

University of Alberta

**CATALYTIC COMBUSTION FOR MITIGATION OF LEAN
METHANE EMISSION**

by

Rajab M. Litto ©

A thesis submitted to the Faculty of Graduate Studies and Research
in partial fulfillment of the requirements for the degree of
Doctor of Philosophy

in

Chemical Engineering

Department Chemical and Material Engineering

Edmonton, Alberta

Fall, 2008



Library and
Archives Canada

Bibliothèque et
Archives Canada

Published Heritage
Branch

Direction du
Patrimoine de l'édition

395 Wellington Street
Ottawa ON K1A 0N4
Canada

395, rue Wellington
Ottawa ON K1A 0N4
Canada

Your file *Votre référence*
ISBN: 978-0-494-46362-8
Our file *Notre référence*
ISBN: 978-0-494-46362-8

NOTICE:

The author has granted a non-exclusive license allowing Library and Archives Canada to reproduce, publish, archive, preserve, conserve, communicate to the public by telecommunication or on the Internet, loan, distribute and sell theses worldwide, for commercial or non-commercial purposes, in microform, paper, electronic and/or any other formats.

The author retains copyright ownership and moral rights in this thesis. Neither the thesis nor substantial extracts from it may be printed or otherwise reproduced without the author's permission.

AVIS:

L'auteur a accordé une licence non exclusive permettant à la Bibliothèque et Archives Canada de reproduire, publier, archiver, sauvegarder, conserver, transmettre au public par télécommunication ou par l'Internet, prêter, distribuer et vendre des thèses partout dans le monde, à des fins commerciales ou autres, sur support microforme, papier, électronique et/ou autres formats.

L'auteur conserve la propriété du droit d'auteur et des droits moraux qui protègent cette thèse. Ni la thèse ni des extraits substantiels de celle-ci ne doivent être imprimés ou autrement reproduits sans son autorisation.

In compliance with the Canadian Privacy Act some supporting forms may have been removed from this thesis.

Conformément à la loi canadienne sur la protection de la vie privée, quelques formulaires secondaires ont été enlevés de cette thèse.

While these forms may be included in the document page count, their removal does not represent any loss of content from the thesis.

Bien que ces formulaires aient inclus dans la pagination, il n'y aura aucun contenu manquant.

■ ■ ■
Canada

This work is dedicated to my dearest son, the late Mohammed, whose life came and was lost during this work. I also would like to dedicate this thesis to my parents who have been a major influence in my life and have supported me wholeheartedly in all my endeavors. Mom and dad, my accomplishments can be rooted to you, who have helped me to shape my academic career as far back as *shule ya vidudu* (pre-school).

ABSTRACT

The global warming problem might be the greatest threat ever to the future of mankind, and scientists have concluded that human activities are the main cause. Energy related activities are the major source of the greenhouse gas (GHG) emission, which enhance the global warming problem.

Leaks in natural gas transmission facilities are the main sources of fugitive methane emissions. Unfortunately, these emissions are difficult to mitigate. Because of their low concentration, conventional combustion cannot destroy them. The present study aims at evaluating the possibility of using catalytic reactor to reduce fugitive methane emissions in the natural gas sector. The proposed reactor is a catalytic flow reversal reactor (CFRR), which has already been proved to work well with lean methane concentrations in coal mine. The natural gas compressor station is a major source of fugitive methane emissions, and it is a focus of this work. The fugitive methane has a lean methane concentration in atmospheric air. Thus, finding a means of concentrating the methane to meet CFRR feed quality is the initial task to be performed. Computer modelling of the flow patterns inside the building is used to show the influence of ventilation openings, ambient temperature and leak location. Simulations show that for a typical building most methane emitted inside will exit through the ridge vent provided the main doors remain closed. When the extraction rate through the ridge vent is controlled, the methane concentration can satisfy the CFRR feed quality.

The CFRR performance was studied in some detail. Two catalysts are evaluated; one is a non-noble metal in the form of rashig rings in a packed bed, and the other a commercial Pd monolith. The activity of the Pd catalyst was studied and the feed and products influence, are reported. It is shown that the Pd catalyst is much more active than the non-noble metal one, and this has implications for reactor design.

It is shown that the reactor insulation has a significant influence on reactor performance, especially for smaller diameter reactors. The correct combination of switch time and velocity is also important.

Overall, it will be shown that this proposed technology offers promising results for methane emission abatement.

ACKNOWLEDGEMENT

First and foremost, I sincerely would like to thank my supervisor, Prof. Robert Hayes, for all help, patience and guidance over the past few years. His enthusiasm, optimism, insight and professionalism were indispensable in turning an original idea into sound engineering work. He supported, motivated and encouraged me during the critical and frustrating moments of my years of studies. The most important is that his elaborative explanations, intensive and constant guidance in introducing me into catalytic combustion expertise. Also, I greatly value the help, support and advice from my thesis supervisory committee.

I am grateful for personal and valuable professional discussion, in our computational fluid dynamics laboratory, with my colleagues, including Stephen Salomons (also helped in setting up catalysis experiment at Darmsdat laboratory in Germany), Amika Kwashaha, Atryee Basu, Adrian Fuxman (also initiated the Comsol Multiphysics program), Anant Pandya and Hermant More, which provided a positive working environment and the best friendship ever. Thank you, Dr. Joe Mmbaga for the untiring help, critics, discussions and conversation over the years, Dr. Ben Liu and Dr. Samy Mukadi for providing me with professional ideas. I also extend my gratitudes to Bob Barton and departmental computing resource team.

I acknowledge the financial support from NRCan, Course (AERI) and NSERC as well as technical input from New Paradigm Engineering, BP Canada, Enerflex System Ltd, Clearstone Engineering, Transcanada Energy and Umicore AG.

Finally, a very special appreciation is due to my wife Rehema, daughter Amina, sons Misama and the late Mohammed, not only for enduring my long absence for so long time but for your constant encouragement and unreserved support in every circumstance. Your love, sacrifice, patience and understanding have helped tremendously throughout these years and made the completion of this work possible.

Table of Contents

1	Introduction	1
1.1	Background	1
1.2	Motivation	3
1.3	Scope of work	5
1.4	Thesis organization	6
1.5	Remarks	7
2	Overview	9
2.1	Global climate change	9
2.2	Global climate change mechanism	16
2.2.1	Natural sources	18
2.2.2	Human induced sources	19
2.3	Greenhouse gases	20
2.3.1	Major greenhouse gases.	20
2.3.2	Global warming potential	25
2.3.3	Atmospheric aerosol and global dimming	25
2.4	Anthropogenic enhancement	26
2.4.1	The Kyoto protocol	27
2.4.2	Emissions from energy sector	27
2.4.3	Possible solutions for methane mitigation	31

3	Oil and natural gas sector	33
3.1	Introduction	34
3.1.1	Methane emission	34
3.2	Fugitive emission	37
3.2.1	Canadian fugitive methane emission	40
3.2.2	Efforts in combating fugitive methane	42
3.2.3	Problem facing fugitive methane mitigation	43
3.3	Natural gas transportation	44
3.4	Natural gas compressor stations	44
4	Capturing emissions from a natural gas compressor station	50
4.1	Modelling methane fugitive flow	50
4.1.1	Methodology	51
4.1.2	Description of building models	53
4.2	Turbulence modelling	56
4.2.1	Model equations	58
4.2.2	Boundary conditions	61
4.2.3	Solution methods	63
4.2.4	Preliminary experiments	64
4.2.5	Modes of operation	66
4.3	Results	67
4.3.1	Free flow in small building	67
4.3.2	Forced extraction in small building	72
4.3.3	Free flow in large building	83
4.3.4	Forced extraction in large building	83
4.3.5	Boundary flows	87
4.4	Observations	89
5	Methane catalytic combustion review	92
5.1	Background	92
5.2	General catalytic combustion	94
5.3	Combustion catalyst	97

5.3.1	Transition metal oxides	98
5.3.2	Noble metals	99
5.4	Reaction kinetics and mechanism	109
5.4.1	Mechanism for catalytic combustion	111
5.4.2	Multi-Step surface mechanisms	112
5.4.3	Surface reaction over platinum catalyst	114
5.4.4	Surface reaction over palladium catalyst	121
5.5	Kinetic models	134
5.5.1	Detailed catalytic surface mechanism kinetics	134
5.5.2	Global reaction kinetics	140
6	Investigation of Pd catalyst activity	151
6.1	Experimental equipment	151
6.2	Experimental procedures and results	156
6.3	Temperature programmed experiments	156
6.3.1	Inlet compositions	156
6.3.2	Experimental procedure	158
6.3.3	Reactor temperature measurement	158
6.3.4	Ignition and extinction curves	168
6.3.5	Summary of ignition extinction experiments	192
6.4	Concentration programmed experiments	195
6.4.1	Results and discussion	197
6.5	Summary	217
7	Kinetic modelling of methane combustion	218
7.1	Global rate models	219
7.1.1	Reactor model	220
7.1.2	Reactor model - implementation and solution	231
7.1.3	Choice of an optimisation routine	231
7.1.4	Development of the rate model	233
7.1.5	Choice of experimental data and implementation method	233
7.1.6	Optimization results	237

7.1.7	Modelling the full curve	244
7.2	Mechanistic model	251
7.2.1	Introduction	251
7.2.2	Reactor model	252
7.2.3	Performance of mechanism	253
7.2.4	Effect trends comparison	265
7.3	Concluding remarks	274
8	Catalytic flow reversal reactor: Background and model development	275
8.1	Introduction	275
8.2	Heat trapping in a reverse flow reactor	276
8.3	Literature review of reverse flow reactors	279
8.4	Reverse flow reactor configurations	282
8.5	Pilot reactor at CTEC Varennes	283
8.6	Modelling the CFRR	287
8.6.1	Introduction to reactor modelling	287
8.6.2	Basic transport equations	289
8.6.3	Reaction kinetics	293
8.6.4	Diffusion in the catalyst	293
8.6.5	Transport properties inside the reactor	294
8.6.6	Auxiliary equations	297
8.6.7	Boundary and initial conditions	298
8.6.8	Solution methodology	301
8.7	Summary	301
9	Parametric studies of the CFRR for lean methane combustion	302
9.1	Introduction	302
9.2	Energy extraction and reactor optimisation	303
9.3	Parametric study of CFRR	305
9.3.1	Comparison of catalyst activity	305
9.3.2	Velocity and switch time	317
9.3.3	Thermal properties	322

9.3.4	Reactor geometry	328
9.3.5	Initial condition	332
9.4	Discussion	333
10	Conclusions and recommendations	334
10.1	Conclusion	335
10.1.1	Fugitive emission capture	335
10.1.2	Catalytic activity	335
10.1.3	Performance of CFRR	336
10.2	Recommendation and future work	337
	References	338
A	Single channel model derivation	363

List of Tables

2.1	Atmospheric concentration of major GHG (IPCC,2007)	24
2.2	GWP for the major GHG (IPCC,1996)	25
2.3	Canadian GHG emission trends by sector since 1990	30
3.1	Annual estimates of the global anthropogenic methane emission into atmosphere (source: Seinfeld and Pandis (2006))	33
3.2	CH ₄ emissions from oil and natural gas sector from selected countries (Source:Methane to market website,2006)	37
4.1	Summary of results for the small compressor building with quiescent air at 293 K operated in free flow mode. Conditions at ridge vent. . .	68
4.2	Summary of results for the small compressor building with an imposed wind velocity of 2 ms ⁻¹ blowing from north to south. Operated in free flow mode at 293K. The leakage rate was 2.7 kg/h. Conditions at the ridge vent	69
4.3	Summary of results obtained for the small compressor building with quiescent air at 293 K operated in free flow mode, with added piping in the building. conditions at the ridge vent.	72
4.4	Summary of results obtained for the large compressor building with quiescent air at 293 K operated in free flow mode (with louvers on the current side of the wall), total leakage rate was 278 kg/h and the area of the ridge vent was 38.4 m ² . conditions at the ridge vent. . . .	84

5.1	Elementary reaction mechanism schemes for catalytic methane combustion over Pt.	116
5.2	Reduced Deutschmann Mechanism	121
5.3	Deutschmann Hydrogen combustion on Pd catalyst	124
5.4	Elementary reaction mechanism schemes for catalytic methane combustion over Pd.	126
5.5	Global reaction kinetics expressions for catalytic methane combustion over palladium based catalyst.	149
6.1	Gas Composition for light-off experiments.	157
6.2	Positions of Thermocouple	159
6.3	Ignition and extinction temperature based on thermocouple T3.	194
6.4	Methane conversion in pulse input concentration programmed experiments at 673 K.	201
6.5	Methane conversion in pulse input concentration programmed experiments at 723 K.	202
6.6	Methane conversion in step input concentration programmed experiments at 673 K.	208
6.7	Methane conversion in step input concentration programmed experiments at 723 K.	209
6.8	Methane conversion in ramp input concentration programmed experiments at 673 K nominal.	215
6.9	Methane conversion in ramp input concentration programmed experiments at 723 K nominal.	216
7.1	Summary of parameter values for the models A and B:	239
7.2	Elementary reaction mechanism schemes for catalytic methane combustion over Pd catalyst.	254

List of Figures

2.1	Global mean surface temperatures, for annual and five years average between 1880 - 2007 (Source:NASA(2007))	10
2.2	Drought in Spain during the 2003 European heat wave, the drought was the worst since the 1940s. (Source: BBC News Online(2003).) . .	11
2.3	Flooding in New Orleans, caused by the hurricane Katrina. This demonstrate the potential loss of human life and infrastructure due to the impact of global warming. (Source: ABC News online(2005)) .	13
2.4	The two photographs provide the trend and rate of snow diminishing at the top of Mount Kilimanjaro. The top photograph was taken from the international space station on 1993 and shows that the mountain was covered by snow and glacier. Seven years later, the bottom photograph, shows that the snow and glacier are rapidly disappearing. (Source: NASA(2007))	14
2.5	A typical diagram of the earth's annual global mean energy balance. (Source: Seinfeld and Pandis (2006))	17
2.6	Atmospheric CO ₂ concentration over last 10,000years (and insert since 1750). (Source: IPCC(2007))	21
2.7	Atmospheric methane concentration over last 10,000years (and insert since 1750). (Source: IPCC(2007))	23
2.8	Atmospheric N ₂ O concentration over last 10,000 years (and insert since 1750). (Source: IPCC(2007))	24

2.9	Estimation of each GHG contribution to the global anthropogenic emissions based on GWP for 100 year period (IPPC,1995).	28
2.10	Canadian GHG emissions trend 1990 - 2005	29
3.1	Sectoral Breakdown of Canada's GHG emission in 2005.(Source: Environment Canada)	41
3.2	Trend of methane emission in Canada.(Source: Environment Canada)	42
3.3	A typical single compressor building.	45
3.4	The natural gas IC engine in one compressor building.	47
3.5	Natural gas pipeline and junction	48
4.1	The small building as modelled in Airpak showing the sources of methane leakage in the building. The blocks represent equipment inside the building.	53
4.2	Two side views of the small building used as a model in this work. The top view is the south face with a single large door; the bottom view is the north face with the large roll-up door and a smaller door.	54
4.3	Two side views of the large compressor building used as a model in this work. The top view is the east elevation with seven exterior doors; the bottom view is the west elevation with seven exterior doors and seven emergency doors. The big sliding doors are on the south and north sides of the building, and are not shown in the drawing.	56
4.4	Transverse momentum distributions - E-R model.	65
4.5	Effect of external temperature on the mass flow rate through the ridge vent. A negative value indicates a flow out of the building. . .	70
4.6	Pressure profile in the middle of the building as a function of the external temperature. The pressure profile depends on the temperature.	71
4.7	Airflow pattern inside the building for (left) ambient temperature below 273 K and (right) ambient temperature is above 273 K.	71

4.8	Fraction of methane captured through ridge vent using forced extraction in the small building with doors closed, at three leak rates. Above about four room changes an hour most of the methane is captured. The ambient temperature was 303K.	74
4.9	Mole percentage of methane in the ridge vent effluent obtained using forced extraction from the small compressor building with the doors closed. The ambient temperature was 303K. The effect of extraction rate and leakage rate are shown.	75
4.10	Fraction of methane captured through ridge vent using forced extraction in the small compressor building with the large roll-up door opened. The ambient temperature was 303K.	76
4.11	Mole percentage of methane in the ridge vent effluent obtained using forced extraction from the small compressor building with the roll-up door opened. The ambient temperature was 303K. The effect of extraction rate and leakage rate are shown.	77
4.12	Velocity vector in the small compressor building operating with option 1 under controlled extraction. The velocity vectors were taken : (a) at the south side louvers position. (b) at the roll-up door position. (c) at the engine, turbocharger and exhaust pipe position, which is the hottest position in the building and near the north-east louver. (d) slightly further along the engine position. Plane of vector is the building cross section.	78
4.13	Velocity vector in the small compressor building operating with option 2 under controlled extraction mode. Building slices taken at the same position as in Figure 4.12.	79

4.14	Profile of methane mole fraction in the small compressor building operating with option 1 under controlled extraction mode. The mole fraction profiles were taken at : (a) at the south side louvers position. (b) at the roll-up door position. (c) at the engine, turbocharger and exhaust pipe position, which is the hottest position in the building and also corresponds to position of the north-east louver, and (d) the engine position.	80
4.15	Profile of methane mole fraction in the small compressor building operating with option 2 under controlled extraction mode. The mole fraction profile were taken at the same position as in figure 4.14. . . .	81
4.16	Fraction of CH ₄ captured through ridge vent using forced extraction in the small compressor building with doors closed. At 273 K ambient temperature.	82
4.17	Mole percentage of CH ₄ in the extracted stream versus extraction rate at different leak rate in the small compressor building. At 273 K ambient temperature.	82
4.18	Fraction of methane captured using forced extraction in the large compressor building with the doors closed. Above about five room changes most of the methane is captured. Louvers on the east wall at (a) the top (b) the bottom.	85
4.19	Mole percentage of methane in the extracted stream versus extraction rate at different leak rate in the large compressor building. The louvers location on the east wall are (a) the top and (b) the bottom.	86
4.20	Behaviour of large opening boundary condition (a) ambient temperature is above 273 K (b) ambient temperature is below 273 K	87
4.21	Velocity vectors in the small compressor building operating with option 1 with controlled extraction. The velocity vectors were taken: a). at the engine, which is the hottest spot in the building, shown in x-plane. b). near the bottom of the building, shown in y-plane. c). taken at upper level of the building, in y-plane.	88

4.22	Velocity vectors in the small compressor building operating with option 2 with controlled extraction. The velocity vectors were taken: a) at the roll-up door position, shown in x-plane. b) Near the bottom of the building, shown in y-plane. c). taken at upper level of the building, in y-plane.	90
5.1	Plot of the hydrocarbon conversion on catalytic combustion as function of temperature (Lee and Trimm (1995)).	95
5.2	Schematic of catalytic surface reaction regimes (Chen et al. (2000)).	97
5.3	Generic Thermal gravimetric profile showing the hysteresis for decomposition of PdO to Pd and its reformation	102
5.4	Methane conversion vs reaction temperature profiles for different PdO based catalyst (Ciuparu and Pfefferle (2001)).	108
5.5	Detailed Langmuir - Hinshelwood mechanism	112
5.6	Eley - Rideal Mechanism	113
5.7	Mars-van Krevelen Mechanism	113
5.8	Proposed mechanism for surface methane combustion reaction as proposed by Oh et al.(1991).	122
5.9	Proposed mechanism for surface methane combustion reaction (Cullis and Willat, 1983).	123
5.10	Methane dissociative adsorption on catalyst surface	128
5.11	Mechanism which was proposed by Fujimoto et al. (1998)	128
5.12	Redox mechanism as proposed by Li et al. (2003)	130
5.13	Scheme A of the mechanism proposed by Demoulin et al. (2005)	131
5.14	Scheme B of mechanism proposed by Demoulin et al. (2005)	132
5.15	: Processes assumed to take place during catalytic methane combustion reaction over PdO/ZrO ₂ catalyst, (a) surface reaction without contribution of redox reaction, leading to scrambling of CO ₂ , (b) Scrambling of O ₂ (c) and Redox mechanism	133
6.1	Diagram showing the experimental setup and flows, adapted from Salomons(2008)	153

6.2	Experimental setup photograph(Courtesy of Salomons (2008))	154
6.3	Squared channels monolith loaded with 80 g ft^{-3} Pd was used.	155
6.4	Temperature ramp profile for the gas mixture with 500 ppm methane and 6% oxygen, pretreated (run 146_2).	160
6.5	Temperature ramp profile for the gas mixture with 1000 ppm methane and 6% oxygen, pretreated case (run 147_1).	161
6.6	Temperature ramp profile for the gas mixture with 1000 ppm methane and 20% oxygen, pretreated (run 153_1).	161
6.7	Temperature ramp profile for the gas mixture with 2000 ppm methane and 6% oxygen, pretreated case (run 149_1).	162
6.8	Temperature ramp profile for the gas mixture with 9000 ppm methane and 20% oxygen, pretreated (run 151_1).	162
6.9	Variation of radial temperature difference with time for the gas mix- ture with 500 ppm methane and 6% oxygen, unpretreated (run 146_3).164	
6.10	Variation of radial temperature difference with time for the gas mix- ture with 1000 ppm methane and 6% oxygen, unpretreated (run 147_2).165	
6.11	Variation of radial temperature difference with time for the gas mix- ture with 2000 ppm methane and 6% oxygen, unpretreated (run 149_2).165	
6.12	Variation of radial temperature difference with time for the gas mix- ture with 9000 ppm methane and 6% oxygen, unpretreated (run 151_2).166	
6.13	Variation of axial temperature difference with time for the gas mix- ture with 500 ppm methane and 6% oxygen, unpretreated (run 146_3).166	
6.14	Variation of axial temperature difference with time for the gas mix- ture with 1000 ppm methane and 6% oxygen, unpretreated (run 147_2).167	
6.15	Variation of axial temperature difference with time for the gas mix- ture with 2000 ppm methane and 6% oxygen, unpretreated (run 149_2).167	
6.16	Variation of axial temperature difference with time for the gas mix- ture with 9000 ppm methane and 6% oxygen, unpretreated (run 151_2).168	
6.17	Ignition and extinction curves for 500 ppm CH_4 and 6% O_2 , based on themocouple T3.	170

6.18	Ignition and extinction curves for 1000 ppm CH ₄ and 6% O ₂ , based on thermocouple T3.	170
6.19	Ignition and extinction curves for 2000 ppm CH ₄ and 6% O ₂ , based on thermocouple T3.	171
6.20	Ignition and extinction curves for 9000 ppm CH ₄ and 6% O ₂ , based on thermocouple T3.	171
6.21	Ignition curve as function of methane inlet concentration, pretreated case, 6% O ₂ , based on thermocouple T3.	172
6.22	Extinction curve as function of methane inlet concentration, pretreated case, 6% O ₂ , based on thermocouple T3.	172
6.23	Ignition curve as function of methane inlet concentration, untreated case, 6% O ₂ , based on thermocouple T3.	173
6.24	Extinction curve as function of methane inlet concentration, untreated case, 6% O ₂ , based on thermocouple T3.	173
6.25	Temperature hysteresis between inlet (T3) and outlet (T4) during heating and cooling.	176
6.26	Comparing effect of pretreatment on temperature hysteresis between inlet (T3) and outlet (T4) during heating and cooling.	176
6.27	Ignition extinction curves for 500 ppm methane, pretreated and untreated cases, based on thermocouple T4.	177
6.28	Ignition extinction curves for 1000 ppm methane, pretreated and untreated cases, based on thermocouple T4.	177
6.29	Ignition extinction curves for 2000 ppm methane, pretreated and untreated cases, based on thermocouple T4.	178
6.30	Ignition extinction curves for 9000 ppm methane, pretreated and untreated cases, based on thermocouple T4.	178
6.31	Ignition and extinction curves for 1000 ppm methane in 20% O ₂ , based on thermocouple T3.	179
6.32	Ignition and extinction curves for 5000 ppm methane in 20% O ₂ , based on thermocouple T3.	180

6.33	Comparison of ignition and extinction curves of 6% and 20% O ₂ with 1000 ppm CH ₄ , pretreated case, based on thermocouple T3.	181
6.34	Comparison of ignition and extinction curves of 6% and 20% O ₂ with 1000 ppm CH ₄ , unpretreated case, based on thermocouple T3.	181
6.35	Ignition/extinction curves for 20 % oxygen with 1000 ppm methane, based on thermocouple T4.	182
6.36	Comparing effect of pretreatment on temperature hysteresis between inlet (T3) and outlet (T4) during heating and cooling.	182
6.37	Effect of adding 10% H ₂ O to the feed with 6% O ₂ and 5000 ppm CH ₄ , based on thermocouple T3.	183
6.38	Effect of adding 10% H ₂ O to the feed with 6% O ₂ and 5000 ppm CH ₄ , based on thermocouple T4.	184
6.39	Comparing effect of pretreatment on temperature hysteresis between inlet (T3) and outlet (T4) during heating and cooling.	184
6.40	Ignition and extinction curves for 1000 ppm H ₂ added into 2000 ppm CH ₄ with 6% O ₂ , based on thermocouple T3.	185
6.41	Ignition and extinction curves for 1000 ppm H ₂ added into 2000 ppm CH ₄ with 6% O ₂ , based on thermocouple T4.	186
6.42	Effect of H ₂ addition on ignition - extinction curves, 2000 ppm CH ₄ , pretreated case based on thermocouple T3.	186
6.43	Effect of H ₂ addition on ignition - extinction curves, 2000 ppm CH ₄ , unpretreated case based on thermocouple T3.	187
6.44	Temperature as function of time for 2000 ppm CH ₄ and 6% O ₂ with 1000ppm added H ₂ , based on thermocouple T3.	187
6.45	Ignition and extinction curves for 1000 ppm CO and 2000 ppm CH ₄ , based on thermocouple T3.	188
6.46	Effect of adding 1000 ppm CO to the feed of 5000 ppm CH ₄ in 6 % O ₂ , pretreated, based on thermocouple T3.	189
6.47	Effect of adding 1000 ppm CO to the feed of 5000 ppm CH ₄ in 6 % O ₂ , unpretreated, based on thermocouple T3.	189

6.48	Effect of CO ₂ on conversion for 2000 ppm CH ₄ in 6 % O ₂ , pretreated, based on thermocouple T3.	190
6.49	Effect of CO ₂ on conversion for 2000 ppm CH ₄ in 6 % O ₂ , unpretreated, based on thermocouple T3.	191
6.50	Comparing effect of pretreatment on temperature hysteresis between inlet (T3) and outlet (T4) during heating and cooling.	191
6.51	Variation of extinction temperature for 6% and 20% O ₂ , based on thermocouple T3	193
6.52	Variation of ignition temperature for 6% and 20% O ₂ , based on thermocouple T3	193
6.53	Methane pulse input for concentration programmed experiments. . .	195
6.54	Methane steps input for concentration programmed experiments. . .	196
6.55	Methane ramps input for concentration programmed experiments. .	197
6.56	Inlet and outlet methane concentration as function of time for pulse experiment at 673 K and 723 K.	198
6.57	Outlet CO ₂ concentration as function of time for pulse experiment at 673 K and 723 K.	198
6.58	Temperature variation against time during pulse concentration programmed experiments. Nominal temperature of 673 K was fixed at inlet.	199
6.59	Temperature variation against time during pulse concentration programmed experiments. Nominal temperature of 723 K was fixed at inlet.	199
6.60	Comparison of temperature near the inlet and outlet of the reactor in pulse experiment at nominally fixed temperature of 673 K.	200
6.61	Comparison of temperature near the inlet and outlet of the reactor in pulse experiment at nominally fixed temperature of 723 K.	200
6.62	Comparison of temperature near the inlet, middle and outlet of the reactor in one pulse period at nominally fixed temperature of 673 K.	203
6.63	Comparison of temperature near the inlet, middle and outlet of the reactor for one pulse period at nominally fixed temperature of 723 K.	203

6.64	Methane concentration as function of time for step at inlet and outlet of reactor. Nominal temperature in front of reactor was fixed at 673 and 723 K.	205
6.65	Temperature variation against time during steps concentration programmed experiments. Nominal temperature of 673 K was fixed at inlet.	205
6.66	Temperature variation against time during steps concentration programmed experiments. Nominal temperature of 723 K was fixed at inlet.	206
6.67	Comparing the reactor temperature near the inlet and outlet for step experiments at fixed nominal temperature in front of reactor of 673 K.	206
6.68	Comparing the reactor temperature near the inlet and outlet for step experiments at fixed nominal temperature in front of reactor of 723 K.	207
6.69	Comparing the reactor outlet temperature for step experiments for fixed nominal temperature in front of reactor of 673 and 723 K.	207
6.70	Comparison of temperature near the inlet, middle and outlet of the reactor in one pulse period at nominally fixed temperature of 673 K.	210
6.71	Comparison of temperature near the inlet, middle and outlet of the reactor for one pulse period at nominally fixed temperature of 723 K.	210
6.72	Methane concentration as function of time for ramp experiments at inlet and outlet of reactor. Nominal temperatures in front of reactor was fixed at 673 K and 723 K.	212
6.73	Temperature variation against time during ramp concentration programmed experiments. Nominal temperature of 673 K was fixed at inlet.	212
6.74	Temperature variation against time during ramps concentration programmed experiments. Nominal temperature of 723 K was fixed at inlet.	213
6.75	Comparison of reactor temperature near the inlet and outlet as function of time for ramp experiment at fixed nominal temperature of 673 K.	213

6.76	Comparison of reactor temperature near the inlet and outlet as function of time for ramp experiment at fixed nominal temperature of 723 K.	214
6.77	Comparison of reactor outlet temperature as function of time for ramp experiment at fixed nominal temperature of 673 and 723 K. . .	214
7.1	Flat slab of porous catalyst	227
7.2	The six experimental extinction curves used in the optimization procedure. The lines show the experimental data and the circular symbols the points from each curve used in optimizer.	236
7.3	Observed and predicted extinction curves for Model A1.	240
7.4	Differences between predicted and observed values at the data points used in the optimization for Model A1.	240
7.5	Observed and predicted extinction curves for Model B1.	241
7.6	Differences between predicted and observed values at the data points used in the optimization for Model B1.	241
7.7	Observed and predicted extinction curves for Model A2.	242
7.8	Differences between predicted and observed values at the data points used in the optimization for Model A2.	242
7.9	Observed and predicted extinction curves for Model B2.	243
7.10	Differences between predicted and observed values at the data points used in the optimization for Model B2.	243
7.11	Model and experimental ignition-extinction curves, Run 146_3, 500 ppm methane.	245
7.12	Model and experimental temperature curves, Run 146_3, 500 ppm methane.	245
7.13	Model and experimental ignition-extinction curves, Run 147_2, 1000 ppm methane.	246
7.14	Model and experimental temperature curves, Run 147_2, 1000 ppm methane.	246

7.15 Model and experimental ignition-extinction curves, Run 149_2, 2000 ppm methane.	247
7.16 Model and experimental temperature curves, Run 149_2, 2000 ppm methane.	247
7.17 Model and experimental ignition-extinction curves, Run 151_2, 9000 ppm methane.	248
7.18 Model and experimental temperature curves, Run 151_2, 9000 ppm methane.	248
7.19 Model and experimental ignition-extinction curves, Run 162_2, 500 ppm methane and 10% water.	249
7.20 Model and experimental temperature curves, Run 162_2, 500 ppm methane and 10% water.	249
7.21 Model and experimental ignition-extinction curves, Run 168_2, 2000 ppm methane and 8000 ppm carbon dioxide.	250
7.22 Model and experimental temperature curves, Run 168_2, 500 ppm methane and 8000 ppm carbon dioxide.	250
7.23 Effect of catalyst loading on methane conversion.	256
7.24 Effect of catalyst loading on reactor temperature.	256
7.25 Effect of initial catalyst coverage on methane conversion.	258
7.26 Variation of surface coverage with temperature. Initial oxygen fractional coverage was zero.	259
7.27 Variation of surface coverage with temperature. Initial oxygen fractional coverage was 0.5.	259
7.28 Variation of surface coverage with temperature. Initial oxygen fractional coverage was 0.75.	260
7.29 Variation of surface coverage with temperature. Initial oxygen fractional coverage was 1.0.	260
7.30 Variation of surface coverage and methane concentration with time.	261
7.31 Close look of effect of initial surface coverage	261
7.32 Close look of effect of initial surface coverage	262
7.33 Close look of effect of initial surface coverage	262

7.34	Oxygen desorption effect on methane conversion at actual value of activation energy.	264
7.35	Effect of oxygen desorption by varying its activation energy.	264
7.36	Ignition curves comparing the effect of methane initial concentration.	266
7.37	Extinction curves comparing the	266
7.38	Ignition-extinction curves comparing the effect of methane initial concentration.	267
7.39	Temperature ignition curve comparing the effect of methane initial concentration.	267
7.40	temperature extinction curves comparing the effect of methane initial concentration.	268
7.41	Temperature ignition-extinction curves comparing the effect of methane initial concentration.	268
7.42	Ignition -extinction curves showing the effect of low methane initial concentration.	269
7.43	Ignition - extinction curves showing the effect of higher methane initial concentration.	269
7.44	Ignition curves comparing the effect of oxygen concentration.	270
7.45	Extinction curves comparing the effect of oxygen concentration.	271
7.46	Ignition - extinction curves comparing the effect of oxygen concentration.	271
7.47	Ignition - extinction curves comparing the effect of water in the feed.	272
7.48	Ignition - extinction curves comparing the effect of carbon dioxide presence.	273
8.1	Typical arrangement for a CFRR in (a)forward flow and (b)reverse flow reactor mode(from Hayes(2004)).	277
8.2	Illustration of heat trap effect in the reverse flow reactor (from Hayes(2004)).	278

8.3	Common catalytic flow reverse reactor configuration, (a) single bed without inerts, (b) single bed with inerts and, (c) and (d) multiple beds.	284
8.4	Diagram of the pilot scale CFRR at CTEC Varennes showing the configuration used by Salomons (2004). The catalyst was a packed bed and the inert sections were monoliths. The letters indicate thermocouple locations. Kushwaha (2003) used the same reactor and included different inert materials in her study. Diagram from Salomons (2003).	299
8.5	Two dimensional axi-symmetrical model for the CFRR used in the parameter study. (a) shows the sub-domains in the model and (b) shows a finite element mesh of the domains generated in COMSOL Multiphysics modelling package.	300
9.1	Centerline axial temperature profile for the base case with packed bed catalyst. The temperature continues to increase with each cycle, and a stationary state was approached.	307
9.2	Centerline axial temperature profile at the end of 60 th forward cycle, comparing packed bed and Pd monolith catalyst.	308
9.3	Centerline axial temperature profile progression for reactor with Pd monolith catalyst with loading at 15 g/ft ³	308
9.4	Methane concentration variation along length of reactor at centerline, comparing between the packed bed and Pd monolith catalyst activity.	309
9.5	Radial temperature profile at the end of selected half - cycles forward flow, comparing packed bed and Pd monolith catalyst.	311
9.6	Radial temperature profile at the end of selected cycles reverse flow, comparing packed bed and Pd monolith catalyst.	311
9.7	Symmetrical model of new proposed CFRR reactor to be used with Pd Monolith catalyst. Position P1 and P2 are possible position for catalyst.	312

9.8	Methane concentration variation along centerline of reactor, comparing catalyst activity in the packed bed and new Pd monolith catalyst configuration.	313
9.9	Temperature profile along centerline at end of 5 th half cycle, comparing a packed bed and new Pd monolith configuration.	314
9.10	Temperature profile along centerline at end of 60 th half cycle, comparing a packed bed and new Pd monolith configuration.	314
9.11	Surface plot of methane concentration showing the length of reactor zone used for reaction, left side is packed bed and right side is Pd monolith at P2. Red indicates high methane concentration and blue for zero concentration.	315
9.12	Centerline axial temperature profile in CFRR with packed bed catalyst.	316
9.13	Centerline axial temperature profile in CFRR with Pd monolith at P2.	316
9.14	Centerline temperature profile after 60 cycles for different combinations of velocity and switch time on monolith reactor.	318
9.15	Centerline temperature profile after 60 cycles for different combinations of velocity and switch time on packed bed reactor.	318
9.16	Centerline methane profile after 60 cycles for different combinations of velocity and switch time on monolith reactor.	319
9.17	Centerline methane profile after 60 cycles for different combinations of velocity and switch time on packed bed reactor.	319
9.18	Centerline temperature profile at end of cycle 60 for different cycle time, in Pd monolith. The larger cycle time shows more motion of the profile.	320
9.19	Centerline temperature profile at the mid-point for operation using superficial velocity of 0.1 m/s and switch time of 1050 s, in pd monolith . Stationary state was attained after 12 cycles.	321
9.20	Centerline temperature profile at the mid-point or operation using superficial velocity of 0.7 m/s and switch time of 150 s, in Pd monolith. The stationary state was not attained even with 60 cycles.	322

9.21	The centerline axial temperature profile at the end of cycle 60 (forward) for different thermal mass. For packed bed, the highest temperature and the least movement are seen with the highest thermal mass.	323
9.22	The centerline axial temperature profile at the end of cycle 60 (reverse) for different thermal mass. For packed bed, the highest temperature and the least movement are seen with the highest thermal mass.	323
9.23	The centerline axial temperature profile at the end of cycle 60 (forward) for different thermal mass. For Pd monolith P2, the highest temperature and the least movement are seen with the highest thermal mass.	324
9.24	The centerline axial temperature profile at the end of cycle 60 (reverse) for different thermal mass. For Pd monolith P2, the stable temperature and the least movement are seen with the highest thermal mass.	324
9.25	Centerline axial temperature profile for different thermal conductivities at the end of cycle 60. The effect is relatively minor in a packed bed.	326
9.26	Centerline axial temperature profile for different thermal conductivities at the end of cycle 60. For reactor with Pd monolith P2, the effect is relatively minor.	326
9.27	Axial temperature profiles after 60 cycles at varying values of wall thermal capacity, in reactor with Pd monolith P2.	327
9.28	Axial temperature profiles after 60 cycles at various insulation thickness and constant reactor diameter. Above 200 mm thickness the effect is insignificant.	329
9.29	Axial temperature profiles after 60 cycles at various insulation thickness and constant reactor diameter. Above 200 mm thickness the effect is insignificant.	329

9.30	Axial methane profiles after 60 cycles at various insulation thickness and constant reactor diameter. Above 20 cm thickness the effect is insignificant.	330
9.31	Axial temperature profiles after 60 cycles at various reactor diameter in packed bed.	331
9.32	Axial temperature profiles after 60 cycles at various reactor diameter in reactor with Pd monolith P2.	331
9.33	Axial temperature profiles progression starting from arbitrary initial temperature profile in reactor with Pd monolith P2.. . . .	332
9.34	Axial temperature profiles progression starting from arbitrary initial temperature profile, in reactor with Pd monolith P2.	333
A.1	Section of monolith channel	363

Symbol	Description	Unit
A	Pre-exponential factor in Arrhenius equation	$\text{m}^3\text{s}^{-1}\text{m}_{cat}^{-3}$
a	Surface area	m^2
a_m	Channel perimeter	m
a_v	Surface area per unit volume	m^2m^{-3}
C	Gas molar concentration	mol m^{-3}
C_A	Gas molar concentration of specie A	mol m^{-3}
C_p	Constant pressure specific heat capacity	$\text{J kg}^{-1}\text{K}^{-1}$ or $\text{J mol}^{-1}\text{K}^{-1}$
D	Dispersion or Diffusion coefficient	m^2s^{-1}
D_{AB}	Molecular diffusion Coefficient	m^2s^{-1}
Da	Damköhler number	
D_C	Characteristic diameter of a particle	m
D_I	Dispersion coefficient	m^2s^{-1}
D_H	Hydraulic diameter	m
D_K	Knudsen diffusion coefficient	m^2s^{-1}
D_R	Reactor internal diameter	m
D_S	Diameter to outside of substrate	m
D_{WC}	Diameter over washcoat perimeter	m
d_p	Particle diameter	m
E	Activation energy	J mol^{-1}
F	Force	N
G	Monolith radial factor	
Gz	Gratz number	
g	Acceleration due to gravity	m s^{-2}
h	Heat transfer coefficient	$\text{W m}^{-2}\text{K}^{-1}$
h	Enthalpy	J kg^{-1}
I	Identity matrix	
J_j	Diffusive mass (or mole) flux	$\text{kg m}^{-2}\text{s}^{-1}$
K	Permeability	m^{-2}
K_{eq}	Thermodynamic equilibrium constant	

K_i	Reaction coefficient	<i>various units</i>
k	Thermal conductivity	$\text{W m}^{-1} \text{K}^{-1}$
k_f	Effective axial thermal conductivity	$\text{W m}^{-1} \text{K}^{-1}$
k_m	Mass transfer coefficient	m s^{-1}
k_w	Effective wall thermal conductivity	$\text{W m}^{-1} \text{K}^{-1}$
L	Length	m
L_c	Effective washcoat thickness	m
Le	Lewis number	
M	Molecular mass	g mol^{-1}
Nu	Nusselt number	
P	Perimeter	m
Pe	Peclet number	
Pr	Prandtl number	
p	Pressure	N m^{-2}
q	Heat flux	W m^{-2}
Re	Reynolds number	
R_{es}	Residual	
R_i	Reaction rate	$\text{mol m}^{-3} \text{s}^{-1}$
R_g	Universal gas constant	$8.314 \text{ J mol}^{-1} \text{K}^{-1}$
r	Radius	m
T	Temperature	K
t	Time	s
S	Sticking coefficient	
Sc	Schmidt number	
Sh	Sherwood number	
S_h	Source term	
u	Radial velocity	m s^{-1}
\vec{u}	Velocity vector	m s^{-1}
V	Volume	m^3
v	axial Velocity	m s^{-1}
v_s	Superficial velocity	m s^{-1}

X	Fractional conversion	
Y	Gas phase mole fraction	
y	Mole fraction	
ΔH	Combustion enthalpy	J mol^{-1}
Δp	Pressure drop	N m^{-2}

Greeks symbols

α	Thermal diffusivity	$\text{m}^2 \text{s}^{-1}$
β	Thermal expansion coefficient	m^{-1}
ϵ	Porosity	
ϕ	Thiele modulus	
η	Effectiveness factor	
τ	Tortuosity factor	
ρ	Density	kg m^{-3}
μ	Viscosity	$\text{kg m}^{-1} \text{s}^{-1}$
θ	Surface coverage	
Γ	Surface site density	moles m^{-2}
τ	Stress tensor	N m^{-2}

Subscripts

a	axial	ads	adsorption
af	axial fluid	app	apparent
as	axial solid	ak	activation
cat	catalyst	eff	effective
eq	equivalent	f	fluid
fk	forward	g	gas
i	component	m	mass
r	radial	ref	reference

rf	radial fluid	rk	reverse
rs	radial solid	s	solid
t	turbulent	te	turbulent energy
v_{ik}	stoichiometric coefficient	w	wall
0	initial value	β	temperature exponent

Superscripts

T	transpose	β_k	temperature exponent
μ_{ik}	coverage exponent		

List of acronyms

ABC	ABC News Agency
AGO	Australian Greenhouse Office
BBC	British Broadcasting Cooperation
BP	British Petroleum
CANMET	Canada Centre for Mineral and Energy Technology
CFD	Computational Fluid Dynamics
CFRR	Catalytic Flow Reversal Reactor
CPI	Cells Per Inch
DNS	Direct Numerical Simulation
EEA	European Environment Agency
EIA	Energy Information Administration
EPA	Environmental Protection Agency
EU	European Union
GDP	Gross Domestic Product
GHG	Greenhouse Gases
GPS	General Pattern Search
GWP	Global Warming Potential
HCFC	Hydrochlorofluorocarbon
HFC	Hydrofluorocarbon
IC	Internal Combustion Engine

IEA	International Energy Agency
IPCC	Intergovernment Panel of Climate Change
IR	Infra Red
LES	Large Eddy Simulation
LHHW	Langmuir Hinshelwood Hougen Watson
LM	Levenberg - Marquardt method
MASI	Most abundant surface intermediate
MARI	Most Abundant Reaction Intermediate
MLT	Multi-component and Multi-method analyzer
MMTCE	Million Metric Tonnes Carbon Equivalent
Mt	Mega tonnes
NASA	National Aeronautics and Space Administration
PDE	Partial Differential Equation
PFC	Perfluorocarbon
RANS	Reynolds Average Navier Stokes
RFO	Reverse Flow Operation
RNG	Re-Normalized Group
TCPL	TransCanada Pipeline
TFID	Thermal Flame Ionization
TOF	Turn Over Frequency
TWC	Three Way Catalyst
UNFCC	United Nation Framework for Climate Change
USA	United State of America
UNEP	United Nation Environmental Programme
VOC	Volatile Organic Compounds
WMD	World Meteorological Organisation

Introduction

1.1 Background

The province of Alberta is widely acknowledged as a fossil fuel giant. This resource rich province has abundant reserves of coal, crude oil, oil sands and natural gas, which have brought wealth to much of its population, but at the same time have made the province a leading emitter of Greenhouse Gases (GHG). It has the highest GHG emission per capita of all the provinces in Canada. GHG emissions are currently a high priority topic on the environmental agenda in both the national and international arenas. Alberta has specialised resource-based industries, linking the economic growth of Alberta to increased GHG emissions, thus presenting a unique challenge in addressing this issue and developing an effective and comprehensive approach to emissions mitigation (Alberta Environment, 2007). Currently, the government of Alberta has targeted large emitters of GHG, requiring them to reduce their carbon emission intensity by 12% by January 1, 2008. It has also introduced emission trading credits starting July, 2007. In emission credit trading in Alberta, Henton (2007) reported that companies have three options;

1. to pay \$15/tonne for every tonne over their limit;
2. to purchase credits on the market from companies that have taken steps in Alberta to reduce emissions, or

3. they can purchase credits from other regulated industries that have reduced their emissions by more than the required minimum.

Since the industrial revolution, human activities, in particular energy related activities, have caused an increase in GHG concentration in the atmosphere, and thus enhanced a natural greenhouse effect. Scientific evidence suggests that continued enhancement of the greenhouse effect will have severe social and economic consequences for planet earth, because it is a potential initiator of catastrophic global climate changes. To avoid this threat, it is necessary to reduce, or at least to stabilize, anthropogenic GHG emissions. Environmental problems do not recognise country border limits, and thus a worldwide collective action is required. Many countries have recognized this fact and made an initiative for a collective effort, which has led to the signing of international environmental agreements.

Establishment of the Intergovernment Panel on Climate Change (IPCC), under the umbrella of the world Meteorological Organization (WMO) and United Nations Environmental Programme (UNEP), to assess relevant information on climate change, its impacts, adaptations and mitigation, followed by the signing of the UN Framework Convention on Climate Change (UNFCCC), in which the problem of GHG was recognised at the highest level and agreed on the need to stabilize its concentration in the atmosphere, and finally the Kyoto Protocol agreement were major achievements towards the development of international GHG abatement solutions and commitments. Under the terms of the Kyoto Protocol, the governments of many countries, including Canada, committed to reduce GHG emissions. Industrialized countries which currently release much of GHG committed to reduce GHG emission to 5% below those of 1990. This reduction is expected to be achieved no later than 2012. Initially, the USA voluntarily committed to a more ambitious target of reducing GHG emissions to 7% below the 1990 level, but later, it changed its mind and abandoned the Kyoto protocol in favour of their own voluntary reduction scheme. The European union (EU) wanted a tougher treaty, and committed itself to 8% reduction, while Japan and Canada committed to reduce GHG to 6% below the 1990 emission level for the years 2008 - 2012. The Kyoto Protocol does not specify GHG reduction targets for developing countries,

but instead gives them opportunities to generate inflow of technology and capital through the clean development mechanism. In other words, global per capita GHG emissions need to be lowered to stabilize GHG atmospheric concentration so that the consequences of global warming may be reduced.

A significant fraction of GHG originates from the use of energy, primarily because fossil fuels (coal, oil and natural gas) are currently used to satisfy most of the global energy demand. Of the fossil fuels, natural gas has the lowest combustion emissions of GHG per unit of energy, and there is much interest in switching from oil and coal to natural gas. However, while natural gas is significantly cleaner than other fossil fuels, significant non-combustion GHG emission occurs during extraction, production, processing, transmission, storage and distribution of natural gas.

In the oil and natural gas sector, methane emission mainly occurs through leakage and venting of gases during normal operation, maintenance and system upset. Here, the term venting is used to describe streams that can be isolated as concentrated streams, whereas leakage refers to streams that, although initially concentrated, can quickly become diluted with air, and thus tend to have low methane concentration. Typically, concentrated streams are easier to address, whilst leakages tend to suffer more variability in flow rate and concentration, and are more difficult to deal with. Additionally, a problem in mitigating leakages is to capture the methane so that it can be directed to a destruction source.

1.2 Motivation

IPCC (2001) stated that, "There is new and stronger evidence that most of the global warming observed over the last 50 years is attributable to human activities". Concern over the short and long-term impacts of global warming on global economies, ecosystem and human habitat has led to recognition that a reduction in the rate of atmospheric GHG loading may help to slow its progress; thus UNFCCC urged and promoted the need to reduce and stabilize GHG emissions as stated in its article 2 :

...stabilization of Greenhouse gases concentrations in the atmosphere at a level that would prevent dangerous anthropogenic interference with the climate system..

Although carbon dioxide (CO₂) emissions are the largest anthropogenic contributors to global climate change, the abatement of carbon dioxide presents an operational cost to the company without any potential for revenue generation. This has forced the international community to find a motivational approach. Among possible approaches is a comprehensive market based solution in which a global system for tradeable permits for sinks and sources of major GHG is being established. Also, a cost-effective abatement of non-CO₂ GHG (CH₄, N₂O, HFCs, PFCs, and SF₆) can be relatively inexpensive and might also have an economic benefit. A strategy to reduce methane emissions may achieve the same goal at considerably lower costs than a carbon dioxide only strategy. Owing to the shorter life time of methane in the atmosphere and its higher Global Warming Potential (GWP) compared to carbon dioxide; the stabilization of GHG can be observed in a shorter period of time. Methane emissions reductions could reduce costs substantially in meeting the Kyoto Protocol emissions targets. Crutzen (1991) suggested that stabilisation of atmospheric methane may most easily be achieved by methane emission reduction from fossil fuel and landfill sources.

Among the primary GHG of carbon dioxide (CO₂), methane (CH₄) and nitrous oxide (N₂O), the main contribution to global warming is made by carbon dioxide (about 64%), with the next largest contribution made by methane (about 19%) (Moore et al., 1998). GHG emissions are reported in terms of equivalent carbon dioxide emissions on a mass basis, usually calculated based on a warming potential for a 100 year lifecycle. Using this method, methane has a GWP 23 times that of carbon dioxide, that is, one tonne of methane is equivalent to 23 tonnes of carbon dioxide. The combustion of methane thus offers the possibility of a net reduction in GHG potential of 88%. There are additional motivations for addressing methane. The atmospheric concentration of methane has been increasing at about 0.6% per year (Steele et al., 1992), and has more than doubled over the last two centuries (Watson et al., 1995). In contrast, the carbon dioxide atmospheric concentration is

increasing at about 0.4% per year. Reduction in methane emissions will produce substantial benefits in the short-term. Methane has a shorter atmospheric lifetime than other GHG: Methane lasts around 12 years in the atmosphere, whereas carbon dioxide lasts about 120 years (Houghton et al., 1992). Owing to methane's high effectiveness and short atmospheric lifetime, stabilization of methane emissions will have a more immediate impact on mitigating potential of global climate change. A key challenge in the reduction of GHG is the mitigation of adverse economic impacts. Because methane is a source of energy as well as GHG, its emissions reduction strategies have the potential to be low cost, or even profitable, provided that the energy from the emissions is effectively used.

In the natural gas sector the methane leakage occurs throughout the chain of activities, resulting from leaky seals, valves, pipe joints, compressors, etc. These emissions are expected to increase with increasing natural gas consumption, although at a lower rate than the rate of growth in the overall market. Improved management and maintenance, plus advances in technology, can potentially reduce the leakage and venting of methane from all parts of the operation.

1.3 Scope of work

For the reasons cited in the foregoing, the significance of promoting strategies to reduce the amount of methane discharged into the atmosphere is apparent. The objective of this work was to investigate and evaluate the possibility of using catalytic reactor based solutions for lean methane emissions. To meet the overall challenge, the main effort is concentrated on a natural gas compressor station which can provide a convenient starting point for reduction efforts. The study covers three major issues relevant to this application of methane abatement, which are:

- An investigation of the feasibility of capturing lean methane emissions that occur inside natural gas compressor buildings.
- A study of catalytic issues, including catalyst type and rate modelling.

- An investigation of the performance of the catalytic flow reversal reactor for this application.

The work brings an understanding of the issues involving methane emissions in natural gas compressor stations and the efficacy of capturing these emissions for subsequent destruction. It also gives an improved fundamental understanding of the operating characteristics of reverse flow reactors and the kinetics of catalytic methane combustion over Pd based catalysts.

1.4 Thesis organization

This thesis presents experimental and numerical investigations on mitigation of the lean methane emissions from a natural gas compressor station. The primary goal is to demonstrate that catalytic combustion in a flow reversal reactor can achieve the mitigation goal. The thesis is organised into three major parts, to cover each of the areas described in Section 1.3.

Part one examines opportunities for mitigating lean methane emission from the oil and natural gas sector; emphasis is placed on the natural gas compressor station. The main focus of this part was to investigate a low cost capture method to be implemented for emissions occurring in an enclosure like the natural gas compressor station. Part one includes Chapters 2, 3 and 4. Chapter 2 gives the general overview on global climate change, to bring an understanding of the basic concepts, science, economic, social, human influence and other environmental issues surrounding the problem. Also the lean methane emission problem is introduced. The magnitude, challenges and opportunities facing the methane emission problem in the oil and natural gas sector is the theme for Chapter 3. Chapter 4 takes a close look at methane emission in a natural gas compressor buildings and proposes a simple low cost capture method for emission originating inside the enclosure. Extensive numerical experiments were done to assess different scenarios.

The second part deals with the fundamentals of catalysis and lean methane catalytic combustion, and includes Chapters 5, 6 and 7. Chapter 5 is a review of

methane catalytic combustion. In Chapter 6 a detailed experimental set-up for methane catalytic studies is presented, and then experimental procedures, analytical equipment, catalyst properties and results obtained are discussed. In Chapter 7, a description of a detailed global model and a surface reaction mechanism and results obtained through modelling experiments is presented before a comparison is made between the experimental and simulation results.

The third part covers the fundamental technology of the catalytic flow reversal reactor, which is the technology used in this project, and comprises Chapters 8 and 9. Chapter 8 gives an extensive review of the basic concepts, operation and past work related to catalytic flow reversal reactors (CFRR). Chapter 9 deals with a parametric study of CFRR through modelling experiments, and investigates the performance of a monolith CFRR using a commercially available catalyst. Its performance is compared to the existing packed bed CFRR reactor. In general, this part investigates reactor performance and suitability of the technology for mitigation of fugitive methane emission. Influence of different parameters on performance of the reactor, and suitability of using the commercial catalyst which was analysed and tested in part two of this work, will be the main factors of this investigation.

Finally, in Chapter 10, conclusions and recommendations on the technology suggested for abatement of fugitive methane emission in the oil and natural gas sector are outlined. Also, the issues which were raised in this work but due to time constraint were not fully analysed will be pointed out for follow-up research, since they are useful and important in realizing the understanding and full utilization of the technology.

1.5 Remarks

Leaked methane emission from a single source may be negligible, but if all sources in the oil and natural gas sector are combined, the amount of methane emitted to atmosphere is considerable, and thus initiative and commitment are needed to reduce them. The study of lean methane emission capture, catalytic mitigation

and manipulation creates a step forward in combating lean methane emission in specific from the oil and natural gas sectors as well as GHG emission in general, which is presented comprehensively in the following chapters.

Overview

2.1 Global climate change

Global climate change is widely considered to be one of the most important issues on the current international environmental agenda. The term **global climate change** can literally be defined as an average change in all features associated with weather, which includes temperature, precipitation, wind patterns, etc, over a specific period of time for the world as the whole (Environment Canada, 2007). Actually, climate change is a natural phenomenon, the ice ages and intervening warm periods are examples of natural climate changes which are constantly occurring (Environment Canada, 2007). The current trend, rate and magnitude of climate changes are different from those observed in the past (Environment Canada, 2007). Many scientists agree that global climate changes are at present happening at a very rapid rate and pose a great challenge to humankind (IPCC, 2007).

There is much scientific evidence which suggests that global climate change is currently occurring at so high a rate that the chance for the earth ecosystem to adopt itself naturally will be enormously difficult. IPCC (2007) has projected that global climate change over the next 100 years will surpass by a significant amount any such change of the last 10,000 years. For example, the mean annual global mean surface temperature is projected to rise by 1.4 - 5.8 °C by 2100 and the global mean sea level will rise by 15 - 95 cm (IPCC, 2007). Such an increase

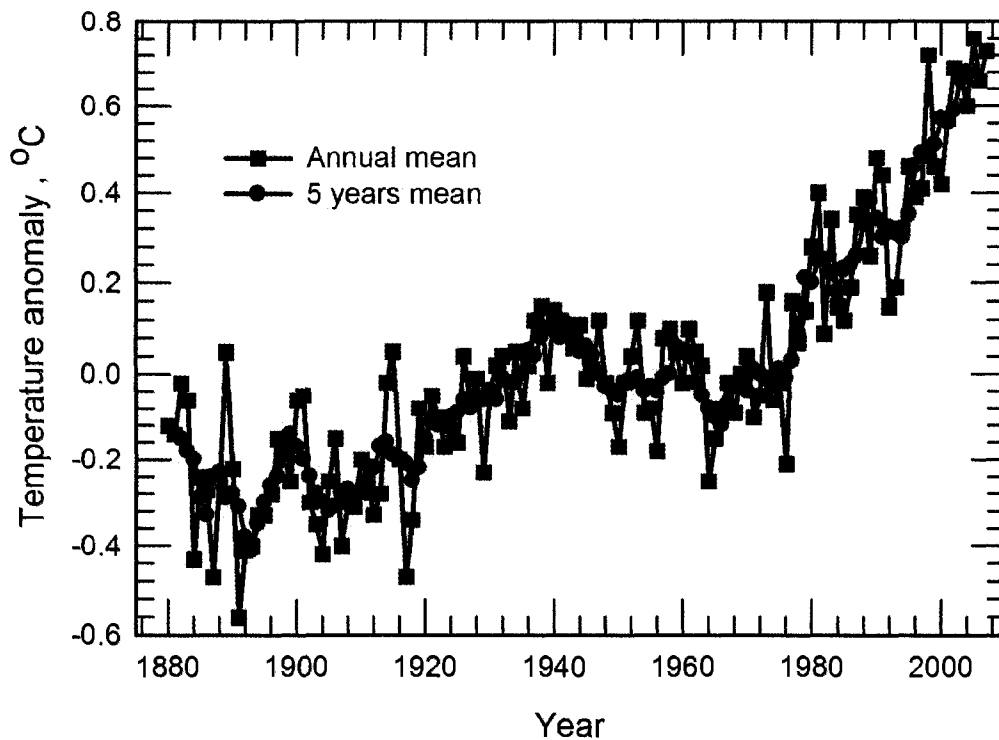


Figure 2.1: Global mean surface temperatures, for annual and five years average between 1880 - 2007 (Source:NASA(2007))

will be highly disruptive. The rising temperatures could bring large-scale drought to critical agricultural regions worldwide. Also, it may cause serious civil unrest and mass migrations due to the spreading of insecurity in water and food supplies (Environment Canada, 2007). In general, abrupt global climate change will cause severe insecurity in terms of ecosystems, species survival, hydrology, water availability, food availability, human habitant, health and security , as well as physical infrastructures (Environment Canada, 2007).

Recent years have been among the warmest since 1880 (Dlugokencky et al., 2003). Figure 2.1 shows the annual increase of average global temperature rise from the start of the industrial revolution to the recent past. It is seen that the average global temperature started to rise rapidly and steadily from the mid 1990s and continues to rise.

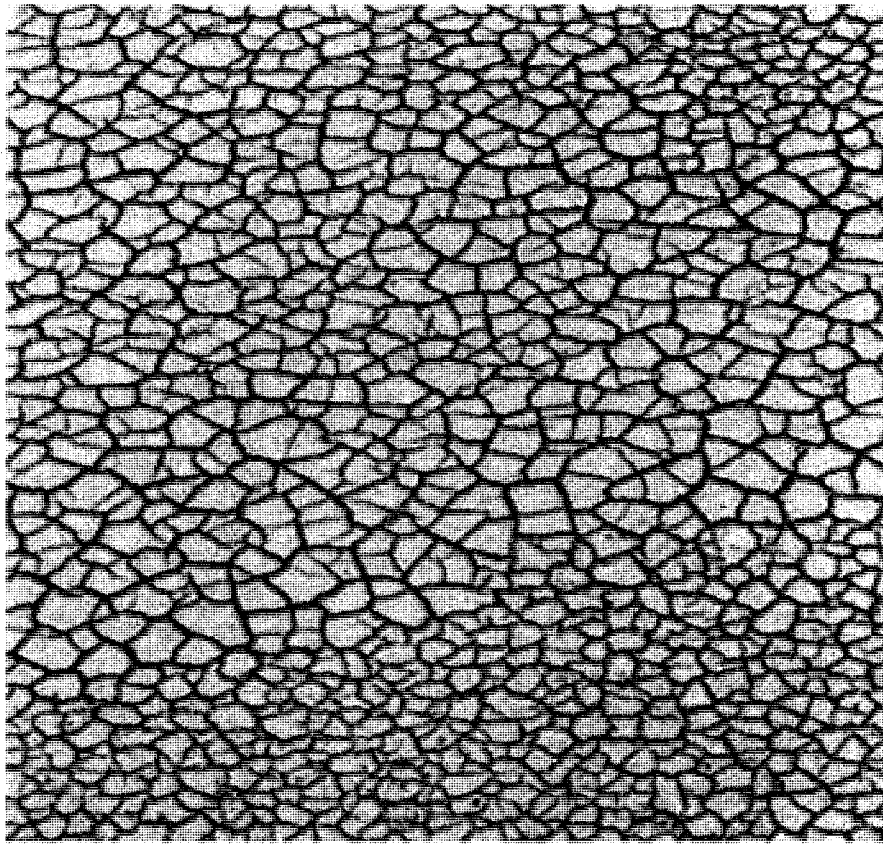


Figure 2.2: Drought in Spain during the 2003 European heat wave, the drought was the worst since the 1940s. (Source: BBC News Online(2003).)

Most scientists agree that the impact of global climate changes on earth is overwhelming and should not be left unchecked, otherwise it could make life on this planet extremely difficult. Some of the obvious impacts considered to be a result of global warming are:

(a) Heat wave: Severe heat waves lead to increases in heat related illness and death, especially in urban areas and among the elderly, the young, the ill and the poor. An example is the European heat wave of 2003. The summer of 2003 was one of the hottest ever in Europe; and led to a health crisis in certain European countries as well as having considerable impact on agriculture.

More than 50,000 people, mostly elderly, died, many acres of forest burnt down,

melting glaciers caused avalanches, and crop yield was low. As the planet heats up, droughts (as seen in Figure 2.2) are expected to become more frequent and severe in some locations. Sustained drought makes wildfires more likely, and crops and trees more vulnerable to pest infestations and diseases. Generally, local land use and land cover changes can exacerbate the climate change-driven increase in drought risk. For the Canadian case, Environmental Canada (2007) reported that Canada's temperature has generally been increasing nationwide and remained above normal since 1996. It shows a warming trend on average of about 1.2 °C over the period of 1948 - 2005.

(b) Storms: Higher temperatures can create conditions for more severe weather events, including thunderstorms, and increased frequency of tornadoes, tropical storms, hurricanes and El-Niño which can lead to risk of life and property. For example, El-Niño in 1997 caused huge problems around the world, from drought to flood and food shortages (McPhaden, 1999).

The recent frequent hurricanes, such as Hurricane Katrina in 2005, (see Figure 2.3), illustrate the fear and loss facing mankind that could result from global climate change.

(c) Glacier melting: Over the past 150 years, the majority of mountain glaciers and snow covers has been shrinking in both hemispheres. Many glaciers and ice caps at lower altitude are now disappearing and scientific predictions show that the majority of them will be gone by the year 2100 (Houghton et al., 2001). As glaciers continue to shrink, summer water flows will drop sharply, disrupting an important source of water for irrigation and power in areas that rely on mountain watersheds. The vanishing ice and glacier at Mount Kilimanjaro is an obvious example of glacier melting (Revkin, 2004). During the last few decades, the permanent snow and ice on the summit of Mount Kilimanjaro has almost completely disappeared. This loss is primarily due to increasing average annual temperatures in the region, and scientists are speculating that the glaciers could be completely gone from Mount Kilimanjaro by the year 2015; Revkin (2004) cited the vanishing ice on Mount Kilimanjaro as an icon of global warming. This ice cap formed more than



Figure 2.3: Flooding in New Orleans, caused by the hurricane Katrina. This demonstrate the potential loss of human life and infrastructure due to the impact of global warming. (Source: ABC News online(2005))

11,000 years ago, 80% of the ice fields have been lost in only the last century. The disappearance rate is illustrated in Figure 2.4 of Landsat images from 1993 and 2000. In the 1993 image a significant ice cap can be seen but only small percentage in the more recent images.

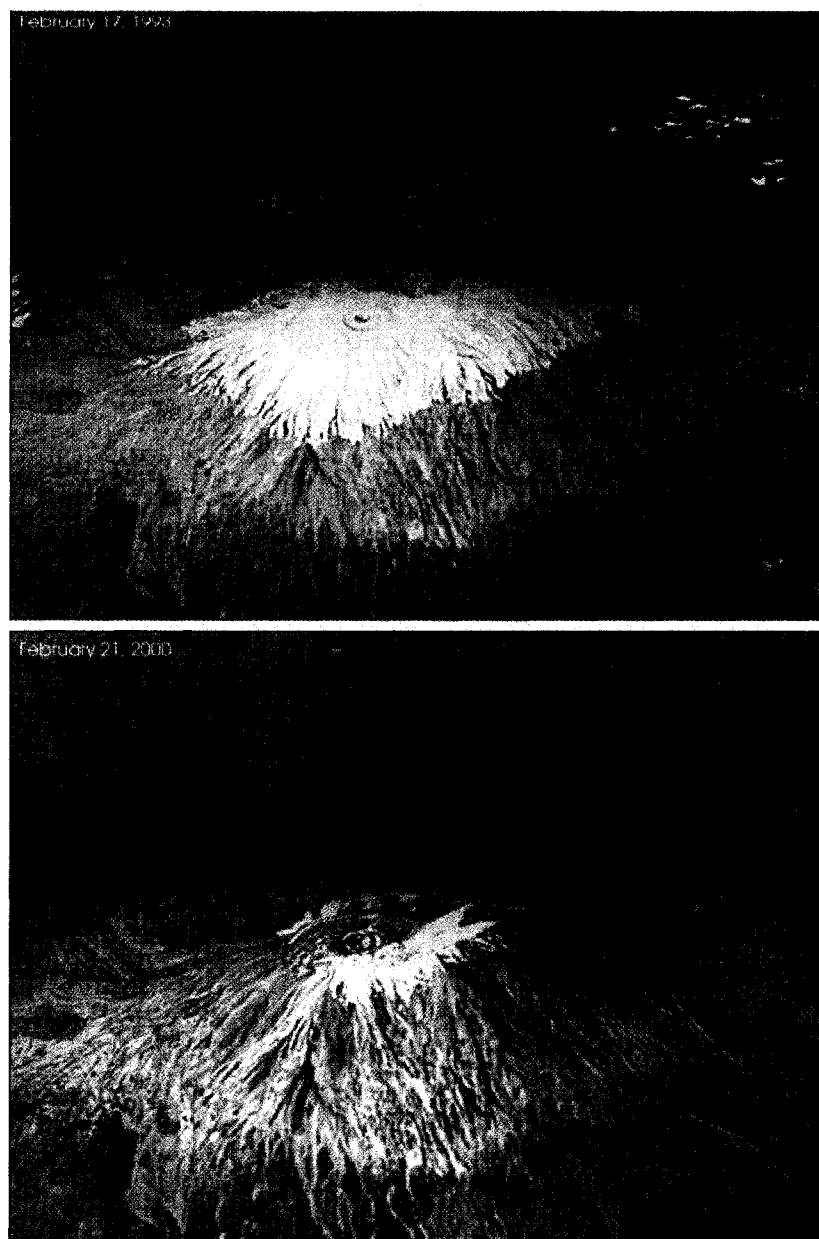


Figure 2.4: The two photographs provide the trend and rate of snow diminishing at the top of Mount Kilimanjaro. The top photograph was taken from the international space station on 1993 and shows that the mountain was covered by snow and glacier. Seven years later, the bottom photograph, shows that the snow and glacier are rapidly disappearing. (Source: NASA(2007))

(d) Precipitation: Global climate change accelerates the cycle of rainfall and evaporation, destroying the balance of water supply and demand, and even possibly expanding the worldwide gap in water availability i.e. there would be some areas that were frequently flooded while others will be constantly suffering from drought and water shortages (NASA, 2007). A warmer climate will bring an increase in precipitation worldwide, especially during winter and in mid- to high latitudes, according to climate model projections (NASA, 2007). In addition, more precipitation is expected to fall in downpours and heavy snowstorms leading to increased flooding and damages (NASA, 2007). As climate change increases the risk of flooding, human changes in land use and land cover can also contribute to the growing risk of flooding.

(e) Ocean warming, raising sea levels and coastal flooding: Global climate changes are expected to raise the global temperature; the higher temperatures will increase melting of mountain glaciers, increase ocean heat content and cause ocean water to expand. Largely as a result of these effects, the sea level keeps rising year after year. IPCC (2007) reported that global average sea level rose at an average rate of 1.8 mm per year for the period 1961 to 2003. They further observed that between the year 1993 and 2003, the average rate of sea level increase was higher at about 3.1 mm per year. Over the past 100 years the sea level has risen between 10 - 25 cm, and is projected to rise a further 15 - 95 cm during the next 100 years. The high sea level intensifies erosion along coast land. On average 50 - 100 metres of beach are lost for every metre of sea level rise. Also, many people who live in places like Bangladesh and Florida are in danger of being displaced by the rising sea level (Houghton et al., 2001).

(f) Agriculture: Global climate changes will directly and seriously affect agriculture, for instance some agricultural crops and animals species will be adversely affected by high temperature and changing weather. It is expected that some species will become extinct. Melting permafrost is forcing the reconstruction of roads, airports and buildings and is increasing erosion and frequency of landslides. Also, it will harm subsistence livelihoods. Reduced sea ice and ice shelves, and changes in

snowfalls which will likely reduce some cold-weather recreations like skiing and snow boarding. Pest infestations can affect native plants and animals that provide food to many people.

(g) Human health: Human health will be affected in many different ways, and in extreme cases, it is expected that many lives will be lost. Direct causes will include intensified heat waves and diseases. Indirect causes will include expanded geographical sphere of activities of organisms carrying contagious diseases and their extended period of activities will result in an increase in contagious diseases. Higher temperatures allow mosquitoes that transmit diseases such as malaria and dengue fever to extend their ranges and increase both their biting rate and their ability to infect humans. (Environment Canada, 2007).

(h) Energy demand: In our daily life, it will be observed that our heating energy consumption will be reduced due to global climatic changes, while on the other hand our water usage and cooling energy demand will be enormously increased.

Astonishingly, eleven of the last twelve years rank among the warmest years on record (IPCC, 2007), and this is a clear indicator of the natural pattern changes of the global climate. Thus the world must stand together to try to reverse the trend before it is too late. It is important to understand the sources which lead to that rapid global climate changes to arrive at a solution or means of reversing and/or stabilizing the situation. In the next section the factors which lead to rapid global climate change will be mentioned and briefly discussed.

2.2 Global climate change mechanism

The physical principles of climate change are best illustrated by considering the earth's global energy balance. The sun is the primary source of energy driving the climate. When solar energy enters the atmosphere, some of it is reflected and some of it is absorbed by the earth's surface (e.g. atmosphere, oceans, ice, land, and various forms of life etc) and re-radiated back to the space at longer wave-lengths (infra-red radiation). If the atmospheric energy system is in equilibrium,

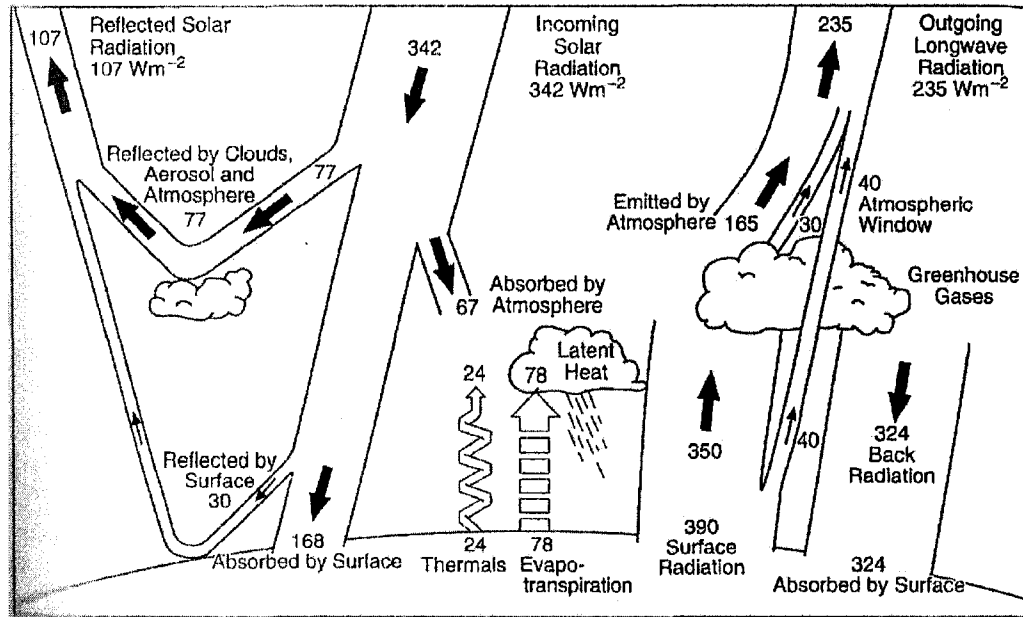


Figure 2.5: A typical diagram of the earth’s annual global mean energy balance. (Source: Seinfeld and Pandis (2006))

the incoming solar radiation and outgoing thermal long-wave radiation balance. Some of the re-radiated infra-red energy passes through earth’s atmosphere back into space; however, the majority is intercepted by a number of minor gases in the atmosphere. Although these gases are relatively transparent to sunlight they are responsible for absorbing most of the infra-red radiation from the earth and re-radiating much of it back to the earth’s surface. These gases act in a sense as an insulating blanket. This phenomena, of re-radiating the infrared radiation back to earth, is generally called “the greenhouse effect” and the absorbing gases that cause the greenhouse effect are called greenhouse gases (GHG).

The energy absorbed by GHG warms the earth and helps to maintain the temperature that sustains life on our planet. There is a delicate long term balance between the outgoing radiation and incoming solar energy. Any change in the factors that affect this process or the energy distribution itself, will change our climate (Environment Canada, 2007). The proportion of GHG is less than 1% of

the total atmospheric gases, thus slight changes in atmospheric concentration of GHG has the potential to alter the earth's energy balance and thus cause climate changes (Environment Canada, 2007). Figure 2.5 summarizes the global energy balance schematically.

Most GHG occur naturally, however, modern industries and new lifestyle have led to new sources of GHG, as well as to new GHG. The two main sources which contribute to the increase of the GHG can thus be categorised as natural and human induced ones.

2.2.1 Natural sources

Over the history of the Earth, the climate has changed. Some changes are global in scale, while others have been regional or hemispheric. There are a number of natural factors that contribute to changes in the Earth's climate over various time scales. It has been identified that GHG are an important factor in influencing the global climate changes. The sources of natural occurring GHG are respiration of plants and animals, transpiration, evaporation, decay of materials, natural wetlands, etc. Two major natural atmospheric factors which influence the global climate change are:

- (a.) *The greenhouse effect:* The main natural GHG are water vapour, carbon dioxide, methane and nitrous oxide. The natural greenhouse effect helps to warm the surface and the troposphere (lowest layer of the atmosphere), keeping it 33 °C warmer than it would otherwise be (Environment Canada, 2007). Thus, the greenhouse effect and GHG are vital in sustaining life in this planet.
- (b.) *Aerosols:* Aerosols are very fine particles and droplets that are small enough to remain suspended in the atmosphere for considerable periods of time. They both reflect and absorb incoming solar radiation. Changing the type and quantity of aerosols in the atmosphere affects the amount of solar energy reflected or absorbed (Environment Canada, 2007).

2.2.2 Human induced sources

Since the industrial revolution, a strong interaction between human activities, resulting GHG and their influence on global climate changes has been observed (Environment Canada, 2007). There has been a marked increase in the emissions of GHG in proportion to industrial expansion. Human activities influence the increase of GHG through the following major activities:

- (a.) *Enhancing the greenhouse effect:* Naturally occurring greenhouse gases (e.g. water vapour, carbon dioxide, methane, nitrous oxide) keep the Earth warm enough to support life. Scientific studies show that a variety of human activities release GHG. These include agricultural activities, deforestation, burning of fossil fuels for producing electrical energy, heating and transportation. By increasing their concentrations and by adding new greenhouse gases like CFCs, humankind is capable of enhancing the natural greenhouse effect.
- (b.) *Land Use Change and deforestation:* As humans replace forests with agricultural lands, or natural vegetation with asphalt or concrete, they substantially alter the way the Earth's surface reflects sunlight and releases heat. All these changes also affect regional evaporation, runoff and rainfall patterns as well result in reduction of a natural sink of GHG.
- (c.) *Atmospheric aerosols:* Humans are adding large quantities of fine particles (aerosols) to the atmosphere, both from agriculture and industrial activities. Although most of these aerosols are soon removed by gravity and rainfall, they still affect the radiation balance in the atmosphere. Whether this effect adds to or offsets any warming trend depends on the quantity and nature of the particles as well as the nature of the land or ocean surface below.
- (d.) *Population increase:* Population increase is another social force driving GHG emissions, because it changes land-use patterns and frequently leads to increased usage of fossil fuel.

Scientists have positively associated human factors with the rapid unusual rate of global climate change and that is why The United Nations Framework Convention

on climate change defines climate change as: *"a change of climate which is attributed directly or indirectly to human activity that alters the composition of the global atmosphere and which is in addition to natural climate variability observed over comparable time periods"*. In other words, the UNFCCC uses the term climate change to mean only those changes that are considered to be brought about by human activities.

2.3 Greenhouse gases

Worldwide collective intervention is needed to combat global climatic changes, otherwise the projected global climate change will be extreme in the near future. Rising temperatures are primarily due to the buildup of GHG in the atmosphere mostly from the increasing usage and production fossil fuels. GHG comprise less than 1% of the atmospheric gases and their levels are determined by a balance between the processes that generate and destroy them. The emissions of GHG have been rising since the start of the Industrial Revolution, causing temperatures to climb as shown in Figure 2.1. Thus, the pace of global climate change is closely related to GHG concentration. Human activities affect GHG levels either by introducing new sources or by interfering with natural sinks. Since enhancement of GHG emissions by human factors has been identified and singled out as a major cause of global climate change, the reduction and/or stabilization of GHG emission will reduce if not eliminate the harmful impact and stabilize the earth's ecosystem.

2.3.1 Major greenhouse gases.

Most GHG occur naturally. However, modern industry and lifestyles have led to new sources of GHG, as well as to the emission of entirely new GHG. Among them the most important are:

- (a.) *Water Vapour*: Water vapour comes from natural respiration, transpiration, and evaporation. Water vapour is a natural GHG and by far the most common, with an atmospheric concentration of nearly 1%, compared with less than 0.04% for carbon dioxide. The effect of human activity on global water

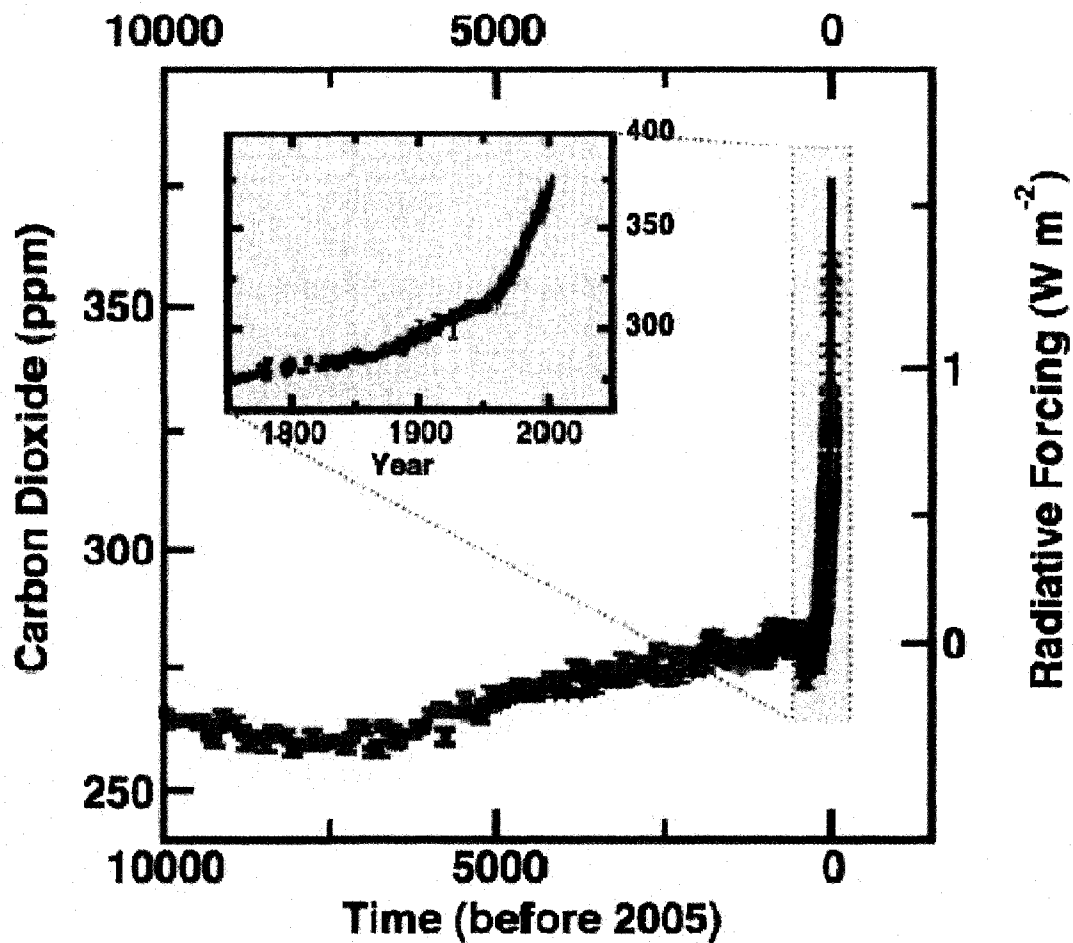


Figure 2.6: Atmospheric CO₂ concentration over last 10,000years (and insert since 1750). (Source: IPCC(2007))

vapour concentrations is considered negligible (EPA, 1998), and thus UNFCCC does not consider it as one of the GHG.

(b.) *Carbon dioxide (CO₂)*: Carbon dioxide comes naturally from the decay of materials and the respiration of plant and animal life. Its major human-induced sources are the combustion of fossil fuels and deforestation.

It is removed from the atmosphere through photosynthesis and ocean absorption. CO₂ is the most abundant GHG from anthropogenic enhancement

sources and mainly comes from the energy sector. The annual CO₂ growth rate is 1.4 ppm as reported by IPCC (IPCC, 2007). A complete trend of atmospheric CO₂ concentration over the last 10,000 years up to year 2005 is shown in Figure 2.6.

- (c.) **Methane (CH₄):** Methane is another naturally occurring GHG although human activities have affected its atmospheric concentration. Although there is less methane than carbon dioxide in the atmosphere, methane is a stronger GHG than carbon dioxide. Natural methane sources include decaying of garbage, termites, oceans and wetlands. Human induced source include agriculture activities, domestic sewage, landfills, fossil fuel production and utilization. Atmospheric methane concentration is observed to increase by 1% per year (Steele et al., 1987) while IPCC (2007) reported a decrease in growth rate since 1990. Figure 2.7 shows the atmospheric concentration of methane over 10,000 years before 2005.
- (d.) **Nitrous oxide (N₂O):** Nitrous oxide is another naturally occurring GHG whose atmospheric concentration has increased as a result of human activities. Soils and oceans are the primary natural source of N₂O. Humans contribute through soil cultivation and use of nitrogen fertilizers, nylon production, and the burning of organic material and fossil fuels. The growth rate of N₂O remained constant since 1980 (IPCC, 2007). Atmospheric concentration of N₂O was increasing quickly in the recent past as shown in Figure 2.8.
- (e.) **Artificial GHG:** Other important GHG are created by human activity and can be called artificial GHG. They did not exist in nature before the industrial revolution, and include chlorofluorocarbons (CFC), hydrochlorofluorocarbons (HCFCs), perfluorocarbons (PFCs) and hydrofluorocarbons (HFCs). They have been in wide use as coolant gases in air conditioners and refrigerators, and also as industrial cleansing agents. CFC are the strongest GHG; for example, HFC 134a has a GWP of 3400 times that of carbon dioxide in terms

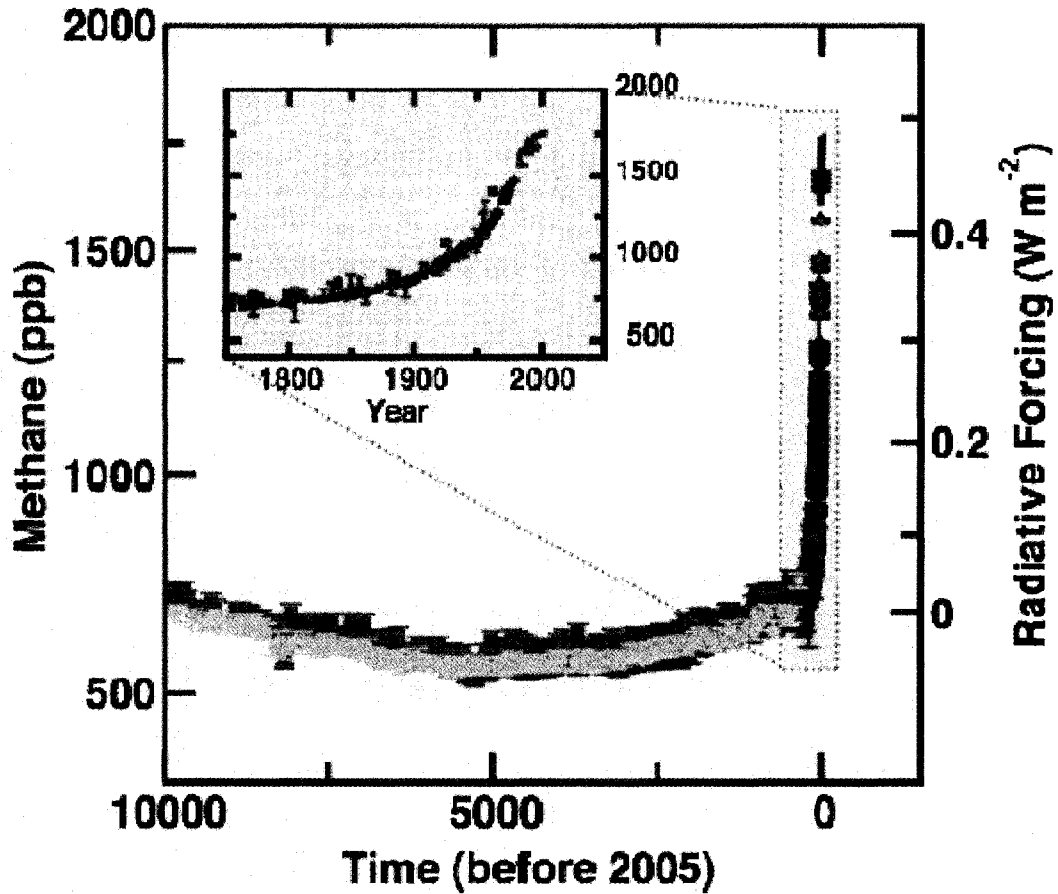


Figure 2.7: Atmospheric methane concentration over last 10,000years (and insert since 1750). (Source: IPCC(2007))

of the 20 year span. For this reason, despite of their small volume fraction in the atmosphere, such gases account for about 10% of the contribution to the global warming by all GHG.

Table 2.1 summarizes the value of atmospheric concentration of major GHG since pre-industrial revolution period and the near past. The initial rate of increase of methane was very high. Although the rate of increase has slowed down, it has the highest atmospheric concentration rate of increase.

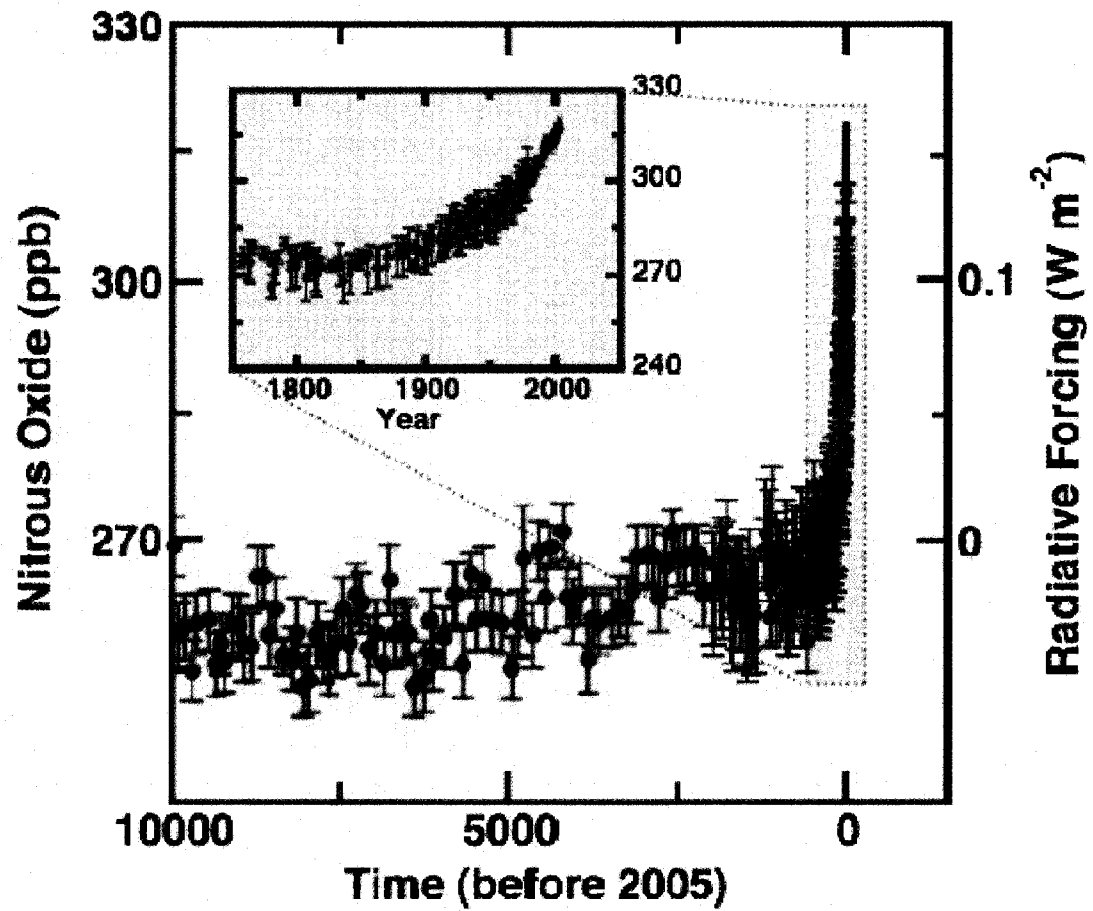


Figure 2.8: Atmospheric N₂O concentration over last 10,000 years (and insert since 1750). (Source: IPCC(2007))

Table 2.1: Atmospheric concentration of major GHG (IPCC,2007)

Gas	units	Atmospheric Concentration				
		Pre-1750	1992	1995	1998	2005
CO ₂	[ppm]	280	355	360	365	379
CH ₄	[ppb]	715	1710	1735	1745	1774
N ₂ O	[ppb]	270	302	311	314	319

2.3.2 Global warming potential

Different GHG exert different effects on the earth's energy balance. To measure and compare the impact of various GHG on global warming, the concept of global warming Potential (GWP) was introduced by the IPCC in its 1990 report. GWP reflects the relative strength of individual GHG with respect to its impact on global warming over a defined period of time.

GWP is defined as the cumulative radiative forcing between the present and some future time caused by a unit mass of GHG emitted now, expressed relative to carbon dioxide. Table 2.2 shows the GWP of major GHG as developed by IPCC. GWP takes into account the differing atmospheric lifetimes and abilities of various GHG to absorb radiation. The most commonly cited GWP are based on the 100 year period.

Table 2.2: GWP for the major GHG (IPCC,1996)

Gas	Atmospheric lifetime	GWP Time horizon		
		20 years	100 years	500 years
	[years]	[kg/kgCO ₂]	[kg/kgCO ₂]	[kg/kgCO ₂]
CO ₂	50 - 100	1	1	1
CH ₄	12	62	23	7
N ₂ O	114	275	296	156
HFC-23	260	9400	12000	10000

2.3.3 Atmospheric aerosol and global dimming

Research has shown that atmospheric aerosols make clouds, which reflect most of the sun's rays back into the space. This leads to an effect known as *global dimming*, in which less energy from the sun reaches the earth. At first, it sounds like an ironic saviour to the global climate change problem. However, it is believed that global dimming is responsible for the droughts that occurred in Sahel region in the 1970s and 1980s, where many people died. The reason for the Sahel drought was that the

northern hemisphere oceans were not warm enough to allow rain formation. Also, aerosols are relatively short-lived in the atmosphere so their effect can not offset the effect of the much longer lived GHG (Watson et al., 1996).

Global dimming also hides the true power of global warming. By cleaning up atmospheric aerosol pollutants without tackling GHG emissions, a rapid warming has been observed, and various human health and ecological disasters have resulted, as witnessed during the European heat wave of 2003.

2.4 Anthropogenic enhancement

Human activities have led to an increase in GHG atmospheric concentration and thus have enhanced the greenhouse effect. Already in the 20th century, the global mean surface temperature has increased by 0.6 °C (Watson et al., 1995). Other evidences as mentioned in previous sections, give a signal to humankind to act before it is too late. The problem is a global issue and needs a collective global action to deal with it. The largest contributor to anthropogenic GHG emissions in both absolute and growth terms is energy sector, the increase is equally accounted for by an increase in production and utilization of fossil fuel. This makes all countries which are principal producers of oil and natural gas important sources of anthropogenic GHG emissions. The increase in emissions from other sectors is also significant, but the pace is somewhat slower.

The emissions increase are closely linked to the impact of energy efficiency, regulations and practice. For example, in electricity generation, emissions are projected to increase significantly if fossil fuel becomes the preferred fuel source, while hydro and nuclear sources will reduce GHG emissions tremendously. however, the concern about nuclear reactor safety, radioactive material waste management, nuclear weapon proliferation and cost limits the liability of nuclear energy utilization.

Carbon dioxide is the most abundant GHG from an anthropogenic source, and mostly comes from burning fossil fuels. Fuel-switching strategy, switching from coal and oil to natural gas, has been suggested by IPCC (2001) as an interim measure to reduce the GHG emissions from the energy sector. Because natural gas emits

less carbon dioxide per unit energy generated, and carbon dioxide contributes more to global warming than all other GHG combined, there is an incentive in fuel switching. A combination of cost, convenience and environmental benefits are promoting the extensive use of natural gas, and world energy outlook projects a continued rise in demand and production of natural gas at least through 2030. The poor quality of methane emissions estimates currently available and the high GWP of methane, put many in doubt if methane leakage and emissions from natural gas industries operations were large enough to reduce substantially or even eliminate the benefits of low carbon dioxide emissions. There are also potential issues about availability of methane in sufficient quantities to justify mitigation.

2.4.1 The Kyoto protocol

In addressing the issue of global climate change, the world came together under UNEP, IPCC and UNFCCC and made an agreement and commitment on mitigation of global climate change, by stabilizing atmospheric GHG concentrations. In 1997, the Kyoto protocol was adopted in which policy and strategies for reduction of GHG emissions were defined. Canada is among the countries which ratified the Kyoto protocol and thence committed itself to reduce GHG emissions between the years 2008 and 2012 to 6% below the level recorded in 1990. According to the Kyoto protocol, there are six important GHG to deal with namely; carbon dioxide (CO₂), methane (CH₄), nitrous oxide (N₂O), and halon carbon families (CFC). CO₂, CH₄ and N₂O are estimated to account for more than 80% of the overall global warming effect arising from human activities (*UNFCCC, 2003*). Figure 2.9 shows the estimation of the contribution of each major GHG to global anthropogenic emissions.

2.4.2 Emissions from energy sector

Energy related activities are the primary source of anthropogenic GHG. The main GHG emissions from the energy sector are CO₂, CH₄ and N₂O. Fossil fuels, chiefly coal, oil and natural gas, now supply most of the world's energy. Only a small amount comes from renewable sources, which do not release GHG into the atmo-

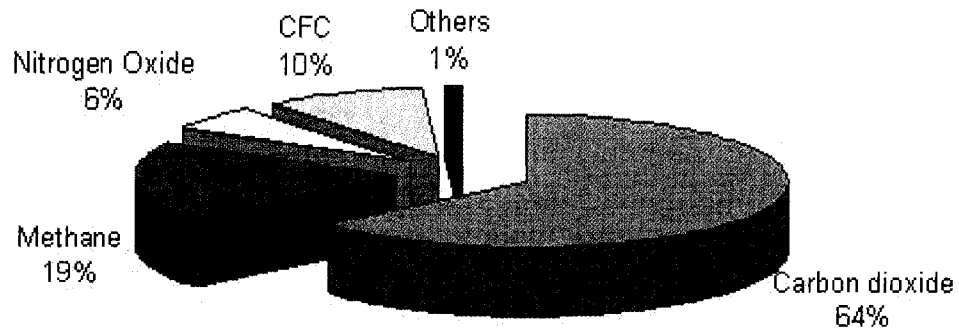


Figure 2.9: Estimation of each GHG contribution to the global anthropogenic emissions based on GWP for 100 year period (IPPC,1995).

sphere. If renewable sources could manage to satisfy more energy demand, the fossil fuels to be burnt will be reduced and hence more GHG emissions will be avoided. The major emission from fossil fuel combustion is CO₂. EPA(2007) estimated approximately 25,575 Tg of CO₂ were added to the atmosphere globally by fossil fuel combustion in 2002. Apart from CO₂, fossil fuel combustion also emits other major GHG, namely CH₄ and N₂O. The oil and natural gas sector account for over 20 percent of global anthropogenic methane emissions (Fernandez et al., 2003; Methane to Market, 2005). In 2005, Canada was estimated to emit 747 mega tonnes of CO₂ equivalent, which is about a 27% increase from 1990 emission and 35% over the Kyoto target. Alberta and Ontario are the two provinces in Canada with the highest GHG emission; together they contribute more than a half of Canadian GHG emission.

Total GHG emissions in Canada in 2005 and 2004 were about 747 Mt CO₂ equivalent which represents a slight increase from 2003 levels. Overall, the long term trend indicates emissions in 2005 were 25.3% and 32.7% above the revised 1990 level and the Kyoto target respectively, as shown in Figure 2.10. During the 15 years (1990 - 2005) GHG increase in Canada was higher than population increase, which was 16.5% and approximately equalled the increase in energy utilization which

increased by 23%. The flattening of the growth curve between 2003 and 2005, as shown in Figure 2.10, is due primarily to a significant reduction in emissions from electricity production (reduced coal and increased hydro and nuclear generation, also fuel switching which resulted in natural gas based generation offsetting other fossil fuels which have higher GHG emission intensity), coupled with reduced demand for heating fuels due to warmer winters and a reduced rate of increase in fossil fuel production. Long term growth, nevertheless, remains large. Between 1990 and 2005 a significant increase in oil and natural gas production, much of which have been provided to the USA, has resulted in a significant increase in the emissions associated with the production and transportation of fossil fuel. In 2005, total emissions associated with these operations were 73 Mt, a 162% increase over the 1990 level of 28 Mt.

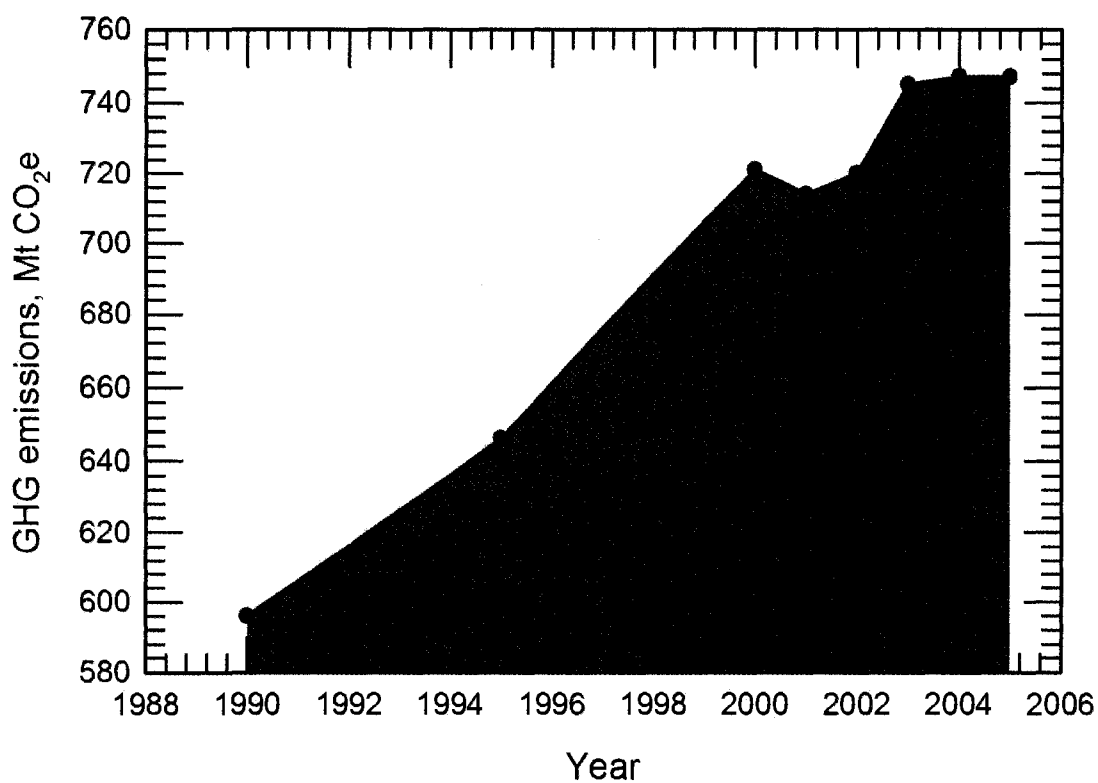


Figure 2.10: Canadian GHG emissions trend 1990 - 2005

Table 2.3: Canadian GHG emission trends by sector since 1990

Sector	Year							
	1990	1995	2000	2001	2002	2003	2004	2005
Energy sector[Mt]	473	513	589	582	592	613	593	609
Industrial sector[Mt]	54	57	49	48	50	50	51	54
Agriculture sector[Mt]	46	61	61	60	59	54	55	57
Forestry [Mt]		2	2	2	6	22	8	
Wastes[Mt]	23	22	24	25	24	27	29	28
Total[Mt]	596	646	721	714	720	745	747	747
GDP[Billions 1997\$]	708	773	946	961	989	1013	1046	1079
GHG Intensity [Mt/\$B GDP]	0.84	0.84	0.76	0.74	0.73	0.74	0.72	0.69

Other fossil fuel activities, such as exploration, production, transportation, storage and distribution, also emit GHG, which mainly consists of methane (CH₄). The relative importance of methane and therefore of the oil and natural gas sector, might increase as a consequence of the emission reduction measures for carbon dioxide and artificial GHG that are taken in the context of international climate and ozone policies. However, a significant technical and economical reduction potential is believed to be possible. Therefore, the focus of this work is methane emission in the oil and natural gas sector.

Energy-related activities are by far the largest source of GHG emissions in Canada. The Energy Sector includes emissions of all GHG from the production of fuels and their combustion for the primary purpose of delivering energy. Emissions in this sector are classified as either fuel combustion or fugitive releases. Fugitive emissions are defined as intentional or unintentional releases of GHG from the production, processing, transmission, storage, and delivery of fossil fuels.

Overall, the net Canadian GHG emission has increased significantly between 1990 and 2005, with the net increase in annual GHG being about 151 Mt. Over the same period emission from the energy sector and transportation increased by about 137 Mt, accounting for more than 90% of overall increase. In the same

period it can be noted that fuel combustion-related emissions increased by 25.3%, while emissions from fugitive releases rose by 54%. At national levels, it has been observed that the variation of GHG emission and GDP have the same trend. So using GHG intensity (i.e ratio of GHG emission and GDP) is a good basis to compare GHG emission of one nation to another, For Canada The GHG intensity generally is decreasing year after year, and between 1990 and 2005 the Canadian GHG intensity decreased by about 17.8%. Table 2.3 summarizes the facts stated above.

2.4.3 Possible solutions for methane mitigation

Methane emission occurs from exploration, production transportation, storage and distribution in the oil and natural gas sector. A number of technologies are possible for abatement of methane emissions which are:

(a.) **Combustion:** This technology converts methane to a less harmful form , i.e. carbon dioxide and water. There are two possible ways to accomplish this. The first possibility is homogeneous combustion, which can be implemented either as flaring (most common in the oil and natural gas sector) which is cheap, but heat energy can not be recovered. Sometimes supporting fuel is needed to accomplish the combustion, or as thermal homogeneous combustion which is not commonly in use for abatement of methane. It is used when the methane concentration is within the flammability limits and there is a need to recover heat through a heat exchanger.

Another possible combustion technology is catalytic combustion, which involves use of a catalyst bed to enhance the oxidation reaction. The main advantage of this technology is that it can operate outside the flammability limits and does not produce flame.

(b.) **Biological Degradation:** This method uses the ability of certain microorganisms, such as methanotrophs, to break down emthane into water and carbon dioxide. The biofilter is the most common biotechnology, but also

there is a possibility of using bioscrubbers and trickling filters. It is not very effective in a cold environment and with a large volume of emissions.

(c.) *Adsorption*: This is a less effective technology for methane and is seldom used in industries. It needs highly porous adsorbents and very large beds in treating methane.

A useful summary of classical mitigation options for methane is provided by the IEA (IEA GHG, 1999). For some specific solutions for the oil and natural gas sector, the paper by Hayes (2004) is also recommended. Restricting our mitigation options to combustion, there are two possibilities. Conventional (homogeneous) combustion is the most common type used, and often consists of a flare. Flares can be used for concentrated streams and for large volumes. The drawback of flares is that they are unpopular with the general public, and require the use of a support fuel if the heat content of the emission stream is not sufficiently high. Although the flame can be hidden from view in other types of thermal reactors, the constraint of the flammability limits remains. Methane emissions (especially fugitives) often consist of a low concentration mixture of methane and air that cannot be destroyed by conventional combustion, because their composition is outside of the flammability limits (about 5% to 16% by volume for methane in air). Furthermore, many of these streams have variable composition and flowrate. These variations can occur over time scales varying from hours to days or months. For many streams catalytic combustion is a viable option, in which a suitable catalytic reactor is used to destroy the hydrocarbons. Catalytic combustion is a flameless combustion process that can be used to oxidise emissions that cannot sustain a conventional flame. Furthermore, catalytic combustion occurs at temperatures lower than conventional combustion processes and thus produces fewer harmful by-products. The combustion unit is usually smaller than a conventional firebox and can be located in areas where conventional, fired units would not be allowed (Hayes and Kolaczowski, 1997).

Oil and natural gas sector

Methane is the most abundant hydrocarbon in the atmosphere (Seinfeld and Pandis, 2006) and the second most abundant GHG. Seinfeld and Pandis (2006) showed that there is imbalance between the current global source and sink of methane which leads to accumulation of methane in the atmosphere. Most methane emitted into the atmosphere comes from anthropogenic sources. Among anthropogenic sources, methane from the energy sector is growing faster compared to others as shown in Table 3.1. Also review data from AGO, EEA, EPA, IPCC, and UNFCCC made it clear that energy sector activities, other than fuel combustion, emit large quantities of GHG. These emissions primarily are methane from oil and natural gas sector.

Table 3.1: Annual estimates of the global anthropogenic methane emission into atmosphere (source: Seinfeld and Pandis (2006))

Anthropogenic source [Tg/year]	Base Year		
	1980's	1990	1992
Energy	75	97	110
Landfills	40	35	40
Ruminants	80	90	115
Rice agriculture	100	88	-
Biomass burning	55	40	40

3.1 Introduction

The oil and natural gas sector is very large and diverse, including various activities such as search, exploration, development, production, gathering, processing and storage of both petroleum and natural gas. It also deals with the reclamation, long term monitoring, control and treatment of sites disturbed because of the activities mentioned above. Oil and natural gas are the two most important fuels that drive global development. Thus, the oil and natural gas sector faces challenges as well as opportunities in providing clean, economically viable, environmentally sound, and socially acceptable energy that are essential for global economical growth, environmental protection and social progress. The upstream activities include production, gathering, processing and storage, and are of interest in this work. Public pressure, environmental legislation and the internal requirement of achieving sustainable development, gives the oil and natural gas sector the responsibility of reducing or eliminating the emissions occurring within the sector, in particular the GHG.

3.1.1 Methane emission

Methane is emitted from a variety of natural and human influenced sources, including landfills, the oil and natural gas sector, agricultural sector, coal mining, etc.. Apart from being a potent GHG, methane is also a clean energy source and the primary constituent of natural gas. Thus any effort in preventing or capturing the methane emissions can provide significant energy, economic, and environmental benefits (EPA, 2006). Although, the oil and natural gas sector is not a major anthropogenic source of methane emission, to prevent and/or reduce methane emission has been a main objective of this sector for improving the safety and economics of its operations. The oil and natural gas sector is comprise of wells, processing facilities, transmission pipelines, storage and end consumers, with methane making up about 95% of the processed gas. It is estimated that this sector releases about 343 million metric tons carbon equivalent (MMTCE) of methane to the atmosphere and accounts for about 18% of total global emissions by sectors (EPA, 2006). Thus,

methane emission reduction can be instrumental in attempting to find the optimal balance between economical, safety, operational and environmental benefits, because methane emission is a revenue loss for the oil and natural gas sector as well as a potent GHG.

The oil and natural gas sector satisfies most of the global energy demand, and thus is responsible for a large percentage of global GHG emission, mostly carbon dioxide. The carbon dioxide emissions are the result of energy usage (fuel combustion), but there are other GHG emissions originate from the oil and natural gas sector. Most of these non-carbon dioxide emissions, including methane, are not the result of fuel combustion. Energy-related activities other than fuel combustion, such as the production, transmission, storage, and distribution of fossil fuels, emit large quantities of GHG, primarily lean methane. Methane emissions are the second largest contributor of the GHG emissions after carbon dioxide. Lean emissions from compressor, metering and regulating stations account for the majority of the methane emissions from the oil and natural gas sector.

Methane emission from the oil and natural gas sector can be characterized by the stage of activities from initial production to delivery for end use. Significant emissions occur in the following areas:

- 1. Production:** Wells are used to extract the natural gas from underground formations. Wells and associated piping, treatment and processing equipment form the production part of this sector. The majority of emissions produced during production are vent and leakage emissions from the associated equipment like separators, meters, dehydrators, gathering pipelines and pneumatic control devices which are often gas powered.
- 2. Processing:** The main objective of this unit is to ensure that the natural gas meets the quality standard for transmission by removing condensate, particulates and other compounds. Leak emissions from compressors are the main source of processing related methane emissions.
- 3. Transmission and Storage:** High pressure, large diameter pipelines are used to transport natural gas to end users. Pressure in the system is maintained by

compressor stations, which, together with metering and regulating stations, account for the majority of methane emissions in the transmission stage. Storage facilities, which are underground formations into which natural gas is injected and kept during times of low demand, produce emissions mainly from the compressor and dehydrators.

- 4. Distribution:** Low pressure emissions occur as leakage in the pipeline which transmit natural gas to consumers. Also leakage can occur at metering and pressure regulation stations as well as at the customer meters.

Within each of these areas, the source of methane emissions can be equipment (such as pneumatic controllers, valves, compressors, offshore platforms), or mode of operation (such as start-up, normal operation, maintenance, system upset, system mishap). Emissions can be categorized as leakage, vent or incomplete combustion. Methane emissions vary from facility to facility, and are largely a function of operation, maintenance procedure, equipment condition and age. Table 3.2 presents some typical methane emissions from the oil and natural gas sector of a few selected countries world wide. Leaks are hard to detect and next to impossible to eliminate completely, thus emissions are always present. To make the situation worse these leakages are quickly mixed with atmospheric air which makes their capture and abatement a real headache for this sector. Usually, such leakages are known as fugitive emissions.

Release of methane is of concern because methane is a chemically reactive GHG and 23 times (from a GWP point of view) more potent than the more-abundant but largely-unreactive carbon dioxide. According to researchers, the main sink for methane in the atmosphere is reaction with the tropospheric hydroxyl radical (OH) which is directly linked to the production of ozone in the troposphere, thus reductions in methane emissions will stabilize both methane as well as ozone concentration in the atmosphere worldwide. This would help to realize the reduction of the global climate change impacts in the near future. IPCC (2001) projected that within the next 25 years or so, methane emissions can be stabilized. Otherwise, the increase in methane concentration in the atmosphere will reduce the concentration

Table 3.2: CH₄ emissions from oil and natural gas sector from selected countries
(Source: Methane to market website, 2006)

Country	CH ₄ emissions [MMTCE]		
	1990	2000	2010 (projection)
Russia	91.6	69.1	74.7
United State	40.3	37.8	39.6
Ukraine	19.6	16.4	10.8
Venezuela	11.0	14.3	18.6
Uzbekstan	7.4	9.2	11.7
India	3.5	6.7	15.0
Canada	4.7	6.4	6.5
Mexico	3.0	4.2	6.0
Argentina	2.2	3.7	8.3
Thailand	0.8	2.3	4.3
China	0.2	0.4	1.3

of tropospheric OH, and will lead to a reduced rate of methane removal as well as a decrease in ozone concentration.

3.2 Fugitive emission

In the oil and natural gas sector, methane emissions can be reduced by upgrading technology or equipment, for example the use of low-emission regulator valves will reduce or eliminate venting, and improving management practices and operational procedures can help to reduce venting and leaks. Implementation of these cost effective measures can lead to reduced methane emission and increased revenue, but an effective abatement method is still needed to deal with methane emission in this sector because it is impossible to eliminate all leakages in the system. The transportation system of natural gas is prone to unexpected or unplanned leakage,

these leakages quickly mix with atmospheric air to make a lean solution. The rate and place of leakage are usually unknown before hand, thus it is difficult to identify and quantify them. Individual leaks from gas transmission and distribution systems may seem relatively minor, but collectively, leakage from these systems can be substantial.

The most common means of transportation for natural gas is through a pressurized pipeline (typical pressure is between 80 and 100 bar), compressor stations are located at every 100 to 150 km along the pipeline, to overcome the pressure drop. Major gas pipeline networks can be found in the USA, which has about 400,000 km, and the former Soviet Union, which has about 214,000 km, as reported in 1994 and 1993 respectively. In Canada, TransCanada Pipeline owns a 37,000 km pipeline network that contains 110 compressor stations, 1200 metering facilities and over 500 valve sites. Although a variety of data have been published on methane emissions, such data should be taken as general estimates only, because most of the data rely on assumptions, and more reliable data will only emerge as additional emission audits are undertaken. It is estimated that the main contributors to global methane emissions are agriculture (44%), landfills and biomass burning (22%), coal (12%) and the oil and natural gas industry (15%) (Moore et al., 1998). The 15% of emissions from the oil and natural gas industry equals about 47 Mt/y (1081 Mt/y of CO₂ equivalent), using 1990/92 data (Moore et al., 1998). Overall, it has been estimated that fugitive methane emissions account for about 50% of the GHG emissions of the Canadian conventional oil and natural gas sector. For 2005 Environment Canada estimated total GHG emissions at 747 Mt of carbon dioxide equivalent, of which about 8.8% are fugitive methane emissions from the oil and natural gas sector (1.8 Mt of fugitive methane annually). Canada is responsible for about 2% of the global GHG emissions. There is a certain degree of inconsistency in the data, as noted, and it is probable that methane emissions are significantly under estimated. But currently UNFCCC requires countries to submit an annual GHG inventory report using UNFCCC reporting guidelines, and this will help to standardize and harmonize the global fugitive emission inventory.

Oil and natural gas are the lifeblood of the global economy, accounting for more

than 90 percent of the energy consumed. To meet projected energy demand, production, processing and transportation of the oil and natural gas have to increase, at the same time the methane emission from leakage also is expected to increase, although not by the same magnitude as the increase in demand due to superior modern technology.

Definition of fugitive methane emissions differs from one group to another. Some of the definitions for fugitive emissions are:

- **Generic definitions - 1 :** Emissions not caught by a capture system which are often due to equipment leaks, evaporative processes and wind blown disturbances (*source California Air Resource Board*)
- **Generic definition - 2:** Uncontrolled emission to air, water or land. Example: material released from a pipeline coupling.
- **Generic definitions - 3:** Means gas, liquid, solid, vapour, fume, mist, fog or dust containing a controlled product that escapes from process equipment, emission control equipment, a product or a device in the workplace or from any facility which constitutes a workplace or part of workplace (*source Canadian Labour safety*)
- **UNFCC Definition:** Fugitive emissions from fossil fuels are intentional or unintentional releases of GHG from the production, processing, transmission, storage and delivery of fossil fuels. Released gas that is combusted before disposal (e.g. flaring of natural gases at oil and natural gas production facilities) is considered a fugitive emission. However, if the heat generated during combustion is captured for use (e.g. heating or sale) then the related emissions are considered fuel combustion sources. (*Environment Canada, 2006*)
- **Oil and natural gas definition:** Fugitive emissions are unintended releases of GHG to the atmosphere. This category includes fugitive equipment leaks, accidents and equipment failures. Fugitive equipment leaks are emissions from equipment component that leak as a result of wear, poor design or improper installation.

Fugitive emissions are sources of direct and indirect GHG emissions in many countries, and from numerous studies it has been identified that leaks from compressor stations are the largest source of single location fugitive emissions. The vented emissions are a point source emission that can be more easily captured and directed for mitigation while fugitive methane from leakages are not that easy.

Global fugitive emissions are difficult to quantify accurately, since only estimated values are available. The accuracy of these values remains uncertain, as different countries or companies use different estimation methods. IPCC and UNFCCC are working to harmonize the system of estimation by issuing guidelines and requesting each country to submit its inventories each year based on these guidelines.

In the period 1990 - 2004, many countries exceeded their Kyoto protocol targets. Countries which reduced their GHG emissions are (*their targets are in brackets*) Lithuania to -60.4% (-5%), Russian Federation to -32% (-5%), Czech Republic to -25% (-8%), Germany to -17% (-8%) and United Kingdom to -14.3% (-8%). Countries still experiencing GHG growth are for example, Japan 6.5% (-6%), Canada 25% (-6%), Greece 27% (-8%), Spain 49% (-8%) and Turkey 72.6% (-8%).

3.2.1 Canadian fugitive methane emission

Canada contributes about 2% of total global GHG emissions. It is one of the highest per capita emitters, largely the result of its size, climate (i.e., energy demands), and richness in fossil fuel resources. In 2005, Canada is estimated to have emitted 747 megatonnes of CO₂ equivalent (Mt CO₂ eq) of GHG to the atmosphere, an increase of 0.4% over the 745 Mt recorded for the year 2003. This is considerably less than the 5% increase that occurred between 2001 and 2005. Also the GHG emission per capita increased from 21.5% in 1990 to 23.1% in 2005. The energy sector accounts for more than 80% (that includes combustion end use) of Canada's GHG emission, while the fugitive methane emissions account for about 50% of the GHG emissions from the Canadian conventional oil and natural gas sector, thus fugitive methane emission from oil and natural gas sector in Canada is significant

and proper attention is required. The management of fugitive methane emission is part of the overall country's strategy towards reduction and/or elimination of GHG.

Figure 3.1 illustrates the significance of combating GHG emission in Canadian

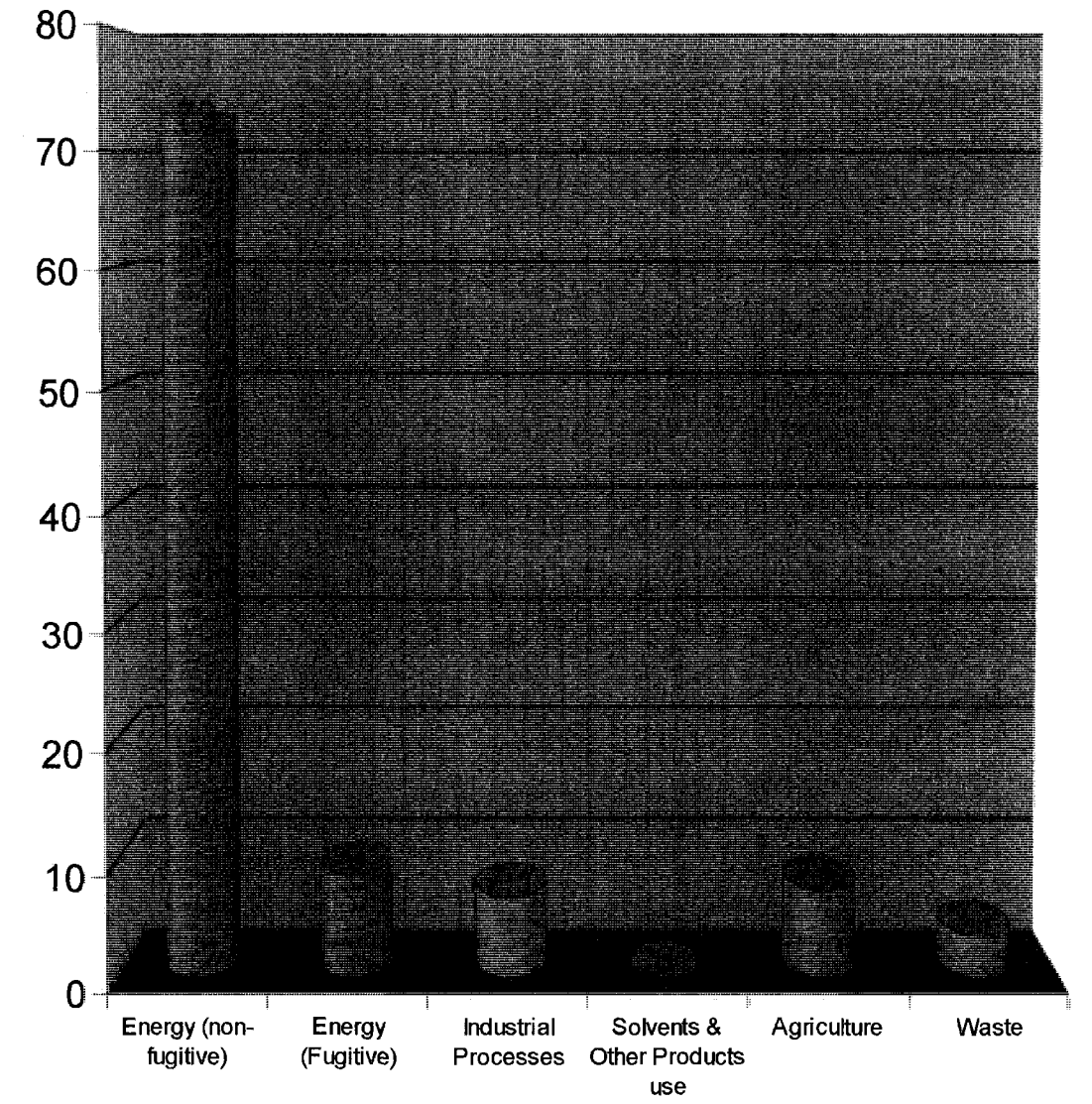


Figure 3.1: Sectoral Breakdown of Canada's GHG emission in 2005.(Source: Environment Canada)

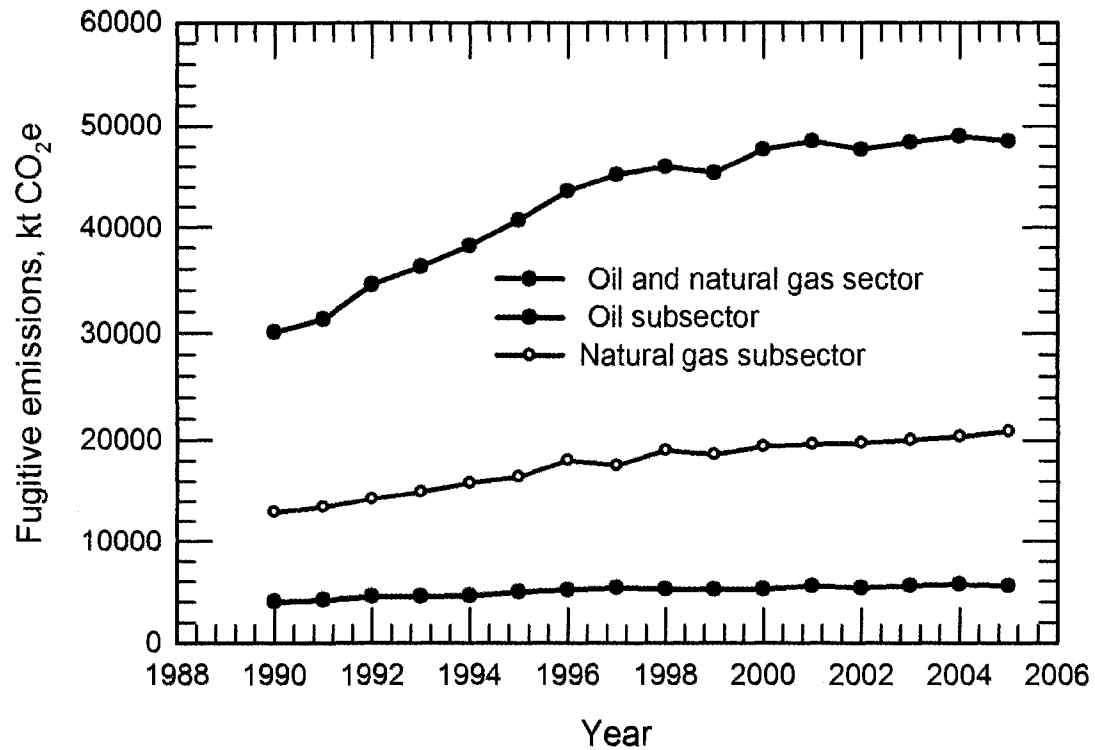


Figure 3.2: Trend of methane emission in Canada.(Source: Environment Canada)

energy sector. Even the fugitive GHG emission from Canadian energy sector alone is greater than the GHG emission from any other sector.

The trend of methane emission from the energy sector in Canada is summarized in Figure 3.2. This figure shows that the GHG emission from the oil and natural gas sector in Canada increasing from 1990 and reaching a plateau in the year 2000. Further , it shows that fugitive sources and natural gas are leading producers of GHG emissions.

3.2.2 Efforts in combating fugitive methane

Mitigation of fugitive methane or GHG emissions in general is not only an environmental issue, it also has aspects related to the economy (including trade and competitiveness), social aspects and concerns about equity between generations.

These issues have competing interests which must be addressed in deciding the mitigation method to be adopted. Thus, the mitigation of GHG emission is an optimizing challenge for sustainable development.

Natural gas use is widely recognized as a means of reducing carbon dioxide emissions when substituted for other fossil fuels. Natural gas produces less carbon dioxide when combusted than either coal or oil per unit of energy produced. Natural gas use retains its advantage as an instrument to combat climate change, unless the leakage from the natural gas network exceeds 6% to 11% of the throughput. With this reasoning, natural gas production and utilization is going to increase and hence so will the fugitive methane emission from this sector.

In oil and natural gas systems, methane emissions can be reduced by upgrading technologies and equipment (such as use of low emission regulator valve), by improving management practices and operational procedures. Implementation of these measures can lead to reduced product losses, lower methane emissions and increased revenues. These cost-effective measures vary greatly from country to country, also from company to company, based on the level of physical and institutional infrastructure. These cost-effective approaches will reduce the methane emission but will never eliminate them, because leaks can not be completely eliminated in the oil and natural gas sector. Joints, flanges and valves may leak to some extent and represent a chronic problem in the oil and natural gas system. These individual leaks are most likely limited to a few cubic millimetres per day (10^{-6} m^3), but taking into account the number of this type of equipment in the given gas network, the sum of their leakage may contribute significantly to total fugitive emissions. Compressor stations, metering stations and valve stations are the location where a good number of such pieces of equipment can be found, and that is why the focus is on compressor stations.

3.2.3 Problem facing fugitive methane mitigation

The low concentration and variable flow rate of fugitive methane sources presents major challenges for mitigation. The key factors that affect the amount of fugitive

emissions from a given operation are the amount and type of infrastructure employed, the integrity of the system, and the incentives or requirements to reduce fugitive emissions. The first challenge is to capture the methane, which may consist of a very lean mixture, and then direct it to a destruction device. Fugitive methane emissions may be in low concentration relative to air (below flammability limits of about 5% to 16%), and thus cannot be destroyed by conventional combustion.

3.3 Natural gas transportation

The transportation system for natural gas from production location to consumers consists of a network of pipelines designed for quick, safe and efficient delivery. Raw natural gas can either originate from oil wells (these are termed as associated natural gases and can either be free natural gas or dissolved in crude oil), or gas well and condensate well (these are known as non-associated natural gases and usually contain little or no crude oil). The main component of natural gas is methane, but it is also common to find higher hydrocarbons, carbon dioxide, water vapour, nitrogen and other compounds. If H_2S is present in the natural gas, the natural gas is called sour natural gas and more care in handling is needed because sour natural gas is poisonous.

Natural gas is transported at high pressure in the pipeline, at pressures from 15 bar to over 100 bar. The high pressure is necessary to reduce the volume of natural gas transported, as well as to provide a force to move natural gas through the pipeline network.

3.4 Natural gas compressor stations

When the natural gas flows through the pipeline network, it loses pressure owing to friction. The natural gas is periodically re-compressed in compressor stations, located at distances of 100 to 150 km apart. These compressor stations typically contain between one and fifteen compressors. The size of the compressor station and the number of compressors varies based on the diameter of the pipe and the

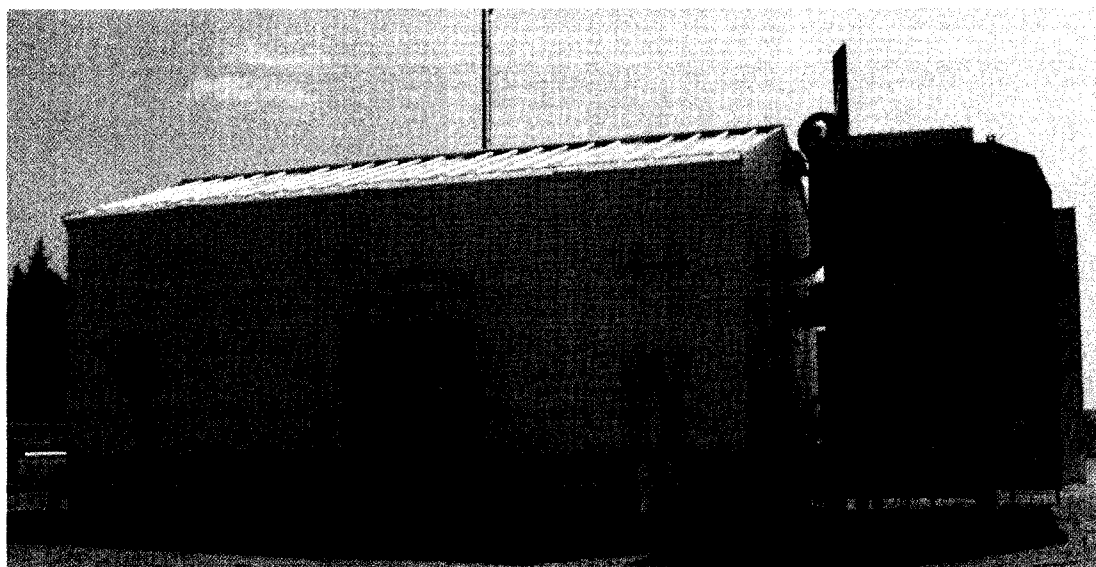


Figure 3.3: A typical single compressor building.

volume of natural gas to be transported. The basic components of the compressor station are similar, and a typical single compressor building is shown in Figure 3.3. There are three major types of compressors available in the market, which include centrifugal compressors (produce high-pressure discharge by converting angular momentum imparted by the rating impellers, and are designed to work for higher capacity), reciprocating compressors (are positive displacement machines, single-stage are generally used for pressure in the range of 70 - 100 psig, while the two-stage are used for higher pressure ranges of 1000 - 1500 psig), and rotary screws compressors (also positive displacement machines, capacity control for these type of compressors is accomplished by variable speed and variable compressor displacement). compressors may be driven by almost any prime mover including an electric motor, steam turbine, combustion engine and internal combustion engine. Historically, electric motors were the dominant prime mover used. The use of natural gas engines has become a popular alternative, because they reduce operating cost by lowering power demand and electric energy consumption. These large piston engines resemble automobile engines, only they are many times

larger as shown in Figure 3.4. They use natural gas from the pipeline for fuel. Reciprocating pistons, located in cylinder cases on the side of the unit, compress the natural gas. The compressor pistons and the power pistons are connected to a common crankshaft, hence the name "integral." The advantage of reciprocating compressors is that the volume of natural gas pushed through the pipeline can be closely adjusted to meet small changes in demand.

Centrifugal compressors powered by natural gas fueled turbines are also used. The centrifugal compressor is similar to a large fan inside a case, which pumps the natural gas as the fan turns. A small portion of natural gas from the pipeline is burned to power the turbine. Electric motor/centrifugal compressor, where the centrifugal compressor is driven by a high voltage, electric motor is another alternative. One advantage of electric motors is that they need no air emission permit because no hydrocarbons are burned as fuel. However, a highly reliable source of electric power must be available near the station. IC engine and turbines are the most common prime movers used in natural gas compressor stations. Before the natural gas enters the compressor unit, all free liquids or any other dirt particles are removed from the natural gas stream by passing it through a dehydrator.

There are three main sources of methane emissions in compressor stations. The first is emissions resulting from incomplete combustion in the engine. The second results from instrument venting, whilst the third source is leaks in valves, flanges, dry gas seals and other equipment inside the building, Figures 3.4 and 3.5 show some of the natural gas systems which are prone to leak. As noted, the focus in this work is the emissions in the building; however, for completeness the other two sources are described briefly.

As noted, either turbines or natural gas IC engines are used to drive the compressors. While the methane emissions from natural gas turbines are fairly low, the IC engine emissions are significantly higher. These engines are operated in either lean burn (excess oxygen) or with a stoichiometric air/fuel ratio. The lean burn system produces less NO_x (up to 90% less) and has better fuel economy than stoichiometric engines. Unfortunately, owing to a lower combustion temperature, the amount of methane in the exhaust gas of a lean burn engine is up to four

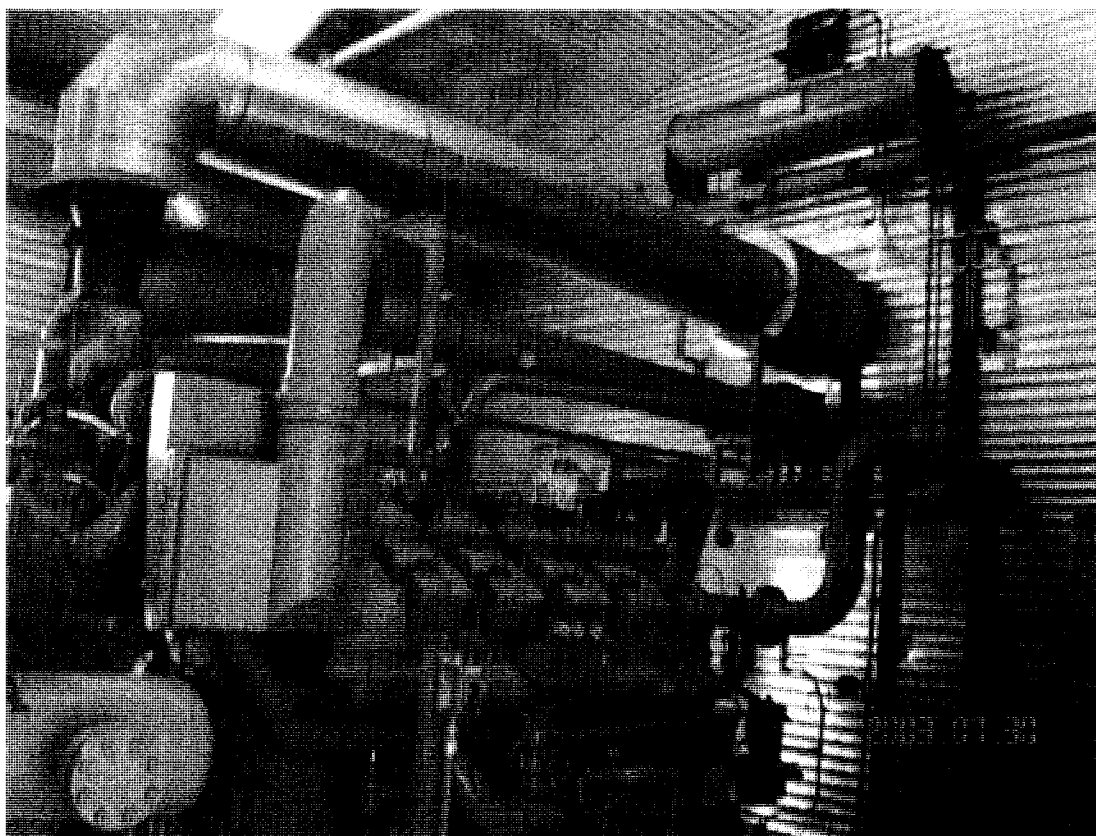


Figure 3.4: The natural gas IC engine in one compressor building.

times higher than for the stoichiometric version. From an economic perspective, the lean burn system is superior, and most units run in this mode. From an environmental perspective, the lean burn engine offers the advantage of low NO_x ; however, normal lean burn operation may not yield sufficiently low NO_x values to meet some regulations, and thus some operators use stoichiometric operation in certain locations (e.g., California). Although the base NO_x emissions are high from a stoichiometric engine, the end of tailpipe emissions can be reduced to acceptable limits, and below that of lean burn operation, through the use of a three-way catalytic converter (TWC), like those used on automobiles for the past two decades. If the NO_x is within acceptable limits with lean burn operation, catalytic converters are not usually used, and the emissions of methane are relatively high. A typical

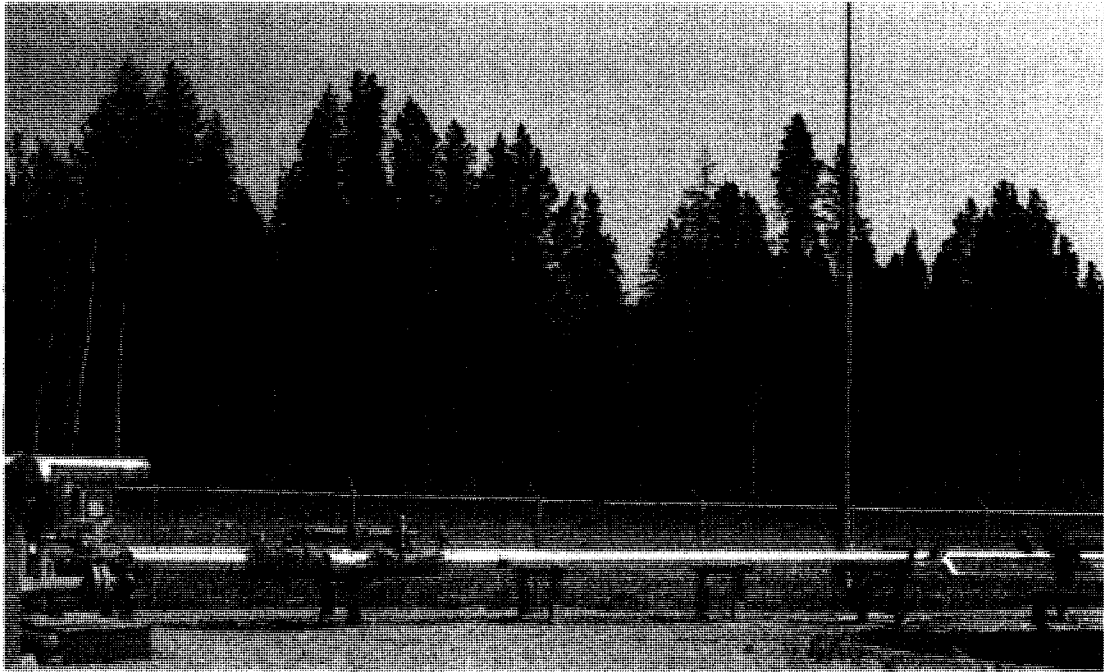


Figure 3.5: Natural gas pipeline and junction

115 litre displacement natural gas lean burn engine running at 1200 rpm produces about 61 tonnes per year of methane (1400 tonnes of carbon dioxide equivalent), which increases as the engines age (according to the data provided by Enerflex Inc.).

The second emission source is instrument vents, which result from the use of natural gas as the supply medium for the pneumatic instruments used to control, for example, temperature and pressure. Pneumatic devices are often powered by natural gas because the high-pressure gas is readily available. These devices, however, bleed natural gas into the atmosphere during normal operation. This gas may be collected as a concentrated stream and vented outside of the building.

The third source of methane emissions in compressor stations is leaking equipment. This source tends to be more prominent in older sites that are used to compress sweet natural gas. Because of the danger from sour natural gas (natural gas containing H_2S) leaks, stations that compress sour gas are much more tightly

monitored and controlled than those pumping sweet gas. Methane losses through the compressor seal can range up to the tens of tonnes per year, and a single leaking valve can yield up to 1000 tonnes a year. Although the methane from leaks is of high concentration at the leak source, it may quickly become diluted as it moves into the building and mixes with air, although in some cases the seal leaks may be collected and vented externally

To illustrate the magnitude of the emissions problem, numbers from a typical site are given. These data were provided by Clearstone Engineering, Calgary, Alberta. The site in question was a compressor station containing five compressors (four at 1650 hp and one at 1450 hp), a glycol dehydrator and two electric power generators. Natural gas was used to operate the instruments. Overall, 68% of the GHG emissions result from the fuel combustion in the engines, and the rest was mostly methane. Methane emissions from the building were about 930 tonnes a year, and a further 400 (estimated) tonnes per year resulting from incomplete combustion in the engines. The breakdown of the 930 tonnes was: 49% from instrument venting, 36% from the produced water tank vent, 7% from fugitives, 7% from the glycol dehydrator and 1% from non-leaking sources. The economic value of this methane at \$ 10 a GJ is about \$ 1,000,000 a year.

Compressor station

This chapter presents an evaluation of the possibilities and limitations of using the natural gas compressor building enclosure as a collector of emissions occurring inside it. Detailed analysis of airflow patterns and methane distribution, with influences of methane concentration, building openings, leak location and extraction rate of the emissions was performed using computer simulation. The results obtained are presented and discussed. This Chapter is an extended version of a paper titled, "Capturing fugitive methane emission from natural gas compressor station buildings" published in The Journal of Environmental Management, authored by Litto et al. (2007).

4.1 Modelling methane fugitive flow

The main objective is to collect and capture methane leaking inside the building and then direct the captured lean methane mixture to a catalytic combustion device, which in this case is a catalytic flow reversal reactor (CFRR). So the target in the capture operation is to meet the minimum feed quality required by the CFRR. The CFRR is discussed in Chapters 8 and 9.

4.1.1 Methodology

Industrial ventilation is required to satisfy indoor air quality requirements to achieve the best operational performance, and to help efficient removal of any emission/pollutants occurring inside the building enclosure. The detailed understanding of airflow patterns helps to improve the ventilation performance as well as to design the capture method for the emission/ pollutants originating inside the building. Computer simulation has been extensively and efficiently used in analyzing the details of indoor air flow patterns and distribution in building enclosures (Awbi, 1989), so it can help to study and analyse the emission capture strategies.

The focus of this work was to develop an understanding of the flow pattern of fugitive CH₄ emissions in a typical compressor building, and to show how CH₄ leaking inside the structure can be captured. As discussed later, it is desired to deliver a methane stream of about 1% by volume, and not to be less than 0.2% by volume, as this value is a feed quality requirement of the chosen mitigation equipment.

In exploring different scenarios, computer modelling was used to simulate the flow of the CH₄ in the building. The modelling was achieved by solving the appropriate partial differential equations that govern the conservation of momentum, mass and energy (see details of equations formulation in Section 4.2.1).

In numerical simulation, the flow domain is subdivided into a finite number of non-overlapping grids or regions, which are called volumes, cells or elements, and then the numerical technique is applied to solve the governing equations in an iterative manner. Techniques which are most popular in numerical simulations are finite difference, finite volume, finite elements, and spectral method (Versteeg et al., 1995). The finite difference methods are based upon approximations which permits replacing differential equations by finite difference equations in structured or unstructured grids. These finite difference approximations are algebraic in form and relate the value of the dependent variable at a point in the solution region to the values at some neighbouring points. The finite difference approximations usually are based on truncated Taylor series. The finite volume method is a spe-

cial case of the finite difference method, in which the integration of the governing equation is done over entire control volumes of the solution domain. The finite element method is a more powerful and versatile numerical technique for handling problems involving complex geometries and inhomogeneous media method (Versteeg et al., 1995). The finite element method uses simple piecewise functions valid on elements to describe the local variations of unknown variables. Spectral methods approximate the unknowns by means of truncated Fourier series or series of Chebychev polynomials; the approximations in this method are not local but valid throughout the entire computational domain, mostly used for specialized applications (Versteeg et al., 1995).

Computational Fluid Dynamics (CFD) uses a fundamental set of partial differential equations that describe the essence of the fluid flow to give an insight of actual transport phenomena occurring inside the flow region (in this case is the building enclosure) through numerical simulation thereby avoiding the need for expensive experiments. Also CFD makes the study of hazardous systems easier. Despite the advantages, the results from CFD should always be handled with caution, since there are errors introduced through assumptions, inaccuracy initiated due to numerical truncations, difficulties in setting boundary conditions, limitations of computer capacities as well the equation model can contribute to the uncertainties too. In this work, CFD was used to analyze and study the airflow patterns in the industrial building enclosure of a natural gas compressor station, to get insight of the airflow pattern which will help to determine an appropriate capture technology for the methane emissions occurring inside the building.

The numerical solution of the equations was done using a finite volume technique. A commercial software package, Airpak V2.1 was used. Airpak is a computational design tool for ventilation systems. Airpak uses the Fluent solver engine for concentration, energy and fluid flow calculations. The tool provides complete mesh flexibility, and allows the solution of flow in complex geometries using unstructured meshes (Fluent Inc., 2002). The solution domain was defined by the confining walls of the building. The engine, compressor, dehydrator, and other equipment were modelled as simpler rectilinear or cylindrical shapes as shown

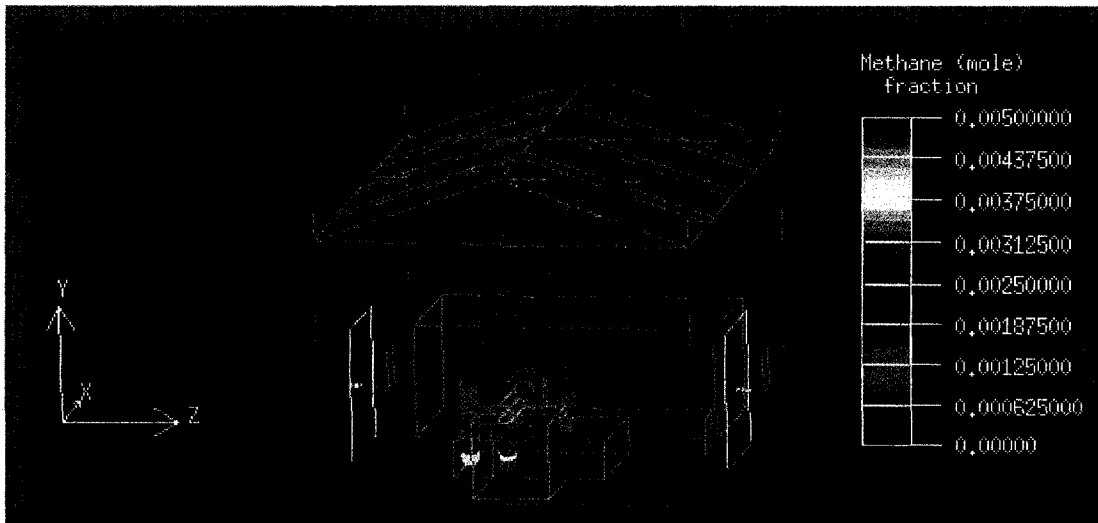


Figure 4.1: The small building as modelled in Airpak showing the sources of methane leakage in the building. The blocks represent equipment inside the building.

in Figure 4.1. The engine, compressor, dehydrator and exhaust pipe were treated as heat sources, and were the only source of heat in the building. The emission sources were imposed near the engine as shown in Figure 4.1. The three plumes of methane were modelled. Steady state numerical simulations were performed.

4.1.2 Description of building models

Airflow in a building enclosure is complex and can involve all three types of convection, i.e. natural, forced and mixed convection. In this work natural and mixed convection were considered.

Two buildings were modelled in this work. Both buildings were based on existing natural gas compressor stations located in the Province of Alberta, Canada. A typical expected range of emission rates was used, based on information from several sources, for example TransCanada PipeLines Limited and Clearstone Engineering Limited in some of their industry presentations that they made, and made available to us. The first (small) building model, is situated at Pembina BP energy

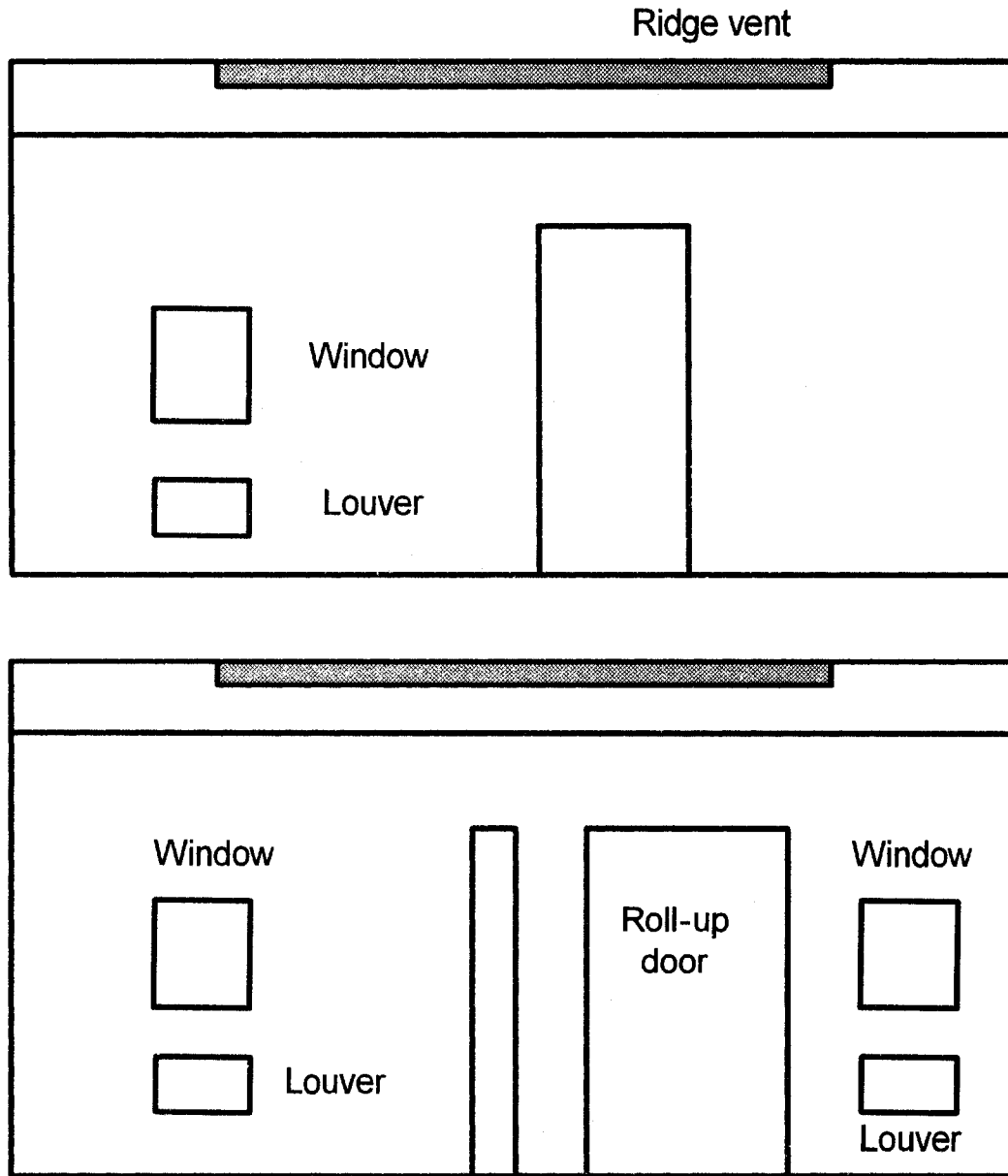


Figure 4.2: Two side views of the small building used as a model in this work. The top view is the south face with a single large door; the bottom view is the north face with the large roll-up door and a smaller door.

site. It houses a single combination of engine and compressor. The building is 12.7 m long, 7.3 m wide and 6.5 m high (see Figure 4.2). There are three louvers provided for ventilation, two doors on the north side (a large roll-up door, measuring 2.55 m wide by 4.37 m high and a smaller door measuring 1 m wide by 4.37 m high) and double doors on the south side measuring 1.91 m wide by 4.37 m high (see details in Figure 4.2). Three windows are present, but these windows together with the smaller north door are usually closed. The larger doors are often opened in the summer to provide additional ventilation, and are closed in the winter. A ridge vent along the top of the roof is used to assist extraction of building air. Fans are present to assist in ventilation, but are typically only used when large unexpected leaks occur.

The compressor is powered by a Waukesha Model L5108 GSI, 12 cylinder, 84 litre, turbocharged, intercooled 1050 HP natural gas engine. Estimated methane emissions from this engine are 61 tonnes a year, based on data provided by Enerflex Systems Ltd., Edmonton, Alberta.

The second building modelled is located at Marten Hill, Alberta and contained thirteen compressors. It is 77 m long, 9.9 m wide and 6.8 m high (see Figure 4.3). For ventilation, it has twelve louvers on the upper part of eastern wall. There are two large sliding doors, one each on the north and south ends, measuring 3.7 m wide by 3.1 m high, and seven exterior doors (measuring 1.0 m wide by 2.2 m high) each on the west and east sides. Also, there are seven emergency doors on the west side, but these are usually closed. A 0.5 m ridge vent along the top of the roof is used to assist extraction of building air. Fans are present to assist in ventilation, but again are typically only used when large unexpected leaks occur. In typical operation, eight out of thirteen compressors are running with the others being used as backup. These compressors are driven by Waukesha 7042 GSI natural gas fueled engines.

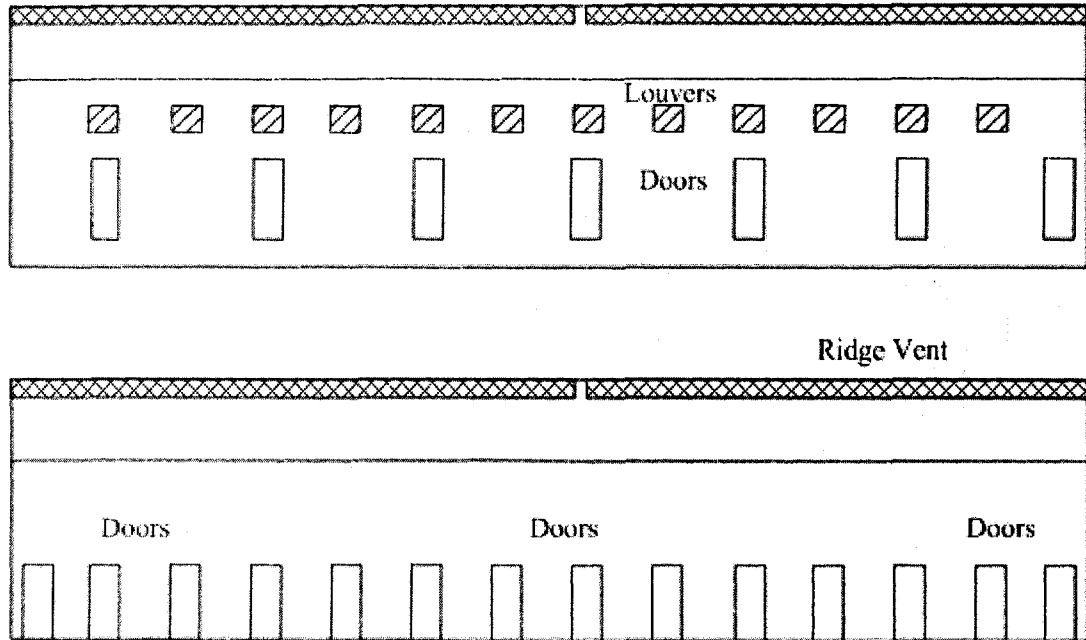


Figure 4.3: Two side views of the large compressor building used as a model in this work. The top view is the east elevation with seven exterior doors; the bottom view is the west elevation with seven exterior doors and seven emergency doors. The big sliding doors are on the south and north sides of the building, and are not shown in the drawing.

4.2 Turbulence modelling

It has been observed that most airflow in the building enclosure is turbulent (Chen, 1996). Turbulence can be identified as a chaotic state of fluid motion, and is characterized by irregularity, diffusivity, large Reynolds number, 3-D vortices fluctuations and dissipation. To predict and analyse the fluid flow accurately, the CFD requires appropriate models for turbulence. Generally, turbulence flows are predicted using three major approaches, which are:

Direct Numerical Simulation (DNS): The DNS method is the most exact way to model turbulence. The unsteady three-dimensional Navier Stokes equations are solved without averaging or approximation. However, this method

requires a very fine mesh and a very small time step to establish the flow field to the smallest length (Kolmogorov) scale (Rodi and Fueyo, 1993). This requires a very long computational time. In consideration of typical industrial building size and computational resources needed, simulation of indoor airflow is not realistic with this method.

Large Eddy simulation (LES): Deardorff (1970) hypothesized that the turbulent motion could be separated into large and small eddies. The main contribution to turbulent transport comes from the large-eddy motion, and the effect of small eddies are modelled by incorporating a subgrid scale eddy viscosity. The method came to be known as Large Eddy Simulation (LES). This method provides better results, however, a large computing resource is required. Therefore, LES is rarely applied for simulation of indoor airflows. Like DNS, LES requires computers that are more powerful than those typically available to be effectively applicable to room airflow simulation.

Turbulence transport models: In engineering, predictions of turbulent flow rely heavily on the statistical Reynolds Average Navier-Stokes (RANS) equations. The RANS equations, which look very similar to the original governing Navier-Stokes equation, describe the behaviour of the mean flow. This greatly reduces the computational expenses of solving the equation. However, averaging the Navier-Stokes equation to obtain RANS equation introduces closure problems. RANS models come in wide variety of forms. Each attempts to close the system in some physically realistic way, with the more complex models representing more of the underlying turbulence physics.

In developing RANS, detailed description of turbulent motion in all time and space is not of much interest. An averaging process can be used to decompose the instantaneous turbulent variables into the mean value and fluctuation parts,

$$\vec{\vartheta} = \bar{\vartheta} + \vartheta' \quad (4.1)$$

where ϑ can represent any of the velocity components, pressure or temperature. Most popular methods of statistical averaging used in turbulence decomposition are ensemble average and mass-weighted averages. A more comprehensive description of statistically averaging of turbulence variables can be found in the book by Libby (1996).

4.2.1 Model equations

The modelling of the building flow requires the solution of the governing conservation and transport equations. These include turbulent momentum, mass and energy balance equations that incorporate the effects of mixed or natural convection. Turbulence flows were predicted by the Reynolds Averaged Navier-Stokes Equations (RANS). RANS models come in wide variety of forms, each closes the system in some way, with the more complex models capturing more details of the underlying turbulence physics. The steady state RANS equations take the following form.

The continuity equation is given as follows:

$$\nabla \cdot (\rho \tilde{u}) = 0 \quad (4.2)$$

Equation 4.2 is the steady state continuity equation at a point in a compressible fluid (Bird et al., 2001).

The momentum transport equation (Bird et al., 2001) is:

$$\nabla \cdot (\rho \tilde{u} \tilde{u}) = -\nabla p + \nabla \cdot \tilde{\tau} + \rho \tilde{g} + \tilde{F} - \nabla \cdot (\overline{\rho u' u'}) \quad (4.3)$$

Where \tilde{F} represents an other forces term that may arise from resistance , etc., The steady state momentum equation contains two stress tensors one representing normal stress tensor and the other one is a turbulent stress tensor which is generally known as Reynold stress. The two tensors can be written as follows:

The normal stress tensor:

$$\tilde{\tau} = \mu \left[(\nabla \tilde{u} + \nabla \tilde{u}^T) - \frac{2}{3} \nabla \cdot \tilde{u} I \right] \quad (4.4)$$

The Reynolds stress is assumed to be proportional to the local mean velocity gradient in analogy to the normal viscous stress :

$$\overline{\rho u' u'} = \frac{2}{3} k_{te} I - \mu_t (\nabla \tilde{u} + \nabla \tilde{u}^T) \quad (4.5)$$

Where μ_t is the turbulent (eddy) viscosity, which is not a fluid property like the molecular viscosity, but it is a flow property that depends strongly on the state and intensity of turbulence. k_{te} is the turbulent kinetic energy and the identity matrix I represents the Kronecker delta.

Species balance equations for each species , Y_i , involved in the system are represented by a convection-diffusion equations which can be written as (Bird et al., 2001):

$$\nabla \cdot (\rho \tilde{u} Y_i) = \nabla \cdot J_i + S_{h,i} \quad (4.6)$$

Equation 4.6 solve for N-1 species (N being a total number of species in the system). For turbulent flow, the mass diffusion term is calculated with the following expression.

$$\tilde{J}_i = - \left(\rho D_{i,m} + \frac{\mu_t}{Sc_t} \right) \nabla Y_i \quad (4.7)$$

where

$$Sc_t = \frac{\mu_t}{\rho D_t} \quad (4.8)$$

The energy equation for fluid phase is written in terms of sensible enthalpy h , as:

$$\nabla \cdot (\rho h \tilde{u}) = \nabla \cdot [(k + k_t) \nabla T] + S_h \quad (4.9)$$

Enthalpy can be estimated as

$$h = \int_{T_{ref}}^T C_p dT$$

and k and k_t are molecular conductivity and the conductivity due to turbulence respectively. The conductivity due to turbulence can be estimated as:

$$k_t = \frac{C_p \mu_t}{Pr_t}$$

The source term S_h represents other volumetric energy sources.

For multicomponent mixing flows, the transport of enthalpy owing to species diffusion can have significant effect on the enthalpy field. It can be estimated from the following term:

$$\nabla \cdot \left[\sum_{i=1}^n (h_i) J_i \right] \quad (4.10)$$

When the Lewis number, defined as:

$$Le_i = \frac{k}{\rho C_p D_{i,m}} \quad (4.11)$$

is far from unity this term should not be neglected.

For conducting solids, the energy balance equation includes the heat flux due to conduction and volumetric heat sources within the solid:

$$0 = (k\nabla T) + S_h \quad (4.12)$$

The additional term on these Reynolds-averaged transport equations accounts for the turbulence, and many RANS models assume a constitutive algebraic relationship between the Reynolds stress tensor and the mean flow gradients. The most common relation is eddy (or turbulent) viscosity model based on the Boussinesq assumption that the turbulent stress tensor can be expressed in terms of the mean rate of strain in the same way as the viscous stress for Newtonian isotropic fluid, except the coefficient of molecular viscosity is replaced by eddy viscosity. The same principle applies to other constitutive relations for the flux of species and heat.

Classic eddy viscosity models include mixing length models such as the zero equation, one equation and two equation eddy viscosity models. The two equation model, often referred to as the standard $k-\epsilon$ model, is the most widely used turbulence model in engineering practice. There are several variations of $k-\epsilon$ model. Many studies have used the $k-\epsilon$ model for indoor airflow analysis (Awbi, 1989; Stathopoulos and Zhou, 1995; Chen and Xu, 1998).

To decrease computational time, Chen and Xu (1998) developed a zero equation model specifically for modelling building enclosure airflows and heat transfer. This

model uses an algebraic equation to calculate the local eddy viscosity, instead of the differential equation used for the $k-\epsilon$ models. Chen and Xu (1998) tested this model on four airflow types: displacement ventilation, natural ventilation, forced convection and mixed convection. They found good agreement between the indoor zero equation model predictions and experimental data, and, in some cases the zero equation model outperformed the $k-\epsilon$ model. Srebric et al. (1999) provided further validation of this approach by comparing the predictive ability of the zero equation models to experimental data for three additional cases of airflow in the enclosure. These included natural convection with infiltration, forced convection and mixed convection with displacement ventilation. They found good agreement between the computed and measured air velocity and temperature profiles. The four eddy viscosity models used in Airpak v2.1 are the mixing - length zero equation turbulence model, the indoor zero equation turbulence model, the standard $k-\epsilon$ and the renormalization group (RNG) $k-\epsilon$ models.

4.2.2 Boundary conditions

The boundary conditions are important for the solution of fluid flow systems. The accuracy of the flow prediction is sensitive to these boundary conditions and the assumptions used (Awbi, 1989), because the flow inside the enclosure is driven by the boundary conditions. The following boundary conditions were imposed.

Free boundary condition: In this case it is assumed that the following condition holds at all major openings.

$$\frac{\partial u_i}{\partial x_i} = \frac{\partial T}{\partial x_i} = \frac{\partial p}{\partial x_i} = 0 \quad (4.13)$$

$$\text{or simply } \nabla \vartheta \cdot n = 0 \quad (4.14)$$

This means that there is zero gradient normal to the free boundary surface. All dependent variables are assumed unknown at the inflows. The variable u , T and p at the free boundary will assume the value of the source where flow originates, while p will assume the value of sink.

Free boundary condition was applied to all openings (including door, ridge vent, louvers) during free flow mode of operation. For forced extraction, the mass flow rate was specified on the ridge vent but for the other openings, the free boundary condition continued to be imposed. When the external wind effect was investigated, velocity was imposed on the side facing the wind direction.

Solid boundary conditions: This type of boundary condition includes walls, floor, roof, and all equipment in the building enclosure. The general boundary condition applied was a no slip condition at the solid surface.

For transport equation:

$$\tau = \mu_{eff} \frac{\partial u_i}{\partial x_i} \quad (4.15)$$

A convective heat flux for the energy balance equation is used

$$q = h(T_w - T) \quad (4.16)$$

where the heat transfer coefficient, h , at the boundary surface used in Equation 4.16 is calculated by the following relationship, if the $Le \gg 1$:

$$h = \frac{\mu_{eff} C_p}{Pr_{eff} \nabla x_j} \quad \text{and} \quad \mu_{eff} = \mu + \mu_t \quad (4.17)$$

For the equipment inside the building, the surface temperatures were fixed for those bodies generating heat, which include the engine, compressor and exhaust pipe. These units provide the heat sources inside of the building. The mass flux at the walls was set to zero. Boundary conditions also include the ambient (exterior) condition. In this way, the overall influence of dynamic weather conditions on airflows is established.

4.2.3 Solution methods

Airpak V2.1 uses the control volume method to convert governing equations, presented in the previous section, to algebraic equations that can be solved numerically. This technique integrates the governing equations at each control volume, which results in discrete governing equations that conserve each quantity on control volume basis. The discretized governing equations are linearized and take an implicit form with respect to dependent variables.

To accelerate the convergence, the algebraic multi grid method, with first order up winding and under-relaxation was used. Unstructured meshes were used in this work, fine meshes were used near objects where gradients of temperature and velocity might be very high, and coarse meshes were applied to all other places where the gradient was small. For the small building about 300 000 hexahedral mesh elements were used, and for the large one about 3 500 000 hexahedral elements were used. Mesh refinement studies indicated this to be sufficient.

In natural convection, flow is buoyancy-driven, where the buoyancy is caused by the change in fluid density due to variation of temperature and/or fluid concentration in the domain. Since in this case, the concentration of interest is very small thence its variation in the the domain is negligible. But in Airpak, Boussinesq model and/or the ideal gas law is used in calculating the gas density in which the effect of concentration was either indirectly incorporated in the formulation or its influence in density change was considered negligible. Airpak uses the the Boussinesq approximation to account for the density driven flow, along with the ideal gas assumption. This model treats density as a constant value in all solved equations, except for the buoyancy term in the momentum equation:

$$(\rho - \rho_0) \approx \rho_0 \beta (T - T_0) \quad (4.18)$$

where ρ_0 is the (constant) density of the flow, T_0 is the operating temperature, and β is the thermal expansion coefficient. This equation is obtained by using the Boussinesq approximation $\rho = \rho_0(1 - \beta T)$ to eliminate ρ from the buoyancy term. This approximation is accurate as long as changes in actual density are small;

specifically, the Boussinesq approximation is valid when $\beta(T - T_0) \ll 1$

General assumptions:

The following assumptions were taken into consideration during problem formulation. These assumptions are:

1. The flow is steady state
2. Flow enters or leaves the building enclosure at the openings only, no flow due to infiltration.
3. Ambient conditions are uniform and constant as specified

4.2.4 Preliminary experiments

As stated above, Airpak v2.1 is equipped with four different turbulence models which can be used in this work. Stability and suitability of these models to solve the current problem needed to be evaluated, to find one which will give an optimum solution and stable results. Preliminary experiments were done to achieve this.

The stability of the residual was the deciding factor in choosing the optimal turbulence model. During the solution process, convergence can be monitored dynamically through residual plots. The residual normally decays towards zero as the solution converges, and thus can help to determine the stability of the model and hence decide on a suitable and optimal turbulence model.

Keeping all other conditions constant, the preliminary experiments were conducted using the four turbulence models in turn. From the residual plots obtained as presented in Figure 4.4 (a - d), both k- ϵ models and the mixing length zero equation model do not satisfy the continuity equation, as their continuity residuals blow-out with time, and hence cause instability in the flow. The indoor zero equation model was stable and satisfied the continuity equation quite well, and its residuals continue to decay as the simulation progress.

Results of the preliminary experiments indicated that the k- ϵ models and mixing length zero equation model have stability problems, particularly on the continuity

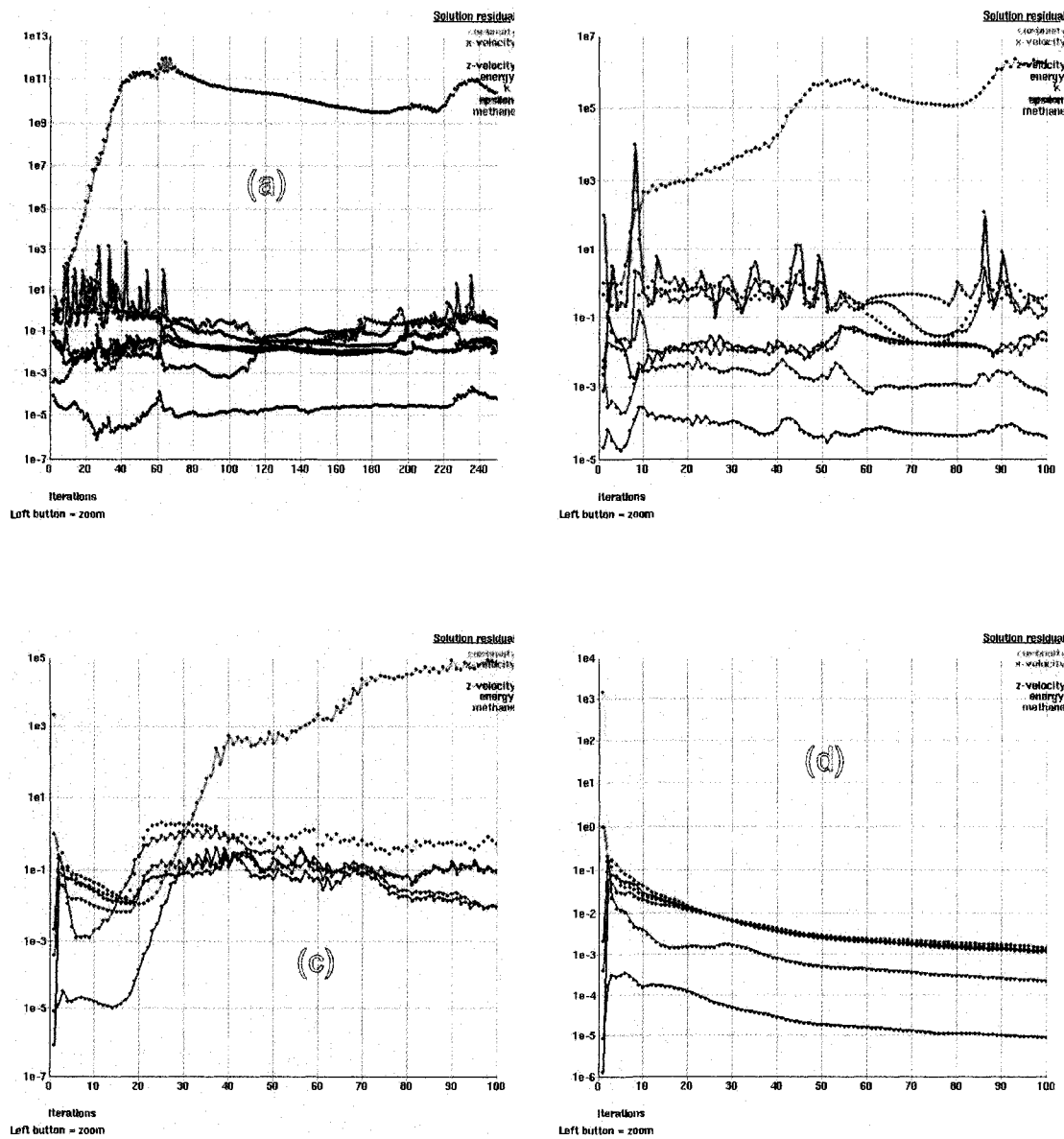


Figure 4.4: Residual plot of trial experiments for assessing the suitability turbulence models. The residuals were obtained by using the: (a) standard k-ε model. (b) RNG k-ε Model, (c) mixing length zero equation model and (d) indoor zero equation model.

equation, whilst the indoor zero equation model proved to be very stable. Chen and Xu (1998) recommends that the k- ϵ model should be used for fully developed turbulence flows, and the Airpak manual suggests that k- ϵ model should be used for flow with very high Reynolds number. Based on these arguments and the preliminary experiments results together with the fact that the Reynolds number of the flow in this work is about 4200 which indicates that the flow is in transition turbulence. Hence, the indoor zero equation model was chosen for reason of stability of simulated flow. In this model, the eddy viscosity is calculated by the relation proposed by Chen and Xu (1998) as follows:

$$\mu_t = 0.03874\rho vL \quad (4.19)$$

The indoor zero equation turbulence models can be used in natural, forced and mixed convection as well as displacement ventilation, where L is the distance to the nearest wall and v is the magnitude of the local velocity.

4.2.5 Modes of operation

The use of the stack effect, which utilizes the buoyancy principle, is the most common strategy in ventilation operation. The strategy uses the density difference between warm air inside the building and the cooler air outside. In this mode of operation, building outflow is expected to occur through the ridge vent located at the apex of the roof. One of the key parameters, especially when retrofitting a building to mitigate emission, is to minimize the effect on operation by the implementation of mitigation technology. Indeed, it is not permitted to stop operation, for retrofitting to be done. Therefore, it was assumed that collection of CH₄ emissions will occur through the ridge vent. The following sections begin by illustrating the flow patterns that are expected in existing situations, that is, a model with natural flow and a free boundary at the ridge vent ("free flow" mode). In the second part, a forced extraction rate was imposed at the ridge vent, which is equivalent to installing an extractor that operates at a specified flow rate. The effect of parameters on the capture efficiency and CH₄ concentration in the effluent stream

were investigated. The parameters are operating modes of building ventilation openings (doors, louvers, etc), ambient conditions, ridge vent size and leak rate.

4.3 Results

Results are presented in four different categories based on the experimental conditions used. These consist of the two buildings with free flow and forced extraction from each one.

4.3.1 Free flow in small building

The first results presented were obtained with quiescent air surrounding the small building at an ambient temperature of 293 K. For these simulations, the free flow mode was used. Four combinations of operating mode were explored, denoted as follows: Option 1, all doors closed, Option 2, only north side roll up door open; Option 3, north roll-up and south door open; and Option 4, all of the doors were open. Two ridge vent sizes were used, with areas of 5 m² and 1 m². Three fugitive leak sources were imposed near the engine, with a total leak rate of either 2.7 kg/h or 270 kg/h. Figure 4.1 shows the position of imposed leaks. The principal variables of interest are the fraction of leaking CH₄ flowing through the ridge vent, the average CH₄ concentration in this stream, the temperature of the stream and the total mass flow of the stream. Table 4.1 shows a summary of the results obtained for the above conditions.

Several trends are evident from the data. If we consider that the methane flowing through the ridge vent can be captured, we see that the best capture rate is obtained when all of the doors are closed. With the louvers located near the bottom of the building, and the temperature within the building an higher than ambient, the stack effect naturally leads to a flow upwards. As the doors are progressively opened, more methane flows through these openings, giving a low capture rate. There is no meaningful difference between capture rates for the different vent sizes when the doors are closed; however, the larger vent is generally superior

Table 4.1: Summary of results for the small compressor building with quiescent air at 293 K operated in free flow mode. Conditions at ridge vent.

Option	Leak rate [kg/h]	Vent size [m ²]	%Methane captured	Mole% methane	Mass flow rate,[T/h]	Temperature [K]
1	2.7	5	97.4	0.037	10.4	309
2	2.7	5	88.0	0.014	24.5	302
3	2.7	5	82.8	0.013	24.8	302
4	2.7	5	65.3	0.010	24.9	302
1	270	5	96.3	0.43	10.5	306
2	270	5	78.9	0.14	25.0	301
3	270	5	70.0	0.13	25.1	301
4	270	5	64.8	0.11	27.5	300
1	2.7	1	99.7	0.061	6.4	309
2	2.7	1	36.1	0.023	6.4	306
3	2.7	1	32.4	0.021	6.2	306
4	2.7	1	29.4	0.019	6.1	306
1	270	1	98.1	0.67	6.8	305
2	270	1	36.5	0.25	7.0	304
3	270	1	13.5	0.093	7.0	300
4	270	1	22.3	0.17	6.5	301

when the doors are opened. Concentration of methane in the ridge vent stream is generally below the targeted effluent concentration when the leak rate is low, although it increases to an acceptable level for high emission rates. For these levels of emissions, however, it would likely be better to eliminate the leaks rather than simply to mitigate them by combustion. The temperature of the effluent stream is the highest when the doors are closed, which corresponds to the lowest mass flow rate. The temperature rise is fairly low in all cases. Note that under free flow mode the total exchange rate in the building corresponds to about 13 building changes

Table 4.2: Summary of results for the small compressor building with an imposed wind velocity of 2 ms^{-1} blowing from north to south. Operated in free flow mode at 293K. The leakage rate was 2.7 kg/h. Conditions at the ridge vent

Option	Vent size [m ²]	%Methane captured	Mole% methane	Mass flow rate, [T/h]	Temperature [K]
1	5	98.6	0.037	9.2	304
2	5	99.4	0.013	25.0	300
3	5	65.2	0.009	23.2	300
4	5	48.5	0.006	23.1	300
1	1	98.2	0.086	4.5	302
2	1	38.2	0.025	6.1	301
3	1	15.3	0.015	4.0	300
4	1	16.0	0.016	4.1	300

per hour.

Table 4.2 summarizes the results obtained for the small compressor building with an imposed velocity of 2 m/s blowing from north to south. The imposed wind was approximated the effect by imposing an additional input velocity on the open doors. This method is an approximation, but serves to illustrate the effect of additional airflow through the doors. In any case, the capture rate with the doors open remains low. The ambient temperature was 293 K and the leakage rate was 2.7 kg/h. There is little effect when the doors are closed. When the north door is open and the others closed, a slight increase in the capture rate is observed, whilst in other cases the capture decreases. The concentration is also below the minimum target desired.

Figure 4.5 shows the effect on the mass flow rate through the ridge vent as the temperature outside the building is lowered. These results were obtained with a leak rate of 2.7 kg/h with the doors closed. From the graph it can be observed that the mass flow rate decreases as the ambient temperature falls, and when the ambient temperature is below 0°C the flow through the ridge vent is positive,

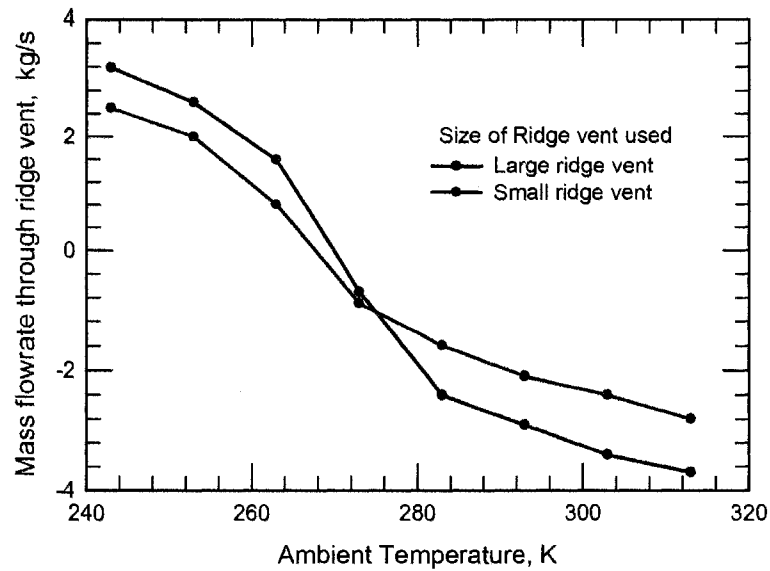


Figure 4.5: Effect of external temperature on the mass flow rate through the ridge vent. A negative value indicates a flow out of the building.

which means the flow direction is into the building. This effect is related to the pressure differential between the inside and outside of the building, which in turn depends on the buoyancy effects generated by the temperature inside. Figure 4.6 shows the change in the pressure profile (difference between internal and external pressure) as the ambient temperature changes. At high ambient temperature, the external pressure gradient decreases faster than the internal pressure, thus forcing flow out through the ridge vent. As the temperature falls, the rate of change within the building also changes, until at low temperature the pressure at the top of the building is higher outside than inside. This pressure differential forces flow inwards through the ridge vent. Figure 4.7 shows the effect on the circulation pattern as a function of the ambient temperature. The complexity of the flow pattern, and the temperature effect is evident. The methane exits through the louvers and in this case, no methane can be captured at the ridge vent.

In the results discussed above, the building was considered to have no obstacles on flow space above the engine, compressor, etc. Simulations were repeated with

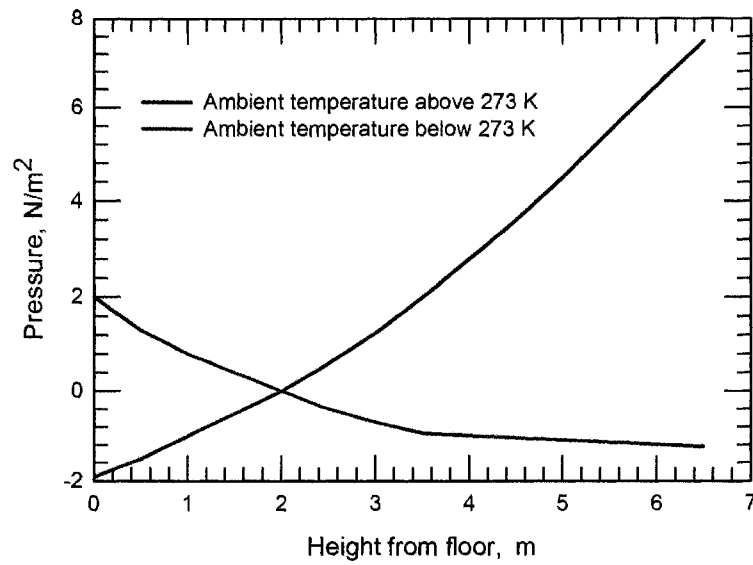


Figure 4.6: Pressure profile in the middle of the building as a function of the external temperature. The pressure profile depends on the temperature.

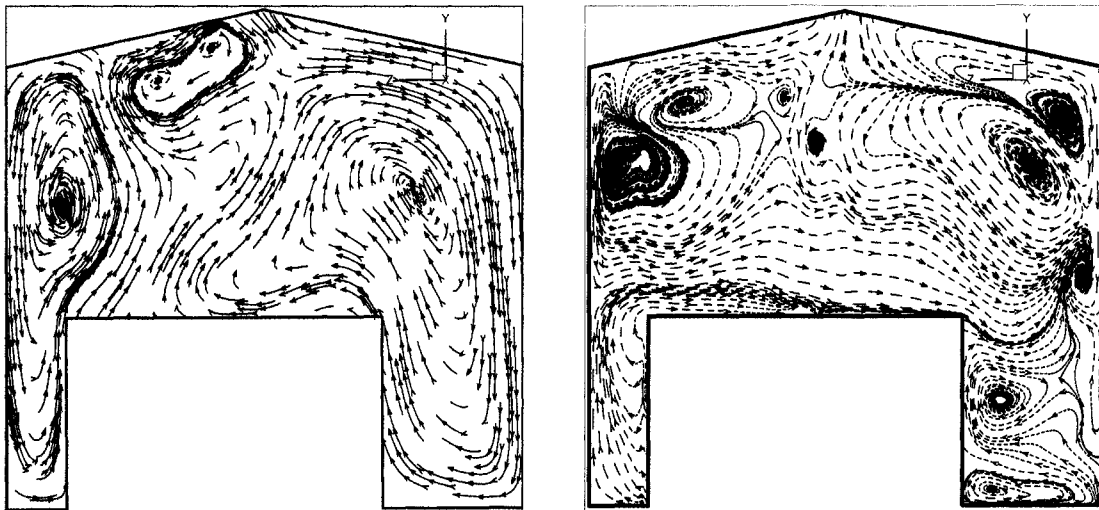


Figure 4.7: Airflow pattern inside the building for (left) ambient temperature below 273 K and (right) ambient temperature is above 273 K.

Table 4.3: Summary of results obtained for the small compressor building with quiescent air at 293 K operated in free flow mode, with added piping in the building. conditions at the ridge vent.

Option	Leak rate [kg/h]	vent size [m ²]	% Methane captured	Mole % methane
1	2.7	5	93.5	0.034
2	2.7	5	91.8	0.013
3	2.7	5	88.9	0.013
4	2.7	5	85.6	0.011
1	270	5	97.7	0.45
2	270	5	82.5	0.15
3	270	5	77.3	0.14
4	270	5	64.8	0.11
1	2.7	1	88.5	0.052
2	2.7	1	49.1	0.025
3	2.7	1	39.5	0.020
4	2.7	1	39.9	0.020
1	270	1	99.9	0.71
2	270	1	32.7	0.23
3	270	1	43.3	0.10
4	270	1	8.4	0.067

some additional piping added in the flow space, and the results are summarized in Table 4.3. The general trend is the same as observed before, although some variations were seen in methane capture and concentration.

4.3.2 Forced extraction in small building

Simulation of the free flow mode of operation gives a good insight into the nature of the flow patterns within a typical building. The general observation is that for

a low leakage rate the concentration of methane at the ridge vent is below the minimum target required. This low concentration is the result of the high mass flow rate that is induced by natural convection forces. The large flow rate implies that a large reactor would be required, which adds unnecessarily to the capital cost. Further, for low ambient temperature, the natural flow rate is through the vent into the building, that is, the methane emissions leave via the louvers, and not the ridge vent. Considering that some extraction device is required to direct the effluent into the reactor, the effect of controlling the exhaust gas flow rate through the ridge vent was investigated, by imposing a constant mass flow rate at the ridge vent.

Experiments on the controlled extraction mode of operation were performed using building operating Option 1 and 2 only, since these were the options that gave a promising result in the free flow experiments. Several extraction rates combined with different leak rates were used. Figure 4.8 shows the effect of extraction rate on the fraction of methane recovered at three different leak rates with an ambient temperature of 303 K. The operating mode was Option 1, all doors closed. It is seen that the fractional recovery is essentially independent of the leak rate, and depends only on the extraction rate. Above about four building changes an hour essentially all of the leaking methane is captured. Figure 4.9 shows how the concentration of the methane in the extracted stream varies with the extraction and leakage rates. In this case, it is clear that the methane concentration increases with leak rate, and decreases with extraction rate. These results follow intuitively from normal dilution rules. It is clear from this figure that controlling the extraction rate can give suitable feed for the CFRR (between 0.1 and 1% volume CH_4). Figures 4.10 and 4.11 show the effect of extraction rate on the fraction of methane recovered and concentration of methane in the extracted stream respectively for operation with Option 2. It is clear that methane concentration and capture rate are greatly reduced by opening the large doors.

Figures 4.12 and 4.13 show the velocity patterns in the building for Options 1 and 2 respectively. It is clearly seen that the buoyancy effect induces strong recirculation patterns, which are expected to cause efficient mixing of the methane, which leads to difficulty in capturing concentrated methane emissions. Strong

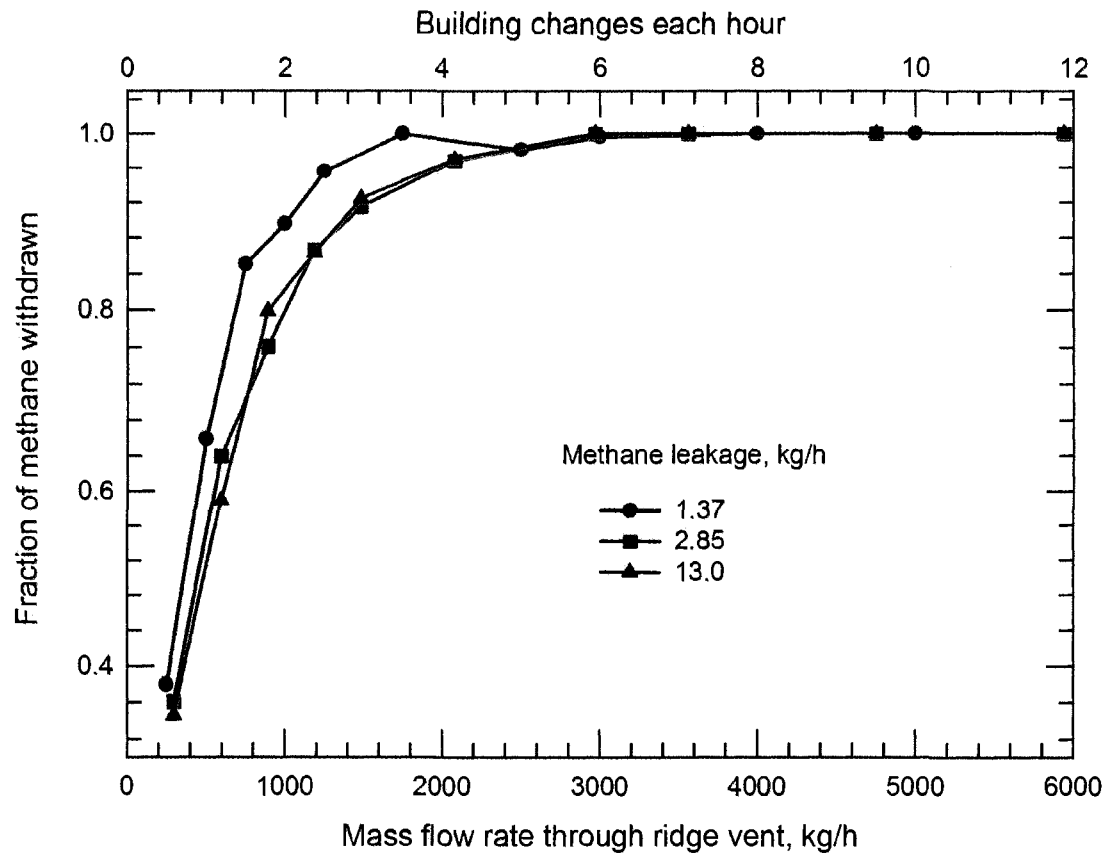


Figure 4.8: Fraction of methane captured through ridge vent using forced extraction in the small building with doors closed, at three leak rates. Above about four room changes an hour most of the methane is captured. The ambient temperature was 303K.

upward flows are seen around the hot engine. The effect of ventilation openings (doors and louvers) on the fugitive methane capture can be observed by comparing the velocity patterns in Figure 4.12, (Option 1) to those in Figure 4.13 (Option 2). In Figure 4.12, air enters only through the louvers, and the gas exits only through the ridge vent after being mixed in the building. In Figure 4.13 (b), it is seen that significant exchange of building and external air occurs through the open door. The cold air flows into the building at the bottom of the opened door, mixes with the

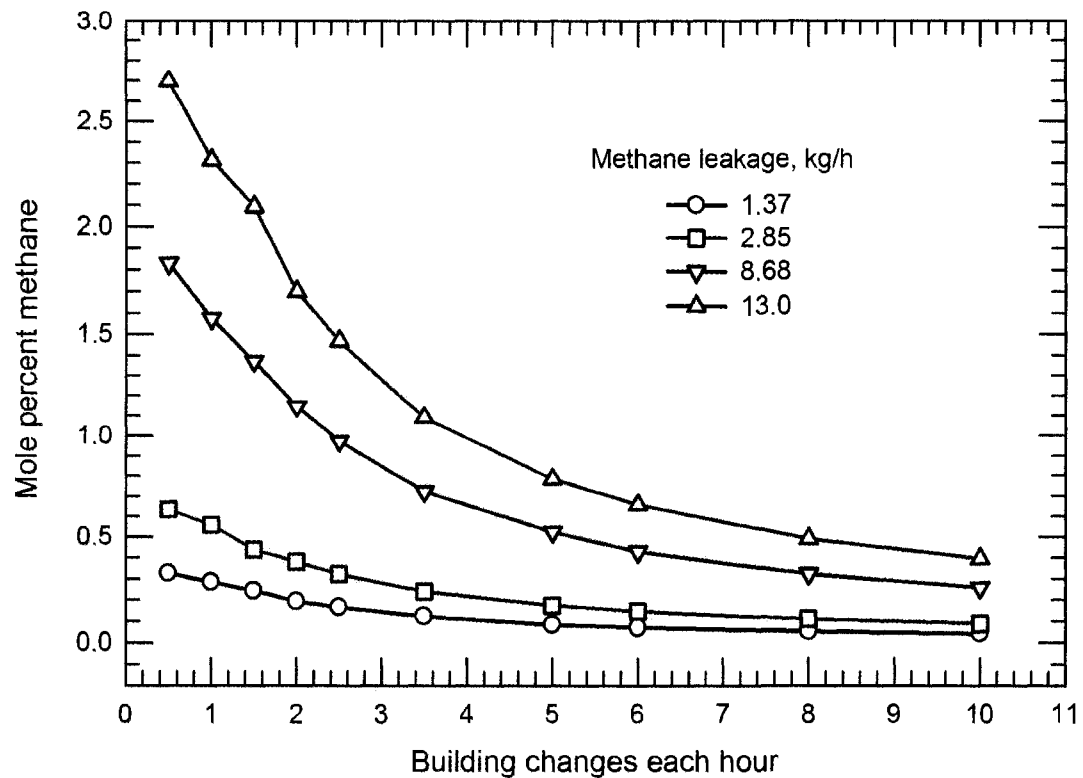


Figure 4.9: Mole percentage of methane in the ridge vent effluent obtained using forced extraction from the small compressor building with the doors closed. The ambient temperature was 303K. The effect of extraction rate and leakage rate are shown.

gases inside the building and then flows out the building at the top of the opened door. This makes the maximum capture of the fugitive methane impossible, and explains why earlier it was suggested that the best way to operate is with all doors closed. It is clear that opening the doors has a strong effect on the flow and recirculation patterns.

Methane mole fraction profiles in the building are shown in Figures 4.14 and 4.15. Generally, speaking, the CH_4 mole fraction at the bottom of the building is lower, and increases as one ascends to the top of the building. Figure 4.14 shows

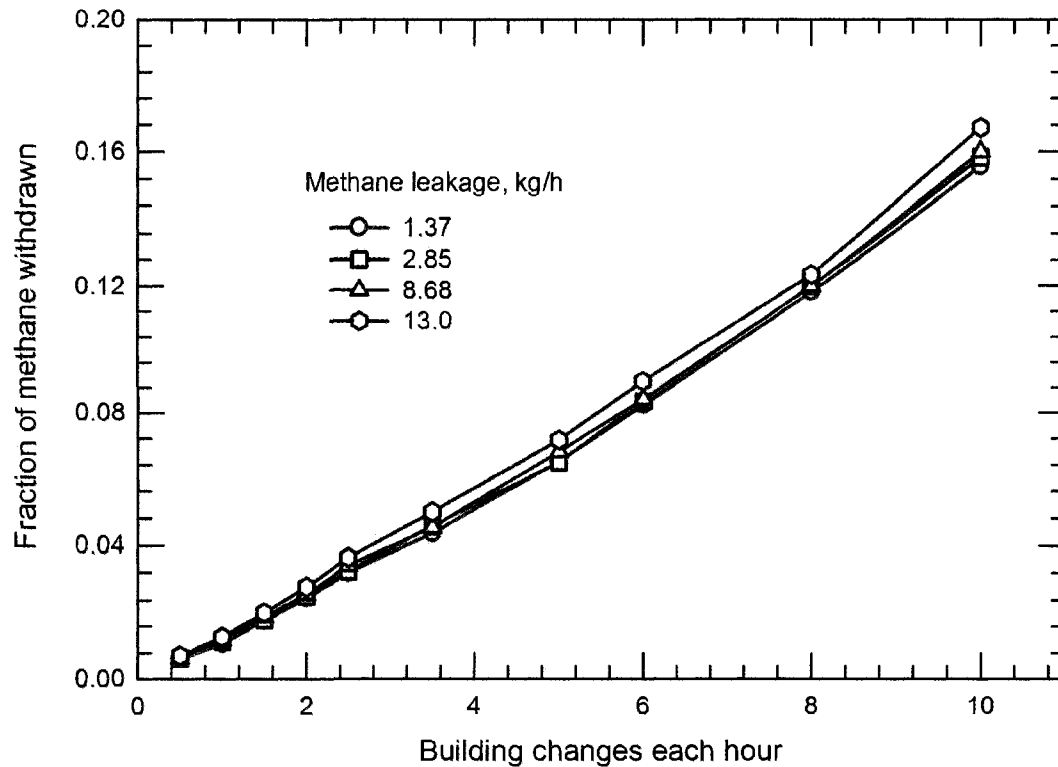


Figure 4.10: Fraction of methane captured through ridge vent using forced extraction in the small compressor building with the large roll-up door opened. The ambient temperature was 303K.

that by closing the doors, the goal of raising the concentration of methane in the captured stream to meet the target requirements can be achieved. Operating with Option 2, where the large roll-up door is open, not only increases the air dilution inside the building but also provides an escape route for the fugitive methane emitted in the building. Profiles of methane mole fraction shown in Figure 4.15 suggest that with the doors open, the concentration of methane in the building will be very low.

In the free flow mode, the flow rate through the ridge vent was affected by the ambient temperature. Thus, when operating with ambient temperature below 273 K, the net flow through the ridge vent was into the building. When imposing a

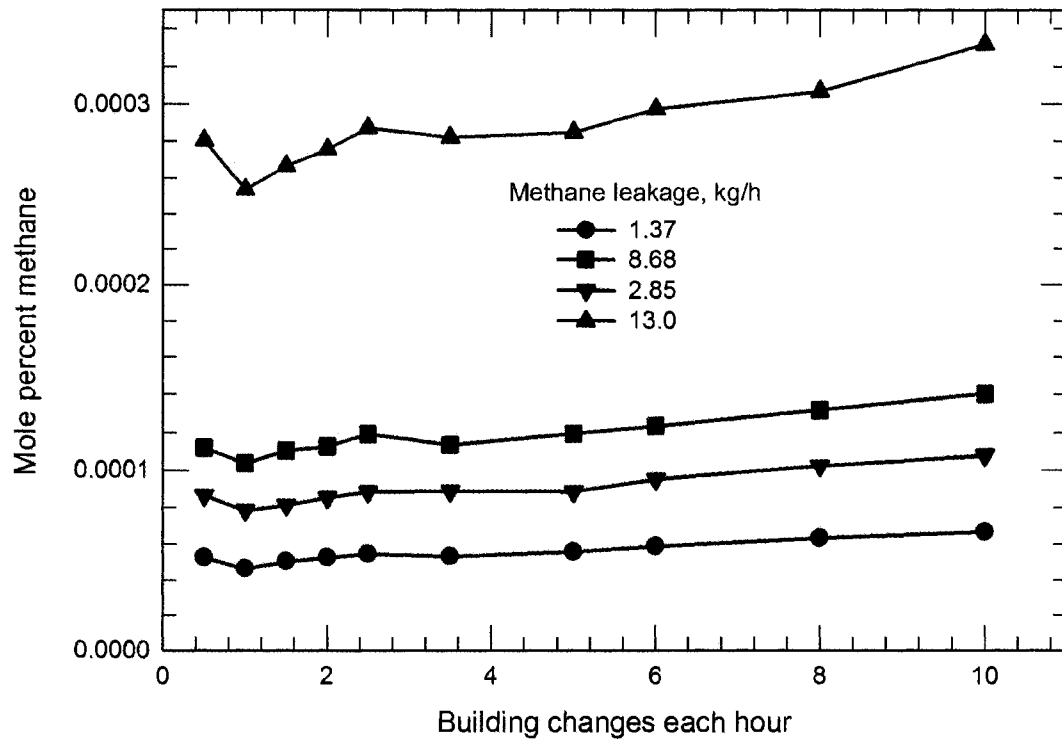


Figure 4.11: Mole percentage of methane in the ridge vent effluent obtained using forced extraction from the small compressor building with the roll-up door opened. The ambient temperature was 303K. The effect of extraction rate and leakage rate are shown.

flow at the vent, this reversal is obviously impossible. To test the effect of ambient temperature, simulations were performed with ambient temperature below 273 K, and no effect on the flow was observed. Typical results are shown in Figure 4.16 and 4.17. The results are essentially the same as those observed with ambient temperature is above 273 K (see Figure 4.8 and 4.9). Thus, ambient temperature has essentially no effect on the flow rate or concentration of effluent of the ridge vent effluent.

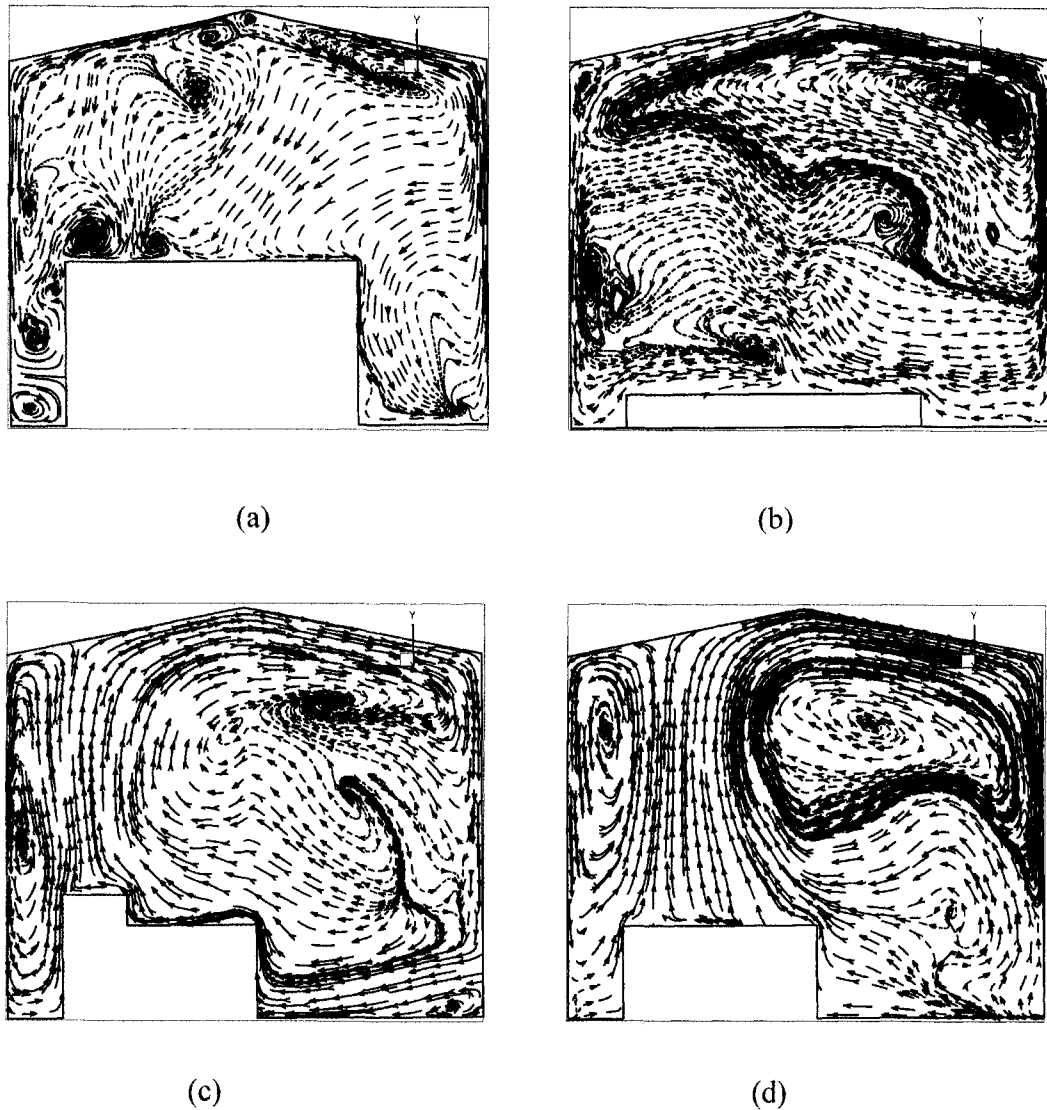
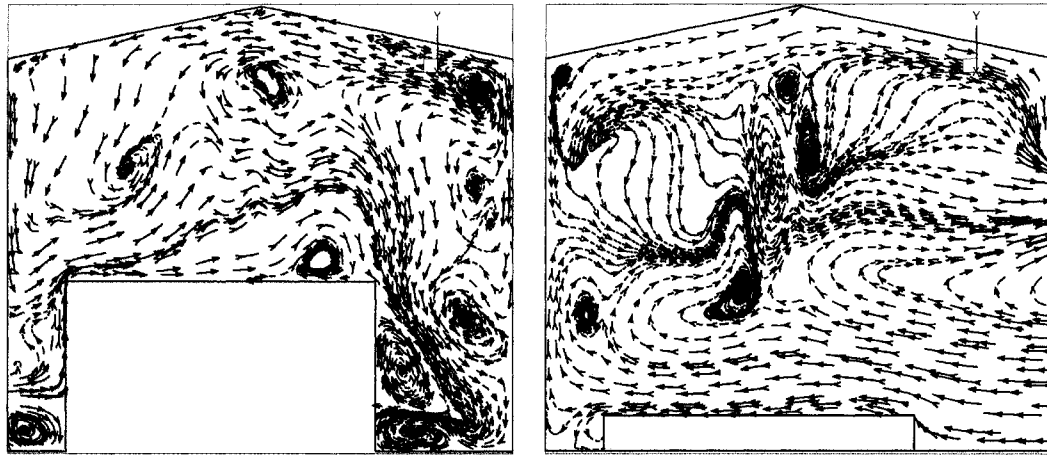
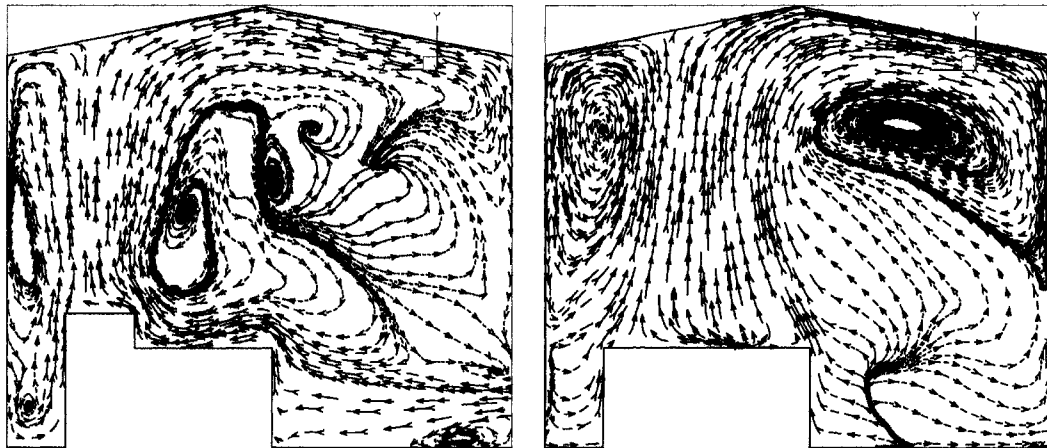


Figure 4.12: Velocity vector in the small compressor building operating with option 1 under controlled extraction. The velocity vectors were taken : (a) at the south side louvers position. (b) at the roll-up door position. (c) at the engine, turbocharger and exhaust pipe position, which is the hottest position in the building and near the north-east louver. (d) slightly further along the engine position. Plane of vector is the building cross section.



(a)

(b)



(c)

(d)

Figure 4.13: Velocity vector in the small compressor building operating with option 2 under controlled extraction mode. Building slices taken at the same position as in Figure 4.12.

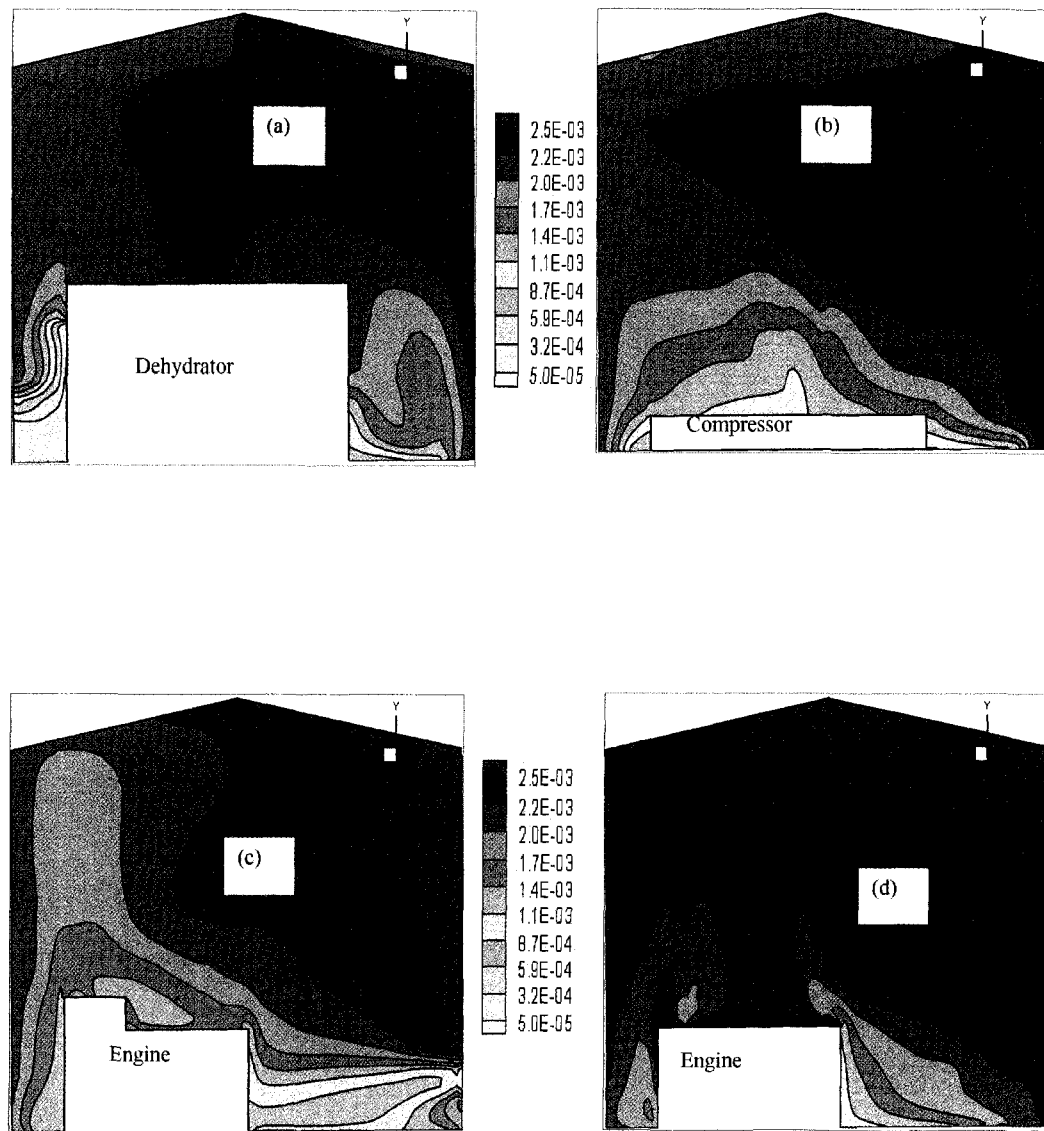


Figure 4.14: Profile of methane mole fraction in the small compressor building operating with option 1 under controlled extraction mode. The mole fraction profiles were taken at : (a) at the south side louvers position. (b) at the roll-up door position. (c) at the engine, turbocharger and exhaust pipe position, which is the hottest position in the building and also corresponds to position of the north-east louver, and (d) the engine position.

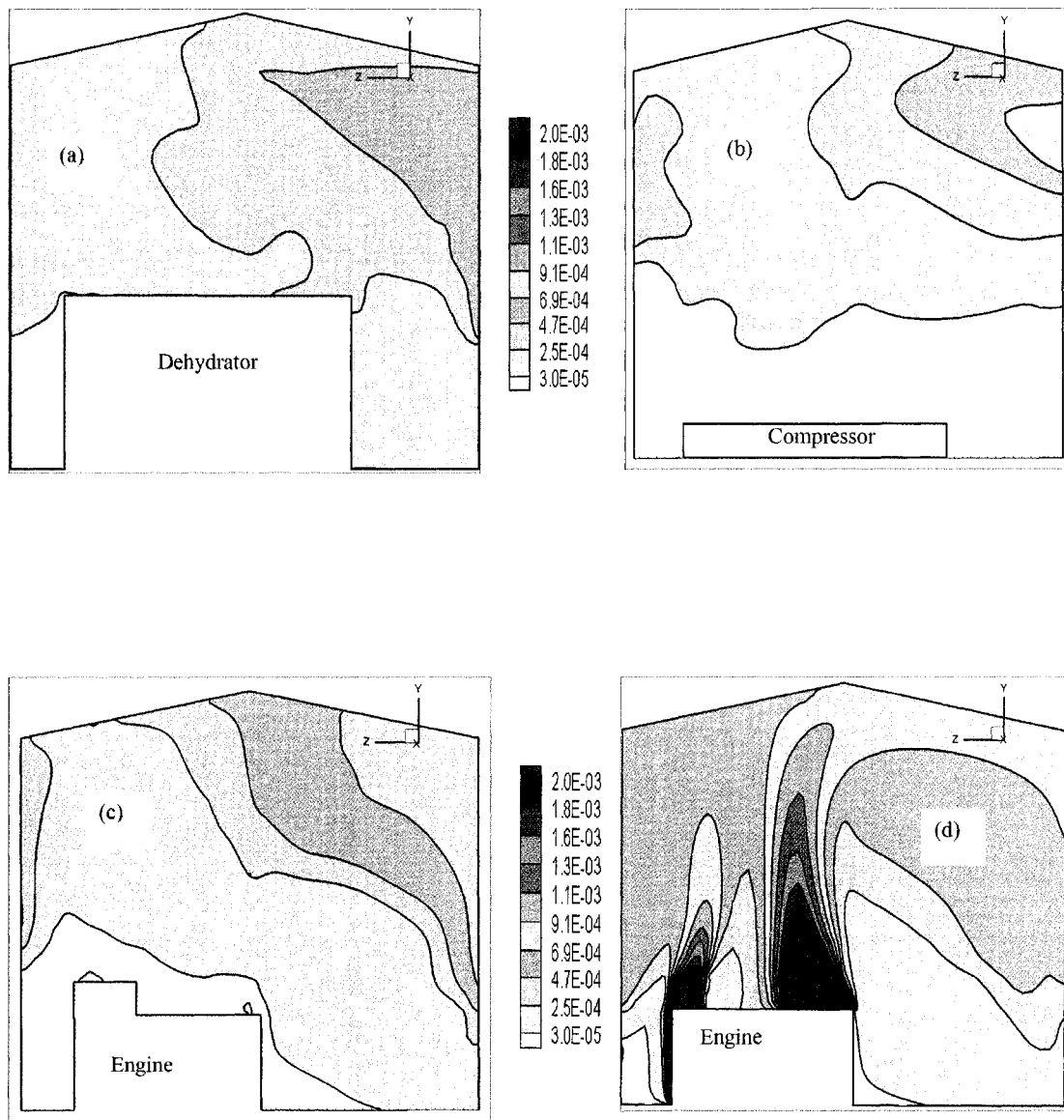


Figure 4.15: Profile of methane mole fraction in the small compressor building operating with option 2 under controlled extraction mode. The mole fraction profile were taken at the same position as in figure 4.14.

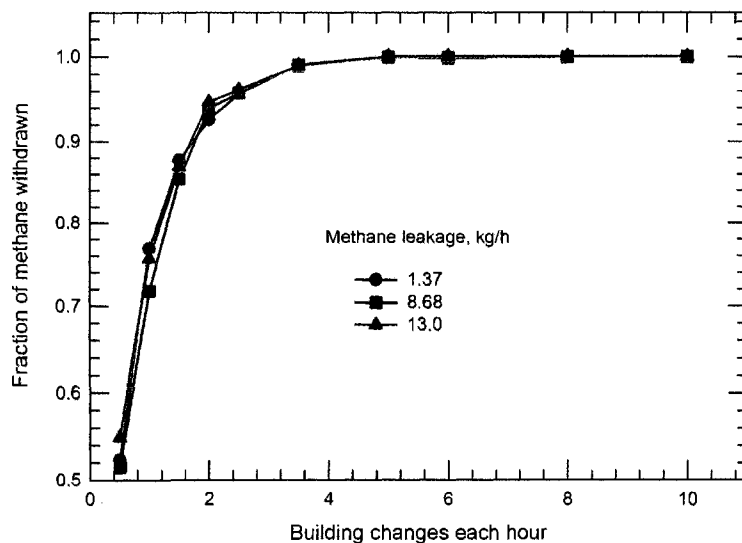


Figure 4.16: Fraction of CH₄ captured through ridge vent using forced extraction in the small compressor building with doors closed. At 273 K ambient temperature.

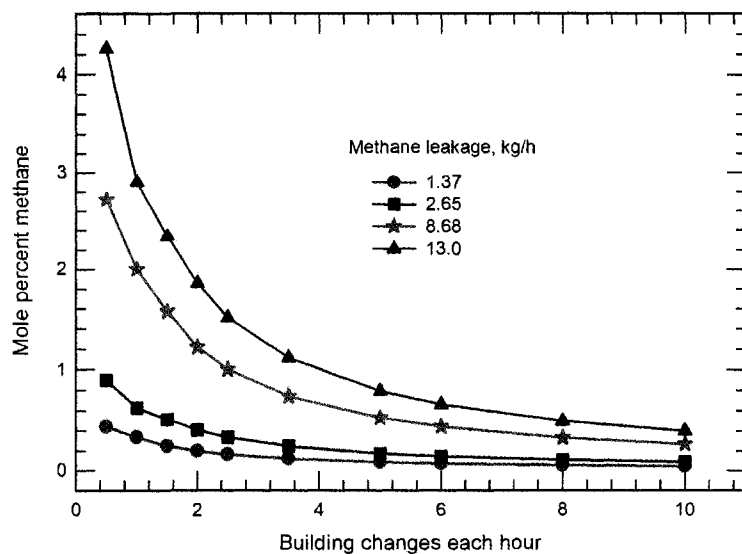


Figure 4.17: Mole percentage of CH₄ in the extracted stream versus extraction rate at different leak rate in the small compressor building. At 273 K ambient temperature.

4.3.3 Free flow in large building

The simulation of the large building was done with an ambient temperature of 293 K. For the case of free flow mode, five building operating options were explored, denoted as follows: Option A, all doors are opened, Option B, only north and south side doors are closed; option C, north, south and east doors are closed, Option D, north, south and west doors are closed and Option E all doors are closed. In all options the louvers and ridge vents are used to ventilate the building unless stated otherwise. Two different cases were considered in regards of louvers location. In Case 1 the louvers were located at the top of the building (the current operating position) and in Case 2 the louvers were located at bottom of the building, as in small compressor building. In this latter case, the louvers were located between the doors. The fugitive leak sources were imposed and distributed around the building, with a total leakage rate of 278 kg/h. Table 4.4 shows a summary of the results obtained from simulation done with above conditions. For the free flow case the trend is the same as observed in the small building. Opening the doors increases the flow rate through the ridge vent and reduces the concentration. As previously observed, the concentration through the ridge vent is below that required.

4.3.4 Forced extraction in large building

Experiments using the controlled extraction mode of operation were done using Cases 1 and 2, with Option E. Several extraction and leakage rates were used. Figure 4.18 shows the effect of extraction rate on the fraction of methane recovered at different leak rates with the louvers located at the top and bottom of the east wall. It can be seen that the fractional recovery is essentially independent of the leak rate, and depends only on the extraction rate, as was observed in the small compressor building. The methane mole fraction in the ridge vent effluent is shown in Figure 4.19 for both cases. These results suggest that the CFRR feed quality requirements can be achieved by controlling the extraction rate. Further, these figures suggest that the location of the louvers has only a small effect on methane recovery fraction

Table 4.4: Summary of results obtained for the large compressor building with quiescent air at 293 K operated in free flow mode (with louvers on the current side of the wall), total leakage rate was 278 kg/h and the area of the ridge vent was 38.4 m². conditions at the ridge vent.

Option	Louvers position	% Methane captured	Mole % methane	Mass flow rate, [$\frac{T}{h}$]	Temperature [K]
A	Top	93.2	0.204	235	294
B	Top	100.0	0.231	215	299
C	Top	98.1	0.265	183	301
D	Top	94.1	0.269	171	301
E	Top	81.7	0.533	77	304
A	Bottom	91.5	0.210	218	292
B	Bottom	98.2	0.245	203	299
C	Bottom	100.0	0.300	171	301
D	Bottom	95.8	0.303	160	302
E	Bottom	68.2	0.602	57	305

and concentration. Although at low extraction rate a difference in performance due to louvers location can be observed, in practice it is not recommended to operate the building at such low extraction rates.

Velocity vector and methane mole profiles for the large compressor building generally follow the similar patterns as those observed in the small compressor building. The opening or closing of the doors, and the location of the louvers, has been shown as the main factor in achieving good capture and above target methane concentrations in the effluent stream.

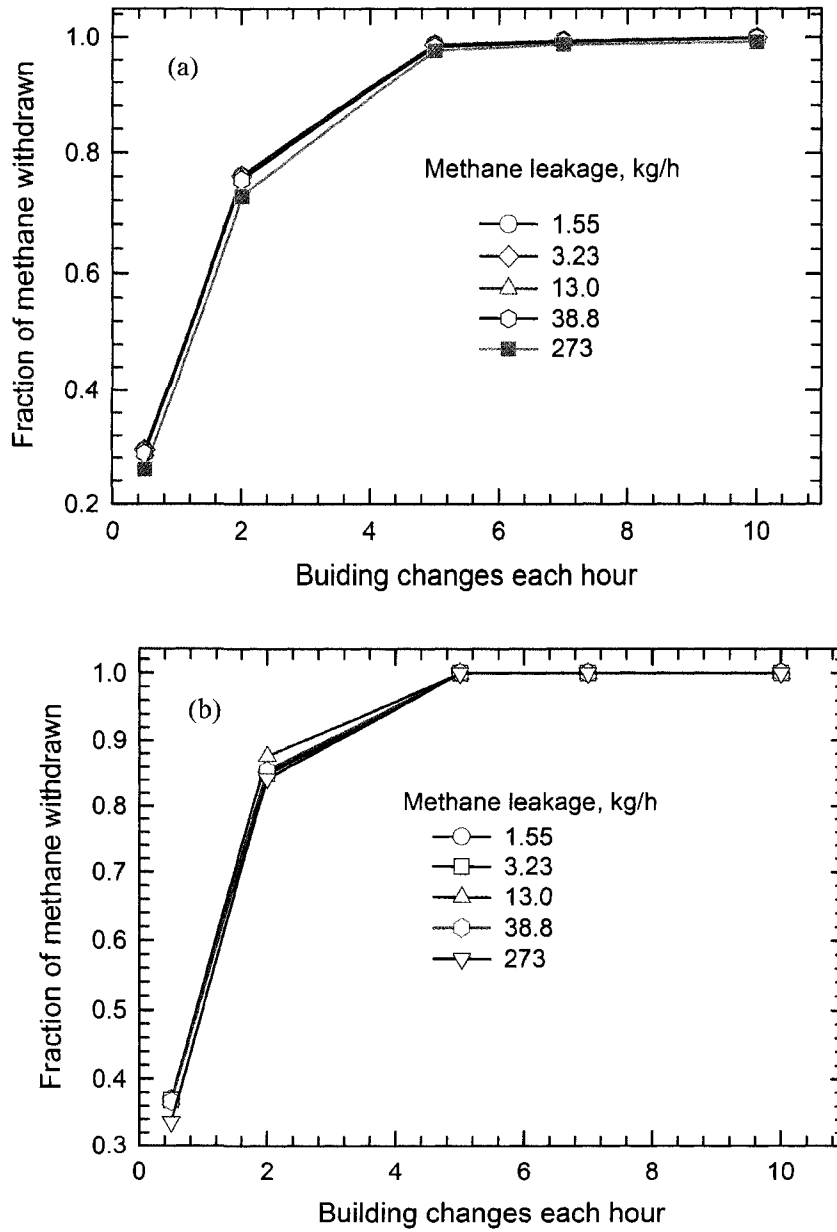


Figure 4.18: Fraction of methane captured using forced extraction in the large compressor building with the doors closed. Above about five room changes most of the methane is captured. Louvers on the east wall at (a) the top (b) the bottom.

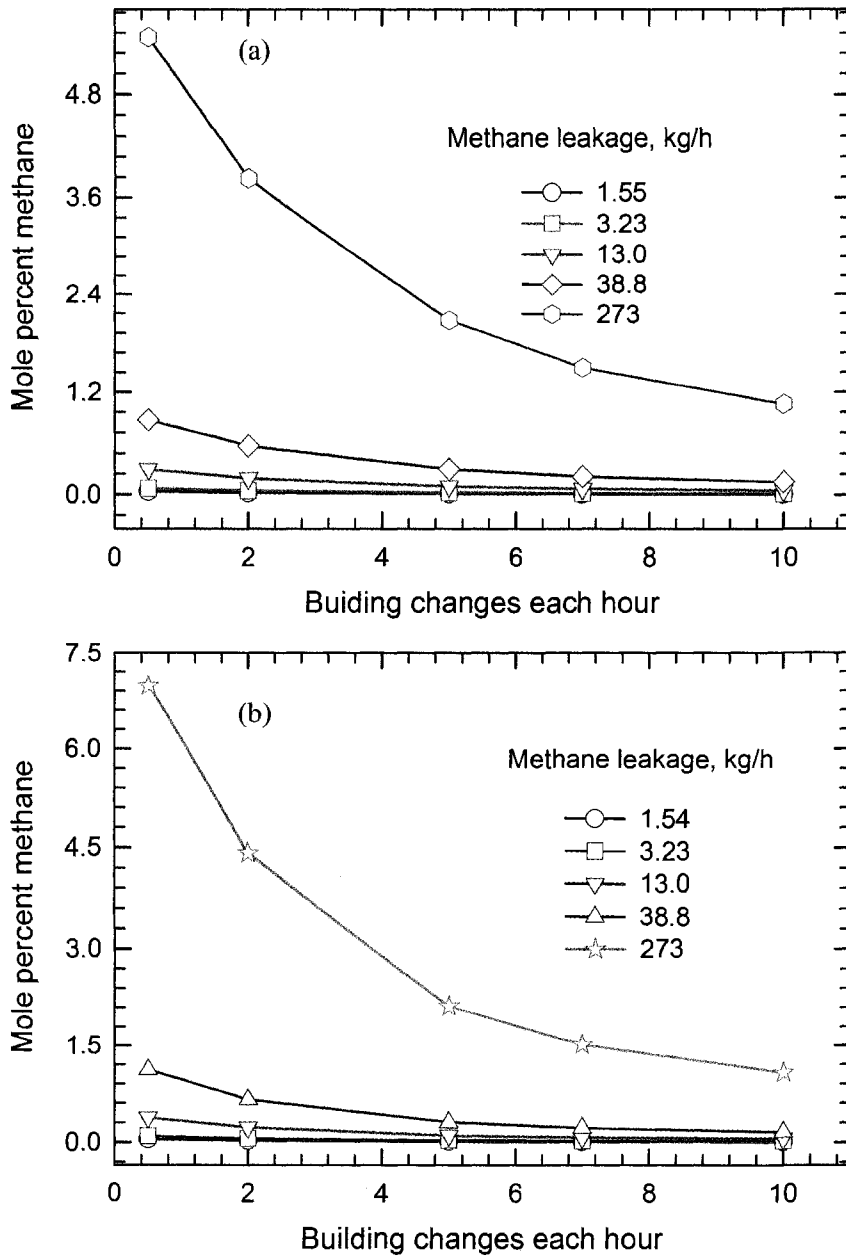


Figure 4.19: Mole percentage of methane in the extracted stream versus extraction rate at different leak rate in the large compressor building. The louvers location on the east wall are (a) the top and (b) the bottom.

4.3.5 Boundary flows

Airflow through the large openings, where a free boundary condition was imposed, was observed to be bidirectional flow as shown in Figure 4.20. The behaviour shown in this experiment agrees with observation in the work of Gan (2000). The bottom part of the opening acts as inlet and the upper part as outlet, for ambient temperature above 273 K. When the ambient temperature falls below 273 K the trend reverses, where the bottom part now becomes the outlet and the upper part the inlet as shown in Figure 4.20 (a) and (b) respectively.

It can also be observed that when cold air from outside enters the building, it flows towards the hot spot, which in this case is the engine location. Figure 4.21

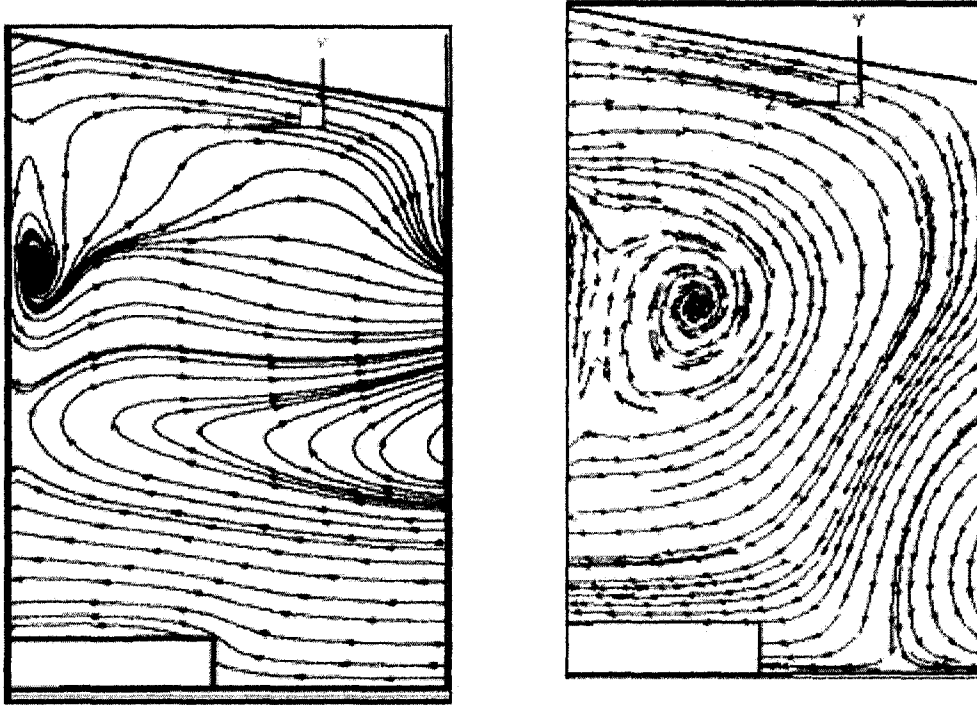


Figure 4.20: Behaviour of large opening boundary condition (a) ambient temperature is above 273 K (b) ambient temperature is below 273 K

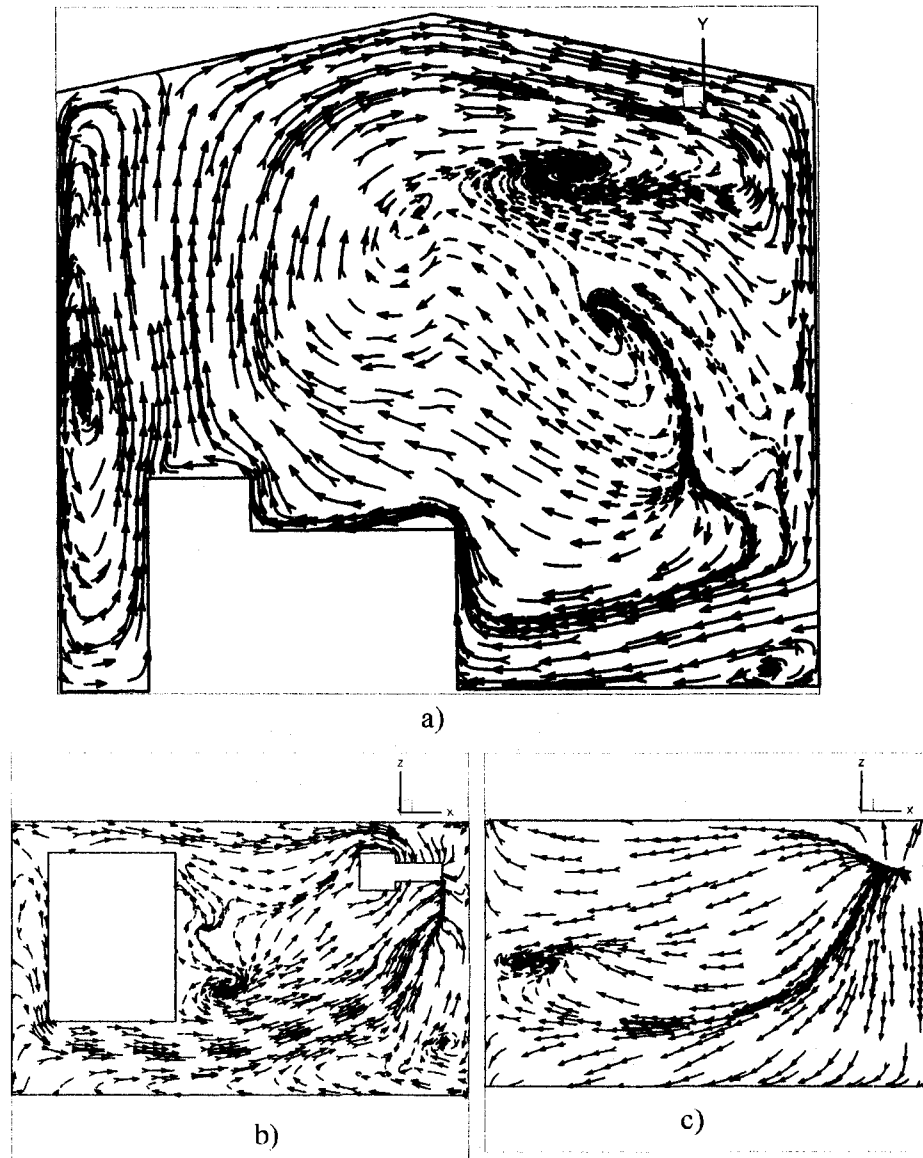


Figure 4.21: Velocity vectors in the small compressor building operating with option 1 with controlled extraction. The velocity vectors were taken: a). at the engine, which is the hottest spot in the building, shown in x-plane. b). near the bottom of the building, shown in y-plane. c). taken at upper level of the building, in y-plane.

and 4.22 shows sectional aerial view of the velocity patterns in the building. Figure 4.21 (a) shows that the hot air above the engine rises up and mixes with cold air it comes in contact with. Figure 4.21 (b) shows a slice of plane at lower part of the building where the air is relatively cold, in which the cold air is shown to be moving towards the engine location to replace the rising hot air. Figure 4.21 (c) shows the phenomena in the upper part of the building. The hot air, is seen to be moving away from the engine location to give room for the cold air; the movements are facilitated by the buoyancy principle.

The effect of ventilation opening in fugitive methane capture operation can be observed by looking to the velocity patterns in Figure 4.22, where option 2 (Only roll-up door was opened) was used in operating the building. The cold air flows into the building at the bottom of the opened door, and mixes thoroughly with the gases inside the building and then flows out the building at the top of the opened door. This makes the maximum capture of the fugitive methane impossible. The flows inside the building are governed by the stack effect, while the flow from outside to inside of the building and vice versa are due to the pressure differences.

4.4 Observations

Fugitive methane emissions in the oil and natural gas sector are a major contributor to greenhouse gases emissions. At the same time, they are potentially much easier to reduce or eliminate than gases such as carbon dioxide, which is very expensive to capture and sequester using current technology. Fugitive emissions in natural gas compressor stations can potentially be collected using the building itself. Possibly the most important variable that affects the capture rate is the opening of the large doors. The large doors are often opened in the summer to keep the building cool. Using controlled extraction rates with doors closed, typical emission rates can lead to an acceptable feed for a reverse flow catalytic reactor. To increase the reduction of GHG emissions, this effluent can also be potentially combined with instrument vent streams,

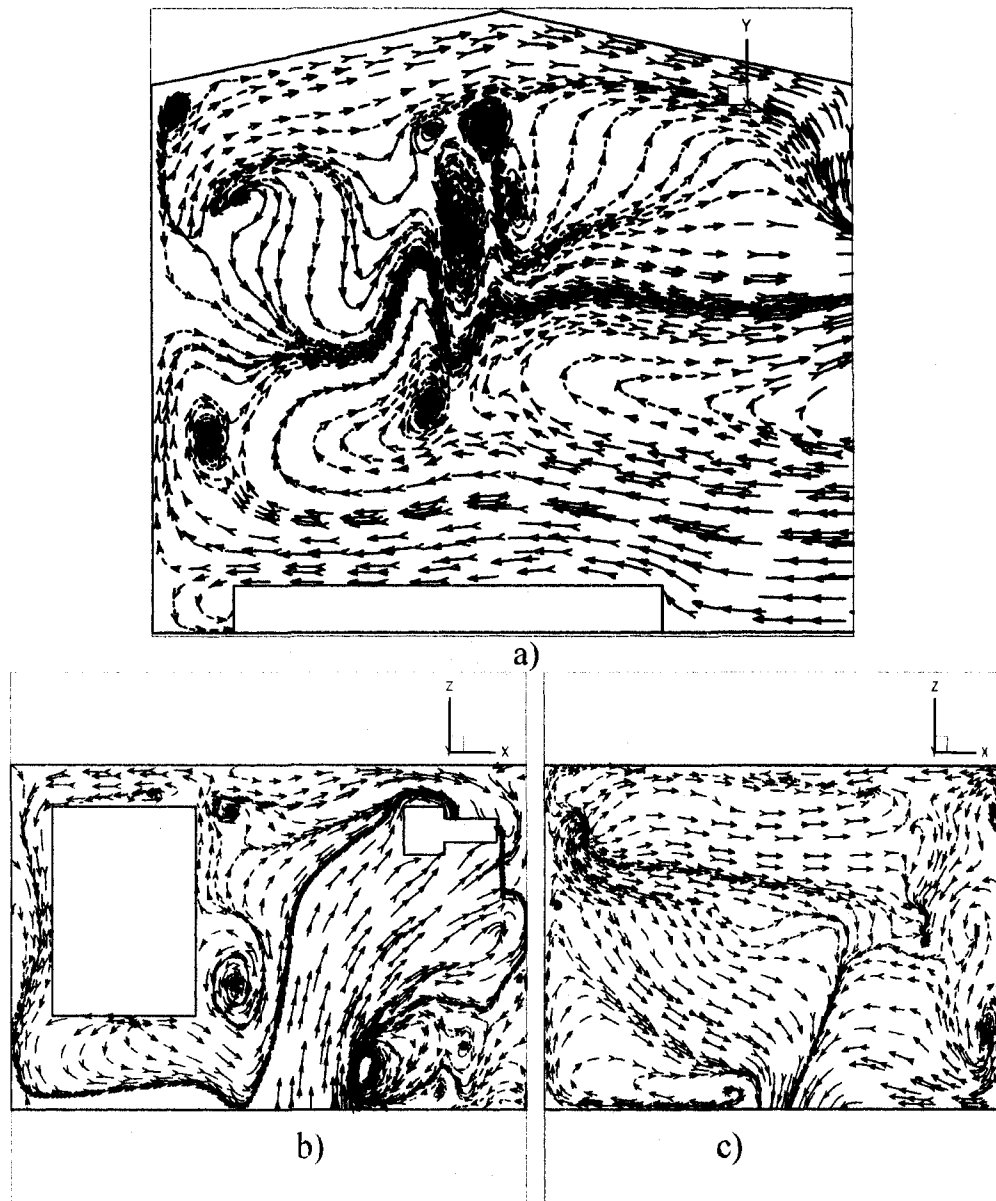


Figure 4.22: Velocity vectors in the small compressor building operating with option 2 with controlled extraction. The velocity vectors were taken: a) at the roll-up door position, shown in x-plane. b) Near the bottom of the building, shown in y-plane. c). taken at upper level of the building, in y-plane.

or the engine exhaust stream, which also contains significant methane and carbon monoxide.

Validation of simulation results is very important, but in conducting validations, the following must be taken into consideration; the parameters to be validated, equipment and manpower requirements and the cost implication. For this work, the physical validation was not possible since it requires extensive involvement of expensive equipment and manpower, there are many parameters to be validated, and the validation requires time to perform. This implies the cost of validation is very high. However, the local validation was done by checking the mass and species balance in the building enclosure domain which came out to be within the required tolerance.

Methane catalytic combustion review

5.1 Background

From prehistoric times, fossil fuels have been used as a source of energy, and currently, more than 90% of global energy demand is satisfied by fossil fuel (Anderson, 1996). The use of combustion processes in the energy sector is growing rapidly, because to a large extent global economic and technological development depends on energy utilization (Anderson, 1996). At the same time, fossil fuel combustion is one of the major sources of environmental pollution, which means environmental impacts have become a critical factor in energy sector development and planning. The increasing global energy demand leads to an increased utilization of combustion processes, but tightening environmental pollution regulations yield a challenging task of minimizing pollution and increasing the efficiency of the combustion processes. Thus, colossal efforts are needed to make fossil fuel combustion more efficient and environmentally acceptable.

Among the fossil fuels, natural gas is considered to be a very clean fuel. It contains low amounts of nitrogen, sulphur, and has the highest ratio of H:C. Its combustion thus tends to yield the lowest amount of pollutants per unit of energy produced, as well as having higher energy yield at lower cost. In principle, the combustion of natural gas produces only water and carbon dioxide together with energy. However, in reality conventional combustion can only occur within the

given flammability limits and the heat of reaction can raise the temperature during combustion to over 2000 K, where the formation of nitrogen oxides can occur. N_2O is considered to be one of the significant GHG and is highly persistent in the atmosphere, forming the main source of NO in the stratosphere.

There are three different mechanisms that lead to nitrogen oxides formation during combustion. These are **thermal NO_x** which is formed by coupling oxygen and nitrogen in the air through the Zeldovich mechanism, which is kinetically limited to a temperature below 1700 K. Above this temperature, its production doubles every time the temperature increases by 40 K. **Fuel bound NO_x** (not significant with methane) is formed by oxidation of nitrogen compounds present in the fuel, and **prompt NO_x** is formed by a fast coupling of nitrogen from the air with radicals formed during the reaction (Hayes and Kolaczkowski, 1997; Ciuparu et al., 2002). Other combustion products can be sulphurous oxides which are mostly produced due to the presence of impurities of sulphur-based compounds in the feed stock. Carbon monoxide and hydrocarbon can also be present in the products if the combustion is incomplete. Their production rate decreases with increasing reaction temperature.

Nitrogen oxides are products of conventional homogeneous flame combustion where air is the combustion medium. The sulphur and nitrogen content in natural gas is negligible and there is no evidence reported on formation of prompt NO_x in natural gas combustion, thus all efforts in natural gas combustion are aimed at reducing thermal NO_x . Thermal NO_x can be reduced by decreasing reaction temperature and residence time, but this action will promote the formation of carbon monoxide and unburned hydrocarbon. The major concern of using natural gas as fuel is that the methane is a potent GHG with GWP much higher than that of carbon dioxide; thus large emission of unburned methane would be a big environmental concern. An alternative technology which will operate at much lower temperature to ensure elimination of thermal NO_x formation and at the same time be able to achieve a complete combustion of methane is thus desirable.

Various approaches have been investigated in the effort to minimize pollution from combustion and to increase combustion efficiency. Catalytic combustion

technology offers a solution in achieving complete combustion at lower reaction temperature and giving lower pollution emission without sacrificing system performance (Hayes and Kolaczkowski, 1997). Also, it enables a wide range of fuel concentration to be oxidized over a suitable catalyst, without a flame. Catalytic combustion can operate at higher air/fuel ratios than homogeneous combustion, and maximum attainable combustion temperature depends on the air/fuel ratio used (Heck et al., 1995). Furthermore, the selectivity of methane catalytic combustion has been observed to be excellent as no other products than carbon dioxide and water are usually formed (Lee and Trimm, 1995).

5.2 General catalytic combustion

Catalysis and combustion have a long partnership, which originated in 1818 when Sir Humphrey Davy discovered that platinum wire can sustain flameless combustion. In 1836, Jöns Jacob Berzelius introduced the term catalysis and catalytic reaction. Since then, catalysis has become important in modern chemical processing plants, engineering research and innovation. In recent years, the interest in catalytic methane combustion has increased considerably after finding potential applications in many industrial processes: such as catalytic combustion for power generation (Lee and Trimm, 1995; Deutschmann et al., 2000; Zhu, 2001; Lyubovsky et al., 2003), catalytic mitigation of fugitive methane emissions (Salomons et al., 2003), reducing emission in exhaust of combustion systems (Lampert et al., 1997; Fujimoto et al., 1998; Au-Yeung et al., 1999a; Liu et al., 2001a; Liu et al., 2001c; Gelin and Primet, 2002) and catalytic partial oxidation for the production of many important chemical raw materials (intermediates) for synthesis of highly valuable chemical products and applications in new technologies like fuel cells. The catalytic combustion of methane has been intensively studied (Gelin et al., 2003) but remains incompletely understood.

Methane is the main component of natural gas and the most stable hydrocarbon, therefore it is the most difficult to oxidize. Methane combustion is highly exothermic, and its complete combustion can be represented by the following global overall

reaction:



The actual global rate of catalytic reaction is governed by the rate of surface kinetic, the rate of diffusion of reactants from the bulk of flowing gas to the surface, adsorption onto catalyst, desorption of the products from the surface and diffusion of the product into bulk flowing gas. These processes occur simultaneously and the slowest one limits the overall reaction rate. Thus a complete description of heterogeneous catalytic combustion processes requires coupling of reactive flow with the catalytic surface reaction. Combustion processes are highly exothermic, which give rapid increases in temperature once the reaction starts. Thus to improve the

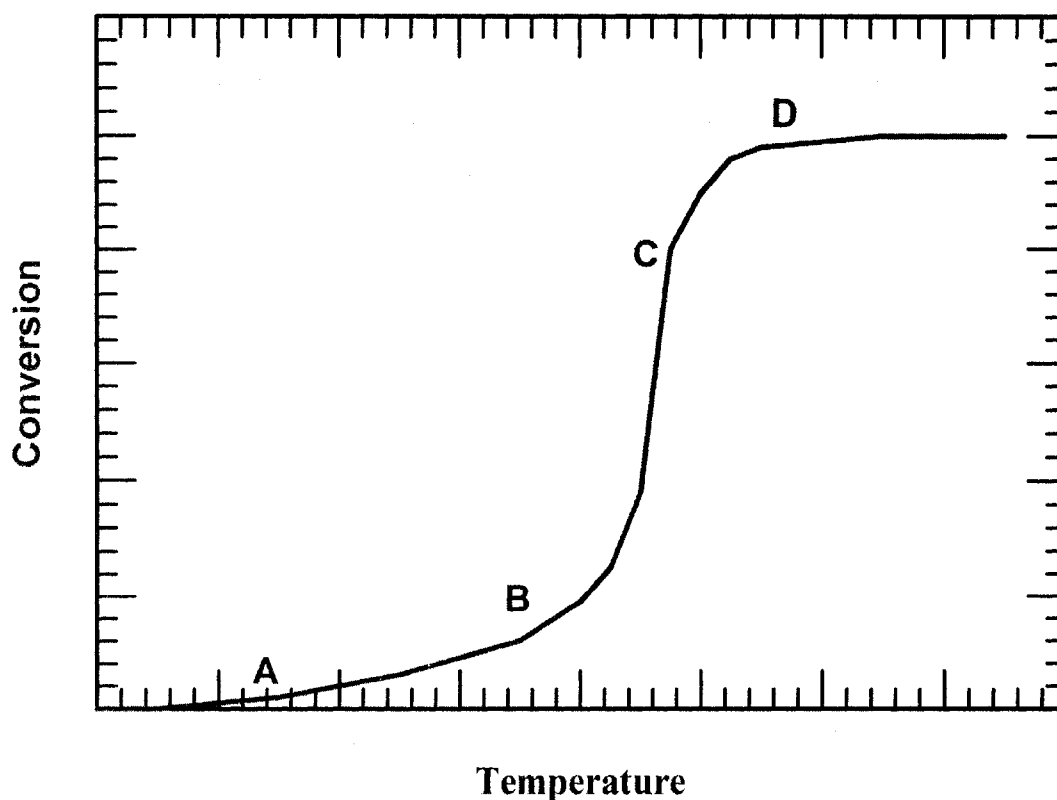


Figure 5.1: Plot of the hydrocarbon conversion on catalytic combustion as function of temperature (Lee and Trimm (1995)).

performance of catalytic combustion a clear understanding and knowledge of relationship between catalyst activity, heat transfer, mass transfer, surface temperature, bulk temperature and process stability is needed.

The general pattern of catalytic combustion of hydrocarbon is well established and the generalized plot of rate of surface reaction as function of temperature can be represented by an S-shaped plot as shown in Figure 5.1 (Lee and Trimm, 1995). As summarized in Figure 5.1, a typical catalytic combustion process passes through the following phases depending on reaction temperature employed:

- At low temperatures the reaction is controlled by the intrinsic surface kinetics, represented by section A - B.
- In the intermediate temperature region the reaction rate may become mass transfer controlled and thus catalytic activity is less important in this region, represented by section B - C.
- At higher temperature there can be a significant contribution from gas phase homogeneous reactions to the overall reaction rate, represented by section C - D. Lee and Trimm (1995) stated that mass and heat transfer become more important once light-off is achieved. Through their experiments, Ibashi et al. (2003) working with a PdO/ZrO₂ catalyst suggested that a thickness of the active catalyst needed to minimize the impact of mass transfer influence in the catalytic methane combustion is about 10 - 15 μ m.

The catalytic combustion general behaviour pattern also can be plotted as temperature of upstream exhaust gas against Damköhler numbers as shown in the Figure 5.2. Damköhler number describes mass transfer with chemical reaction. There are many forms of Damköhler number (Da), the one referred to here is the ratio of rate of reaction in the catalyst layer to rate of external diffusion from the gas phase to the catalyst surface as given by Hayes and Kolaczkowski (1997). Depending on the state of the catalyst, the catalytic reactor can be operated in any of the following three regimes: region A, the Damköhler number is low, the kinetics of the intrinsic surface reaction dominates over diffusion effects. At moderate Damköhler

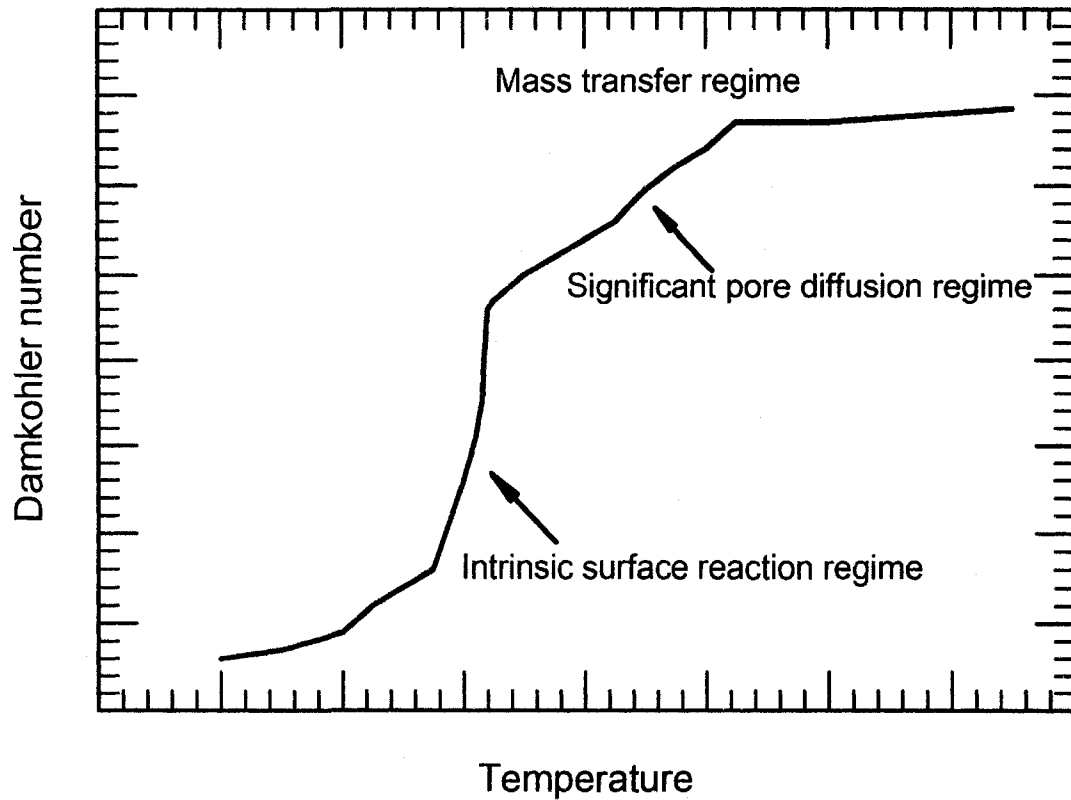


Figure 5.2: Schematic of catalytic surface reaction regimes (Chen et al. (2000)).

number in region B, pore diffusion becomes significant and dominating while at higher Damköhler number in region C, mass transfer is a significant factor (Chen et al., 2000).

5.3 Combustion catalyst

Catalytic combustion has several advantages compared to conventional combustion, but there are many issues that must be addressed in designing an appropriate catalytic combustion system. Catalyst systems generally consist of an active component and a support. A large number of permutations and combinations exist and more complexity is introduced because components which are themselves active

catalysts may be used as supports (Choudhary et al., 2002).

For catalytic methane combustion, both transition metal oxides and noble metals have been used as catalysts. They can be used with or without support, but supported catalysts are the most popular. The main advantage of supported metal catalysts is that the catalysts is dispersed over a large surface area of the support, which results in a very high surface to volume ratio, allowing for a greater ease of reaction compared to an unsupported catalyst. Supported catalysts may show higher activity and stability than unsupported catalyst due to the interaction between catalyst and support. The support can take different shape, like saddles, cylinders, spheroids, metallic mesh, monolithic honey combs, etc. Good supports need to have high thermal stability, low volumetric shrinkage with temperature, high surface area, low density, low heat capacity, high resistance to attrition, poisoning and mechanical shocks (Hayes and Kolaczkowski, 1997). The following subsections will briefly discuss some of the transition metal oxides and noble metal catalysts which are reported to be more successful catalysts for methane catalytic combustion.

5.3.1 Transition metal oxides

Transition metal oxides are relatively inexpensive and have the ability to suppress fuel NO_x formation. However, they are not widely used because of relatively low catalytic activity per site and higher ignition temperatures (Choudhary et al., 2002). Various metal oxides have been studied, including single transition metal oxides and mixed transition metal oxides (which include doped metal oxides, perovskites, spinels and others). Despite having lower catalytic activity per site, transition metal oxides particularly perovskite type, still receive wide attention.

Perovskite-type oxides are mixed oxides with specific structure, of general formula ABO_3 , where lanthanide elements usually are at site A position and the first row transition metals at site B position. Perovskites are relatively cheaper, comparatively active and more thermally stable for methane catalytic complete combustion applications (Prasad et al., 1984; Zwinkels et al., 1993), they have been frequently

studied and proved to be a valuable alternative to noble metals. Choudhary et al. (1992) showed that LaBO_3 ($B = \text{Mn, Co, Fe and Ni}$) perovskites have comparatively high catalytic activity for complete combustion of hydrocarbons. The B ion is the one which is responsible for catalytic activity, while the La^{3+} cation brings in structural stability.

5.3.2 Noble metals

Noble metal catalyst show higher activity than transition metal oxides for catalytic methane combustion, and thus most research has been directed towards this class of catalyst. Apart from having higher catalytic activity per site, noble metal catalysts also show a greater resistance to sulfur poisoning (Lampert et al., 1997) but have low thermal stability. Palladium and platinum catalysts have been the most widely accepted as being the most effective catalysts for the catalytic combustion of methane (Gelin et al., 2003). The use of noble metals other than palladium and platinum is limited because of their high volatility, ease of oxidation and limited supply. Gellin et al. (2003) noted that when platinum or palladium is deposited on conventional supports (like silica and alumina) a high degree of dispersion can be achieved, which provides a large catalytic contact. The focus of this work is on supported palladium catalysts.

The performance of a particular catalyst is influenced by several factors, including the ratio of oxygen to methane in the feed, method of catalyst loading on the support, nature of the support itself, sensitivity to catalyst structure, extent and nature of catalyst pretreatment, presence of other components in the feed mixtures (e.g. water, carbon monoxide, sulphurous compounds, e.t.c) and reaction conditions. In the following paragraphs, these factors will be briefly discussed for the case of a palladium catalyst.

There are many studies of the complete combustion of methane over palladium and platinum catalyst, see for example, Hayes and Kolaczkowski (1997), Roth et al. (2000), Dupont et al. (2001), Groppi (2003), Demoulin et al. (2004), Araya et al. (2005), Escandon et al. (2005) and Kraikul et al. (2005). Various aspects of catalytic

behaviour of these catalysts have been discussed and investigated experimentally as well as numerically. The complicated behaviour, particularly for Pd catalysts, remains an area of substantial research and debate. The chemical properties and morphology of these catalyst have been observed to change as a function of reaction conditions, resulting in an increase or decrease in the catalyst activity. Factors considered to influence these changes for a given supported catalyst are as follows:

(a) Support : Platinum and palladium are usually dispersed on a support to increase active surface area. The support may also provide enhancement of thermal stability and resistance to poisoning of the catalyst. Sometimes the supports also take an active role by either promoting or hindering particular catalytic reactions. Thus, supports strongly influence the performance and activity of the catalytic system as well as the life of catalyst. The most commonly used supports in catalytic methane combustion are alumina (Briot and Primet, 1991; Müller et al., 1996; Groppi et al., 1999; Escandon et al., 2005), zirconia (Pecchi et al., 1998; Müller et al., 1999), silica (Narui et al., 1998; Kikuchi and Takahashi, 1997; Araya et al., 2005; Okumura et al., 2006) and metal oxides (Wang and Chang Xie, 2001; Li and Flytzani-Stephanopoulos, 1999). Studies show that the activities of supported catalysts are not constant with time (Farrauto et al., 1995; Euzen et al., 1999; Datye et al., 2000; Gelin and Primet, 2002; Escandon et al., 2005). Possibly this can be caused by a loss in catalytic surface area due to catalyst particle sintering when exposed to high temperature. Demoulin et al. (2004) reported that titania- and tin- supported Pd catalysts show higher activity for methane combustion compared to alumina supported catalysts at low temperature using high throughput experiments.

Catalyst dispersion on the support is favoured as the substrate-gas interfacial free energy increases. Thermal stability of a catalyst system (particularly the sintering inhibition) is an important factor for support choice. In the literature, it has been observed that the ability of the support to inhibit sintering varies according to the variation of interfacial free energy between support and

catalyst in the following order

$$\text{ZrO}_2 \left(1130 \left[\frac{\text{erg}}{\text{cm}^2} \right] \right) \gg \text{Al}_2\text{O}_3 \left(925 \left[\frac{\text{erg}}{\text{cm}^2} \right] \right) \gg \text{SiO}_2 \left(605 \left[\frac{\text{erg}}{\text{cm}^2} \right] \right) \quad (5.2)$$

Equation 5.2 implies that a catalyst supported on silica will sinter faster than those supported on alumina and zirconia, or zirconia and alumina have preferable high thermal stability. This trend is supported by the experimental observations of Lee and Trimm (1995) and Escandon et al. (2005).

Zirconia and alumina have a high value of free energy and thus inhibit the mobility of Pd species. Also, it is worthwhile to note that at a temperature of around 1275 K, the γ -phase of alumina transforms to the more thermodynamically stable α -phase (Hayes and Kolaczkowski, 1997). This transformation is also known as sintering, which is a thermally activated process and physical in nature, can occur on support, catalyst itself or both. Sintering leads to loss of surface area, which will block most of the catalyst inside the support's pores or fuse the catalyst together. This significantly decreases the catalyst surface area available for the reaction and hence a drastic decrease in activity will be observed. When the supports are modified by the addition of promoters such as La and Y, their stabilization of Pd species may be greatly altered. Various attempts have been made to stabilize the alumina supports against thermal deactivation (Beguin et al., 1991; Church et al., 1993; Loong et al., 1997; Chen et al., 2001), addition of La to alumina results in an inhibition in the catalyst support interaction between Pd and alumina. Other supports such as ZrO_2 and SiO_2 have been examined either as single materials or in combination with others (Wang et al., 1997). ZrO_2 has captured much attention because it is considered to be one of the most promising support materials. The stabilization of ZrO_2 by yttrium (Y) (Labalme et al., 2000) or doping with cerium (Kenevey et al., 2001) has proven to be successful with respect to activity of supported Pd catalysts.

Palladium is unusual in its thermodynamic properties; thermodynamically the stable phase can be either metallic Pd or PdO depending on oxygen partial

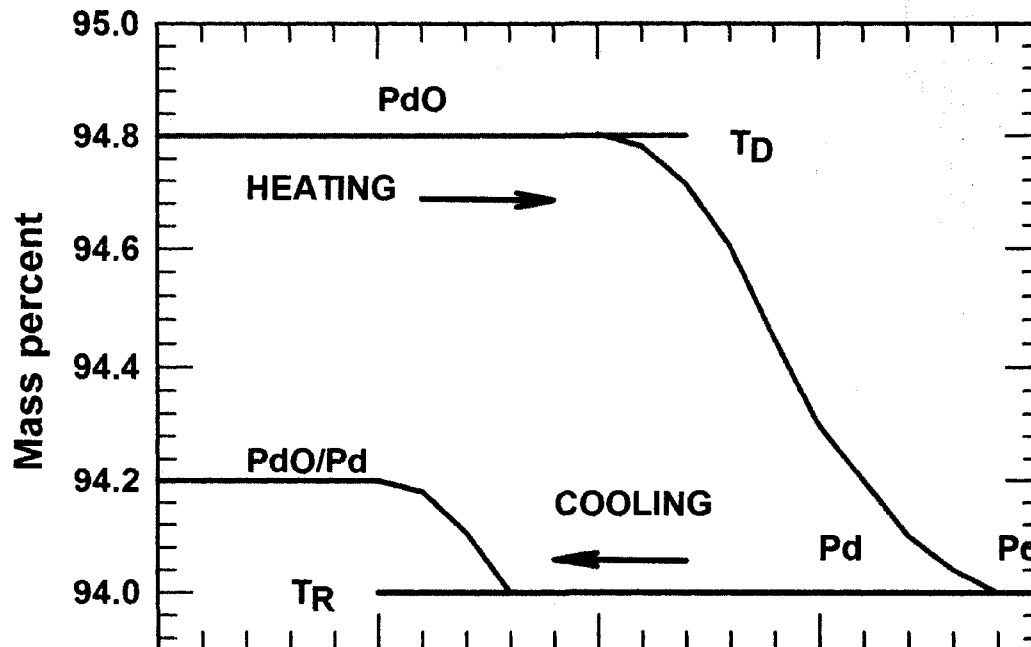


Figure 5.3: Generic Thermal gravimetric profile showing the hysteresis for decomposition of PdO to Pd and its reformation

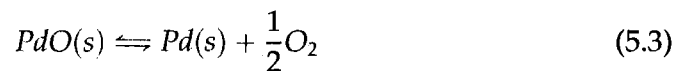
pressure and temperature. At atmospheric pressure, in air, the stable phase is PdO at temperatures below 1100 K, while metallic Pd is stable above this temperature (Farrauto et al., 1995). The hysteresis for decomposition of PdO to Pd and its reformation has been found to be strongly dependent on the nature of the support. Among other supports, zirconia is reported as having the largest gap between the reduction and re-oxidation temperature (Farrauto et al., 1995) and exhibits high thermal stabilities. Upon heating and cooling under air or reaction conditions, the hysteresis between the decomposition and reformation of PdO has been observed and discussed (Farrauto et al., 1992; McCarty, 1995; Hayes and Kolaczkowski, 1997; Ciuparu and Pfefferle, 2001).

Farrauto et al. (1995) showed that PdO supported on alumina rapidly decomposes completely to Pd at about 1100 K upon heating. By contrast, during

cooling, re-oxidation does not occur until temperature reached 950 K, see Figure 5.3. In addition to hysteresis, the Pd/Al₂O₃ exhibited a peculiar lack of reversibility upon re-oxidation. Cullis and Willatt (1984) suggested that the choice of support may affect both magnitude of oxygen uptake and its dependence on temperature. Roth et al. (2000) discussed on the possibility of formation of low activity species like Pd(OH)₂ on the surface of PdO.

The high affinity of Pd to oxygen can be linked to its high combustion activity, superior to other noble metals. When compared to Pt, Cullis and Willat(1983) found out that at 673 K, the oxygen uptake capacity of Pd catalyst is more than 100 times when compared to Pt catalyst. This observation was later correlated with the relative activities of the two catalyst by Muto et al. (1996).

At normal conditions Pd catalysts exist as PdO, thus its catalytic activity depends on the rate and extent of PdO decomposition and re-oxidation which thermodynamically can be expressed as:



The stability of Equation 5.3 and hence Pd catalytic activity depend upon temperature and oxygen partial pressure, or simply the decomposition temperature of PdO depends on the O₂ partial pressure (Hayes and Kolaczkowski, 1997).

$$P_{O_2}^{0.5} (1 \text{ atm})^{-0.5} = \exp \left(\frac{-11273}{T} - 2.89 \log_{10} T + 18.57 \right) \quad (5.4)$$

The transition temperature of PdO to Pd equilibrium decomposition can be determined by using Equation 5.4, which expresses the decomposition pressure as a function of temperature. The equation was developed by Hayes and Kolaczkowski (1997).

- (b) Precursor:** It is important to note that the catalyst precursor can influence the catalyst activity. Cullis and Willat (1983) observed experimentally that the presence of residual chlorine ions originating from the precursor strongly

inhibit the conversion of methane. Presence of chlorine create a competition for an active site between oxygen and chlorine.

Hick et al. (1990) reported that catalysts prepared from a chlorinated precursor showed a low TOF rate initially and increased as the reaction progressed. They associated the slow TOF increase with slow decomposition of Pd poisoned by chlorine to active PdO species. Roth et al. (2000) observed that the activity of methane combustion is strongly inhibited by chlorine presence, but the chlorine ions could be slowly removed under reaction conditions in the form of HCl. Demoulin et al. (2005) observed that a chlorinated precursor caused a low activity for zirconia supporting palladium in comparison to other researchers who reported higher activity for zirconia supports.

- (c) **Catalyst dispersion and structure:** It has been observed that both catalyst particle size and morphology can change during the reaction (Garbowski et al., 1994; Lee and Trimm, 1995). Fujimoto et al. (1998) and Farrauto et al. (1995) observed that sintering and re-dispersion of Pd species under different environments is responsible for a change of particle sizes. At elevated reaction temperatures substantial changes in the morphology of Pd and PdO can occur, which will have serious consequence for the activity. For example Ciuparu et al. (2002) observed that on Pd re-oxidation, the large particles are broken into many different crystalline domains, thus increasing the surface area available for reaction.

It is not clear what influence particle size has on activity, some studies have demonstrated a strong dependence of activity on particle size (Hicks et al., 1990; Briot and Primet, 1991). Hick et al. (1990) observed that TOFs for methane catalytic combustion of 1.3 s^{-1} and 0.02 s^{-1} for large and small particles respectively. Their experiments were conducted at 608 K on pre-reduced Pd/Al₂O₃ and Pd/Y-ZrO₂ catalysts. Müller et al. (1997), working at a temperature of 600 K on Pd/ZrO₂, observed a TOF increase from 0.035 s^{-1} to 0.17 s^{-1} when the particle size was varied from 6 to 12 nm. Other researchers have concluded otherwise. Baldwin and Burch (1990) studied Pd/Al₂O₃ at

different temperatures and observed a wide variation of activities without a clear relationship between TOF and particle size. Ribiero et al. (1994a) and Muto et al. (1996) observed a slight increase in TOF as the particle size varied, but they concluded that methane catalytic combustion on Pd/Al₂O₃ is not structure sensitive, the changes in TOF might be attributed to factors other than particle size effect. When catalyst particles are in critical sizes the relative concentrations of surface sites with given coordination neighbours changes rapidly when the particle size changes, this means the surface structure of catalyst changes. Fujimoto et al. (1998) suggested that changes of oxidation state and morphology of the Pd in the presence of reaction mixture as well as product inhibition effects could be a cause of TOF variation as observed by different researchers and not the effect of particle size.

(d) Pretreatment: Catalyst activity was found to be highly sensitive to pretreatment procedures. The effect of pretreatment on the activity of Pt and Pd catalysts was studied by different researchers, either under reducing or oxidizing conditions. Pretreatment under reducing conditions is usually done with H₂. In all studies done increased transient and steady state catalyst activity was observed. Cullis and Willat (1983) investigated the activity of Pd/Al₂O₃ after pretreatment with H₂ and He, He, or O₂. The catalyst under H₂ and He exhibited higher transient activities than the other two. For pretreatment under oxidizing conditions, O₂ is usually employed and results in decreases in the transient and steady state activity. Reactant gas mixtures were also used for oxidizing condition pretreatment of catalyst and their performance were better than employing O₂ (Lee and Trimm, 1995). Generally, it can be said that catalysts pretreated under reducing conditions have a higher activity than those treated under oxidizing atmospheres (Müller et al., 1997; Baldwin and Burch, 1990; Cullis and Willatt, 1983). Reducing pretreatment has been observed experimentally to increase catalyst activity for Pd supported on titania, tin, alumina and zirconia (Demoulin et al., 2005). Further, Demoulin et al (2005) suggested that even though the reducing pretreatment

is important in improving the catalyst activity, the extent of its effectiveness mainly depends on the type of support involved. It is obvious now that the composition of the surface and thermal history of the catalyst are decisive determinants of the catalyst activity.

(e) Poisoning and feed quality: Interaction between catalyst and either impurities in the reactants, source of catalyst materials or products of reaction are cause of deactivation of catalyst. Poisoning causes catalyst deactivation and arises as a result of chemisorption of species that are present in the reactor feed. Poisoning can be an irreversible or reversible process. The most common poison is sulphur. Sulphur poisoning of catalysts has been extensively investigated (Lampert et al., 1997; Dupont et al., 2004; Kraikul et al., 2005). The adsorption of sulphur on most catalysts has strong effects on catalytic properties which lead to the reduction of catalytic performance and activity.

Natural gas typically has low sulphur content; however, the presence of even a trace amount of sulphur compound can severely poison the methane combustion catalyst. Sulphur species may exist in the form of sulphur dioxide, sulphate or sulphide. Kharulin et al. (2005) have shown that the presence of 100 ppm H_2S can raise the ignition temperature of Pd/Al_2O_3 by $150^\circ C$, as well causing a loss of catalyst activity by more than 90% by poisoning. The loss of activity was attributed to the irreversible adsorption of sulphur species on the catalyst. The support has also been found to play an important role in the sulphur poisoning process. Alumina supported catalysts deactivate slowly in comparison with silica supported catalysts (Kraikul et al., 2005).

Another crucial poisoning agent is chlorine compounds. The chlorine can originate from the precursor salts or other impurities, either in supports or the feed itself. The effect of chlorine poisoning on activity of supported platinum and palladium based catalysts was widely studied (Simone et al., 1991; Cullis and Willatt, 1984). In the case of palladium, it was proposed that Cl ions, regardless of its source, would mainly be localized on the support and during catalytic reaction, Cl ions desorbed in the form of HCl, the evolved

HCl will then compete with reactants on the metal active sites. By blocking the active site, HCl inhibits the catalytic reaction as well as decreases the catalytic activity of the catalyst. For the case of platinum based catalysts, apart from the Cl ion on the support, there also existed second type of Cl ion which mainly can be found at platinum - alumina interfaces possibly as bridging species between platinum and alumina and directly influencing the adsorptive and catalytic properties of the platinum (Gelin et al., 2003). Other halogen and bromide compounds have similar inhibiting effects on Pd and Pt supported catalysts.

Lee and Trimm (1995) suggested that the feed $O_2:CH_4$ ratio has a strong effect on the oxidation of methane. Under O_2 rich conditions, CH_4 is oxidized to CO_2 over Pt and Pd catalyst. However, under O_2 deficient condition the formation of CO was observed over Pt and Pd. It has also been observed that the presence of CO_2 and H_2O inhibit the methane combustion reaction. Inhibition by H_2O is considered to be more severe than that of CO_2 .

During the catalytic combustion of CH_4 , it was observed that some carbon was deposited on the catalyst (Lee and Trimm, 1995). This carbon has no effect on the activity of the catalyst, and it was found that the rate of methane combustion was independent of the deposition of carbon on the Pd catalyst. Also it was reported that deposition of carbon on Pt catalysts first reduces activity but the system recovers within 15 min (Lee and Trimm, 1995).

- (f) Deactivation (time-dependent catalytic activity):** Pt and Pd exhibit very different reactivities towards oxygen. In the presence of oxygen, Pt and Pd oxidize into PtO_2 and PdO respectively. At lower temperatures PtO_2 is highly unstable and volatile compared to PdO, so metallic Pt will always remain available. PdO is very stable for temperatures below 1100 K. This explains why at lower temperatures the catalytic active state is metallic Pt for Pt and PdO for Pd. The existence of hysteresis in reaction rates has been observed during methane combustion over Pd-based catalysts (Ciuparu and Pfefferle, 2001). The catalyst activity increases with temperature and reaches a maxi-

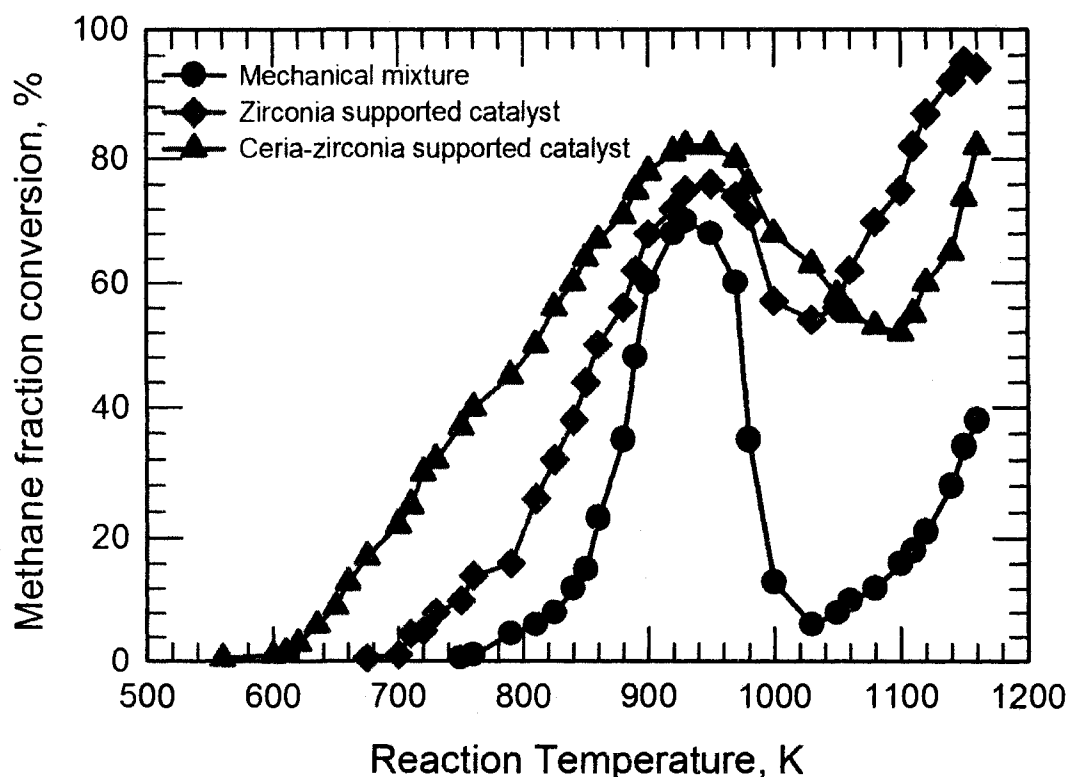


Figure 5.4: Methane conversion vs reaction temperature profiles for different PdO based catalyst (Ciuparu and Pfefferle (2001)).

imum around 975 K, and then decreases as the temperature increased showing a negative activation phenomena associated with thermal decomposition of PdO to Pd. As PdO is completely reduced to metallic Pd the activity increases again with temperature, as seen in Figure 5.4.

At lower temperature PdO is thought to be catalytically active for CH₄ combustion (McCarty, 1995). The transformation from PdO to Pd generally leads to a drop in catalyst activity as the temperature is increased. However, as shown by Ciuparu and Pfefferle (2001), Lyubovski and Pfefferle (1999) metallic Pd could be more active than PdO for methane combustion at higher temperature.

(g) Effect of loading: The effect of platinum and palladium loading on the support for catalytic methane combustion was investigated by Cullis and Willat (1983). They showed that reaction rate increased with an increasing loading of platinum over range of 0.1% - 0.2 wt%. Similar observation was observed for Pt and Pd catalyst supported on γ -alumina for the loading range of 2.7 - 10 wt%. They also noted that although the overall reaction rate was observed to increase, the activity per unit metal surface area decreased with increasing loading.

Otto (1989) used a loading range of 0.027 - 100 wt% of platinum catalyst to investigate its effect on the catalytic reaction rate. Results showed that below 1.4 wt%, the catalytic reaction rate was almost constant, while above 1.4 wt% the rate increase with increasing loading till it reach maximum at around 5 wt%. Above 10 wt% the catalytic reaction rate decreased significantly.

(h) Reaction condition: Methane oxidation is a highly exothermic reaction, which strongly couples the surface temperature with reaction rate and thus catalyst activity. Also, the reaction temperature can be high enough to allow the oxidation - reduction process of PdO - Pd to take place along side methane combustion, and this will complicate the catalytic process. The presence of water in the feed stock or from combustion product has an inhibition effect on the catalytic combustion process.

The effect of reaction temperature on catalyst activity have been studied by Briot and Primet (1991), Ribiero et al. (1994a) and Uchida et al. (1994) who found that methane oxidation rates do not always increase with increasing temperature, but one observed to increase initially with rise in reaction temperature, but decrease after reaction temperature exceed 700 ° C.

5.4 Reaction kinetics and mechanism

Current research focuses on reactor design to increase efficiency and productivity. As a result, a knowledge of physical and chemical processes occurring on catalytic

surfaces and their coupling with the flow field is important.

Detailed heterogeneous multi-step chemical kinetics and reaction mechanism are sometimes used to describe the transformation of reactants to products at a molecular level. Traditional kinetic studies involve global kinetics where the catalyst activity is viewed as a function of measured quantities like composition, pressure and temperature. This information can be determined from experimental data, and used to fit empirical rate expressions. Different kinetic expressions may fit data equally well, making it impossible to discriminate between different reaction mechanisms. Further, it is dangerous to extrapolate global expressions outside the range of conditions the parameters were fitted for (Hayes and Kolaczkowski, 1997).

On studying multi-step surface kinetics, the kinetics of the elementary reaction making up the reaction mechanism is required to be known in detail. Since realistic reaction mechanisms can not be established by global overview alone, different in situ techniques may be used to establish a reaction mechanism by identifying key reaction intermediates. This is the reason why research in chemical kinetics in addition to measurement of reaction rates also involves the study of reaction intermediates by computational (Deutschmann et al., 1996; Gelin and Primet, 1999; Müller et al., 1999), spectroscopy (Demoulin et al., 2005; Narui et al., 1999; Dartye et al., 2000), isotopic labeling (Au-Yeung et al., 1999a; Ciuparu et al., 2001), and other in situ methods of identifying and measuring the reaction intermediates. Once reliable data for key intermediates become available these data constrains the reaction mechanisms and thereby the predicted macroscopic kinetics. This approach enables discrimination between different reaction mechanisms.

For a number of reactions in heterogeneous catalysis, it has been found experimentally that reaction orders and activation energies vary with the reaction conditions (Lee and Trimm, 1995; Ciuparu and Pfefferle, 2001; Liu et al., 2001a). Intuitively one might expect this to be caused by a complex reaction mechanism, e.g. a change in rate limiting step or reaction pathway, this expectation is, however, not necessarily correct. Kinetic in heterogeneous catalysis is highly non-linear due to different stoichiometric, vastly different rates among elementary steps, competition for active sites among intermediates, and non-linearity of rate constants in tem-

perature. This means that even simple reaction mechanisms like that of methane combustion may lead to more complicated kinetics which display variable reaction orders and activation energies.

5.4.1 Mechanism for catalytic combustion

For catalytic methane combustion mechanisms, many researchers prefer to use a single step global surface reaction represented by Equation 5.1. However, this is a simplification, since the actual surface reaction mechanism involves many gas and surface species in a number of elementary reactions. The single step global surface reaction kinetics is preferred because of limited knowledge of the elementary reaction kinetics, unavailability of kinetic data for elementary reactions involved and knowledge of what occurs on the catalyst surface. The simple global chemical kinetic model can predict surface ignition/extinction temperatures of lean methane - air mixtures very well. Since surface ignition temperatures of methane-air catalytic combustion are low, about 900 K (Williams et al., 1991), the heterogeneous ignition process is dominated by the surface reaction due to its much lower activation energy compared to those of gas phase reactions. As calculations with a single-step reaction do not involve radicals, the well predicted ignition temperatures of lean methane - air mixture by Song et al.(1991) suggested that, under fuel - lean conditions, the interaction between catalytic and gas phase reactions is not important because the heterogeneous ignition is driven by the heat release by surface reaction. However, for high temperature conditions (≥ 1200 K), the interaction between catalytic and homogeneous reactions via radicals such as hydroxyl (OH) and oxygen atom may potentially affect the ignition process (Pfefferle et al., 1989; Griffin et al., 1992). To include the radical interaction between surface and gas phase at high temperatures, Markatou et al. (1993) modified the single step surface reaction model by introducing a coefficient to regulate the amount of OH desorbing from surface. The value of this coefficient was determined from experimental data. Their results show that the OH desorbed from the surface enhances the gas phase reactions and, hence, the generation of radicals in the boundary layer for

surface temperatures above 1300 K. So, Markatou et al. (1993) suggested the need of detailed surface kinetics and gas-surface energy balance to properly couple gas phase and surface processes in catalytic combustion calculations.

5.4.2 Multi-Step surface mechanisms

Catalytic methane oxidation by using multiple-step surface reactions have been reported by Hickman and Schmidt (1992), Deutschmann et al.(1994), Behredt et al. (1995), Bond et al (1996), and Chou et al. (2000). Most of the multi-step surface reaction mechanisms were developed using well established principles which are:

- **Langmuir - Hinshelwood (LH) type surface reaction mechanism:** This mechanism requires both reactants to be adsorbed on the catalyst surface, and must be in thermal equilibrium. Also, the adsorbed reactants are required to be close to each other prior to reaction to form the product. In this reaction mechanism, the surface catalyzed reactions usually took place between two adsorbed species. The adsorption of species can either be molecular adsorption or dissociative adsorption. Figure 5.5 illustrates an adsorption mechanism as it occurs in a Langmuir-Hinshelwood mechanism.

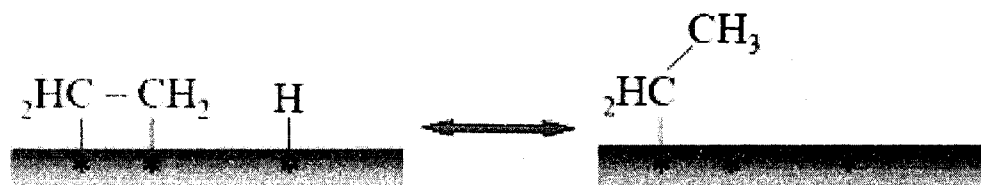


Figure 5.5: Detailed Langmuir - Hinshelwood mechanism

- **Eley- Rideal mechanism:** In an Eley-Rideal mechanism an atom from the gas phase scatters directly off a previously adsorbed atom and forms the reaction product.

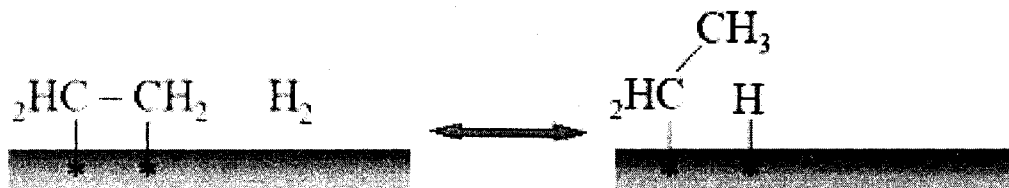


Figure 5.6: Eley - Rideal Mechanism

The main assumption here is that the surface of catalyst is completely covered by one of the reactant species and another reactant species from a bulk gas phase come into contact to form a product, as illustrated in Figure 5.6.

- Mars-van Krevelen mechanism:** It states that oxygen is introduced into the methane from the catalyst surface. Hence, the catalyst is reduced in this step. Subsequently, the catalyst is replenished with oxygen from the gas phase - and the catalyst is re-oxidized, this mechanism is also known as a redox mechanism and Figure 5.7 demonstrate the mechanism.

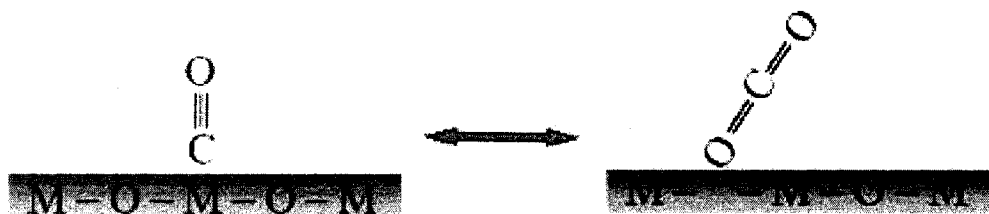


Figure 5.7: Mars-van Krevelen Mechanism

By using the framework of these principal surface reaction mechanisms, improved and more detailed surface mechanisms were developed by different research groups. The mechanisms consist of several basic elementary reactions: adsorption of reactants and intermediate species, surface reactions of adsorbed species, and desorption of products and intermediate species. These surface reactions can contain several elementary reactions and a large number of species. The

elementary reactions are described by the kinetics of surface reactions and thermodynamic equilibrium of adsorption and desorption of species. The different state of palladium and platinum under reaction conditions is a key to the development of a reaction mechanism for combustion of methane. For each catalyst type some simple detailed surface reaction mechanisms proposed in literature are discussed in the following sections.

5.4.3 Surface reaction over platinum catalyst

Due to high temperature conditions and very fast chemistry of catalytic combustion process, a direct experimental investigation of the elementary steps of reaction mechanism is difficult under realistic conditions. Therefore, modelling work is always essential in examining and validating the reaction behaviour under underlying detail elementary steps kinetics models. Detailed methane catalytic combustion mechanism over supported Pt catalyst have been extensively studied. The detailed reaction mechanism for premix methane-air catalytic combustion over platinum is widely tested and well developed and is reportedly able to reproduce experimental results by numerical modeling. These proposed mechanism will be presented and discussed below.

Simple reaction mechanism: A detailed multi-step surface reaction mechanism was proposed by Deutschmann et al. (1994). The mechanism was developed to predict ignition and steady state operation. This scheme includes 10 surface species and 24 elementary reaction steps. These reaction steps include adsorption and desorption of reactants and products, as well as surface reaction. The scheme assumes methane is irreversibly adsorbed on the catalyst surface, validation was done using a stagnation flow reactor. Thermo-chemical and kinetic data used were taken from the literature. The scheme was further modified and improved by Deutschmann et al. (1998), Goralski and Schmidt (1999) and Deutschmann et al. (2000). The details of the mechanism are presented in Table 5.1. In this mechanism, oxygen adsorption into catalyst surface is accomplished by two independent competing adsorption reaction, i.e. reaction 2 and 3 in Table 5.1.

Bond et al. (1996) proposed another mechanism for methane combustion on platinum catalyst, which used both LH and Eley-Rideal steps. Chou et al. (2000) improved Bond's mechanism, and the improved scheme contains 16 species and 23 elementary reactions. The detail of this mechanism is presented in Table 5.1.

Another elementary heterogeneous mechanism was proposed by Vlachos and co-workers which includes the work by Bui et al. (1997), Mhadeshwar et al. (2002) and Aghalayam et al. (2003). They developed a detailed reaction mechanism for methane combustion on platinum, which they called a "C1 Reaction Mechanism". Their scheme consist 10 species and 62 surface reactions, as shown in Table 5.1. In their proposed mechanism the surface reactions are divided into five classes as follows

- (a.) Adsorption and desorption of reactants, main products and intermediates.
- (b.) Pyrolytic hydrogen abstraction from CH_x species.
- (c.) Oxygen-assisted and hydroxyl-assisted hydrogen abstraction from CH_x species.
- (d.) Reactions of O and H to form OH, HO_2 , H_2O and H_2O_2 and their internversions (the H_2/O_2 subset).
- (e.) Reaction for formation of CO and CO_2 from various carbon and Oxygen moieties on the surface.

Thermo, chemical and kinetic data were obtained from both experimental and semi-empirical theoretical calculations (Aghalayam et al., 2003).

Table 5.1: Elementary reaction mechanism schemes for catalytic methane combustion over Pt.

Reaction	Deutschmann Mechanism		C1 (Vlachos) Mechanism		Chou Mechanism	
	A	E [$\frac{kJ}{mol}$]	A	E [$\frac{kJ}{mol}$]	A	E [$\frac{kJ}{mol}$]
Adsorption reaction						
1. $CH_4 + 2^* \rightarrow CH_3^* + H^*$	1.0×10^{-2}		1.0	12.0	0.15	27
2. $O_2 + 2^* \rightarrow 2O^*$	2.3×10^{-2}	0.0	0.003	0.0	0.003	0.00
3. $O_2 + 2^* \rightarrow 2O^*$	1.8×10^{21}	0.0				
4. $CH_3 + ^* \rightarrow CH_3^*$			1.00	0.00		
5. $CH_2 + ^* \rightarrow CH_2^*$			1.00	0.0		
6. $CH + ^* \rightarrow CH^*$			1.00	0.0		
7. $C + ^* \rightarrow C^*$			1.00	0.0		
8. $H_2 + 2^* \rightarrow 2H^*$	4.6×10^{-2}	0.0	0.25	0.0	0.046	0.00
9. $H + ^* \rightarrow H^*$	1.00	0.0	1.00	0.0		
10. $O + ^* \rightarrow O^*$	1.00	0.0	1.00	0.0		
11. $H_2O + ^* \rightarrow H_2O^*$	0.75	0.0	0.70	0.0	0.50	0.00
12. $OH + ^* \rightarrow OH^*$	1.00	0.0	1.00	0.0	1.00	0.00
13. $CO_2 + ^* \rightarrow CO_2^*$			1.00	0.0		

14.	$\text{CO} + * \rightarrow \text{CO}^*$	0.84	0.0	1.00	0.0	0.84	0.00
15.	$\text{CH}_4 + 2\text{O}^* + * \rightarrow \text{CH}_3^* + \text{OH}^*$					0.43	59.20
	Pure surface reactions						
16.	$\text{H}^* + \text{O}^* \rightleftharpoons \text{OH}^* + *$	3.7×10^{21}	11.5			1.0×10^{19}	10.5
17.	$\text{H}^* + \text{OH}^* \rightleftharpoons \text{H}_2\text{O}^* + *$	3.7×10^{21}	17.4				
18.	$\text{H}_2\text{O}^* + * \rightarrow \text{H}^* + \text{OH}^*$			1.2×10^{10}	18.4	1.8×10^{13}	54.2
19.	$\text{H}^* + \text{OH}^* \rightarrow \text{H}_2\text{O}^* + *$			3.5×10^{11}	12.4	1.0×10^{21}	62.5
20.	$\text{OH}^* + \text{OH}^* \rightleftharpoons \text{H}_2\text{O}^* + \text{O}^*$	3.7×10^{21}	48.2				
21.	$\text{OH}^* + * \rightarrow \text{H}^* + \text{O}^*$			5.6×10^{11}	24.4	1.0×10^{12}	20.80
22.	$\text{H}^* + \text{O}^* \rightarrow \text{OH}^* + *$			1.70×10^{10}	12.1	1.0×10^{19}	10.5
23.	$\text{H}_2\text{O}^* + \text{O}^* \rightarrow 2\text{OH}^*$			1×10^{11}	12.6		
24.	$2\text{HO}^* \rightarrow \text{H}_2\text{O}^* + \text{O}^*$			1×10^{11}	18.9	1.0×10^{20}	51.25
25.	$\text{C}^* + \text{OH}^* \rightarrow \text{CO}^* + \text{H}^*$			1×10^{11}	4.0		
26.	$\text{CO}^* + \text{H}^* \rightarrow \text{C}^* + \text{OH}^*$			1×10^{11}	40.3		
27.	$\text{C}^* + \text{O}^* \rightarrow \text{CO}^* + *$	3.7×10^{21}	62.8	1×10^{11}	4.3	5.0×10^{20}	62.5
28.	$\text{CO}^* + * \rightarrow \text{C}^* + \text{O}^*$	1.0×10^{18}	184	1×10^{11}	53.0	1.0×10^{13}	156.5
29.	$\text{CO}^* + \text{O}^* \rightarrow \text{CO}_2^* + *$	3.7×10^{21}	105	1×10^{11}	3.6	4.0×10^{20}	100.80
30.	$\text{CO}_2^* + * \rightarrow \text{CO}^* + \text{O}^*$			1×10^{11}	21.2		
31.	$\text{CO}^* + \text{OH}^* \rightarrow \text{CO}_2^* + \text{H}^*$			1×10^{11}	8.4		
32.	$2\text{CO}^* \rightarrow \text{C}^* + \text{CO}_2^*$			1×10^{11}	31.0		

33.	$C^* + CO_2^* \rightarrow 2CO^*$					1×10^{11}	0.0	
34.	$CO_2^* + H^* \rightarrow CO^* + OH^*$					1×10^{11}	13.6	
35.	$CO^* + H^* \rightarrow CH^* + O^*$					1×10^{11}	80.5	
36.	$CH^* + O^* \rightarrow CO^* + H^*$					1×10^{11}	0.0	
37.	$C^* + H_2O^* \rightarrow CH^* + OH^*$					1×10^{11}	38.1	
38.	$CH^* + OH^* \rightarrow C^* + H_2O^*$					1×10^{11}	0.1	
39.	$CH_3^* + ^* \rightarrow CH_2^* + H^*$	3.7×10^{21}	20			5×10^{12}	25.8	1.0×10^{21}
40.	$CH_2^* + H^* \rightarrow CH_3^* + ^*$					1.0×11^{12}	6.1	
41.	$CH_3^* + O^* \rightarrow CH_2^* + OH^*$					1×10^{11}	20.2	
42.	$CH_2^* + OH^* \rightarrow CH_3^* + O^*$					1×10^{11}	12.5	
43.	$CH_3^* + OH^* \rightarrow CH_2^* + H_2O^*$					1×10^{11}	18.6	
44.	$CH_2^* + H_2O^* \rightarrow CH_3^* + OH^*$					1×10^{11}	5.1	
45.	$CH_2^* + ^* \rightarrow CH^* + H^*$	3.7×10^{21}	20			1.0×10^{11}	25.0	1.0×10^{21}
46.	$CH^* + H^* \rightarrow CH_2^* + ^*$					1×10^{11}	12.2	
47.	$CH_2^* + OH^* \rightarrow CH^* + H_2O^*$					1×10^{11}	19.5	
48.	$CH^* + H_2O^* \rightarrow CH_2^* + OH^*$					1×10^{11}	13.2	
49.	$CH_2^* + O^* \rightarrow CH^* + OH^*$					1×10^{11}	19.9	
50.	$CH^* + OH^* \rightarrow CH_2^* + O^*$					1×10^{11}	19.3	
51.	$CH^* + ^* \rightarrow C^* + H^*$	3.7×10^{21}	20			1×10^{11}	5.4	1.0×10^{21}
52.	$C^* + H^* \rightarrow CH^* + ^*$					1.0×10^{11}	37.6	

53.	$C^* + OH^* \rightarrow CH^* + O^*$					1×10^{11}	45.9		
54.	$CH^* + O^* \rightarrow C^* + OH^*$					1×10^{11}	1.5		
	Desorption reactions								
55.	$CH_3^* + H^* \rightarrow CH_4 + 2^*$	-				1×10^{11}	5.5		
56.	$2O^* \rightarrow O_2 + 2^*$	3.7×10^{21}			$213.2-60 \times \theta_{O^*}$	1×10^{13}	51.0	1.0×10^{21}	216.00
57.	$CH_3^* \rightarrow CH_3 + ^*$					1×10^{13}	38.0		
58.	$CH_2^* \rightarrow CH_2 + ^*$					1×10^{13}	68.0		
59.	$CH^* \rightarrow CH + ^*$					1×10^{13}	97.0		
60.	$C^* \rightarrow C + ^*$					1×10^{13}	150		
61.	$2H^* \rightarrow H_2 + 2^*$	3.7×10^{21}			$67.4-6 \times \theta_{H^*}$	1×10^{13}	20.0	5.0×10^{20}	67.40
62.	$H^* \rightarrow H + ^*$					1.0×10^{13}	60.2		
63.	$O^* \rightarrow O + ^*$					1.0×10^{13}	92.6		
64.	$H_2O^* \rightarrow H_2O + ^*$	1×10^{13}		40.3		1×10^{13}	10.0	1.0×10^{13}	45.40
65.	$OH^* \rightarrow OH + ^*$	1.0×10^{13}		192.8		1.0×10^{13}	63.0	1.5×10^{13}	192.8
66.	$CO_2^* \rightarrow CO_2 + ^*$	1×10^{13}		20.5		1×10^{13}	17.0		
67.	$CO^* \rightarrow CO + ^*$	1.0×10^{13}		125.5		1.0×10^{13}	34.0	8.5×10^{12}	152.50

In Table 5.1:

- Vacant active site is represented by * and B* represent adsorbed specie.
- Units are given as A [mol,cm,s], E [KJ/mol] and S [-].
- For surface reactions and desorption, the reaction rate is given by Equation 5.9 below with $\beta = 0$, except for Deutschmann mechanism reaction 3 where the value of $\beta = -0.5$.
- In all adsorption reactions A denotes a sticking coefficient, except in Deutschmann reaction 3 where A is calculated by equation 5.15.
- In Deutschmann mechanism reaction 2 and 3 represent competing pathways of oxygen adsorption.
- Deutschmann and co-workers used the following relationship to correct the initial sticking coefficient (discussed in detail later in this chapter) of oxygen with the varying temperature.

$$S_{O_2}^o = 0.07 \frac{T_o}{T} \quad (\text{where } T_o = 300\text{K}) \quad (5.5)$$

The schemes above were proposed for complete and partial combustion of methane on platinum catalyst, and take into consideration both reactions which happen on the catalytic surface and the influence of homogeneous (gases) reactions phase on the combustion, because are specifically aimed to be used in catalytic combustion in turbines where higher temperatures are involved. When the main interest is to predict accurately the catalytic conversion when the homogeneous reaction does not play any part, Reinke et al. (2004) introduced what they called a reduced Deutschmann mechanism, which focused only on what happens on the catalyst surface. This reduced Deutschmann mechanism is shown in Table 5.2. It is based on the full scheme of Deutschmann et al. (1998) but eliminates gas phase reactions. The thermo-chemical and kinetic data used are the same as those used in the Deutschmann mechanism.

Table 5.2: Reduced Deutschmann Mechanism

				A(S)	β	E
S1	CH ₄	+ 5*	→ CH ₄ * + 4H*	0.01	0.00	0.00
S2	O ₂	+ 2*	→ 2O*	0.023	0.00	0.00
S3	O ₂	+ 2*	→ 2O*	4.9 × 10 ¹²	-0.50	0.00
S4	H ₂ O	+ *	→ H ₂ O*	0.75	0.00	0.00
S5	H*	+ O*	⇌ OH* + *	1.0 × 10 ¹³	0.00	11.50
S6	OH*	+ OH*	⇌ H ₂ O* + O*	1.0 × 10 ¹³	0.00	48.20
S7	C*	+ 2O*	→ CO ₂ * + 2*	1.0 × 10 ¹³	0.00	62.80
S8	2O*		→ O ₂ + 2*	1.0 × 10 ¹³	0.00	213.20-60 _{O*}
S9	H ₂ O*		→ H ₂ O + *	1.0 × 10 ¹³	0.00	40.30
S10	CO ₂ *		→ CO ₂ + *	1.0 × 10 ¹³	0.00	125.50
S11	OH	+ *	→ OH*	1.0	0.00	0.00
S12	OH*		→ OH + *	1.0 × 10 ¹³	0.00	192.80
S13	CO	+ O* + *	→ CO ₂ * + *	0.84	0.00	0.00

Apart from eliminating gas-phase influence, Reinke et al. (2004) also combined some of surface reactions, for example the four steps of methane chemisorption were combined into one step, see reaction S1 in Table 5.2, also, the CO surface species was ignored by combining two surface reaction to yield surface reaction S7 in Table 5.2. The kinetic parameters of the slowest reaction among the combined reactions was taken to represent the new reaction. The reduced Deutschmann catalytic mechanism was able to predict accurately the catalytic conversion of methane in the absence of the influence of gaseous chemistry (Reinke et al., 2004), and it was validated for the pressure range of 1 - 16 bars (Reinke et al., 2005).

5.4.4 Surface reaction over palladium catalyst

Surface reaction mechanisms for the combustion of methane on palladium catalyst are still very much a matter of debate. Whereas for platinum most agree that

the metallic platinum is the active site, for palladium there are different views. Some publications report that metallic palladium is the active site, while others favour palladium oxide as the active site. For this reason, many kinetic studies of proposed elementary reactions of adsorption, desorption and surface reactions can not be considered with confidence (Moallemi et al., 1999). The debate over the role of PdO and metallic Pd in heterogeneous reaction is not over yet.

Although methane is the simplest hydrocarbon, and Pd-catalyst is acknowledged to be the most efficient catalyst for methane combustion, the combustion mechanism over palladium catalyst is not yet known. Some suggest mechanism of a Langmuir - Hinshelwood type, while others a Mars-van Krevelen type and some tried to fit the Eley-Rideal type. Developing a mechanism for catalytic methane combustion on Pd catalyst is still a "black art", with the majority being constructed on an ad hoc basis relying heavily on intuition, rule of thumb or building from previously published sub-mechanisms. The following are some of the mechanisms proposed in the literature:

Langmuir -Hinshelwood type of Mechanism: Oh et al. (1991) considered that metallic palladium is the active site, and proposed the mechanism illustrated in Figure 5.8.

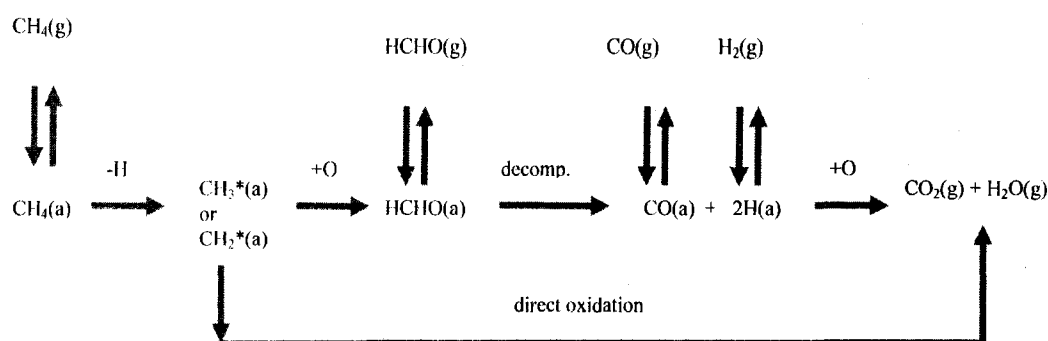


Figure 5.8: Proposed mechanism for surface methane combustion reaction as proposed by Oh et al.(1991).

The chemisorption of methane onto active sites is dissociative, where methyl or methylene radicals are produced by removing hydrogen atom. The adsorbed radicals subsequently react with adsorbed oxygen to produce CO_2 and H_2O or chemisorbed formaldehyde. This chemisorbed formaldehyde is either desorbed as HCHO or dissociate to adsorbed CO and adsorbed H atoms, which either desorbed as CO and H_2 or react with adsorbed oxygen to produce CO_2 and H_2O depending on composition of the reactant mixtures. In their experiments only trace of formaldehyde was detected in the reaction products, which suggests that decomposition of adsorbed formaldehyde intermediate is much faster than desorption (Lee and Trimm, 1995).

Cullis and Willat (1983) proposed the mechanism illustrated in Figure 5.9, where * represents a free surface site for adsorption of methane and (O^*) represents a pal-

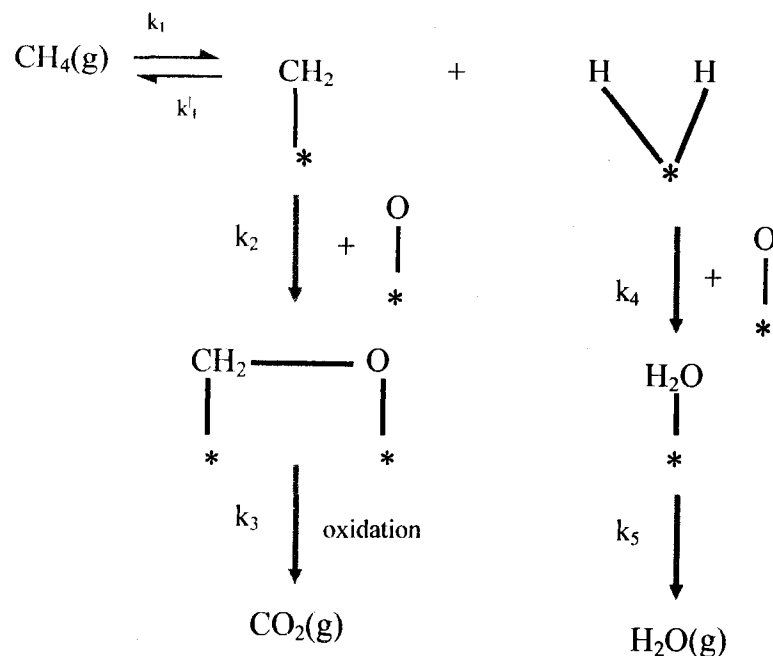


Figure 5.9: Proposed mechanism for surface methane combustion reaction (Cullis and Willat, 1983).

ladium atom attached to a lattice oxygen ion. If it is assumed that k_1 and k_1' are large in comparison with k_2 and k_4 , i.e, the surface coverage by methane is determined solely by the adsorption-desorption kinetics and the surface concentration of oxygen remains effectively constant.

Deutschmann et al. (1996) considered Pd as active site and proposed a reaction mechanism with 4 surface species and 13 surface reactions for H_2 catalytic oxidation. Moallemi et al. (1999) added 5 surface species and 8 surface reactions to form catalytic reaction mechanism scheme in which metallic palladium was considered as an active site. Their scheme adopted the Deutschmann mechanism for combustion of methane on platinum catalyst, but some of the thermo-chemical data were altered to take into account the different site density for palladium, and other values were obtained from the work of Engel and Ertl (1978). The last two reactions were postulated by Engel and Ertl (1978), the sticking coefficient for the adsorption

Table 5.3: Deutschmann Hydrogen combustion on Pd catalyst

				A(S)	E
1.	H_2	+ 2Pd(s)	\rightarrow 2H(s)	0.7	0.0
2.	H	+ Pd(s)	\rightarrow H(s)	1.0	0.0
3.	2H(s)		\rightarrow H_2 + 2Pd(s)	4.8×10^{21}	$84-15\theta_{H(s)}$
4.	O_2	+ 2Pd(s)	\rightarrow 2O(s)	0.4	0.0
5.	O	+ Pd(s)	\rightarrow O(s)	1.0	0.0
6.	2O(s)	+	\rightarrow O_2 + 2Pd(s)	7.1×10^{21}	230
7.	H_2O	+ Pd(s)	\rightarrow 2H ₂ O(s)	0.75	0.0
8.	H ₂ O(s)		\rightarrow H_2O + Pd(s)	1.3×10^{13}	44
9.	OH	+ Pd(s)	\rightarrow OH(s)	1.0	0.0
10.	OH(s)		\rightarrow OH + Pd(s)	1.3×10^{13}	213
11.	H(s)	+ O(s)	\rightleftharpoons OH(s) + Pd(s)	6.5×10^{21}	11.5
12.	H(S)	+ OH(s)	\rightleftharpoons H ₂ O(s) + Pd(s)	6.5×10^{21}	17.4
13.	OH(s)	+ OH(s)	\rightleftharpoons H ₂ O(s) + O(s)	6.2×10^{21}	48.2

of CO is temperature dependent. At 470 K, it reaches its peak value of 0.96 and then decreases with increasing temperature to a value of 0.2 at about 700 K. With this trend, a zero sticking coefficient will be reached above 1000 K. Moallemi et al. (1999) used both extreme values of sticking coefficient of 0.96 and zero, also assumed that every metal atom was available at the catalytic site. Their numerical results suggested a poor performance of their proposed mechanism.

Zhu (2001) proposed a mechanism claimed to capture the effect of water inhibition, variation of catalyst activity during operation, PdO decomposition and reformation hysteresis. The scheme was only partially validated through light-off experimental data. Two types of active site were considered.

Table 5.4: Elementary reaction mechanism schemes for catalytic methane combustion over Pd.

	Reaction	Moallemi Mechanism		Zhu Mechanism		
		A(s)	E [$\frac{kJ}{mol}$]	A(s)	E [$\frac{kJ}{mol}$]	β
1.	$O_2 + 2^* + 2O_{(B)} \rightarrow 2O^* + 2O_{(B)}$			2.1	0.0	-1.00
2.	$O_2 + 2^* + 2_{(B)} \rightarrow 2O^* + 2_{(B)}$			2.1	40	-1.00
3.	$2O^* \rightarrow O_2 + 2^*$			1.2×10^{21}	244	0.00
4.	$2O^* \rightarrow O_2 + 2^*$			1.2×10^{20}	199	0.00
5.	$1_{(B)} + O^* + O_{(B)} \rightarrow 2O_{(B)} + 2^*$			4.2×10^7	144	0.00
6.	$2_{(B)} + O^* \rightarrow 1_{(B)} + O_{(B)} + ^*$			4.2×10^7	159	0.0
7.	$O_{(B)} + O^* \rightarrow O_{(B)} + O^*$			3.7×10^{12}	90	0.0
8.	$1_{(B)} + O^* \rightarrow 1_{(B)} + O^*$			1.2×10^{12}	115	0.0
9.	$H_2 + 2^* \rightarrow 2H^*$	0.7	0.0	0.1	0.0	0.0
10.	$H + ^* \rightarrow H^*$	1.0	0.0	1.00	0.0	0.0
11.	$O_2 + 2^* \rightarrow 2O^*$	0.4	0.0			
12.	$O + ^* \rightarrow O^*$	1.0	0.0			
13.	$H_2O + ^* \rightarrow H_2O^*$	0.75	0.0	0.25		
14.	$H_2O^* \rightarrow H_2O + ^*$	1.3×10^{13}	44.0	3.7×10^{12}	60	
15.	$OH + ^* \rightarrow OH^*$	1.0	0.0	1.00		
16.	$2H^* \rightarrow H_2 + 2^*$	4.8×10^{21}	84.0	3.7×10^{21}	90	
17.	$2O^* \rightarrow O_2 + 2^*$	7.1×10^{21}	230.0	3.7×10^{21}	154	
18.	$H^* + O^* \rightarrow OH^* + ^*$			1.2×10^{21}	426	
19.	$OH^* \rightarrow OH + ^*$	1.3×10^{13}	213.0	3.7×10^{12}	253	
20.	$O^* + H \rightarrow ^* + OH^*$	6.5×10^{21}	11.5	3.7×10^{21}	17.6	
21.	$H^* + OH^* \rightarrow H_2O^* + ^*$	6.5×10^{21}	17.4	3.7×10^{21}	32.6	
22.	$OH^* + OH^* \rightarrow H_2O^* + O^*$	6.5×10^{21}	48.2	3.7×10^{21}	104	
23.	$CH_4 + 2^* \rightarrow CH_3^* + H^*$	0.19	0.0	8×10^4	196	

24.	$\text{CH}_3^* + ^* \rightarrow \text{CH}_2^* + \text{H}^*$	6.5×10^{21}	20.0			
25.	$\text{CH}_2^* + ^* \rightarrow \text{CH}^* + \text{H}^*$	6.5×10^{21}	20.0			
26.	$\text{C}^* + \text{O}^* \rightarrow \text{CO}^* + ^*$	6.5×10^{21}	62.8			
27.	$\text{CO}^* + \text{O}^* \rightarrow \text{CO}_2 + 2^*$	6.5×10^{21}	104.6			
28.	$\text{CO} + ^* \rightarrow \text{CO}^*$	0.96 - 0	0.0	0.4		
29.	$\text{CO}^* \rightarrow \text{CO} + ^*$	1.3×10^{13}	133.9	3.7×10^{12}	151.4	
30.	$\text{CO}_2^* \rightarrow \text{CO}_2 + ^*$			3.7×10^{12}	29	
31.	$\text{CO}^* + \text{O} \rightarrow \text{CO}_2^* + ^*$			3.7×10^{21}	76	
32.	$\text{CO}^* + \text{O} \rightarrow \text{CO}_2^* + ^*$			1.2×10^{21}	101	
33.	$\text{CO}^* + \text{OH}^* \rightarrow \text{CO}_2^* + \text{H}^*$			3.7×10^{21}	91	
34.	$\text{C}^* + \text{O}^* \rightarrow \text{CO}^* + ^*$			3.7×10^{21}	62.8	
35.	$\text{C}^* + \text{O}^* \rightarrow \text{CO}^* + ^*$			1.2×10^{21}	87.8	
36.	$\text{C}^* + \text{OH}^* \rightarrow \text{CO}^* \text{H}^*$			3.7×10^{21}	77.8	
37.	$\text{CH}_3^* + 3^* \rightarrow \text{C}^* + 3\text{H}^*$			1.2×10^{21}	85.1	
38.	$\text{CH}_4 + ^* + \text{O}^* \rightarrow \text{CH}_3^* + \text{OH}^*$			80	81.6	
39.	$\text{CH}_4 + ^* + \text{O}^* \rightarrow \text{CH}_3^* + \text{OH}^*$			20	106.6	
40.	$\text{CH}_3^* + 3\text{O}^* \rightarrow \text{C}^* + 3\text{OH}^*$			3.7×10^{21}	25.1	
41.	$\text{CH}_3^* + 3\text{O}^* \rightarrow \text{C}^* + 3\text{OH}^*$			1.2×10^{21}	50.1	

Mars-van Krevelen Mechanism: For this type of mechanism, authors proposed two main explanations for the different contribution of redox mechanism observed. One of the explanations is offered by Iglesia and co-workers, who proposed that for redox mechanism to occur the pre-request is to have a coordinately unsaturated Pd site on surface of PdO crystallites. Their detailed mechanism is one which was developed by Fujimoto et al. (1998), where the rate determining step is the dissociative chemisorption of methane onto a site pair consisting of adjacent Pd and PdO species. The mechanism is divided into two schemes as follows:

Scheme 1: Methane dissociation on a surface Pd-PdO_x site pair

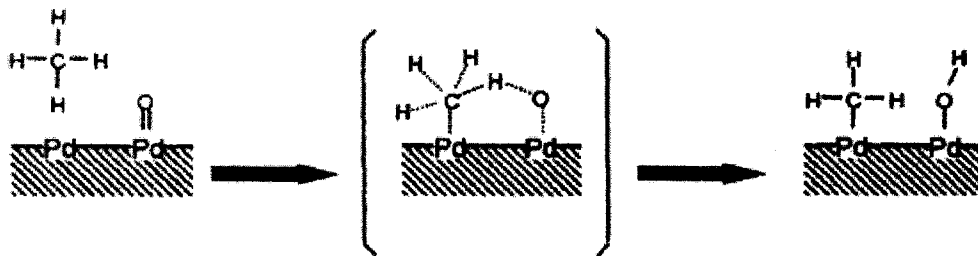


Figure 5.10: Methane dissociative adsorption on catalyst surface

Scheme 2: Pathway of methane combustion on Pd catalyst surface.

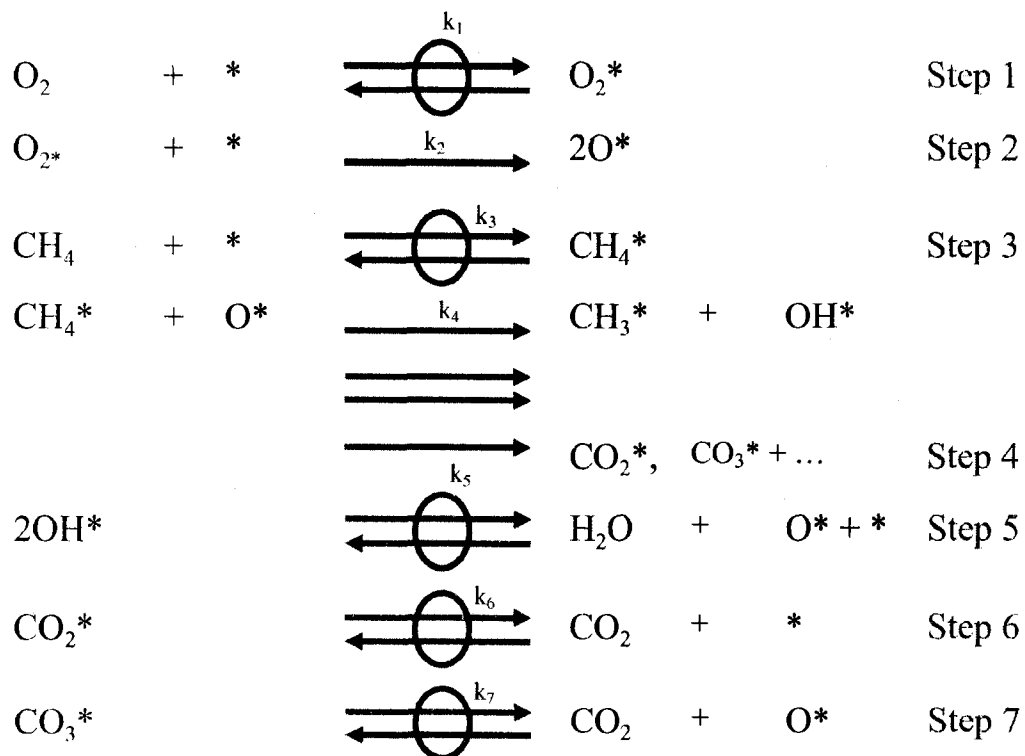


Figure 5.11: Mechanism which was proposed by Fujimoto et al. (1998)

What happens in scheme 1 is that methane from the gas phase is first physically adsorbed on saturated metallic Pd site, and then interacts with neighbouring Pd-O surface species to form surface hydroxyl group Pd-OH, as shown in Figure 5.10. This process extracts H atoms from physically adsorbed methane sequentially. The dissociative chemisorption of oxygen is assumed to be irreversible.

The scheme 2, as illustrated in Figure 5.11, shows the proposed pathways for combustion of methane on crystalline PdO_x. The first step is molecular adsorption of oxygen and its subsequent dissociation to oxygen atom shown in irreversible step 2. C - H bonds in methane are activated in step 4 by a vacancy Pd-PdO pair, following its reversible molecular adsorption in step 3. Initial H - abstraction step is a rate determining step and adsorbed OH species are observed to be the most abundant surface intermediates (MASI). The subsequent H-abstraction steps are not kinetically important because they occur after the first irreversible step and they do not involve the most abundant surface intermediates. Water is proposed to form via recombination of surface hydroxyl group.

Other explanation is that the mechanism consists of the abstraction of hydrogen from adsorbed methane species is a normal surface reaction, where the formation of O₂ - C bonds is more pronounced subjected to redox mechanism. Later, Au-Yeung et al. (1999b) used an isotopically labeled oxygen technique to investigate the methane combustion pathways on PdO catalyst. They concluded that lattice oxygen in PdO is more efficiently used in methane combustion than oxygen atom from the gas phase.

Other redox mechanisms: Other similar redox mechanisms were proposed by Garbowski et al. (1994) and Burch et al. (1995). Li et al. (2003) suggested that O₂ can be easily adsorbed onto the catalyst to form reactive species [PdO]_x. As illustrated in Figure 5.12, they claimed that it is impossible for methane to be adsorbed on the catalyst without adsorbed oxygen. The adsorbed O₂ forms a reactive oxygen species which is helpful for activating methane thus affecting the catalytic activity for methane combustion. Their scheme is as shown in Figure 5.12:

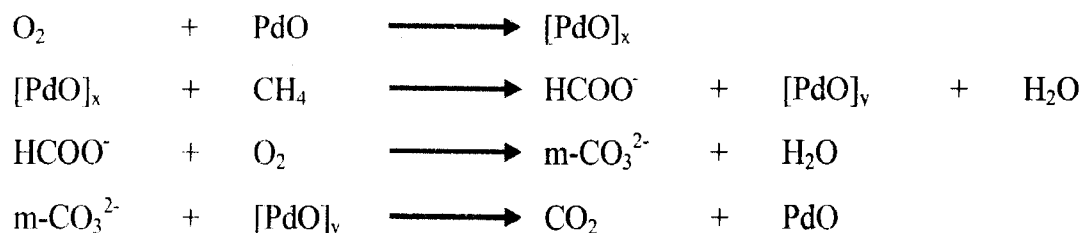


Figure 5.12: Redox mechanism as proposed by Li et al. (2003)

The adsorbed and species are intermediates which form CO and CO₂ respectively. Li et al. (2003) observed that when the O₂:CH₄ < 2, the adsorbed will be converted to CO₂ so no CO will be formed.

Demoulin et al. (2005) proposed the redox mechanism illustrated in Figures 5.13 and 5.14. Their mechanism suggests that under reaction conditions the surface of the palladium particles in Pd/γ-Al₂O₃ catalyst is always in an oxidized state. The oxidation state ranges from surface lacunary [PdO+(n-x)O*] to surface over oxidized [PdO+nO*] of PdO species, or it simply can be said that a palladium surface is always covered by a superficial layer of very reactive oxygen species developed under reaction conditions. They suggested that the activity of PdO depends on the presence of this superficial oxygen layer. This layer is regenerated either by chemisorbed gaseous oxygen, if sufficient oxygen is available, or by the PdO phase, in oxygen deficient condition, or possibly by both mechanisms. They called their scheme a combined surface redox reaction mechanism and divided the scheme into two, scheme A and B, as shown in Figure 5.13 and 5.14, respectively.

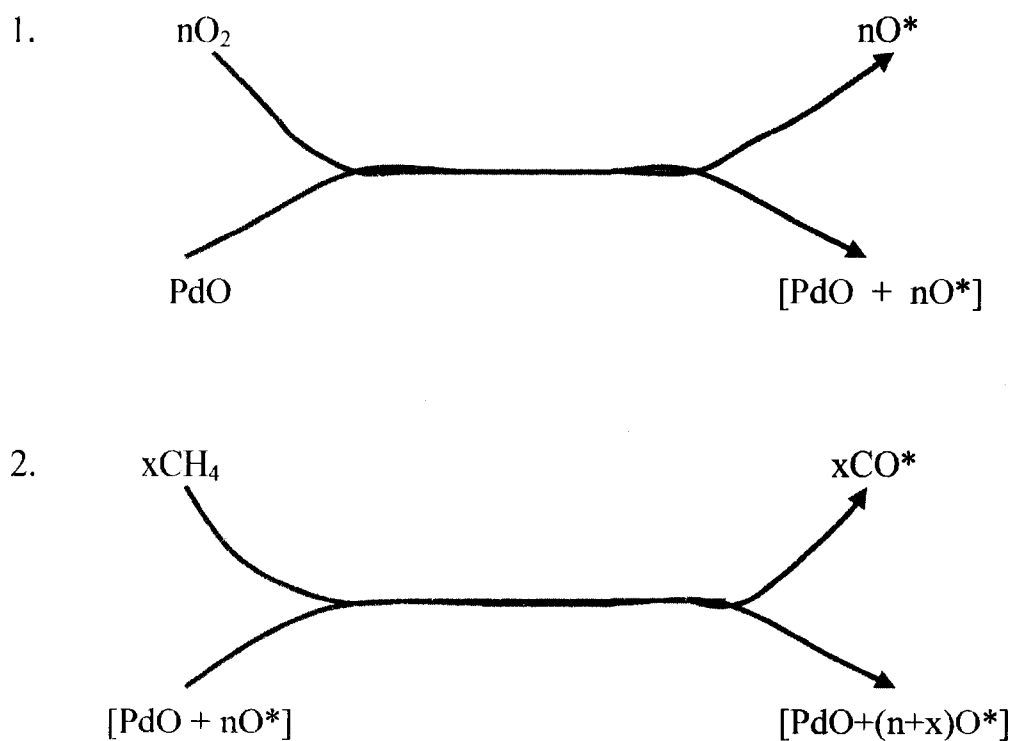


Figure 5.13: Scheme A of the mechanism proposed by Demoulin et al. (2005)

Scheme A:

Step 1: Activation of oxygen and formation of an external layer of O^* species on PdO $[\text{PdO} + n\text{O}^*]$.

Step 2: Consumption of some of O^* species of the external layer of PdO by oxidation of methane to CO^*

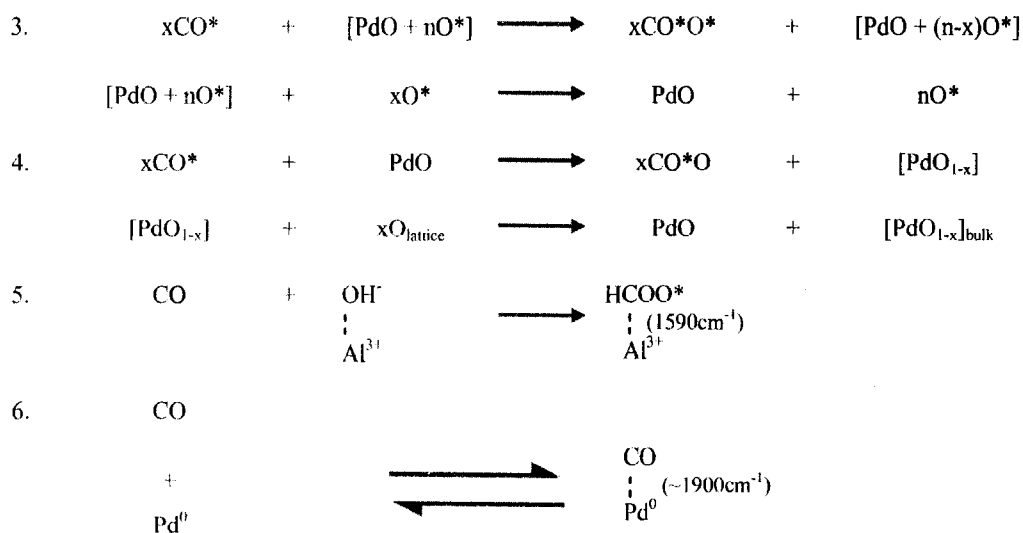


Figure 5.14: Scheme B of mechanism proposed by Demoulin et al. (2005)

Scheme B:

Step 3: oxidation of CO^* to CO_2 by the O^* species and regeneration of active O^* layer.

Step 4: oxidation of CO by surface O atom of PdO , producing CO_2 and empty surface vacancy which is regenerated by lattice O - atom coming from the bulk of the particle.

step 5: CO can alternatively react with surface hydroxyls of alumina and forms formate species or

Step 6: adsorbed onto reduced surface of Pd as bridging carbonyl species.

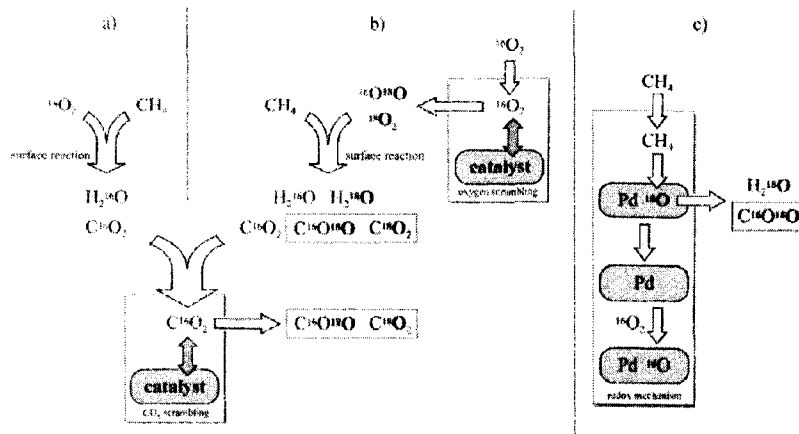


Figure 5.15: : Processes assumed to take place during catalytic methane combustion reaction over PdO/ZrO₂ catalyst, (a) surface reaction without contribution of redox reaction, leading to scrambling of CO₂, (b) Scrambling of O₂ (c) and Redox mechanism .

Muller et al. (1997; 1999) investigated the role of a redox mechanism in the catalytic methane combustion and suggested that the combustion reaction can not only be explained by the contribution of redox mechanism. According to their study, normal surface reactions based on Langmuir-Hinshelwood and Eley-Rideal type of steps also make contribution, as illustrated in Figure 5.15.

Muller et al. (1999) concluded that methane combustion on Pd-based catalyst proceeds partially via redox mechanism. They based their argument on the observation of oxidation mechanism of hydrogen and carbon atom in their experiment.

Eley-Rideal: Haneda et al. (2006) and Seimanides and Stoukides (1986) proposed an Eley-Rideal type of reaction mechanism. This type of mechanism was preferred when the study of detailed mechanism of catalytic methane combustion was beginning, but later Otto (1989) concluded that the Eley-Rideal mechanism is inconsistent with observation. Since then more researchers favoured redox (Mars-van Krevelen) mechanism and the most recent works are focusing on this mechanism as discussed above. The Eley-Rideal type of mechanism has received either little

attention or no attention at all regarding to catalytic methane combustion.

From the above, it can be observed that different mechanisms were proposed for methane catalytic combustion surface reaction over Pd-based catalyst. This demonstrates that there is neither clear agreement nor detailed understanding of the phenomena occurring on the surface of the catalyst during the catalytic combustion reaction, particularly for oxygen rich conditions. Development of a reasonable surface reaction mechanism which will be applicable over a wide range of operating conditions needs to incorporate the significant details of the complicated physiochemical behaviour of Pd-catalyst, methane surface reaction hysteresis and complicated adsorption behaviour of oxygen onto the catalyst surface.

5.5 Kinetic models

The mechanism is a description of all steps that occurs in the reaction. After establishing the reaction mechanism, the next important step is to develop a reaction rate expression of the system. The development of reaction rate expression is often quite difficult, as it has to explain the trends in kinetic behaviour mathematically. If the reaction mechanism is known it may be possible to deduce the form of the rate expression from it, and then determine the numerical value of the constants from experimental data. The models of reaction kinetics for catalytic reactors can be divided into the following two categories. The first category is known as a detailed reaction mechanism in which almost all possible elementary reactions taking place in the system are considered while in the second category the combustion system is represented by a single global reaction rate.

5.5.1 Detailed catalytic surface mechanism kinetics

In recent years, the usage of a detailed catalytic surface reaction mechanism for auto catalyst application has attracted interest, because it is believed that it allows a better prediction of the process occurring in the reactor. This approach is computationally intensive since it involves a large amount of non-linear equations in

its system. The goal of detailed kinetics is to improve the accuracy and having a predictive capability from elementary reactions without relying as much on fitting of experimental data.

For a proposed mechanism, which usually involves elementary reaction steps, the main steps are adsorption of the reactants on the active surface sites, reaction of adsorbed species, and desorption of the reaction products. To have a reasonable model, trustworthy thermo-chemical and kinetic data are required. These data include elementary reactions, sticking coefficients, activation energy, pre-exponential factor, reaction order with respect to species involved in the reaction, and rate coefficients of adsorption, desorption and surface reaction. Some of these data are available in the literature or can be estimated, but some must be obtained experimentally from independent experiments or estimated by using semi-empirical relationships.

Both gas phase and surface species can be produced and depleted by surface reactions. The production rate for each species in the reaction can be represented as:

$$R_i = \sum_{k=1}^{K_s} \nu_{ik} k_{fk} \prod_{i=1}^{N_g+N_s} [C_i]^{\nu'_{ik}} \quad (5.6)$$

where:

K_s = total number of elementary surface reactions including (adsorption/desorption),

ν'_{ik} = stoichiometric coefficients,

k_{fk} = rate coefficient for forward reaction,

$[C_i]$ = concentration of adsorbed species [molm^{-1}],

N_g = number of gas phase species,

N_s = number of surface species.

The forward rate coefficient of activated adsorption, desorption and surface reactions can also depend on surface coverage leading to the following rate expression for the rate coefficient k_{fk}

$$k_{fk} = A_k T^{\beta_k} \exp \left[\frac{-E_{ak}}{R_g T} \right] \prod_{i=1}^{N-s} \theta_i^{\mu_{ik}} \exp \left[\frac{\epsilon_{ik} \theta_i}{R_g T} \right] \quad (5.7)$$

- A_k = pre-exponential factor
- β_k = temperature exponent
- E_{ak} = activation energy of the reaction
- μ_{ik}, ϵ_{ik} = describe the dependence of rate coefficient on the surface coverage
- θ_i = surface coverage for specie i

Equation 5.7 above is reduced or simplified by some authors (Mukadi, 2003) to the following form:

$$k_{fk} = A_k T^{\beta_k} \theta^\mu \exp \left(\frac{-E_{ak}}{R_g T} \right) \quad (5.8)$$

Where μ is the correction to the reaction order of θ_i or departure from power based on the stoichiometric coefficient.

For the gas phase reaction, the temperature dependence of the rate coefficient is described by the modified Arrhenius expression

$$k_{fk} = A_k T^{\beta_k} \exp \left(\frac{-E_{ak}}{RT} \right) \quad (5.9)$$

For reversible reactions, the reverse rate coefficients are calculated by the equilibrium constant using thermodynamic data.

$$k_{rk} = \frac{k_{fk}}{K_{eq}} \quad (5.10)$$

Some authors adjusted the activation energy to allow for a variation with surface site coverage. Chen et al. (2003) proposed the following empirical expression.

$$E_{ak} = E_{ak,0} - \sigma\theta_i \quad (5.11)$$

Where $E_{ak,0}$ is the activation energy taken from the original reaction and σ is an adjusting parameter.

Concentration of surface adsorbed species is directly proportional to the fractional surface coverage and can be related as:

$$C_{sk} = \Gamma\theta_i \quad (5.12)$$

The variation of the surface coverage that is fraction of surface sites covered by specie i is calculated from surface reaction rate according to:

$$\frac{\delta\theta_i}{\delta t} = \frac{R_i}{\Gamma}, (i = N_g + 1, \dots, N_g + N_s) \quad (5.13)$$

Γ is the surface site density of the catalyst (the value for palladium is 1.95×10^{-9} mol/cm² platinum is 2.72×10^{-9} mol/cm², other used 1.66×10^{-5} molm⁻²)

Non-activated adsorption steps follow the kinetic gas theory and different authors express it differently. Veser et al. (2000) used the following:

$$k_{ads,j} = \frac{S_j \left(\frac{1}{\Gamma}\right)}{\sqrt{2\pi M_j R_g T}} \quad (5.14)$$

S_j is the sticking coefficient, which is the ratio of the rate of adsorption to the rate at which the adsorptive strikes the total surface, i.e. covered and uncovered. It is usually a function of surface coverage and temperature. M_j is the molar mass of species j

Reinke et al. (2004; 2005) used the following equation, which was also used by Deutschmann and co-workers, as well as Vlachos and co-workers.

$$k_{ads,j} = C \left(\frac{S_j}{\Gamma^m}\right) \sqrt{\frac{R_g T}{2\pi M_j}} \quad (5.15)$$

where C = the Motz correction factor

$C = (1 - \frac{\theta_{pr} S_i}{2})$ as proposed by Dogwiler et al (1999).

$C = 1$ used in Vlachos mechanism $C=1$.

m = number of adsorption site involved.

Mukadi (2003) used the following expression:

$$k_{ads,i} = \left(\frac{1}{\Gamma^m} \right) \sqrt{\frac{R_g T}{2\pi M_i}} \quad (5.16)$$

The specific surface area of catalyst active site represents the amount of active sites loaded during catalyst preparation. Its value can be used to transform the unit of reaction rate from $\left[\frac{\text{mole}}{\text{m}^2 \text{s}} \right]$ to the more common units preferred $\left[\frac{\text{mole}}{\text{m}^3_{\text{cat}} \text{s}} \right]$.

$$R_i = a_{\text{cat}} R_{fk} = a_{\text{cat}} \sum v_{ik} k_{fk} \Gamma [C_i]^{v_{ik}} \quad (5.17)$$

Parameters of elementary steps are often obtained from independent surface science experiments whenever available, and missing parameters are fitted to experimental data. The parameters from different experiments can differ substantially, especially those in involving adsorption-desorption steps. As a result, most mechanisms are not adequate to be used over wide range of conditions or to define different type of experiments. This problem will magnify further when one considers the complicated relationship of material and pressure. Thermodynamic inconsistency also should not be ruled out.

Sticking coefficient & surface coverage

Adsorption is always an important step in heterogeneous catalytic reaction, unfortunately there is no quantitatively workable dynamical theory of dissociative adsorption which can explain all of the diverse features of the process. For simplicity it is usually assumed that activated adsorption can be defined the same way as surface reactions are defined, and for non-activated adsorption the sticking coefficient should be found to calculate the adsorption coefficient. The sticking

coefficient, S_j , is a measure of the fraction of incident molecules which adsorb upon the surface i.e. it is a probability and lies in the range 0 - 1, where the limits correspond to no adsorption and complete adsorption of all incident molecules respectively. In general, S_j depends upon many variables i.e.

$$S_j = f(\text{surface coverage, temperature, particle size, } \dots) \quad (5.18)$$

In most cases the initial sticking coefficient at given temperature is required and then the necessary correction is made for its variation with temperature. Deutschmann et al. (1996) corrected the sticking coefficient of oxygen with varying temperature by using equation 5.5. The surface coverage of an adsorbed species may itself, however, be specified in a number of ways as:

- i. The number of adsorbed species per unit area of surface (e.g. in molecules cm^2).
- ii. a fraction of the maximum attainable surface coverage i.e.

$$\theta = \frac{\text{Actual surface coverage}}{\text{Saturation surface coverage}} \quad (5.19)$$

- in which case θ lies in the range 0 - 1 .

- iii. relative to the atom density in the top most atomic layer of the substrate i.e.

$$\theta = \frac{\text{Number of adsorbed species per unit area of surface}}{\text{Number of surface substrate atoms per unit area}} \quad (5.20)$$

- in which case θ_{max} is usually less than one, but can for an adsorbate such as H occasionally exceed one. Note :

- a. whichever definition is used, the surface coverage is normally denoted by θ
- b. the second means of specifying the surface coverage is only usually employed for adsorption isotherms (e.g. the Langmuir isotherm). The third method is the most generally accepted way of defining the surface coverage.

- c. a monolayer (1 ML) of adsorbate is taken to correspond to the maximum attainable surface concentration of adsorbed species bound to the substrate.

5.5.2 Global reaction kinetics

Global reaction kinetics of catalytic methane combustion over Pd and Pt has been the subject of study for the past decades and reaction rate equations of various complexities can be seen in the literature. A frequently used model for global kinetics reaction rate equation are power rule and LHHW techniques. In most cases, these equations are established from experimental data, and thus their validation are limited to a particular range of experimental conditions. In the following subsections some of the equations from the literature are briefly discussed.

i) Power rule:

When a single step global surface reaction is considered, it is often assumed that the products have no net effect on the global reaction rate. Thus the reaction rate estimation is limited to fit a general form of power rule rate expression as:

$$(-R_{CH_4}) = k p_{CH_4}^\alpha p_{O_2}^\beta \quad (5.21)$$

$$\text{Where } k = k_0 \exp\left(\frac{-E_{App}}{R_g T}\right) \quad (5.22)$$

The experimental data are used to find the values k_0 , E_{App} , α , and β . The order of reaction with respect to methane universally is agreed to be one (generally is taken as universal unless stated otherwise), and the order with respect to oxygen is zero or close to it. This form of rate expression was used by Escandon et al. (2005), who used pseudo first order model to compare the effect of different catalyst support on the catalyst activity. Cullis et al. (1983), through their experiments using a Pd/Al₂O₃ catalyst, reported that the catalytic reaction of methane is independent of oxygen and proportional to methane concentration to the power of 0.8

$$(-r_{CH_4}) = kp_{CH_4}^{0.8} \quad (5.23)$$

They worked in the temperature range of 450 - 560°C and the value of activation energy for the reaction was found to be 45 kJ/mol.

Common inhibition effect: In some cases the influence of the products and products compounds present in the feed were considered in developing the reaction rate expression. The general power rule reaction rate expression in this case is in the form:

$$(-R_{CH_4}) = kp_{CH_4}^\alpha p_{O_2}^\beta p_{H_2O}^\gamma p_{CO_2}^\eta \quad (5.24)$$

Equation 5.24 is used by many researchers to investigate the influence of each component involved in the methane catalytic reaction. Each individual researcher focused on different aspects, but the main interest was on the effect of water and carbon dioxide, as their effects were appreciated by a majority of researchers. The following are some of the works which focused on the issue of global inhibition in catalytic methane combustion.

Water inhibition: Van Giezen et al. (1999) investigated the influence of water, oxygen and carbon dioxide. Their experimental study determined the global reaction rate expression as shown in Equation 5.25, for methane combustion on PdO/Al₂O₃ catalyst.

$$(-R_{CH_4}) = k \left[\frac{C_{CH_4}^{1.0} C_{O_2}^{0.1}}{C_{H_2O}^{0.8}} \right] \quad (5.25)$$

The value of activation energy was determined to be 151 kJ/mol and 86 kJ/mol for wet and dry feed respectively, variation of activation energy between wet and dry feed proves the intensity and magnitude of water inhibition effect for catalytic methane combustion reaction.

Araya et al (2005) also investigated the effect of hydrophobicity in the catalytic reaction of methane over a Pd/SiO₂ catalyst. The global power rule reaction rate expression fitted was:

$$(-R_{CH_4}) = k_{app} C_{CH_4}^\alpha C_{H_2O}^\gamma \quad (5.26)$$

The value of methane reaction order, α , was taken to be one as general assumption states, while the value of apparent activation energy, k_{app} and water reaction order, γ were determined by optimization method. The optimum value of γ was found to be -0.25, implying a strong inhibition. Further, Araya et al. (2005) observed that hydrophobic of support do not interferes with the reaction, although apart from the inhibition effect, the presence of water also sped up the catalyst deactivation process.

Carbon dioxide inhibition: Other researchers went further and incorporated the effect of all reactants and products in the global reaction rate expression. Ibashi et al. (2003) took a common assumption for the order of reaction with respect to methane and oxygen (i.e 1.0 and 0 respectively), and then the power rule was used to fit their experimental data to find the rest of parameters in Equation 5.24. A PdO/ZrO₂ (10%w/w%) catalyst was used and results showed that products have an inhibition effect on the global reaction. The experimental data fitting result in the global reaction rate expression was:

$$(-R_{CH_4}) = k \left[\frac{p_{CH_4}^{1.0}}{p_{H_2O}^{0.32} p_{CO_2}^{0.25}} \right] \quad (5.27)$$

Water and carbon dioxide significantly inhibit the reaction rate at least to the reaction temperature up to 823 K, and the value of

$$k_{(at\ 673K)} = 2.22 \times 10^{-2} \left[\frac{\text{mol}}{\text{kg}_{cat} \text{sbar}^{0.43}} \right]$$

$$E_{App} = 108 \left[\frac{\text{KJ}}{\text{mol}} \right]$$

apparent reaction constant From their model fitting also the following results were obtained.

Increasing water concentration in the feed was observed to decrease the conversion, markedly. Ibashi et al. (2003) attributed the effect to a reversible adsorption of water on single PdO active site as shown in Equation 5.28,



Ribeiro et al. (1994b) suggested that water dissociatively adsorbed onto a pair of oxidized and reduced sites is responsible for the inhibition. The dissociative adsorption can be represent as:



The *, O* and OH* represent active site, adsorbed oxygen species and adsorbed hydroxyl species respectively. The adsorbed hydroxyls resulting from water dissociatively adsorption impede surface re oxidation during methane oxidation, which result into the catalyst being deprived of oxygen and this is the inhibition effect.

Carbon dioxide inhibition effect is controversial. For example van Giezen et al. (1999) reported no carbon dioxide inhibition effect for up to 5% carbon dioxide in the feed mixture and up to 773 K reaction temperature, others reported very weak inhibition. Fujimoto et al. (1998) suggested that the carbon dioxide inhibition effect is masked by water which compete for adsorption onto the same active sites. Ribeiro et al. (1994b) reported that if carbon dioxide concentration is higher than 0.5% and reaction temperature is higher than 553 K, the reaction order of carbon dioxide is -2, that means there will be a significant carbon dioxide inhibition. The global reaction rate expression in Equation 5.30 was proposed by Ribeiro et al. (1994b) for catalytically combustion of methane on Pd catalyst.

$$(-R_{CH_4}) = k_{eff} \frac{C_{CH_4} C_{O_2}^0}{C_{H_2O}^1 C_{CO_2}^2} \quad (5.30)$$

So far, the mechanism by which carbon dioxide inhibits the rate is unknown, however, it was suggested that CO₂ may react with PdO to form inactive PdO - CO₂ surface species. However in such cases it has been observed that CO₂ might be replaced by H₂O to form PdO - H₂O species, which is more stable and less active than the former, that is why some authors suggested that CO₂ and H₂O compete for the same sites on PdO surfaces. Mechanistic pathways and kinetics of combustion shows the effect of oxygen concentration on reaction rate depends on the operating conditions.

Groppi (2003) proposed the global reaction rate expression as:

$$(-R_{CH_4}) = k \frac{p_{CH_4}}{p_{H_2O}^{0.32} p_{CO_2}^2} \quad (5.31)$$

The apparent activation energy observe was $E_{App} = 108$ kJ/mol which is lower than lowest apparent energy reported by other authors who also considered the water inhibition effect.

Demoulin et al. (2005) through their experimental results concluded that CO₂ presence in the feed plays an important role in the reaction, but its exact role is determined by the type of support employed in the system. It can either increase or inhibit the catalytic reaction. They observed that CO₂ inhibits reaction on alumina support, whereas ceria-zirconia mixed oxide support showed significant increase in activity when CO₂ is present in the feed.

ii) Langmuir-Hinshelwood-Hougen-Watson type model:

Power rule models, although useful, can suffer from some computational problems, especially when the powers are negative. For example, the rate given by equation 5.31 will be infinite in the absences of CO₂ and H₂O, which will be true at the reactor inlet in the absence of added product.

A very popular methodology for developing rate equations is the Langmuir - Hinshelwood - Hougen - Watson (LHHW) method. Briefly, the method consists of proposing a mechanism, which is usually relatively simple. A rate determining

step is assumed and then a rate equation derived. Although the rate equation thus developed is usually empirical, it often has a good mathematical form to represent the reaction. For example, for the reaction:



a typical rate expression for the surface reaction being the rate step might be :

$$(-R_A) = \frac{k(C_A C_B - \frac{1}{k} C_C C_D)}{1 + k_A C_A + k_B C_B + k_C C_C + k_D C_D} \quad (5.33)$$

The numerator is the kinetic driving force and the denominator the inhibition term that results from adsorption. Equation 5.33 can not have a value of infinity in the absence of either reactants or products. Because many reactions have adsorption inhibition, this form of rate equation often gives good results, even if the assumed mechanism is wrong. Rate equations are often proposed in this form, even without attempting to drive them from an assumed mechanism. For example mechanisms, the derivation of a rate equation can be very complex.

For most mechanism which used the LHHW model, the activation of the methane molecule is considered the rate limiting step. Ciuparu et al. (2001; 2003) had a different opinion, and suggested that at low to moderate temperature the reaction is limited by the water desorption step on the catalyst. Ciuparu and Pfefferle (2002) demonstrated that absorbed water remains longer at the surface compared to carbon dioxide, the longer presence of water on the surface was suggested to be responsible for the deprivation of oxygen at reaction temperature, and thus water inhibition is most influential.

Fujimoto et al. (1998), derived the rate equation by using LHHW principles from the mechanism they developed. The global reaction rate expression is:

$$(-R_{CH_4}) = \frac{k_1 k_2 k_3}{3 \left[1 + k_3 C_{CH_4} + Z_1 + K_1 C_{O_2} + (Z_2)^{0.5} + \left(\frac{1}{k_6} + Z_3 \right) C_{CO_2} \right]^2} \quad (5.34)$$

Where

$$Z_1 = \frac{k_1 k_2 C_{O_2}}{3k_4 k_3 C_{CH_4}}, \quad Z_2 = \frac{k_2 k_1 C_{O_2} C_{H_2O}}{3k_4 k_3 k_5 C_{CH_4}}, \quad Z_3 = \frac{k_2 k_1 C_{O_2}}{3k_4 k_3 k_7 C_{CH_4}} \quad (5.35)$$

This equation can be simplified by considering the most abundant surface reaction intermediate (MARI) which in this case is OH^* , implies that the concentration of water is higher. Thence equation 5.34 can be simplified to:

$$(-R_{CH_4}) = \left[\frac{k_4 k_3 k_5 C_{CH_4}}{C_{H_2O}} \right] \quad (5.36)$$

For case, the concentration of CO_2 , CO_2^* or CO_3^* in total become more abundant the global reaction rate expression 5.34 may takes the following form:

$$(-R_{CH_4}) = \frac{k_1 k_2 C_{O_2}}{3 \left[\left(\frac{1}{k_6} + \frac{k_2 k_1 C_{O_2}}{3k_4 k_3 k_7 C_{CH_4}} \right) C_{CO_2} \right]^2} \quad (5.37)$$

Ciuparu and Pfefferle (2001) studied the effect of water on the catalytic activity of a Pd catalyst and found that at low to moderate reaction temperatures, the apparent activation energy was changing with temperature. They, suggested that at low temperature most of the water formed during methane combustion reaction remains adsorbed on the catalyst surface and becomes the limiting factor to the global reaction rate. As reaction temperature rises, the rate of active surface regeneration increases more rapidly than combustion reaction rate, mainly because water desorption rate strongly increases with temperature. Therefore, at higher temperature water concentration on the catalyst surface will be low and then methane activation step will now become a limiting factor. Also, at higher temperature the value of apparent activation energy remains almost constant. Ciuparu and Pfefferle (2001) used Langmuir-Hishelwood method to derive a global reaction rate expression for catalytic methane combustion reaction and their final expression is:

$$(-R_{CH_4}) = k_c C_{CH_4} \theta \quad (5.38)$$

k_c and θ are reaction rate constant and fraction of vacant active catalytic sites on the surface, respectively. By assuming that the methane coverage is very low ($\theta_{CH_4} \approx 0$), expressing the fraction of the vacant sites by the Langmuir isotherm and water concentration expressed as function of methane conversion, then Equation 5.38 can be in the following form:

$$(-R_{CH_4}) = \frac{k_c (1 - x) (C_{CH_4})_0}{1 + 2b_{H_2O} (C_{CH_4})_0} \quad (5.39)$$

Araya et al. (2005) reported that the reaction order with respect to water was $\alpha = -0.25$. To explain this higher reaction order compared to the others, they used Equation 5.39 to justify their results. Araya et al. (2005) used Equation 5.39 to derive equation 5.24, and then to show that the apparent reaction order with respect to water depends on the value of Langmuir isotherm coefficient b_{H_2O} . When $b_{H_2O} C_{H_2O} \gg 1$ then $\gamma = -1$ as they found when using Pd/ZrO₂, otherwise for low $b_{H_2O} C_{H_2O}$ value will lead the value of γ to be $-1 \leq \gamma \leq 0$ agree with their results when using Pd/SiO₃ catalyst.

Au-Yeung et al. (1999a) used the same reaction kinetics expression in Equation 5.34, as derived by Fujimoto et al. (1998), but instead of using concentration term they used partial pressure term. By considering that OH* is MARI, the equation 5.34 in partial pressure terms reduces to the following form:

$$(-R_{CH_4}) = \frac{k_3 k_4 k_5 p_{CH_4}}{P_{H_2O}} \gg k_{eff} p_{CH_4} p_{H_2O}^{-1} \quad (5.40)$$

Hayes et al. (2001) studied the catalytic combustion of methane over Pd-based catalyst and concluded that reaction kinetics of this reaction can be modelled by Mars-van Krevelen type of rate expression which includes the effect of water inhibition. Also they suggested that water inhibition effect is very important even at low concentration of pure dry feed. To them carbon dioxide had no observable effect. They also observed a change in activation energy with temperature. In their reactor model all heat and mass transfer effects were considered, therefore

this change was considered to be a result of mechanistic effects. They proposed a rate equation of the form:

$$(-R_{CH_4}) = \frac{kC_{CH_4}}{1 + KC_{H_2O}} \quad (5.41)$$

The value of the activation energy in the rate constant k was 104 kJ/mol below 811 K and 47.5 kJ/mol above. As noted earlier, the change in activation energy has been observed by others, with a transition temperature ranging from 650 to 875 K, see Hayes et al. (2001) for a summary. Hayes et al. (2001) used a single oxygen pressure, and oxygen was present in large excess.

Golodets et al. (1983) proposed the following global reaction rate :

$$(-R_{CH_4}) = \frac{k_1 C_{O_2} k_2 C_{CH_4}}{k_1 C_{O_2} + k_2 C_{CH_4}} = \frac{k_2 C_{CH_4}}{1 + \left(\frac{k_2}{k_1}\right) \left(\frac{C_{CH_4}}{C_{O_2}}\right)} \quad (5.42)$$

If oxygen concentration is relatively large and $k_1 \gg k_2$, or in other words $1 \gg \left(\frac{k_2}{k_1}\right) \left(\frac{C_{CH_4}}{C_{O_2}}\right)$, thus equation 5.42 can be reduce to:

$$(-R_{CH_4}) = k_2 C_{CH_4} \quad (5.43)$$

which shows that the reaction only depends on methane concentration, but at low oxygen pressure a small oxygen dependence can be observed.

Van de Beld et al. (1996) proposed the global reaction expression in the form below:

$$(-R_{CH_4}) = \frac{k_2 C_{CH_4}}{1 + b_{H_2O} C_{H_2O} + \left(\frac{k_2}{k_1}\right) \left(\frac{C_{CH_4}}{C_{O_2}}\right)} \approx \frac{k_2 C_{CH_4}}{1 + b_{H_2O} C_{H_2O}} \quad (5.44)$$

The simplified form of equation 5.44 is the same of equation 5.38.

Groppi (2003), after proposing the global reaction rate expression, equation 5.27, tried to test other expressions from other authors. Groppi (2003) tested equation 5.38 which was proposed by Ciuparu and Pfefferle (2001) and substituted the concentration term with partial pressure as seen below:

Table 5.5: Global reaction kinetics expressions for catalytic methane combustion over palladium based catalyst.

Reference	Catalyst/ support	Temp.	Activation energy [$\frac{kJ}{mol}$]	Reaction order			Rate equation	Inhibition
				CH ₄	O ₂	H ₂ O		
Araya et al. (2005)	Pd/SiO ₃			1.00	0.00	-0.25	0.00	H ₂ O
Araya et al. (2005)	Pd/ZrO ₂			1.00	0.00	-1.005	0.00	H ₂ O
Ciuparu et al. (2001)	PdO/Al ₂ O ₃			1.00	0.00	-1.00	0.00	H ₂ O
Cullis and Willat (1983)			45	0.80	0.00	0.00	0.00	
Fujimoto et al. (1998)	PdOx/ZrO ₂			1.00	0.00	-1.00	0.00	MASI
Golodets et al. (1983)				1.00	0.00	-1.00	0.00	
Groppi (2003)	Pd/ZrO ₂		108	1.00	0.00	-0.32	-0.25	H ₂ O, CO ₂
Hayes et al. (2001)				1.00	0.00	1.00	0.00	Water
Ibashi et al. (2003)	Pd/ZrO ₂	673K	108	1.00	0.00	-0.32	-0.25	H ₂ O, CO ₂
Monteiro et al. (2001)	Pd black		135	0.70	0.10	-0.80	0.00	H ₂ O
Monteiro et al. (2001)	Pd foil		125	0.70	0.20	-0.90	0.00	H ₂ O
Ribeiro et al. (1994b)	Pd/ZrO ₂		184	1.10	0.10	-1.00	0-2.00	H ₂ O
Van Be Beld (1996)				1.00	0.00	-1.00	0.00	
Van Gazien et al. (1999)	PdO/Al ₂ O ₃	563K	86	1.00	0.10	-0.80	-	water

$$(-R_{CH_4}) = k_c p_{CH_4}^{\gamma} \theta \quad (5.45)$$

also the Langmuir isothermal parameter, θ was expressed according to site balance equation and this yield the the following equation:

$$(-R_{CH_4}) = \frac{k_c p_{CH_4}^{\gamma}}{1 + k_{H_2O} p_{H_2O} + k_{CO_2} p_{CO_2}} \quad (5.46)$$

Equation 5.45 or 5.46 in principle could account for zeroth order with respect to oxygen, first order with respect to methane and negative fractional reaction order with respect with reaction products as realized in power law analysis (Groppi, 2003). He tried to fit the experimental data to equation 5.45 and compared to power law approach, from that he concluded that a further insight on the surface chemistry in needed to obtain a truly physically sound kinetic description. Table 5.5 summarizes the global reaction kinetic expressions found in the literature.

Chapter 6

Investigation of Pd catalyst activity

Supported palladium catalyst is accepted to be the most active catalyst for complete methane combustion. Despite its wide spread use there is no common consensus on the issue of catalytic behaviour. Therefore, to study and model the performance of the CFRR with a commercial Pd monolith catalyst, it is necessary to conduct experiments to determine the performance and activity of the catalysts to be used.

This chapter describes an experimental study of a commercial palladium monolith catalyst, and presents and discusses the experimental results. The purpose of the experiments was to investigate the behaviour of the commercial palladium monolith catalyst under a variety of reaction conditions for complete combustion of lean methane mixtures. Both temperature programmed and concentration programmed experiments were performed. The experiments were designed to provide information on the catalyst activity needed to allow for the development of a kinetic model sufficient for reactor performance prediction.

6.1 Experimental equipment

The experiments described in the following sections were conducted using an experimental reactor system located at the University of Darmstadt, Germany. The apparatus was designed and built by Stephen Salomons, and used for this work by kind permission of Umicore AG and the University of Darmstadt, Germany. Owing

to the constraint on equipment time available only a limited number of experiments were performed, and thus a detailed kinetic study was not a focus of this study. A complete detailed description of the equipment is provided by Salomons (2008) and a brief summary is given here. The diagram of the experimental apparatus is shown in Figure 6.1. The experimental apparatus consists of the following units:

- i) gas source, ii) gas mixing unit, iii) water evaporator,
- iv) heater, v) reactor, vi) labview control system,
- vii) analyzer, viii) sensors and
- ix) flow components (contains valves, piping, flow controller, etc)

The experimental set-up was designed with a fully automated control system, and was run through a computer using LabView, a program for operating, control and measurement storage for the system. The system is computerized so that all valves are opened or closed accurately within the shortest possible time. The flow rates of the inlet gases, which determine the composition of feed to the reactor are set by mass flow controllers. A condenser is positioned between the reactor outlet and analyser unit, to avoid condensation of water in the gas analysers. Figure 6.2 is a photograph of the experimental setup.

Gas source, gas mixing, flow units: There were five gas source units for each of nitrogen (N_2), oxygen (O_2), methane (CH_4), carbon monoxide (CO), carbon dioxide (CO_2) and hydrogen (H_2), each gas is supplied separately in pure form. Each supply line had its own pressure reducer, one-way valve, and mass flow controller, see Figure 6.1. The mixing unit controlled the concentration of a feed to the reactor. The static mixer in front of the reactor unit provided thoroughly mixing to make the feed mixture homogeneous.

Water evaporator and oven: When water is needed, it is added to the system by mixing the incoming gas mixture with liquid water at the evaporator inlet, and then water is vapourized inside the evaporator before entering the reactor. Just before the reactor, there is a large split-tube oven which is designed to heat the reactor feed to the desired temperature.

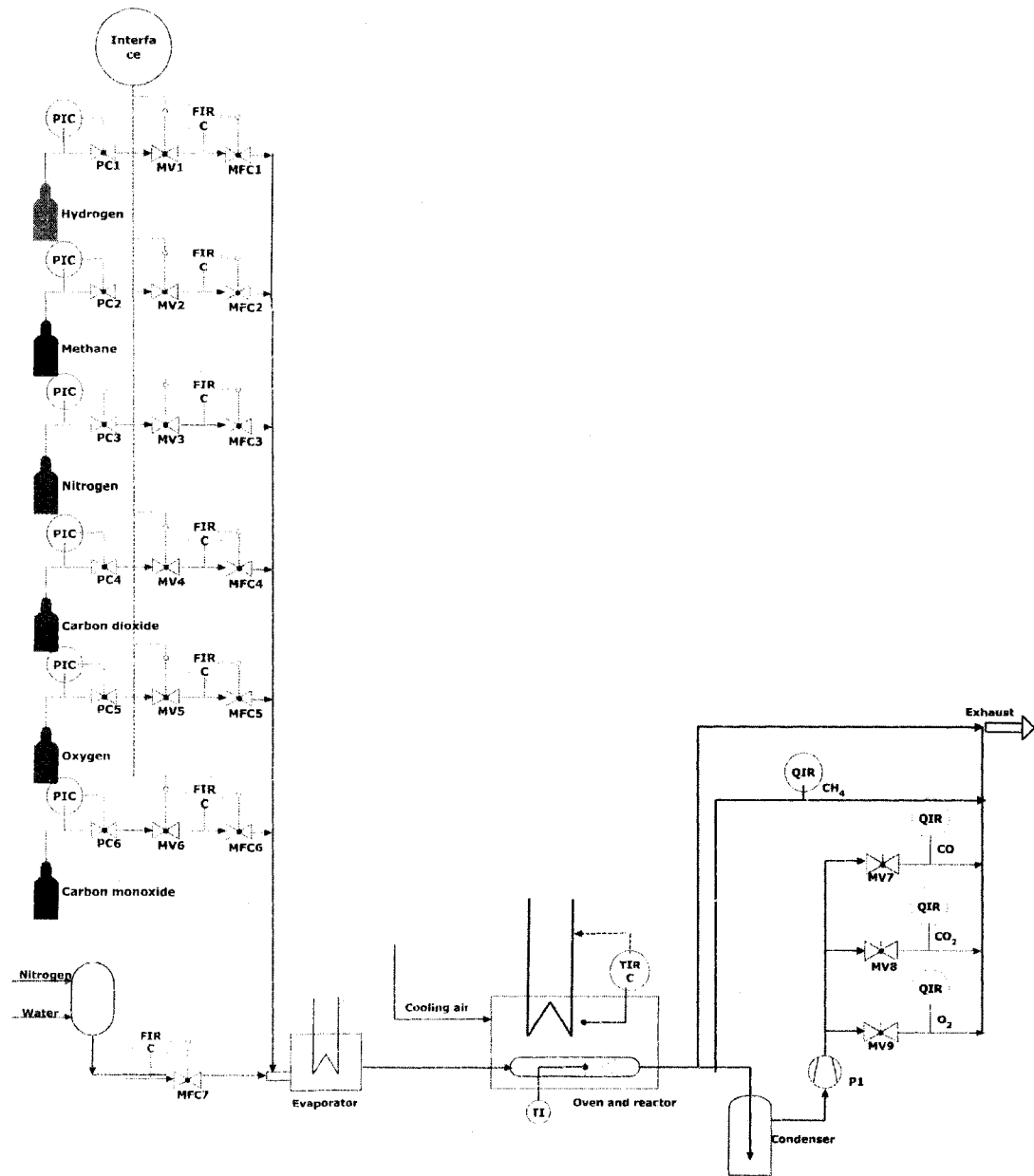


Figure 6.1: Diagram showing the experimental setup and flows, adapted from Salomons(2008)

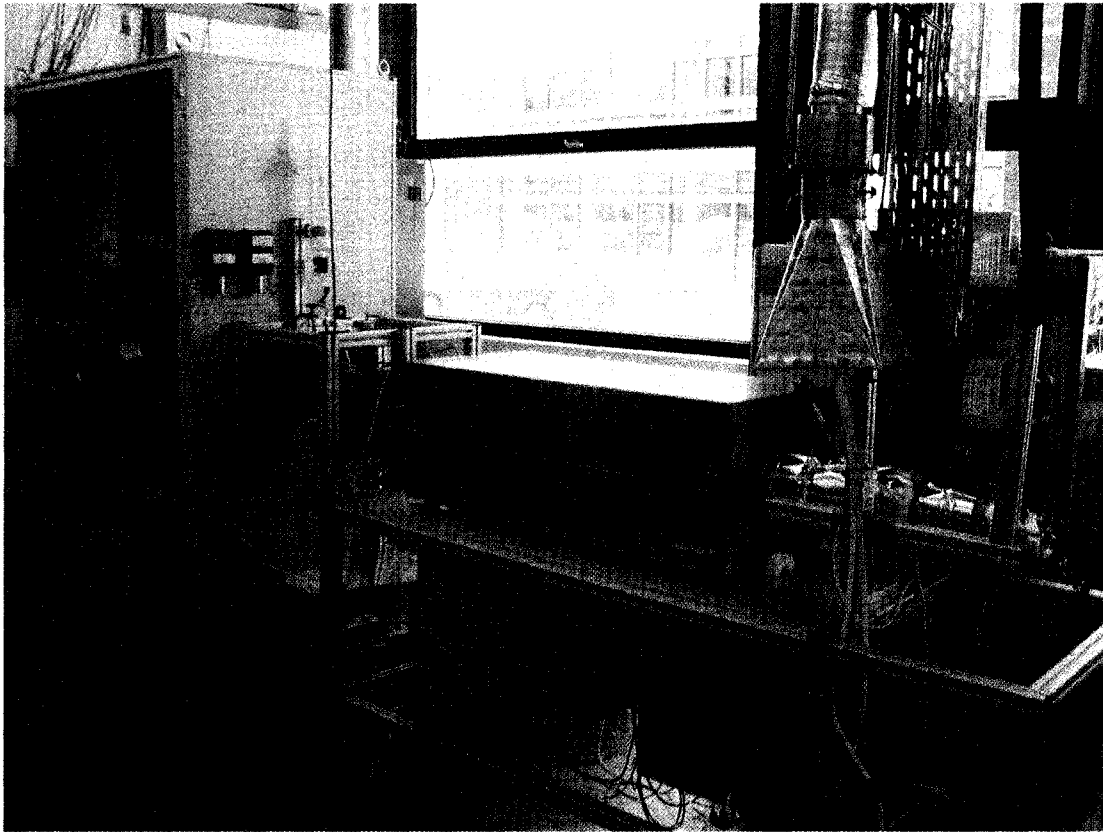


Figure 6.2: Experimental setup photograph(Courtesy of Salomons (2008))

Reactor section and monolith catalyst: The catalyst used in this study was a commercial monolith palladium catalyst supplied by Umicore AG, Automotive Catalysis Division. The palladium loading used was 80 g ft^{-3} . The cordierite monolith support was 26 mm in diameter and 76 mm long, with square channels and cell density of 400 CPI, see Figure 6.3. The nominal total wall thickness is 0.1651 mm, and the inside dimension of the channel is $1.105 \times 10^{-3} \text{ m}$ before washcoat addition. Prior to first use, the catalyst was aged for 20 hours at 473 K in a flow of hot air.

The well insulated laboratory-scale stainless reactor containing the monolith was placed immediately after a large electric heater. The heater allowed the inlet gas temperature to be controlled and ramped at the desired rate. Static

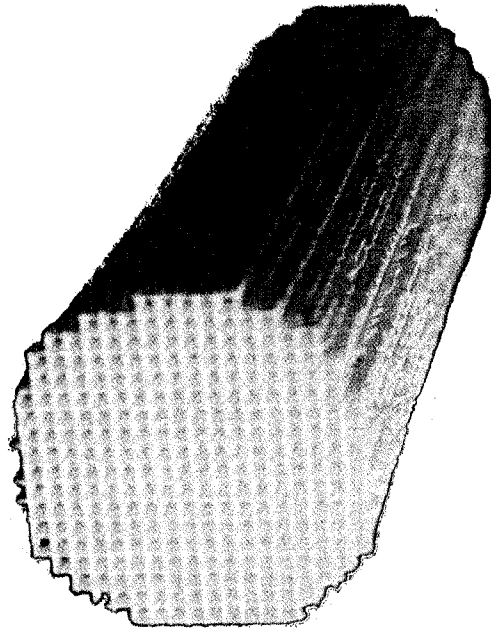


Figure 6.3: Squared channels monolith loaded with 80 g ft^{-3} Pd was used.

mixers placed at the inlet of reactor ensure uniform radial temperature and composition distribution at the monolith inlet.

Analyser unit and sensors: The analyser unit consisted of a thermo flame ionization unit (TFID), multi-component and multi-method analyzer (MLT), and hydrogen monitoring system, although hydrogen was not monitored in this work. TFID is used to measure hydrocarbon in the stream, carbon monoxide, carbon dioxide and oxygen are measured by MLT, carbon monoxide and carbon dioxide measurements utilizes infrared (IR) technique while oxygen uses a paramagnetic sensor. In MLT, all trace of water are to be removed before the mixture enters the equipment so as to prevent damage of IR cells, all measurement are done on dry basis. K - type thermocouples were used to measure temperatures, and a pressure sensor was used to measure pressure. Details on thermocouple placement are given shortly. As noted earlier, all analog measured signal were interfaced to a computer by Labview which records all data.

6.2 Experimental procedures and results

The experiments were planned with the objective of investigating ignition and extinction behaviours, the dependence of catalyst activity on surface temperature and inhibition effect of combustion products or other possible impurities, for a catalytic lean methane combustion on palladium catalyst. Both temperature and concentration programmed experiments were designed to meet these objectives. The gas hourly space velocity (GHSV) used in all experiments was 25000 hr^{-1} , calculated at atmospheric pressure and 298 K.

6.3 Temperature programmed experiments

Temperature programmed experiments were performed to determine the ignition-extinction curve for methane combustion under a variety of feed compositions. This type of experiment gives a large amount of data over a wide temperature range, which is needed for kinetic modelling.

6.3.1 Inlet compositions

A variety of inlet compositions was tested to cover the range of interest. Further, it was desired to determine the effect on reaction rate of both reactants and products. With this objective in mind, the methane concentration was varied from 500 to 9000 ppm. Two oxygen concentrations were used, 6 % and 20 % by volume. 6 % oxygen represents the composition that might be expected in the exhaust from a natural gas fuelled lean burn engine, while 20 % represents combustion in air. The effect of injected water was tested, as well as the effects of hydrogen, carbon monoxide and carbon dioxide. Water and carbon dioxide are both reaction products, as well as being present in the exhaust from a lean burn engine. Carbon monoxide and hydrogen are both present in the exhaust from lean burn engines.

Table 6.1: Gas Composition for light-off experiments.

Experiment Number	Pretreated	CH ₄ ppm [Nominal]	CH ₄ ppm [Valves]
Runs with 6% Oxygen			
146_2	yes	500	515
146_3	no	500	515
147_1	yes	1000	984
147_2	no	1000	984
149_1	yes	2000	1941
149_2	no	2000	1941
151_1	yes	9000	9090
151_2	no	9000	9090
Runs with 20% Oxygen			
153_1	yes	1000	913
153_2	no	1000	997
156_1	yes	5000	4623
156_2	no	5000	4623
Runs with 10% water and 6% Oxygen			
162_1	yes	5000	5715
162_2	no	5000	5715
Runs with 1000 ppm CO and 6% Oxygen			
164_1	yes	2000	1811
164_2	no	2000	1811
Runs with 1000 ppm hydrogen and 6% Oxygen			
165_1	yes	2000	1811
165_2	no	2000	1811
Runs with 8000 ppm CO ₂ and 6% Oxygen			
168_1	yes	2000	1810
168_2	no	2000	1810

Table 6.1 summarizes the gas compositions for the experiments performed. In all cases the balance of the mixture was nitrogen. Unless otherwise specified, the experiments used 6 % oxygen. Note that the nominal and valve methane concentrations refer to the set-point values and the values recorded from the mass flow controllers respectively. In all cases, the fractional conversion was based on the measured value.

6.3.2 Experimental procedure

Two runs of experiments were performed, one run was made on a pretreated catalyst and another on an unpretreated catalyst. Prior to any pretreated experiments, the catalyst was pretreated online with a flow of 7 % hydrogen in nitrogen for 15 minutes. The procedure of the online hydrogen pretreatment is as follows.

The hydrogen pretreatment procedure started with the flow of pure nitrogen to purge the system, at the same time the temperature ramp was started at a rate of 8 K per minute. The 7% hydrogen flow was introduced into the system when the inlet temperature reached 643 K, the 7% hydrogen flow continued for 15 minutes and the temperature ramping continued until the temperature reached 843 K; After this point, the temperature was slowly decreased by ramping down at the same rate until the temperature of 353 K was attained. At this point the system is ready to start the pretreatment run of the experiment. Immediately after completing the pretreatment run, the same experiment was repeated without the 7% hydrogen pretreatment step, and such a run has been called an unpretreated experiment.

6.3.3 Reactor temperature measurement

The reactor temperature was measured using eight K - type thermocouples placed in the monolith channels, and one thermocouple placed in front of the reactor (thermocouple T1). The other thermocouples were inserted into the channels from the reactor exit end and were securely sealed with alumina cement. The position of the thermocouples is summarized in Table 6.2.

The axial position is measured from the front of the reactor to the thermocouple

Table 6.2: Positions of Thermocouple

Thermocouple	Axial position [mm]	Radial position[mm]
T2	20	7.6
T3	1	8.9
T4	70	7.6
T5	70	5.1
T6	1	5.1
T7	35	6.4
T8	35	0
T9	20	6.4

tip, and the radial position is measured from the monolith axis. Both distances are given in millimeter (mm). With hot gas flowing through the system before the temperature ramping was started, the thermocouple in front of the reactor (thermocouple T1) read about 5 K lower than the other thermocouples inside the reactor. The difficulty of measuring accurately the gas temperature in front of the monolith using a thermocouple placed there has been noted by others (Liu, 2000) and thermocouple T1 was not used in the data analysis. The thermal response of the reactor during the ignition - extinction cycle has a large influence on the shape of the ignition - extinction curves. Therefore in the following paragraphs the measured response is examined in some detail. The thermocouple response showed a similar pattern in all experiments. The responses of thermocouple T1 (at reactor front), T3 (1 mm), T2 (20 mm), T7 (35 mm) and T4 (70 mm) for several runs are shown in Figure 6.4 to 6.9.

It can be seen from these figures that during the positive temperature ramp (ignition curve) the temperature at the front of the reactor is higher than that downstream. This effect is expected, certainly in the absence of reaction, because the hot inlet gases transfer heat at the inlet. As the reaction starts to occur, liberating thermal energy, the downstream portion of the reactor can increase in temperature,

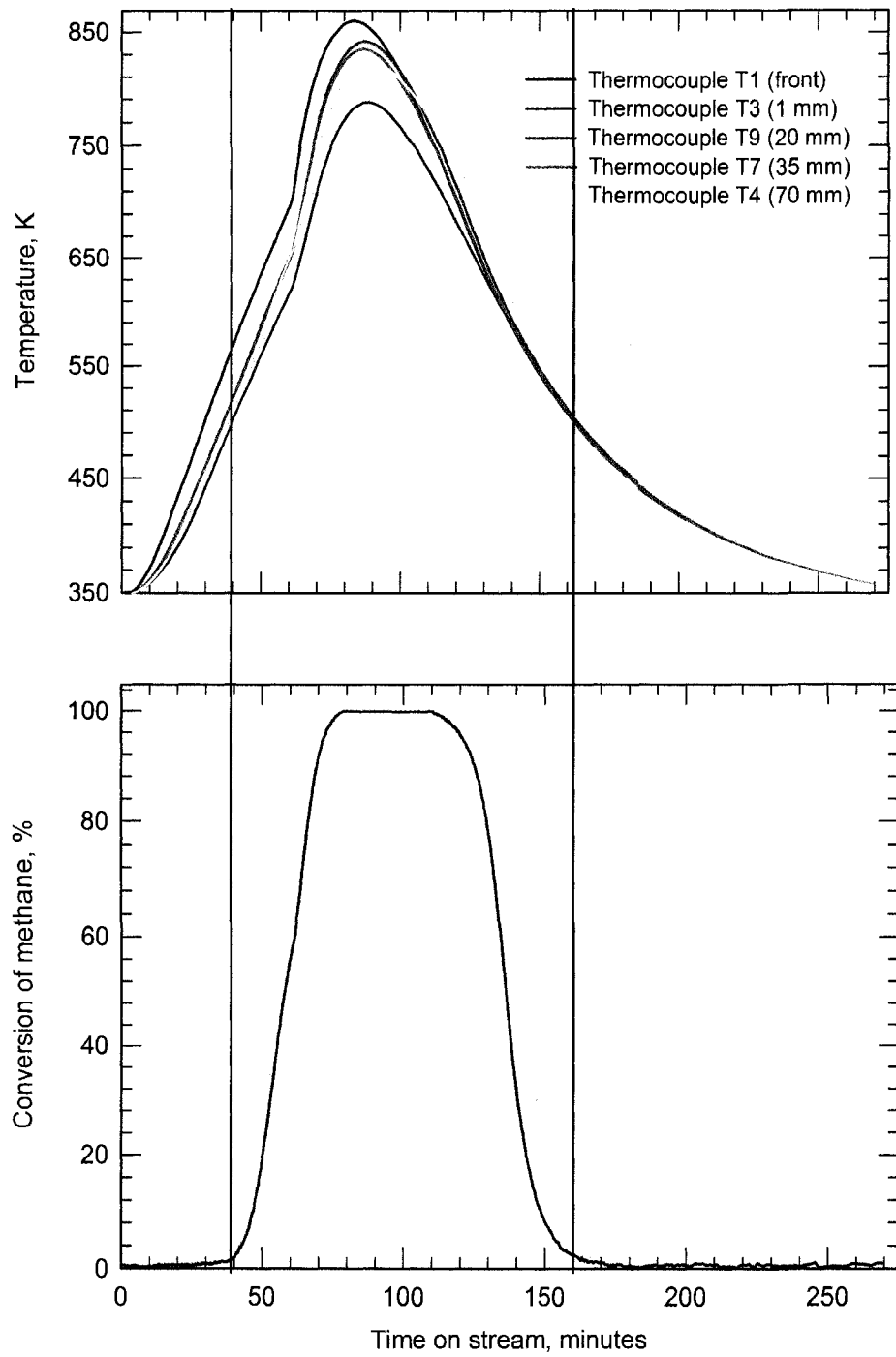


Figure 6.4: Temperature ramp profile for the gas mixture with 500 ppm methane and 6% oxygen, pretreated (run 146.2).

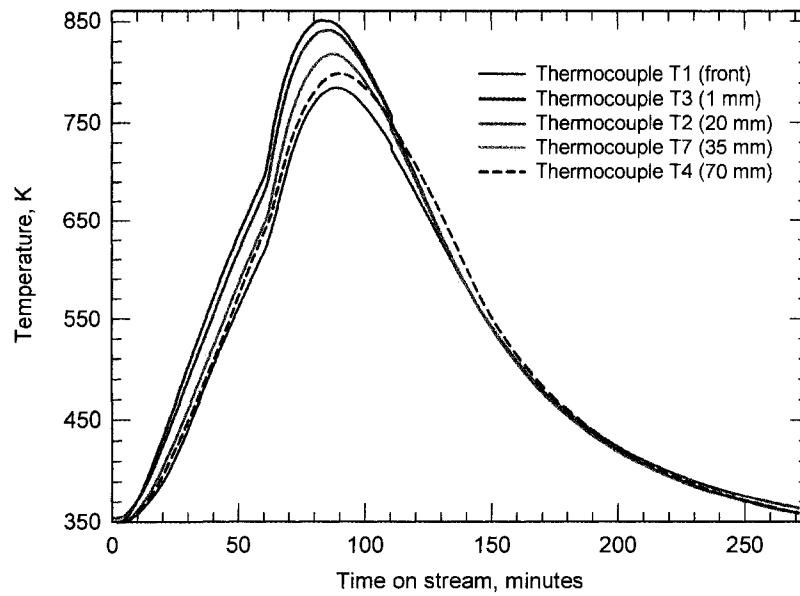


Figure 6.5: Temperature ramp profile for the gas mixture with 1000 ppm methane and 6% oxygen, pretreated case (run 147_1).

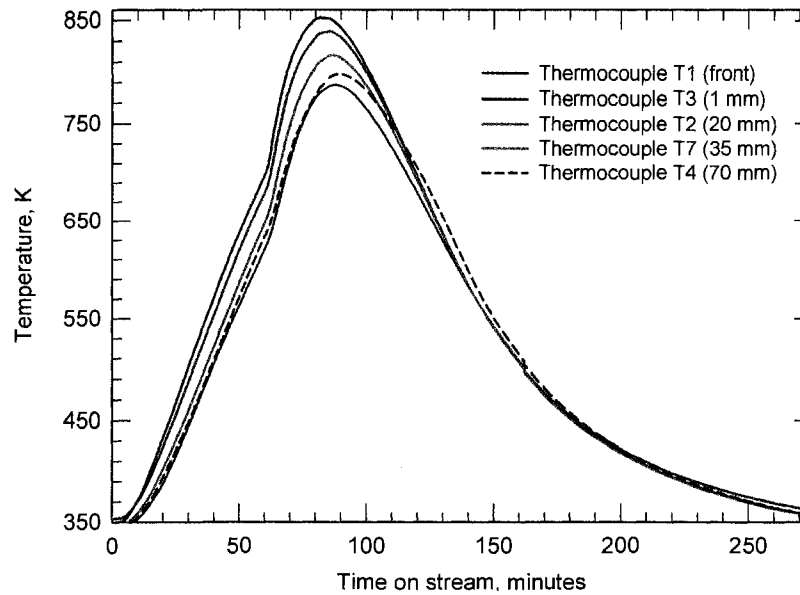


Figure 6.6: Temperature ramp profile for the gas mixture with 1000 ppm methane and 20% oxygen, pretreated (run 153_1).

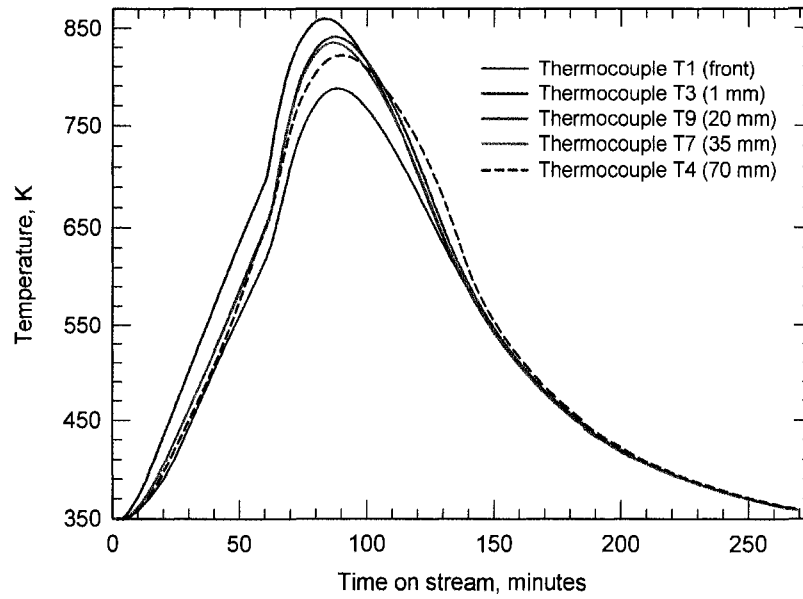


Figure 6.7: Temperature ramp profile for the gas mixture with 2000 ppm methane and 6% oxygen, pretreated case (run 149_1).

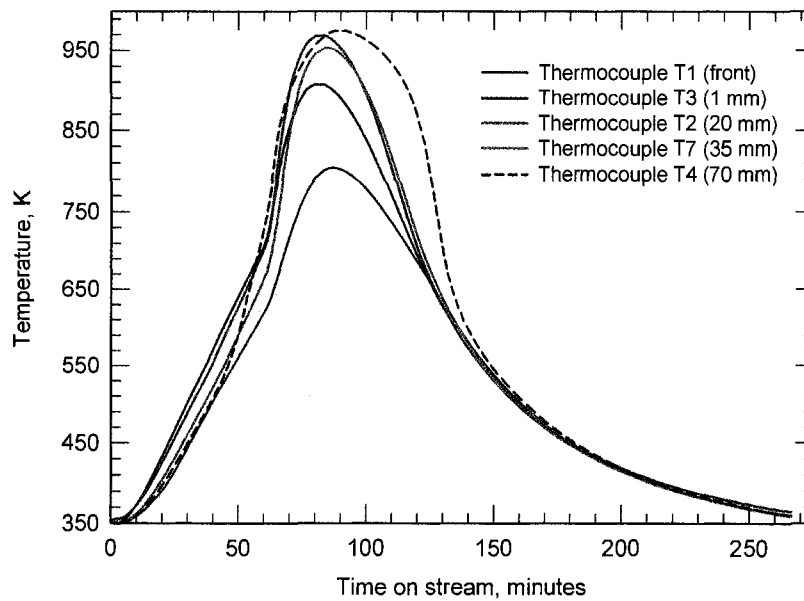


Figure 6.8: Temperature ramp profile for the gas mixture with 9000 ppm methane and 20% oxygen, pretreated (run 151_1).

becoming hotter than inlet region. The temperature rise in the reactor under reaction conditions depends on the methane concentration. Thus with 500 ppm methane the maximum temperature attained was about 850 K (see Figure 6.4) whilst for 9000 ppm methane the maximum temperature attained was more than 950 K (see Figure 6.8). Note also that at the position of maximum temperature (inflection point) for the lowest methane concentration, the front of reactor is the highest temperature, while at 9000 ppm methane, the exit of the reactor is the hottest part. It can also be noted that after about 1 hour the gradients of all ignition temperature curves quickly changed and at higher concentration were merged together.

As the reactor is slowly allowed to cool, the temperature along the reactor length slowly merge. Thus the axial gradient are much smaller for the extinction than for the ignition curve. It was also observed that pretreatment and differing oxygen concentrations had no observable effect on the pattern of the temperature curves.

Figures 6.4 to 6.8 show that the thermal response of the monolith reactor was significantly different for the ignition and extinction curves. This difference has important ramifications for the understanding of the conversion profiles and for the subsequent kinetic modelling of the reaction. Both of these points are discussed in detail later in the thesis. However, before proceeding to those discussions some further graphs are presented that illustrate more clearly the temperature gradients present during the heating and cooling cycles.

Recall from Table 6.2 that pairs of thermocouples were positioned at four axial locations along the reactor, i.e. at 1 mm, 20 mm, 35 mm and 70 mm. The radial distance between each pair, and the radial position varied with each pair; refer to Table 6.2. Figures 6.9 to 6.12 show the temperature differences recorded for each thermocouple pair as a function of time. The corresponding percent conversion is also shown on each graph. There are several important observations to be made from these graphs.

The first is that a significant radial temperature gradient exists during the transient response. The gradients are particularly strong during the ignition curve, and become relatively minor during the extinction curve. The gradients are the largest for the highest methane concentration. Clearly there is significant radial

heat transfer occurring during the ignition.

Figures 6.13 to 6.16 show the axial temperature differences recorded during the ignition and extinction cycles. In general the same conclusion can be drawn, in that during ignition the axial gradients are much larger than that observed during extinction. The implications for the conversion during the ignition - extinction cycles are discussed in the following section. The ramification for modelling are discussed in Chapter 7.

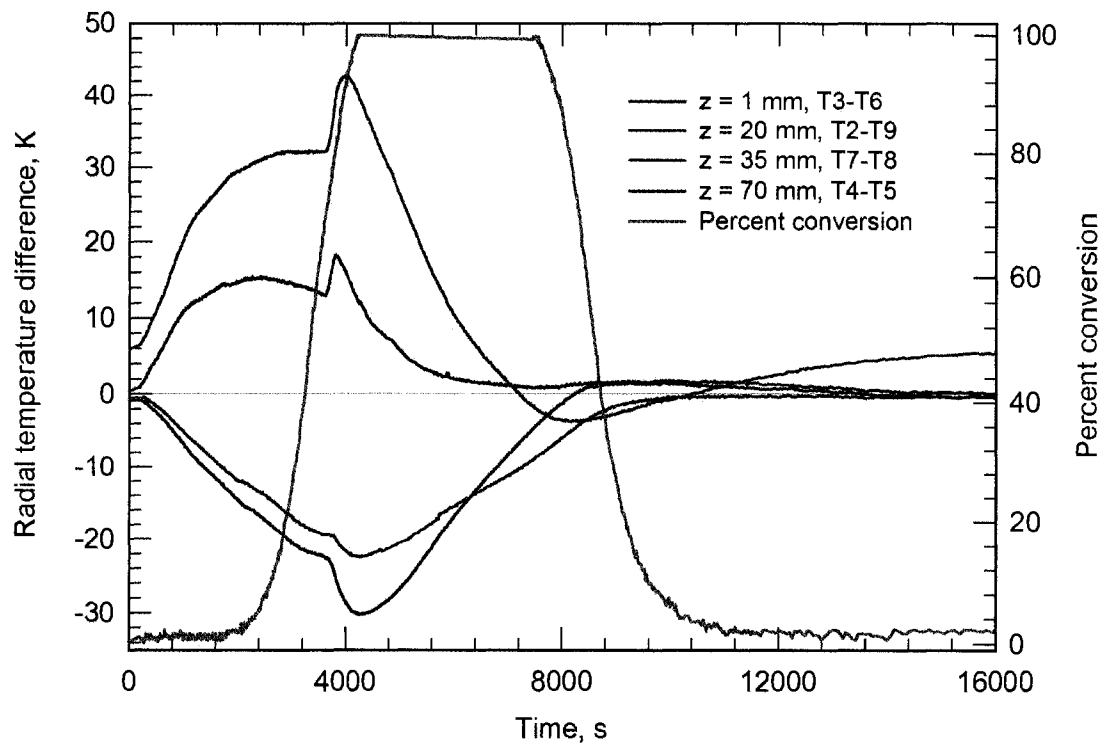


Figure 6.9: Variation of radial temperature difference with time for the gas mixture with 500 ppm methane and 6% oxygen, unpretreated (run 146.3).

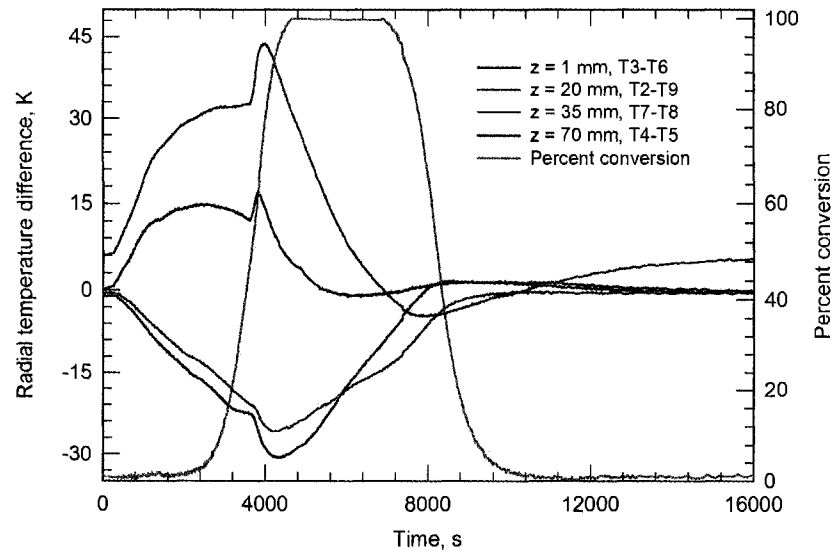


Figure 6.10: Variation of radial temperature difference with time for the gas mixture with 1000 ppm methane and 6% oxygen, untreated (run 147_2).

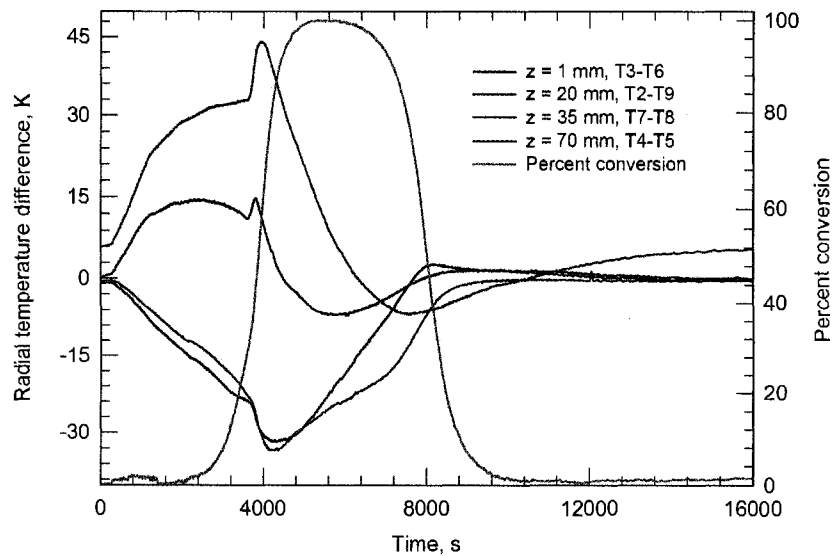


Figure 6.11: Variation of radial temperature difference with time for the gas mixture with 2000 ppm methane and 6% oxygen, untreated (run 149_2).

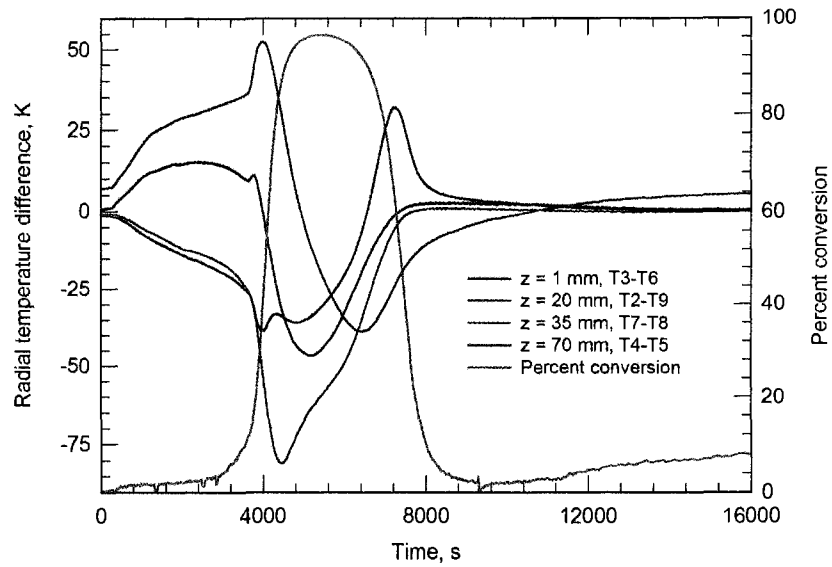


Figure 6.12: Variation of radial temperature difference with time for the gas mixture with 9000 ppm methane and 6% oxygen, untreated (run 151.2).

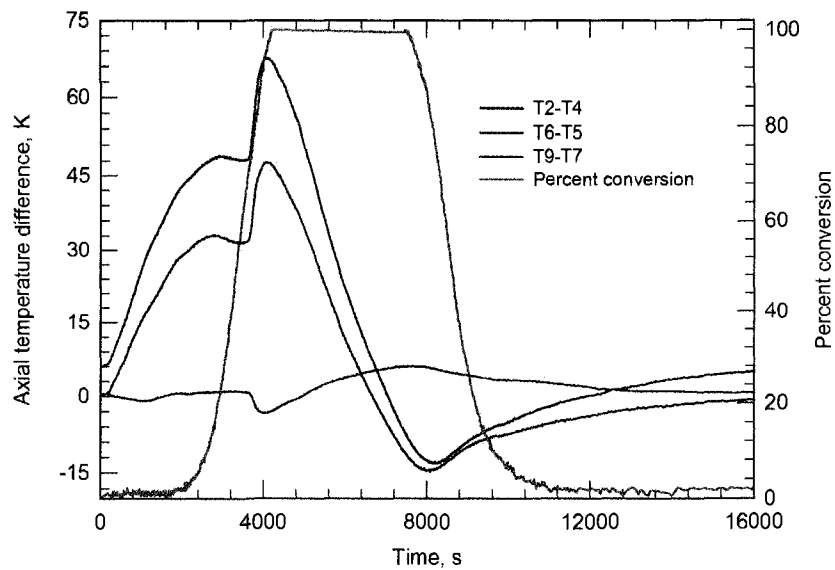


Figure 6.13: Variation of axial temperature difference with time for the gas mixture with 500 ppm methane and 6% oxygen, untreated (run 146.3).

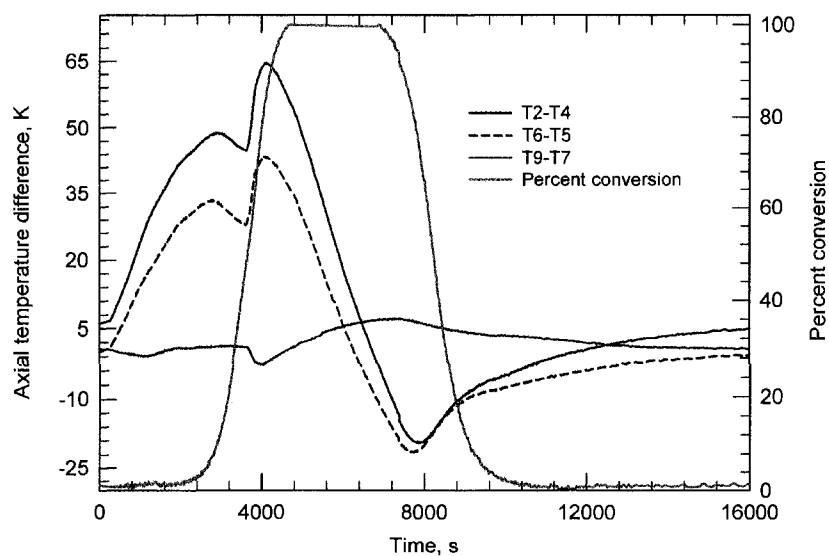


Figure 6.14: Variation of axial temperature difference with time for the gas mixture with 1000 ppm methane and 6% oxygen, unpretreated (run 147.2).

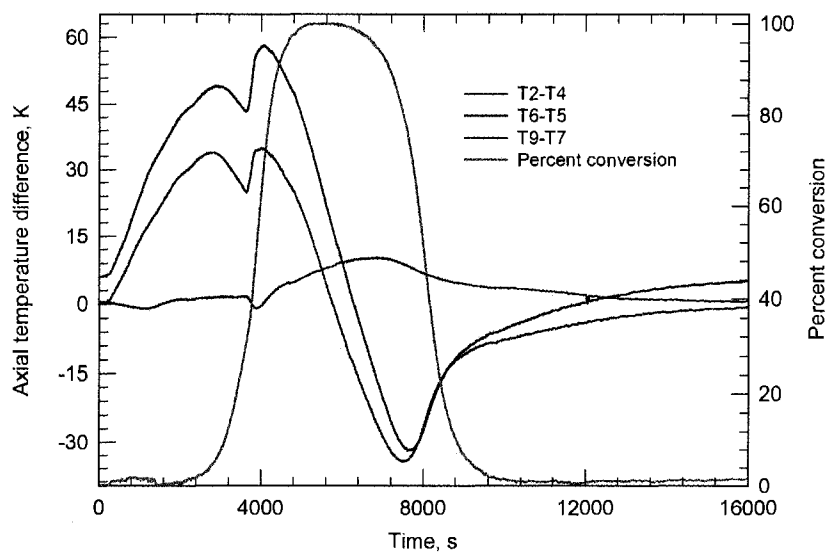


Figure 6.15: Variation of axial temperature difference with time for the gas mixture with 2000 ppm methane and 6% oxygen, unpretreated (run 149.2).

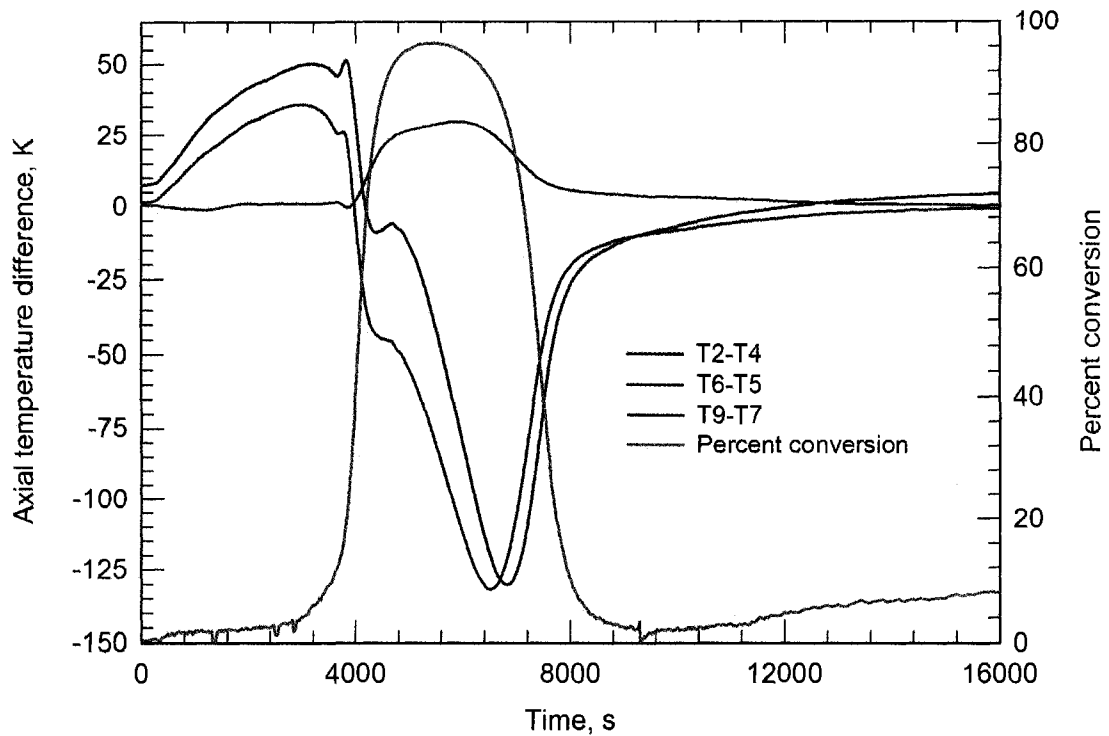


Figure 6.16: Variation of axial temperature difference with time for the gas mixture with 9000 ppm methane and 6% oxygen, untreated (run 151.2).

6.3.4 Ignition and extinction curves

In this section the results obtained from all of the temperature programmed experiments are presented. The results are presented in the form of ignition/extinction curves, in which the temperature recorded by thermocouple 3 are plotted against the fractional conversion. The experimental results will first be presented, with some discussion, and then a further discussion of all of the results will be made afterwards.

Effect of methane concentration

The first set of experiments presented is the ignition and extinction curves for the four cases of varying methane concentration with and without hydrogen pretreat-

ment. Recall from Table 6.1 that these experiments were 146, 147, 149 and 151. Figures 6.17 to 6.20 give the ignition and extinction curves for the four methane concentrations used; 500, 1000, 2000 and 9000 ppm with 6 % oxygen. Each graph shows the complete ignition extinction curve for the pretreated and unpretreated cases. Figures 6.21 to 6.24 then give the ignition branch and the extinction branch plotted with the different methane concentrations shown on the same graph, for the pretreated and the unpretreated cases, to illustrate the effect of the methane concentration.

The general trend follows the classical pattern for ignition/extinction or light-off curves. At low temperature, the catalyst is not active, and a zero conversion is the result. As the temperature is increased, the conversion starts to increase as well, and then as the reaction ignites the conversion rises fairly rapidly to 100 %. Hysteresis is present in the ignition/extinction curve, in that the catalyst shows a higher activity on the extinction branch. The pre-treated catalyst shows more activity for both ignition and extinction branches, although the difference between the pretreated and unpretreated extinction curves is smaller than for the ignition case. Also can be observed that for the ignition curve, there appears to be a change in slope at 690 to 700 K.

The pretreating by hydrogen, which should reduce the surface PdO to Pd, is consistent with some previously reported results in the literature. There is a lot of controversy currently over whether Pd or PdO is the active catalyst for methane oxidation. Indeed, it has been shown that at high temperature in the presence of oxygen the PdO transforms to Pd, which causes a reduction in catalyst activity.

This type of behaviour has led to a hysteresis effect where the reaction extinguishes at a higher temperature than the ignition (opposite to the effect observed here), see Farrauto et al. (1992). Lyubovsky and Pfefferle (1998) discussed the activity of Pd and PdO in detail, and showed that the activity could depend on the composition. However, all of this work achieved the transformation from PdO to Pd by exposing the catalyst to temperatures above about 1100 K, which was not done here. Zheng et al. (2000) showed that the activity of the catalyst depended on where the PdO and Pd were located on the surface, and demonstrated that catalyst

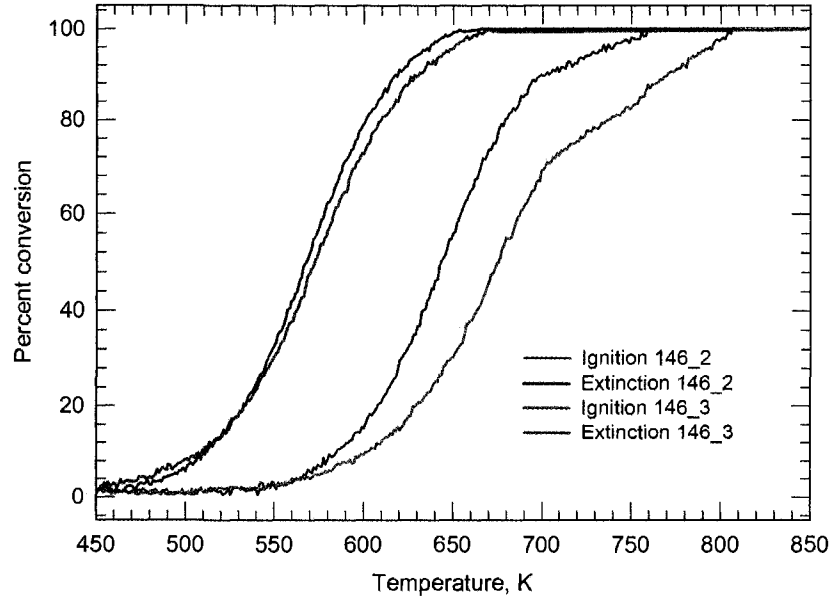


Figure 6.17: Ignition and extinction curves for 500 ppm CH₄ and 6% O₂, based on thermocouple T3.

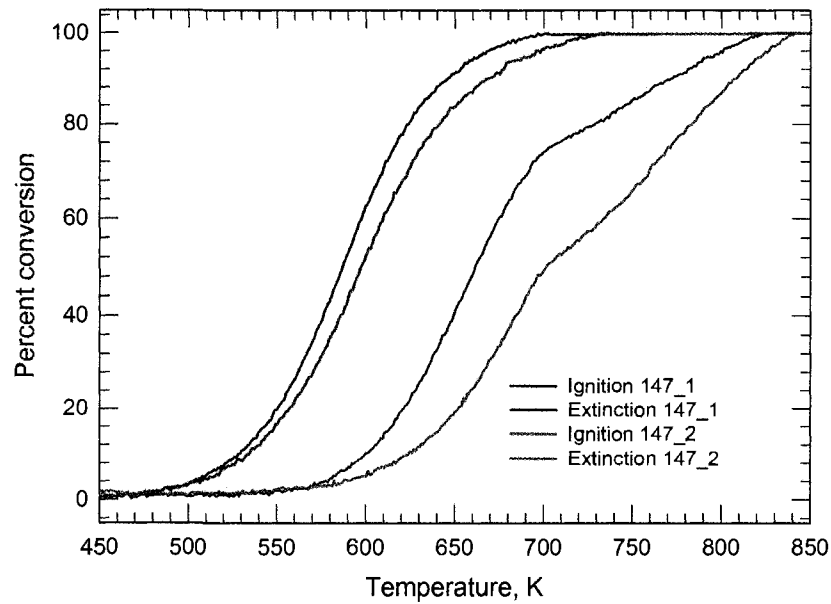


Figure 6.18: Ignition and extinction curves for 1000 ppm CH₄ and 6% O₂, based on thermocouple T3.

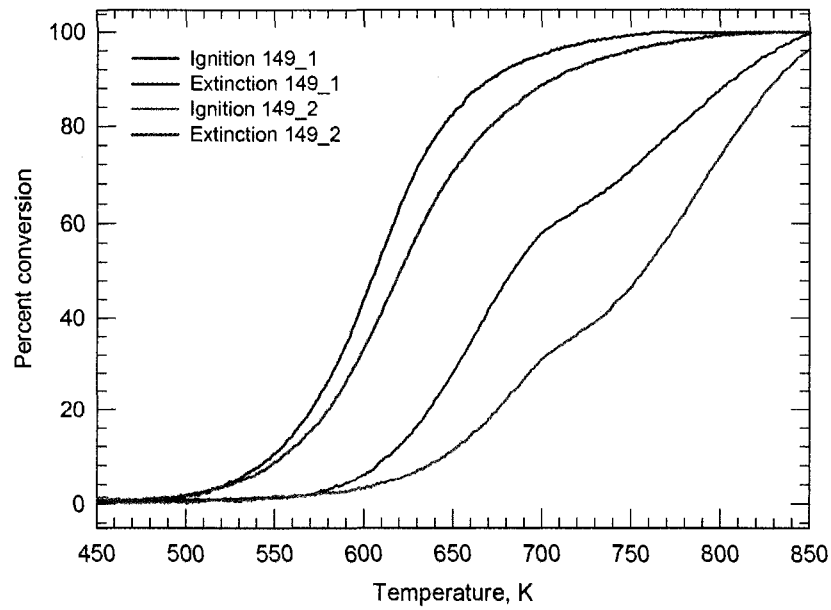


Figure 6.19: Ignition and extinction curves for 2000 ppm CH₄ and 6% O₂, based on thermocouple T3.

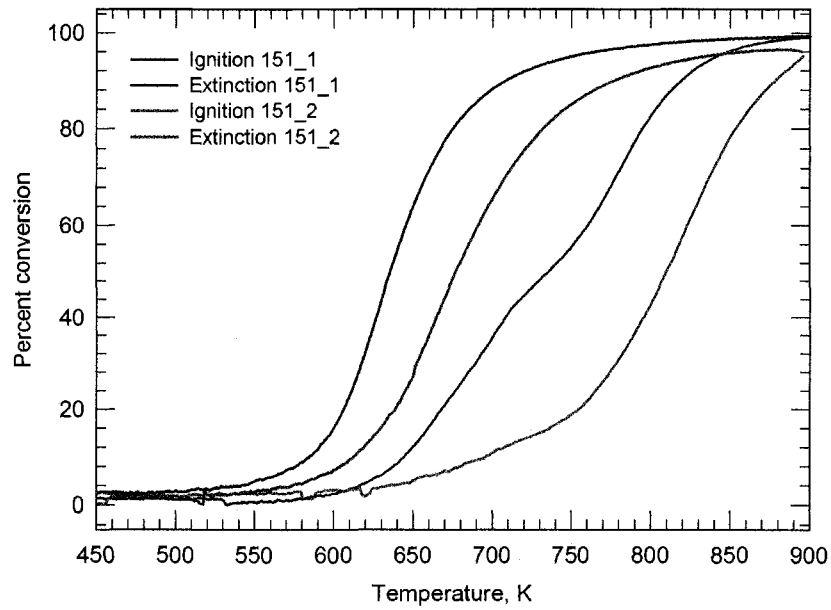


Figure 6.20: Ignition and extinction curves for 9000 ppm CH₄ and 6% O₂, based on thermocouple T3.

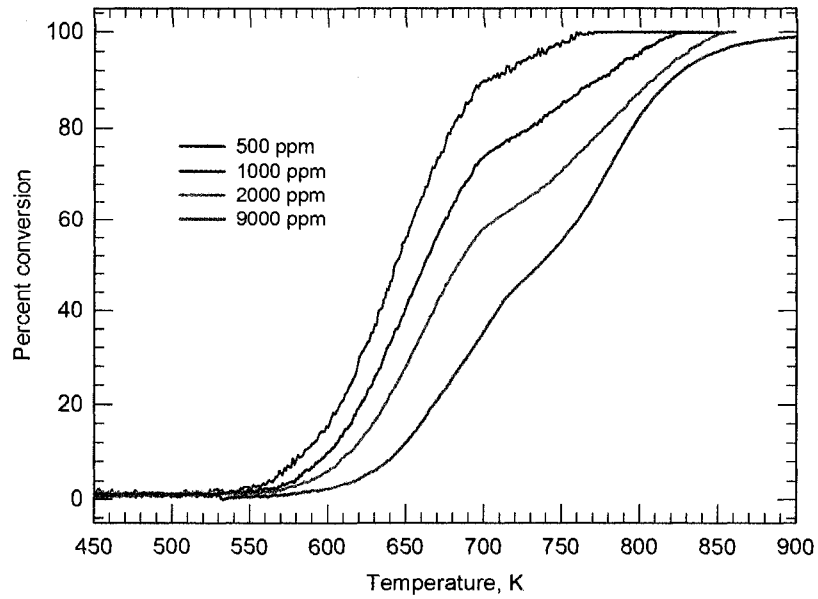


Figure 6.21: Ignition curve as function of methane inlet concentration, pretreated case, 6% O₂, based on thermocouple T3.

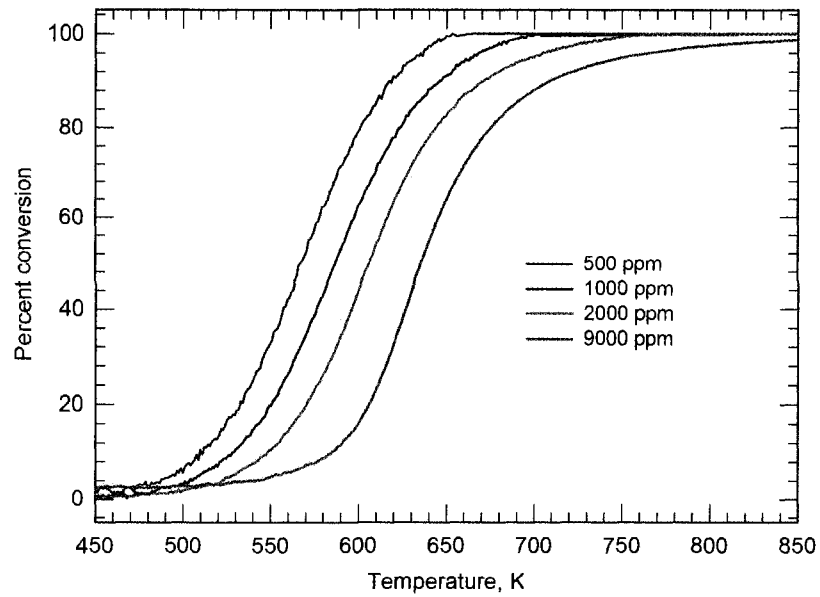


Figure 6.22: Extinction curve as function of methane inlet concentration, pretreated case, 6% O₂, based on thermocouple T3.

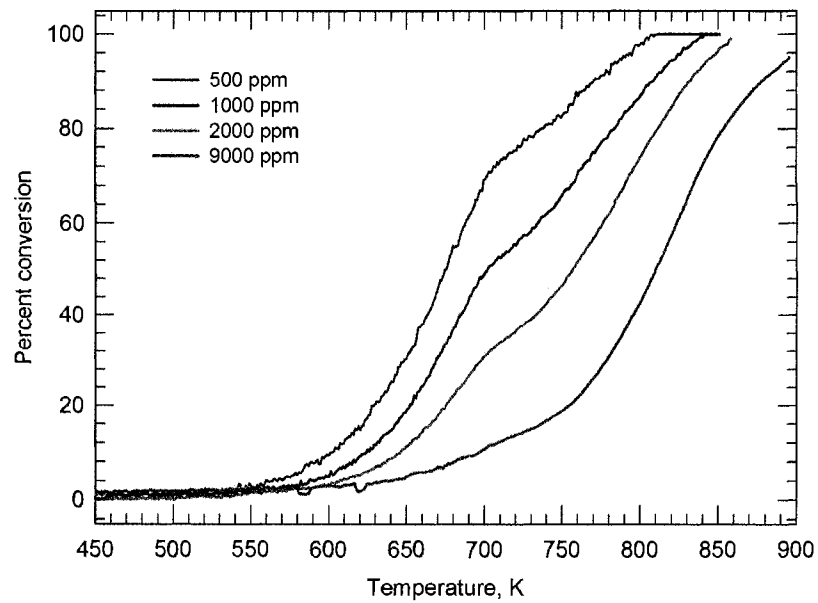


Figure 6.23: Ignition curve as function of methane inlet concentration, untreated case, 6% O₂, based on thermocouple T3.

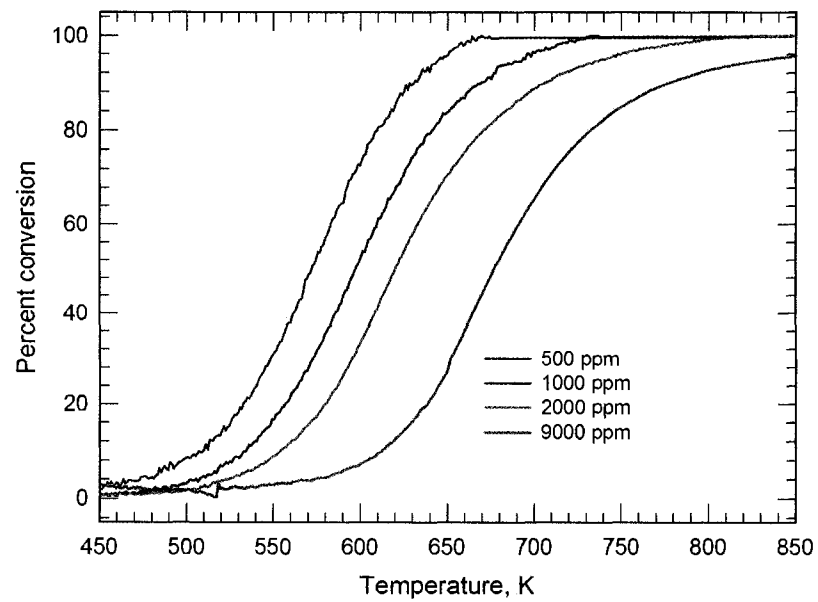


Figure 6.24: Extinction curve as function of methane inlet concentration, untreated case, 6%O₂, based on thermocouple T3.

partially reduced by exposure to hydrogen could result in an increase in catalyst activity up to 15 times.

It was observed that the light-off temperature (50 % outlet conversion) increases as a function of methane concentration. This effect is often observed when there is an inhibition effect by the reactants, as is commonly observed with LHHW type kinetic models. This result is particularly interesting, because it contradicts most of the observations in the literature, which tend to show a reaction rate dependence on methane concentration around first order. See, for example, Cullis and Willatt (1983) or Groppi (2003).

The observed hysteresis in the ignition-extinction curves can often be attributed to one of three factors. For methane combustion over palladium, one observed cause of hysteresis is the transition from PdO to Pd, which causes a loss in activity. This transition is not expected to be important in this investigation, because the reactor was not heated to a sufficiently high temperature to cause the transition. The maximum reactor temperature was about 950 K, and therefore provided that the oxygen concentration is above 2.2 % by volume the decomposition will not occur (Hayes and Kolaczkowski, 1997).

Hysteresis in ignition - extinction curves can also result when the reactant inhibits the reaction, as was observed here. These type of kinetics give rise to multiple steady states which give hysteresis, and it is likely that this is indeed a contributing factor in the present study.

The third source of hysteresis can result from temperature effects. The plots shown so far are presented as a function of the temperature recorded near the inlet of the reactor (Thermocouple T3, 1 mm from the front). However, it was seen from the plots of all of the thermocouples with time over the whole experiment that the temperature profiles within the reactor were different during the heating and cooling cycles. Recall that during the heating, the temperature near the front of the reactor was consistently higher than the temperature further downstream. During cooling, the temperature downstream could be higher or similar to that near the inlet. Furthermore, radial temperature maldistribution was seen to be higher for ignition than for extinction. Because catalyst activity (and hence conversion) is

a function of the local temperature, one has to be careful when considering the hysteresis shown by thermocouple T3.

The concentration and temperature both vary along the axis, therefore it is not possible to separate exactly the causes of the hysteresis from the outlet conversion only. However, some insight can be gained by examining the ignition extinction curves in light of the temperature time response of the different thermocouples. It has been noted that during ignition, the reactor inlet is hotter than the reactor outlet, whilst during cooling the opposite was true. For example, for runs 151.1 (9000 ppm methane) and 146.1 (500 ppm methane), the relationship between T3 and T4 during heating and cooling is represented on Figure 6.25. Figure 6.26 compares the effect of pretreatment on temperature hysteresis between for higher concentration case.

From this figure it is clear that some of the hysteresis is the result of thermal effects. It is instructive to plot the ignition extinction curves using temperatures other than T3. Considering the thermal hysteresis, plotting the ignition extinction curves using T3 will tend to maximize the hysteresis. If we use T4 instead, the effect of the hysteresis should be reduced, because on heating T4 is lower than T3 and the conversion curve will shift to the left. Figures 6.27 to 6.30 show the ignition extinction curves plotted using thermocouple T4.

It is observed from these curves that for the pretreated cases, the hysteresis is much reduced, and indeed disappears at the lowest concentration. For the unpretreated case, there is always some hysteresis present. Overall, one must be careful when interpreting the hysteresis, because of the temperature maldistribution, especially during ignition.

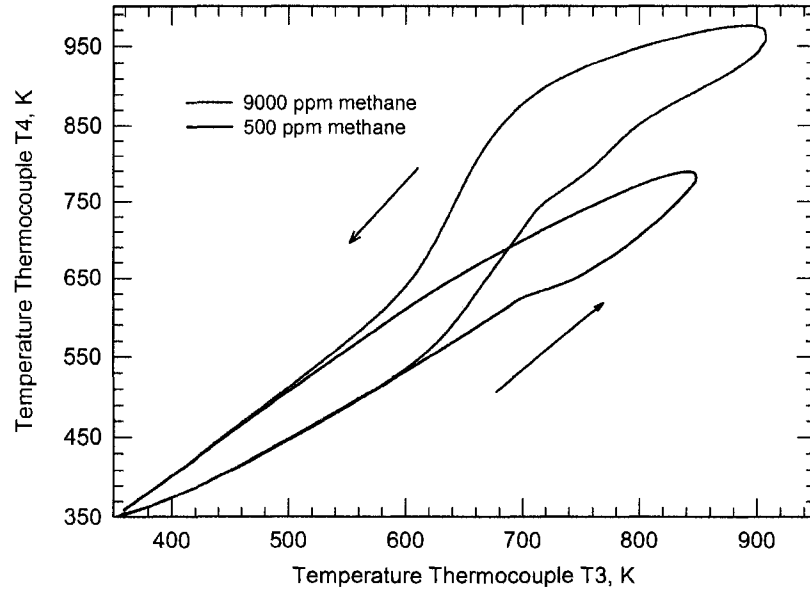


Figure 6.25: Temperature hysteresis between inlet (T3) and outlet (T4) during heating and cooling.

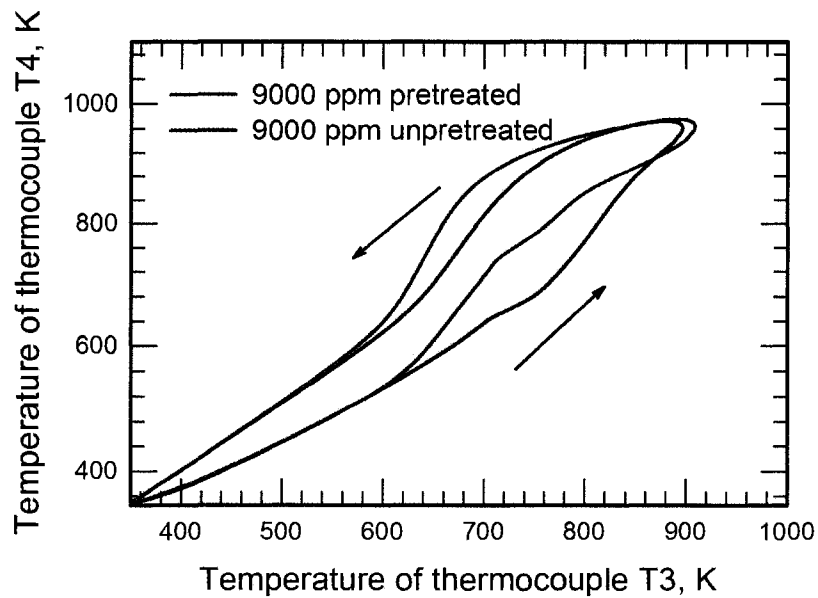


Figure 6.26: Comparing effect of pretreatment on temperature hysteresis between inlet (T3) and outlet (T4) during heating and cooling.

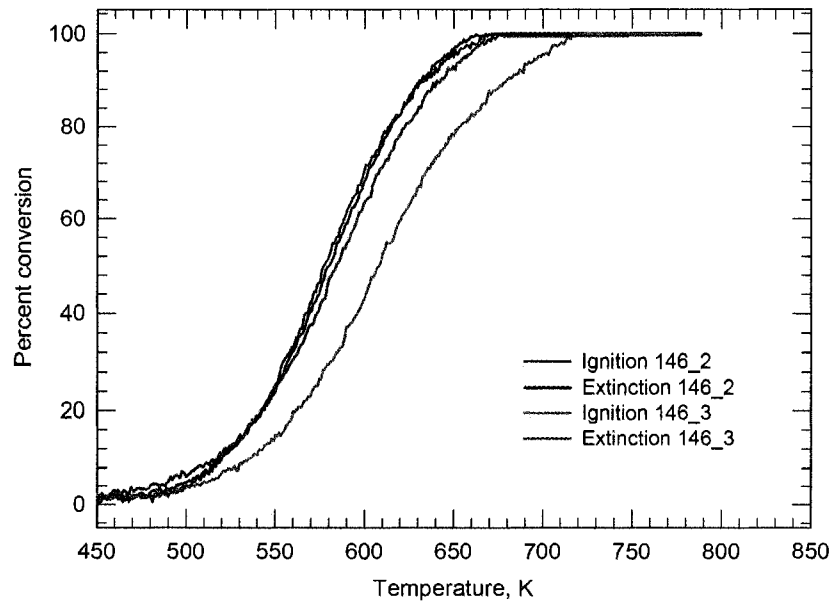


Figure 6.27: Ignition extinction curves for 500 ppm methane, pretreated and unpretreated cases, based on thermocouple T4.

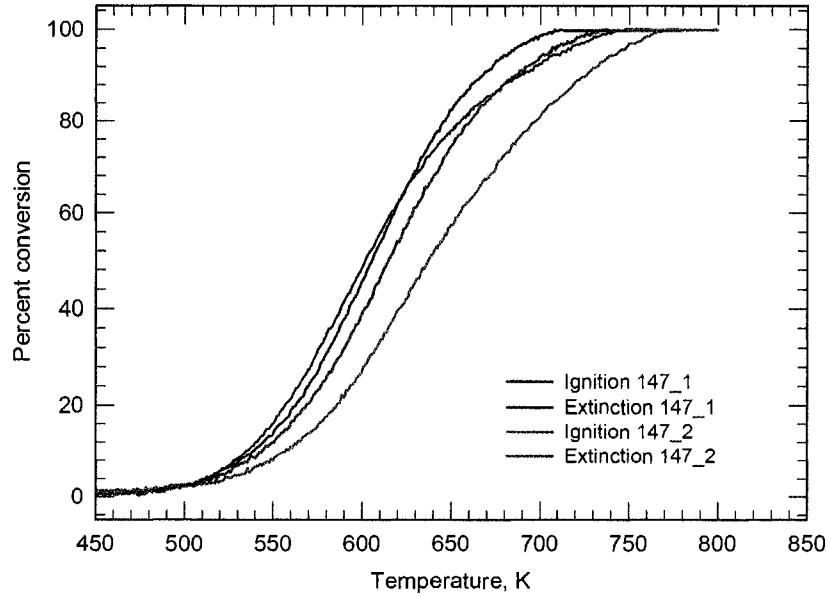


Figure 6.28: Ignition extinction curves for 1000 ppm methane, pretreated and unpretreated cases, based on thermocouple T4.

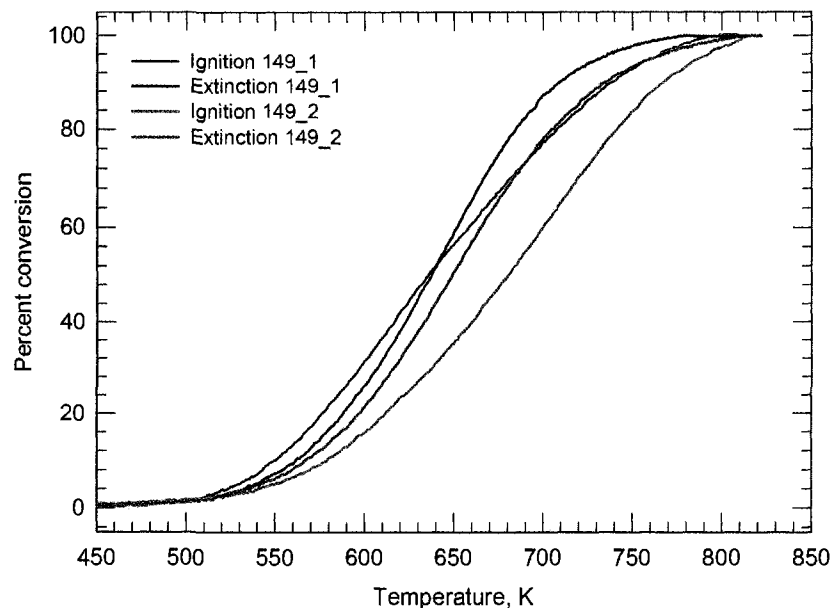


Figure 6.29: Ignition extinction curves for 2000 ppm methane, pretreated and untreated cases, based on thermocouple T4.

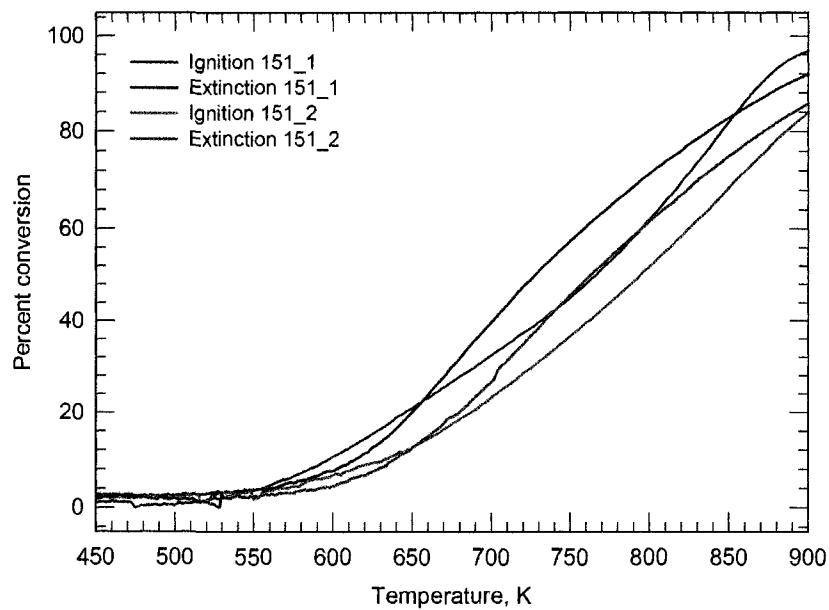


Figure 6.30: Ignition extinction curves for 9000 ppm methane, pretreated and untreated cases, based on thermocouple T4.

Effect of oxygen concentration.

The next graphs show the effect of increasing the oxygen concentration from 6 % to 20 %. Two experiments are presented. The first experiment shown in Figure 6.31 was at 1000 ppm methane and the second shown in Figure 6.32 used 5000 ppm. It is seen that for 20 % oxygen the pretreated and unpretreated cases show essentially the same activity. A possible explanation for the fact that the curves coincide is that the higher oxygen partial pressure causes a rapid reoxidation of the surface from Pd to PdO, thus negating the benefit of pretreatment.

Figures 6.33 and 6.34 compare the ignition extinction curves for 1000 ppm methane with the two oxygen concentrations. Some interesting observations can be made from this comparison.

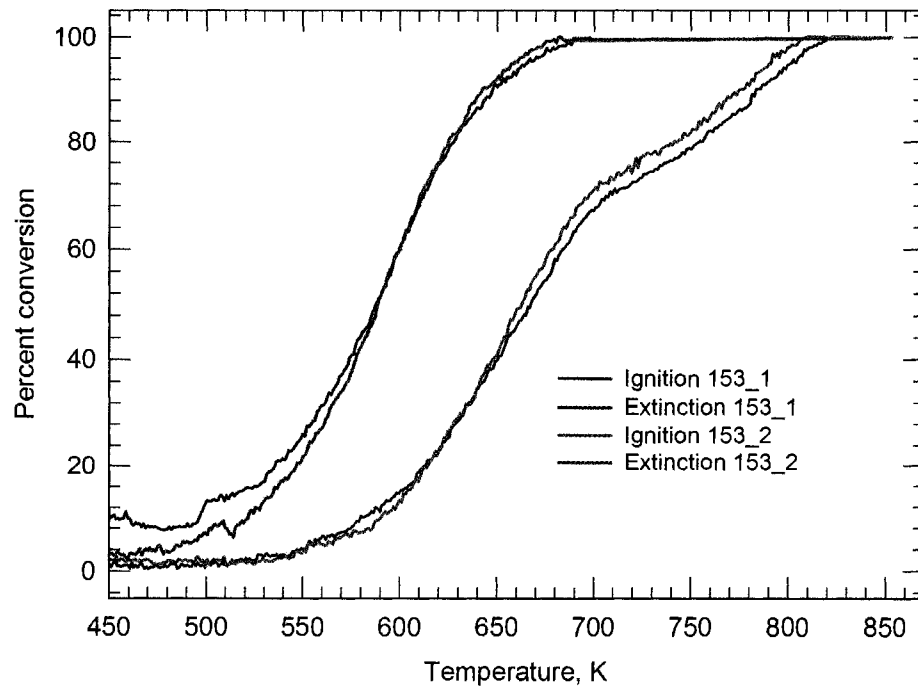


Figure 6.31: Ignition and extinction curves for 1000 ppm methane in 20% O₂, based on thermocouple T3.

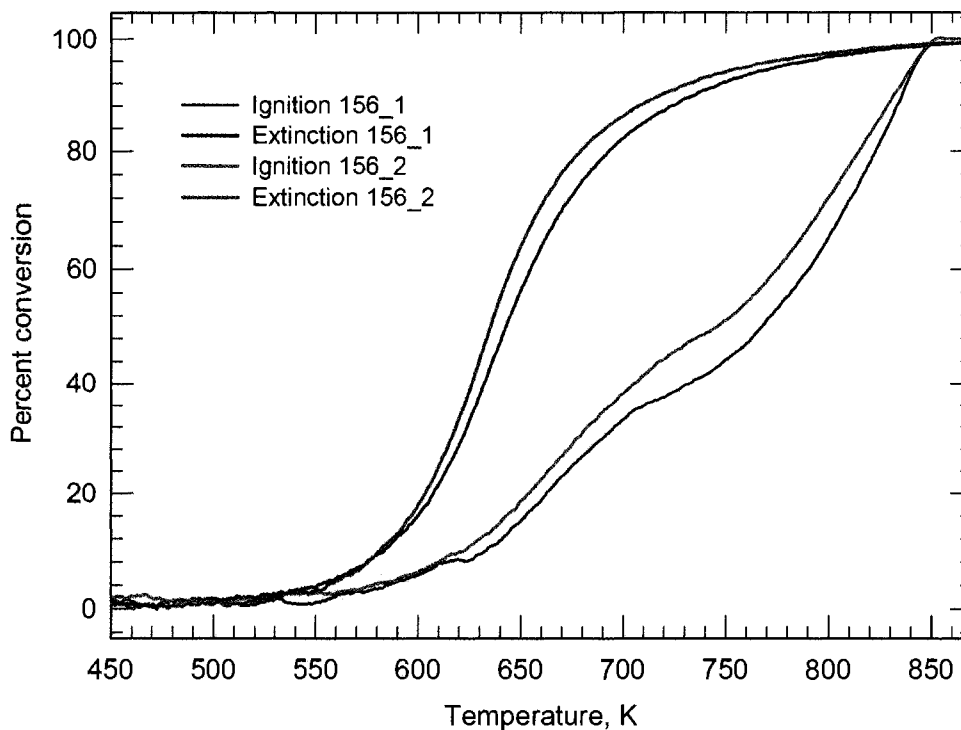


Figure 6.32: Ignition and extinction curves for 5000 ppm methane in 20% O_2 , based on thermocouple T3.

The first observation is that the ignition curves for the 20 % oxygen case follows the ignition curves of the pretreated case at 6 % oxygen. The second observation is that for the unpretreated case, the activity is higher at 20 % oxygen. The latter observation would support the case for a dependence of the reaction on the oxygen concentration. This dependency of the reaction rate on oxygen is usually reported as being close to zero order, and therefore to observe a dependence in these experiments is interesting. However, during the extinction curve the effect of oxygen concentration is much smaller.

Figure 6.35 shows the ignition extinction curve for the case of 1000 ppm methane plotted using thermocouple T4, and it is seen that as before the hysteresis becomes very small. Figure 6.36 shows there is no difference in temperature hysteresis between temperature T3 and T4 at higher oxygen concentration.

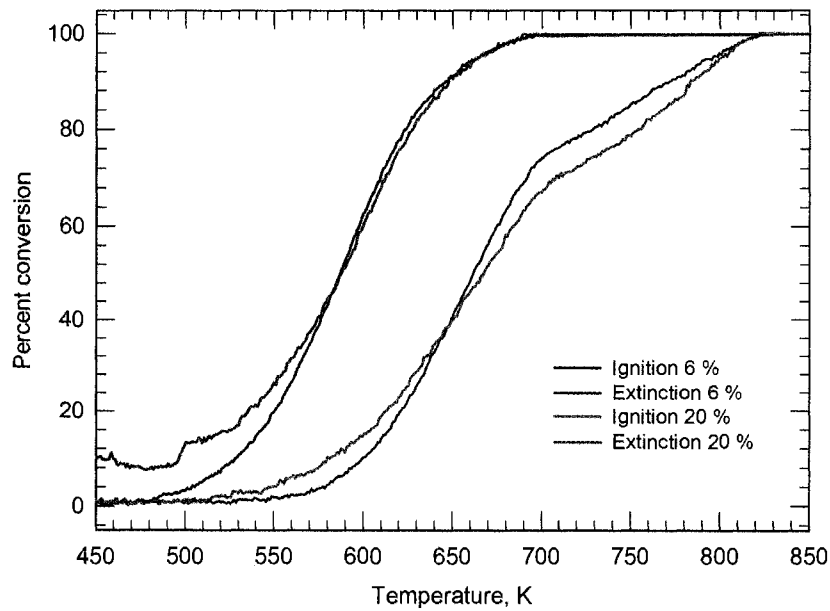


Figure 6.33: Comparison of ignition and extinction curves of 6% and 20% O₂ with 1000 ppm CH₄, pretreated case, based on thermocouple T3.

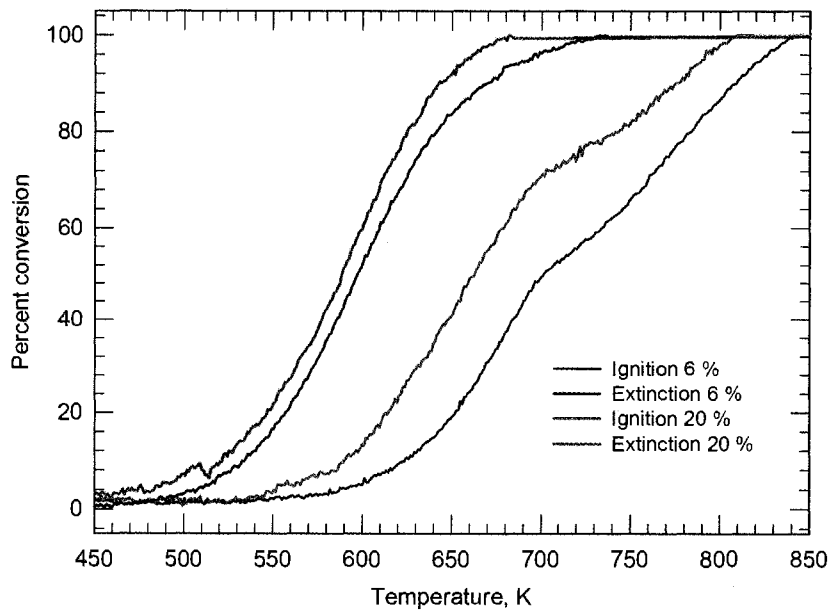


Figure 6.34: Comparison of ignition and extinction curves of 6% and 20% O₂ with 1000 ppm CH₄, untreated case, based on thermocouple T3.

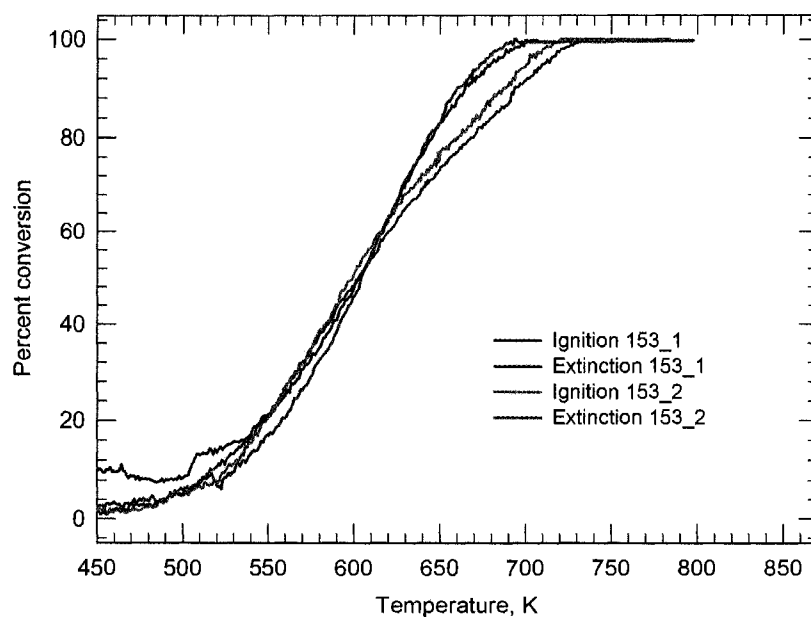


Figure 6.35: Ignition/extinction curves for 20 % oxygen with 1000 ppm methane, based on thermocouple T4.

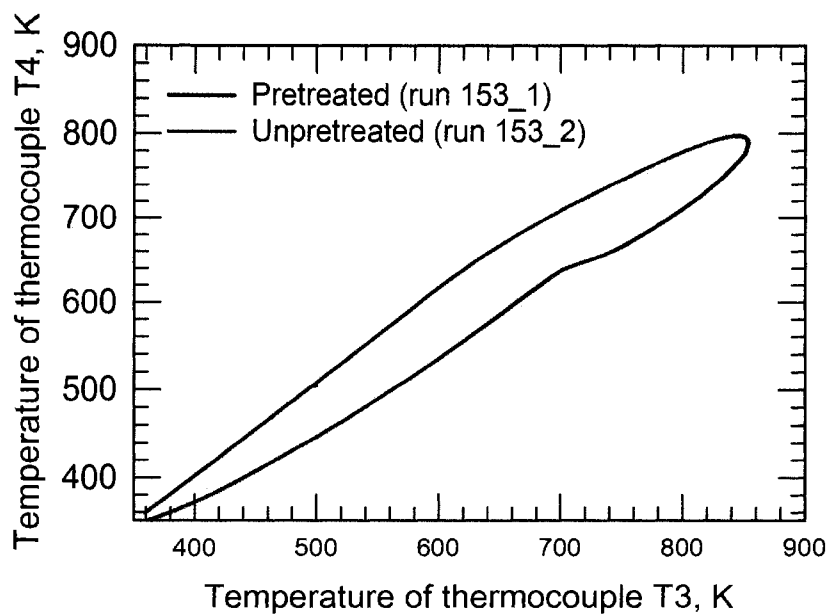


Figure 6.36: Comparing effect of pretreatment on temperature hysteresis between inlet (T3) and outlet (T4) during heating and cooling.

Effect of added water.

Figure 6.37 shows the effect of adding 10 % water to the feed for 5000 ppm methane. The water is seen strongly to inhibit the reaction and almost eliminates the hysteresis (based on thermocouple T3). A very high temperature is required to achieve complete conversion of the methane. Furthermore, the pretreated and unpretreated catalyst acts in essentially the same manner. This result is not surprising, because it has been widely reported (as discussed in Chapter 5) that water strongly inhibits the reaction. If the ignition extinction curves are plotted with thermocouple T4 rather than T3, the result shown in Figure 6.38 is obtained. It now appears that there is some hysteresis with the extinction branch lying to the right of the ignition branch. With added water obvious the temperature hysteresis exist as illustrated by Figure 6.39 but the effect of pretreatment was undermined.

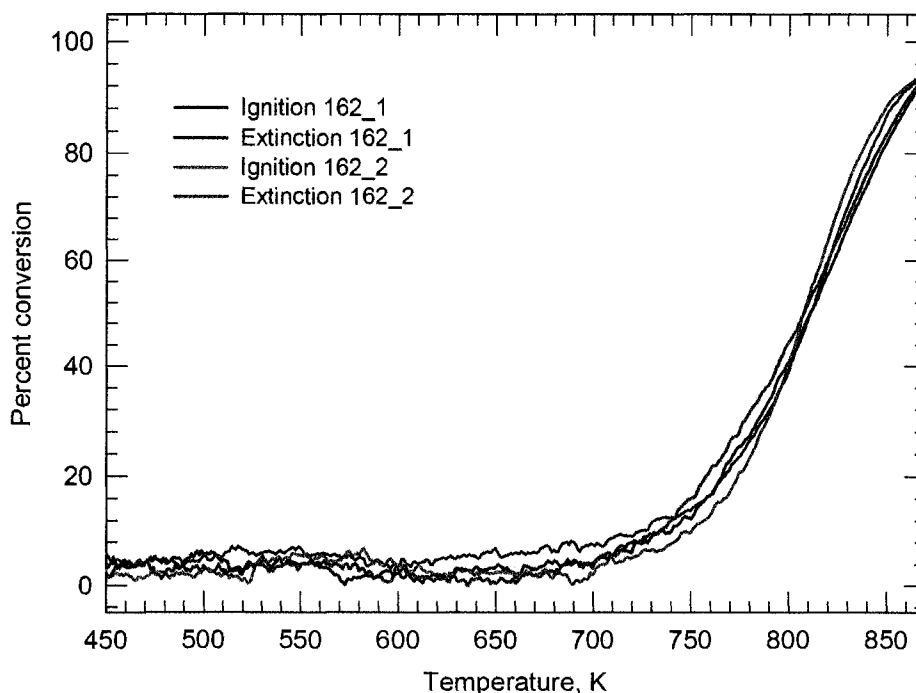


Figure 6.37: Effect of adding 10% H₂O to the feed with 6% O₂ and 5000 ppm CH₄, based on thermocouple T3.

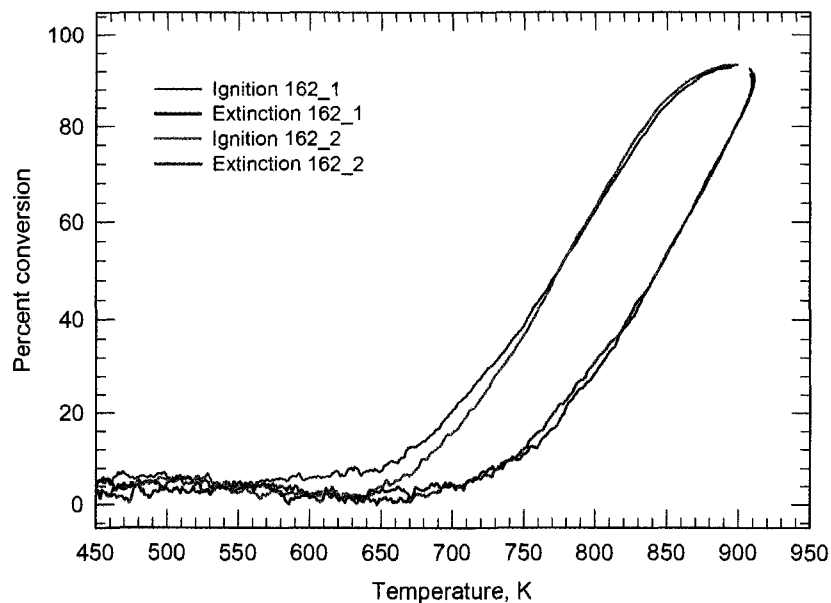


Figure 6.38: Effect of adding 10% H₂O to the feed with 6% O₂ and 5000 ppm CH₄, based on thermocouple T4.

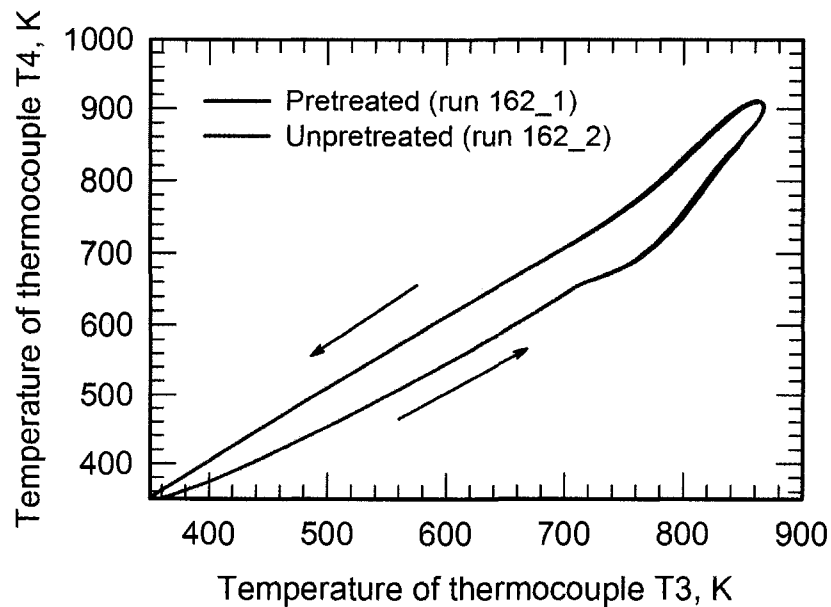


Figure 6.39: Comparing effect of pretreatment on temperature hysteresis between inlet (T3) and outlet (T4) during heating and cooling.

Effect of added hydrogen.

Figure 6.40 shows the effect of adding 1000 ppm of hydrogen to a feed of 2000 ppm methane in 6 % oxygen plotted using thermocouple T3. Figure 6.41 shows the same plot with thermocouple T4. The pattern is similar to that observed without hydrogen, however, there appears to be a sudden increase in methane conversion at about 740 K on the ignition curves.

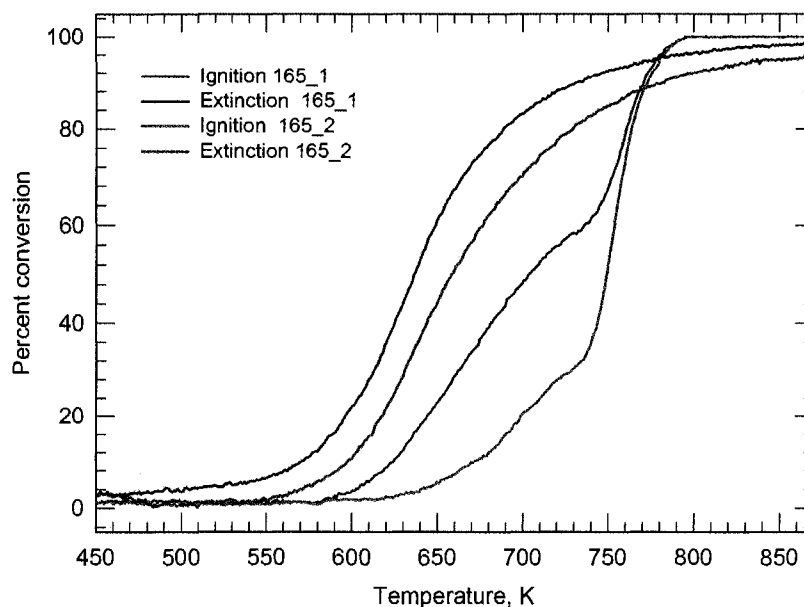


Figure 6.40: Ignition and extinction curves for 1000 ppm H_2 added into 2000 ppm CH_4 with 6% O_2 , based on thermocouple T3.

The results are compared to those obtained without hydrogen in Figures 6.42 and 6.43 for the pretreated and unpretreated cases respectively. From these figures it appears that there is a small inhibition effect for the ignition curves up to about 740 to 750 K, and then a rapid jump in methane conversion. This jump at 750 K could mark the point where the hydrogen suddenly reacts, and the enhanced activity is the result of the exotherm. The temperature profile for the unpretreated case with 1000 ppm hydrogen are given in Figure 6.44. It is observed that there is not any obviously different behaviour in the temperature profiles compared to the other experiments.

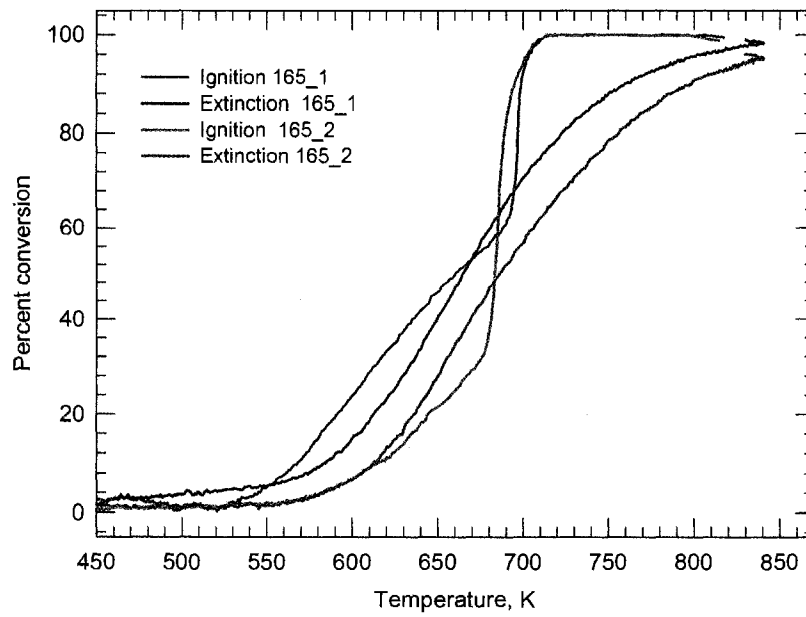


Figure 6.41: Ignition and extinction curves for 1000 ppm H₂ added into 2000 ppm CH₄ with 6% O₂, based on thermocouple T4.

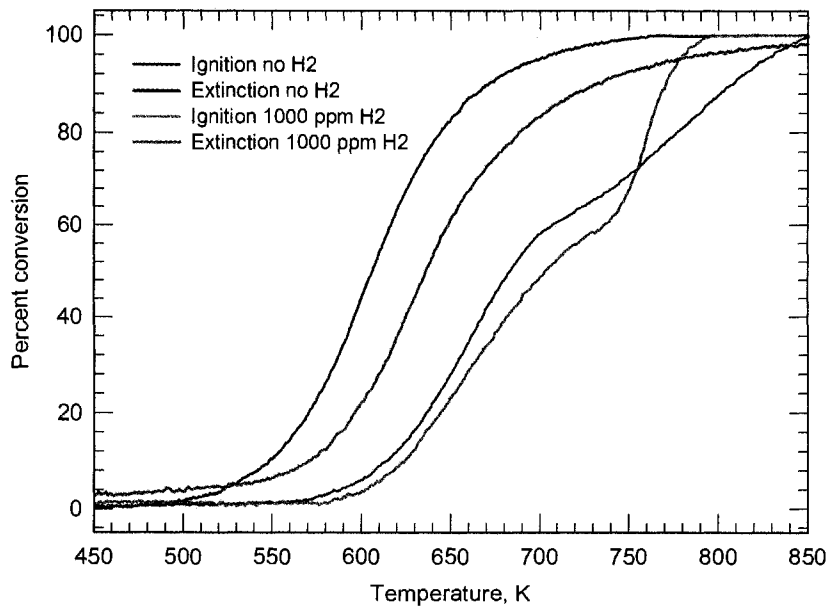


Figure 6.42: Effect of H₂ addition on ignition - extinction curves, 2000 ppm CH₄, pretreated case based on thermocouple T3.

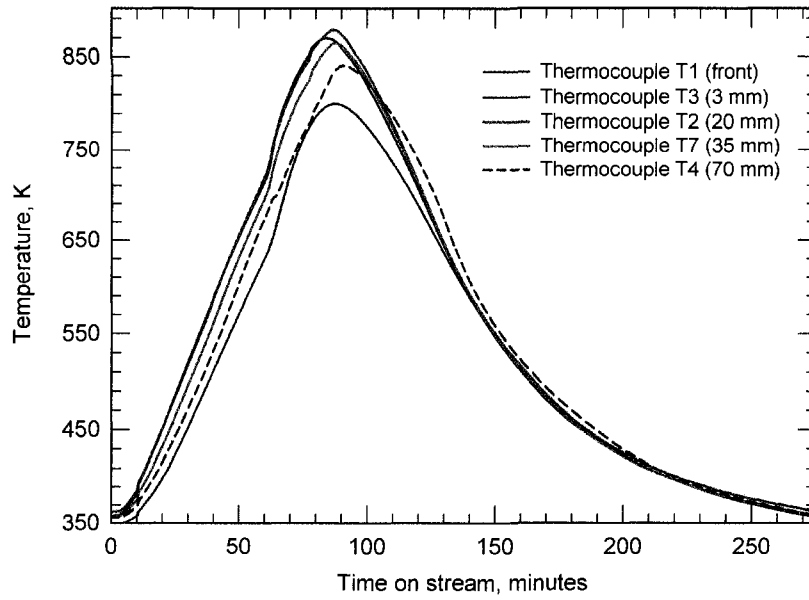


Figure 6.43: Effect of H₂ addition on ignition - extinction curves, 2000 ppm CH₄, untreated case based on thermocouple T3.

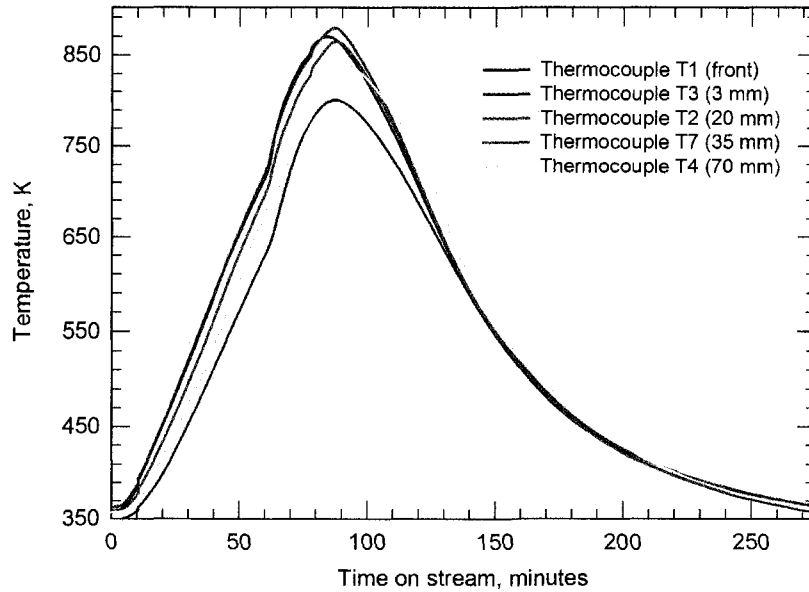


Figure 6.44: Temperature as function of time for 2000 ppm CH₄ and 6% O₂ with 1000ppm added H₂, based on thermocouple T3.

Effect of added carbon monoxide.

Figure 6.45 shows the ignition extinction curves for 1000 ppm added CO, with 2000 ppm methane in the feed. Figures 6.46 and 6.47 show the comparison to the case without CO. The main observation is that CO causes some decrease in activity. Inhibition effect is clear during extinction, while in ignition period, the reaction temperature and pretreatment influence the effect as shown in Figure 6.46 and 6.47.

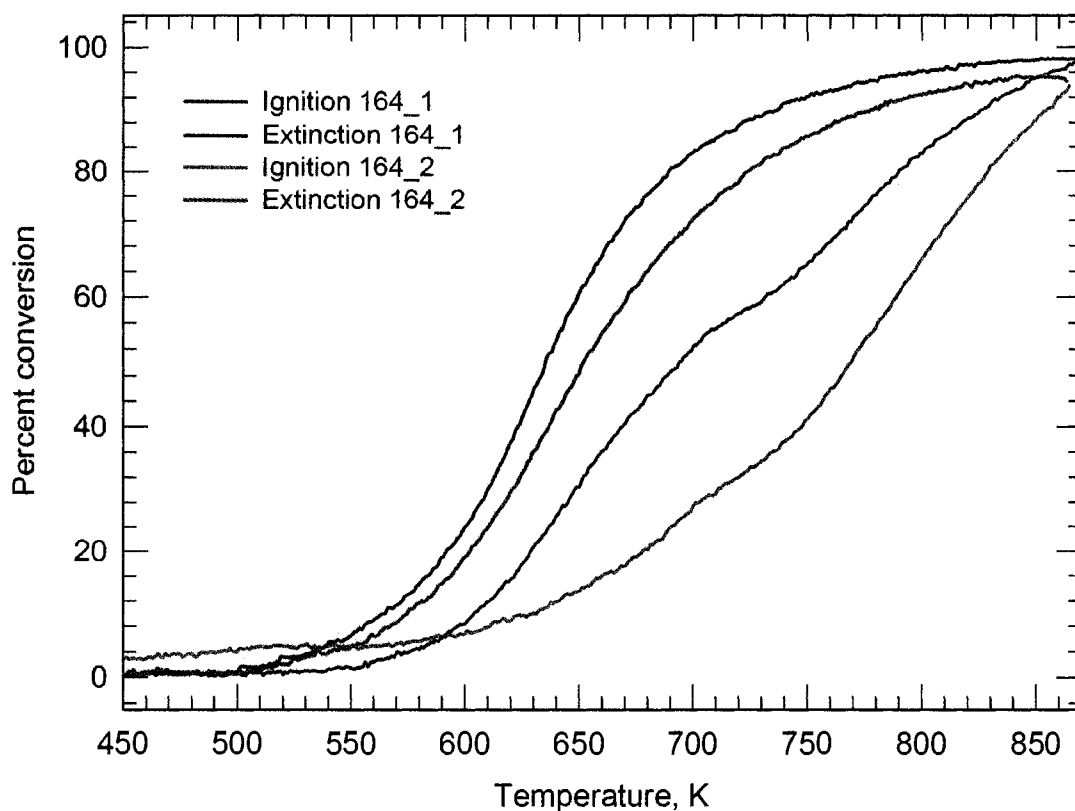


Figure 6.45: Ignition and extinction curves for 1000 ppm CO and 2000 ppm CH₄, based on thermocouple T3.

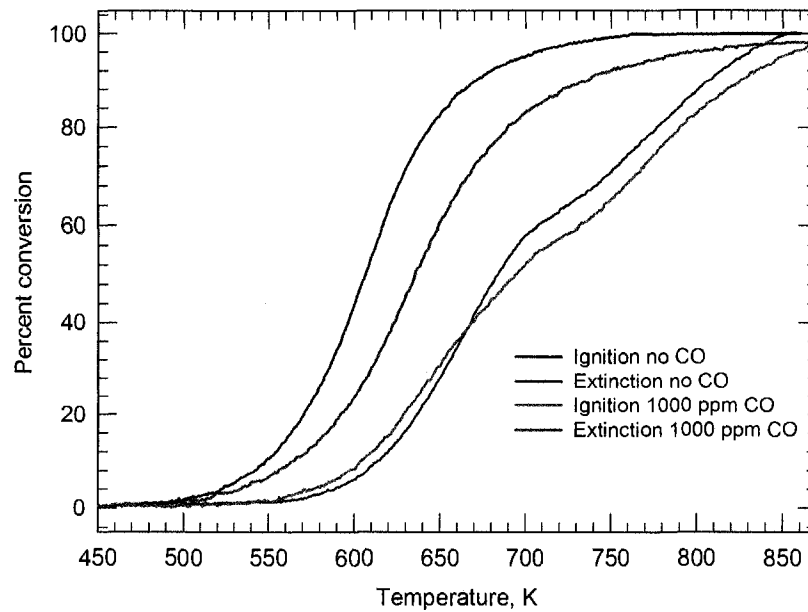


Figure 6.46: Effect of adding 1000 ppm CO to the feed of 5000 ppm CH₄ in 6 % O₂, pretreated, based on thermocouple T3.

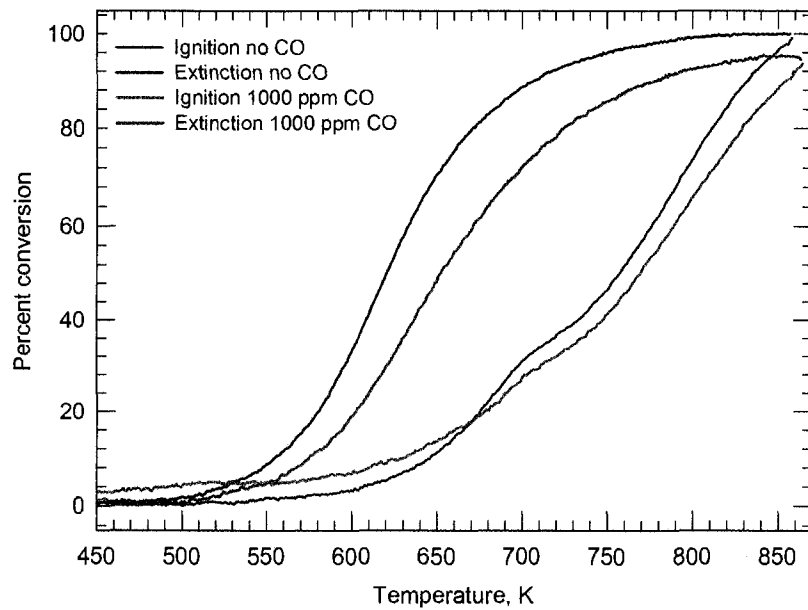


Figure 6.47: Effect of adding 1000 ppm CO to the feed of 5000 ppm CH₄ in 6 % O₂, untreated, based on thermocouple T3.

Effect of added carbon dioxide.

The final result shows the effect of added carbon dioxide. Figure 6.48 and 6.49 show the ignition and extinction curves for the case where 8000 ppm of carbon dioxide was added to a feed of 6 % oxygen and 2000 ppm methane. For both runs, the ignition and extinction curves for 2000 ppm methane are added for comparison purposes. It is seen that for the untreated case there appears to be a small effect on the ignition curve, and in both cases the extinction occurs at a higher reactor temperature in the presence of carbon dioxide. As discussed in Chapter 5, carbon dioxide has been shown by some researchers to inhibit the reaction rate.

Figure 6.50 illustrate the existence of temperature hysteresis and at the same time shows that the effect of pretreatment is negligible in presence of carbon dioxide.

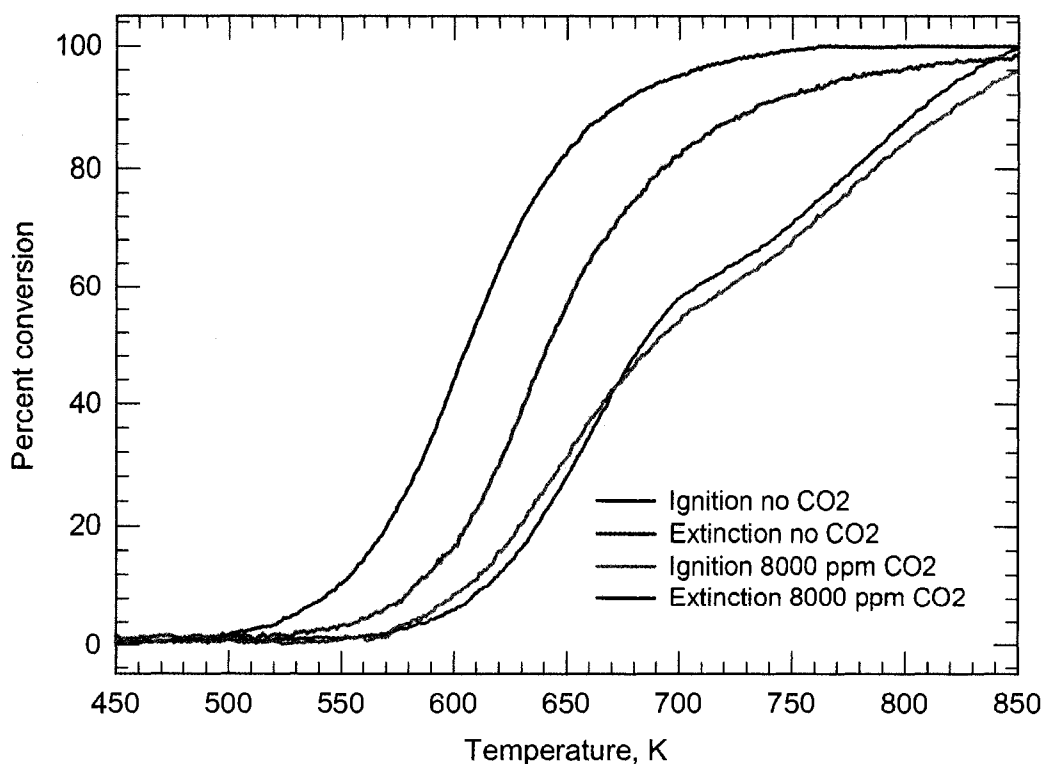


Figure 6.48: Effect of CO₂ on conversion for 2000 ppm CH₄ in 6 % O₂, pretreated, based on thermocouple T3.

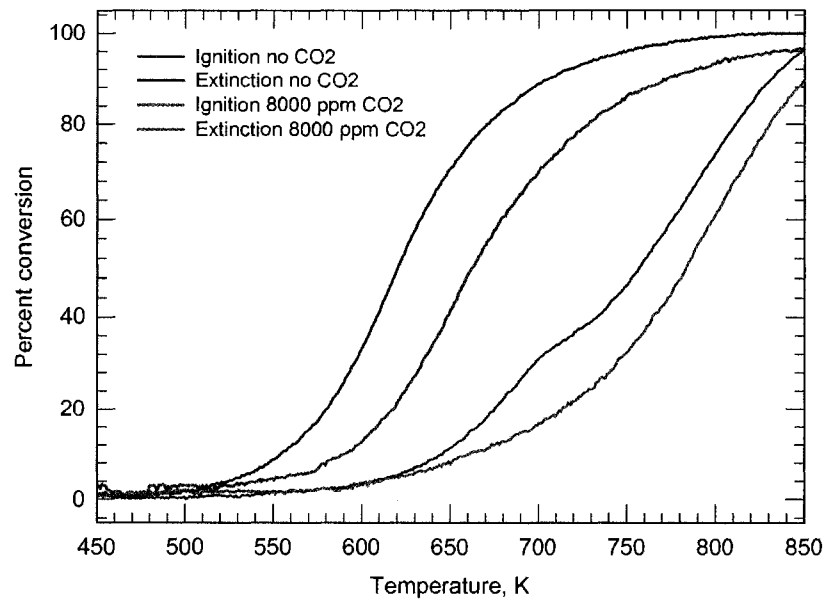


Figure 6.49: Effect of CO₂ on conversion for 2000 ppm CH₄ in 6% O₂, unpretreated, based on thermocouple T3.

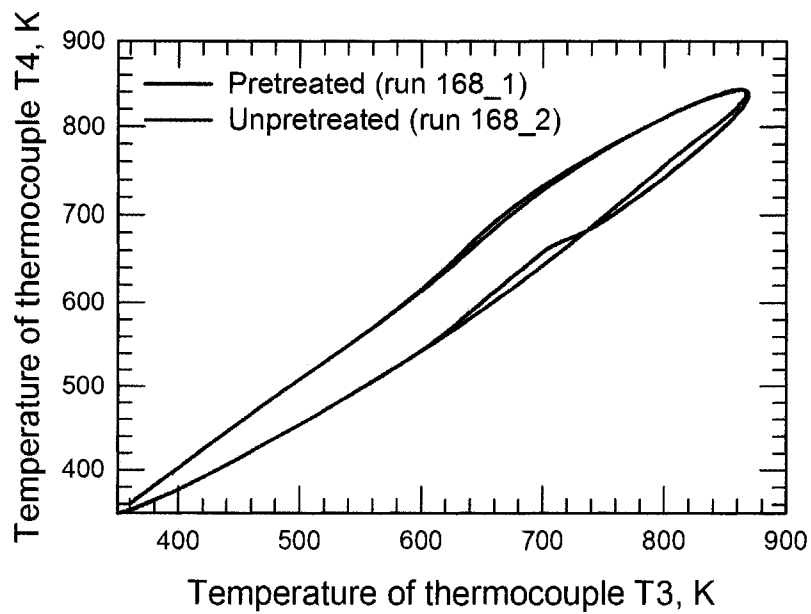


Figure 6.50: Comparing effect of pretreatment on temperature hysteresis between inlet (T3) and outlet (T4) during heating and cooling.

6.3.5 Summary of ignition extinction experiments

The experimental results reveal a number of interesting observations, some of which are contrary to other literature works. It should be pointed out, however, that there is no complete agreement among other workers, as discussed in Chapter 5, and this work likely does not differ more than the current state of disagreement. Further, it points to the necessity of conducting experiments on the catalyst of interest, rather than relying on literature results. Table 6.3 summarizes the ignition and extinction temperatures, were defined as the temperature at which a 50% conversion is first achieved either in ascending or descending respectively, as a function of methane concentration and pretreatment history, for all runs. Tabulated temperatures are based on thermocouple T3. A general observation is that the ignition and extinction temperature increase with increasing methane concentration in the feed for both with and without pretreatment. For the pretreated case the difference between the ignition and extinction temperature is low while for the other case, it is high and increases as the concentration of methane increase in the feed. Also it should be noted that the ignition and extinction temperatures for the case of unpretreated experiments are higher than those of pretreated experiments.

Figures 6.51 and 6.52 show the variation of ignition and extinction temperature with methane for 6% and 20% oxygen. The unpretreated cases always have higher ignition and extinction temperature when compared to pretreated, and in both cases the temperature increases with methane concentration almost linearly. The extinction curves have narrow separation as compared to ignition curves, this holds for 6% and 20% oxygen. The key findings which will affect the resulting kinetic model (kinetic model that accounts for these findings is developed in chapter 7.) are:

1. CH_4 exhibits a self - inhibition, which is contrary to most literature findings.
2. H_2O and CO_2 both inhibit the reaction, which is consistent with the literature.
3. H_2 and CO also appear to show inhibition.

- Increasing O_2 concentration enhances ignition for the unpretreated case but has a fairly small effect during extinction.

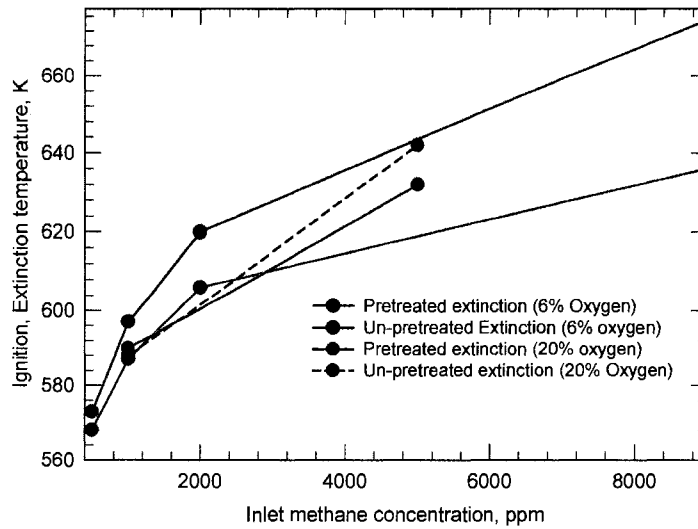


Figure 6.51: Variation of extinction temperature for 6% and 20% O_2 , based on thermocouple T3

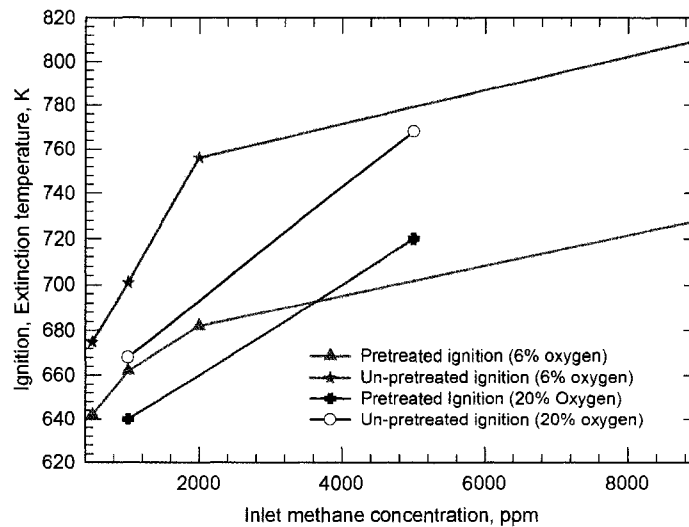


Figure 6.52: Variation of ignition temperature for 6% and 20% O_2 , based on thermocouple T3

Table 6.3: Ignition and extinction temperature based on thermocouple T3.

Experiment	Ignition temperature [K]	Extinction temperature [K]
Without pretreatment		
146.3	675	573
147.2	701	597
149.2	756	620
151.2	810	675
153.2	640	590
156.2	720	632
159.2	796	752
162.2	806	807
164.2	769	648
165.2	750	652
168.2	783	662
With pretreatment		
146.2	642	568
147.1	662	587
149.1	682	606
151.1	728	636
153.1	668	588
156.1	768	642
159.1	nn	nn
162.1	811	810
164.1	681	630
165.1	692	636
168.1	684	642

6.4 Concentration programmed experiments

The dependence of catalyst activity on surface temperature was also studied through concentration programmed experiments. In these experiments the methane concentration in the feed was changed using three different methods, which were pulse, steps and ramp. These experiments were designed to evaluate the influence of surface temperature on palladium monolith catalyst activity, by monitoring the change of methane concentration with time at reactor outlet. The experimental procedures for each category of concentration programmed experiment are detailed in the following:

- **Pulse experiments:** In these experiments the methane concentration was varied using a sequentially larger pulse. The concentration was increased from zero to a desired value, held there for a few minutes, and then decreased back to zero. The concentration was then held at zero for a few minutes before the next pulse was introduced. The concentrations used in the pulses were 500, 1000, 2000, 5000 and 9000 ppm. A typical pulse sequence is given in Figure 6.53.

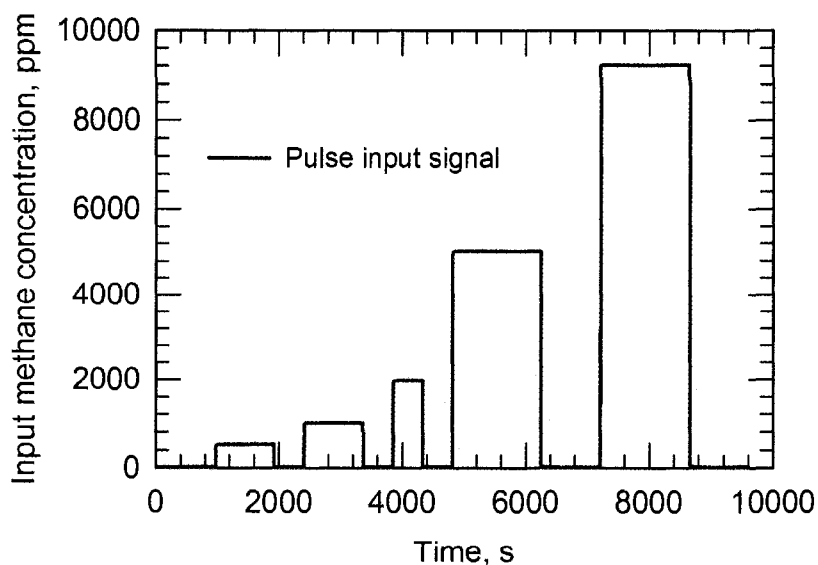


Figure 6.53: Methane pulse input for concentration programmed experiments.

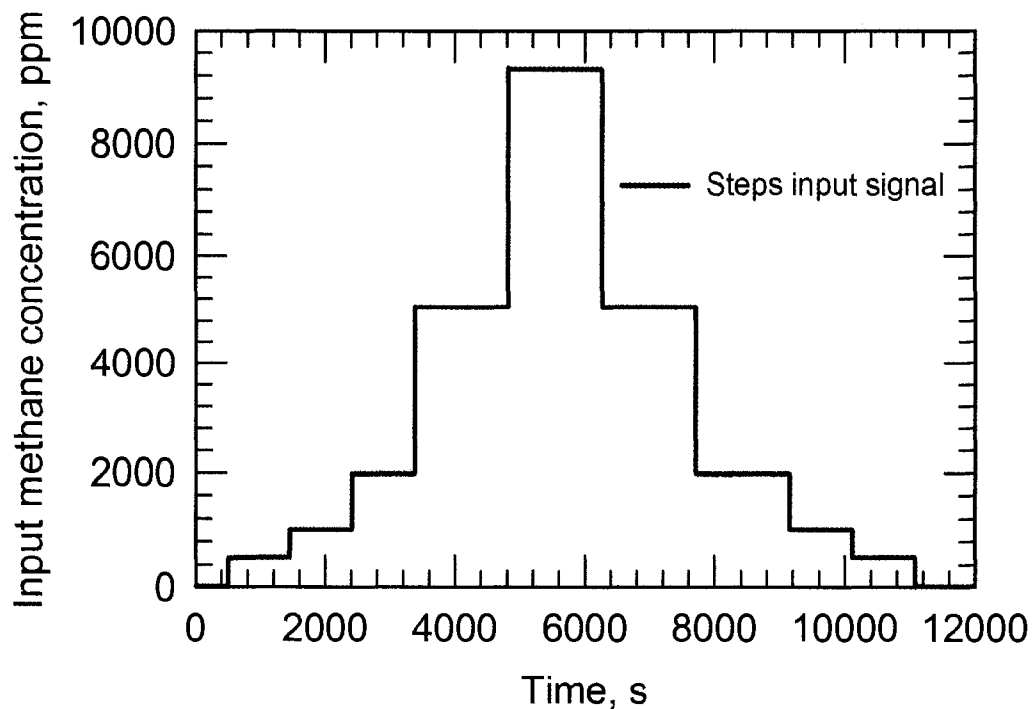


Figure 6.54: Methane steps input for concentration programmed experiments.

- **Steps experiments:** For these experiments the methane concentrations were increased in a stepwise manner from 0 to 9000 ppm, as shown in Figure 6.54. After each step increase the concentration was held constant for a few minutes. The methane concentration for each step was 500, 1000, 2000, 5000 and 9000 ppm.
- **Ramp experiments:** The variation of methane concentration was increased and decreased between 0 and 9000 ppm using a constant ramp concentration. A typical ramp input used is as shown in Figure 6.55. The methane concentration was increased or decreased at a rate of 4.6 ppm per second, and when the maximum concentration of 9000 ppm was reached the flow remained constant for a few minutes before the decrease was started.

The pulse experiments were performed first, followed by two minutes wait time for cleaning the reactor. The pulse experiments were then repeated followed

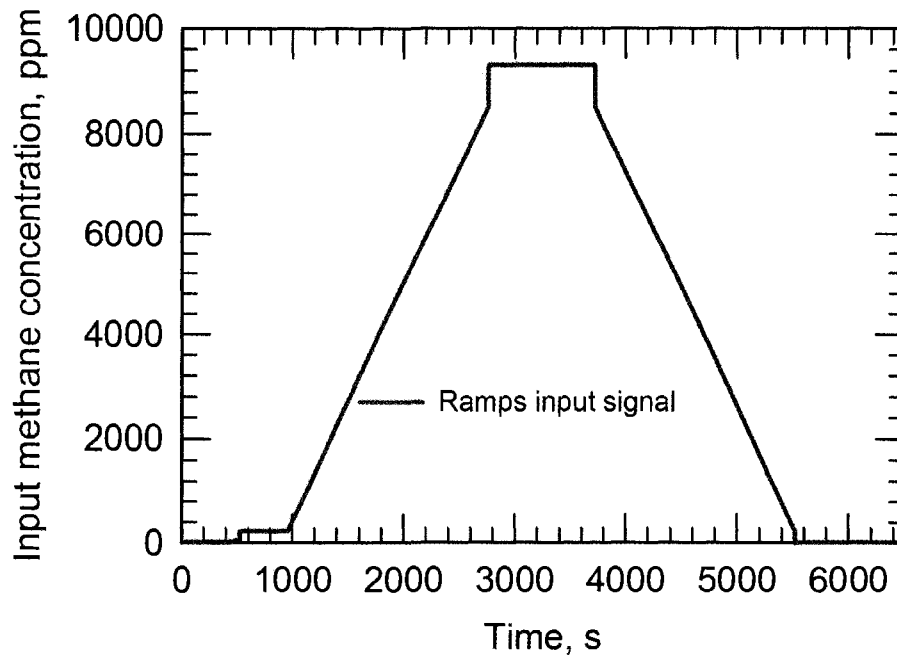


Figure 6.55: Methane ramps input for concentration programmed experiments.

by a further two minutes wait. The ramp experiments were then run in the same manner, and finally the step experiments were performed. The catalyst was not pretreated with hydrogen in these experiments.

6.4.1 Results and discussion

The common trend in all experiments was an increasing conversion with temperature (which is obviously expected). Other features of these experiments are discussed in the following.

(i) Pulse experiment: Figure 6.56 shows the inlet and outlet methane at nominal reactor inlet temperature of 673 K and 723 K. It is evident that the conversion increases with temperature. Figures 6.58 and 6.59 show the temperatures recorded at all of the thermocouples during the experiments, and Figures 6.60 and 6.61 show temperature recorded by thermocouple T3 and T5 only. Tables 6.4 and 6.5 summarize the data in tubular form.

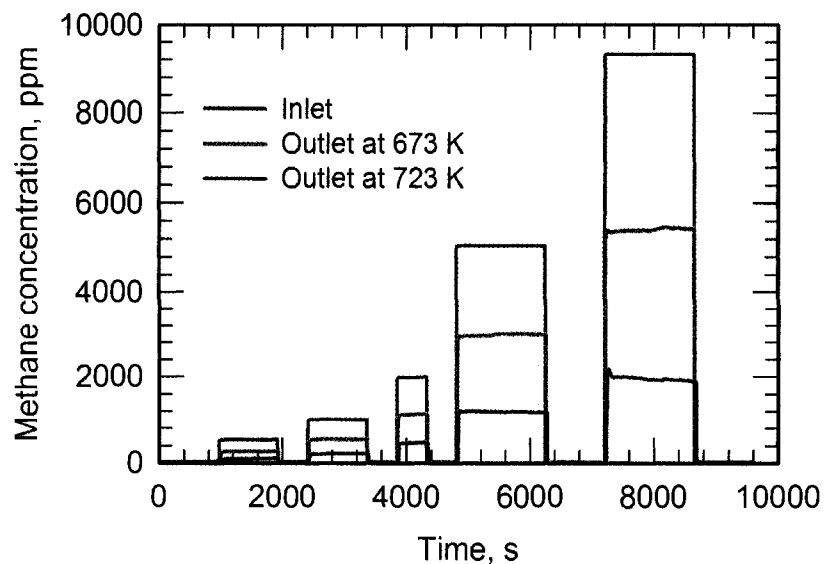


Figure 6.56: Inlet and outlet methane concentration as function of time for pulse experiment at 673 K and 723 K.

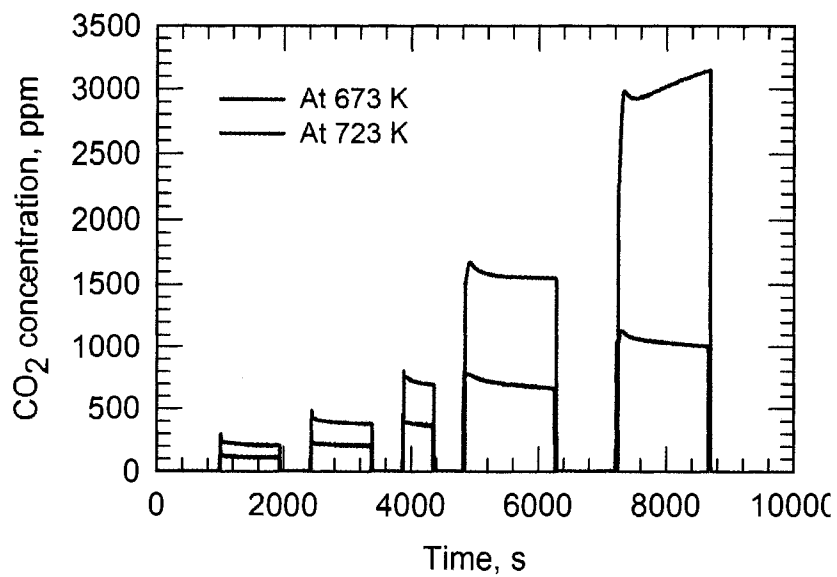


Figure 6.57: Outlet CO₂ concentration as function of time for pulse experiment at 673 K and 723 K.

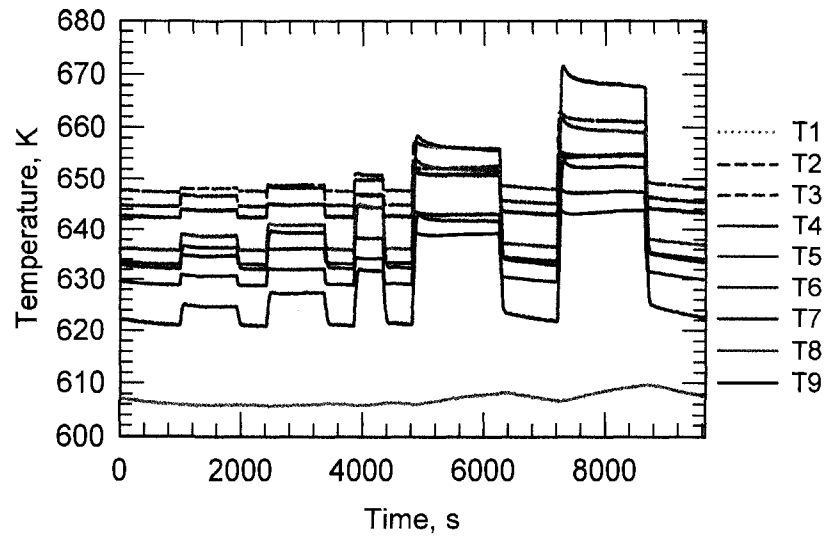


Figure 6.58: Temperature variation against time during pulse concentration programmed experiments. Nominal temperature of 673 K was fixed at inlet.

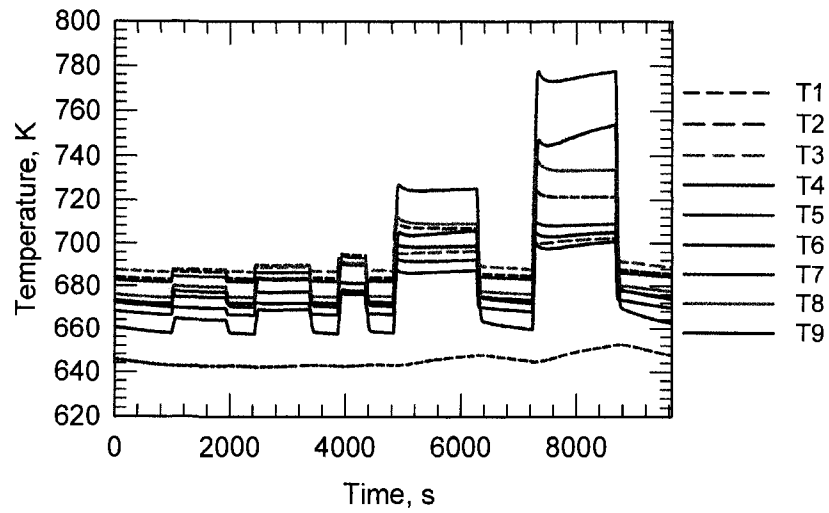


Figure 6.59: Temperature variation against time during pulse concentration programmed experiments. Nominal temperature of 723 K was fixed at inlet.

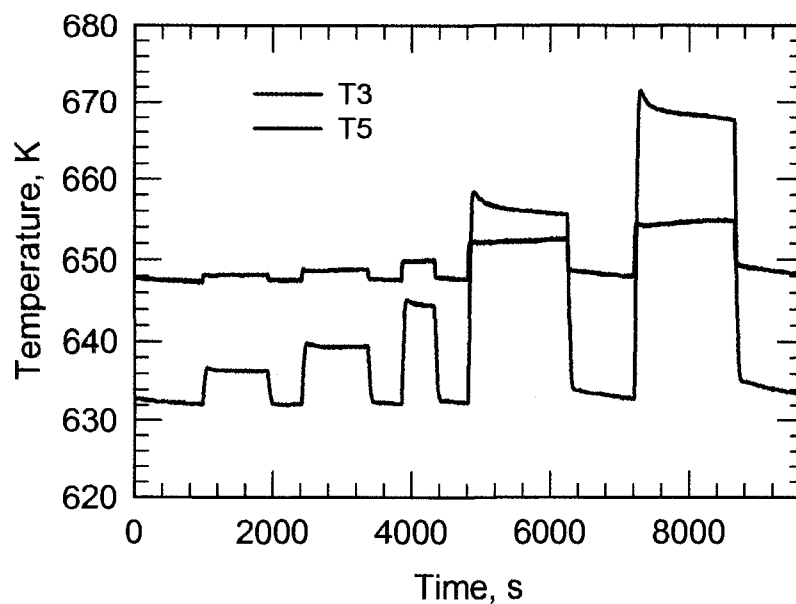


Figure 6.60: Comparison of temperature near the inlet and outlet of the reactor in pulse experiment at nominally fixed temperature of 673 K.

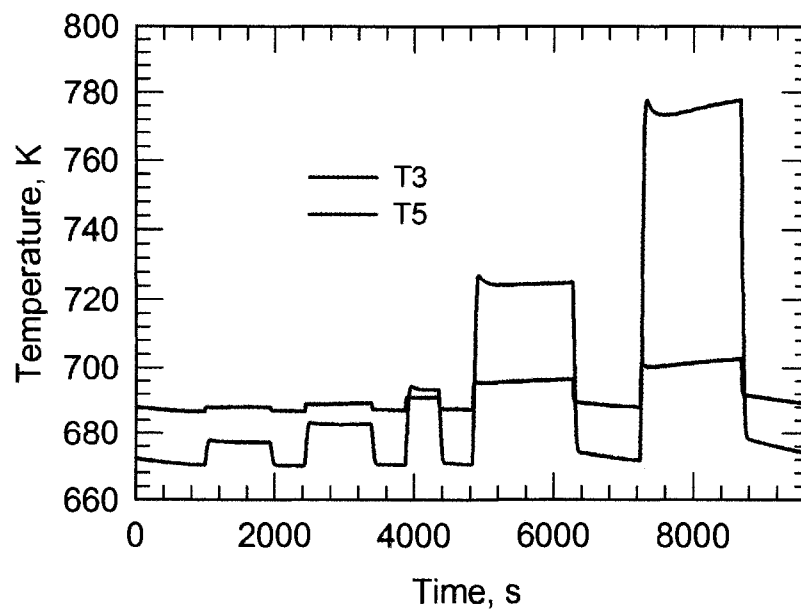


Figure 6.61: Comparison of temperature near the inlet and outlet of the reactor in pulse experiment at nominally fixed temperature of 723 K.

Table 6.4: Methane conversion in pulse input concentration programmed experiments at 673 K.

CH ₄ inlet Conc. [ppm]	CH ₄ outlet conc. [ppm]	% conversion [-]	Front T1 [K]	20 mm T2 [K]	1 mm T3 [K]	70 mm T4 [K]	70 mm T5 [K]	1 mm T6 [K]	35 mm T7 [K]	35 mm T8 [K]	20 mm T9 [K]
0	0	0	607	645	648	622	633	643	634	636	629
526	259	51	606	647	648	625	636	644	635	639	631
0	0	0	606	645	648	621	632	642	633	636	629
1008	545	46	606	648	649	627	639	645	636	641	632
0	0	0	606	645	648	622	633	643	633	636	629
1986	1109	44	606	651	650	631	644	647	638	644	634
0	0	0	606	645	648	622	633	643	634	637	629
5057	2972	41	607	656	652	642	656	651	643	652	639
0	0	0	608	646	648	623	634	643	634	637	630
9315	5393	42	608	661	655	652	668	655	647	659	643
0	0	0	609	646	649	625	635	644	635	638	631

Table 6.5: Methane conversion in pulse input concentration programmed experiments at 723 K.

CH ₄ inlet Conc. [ppm]	CH ₄ outlet conc. [ppm]	% conversion [-]	Front T1 [K]	20 mm T2 [K]	1 mm T3 [K]	70 mm T4 [K]	70 mm T5 [K]	1 mm T6 [K]	35 mm T7 [K]	35 mm T8 [K]	20 mm T9 [K]
0	0	0	644	684	687	659	671	682	672	675	667
527	96	82	643	687	688	664	677	684	675	680	670
0	0	0	642	683	687	658	671	682	672	675	666
1008	219	78	642	690	689	669	683	686	677	684	672
0	0	0	643	684	687	659	671	682	672	675	667
1986	453	77	643	694	691	676	692	690	681	690	676
0	0	0	643	684	687	660	672	683	673	676	667
5057	1193	76	645	707	696	704	723	698	692	709	687
0	0	0	646	685	689	663	674	684	674	677	669
9316	1947	79	648	721	701	747	773	708	704	733	699
0	0	0	650	687	690	668	678	685	677	680	672

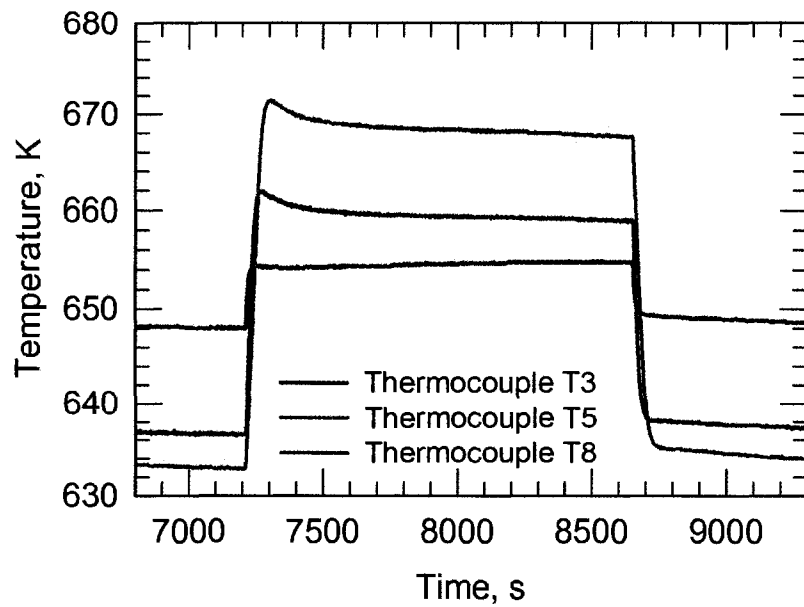


Figure 6.62: Comparison of temperature near the inlet, middle and outlet of the reactor in one pulse period at nominally fixed temperature of 673 K.

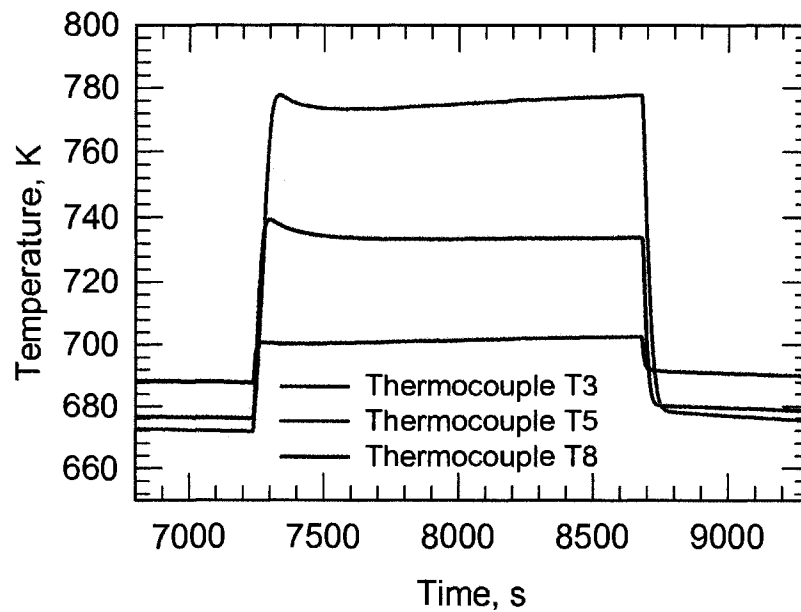


Figure 6.63: Comparison of temperature near the inlet, middle and outlet of the reactor for one pulse period at nominally fixed temperature of 723 K.

The observed temperature distribution with and without reaction is first considered. Prior to any reaction, it was observed that thermocouple T1 read lower than any of the ones located inside the reactor. This observation is consistent with the behaviour observed during the ignition - extinction curves. It was further observed that there were axial and radial gradients present. There was about 10 - 20 K axial as well as radial temperature differences. These gradients again illustrate that the reactor was not adiabatic.

For both cases the fractional conversion was similar for all concentrations, with a possible trend of a small decrease in conversion with increasing concentration. At higher inlet concentration, however, the average reactor temperature was higher. Therefore it can be concluded that these results are consistent with an inhibition effect by methane, which supports the conclusion reached in the temperature programmed experiments.

Examining Figures 6.62 and 6.63, it is notable that thermocouple responses both rise immediately. There is also an overshoot in the thermocouple response, especially thermocouple T5 at 70 mm. These observations illustrate that the reaction starts everywhere in the reactor and there is strong self methane inhibition effect.

(ii) Step experiments: The step experiments were also conducted at nominal inlet temperatures of 673 K and 723 K. Figure 6.64 shows the inlet and outlet methane concentrations recorded during step changes. Figures 6.65 and 6.66 show the temperatures for all of the thermocouples, and Figures 6.67 and 6.68 show temperature of thermocouple T3 and T5 only. The data are presented in tabular form in Tables 6.6 and 6.7.

The same comments can be made regarding the temperature distribution in the reactor in the absence of reaction as were made for the pulse experiments. The temperature recorded by the thermocouples are similar. The step responses are essentially the same as the pulse responses, without the return to zero concentration between steps. It would be reasonable to expect that the temperature distribution and fractional conversion would be similar at each input concentration.

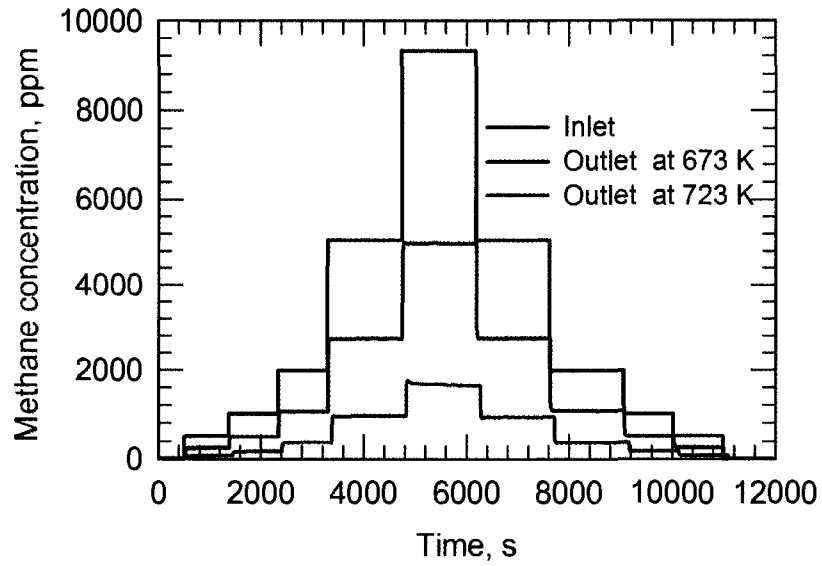


Figure 6.64: Methane concentration as function of time for step at inlet and outlet of reactor. Nominal temperature in front of reactor was fixed at 673 and 723 K.

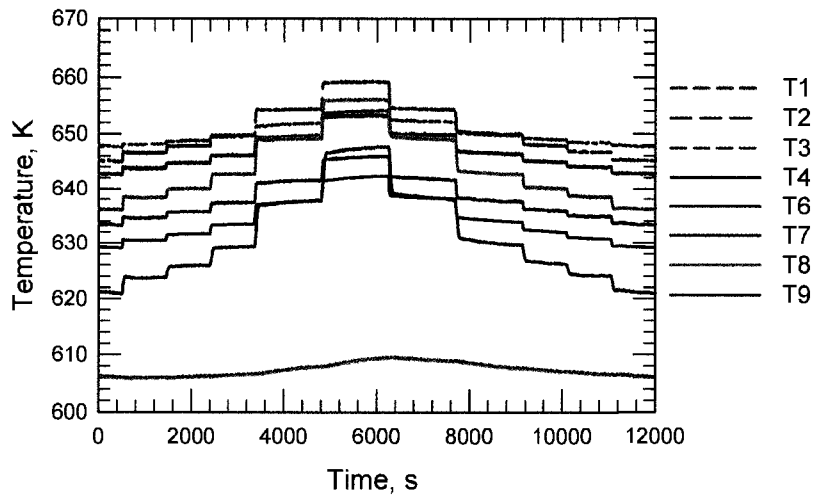


Figure 6.65: Temperature variation against time during steps concentration programmed experiments. Nominal temperature of 673 K was fixed at inlet.

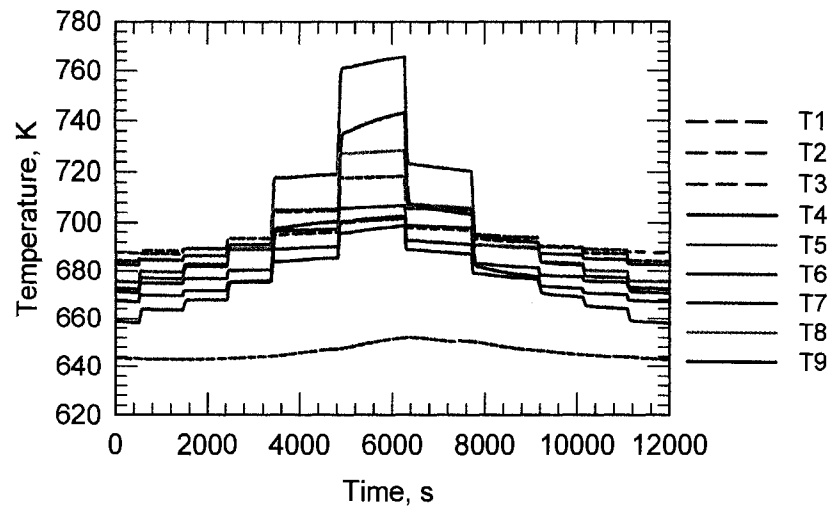


Figure 6.66: Temperature variation against time during steps concentration programmed experiments. Nominal temperature of 723 K was fixed at inlet.

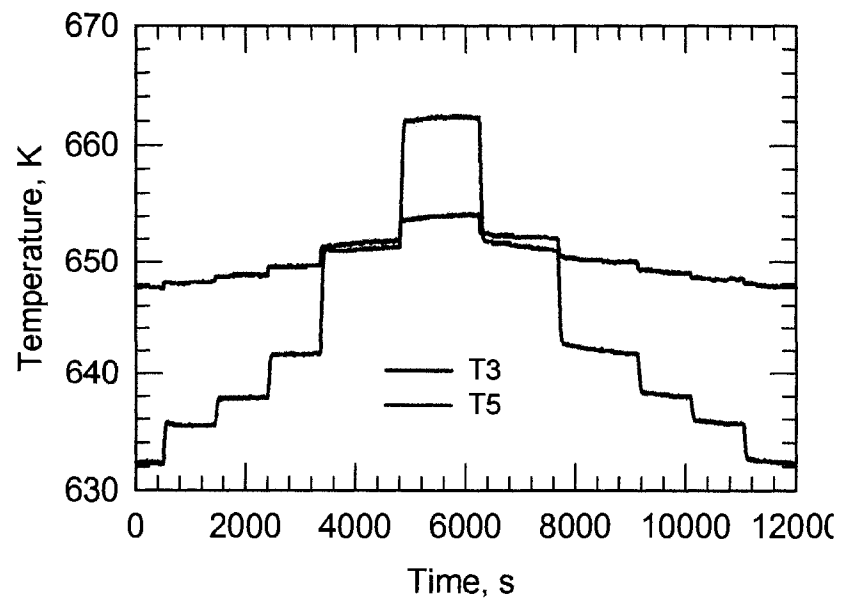


Figure 6.67: Comparing the reactor temperature near the inlet and outlet for step experiments at fixed nominal temperature in front of reactor of 673 K.

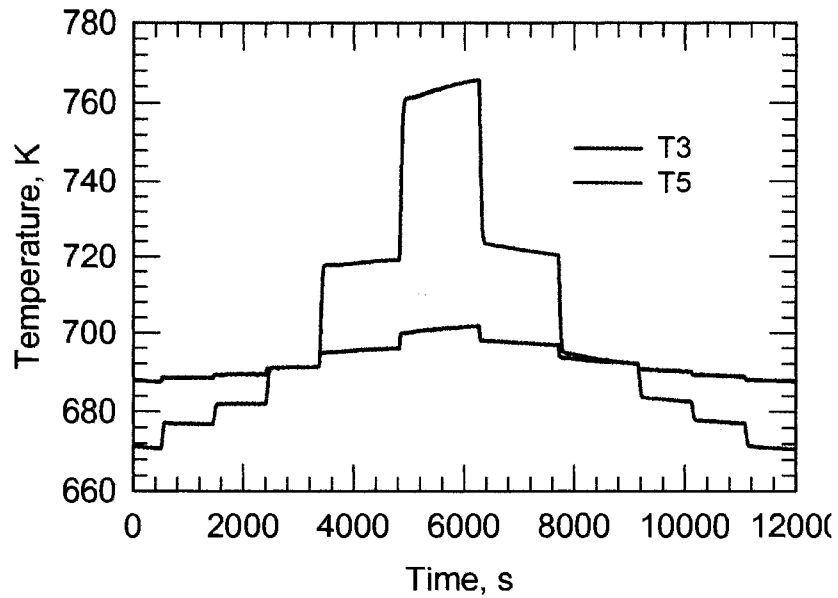


Figure 6.68: Comparing the reactor temperature near the inlet and outlet for step experiments at fixed nominal temperature in front of reactor of 723 K.

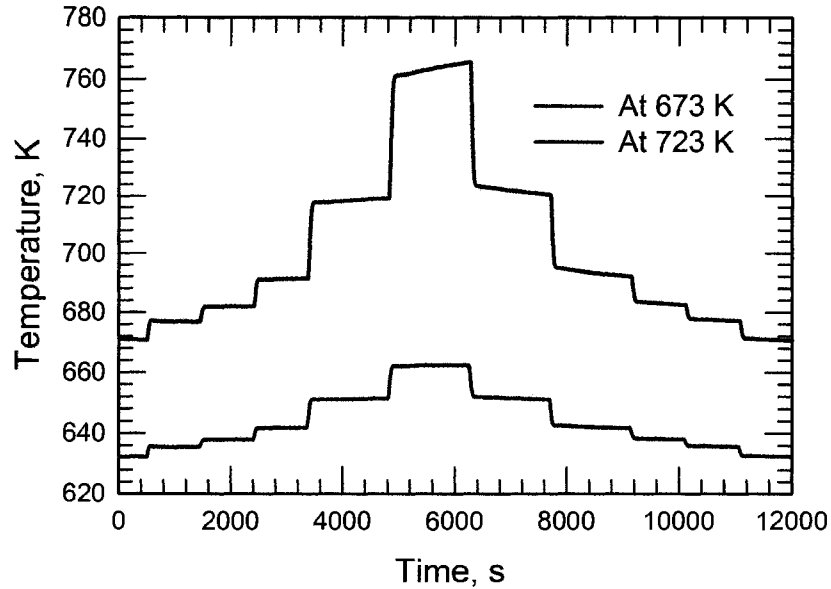


Figure 6.69: Comparing the reactor outlet temperature for step experiments for fixed nominal temperature in front of reactor of 673 and 723 K.

Table 6.6: Methane conversion in step input concentration programmed experiments at 673 K.

CH ₄ inlet Conc. [ppm]	CH ₄ outlet conc. [ppm]	% conversion [-]	Front T1 [K]	20 mm T2 [K]	1 mm T3 [K]	70 mm T4 [K]	70 mm T5 [K]	1 mm T6 [K]	35 mm T7 [K]	35 mm T8 [K]	20 mm T9 [K]
0	0	0	606	645	648	621	632	643	633	636	629
527	255	52	606	647	648	624	635	644	635	638	630
1008	530	47	606	648	649	626	638	645	636	640	632
1988	1093	45	606	650	650	629	642	646	637	643	633
5058	2814	44	607	654	652	637	651	649	641	649	637
9316	5109	45	609	659	654	647	662	653	646	656	642
5058	2831	44	609	655	652	639	652	650	642	649	638
1989	1111	44	608	650	650	630	642	647	638	643	634
1008	545	46	607	648	649	627	638	645	636	640	632
528	269	49	607	647	648	624	636	644	635	639	631
0	0	0	606	645	648	621	633	643	633	636	629

Table 6.7: Methane conversion in step input concentration programmed experiments at 723 K.

CH ₄ inlet Conc. [ppm]	CH ₄ outlet conc. [ppm]	% conversion [-]	Front T1 [K]	20 mm T2 [K]	1 mm T3 [K]	70 mm T4 [K]	70 mm T5 [K]	1 mm T6 [K]	35 mm T7 [K]	35 mm T8 [K]	20 mm T9 [K]
0	0	0	644	685	688	659	671	683	673	676	667
527	75	86	643	687	689	664	677	685	675	680	670
1008	170	83	643	689	689	668	682	686	677	683	672
1989	366	82	644	694	691	676	691	689	680	689	675
5059	958	81	646	704	695	699	718	697	690	705	685
9316	1666	82	650	718	701	738	762	706	702	728	697
5055	936	81	651	705	697	706	723	698	692	707	688
1989	369	81	648	695	693	680	694	691	683	691	678
1009	179	82	646	690	690	670	683	687	678	684	673
528	84	84	644	687	689	665	678	685	676	680	670
0	0	0	643	684	688	658	671	683	673	676	667

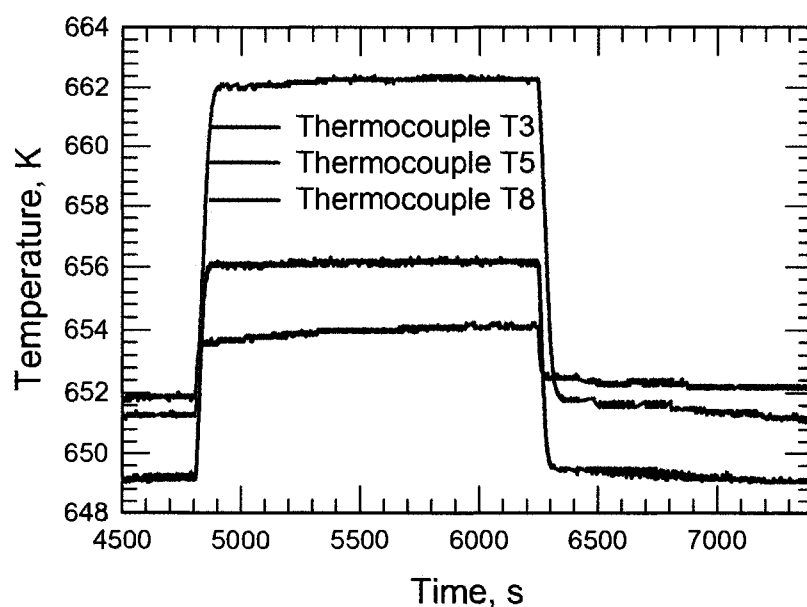


Figure 6.70: Comparison of temperature near the inlet, middle and outlet of the reactor in one pulse period at nominally fixed temperature of 673 K.

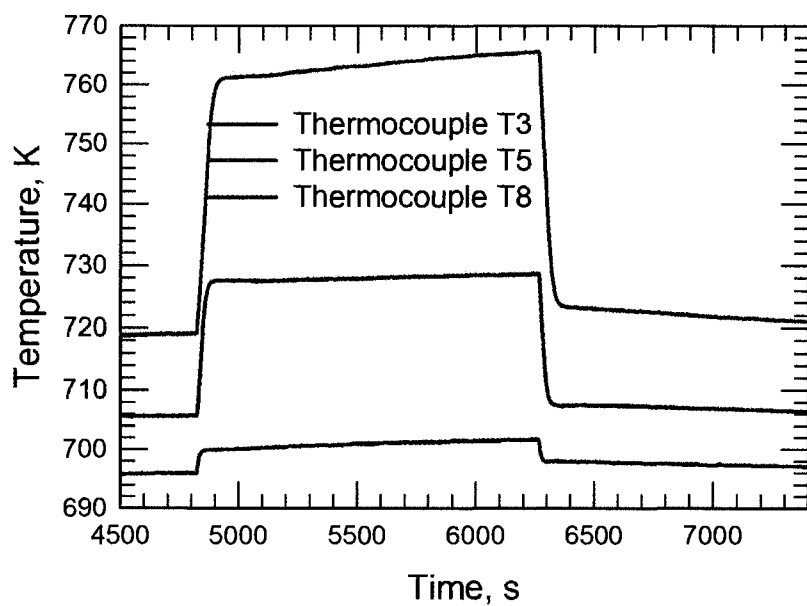


Figure 6.71: Comparison of temperature near the inlet, middle and outlet of the reactor for one pulse period at nominally fixed temperature of 723 K.

If one compares the temperatures and conversion for the pulse and step experiments, it is observed that this is indeed the case. For any given input concentration the fractional conversion is essentially the same, and the thermocouple readings are within a few degrees. This agreement also suggests a good experimental reproducibility. It should also be noted that negligible hysteresis was observed, and the up steps had essentially the same results as the down steps.

Figures 6.70 and 6.71 show that thermocouple responses both rise immediately and almost at the same time as observed in the case of pulse experiments. But in this case the overshoot which was observed to occur for T5 and T8 did not appear. It should be noted that the temperature attained as well as the temperature difference between corresponding temperatures are slightly higher in pulse compared to step experiments, this could be explained by the slow surface poisoning by methane.

(iii) Ramp experiments: Concentration ramp experiments were conducted at nominal reactor inlet temperatures of 673 K and 723 K. The inlet methane concentration was ramped from 0 to 9000 ppm at 4.6 ppm/s. The concentration was held constant at 9000 ppm for a few minutes, and then the descending ramp back to 0 ppm was started. Figure 6.72 shows the inlet and outlet methane concentrations measured during the ramping process. Figures 6.73 and 6.74 show the temperatures recorded by all of the thermocouples, and Figures 6.75 and 6.76 show the temperature of thermocouple T3 and T5 only. Tables 6.8 and 6.9 summarize the data in tabular form.

There were some small differences in behaviour for the ramped response when compared to the pulse and step changes. Comparing the conversions as were used in the pulse and the ramp experiments, significant differences in the fractional conversions can be seen. In both the pulse and step changes the conversion is essentially constant and, for the case of the step cycle no hysteresis was observed.

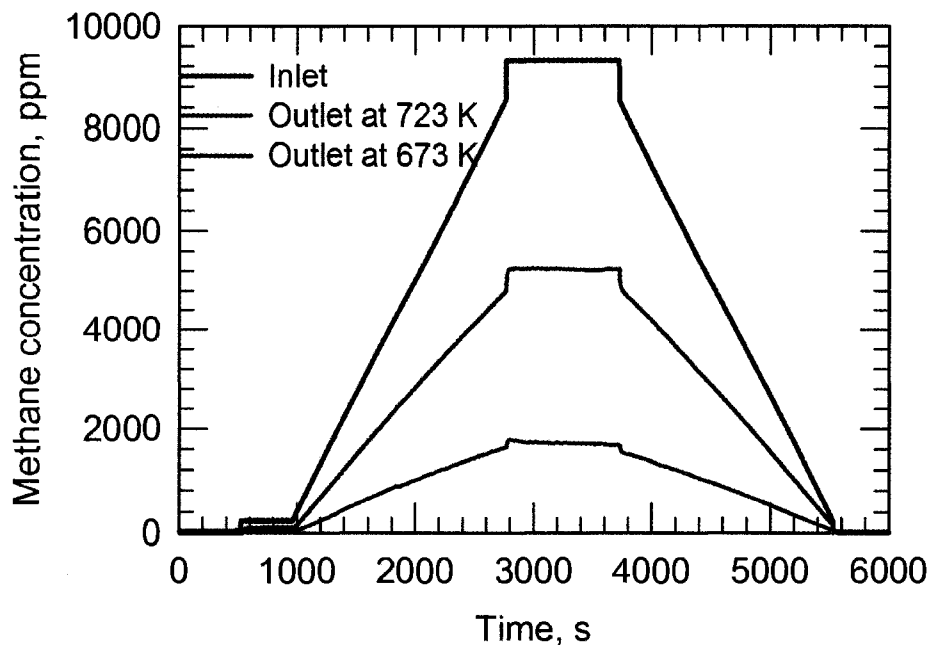


Figure 6.72: Methane concentration as function of time for ramp experiments at inlet and outlet of reactor. Nominal temperatures in front of reactor was fixed at 673 K and 723 K.

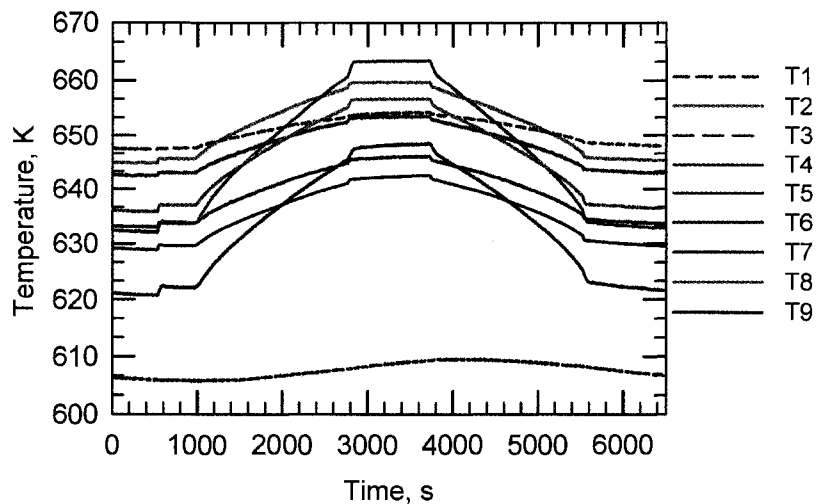


Figure 6.73: Temperature variation against time during ramp concentration programmed experiments. Nominal temperature of 673 K was fixed at inlet.

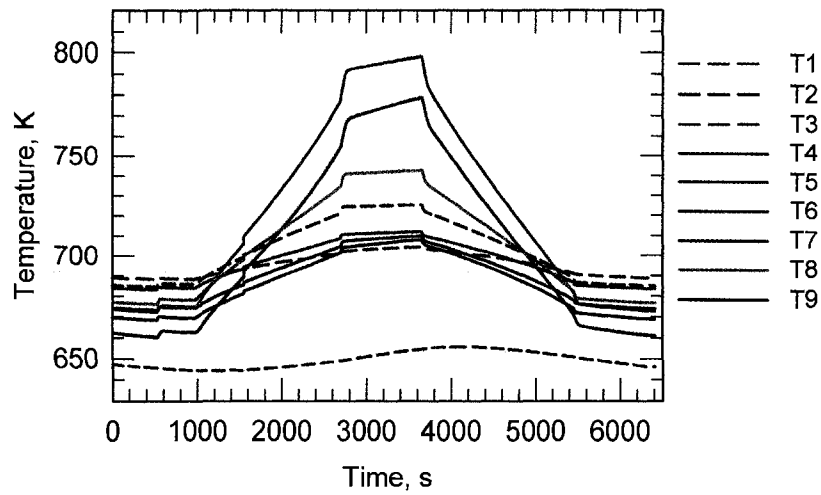


Figure 6.74: Temperature variation against time during ramps concentration programmed experiments. Nominal temperature of 723 K was fixed at inlet.

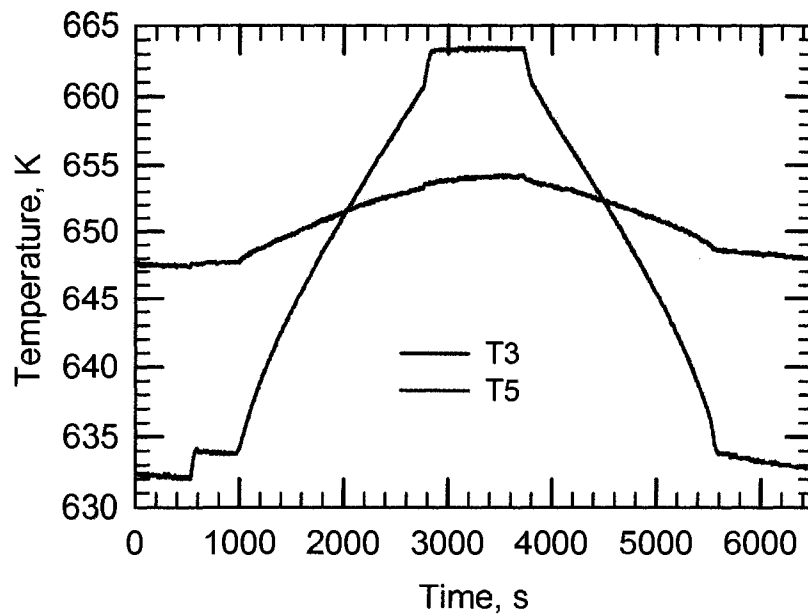


Figure 6.75: Comparison of reactor temperature near the inlet and outlet as function of time for ramp experiment at fixed nominal temperature of 673 K.

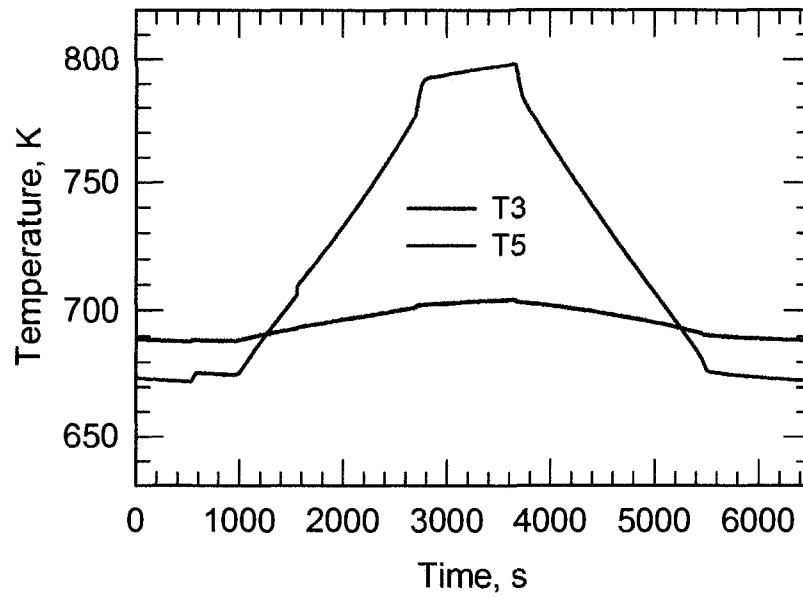


Figure 6.76: Comparison of reactor temperature near the inlet and outlet as function of time for ramp experiment at fixed nominal temperature of 723 K.

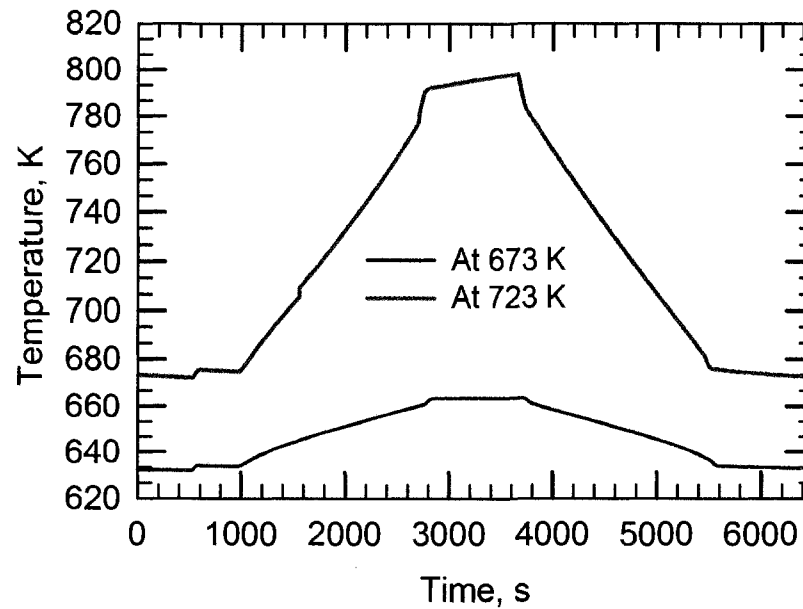


Figure 6.77: Comparison of reactor outlet temperature as function of time for ramp experiment at fixed nominal temperature of 673 and 723 K.

Table 6.8: Methane conversion in ramp input concentration programmed experiments at 673 K nominal.

CH ₄ inlet Conc. [ppm]	CH ₄ outlet conc. [ppm]	% conversion [-]	Front T1 [K]	20 mm T2 [K]	1 mm T3 [K]	70 mm T4 [K]	70 mm T5 [K]	1 mm T6 [K]	35 mm T7 [K]	35 mm T8 [K]	20 mm T9 [K]
500	193	61	606	646	648	623	635	644	634	638	630
1098	539	51	606	648	649	626	638	645	636	640	632
1964	1041	47	606	650	649	629	641	646	637	643	633
5012	2826	44	607	654	651	637	651	650	641	649	637
9316	4796	49	608	659	653	646	661	652	645	655	641
5001	2904	42	609	655	652	640	652	650	642	650	639
2007	1179	41	609	650	650	632	643	647	638	644	635
1006	599	41	609	649	650	628	640	645	637	641	633
508	320	37	608	648	649	627	638	645	636	640	632

Table 6.9: Methane conversion in ramp input concentration programmed experiments at 723 K nominal.

CH ₄ inlet Conc. [ppm]	CH ₄ outlet conc. [ppm]	% conversion [-]	Front T1 [K]	20 mm T2 [K]	1 mm T3 [K]	70 mm T4 [K]	70 mm T5 [K]	1 mm T6 [K]	35 mm T7 [K]	35 mm T8 [K]	20 mm T9 [K]
537	105	80	644	688	689	664	677	685	676	681	671
1004	262	74	644	690	690	670	683	687	678	684	673
2007	624	69	644	695	692	680	695	691	682	692	678
5002	1708	66	645	707	696	710	729	699	693	711	689
9316	2678	71	654	725	704	779	798	712	710	743	708
5005	1640	67	655	710	700	725	740	702	697	715	695
2002	691	66	653	697	695	691	703	693	686	695	683
1002	341	66	652	693	693	680	691	690	682	688	678
502	166	67	651	690	692	674	685	688	680	684	676

For the ramp experiment, however, the fractional conversion tends to decrease much more as the methane concentration increases, and then tends to stay the same or decrease slightly even when the concentration is reduced. It is notable, however, that the temperatures are about the same for the three types of experiments. Clearly there are unsteady state processes occurring at the catalyst surface over the time scale of the ramped experiments.

6.5 Summary

In this chapter experimental results were presented on the catalytic combustion of methane on a palladium catalyst. The findings are that methane, water, hydrogen, carbon monoxide and carbon dioxide all show inhibition effects for the reaction. Pretreating the catalyst with hydrogen can offer an increased initial activity. this activity increase is lost after exposure to an oxidizing environment. The use of the data collected to build a kinetic model for the system is shown and discussed in Chapter 7.

Kinetic modelling of methane combustion

One of the principal objectives of this work was to model the catalytic flow reversal reactor for the combustion of lean methane. As part of this modelling study, the use of palladium catalyst was investigated. A necessary condition for reactor modelling is to have a suitable kinetic model for the reaction. In Chapter 6, the procedure and results for the experimental investigation of methane combustion over palladium catalyst were presented. The purpose of this chapter is to present the results of modelling studies aimed at elucidating the kinetics of the reaction.

The detailed literature review of the catalytic combustion of methane was presented in Chapter 5. In brief, there are two main approaches that are used to model kinetic reactions. A global kinetic model is often used as a simplification of the complex surface mechanisms, see for example Golodets et al. (1983), Cullis and Willat (1983), Ribiero et al. (1994a), Monteiro et al., (2001), Liu et al. (2001a), Ibashi et al. (2003), and Araya et al. (2005). This type of approach leads to relatively simple models that may be applicable over a small range of operating conditions. Usually the constants in the model are obtained by fitting with experimental data using an optimization procedure such as least squares regression analysis. This type of modelling is commonly used in chemical reaction engineering. Global models offer simplicity and speed of computation which, in spite of the advances

in computer technology, is still a significant advantage over more complex models. They may be suitable for engineering design.

The second approach to kinetic modeling treats the surface kinetics at the mechanistic level, where each step in the reaction, from adsorption, multi-step surface reaction and desorption is included. The advantage of this type of model is that they might have a better predictive ability and be more easily extrapolated to new operating conditions. Where fast transients are modelled, with changing surface conditions, a model incorporating explicitly the microscopic steps is really necessary. The drawback of this type of model is the complexity, combined with the fact that the surface mechanism is often unknown. Implementation of such complex models into reactor simulators can also lead to extremely long execution times.

Modelling of catalytic combustion reactions is complicated by the high exothermicity of the reaction, and the importance of heat and mass transfer effects, which are usually significant in these systems. In this chapter, results from both global and mechanistic modelling are presented.

7.1 Global rate models

As discussed in Chapter 5, a global rate model can be written or developed in many ways, but the result is generally considered at best semi-empirical because there are always simplifying assumptions made, and the constants in the model are best fit parameters based on some experimental data. In the most rigorous development of such a model, a reaction mechanism is assumed, and then a rate equation developed using some simplifications. A typical example of this type of rate model is the LHHW type model as developed by Langmuir, Hinselwood, Hougen and Watson. Although the model assumptions are seldom valid, the resulting models nonetheless can be useful design equations. Some models make no pretence at a theoretical basis, and are simply empirical. Some models also include the transport effects in the kinetic parameters, while others do not. The term global model is sometimes used for models that include transport effects, while those that do not are often called intrinsic models. In this thesis, the term

global kinetic model is meant to refer to a non-mechanistic model. For the catalytic combustion of methane on palladium, global rate equations have been shown to be effective for modelling, as reviewed in Chapter 5.

The data used for this investigation are those described in Chapter 6, and the selection of which data to use is described shortly. First, the tools required for determining the rate equation are described, followed by the model development. These tools include an efficient reactor model and a good non-linear optimizer, both of which are now described.

7.1.1 Reactor model

Reactors may be modelled at various levels of complexity, depending on the underlying assumptions. Simple models use less computer time, which can be advantageous, however, overly simplified models will lack sufficient accuracy for design purposes. For heterogeneous reactors, the first choice is whether to use a continuum or a discrete model. In a discrete model, the domain of each phase is considered; that is, the actual physical space occupied by the fluid and solid is considered. Discrete models of an entire monolith reactor (even a relatively small one) would require vast computational resources for their solution, and therefore are not seen. A continuum model based on a volume averaging process is usually used (e.g., Zygourakis (1989); Luoma and Smith (1996)). These models are discussed in more detail in Chapter 8.

It was seen from the data in Chapter 6 that there were axial and radial temperature gradients in the reactor during all experiments. This observation would imply that for the best accuracy a two or three dimensional model should be used to simulate the experimental reactor. However, to couple such a simulator to an optimizer, would be beyond the ability of the available computational resources to solve in a reasonable amount of time. It was therefore decided to use a single channel model. A single channel model represents only a single channel, and rests on the assumption that all of the channels in the monolith experience essentially the same reaction conditions. Clearly this was not the case here, and the assumptions

and approximations made are discussed in further detail presently. Single channel monolith reactor models (e.g. Hayes et al. (1992), Leclerc et al. (1993)) are discrete models.

To develop a single channel model, decisions concerning the number of space dimensions to be used must be made. A real monolith channel does not have axial symmetry, and the washcoat distribution is often not uniform around the perimeter. Therefore, a three dimensional model is really required to represent accurately the behaviour (see for example More et al. (2003)). However, a three dimensional model is extremely expensive to execute, and therefore a two or one dimensional model is preferred. A one dimensional (1D) model is the simplest and easiest to understand. A major advantage is that it uses significantly less computational time than two dimensional (2D) or three dimensional (3D) models. The 1D model ignores radial and angular velocity, temperature and concentration gradients and considers only axial variations. The temperature and concentration in the fluid phase are taken as the mixing cup values. This averaging of the radial values creates a discontinuity at the wall, which is accounted for by the use of heat and mass transfer coefficients.

A 2D model requires the representation of the monolith channels as right cylinders with symmetry about the axis and of the same hydraulic diameter as the channels. The hydraulic diameter is defined as the ratio of the inside perimeter divided by the cross sectional area for one channel. The gas phase temperature and concentration gradient are considered in the radial as well as axial directions. The 2D model can capture the velocity profile in the channel, including the developing flow at the inlet. The steady state model requires the solution of mole and energy balance as well as the momentum balance equations for the fluid phase. A 2D model requires more computational time than the 1D model.

Both 1D and 2D models can account for internal and external mass and heat transfer resistance. The 1D model uses mass and heat transfer coefficients, and provided that they are chosen carefully, the 1D and 2D models can give close agreement. Single channel modelling of monolith reactors is discussed in detail in Hayes and Kolaczkowski (1997). Because of the need for an extremely fast simulator

to couple with the optimizer, it was decided to use a 1D model. Furthermore, because of the assumptions made in developing the model, it was felt that there would be no added benefit to using a more complicated 2D model.

The 1D model can also be written in various forms. As mentioned earlier, a 1D model ignores radial and angular gradients in temperature, concentration and velocity, and considers only axial variations. Sometimes a further simplification is made, and the wall and fluid temperatures are assumed to be the same. This type of model is called a pseudo-homogeneous model. For catalytic combustion applications, there is often a significant difference between the temperature at the wall (where the reaction occurs) and the mean bulk temperature. In this case, the wall is assumed to be a discontinuity and separate mole and energy balance equations are written for the solid phase. These equations are coupled to the fluid equations through mass and heat transfer coefficients. This type model is known as heterogeneous model.

In both models, the effects of diffusion resistance in the washcoat can be included by incorporating an effectiveness factor in the rate expression. The pseudo homogeneous model can run very fast, however it was found here that the heterogeneous model was able to run with sufficient speed in these investigations. An assumption often made in the 1D model is that the fluid flows through the reactor in plug flow. The resulting model is called the plug flow model. Alternatively, some axial dispersion may be included. There are two methods commonly used for modelling tubular type reactors with axial dispersion. These are the dispersed plug flow model (dispersion equation) and the tanks-in-series model (TIS). Pandya (2006) compared both axial dispersion models and the TIS model for simulating and optimizing the kinetics for a diesel oxidation catalyst. He reported that the two models gave similar speed, although the TIS model was more robust under extreme reaction conditions. In this work, the axial dispersion model was chosen because it was found to work over the range of experiments and to execute quickly.

The development of the axial dispersion model is explained in detail in Hayes and Kolaczkowski (1997), and the main equations are given here (adapted from Pandya (2006) and Hayes and Kolaczkowski (1997)). The derivations are also given

in further detail in the Appendix. The axial dispersion is superimposed on to a bulk flow term giving the advection dispersion equation. Consider flow down a channel with catalyst located on or in the wall. If the possibility of the reaction in the gas phase is ignored (a reasonable assumption given the low temperatures used) the steady state gas phase mole balance equation can be written in terms of the mole fraction as:

$$\frac{d}{dz} \left(D_l C_f \frac{dY_{j,f}}{dz} \right) - C_f u_m \frac{dY_{j,f}}{dz} + a_m k_{m,j} (Y_{j,f} - Y_{j,s}) = 0 \quad (7.1)$$

The constant a_m is the effective area for mass transfer from the bulk gas. It is defined as the ratio of the gas volume to the gas/solid interfacial area, which is equivalent to the channel perimeter, P , divided by the cross sectional area of the channel, A_C . This ratio is related to the hydraulic diameter, D_H , for a duct of arbitrary shape by:

$$D_H = \frac{4A_C}{P} = \frac{4}{a_m} \quad (7.2)$$

The mole balance can thus be expressed in terms of the hydraulic diameter:

$$\frac{d}{dz} \left(D_l C_f \frac{dY_{j,f}}{dz} \right) - C_f u_m \frac{dY_{j,f}}{dz} + \frac{4}{D_H} k_{m,j} C_f (Y_{j,f} - Y_{j,s}) = 0 \quad (7.3)$$

D_l is the dispersion coefficient in m^2/s , C_f is the total fluid concentration in mol/m^3 , Y_f and Y_s are mole fractions of the component in fluid and solid respectively. The dispersion coefficient for laminar flow in a circular tube can be calculated from the Taylor-Aris equation:

$$D_l = D_{AB} + \frac{u_m^2 r^2}{48 D_{AB}} \quad (7.4)$$

where D_{AB} is the molecular diffusion coefficient of A in a mixture of A and B, u_m is average velocity and r is the radius of the tube. Equation 7.4 is valid provided that the following condition is met:

$$\frac{L}{r} > 0.16 \frac{u_m r}{D_{AB}} \quad (7.5)$$

The boundary conditions for Equation 7.1 typically imposed are the so-called Dankwerts condition. They are:

$$\left(-D_l \frac{dY_{j,f}}{dz} \right)_{0^+} = u_m [Y_{j,f0} - Y_{j,f(0^+)}] \quad \text{at} \quad z = 0 \quad (7.6)$$

$$\frac{dY_j}{dz} = 0 \quad \text{at} \quad z = L \quad (7.7)$$

In Equation 7.6 the term 0^+ indicates the position at $z = 0$ but inside the reactor. The mole fraction, $Y_{j,f0}$, is the mole fraction of species j in the feed. The solid phase mole balance is:

$$k_{m,j} C_f (Y_{j,f} - Y_{j,s}) = \eta (-R_j)_s \quad (7.8)$$

The effectiveness factor, η , is included to account for diffusion resistance in the porous washcoat. Internal diffusion resistance is discussed shortly. In this equation, the reaction rate has units based on the surface area of the catalyst, that is, the interfacial contact area between the fluid and solid. This definition of the rate is often used in monolith reactor modelling, however it may be preferable to base the rate on unit washcoat volume. To base the reaction rate on the volume of the washcoat, assuming a circular channel with an annular washcoat layer of outside diameter D_{WC} , we can directly transpose the solid phase mole balance equation:

$$A_s k_{m,j} C_f (Y_{j,f} - Y_{j,s}) = \eta (-R_j)_v V_w \quad (7.9)$$

A_s is the washcoat surface area and V_w is the volume. If substituted and simplify, the following expression is obtained:

$$\left(\frac{4D_H}{D_{WC}^2 - D_H^2} \right) k_{m,j} C_f (Y_{j,f} - Y_{j,s}) = \eta (-R_j)_v \quad (7.10)$$

The steady state gas phase energy balance equation is:

$$\frac{d}{dz} \left(k_l \frac{dT_f}{dz} \right) - u_m (\rho C_p)_f \frac{dT}{dz} + \frac{4h}{D_H} (T_s - T_f) = 0 \quad (7.11)$$

where k_l is an effective axial thermal conductivity defined by analogy with the Taylor - Aris diffusion coefficient:

$$k_l = k + \frac{(u_m r \rho C_p)_f^2}{48k} \quad (7.12)$$

The boundary conditions used were a fixed inlet temperature and a zero flux outlet condition.

The solid phase energy balance is transient. If the wall is modelled in one dimension, then all of the thermal mass is lumped into the transient term. Allowing for axial conduction in the wall gives the equation:

$$\begin{aligned} \frac{\delta}{\delta z} \left(k_w \frac{\delta T_s}{\delta z} \right) - h \left(\frac{4D_H}{D_S^2 - D_H^2} \right) (T_s - T_f) \dots \\ - \left(\frac{D_{WC}^2 - D_H^2}{D_S^2 - D_H^2} \right) (\Delta H_R) (-R_{CH_4})_V = (\rho C_p)_s \frac{\delta T_s}{\delta t} \end{aligned} \quad (7.13)$$

Where k_w is the effective thermal conductivity of the wall in W/(mK).

If heat transfer from the ends is ignored, then zero flux boundary conditions can be imposed at each end. It is necessary to have correlations for the external heat and mass transfer coefficients. More (2007) has provided an extensive review of heat and mass transfer coefficients in monolith reactors. Generally speaking, in the developing flow region it is not clear what are the best values to use, whilst in the fully developed region the values lie between those found for constant wall temperature and constant wall flux boundary conditions, and depend on the rate of reaction. Typically, the local Nu value in the system is approximated by interpolating between and using the interpolation formula of Bräuer and Fetting, (1966):

$$\frac{N_u - N_{uH}}{N_{uT} - N_{uH}} = \frac{D_a N_u}{(D_a + N_u) N_{uT}} \quad (7.14)$$

The Damköhler number, D_a , is defined for an arbitrary reaction of component A by:

$$D_a = \frac{\eta (-R_A)_S D_H}{4C_{A,S} D_{AB}} \quad (7.15)$$

The Nusselt number is:

$$N_u = \frac{h D_H}{k_f} \quad (7.16)$$

For constant wall temperature, Tronconi and Forzatti (1992) presented a correlation for simultaneously developing thermal and hydrodynamic boundary layers for a fluid with a Prandtl number of 0.7:

$$N_{uT} = 3.657 + 8.827 \left(\frac{1000}{Gz} \right)^{-0.524} \exp \left(-\frac{48.2}{Gz} \right) \quad (7.17)$$

The Graetz number is defined as:

$$Gz = \frac{D_H}{z} Re Pr \quad (7.18)$$

A correlation for simultaneously developing flow at a Prandtl number of 0.7 with constant wall flux is given in Hayes and Kolaczowski, (1997):

$$N_{uH} = 4.364 + 13.18 \left(\frac{1000}{Gz} \right)^{-0.524} \exp \left(-\frac{60.2}{Gz} \right) \quad (7.19)$$

The Sherwood number can be obtained by substituting the Schmidt number, Sc , for the Prandtl number in the equation for Graetz number, that is, Equation 7.18. The Sherwood number is:

$$Sh = \frac{k_m D_H}{D_{AB}} \quad (7.20)$$

For the 1D model, the pressure drop is usually assumed to be negligible and is ignored. Analytical solution for the preceding PDE that describe the axial dispersion model is not possible, hence a numerical method is required. The solution methodology is discussed shortly.

In spite of the thin washcoat layers in monolith catalytic combustion reactors, it has been shown that diffusion resistance in the washcoat can be significant. See for example, Hayes et al. (2005). The following paragraphs briefly describe diffusion resistance in porous catalyst.

Many textbooks, for example, Satterfield (1970), Hayes and Kolaczkowski (1997), or Froment and Bischoff (1990), provide the background on diffusion in catalysis. Consider, for illustration purposes, a flat slab of porous catalyst of thickness L , see Figure 7.1, where diffusion into the slab occurs only at the face where $x = L$, with the face at $x = 0$ being impermeable.,

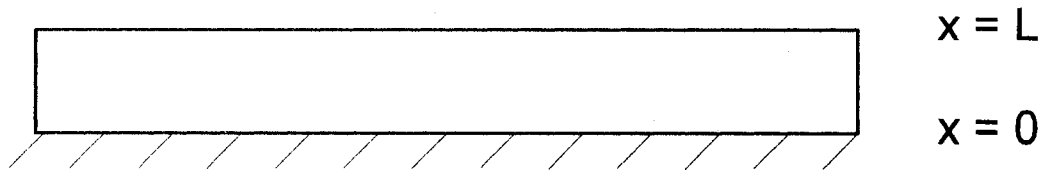


Figure 7.1: Flat slab of porous catalyst

If a reactant A is considered to diffuse into the catalyst, it will undergo a simultaneous reaction as some of the reactants encounter active sites. This reaction will cause a diminution of the reactant, and, as a result, a concentration gradient will develop along the catalyst depth. The magnitude of the gradient will depend on the relative speed of the diffusion and reaction processes. At any point in the catalyst the rate of reaction is given by the intrinsic rate expression evaluated at local concentration and temperature, which will clearly vary within the catalyst. The diffusion of species is modelled using an effective diffusion coefficient, D_{eff} . The mole balance equation for species A is then written:

$$D_{eff} \frac{d^2 C_A}{dx^2} - (-R_A) = 0 \tag{7.21}$$

This equation is the mole balance in a flat plate for simultaneous diffusion and reaction. The equation requires two boundary conditions. At the surface the concentration is given by the surface concentration, while at $x = 0$ the diffusive flux is zero, because it is either a line of symmetry or an impermeable boundary. Thus we write:

$$C_A = C_{A,S} \quad \text{at} \quad x = L, \quad \text{and} \quad \frac{dC_A}{dx} = 0 \quad \text{at} \quad x = 0 \quad (7.22)$$

Note that the rate, $(-R_A)$, has units of $\text{mol}/\text{m}^3 \text{ s}$, that is, the rate is measured in terms of volume of catalyst. It is convenient to put the equation into dimensionless form as an aid in identifying the important dimensionless groups which govern the diffusion/reaction process. Consider a first order reaction:

$$(-R_A) = k_V C_A \quad (7.23)$$

Define the dimensionless concentration as the ratio of the concentration to the surface concentration, $C^* = C_A/C_{A,S}$, and the dimensionless coordinate as $x^* = x/L$. The dimensionless form of the differential equation is:

$$\frac{d^2 C^*}{dx^{*2}} - \left(L^2 \frac{k_V}{D_{eff}} \right) C^* = 0 \quad (7.24)$$

The dimensionless boundary equations are:

$$C^* = 1 \quad \text{at} \quad x^* = 1 \quad \text{and} \quad \frac{dC^*}{dx^*} = 0 \quad \text{at} \quad x^* = 0 \quad (7.25)$$

The equation can be simplified by introducing another dimensionless group, called the Thiele modulus, ϕ , which is defined (for a first order reaction in a flat slab) as:

$$\phi = L \sqrt{\frac{k_V}{D_{eff}}} \quad (7.26)$$

Substitute into Equation 7.24:

$$\frac{d^2 C^*}{dx^{*2}} - \phi^2 C^* = 0 \quad (7.27)$$

Equation 7.24 with the boundary conditions of Equation 7.25 has an analytical solution ((Satterfield, 1970; Thomas and Thomas, 1967; Fogler, 1992; Froment and Bischoff, 1990):

$$C^* = \frac{\cosh(\phi x^*)}{\cosh(\phi)} \quad (7.28)$$

This equation gives the concentration profile in the catalyst and hence the reaction rate at any point can be calculated.

The observed rate for the entire plate is an average of all the local intrinsic rates. It is common to use an effectiveness factor to quantify the effect of the diffusion in the catalyst. This factor is defined as:

$$\eta = \frac{\text{average rate for a catalyst pellet}}{\text{rate evaluate at surface conditions}} \quad (7.29)$$

The ratio of the average rate to the rate calculated at the surface conditions is the effectiveness factor. Using the solution from the mole balance equation, it can be shown that the effectiveness factor is given by:

$$\eta = \frac{\tanh(\phi)}{\phi} \quad (7.30)$$

This result is valid for a first order reaction occurring in an isothermal flat plate of catalyst with a uniform catalyst activity.

For complex non-linear kinetics such as the LHHW type other behaviour is observed. Consider a typical yet simple LHHW model:

$$(-R_A) = \frac{k_V C_A}{(1 + K_A C_A)^2} \quad (7.31)$$

Define the additional dimensionless group:

$$\Gamma = (C_A)_S K_A \quad (7.32)$$

The diffusion reaction equation in a one dimensional plane wall could now be written:

$$\frac{d^2C^*}{dx^{*2}} - \phi^2 \frac{C^*}{(1 + \Gamma C^*)^2} = 0 \quad (7.33)$$

Equation 7.33 does not have an analytical solution, and thus must be solved numerically. This type of non-linear kinetics is interesting because it allows the possibility of effectiveness factors greater than unity. To model the diffusion washcoat, it is necessary to have values for the effective diffusivity and the characteristic washcoat length. The effective diffusion coefficient D_{eff} in the washcoat is calculated by combining the effects of bulk and Knudsen diffusion in the catalyst pores:

$$D_{eff} = \frac{\varepsilon}{\tau} \left[\frac{1}{D_K} + \frac{1}{D_{AB}} \right]^{-1} \quad (7.34)$$

In this equation, the diffusion terms are the Knudsen diffusion coefficient, given by:

$$D_K = 48.5d_p \sqrt{\frac{T}{M}} \quad (7.35)$$

The bulk diffusion coefficient was obtained from the Fuller correlation. For methane diffusing in air, for example, the equation is (Hayes and Kolaczkowski, 1997):

$$D_{AB} = 9.99 \times 10^{-5} \frac{T^{1.75}}{p} \quad (7.36)$$

The mean pore diameter, d_p , is taken as 1×10^{-8} metres (10 nanometres), the catalyst porosity, ε , as 0.5 and the tortuosity factor, τ as 1. These values are based on earlier work that studied effective diffusion coefficients in similar washcoats (Zhang et al., 2004). The characteristic length of the washcoat was taken as 4×10^{-5} metres.

7.1.2 Reactor model - implementation and solution

As noted above the reactor model selected was the heterogeneous dispersed plug flow model in one dimension. This model is comprised of a set of partial differential equations and related algebraic equations. The equations were solved numerically using the Galerkin finite element method. There are currently several products available for the numerical solution of PDE, and for this work the package MONO1D was used. This software package has been developed over the last dozen years by the catalytic combustion group in the department of Chemical and Materials Engineering, University of Alberta. It is designed to model catalytic combustion reactions in monolith reactors. It includes a library of physical properties. Previous users of this code include Liu (2000) and Pandya (2006). The software has been extensively validated against other software and experimental data. For the work of Pandya (2006) the package was modified to enable kinetic parameter optimisation. The major changes for this work involved the addition of the rate function forms that were desired to be tested. Other changes will be discussed as introduced.

7.1.3 Choice of an optimisation routine

Although kinetic models have been used in catalytic converters for more than three decades, there has not been much effort at computer aided tuning. In most cases the tuning is done in a very empirical manner. Montreuil et al. (1992) presented an attempt at systematically tuning the parameters for a TWC using a conjugate gradient method with steady state data. Dubien and Schweich (1998) used a similar method to adjust pre-exponential factors for simple rate expressions from light-off curves.

The most classical approach to the optimization of parameters in rate equations, and the one presented in most standard textbooks, is a re-paramaterisation of the rate equation followed by linear regression. With the increase in computing power, and the advent of user friendly software packages, the use of non-linear regression analysis has become widespread. The Levenberg-Marquardt (LM) method is

commonly used. The LM method is gradient based and shares a common problem with other gradient methods, namely the possibility to achieve a local minimum, especially in complex non-linear problems. Although this problem can be alleviated by using several initial guesses, this step increases the computational expenses especially when a large number of parameters is involved. Also, when modelling reaction mechanisms containing adsorbed species, it is often not a priori obvious what are good initial guesses for the parameters, and thus gradient methods will face difficulty. Under this condition, use of results obtained from gradient based solvers can be misleading. A further drawback of gradient based solvers is that they may be cumbersome to implement, especially if the objective function must be generated by the solution of a complex simulator, for example, a CFD package.

Generalized optimization methods include both deterministic (Schnepper and Stadtherr, 1996; Esposito and Floudas, 1998) and stochastic (Cardoso et al., 1996; Belohlav et al., 1997). Deterministic methods tend to be more complicated to implement. Stochastic methods are simpler, using a random search of the defined parameter space. Stochastic methods have been reported by Wolf and Moros (1997), Kalies et al. (1996). Stochastic methods include simulated annealing and genetic algorithms. Eftaxieas (2002) reported that the increased cost of a simulated annealing algorithm compared to the LM was more than compensated for by its robustness. Among the most recent developments in the area of non-linear optimization are the generalized pattern search (GPS) algorithms (Audet and Dennis, 2003). Compared with the traditional methods, generalized pattern search algorithms provide a higher potential for achieving a global minimum, even when there are large numbers of parameters and the search space is large. They are capable of searching efficiently through parameter spaces where the parameter range is not reliably known. This situation may be found in mechanistic rate models that include adsorbed species. In recent work (Hayes et al., 2003) a GPS algorithm was shown to be superior to a more traditional gradient based Fletcher-Reeves algorithm. Hayes et al. (2003), used light-off curves for the oxidation of CO in their work. GPS algorithms have also proven very useful in other engineering contexts (Burns and Cliff, 1998; Kokkolaras et al., 2001). In this work the GPS methodology

used by Pandya (2006) was adopted.

7.1.4 Development of the rate model

The objective in this part of the work was to develop an empirical rate model that was consistent with the experimental observations. No attempt is made to justify the model mechanistically. However, the model form considers typical and classical forms of rate models that have been successfully used by others (see Chapter 5). The primary observations from the experimental ignition extinction curves for the untreated case (mainly the extinction curves) are that methane, water and carbon dioxide all appear to inhibit the rate. Oxygen did not seem to have a major impact on the rate. Recall from the earlier discussion that for reactions with adsorption inhibition, the classical LHHW form is often developed based on an assumed mechanism and some simplifying assumptions. Here, an empirical equation of the LHHW type is adopted, to give a proposed model of the form:

$$(-R_{CH_4}) = \frac{k_V C_{CH_4}}{(1 + K_1 C_{CH_4} + K_2 C_{CO_2} + K_3 C_{H_2O})^n} \quad (7.37)$$

This equation is expected to be the simplest model that should be able to include all of the effects observed. The first goal was to determine if this model could successfully fit the data.

7.1.5 Choice of experimental data and implementation method

The optimisation procedure requires a comparison between predicted and observed data. In this case, the predicted and observed data used were the outlet fractional conversions. In the first instance, the residual, or objective function, for n data points is defined as:

$$R_{cs} = \frac{1}{n} \sum_{i=1}^n (X_{obs} - X_{pred})^2 \quad (7.38)$$

The goal is to determine the value of the parameters in the proposed kinetic model that gives the lowest possible value of the residual, R_{cs} .

The first step was to choose the data to be used in the optimisation process. The experimental data for the ignition and extinction curves were presented in Chapter 6. Because these data were obtained over a broad temperature range, and included a wider range of concentrations compared to the constant inlet temperature experiments, it was decided to use them. Significant hysteresis was observed. Large temperature gradients were also observed during the ignition part of these curves, and to a lesser extent the extinction curves. The hysteresis observed was thought to be largely a result of the temperature hysteresis.

There are a number of possible choices for modelling the experimental reactor. For example, in the optimisation work of Hayes et al. (2003) and in Pandya (2006) ignition curves were modelled in the simulator. In both works, the inlet reactor temperature was imposed as the inlet boundary condition. The reactor simulator (single channel model) was solved with the appropriate kinetic models assuming that the reactor was adiabatic. Thus both the mole and energy balance equations were solved and the temperature in the reactor was dependent on the imposed inlet conditions and the extent of reaction. This approach is good if the reactor really is adiabatic. However, in this work, it was clear that there were significant radial gradients, which indicated that the adiabatic assumption would not really be valid. During the extinction curves, the radial temperature gradients were smaller, however, there would not be a correspondence between the mole and energy balances because the reactor was not adiabatic during the ignition phase, and it is not evident how to compute the rate of energy transfer to the surroundings. Therefore it was felt that the simultaneous solution of the transient mole and energy balances would not give an adequate representation of the reactor. Rather, the following approach was adopted. First, the extinction curves were used because of the smaller radial and axial gradients present during operation. From each of the extinction curves used (discussed shortly), about 16 to 17 conversions were selected, with the conversion value ranging from approximately 2 to 96 %. These data formed the observed data. The predicted data were then computed

from the simulator as follows. At each data point, the temperature profile in the reactor was extracted from the experimental data file. The temperatures at four axial positions in the reactor were known, at 1 mm, 20 mm, 35 mm and 70 mm. At each of these axial locations, two thermocouples were used. At each location, the two thermocouple values were averaged. Between these points, the temperature was calculated using linear interpolation. In this way, a temperature profile for the reactor was generated. This temperature profile was imposed in the reactor simulation, and the mole balance equation was solved at steady state to generate the predicted conversions.

Solving the steady state mole balance only for the observed temperature profile offers some advantages. First, it is not necessary to have an adiabatic system. Second, solving only the steady state mole balance equation rather than the coupled mole and energy balances in transient form offers a much quicker simulation, which is quite important when performing optimisation studies with many adjustable parameters. The extinction curves used were those for the untreated case, because in the operation of the large scale reactor (described in Chapters 8 and 9) the catalyst would not be pretreated with hydrogen. The four primary runs used are 146.3, 147.2, 149.2 and 151.2 to capture the effect of the methane concentration. Because the model must contain inhibition terms for carbon dioxide and water, the runs with added water (run 162.2) and added carbon dioxide (run 168.2) were included. Note that when these products are not added to the feed, it is not possible to determine independently the effects of products, because their concentrations are correlated by the reaction stoichiometry. The extinction curves and the data points taken from them are shown in Figure 7.2. The points were extracted to cover the range of rapidly changing concentration.

The reactor operated in conditions where washcoat diffusion was expected to be significant. One modelling option often employed for monolith reactor modelling is to incorporate the diffusion effects in the kinetic parameters, to give "global" parameters. Alternatively, the effectiveness factor may be used, as discussed earlier. However, the determination of the effectiveness factor for this type of non-linear kinetics must be made numerically, and this calculation is very expensive in terms

of the CPU time. While it is easily done in the MONO1D software, it takes over a minute for each reactor simulation. Although this time is insignificant in the context of modelling the reactor, it is far too long for use with the optimizer and a model with a large number of adjustable parameters. Therefore the effectiveness factor was approximated using the first order solution. Although this will possibly introduce some error, it is a necessary simplification to achieve computational simplicity. Note also that the resulting rate equation is to be used in the modelling of the full monolith reactor (see Chapter 9) where it is also necessary to make this simplification, thus the model is consistent. This approximation is felt to an improvement over ignoring the diffusion and using lumped parameters.

As noted earlier, the optimizer used was the GPS optimizer contained in the Matlab optimization toolbox. A Matlab script was used to interface the optimizer

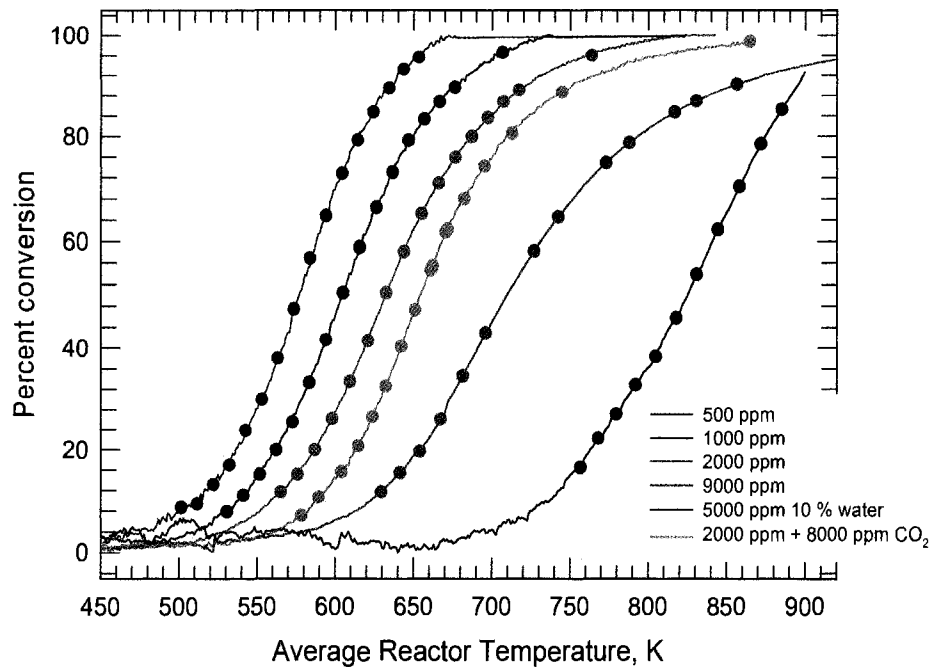


Figure 7.2: The six experimental extinction curves used in the optimization procedure. The lines show the experimental data and the circular symbols the points from each curve used in optimizer.

with the reactor simulator, MONO1D. The main factor to set for the GPS optimizer is the parameter range to be searched, which is unknown. Therefore the parameter range was originally set fairly wide with what were thought to be good values. After the optimization was stopped, the final parameter values were examined. If the values were close to the upper or lower limits of the range specified, then the range was increased and the optimisation re-run. This method was found to be effective.

7.1.6 Optimization results

In this section the results are presented. In the first instance, the optimization was performed using the six extinction curves and the rate equation as proposed in Equation 7.37. All the kinetic parameters are assigned an Arrhenius type temperature dependency, that is:

$$\begin{aligned} k_V &= A_V \exp\left(\frac{-E_V}{R_g T}\right) & K_1 &= A_1 \exp\left(\frac{-E_1}{R_g T}\right) \\ K_2 &= A_2 \exp\left(\frac{-E_2}{R_g T}\right) & K_3 &= A_3 \exp\left(\frac{-E_3}{R_g T}\right) \end{aligned} \quad (7.39)$$

The first objective was to determine the best value for n . In classical LHHW modelling this power usually has the value of either 1, 2 or 3 (less often 4). When the optimisation was performed with the six extinction curves, it was observed that the final value of the constant n was 1.92, and therefore in all other runs (unless specified to the contrary) this value of n was fixed to 2. Following this specification, many different scenarios were tried and the convergence behaviour of the algorithm was observed. Some general observations are given in the following:

- a) Overall, when the residual was less than about 10 for all six runs combined, the solution appeared by eye to be reasonable, and the errors between the observed and predicted conversions were less than 10 %.
- b) There were several different sets of parameter values that could give low residuals (less than 10) and the match between experimental and predicted

curves would appear to be reasonable, and therefore it is not possible to state absolutely what the optimal parameters are, especially considering that there is some experimental error. Therefore no physical meaning should be given to the parameter values finally determined.

- c) After the set of optimized parameters was determined, the simulations were run again for all of the data points. However, in this case the reactor temperature was held constant at the average reactor temperature rather than imposing the temperature profile. The residual changed by an insignificant amount, indicating that it is sufficient to assume an isothermal reactor.

The first result presented shows the best fit parameters obtained on the full model with a power on the denominator of 2. This scenario is called Model A1. The rate model is:

$$(-R_{CH_4}) = \frac{k_V C_{CH_4}}{(1 + K_1 C_{CH_4} + K_2 C_{CO_2} + K_3 C_{H_2O})^2} \quad (7.40)$$

The activation energy was held constant over the entire temperature range. Figure 7.3 shows the difference between the experimental and predicted light-off curves. The predicted light-off curves were generated assuming a uniform reactor temperature. The experimental curves are plotted using the average reactor temperature. Figure 7.4 shows the difference between predicted and observed values for each of the data points used in the optimization. The optimal parameters are given in Table 7.1.

It has been observed in the literature (see, for example, (Liu et al., 2001c)) that the activation energy for methane oxidation can undergo a transition in the temperature range of 650 to 850 K. It was found that setting a transition temperature of, for example, 700 K and allowing different activation energies above and below this value gave an equivalent fit, and the activation energy above 700 K was observed to decline, consistent with the literature observations. This model is referred to as Model B1. In this case, the pre-exponential factor for the high temperature region is fixed so that the value of the rate constant at 700 K is the same for both forms

of the rate equation. The curves are shown in Figures 7.5 and 7.6. It should be pointed out, however, that based on the data obtained here, it is not possible to state whether or not this catalyst exhibited the transition behaviour or not. It can be seen that the run at 9000 ppm methane is fit a little better with model.

It is noted from the comparison of the predicted and observed values that there is generally a smaller deviation at the higher conversions. This is likely an artifact of the method by which the residual is calculated, because the absolute error was used rather than a relative error. The optimisations were repeated with the objective function modified to compute a relative error, thus:

$$R_{es} = \frac{1}{n} \sum_{i=1}^n \left(1 - \frac{X_{pred}}{X_{obs}} \right)^2 \quad (7.41)$$

Table 7.1: Summary of parameter values for the models A and B:

Parameter	Model A1	Model B1	Model A2	Model B2
$A_V T \leq 700 \text{ K}$	2.89×10^5	2.19×10^5	1.64×10^5	1.83×10^5
$E_V T \leq 700 \text{ K}$	3.00×10^4	3.00×10^4	3.00×10^4	3.00×10^4
$A_V T \geq 700 \text{ K}$	2.89×10^5	1.90×10^3	1.64×10^5	1.22×10^3
$E_V T \geq 700 \text{ K}$	3.00×10^4	2.36×10^3	3.00×10^4	8.60×10^2
A_1	2.18×10^{-2}	2.31×10^{-2}	4.50×10^{-3}	8.08×10^{-3}
E_1	5.00×10^4	3.71×10^4	4.50×10^4	4.21×10^4
A_2	4.25×10^{-4}	4.29×10^{-3}	6.30×10^{-4}	5.71×10^{-4}
E_2	5.00×10^4	3.81×10^4	4.76×10^4	4.85×10^4
A_3	2.35×10^{-6}	1.14×10^{-5}	1.36×10^{-4}	1.53×10^{-5}
E_3	8.72×10^4	7.73×10^4	6.25×10^4	7.47×10^4

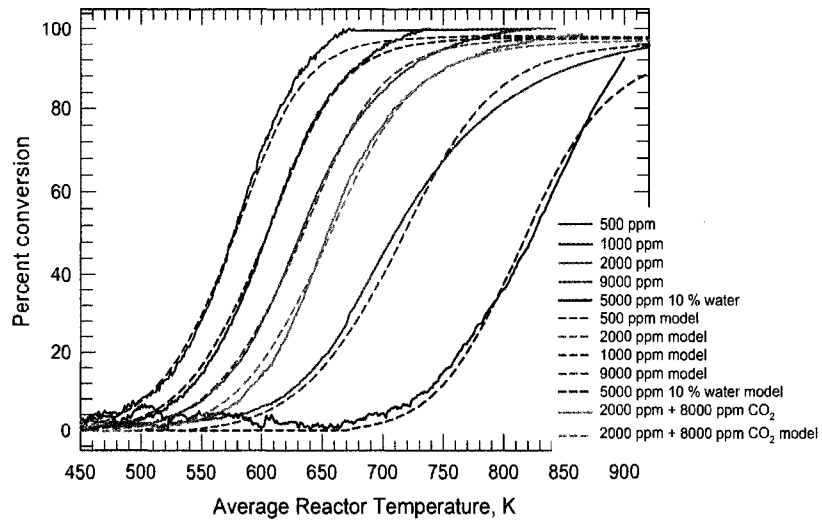


Figure 7.3: Observed and predicted extinction curves for Model A1.

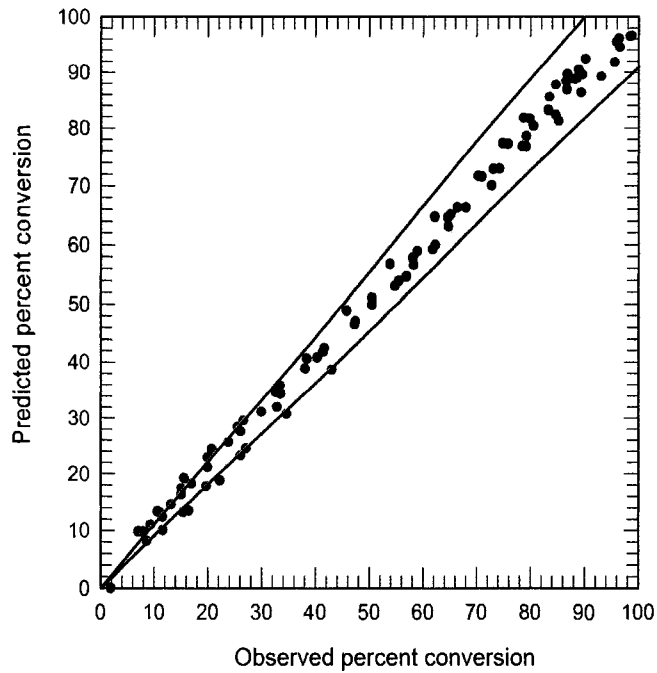


Figure 7.4: Differences between predicted and observed values at the data points used in the optimization for Model A1.

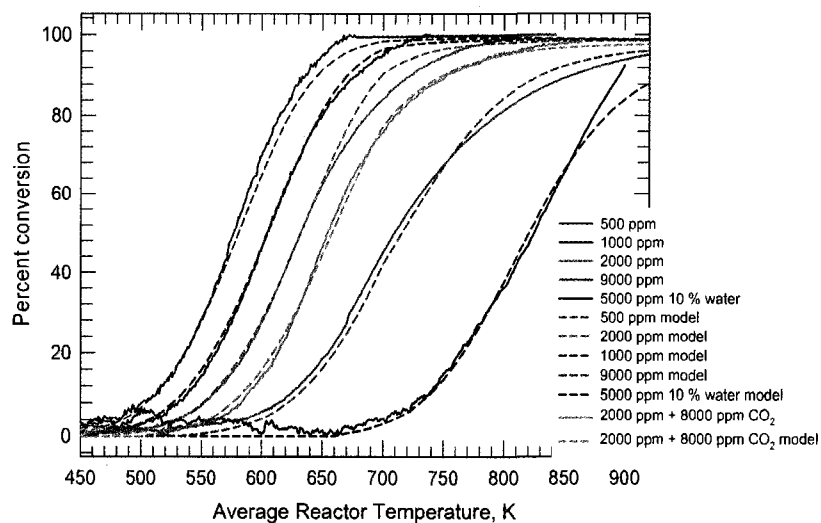


Figure 7.5: Observed and predicted extinction curves for Model B1.

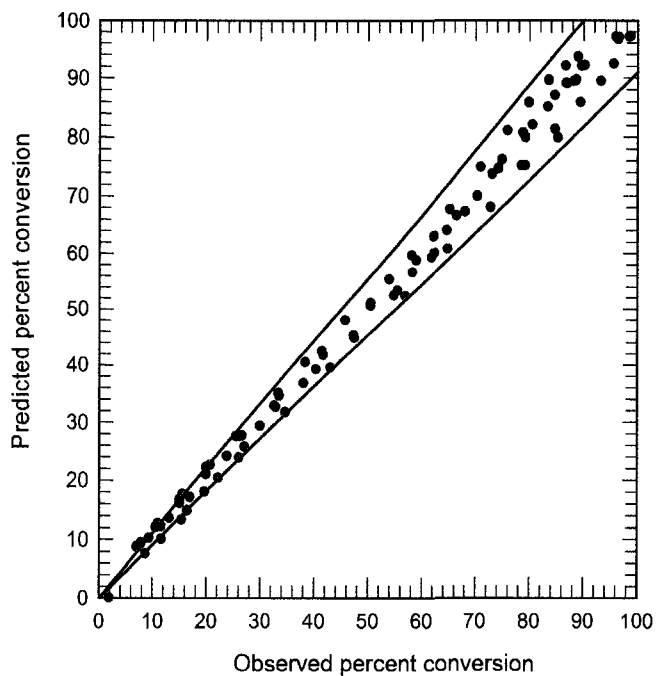


Figure 7.6: Differences between predicted and observed values at the data points used in the optimization for Model B1.

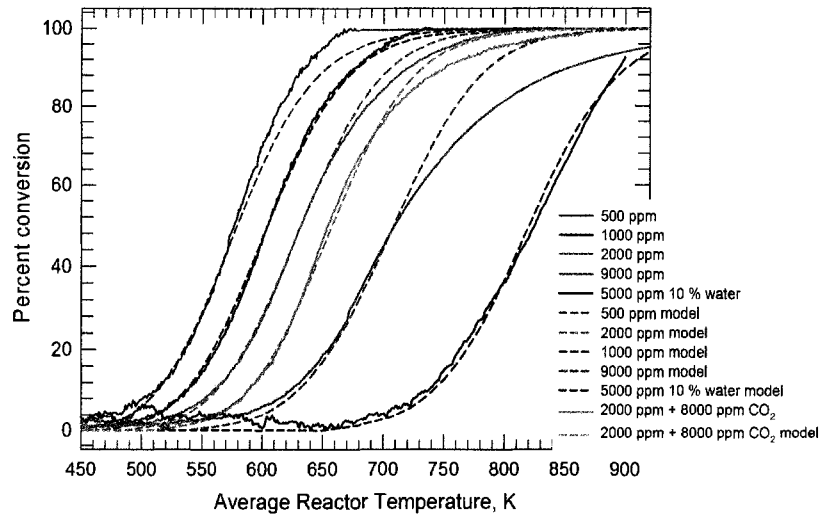


Figure 7.7: Observed and predicted extinction curves for Model A2.

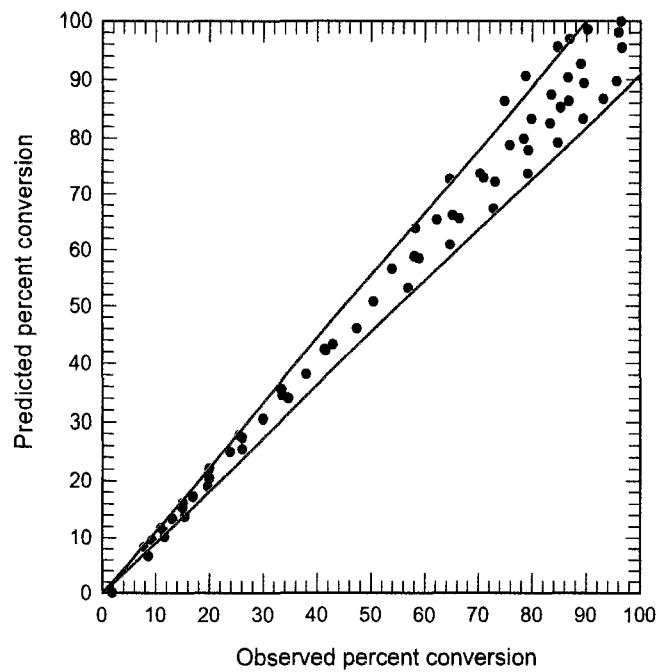


Figure 7.8: Differences between predicted and observed values at the data points used in the optimization for Model A2.

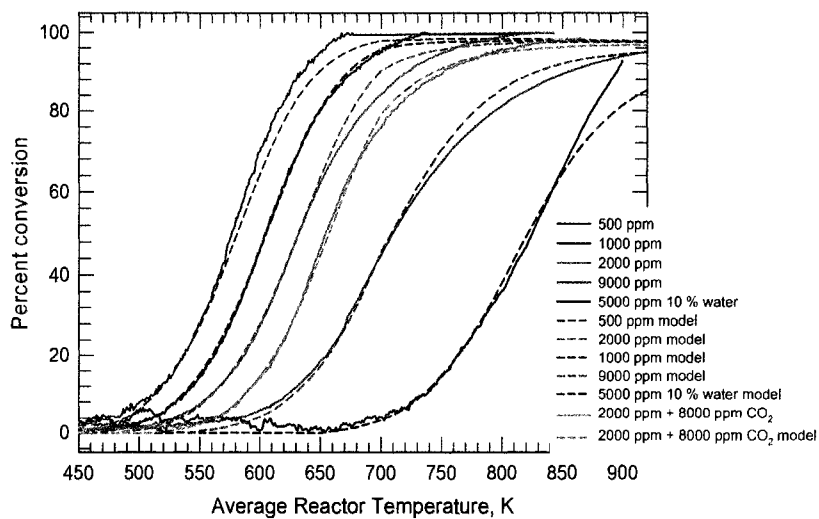


Figure 7.9: Observed and predicted extinction curves for Model B2.

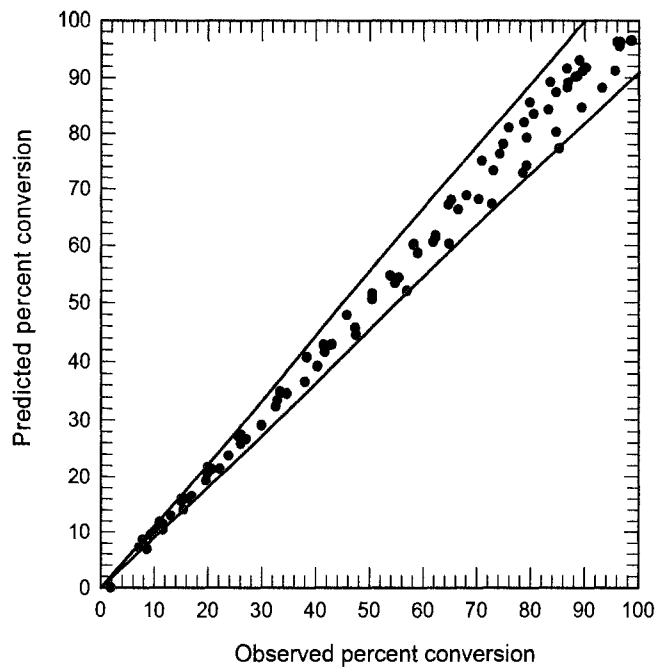


Figure 7.10: Differences between predicted and observed values at the data points used in the optimization for Model B2.

The optimisation for models A and B were repeated, and are denoted models A2 and B2. The results are shown in Figures 7.7 to 7.10 and the parameter values are given in Table 7.1. In this case, it is seen that the run at 9000 ppm methane is fit much better with the two step model.

As noted earlier, there should not be a physical significance attached to the values. Also, there are many additional combinations of parameters that will give a reasonable looking fit, although the residual will be higher. However, for the purpose of evaluating the catalytic flow reversal reactor, the model is felt to be adequate. The parameter set represented by Model B1 was used in this investigation (see Chapter 9).

An additional simulation is presented for interest. The inhibition term for methane in the denominator was excluded. The purpose was to determine if the inhibition terms for the water and carbon dioxide alone could account for the decrease in activity with increasing methane concentration. This model was referred to as Model C. It was found out that this assumption could not result into an acceptable fit.

7.1.7 Modelling the full curve

In this section the Model B1 generated previously was used to generate the full ignition-extinction curves for the six cases used in the optimization. In this instance, the full transient single channel model was used with the solution of the coupled mole and energy balance equations. For each of the six runs, the temperature hysteresis and the conversion curves are shown. For the model data, the plots are based on inlet and outlet temperatures. For the experimental runs, the plots are based on thermocouples T3 (inlet) and T4 (near outlet). The inlet temperature ramp to the model was the experimental ramp recorded by thermocouple T3. The purpose of these plots is simply to give an idea of non-adiabatic performance of the experimental reactor. It is also seen that the model predicts hysteresis in conversion, which is the result of the temperature hysteresis. Figures 7.11 to 7.22 compare the experimental and model B1 results for conversion and temperature curves.

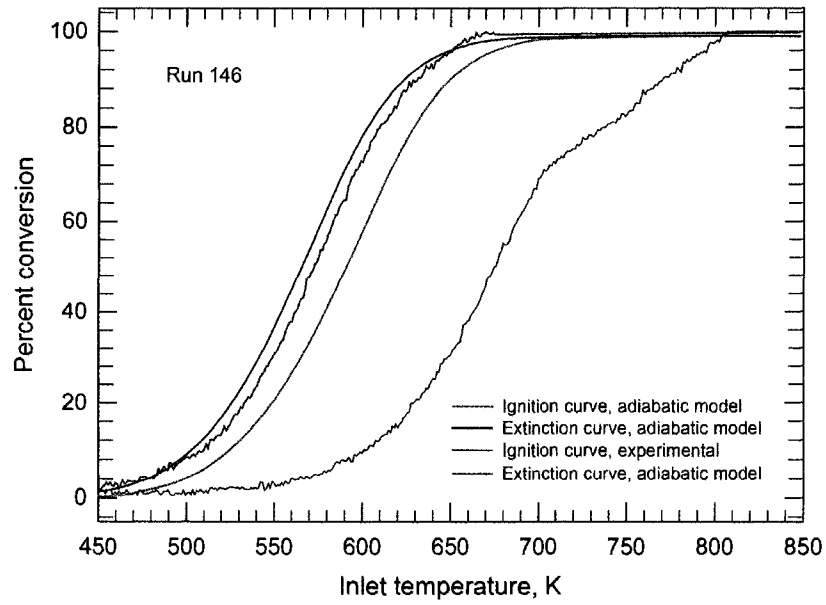


Figure 7.11: Model and experimental ignition-extinction curves, Run 146_3, 500 ppm methane.

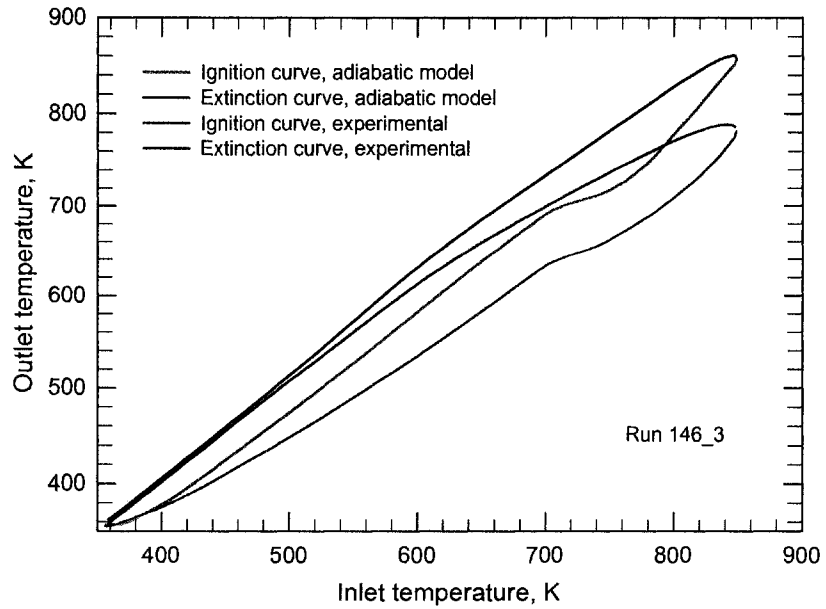


Figure 7.12: Model and experimental temperature curves, Run 146_3, 500 ppm methane.

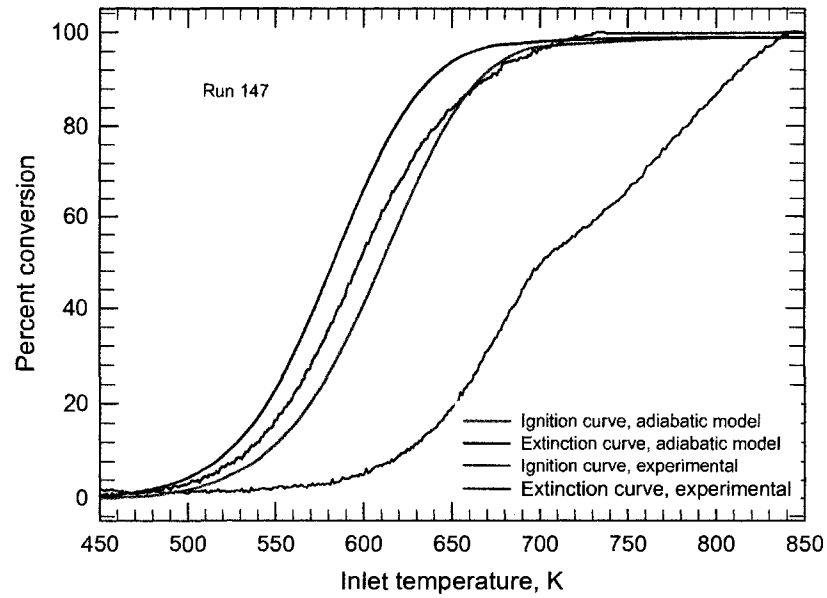


Figure 7.13: Model and experimental ignition-extinction curves, Run 147.2, 1000 ppm methane.

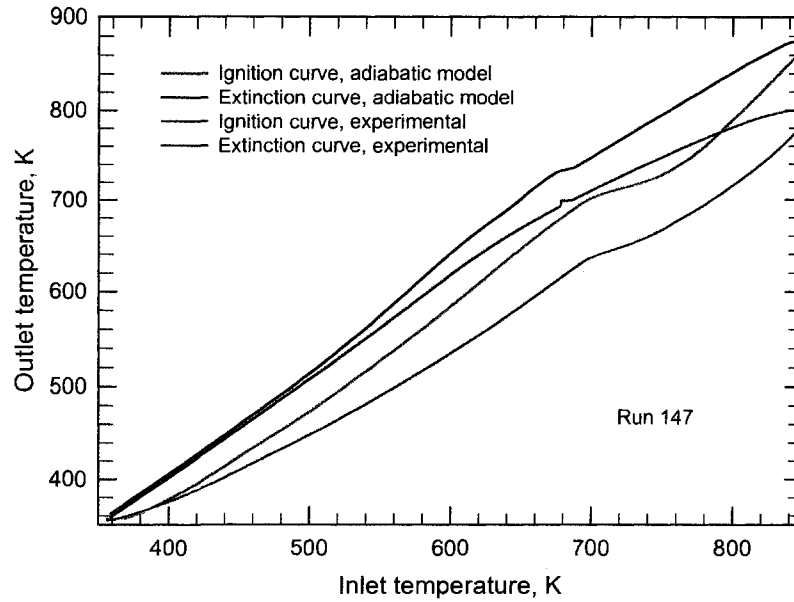


Figure 7.14: Model and experimental temperature curves, Run 147.2, 1000 ppm methane.

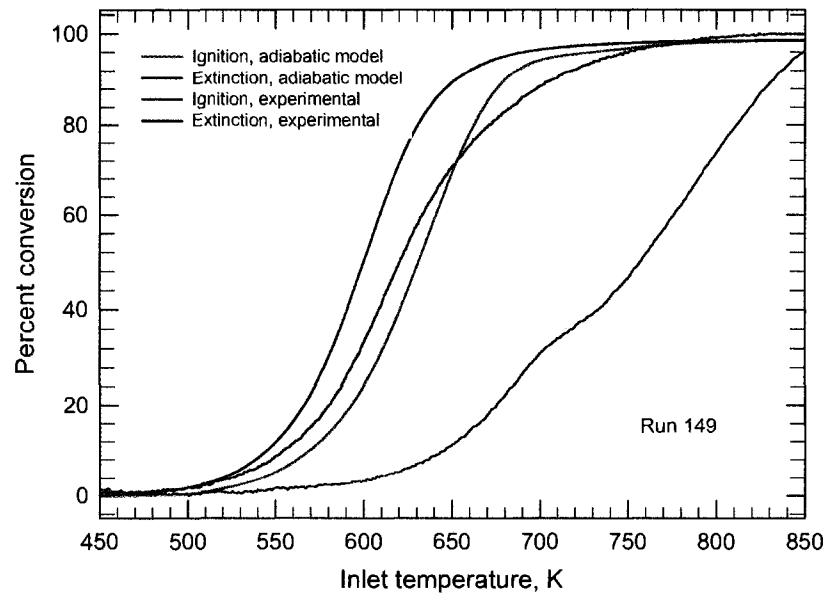


Figure 7.15: Model and experimental ignition-extinction curves, Run 149.2, 2000 ppm methane.

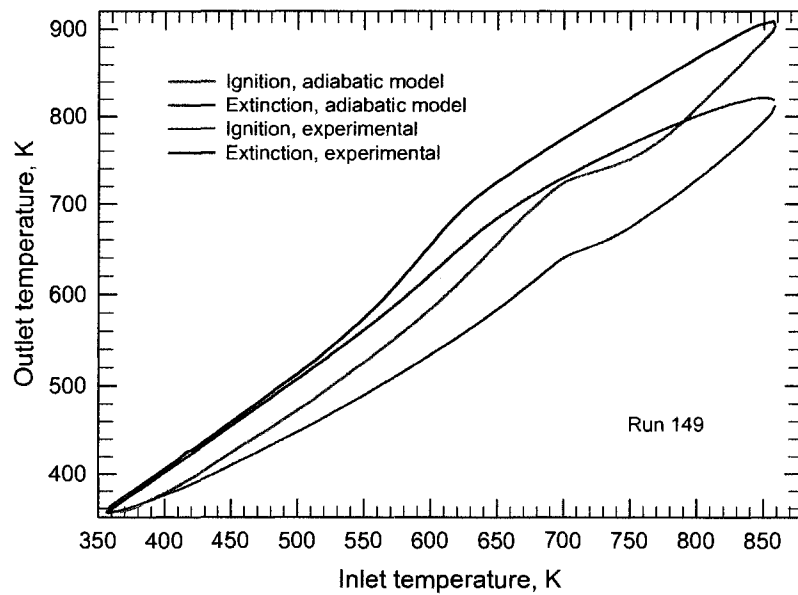


Figure 7.16: Model and experimental temperature curves, Run 149.2, 2000 ppm methane.

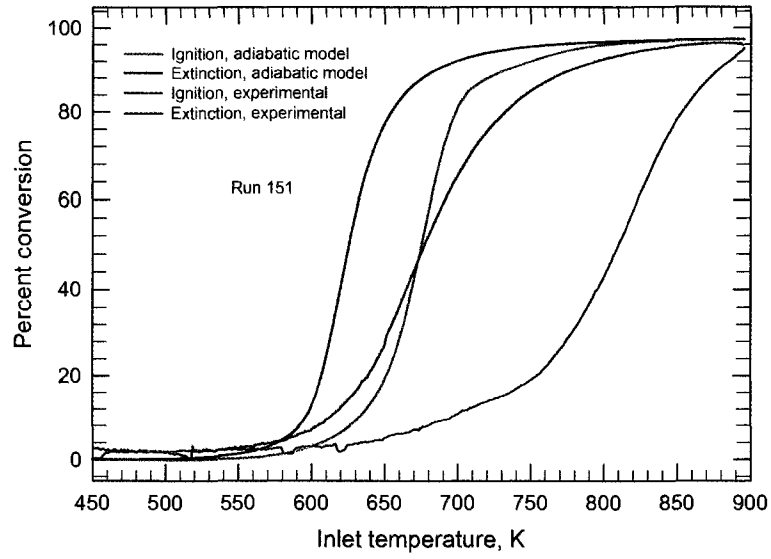


Figure 7.17: Model and experimental ignition-extinction curves, Run 151.2, 9000 ppm methane.

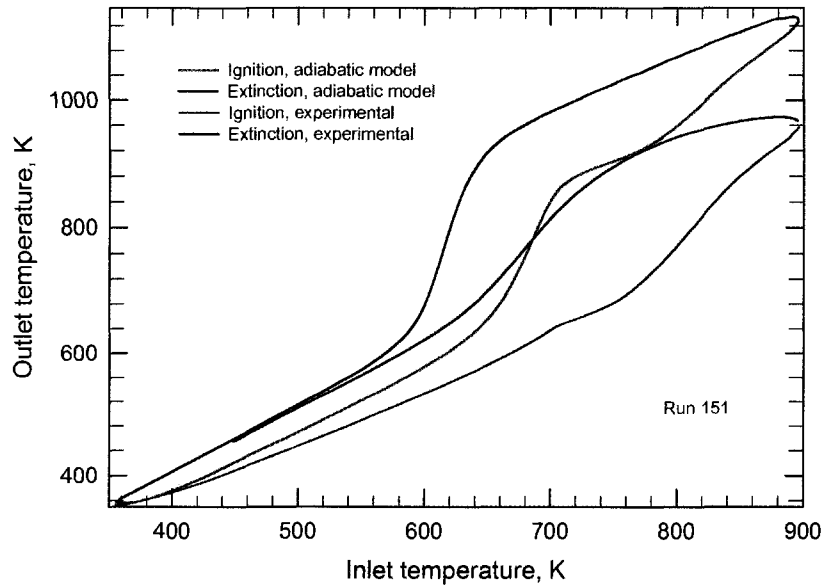


Figure 7.18: Model and experimental temperature curves, Run 151.2, 9000 ppm methane.

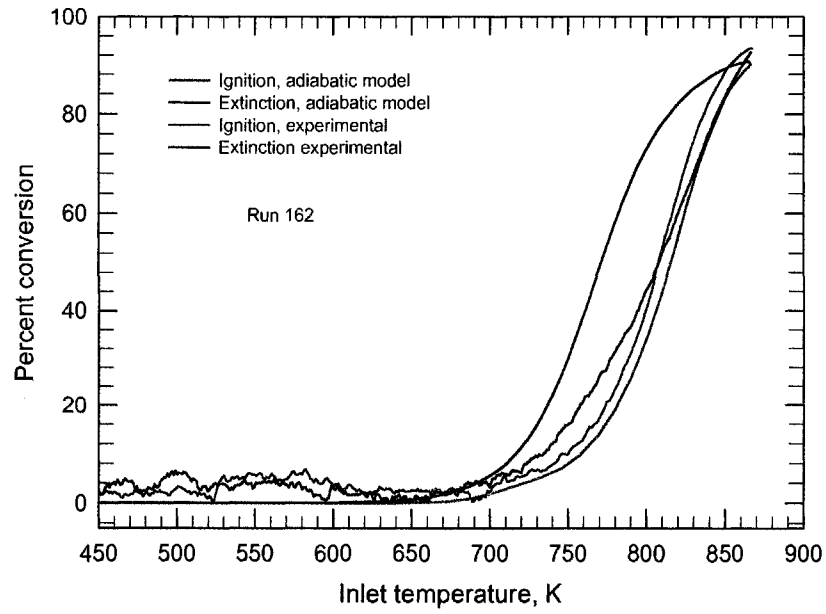


Figure 7.19: Model and experimental ignition-extinction curves, Run 162.2, 500 ppm methane and 10% water.

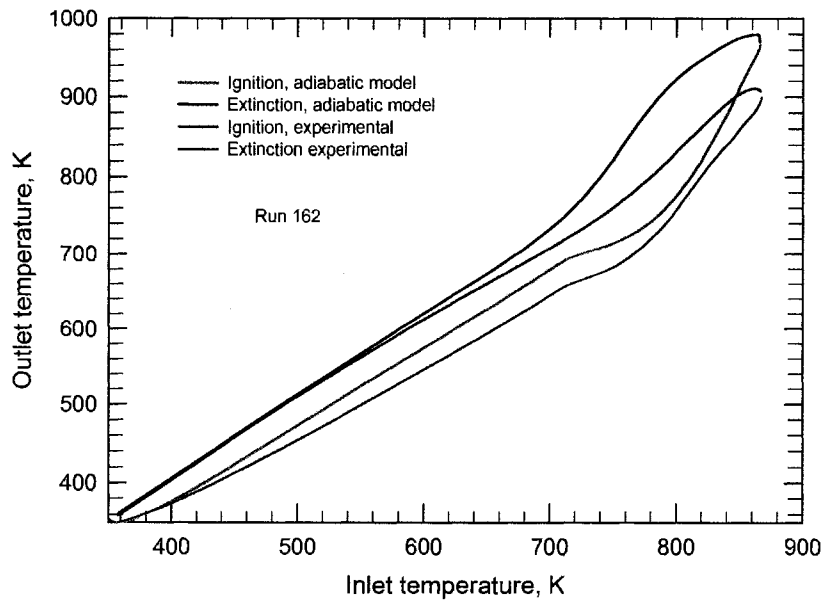


Figure 7.20: Model and experimental temperature curves, Run 162.2, 500 ppm methane and 10% water.

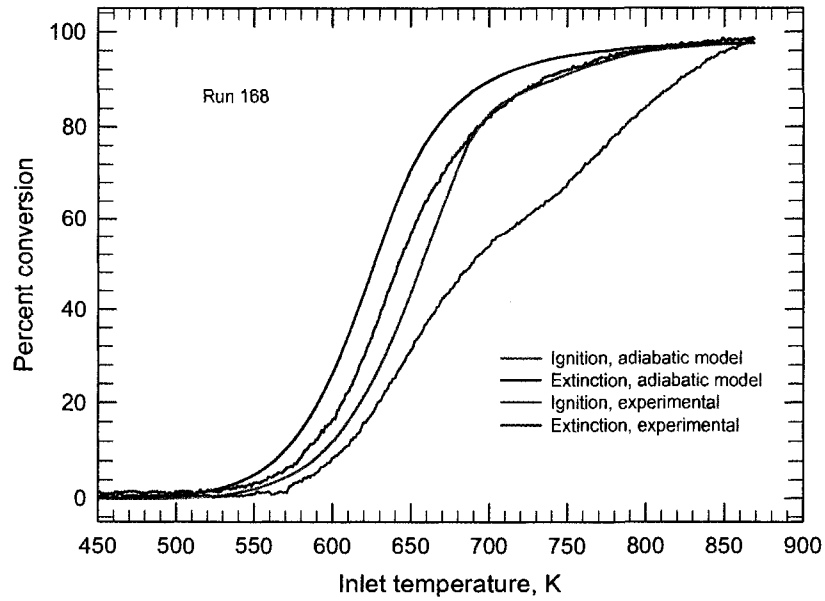


Figure 7.21: Model and experimental ignition-extinction curves, Run 168.2, 2000 ppm methane and 8000 ppm carbon dioxide.

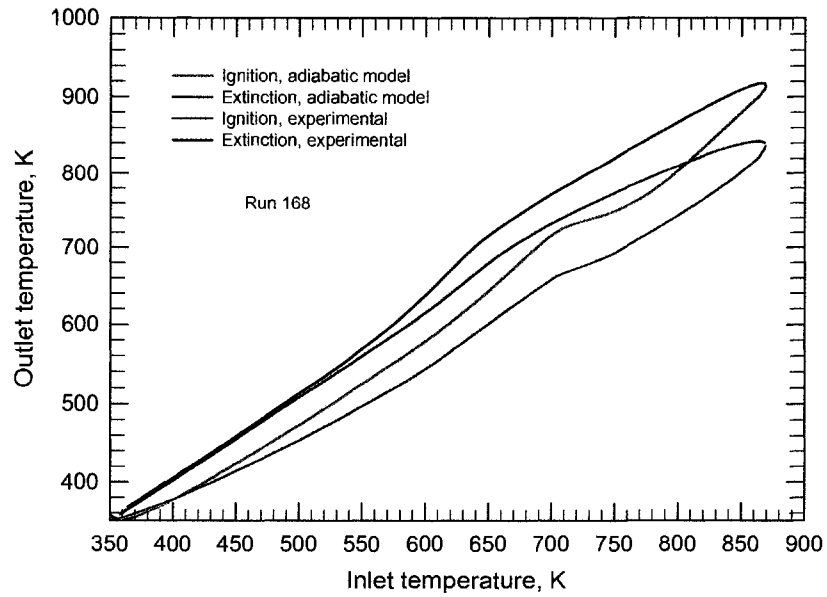


Figure 7.22: Model and experimental temperature curves, Run 168.2, 500 ppm methane and 8000 ppm carbon dioxide.

7.2 Mechanistic model

Understanding the detailed surface reaction mechanism can be useful for improving reactor performance. Development of detailed mechanisms which can capture and predict experimental data and real reactor performance accurately is a challenging task. Due to limited knowledge of the elementary surface reaction kinetics, most numerical studies have been performed with single-step global surface reaction. Global reaction models should be used with care as predictive tools, due to the limitation that the kinetics parameters associated with them are usually fitted to a narrow range of operating conditions. Detailed reaction mechanisms based on elementary steps are better options if they are able to capture the underlying science and physical operations, from a fundamental point of view.

7.2.1 Introduction

As discussed in detail in Chapter 5, extensive experimental and numerical studies have been used to help to understand the fundamentals of catalytic methane combustion and its detailed surface mechanism on noble metals, over a broad range of conditions. Some relevant studies were carried out by Deutschmann et al. (1996)

So far, the detailed surface mechanism for methane catalytic combustion on platinum surface is more extensively studied and thus more widely accepted. For palladium catalyst, the surface mechanism is still in debate and no agreement exists; in most cases the established mechanism for combustion of methane on Pt catalyst has been adopted for use in the case of Pd catalyst, with some minor adjustment. Systematic attempts to develop a methane catalytic multi-step surface mechanism started with the effort of Deutschmann et al. (1996), who proposed a detailed surface mechanism for catalytic hydrogen combustion. A five species and 13 elementary reaction steps mechanism was proposed, and was able to fit their experimental data for lean hydrogen - air mixture combustion. Later, Moallemi et al. (1999) adopted the proposed mechanism and added some more species and elementary surface reaction steps to obtain a methane multi-step surface mechanism with ten species and twenty one elementary reaction steps, although the

proposed mechanism failed to capture hysteresis behaviour of methane combustion on palladium based catalysts. Using the Deutschmann mechanism as a base, Zhu (2001) introduced the oxygen physical adsorption idea to propose another mechanism. Sidwell et al. (2002), also used the hydrogen mechanism proposed by Deutschmann et al. (1996) and Zhu (2001) to build on the methane mechanism by combining the two mechanisms with some modification and adjusting the kinetic parameters.

Among the multi-step surface mechanism discussed in Chapter 5, the one proposed by Deutschmann et al. (1994) for Pt based catalyst was the basis in this analysis, because this mechanism is simple, successfully applied, widely accepted and most proposed Pd mechanisms are based on it. This multi step mechanism was developed with kinetic and thermal data along with several assumptions, such as dissociative adsorption of oxygen and methane, perfect catalyst surface, monolayer coverage, etc. Table 5.1 shows this surface reaction mechanism.

The Deutschmann mechanism is comprised of adsorption of reactants and intermediate species, surface reaction and desorption of products and intermediates species. In total there are 22 elementary reactions and about 20 species.

In this work, the mechanistic models proposed in the literature were tested and compared to the results observed in the experimental study. Although the global model developed earlier in the chapter was felt to be sufficient for the main goal of the thesis (estimating the performance of the large scale reactor), there was the opportunity to compare the trends predicted by the mechanistic models.

7.2.2 Reactor model

The mechanistic model was used in conjunction with a single channel reactor model to investigate the trends in reactor performance. The single channel model was described in some detail earlier in the chapter, and the basic equations that govern it were given. For the work on the mechanistic model, a different simulation software from the one used in optimization study was used. When dealing with a large number of species, the development of an efficient simulator is a challenging task.

The tool adopted was a program developed by Mukadi and Hayes (2002). This software uses the finite volume method to solve the governing partial differential equations for the mole and energy balances. The solver uses the Newton-Krylov method with a GMRES preconditioner. Detailed surface chemistry is included via a "chemistry" module that computes source terms for all reactions. This module contains a database of thermodynamic and other properties such as diffusion coefficient, thermal conductivity, viscosity, etc. The steps in the reaction mechanism are defined by the user. This software was developed for Umicore AG and used with their permission.

The software can model the monolith channel in both 1D and 2D, and it can incorporate washcoat diffusion. Because of the lengthy execution time that resulted when either the 2D model or washcoat diffusion was included, the 1D model without diffusion in the washcoat was used. Although the development version of this software (as described in Mukadi and Hayes (2002)) allowed for execution on a parallel computer, the production version used here does not have this capability.

7.2.3 Performance of mechanism

Mechanistic models for methane combustion were discussed in detail in Chapter 5. For this investigation the Deutschmann mechanism (Deutschmann et al., 1994) was adopted as the basis. The complete Deutschmann mechanism is shown in Table 5.1. Contrary to other researchers who adopted this mechanism for Pd catalyst, in this work the reaction parameters will be used as proposed in the original mechanism. Only the value of activation energy for oxygen desorption was changed to allow the study of its effect on the reactor performance and response as will be discussed later in this chapter.

In the preliminary runs, the complete Deutschmann mechanism was tested, however it was found that when both competing oxygen adsorption steps were included, the temperature required for reaction to commence was extremely high. Furthermore, most literature does not support the competing oxygen adsorption steps on a Pd catalyst, thence reaction number 3 in Table 5.1 was eliminated.

Table 7.2: Elementary reaction mechanism schemes for catalytic methane combustion over Pd catalyst.

	Elementary reaction	A	S	Ea
Adsorption				
R1	$O_2 + 2Pd_{\cdot} \rightarrow 2O_{\cdot}Pd$		2.3×10^{-2}	
R2	$CH_4 + 2Pd_{\cdot} \rightarrow CH_3_{\cdot}Pd + H_{\cdot}Pd$		1.0×10^{-2}	
R3	$CO + Pd_{\cdot} \rightarrow CO_{\cdot}Pd$		8.4×10^{-1}	
R4	$H_2O + Pd_{\cdot} \rightarrow H_2O_{\cdot}Pd$		7.5×10^{-1}	
surface reaction				
R5	$CH_3_{\cdot}Pd + Pd_{\cdot} \rightarrow CH_2_{\cdot}Pd + H_{\cdot}Pd$	3.7×10^{21}		20
R6	$CH_2_{\cdot}Pd + Pd_{\cdot} \rightarrow CH_{\cdot}Pd + H_{\cdot}Pd$	3.7×10^{21}		20
R7	$CH_{\cdot}Pd + Pd_{\cdot} \rightarrow C_{\cdot}Pd + H_{\cdot}Pd$	3.7×10^{21}		20
R8	$H_{\cdot}Pd + O_{\cdot}Pd \rightleftharpoons OH_{\cdot}Pd + Pd_{\cdot}$	3.7×10^{21}		11.5
R9	$H_{\cdot}Pd + OH_{\cdot}Pd \rightleftharpoons H_2O_{\cdot}Pd + Pd_{\cdot}$	3.7×10^{21}		17.4
R10	$2OH_{\cdot}Pd \rightleftharpoons H_2O_{\cdot}Pd + O_{\cdot}Pd$	3.7×10^{21}		48.2
R11	$C_{\cdot}Pd + O_{\cdot}Pd \rightarrow CO_{\cdot}Pd + Pd_{\cdot}$	3.7×10^{21}		62.8
R12	$CO_{\cdot}Pd + Pd_{\cdot} \rightarrow C_{\cdot}Pd + O_{\cdot}Pd$	1.0×10^{18}		184
R13	$CO_{\cdot}Pd + O_{\cdot}Pd \rightarrow CO_2_{\cdot}Pd + Pd_{\cdot}$	3.7×10^{21}		105
Desorption				
R14	$2O_{\cdot}Pd \rightarrow O_2 + 2Pd_{\cdot}$	3.7×10^{21}		$213.2 - 60 \times \theta_{O_{\cdot}}$
R15	$CO_{\cdot}Pd \rightarrow CO + Pd_{\cdot}$	1.0×10^{-13}		125.5
R16	$H_2O_{\cdot}Pd \rightarrow H_2O + Pd_{\cdot}$	1.0×10^{13}		40.3
R17	$CO_2_{\cdot}Pd \rightarrow CO_2 + Pd_{\cdot}$	1.0×10^{13}		20.5

NB: In Table 7.2, A = reaction pre-exponential constant, unit in [mol,cm,s],

S = sticking coefficient, units in [-] and

E_a = activation energy, unit in [kJ mol⁻¹].

Because the reaction temperature was relatively low (below 1000 K) and the reaction is predominantly surface reaction, other simplifications were made, one was: omission of the homogeneous combustion steps, which are not important, as illustrated by Reinke et al. (2004) in their reduced Deutschmann mechanism. However, in this work none of surface reaction steps were combined as Reinke et al. (2004) did. The final mechanism used in this work has 17 species (which include 5 gaseous species and 12 surface species) and 17 reactions (which include 4 adsorption, 4 desorption and 9 surface reactions) as shown in Table 7.2.

(a) Model parameters: The many parameters in the mechanistic model are based on fundamental processes and in the first instance these were not modified. The main adjustable parameter in the model is the catalyst loading factor, a_{cat} . Loading factor, also known by others as specific surface area of the catalyst active sites, is a function of catalyst preparation. It is used in transforming the reaction rate unit into $\text{mole}_A/(\text{m}_{cat}^3 \cdot \text{s})$, this can be achieved either by the following equation:

$$-R_{CH_4} = a_{cat}(-R''_{CH_4}) \equiv \left[\frac{\text{mole}_A}{\text{m}_{cat}^3 \cdot \text{s}} \right] \quad (7.42)$$

or just by transforming the density of active sites, which is given as moles per surface area and is characteristic of a given catalyst to concentration of active sites as:

$$L_A = a_{cat}L_t \quad (7.43)$$

The effect of changing the catalyst loading over the range of $0.25 \text{ m}^2 \text{ m}^{-3}$ to $10.0 \text{ m}^2 \text{ m}^{-3}$ was first investigated. The inlet mole fraction of methane was 0.01 and the temperature ramp was 8 K per minute. Figure 7.23 shows how the activity increases as the catalyst loading increases. The rate of increase of activity is more pronounced at low loading values, and increasing the loading beyond $7.5 \text{ m}^2 \text{ m}^{-3}$ does not significantly improve the activity of the catalyst,

see Figure 7.23. The plot of inlet versus outlet temperature is shown in Figure 7.24.

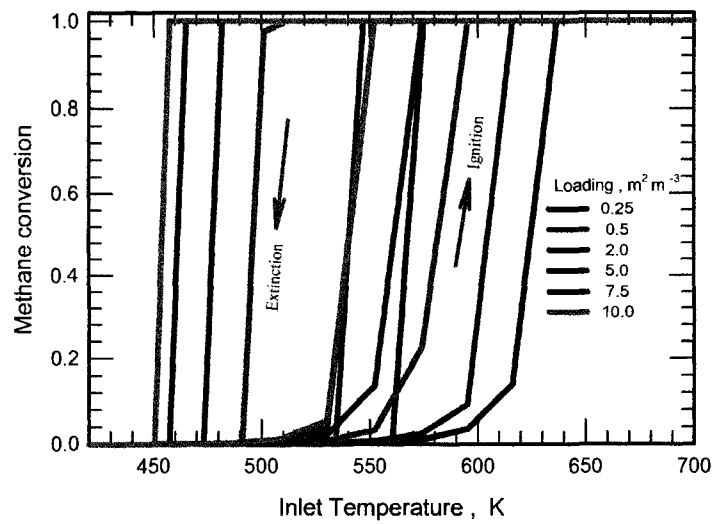


Figure 7.23: Effect of catalyst loading on methane conversion.

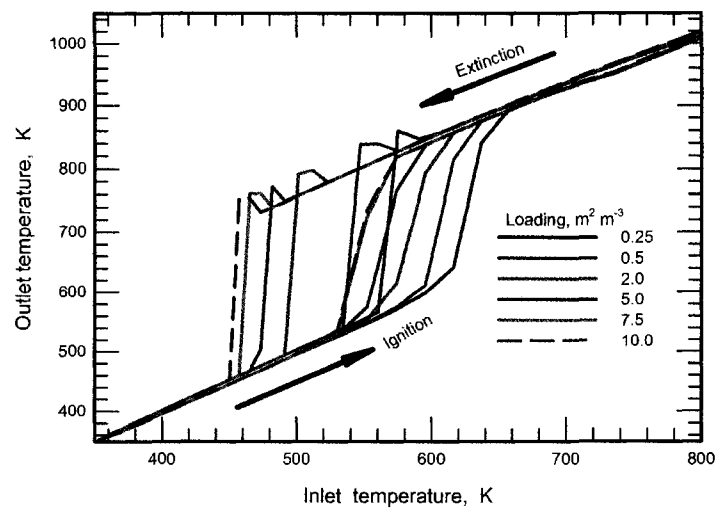


Figure 7.24: Effect of catalyst loading on reactor temperature.

Both temperature - conversion and inlet - outlet temperature plots exhibit hysteresis, as was seen in previous experimental and global modelling studies. Figure 7.23 and 7.24 shows that the hysteresis is more pronounced with high catalyst loading. The loading of $7.5 \text{ m}^2 \text{ m}^{-3}$ was used in further analysis.

- (b) Initial surface coverage: In studying the influence of initial coverage of catalyst surface by adsorbed species, the main interest was on oxygen coverage taking the fact that most researchers believe that the active state of Pd is PdO as well at ordinary conditions the surface of Pd catalyst exists as PdO, thus it is obvious that oxygen adsorption and desorption can be the main factor in controlling and initiating the surface reaction.

In this study, the initial coverage by oxygen was varied from zero to full coverage, while the value of inlet methane concentration and temperature ramping were the same as those used in studying the influence of catalyst loading. Figure 7.25 shows that initial oxygen coverage had no direct influence on the reaction performance. In that figure the curves of methane fractional conversion versus inlet temperature are all the same despite of the changing values of initial oxygen coverage. Figure 7.26 to 7.29 illustrate that immediately at start-up of the catalytic combustion process, the catalyst surface will be fully covered by adsorbed oxygen independent on initial surface coverage started with. In other words, the surface rapidly fills with oxygen regardless of the initial value. This mechanistic model observation confirms that initial surface coverage does not influence the surface catalytic reaction, but at the same time it contradicts the experimental observation that the reduced catalyst was observed to be more active. Clearly the experimental rate of surface oxidation is slower than predicted by the mechanism. Figure 7.30 superimposes surface coverage variation and methane conversion as function of inlet temperature, and shows that the surface reaction starts as soon as the adsorbed oxygen begins to desorb from the catalyst surface. The extinction occurred as the surface becomes recovered by adsorbed oxygen. This observation suggests that for surface reaction to occur, a co-existence of

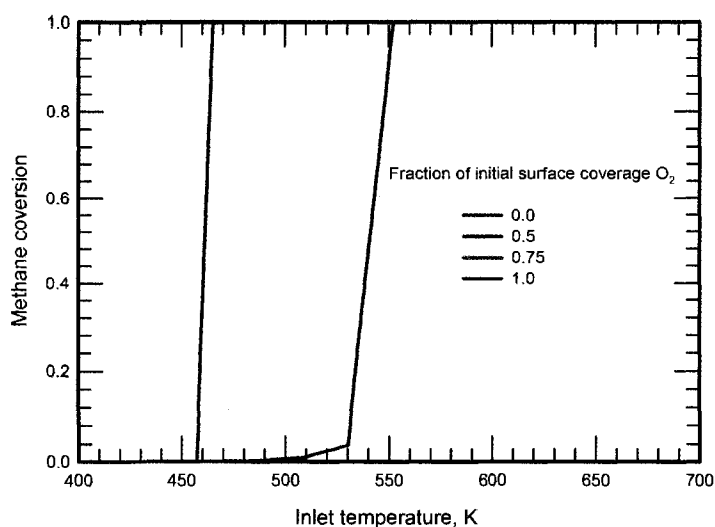


Figure 7.25: Effect of initial catalyst coverage on methane conversion.

adsorbed oxygen species with a vacant active site is necessary. Also, it has been observed that the start of surface reaction depends on the activation energy of the oxygen desorption process. If the activation energy is high, the reaction will start at very high temperature and as the value decreases the starting temperature also decreases, as will be discussed later.

Another important observation, based on the mechanistic model used, is that at any time, the catalytic surface is mainly covered by adsorbed oxygen or by adsorbed oxygen and vacant active sites, as shown in figure 7.26 to 7.29 as well as Figure 7.31 to 7.33, which show the concentration of other surface species. This observation means that other involved elementary reactions are faster than oxygen desorption, and thus oxygen desorption is the main factor controlling the catalytic reaction. Most of other surface species, like $\text{CH}_x\text{-Pd}$, $\text{CO}_2\text{-Pd}$ and OH-Pd , have surface coverage less than 1×10^{-5} which is negligible compared to surface coverage of O-Pd and Pd_\cdot (vacancy sites) at any time.

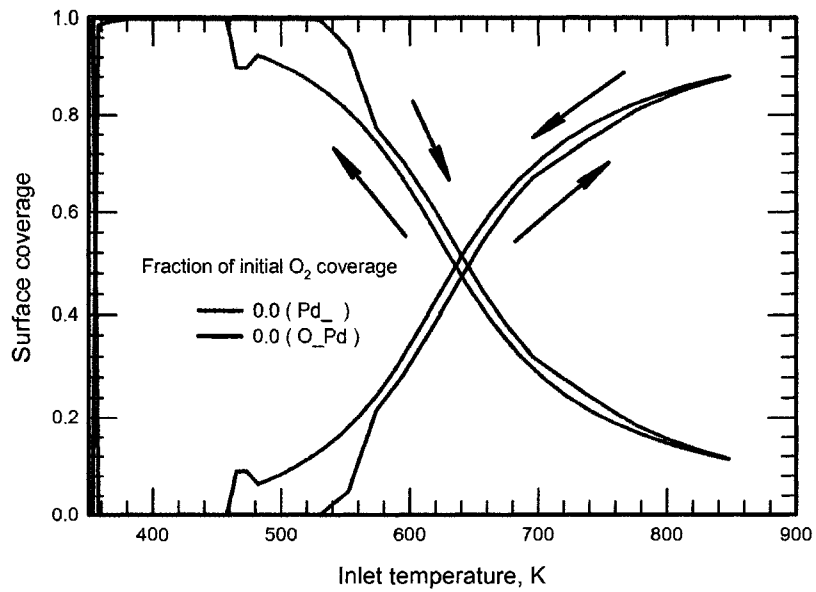


Figure 7.26: Variation of surface coverage with temperature. Initial oxygen fractional coverage was zero.

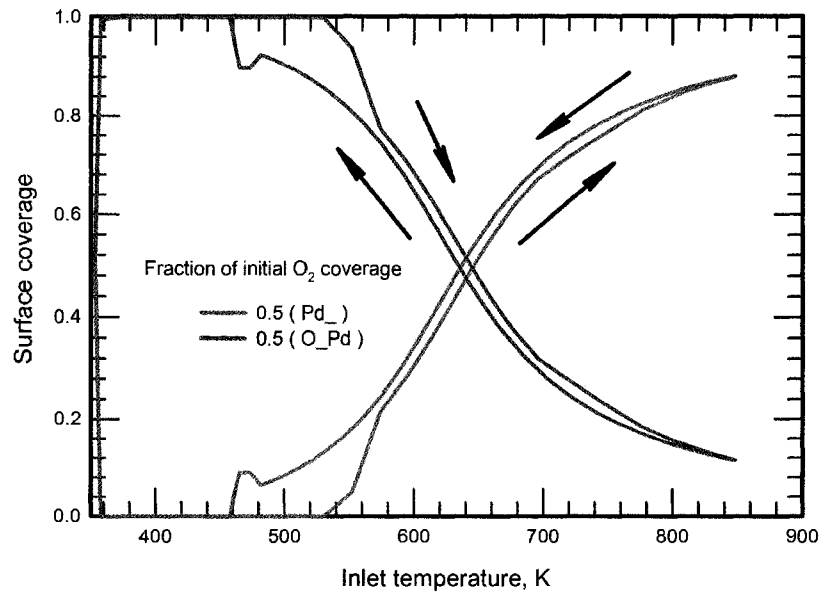


Figure 7.27: Variation of surface coverage with temperature. Initial oxygen fractional coverage was 0.5.

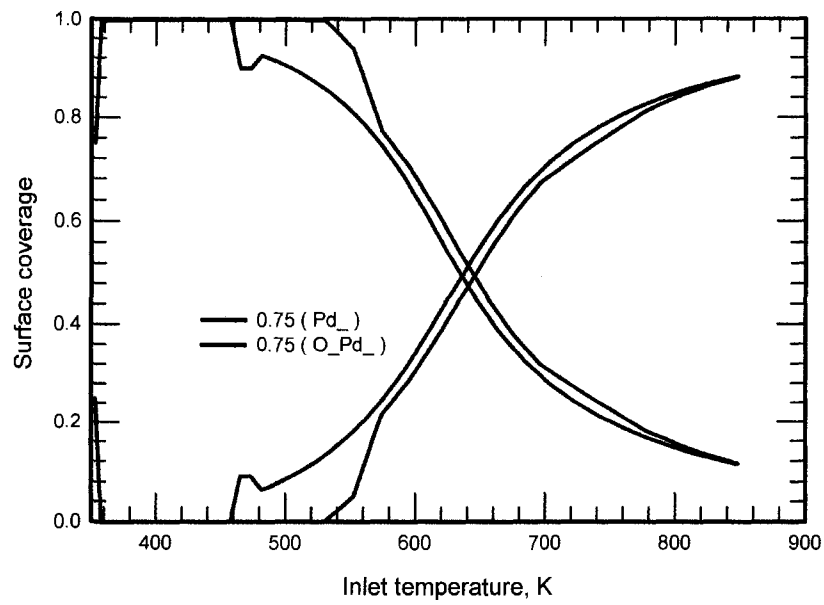


Figure 7.28: Variation of surface coverage with temperature. Initial oxygen fractional coverage was 0.75.

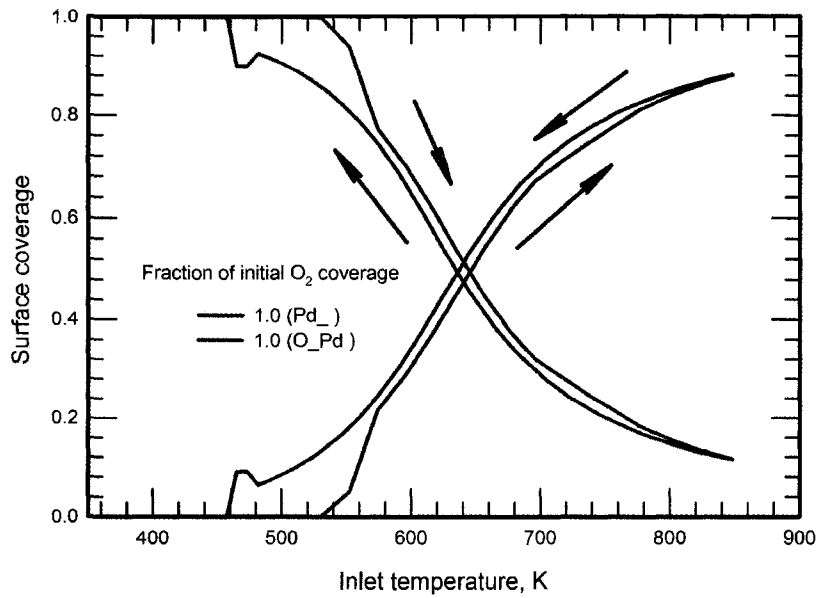


Figure 7.29: Variation of surface coverage with temperature. Initial oxygen fractional coverage was 1.0.

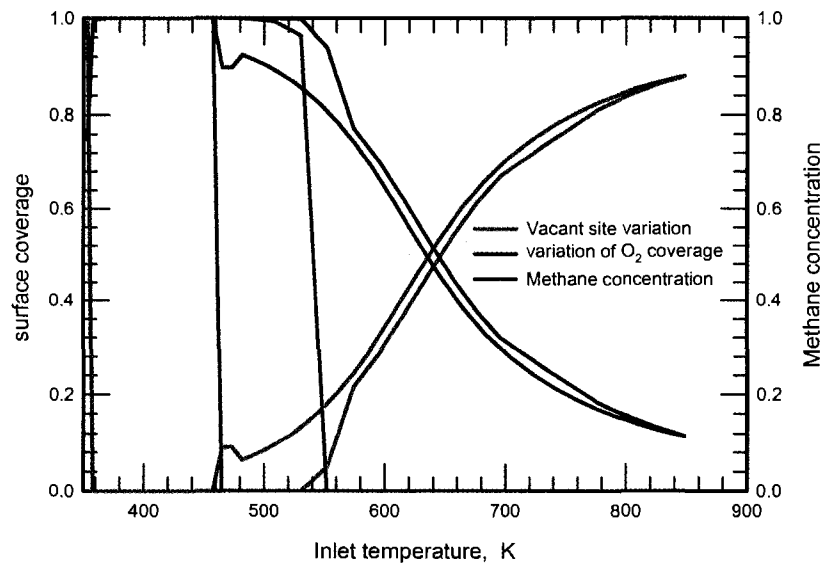


Figure 7.30: Variation of surface coverage and methane concentration with time.

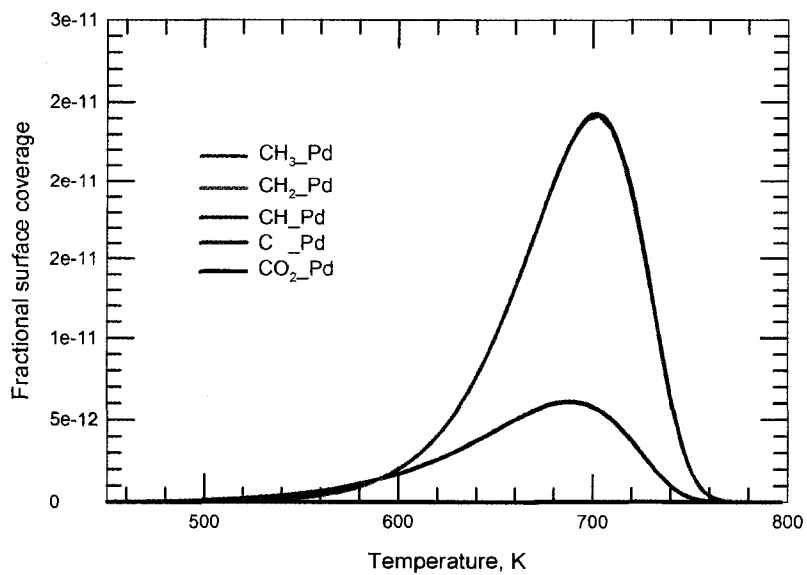


Figure 7.31: Close look of effect of initial surface coverage

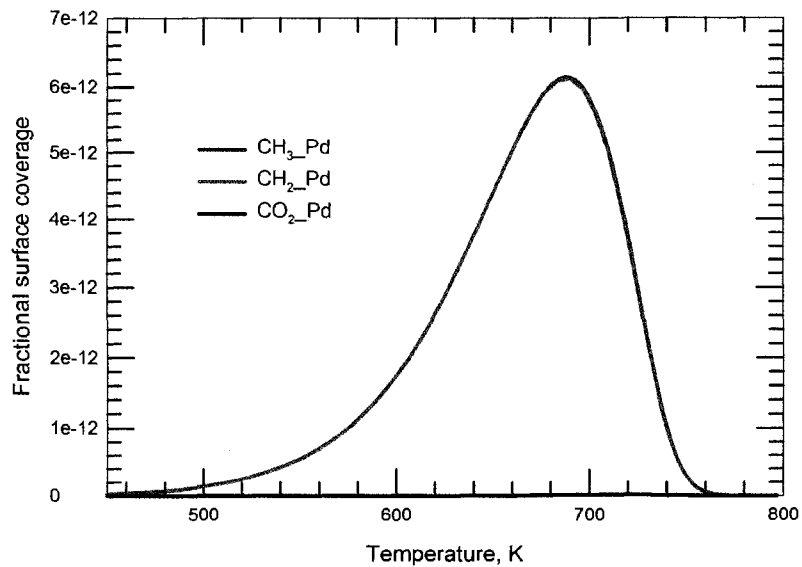


Figure 7.32: Close look of effect of initial surface coverage

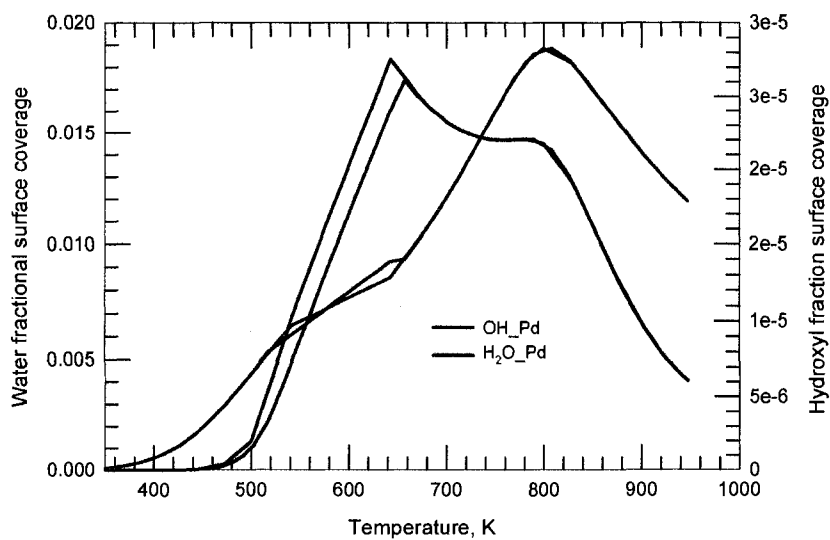


Figure 7.33: Close look of effect of initial surface coverage

- (c) **Effect of Oxygen desorption:** From the result of study of the influence of initial surface coverage, it has been shown that oxygen desorption process is the key element in driving the reaction. The catalyst surface is always rapidly covered by adsorbed oxygen, and it has been seen that methane conversion begins when the desorption of adsorbed oxygen begins. Thus the parameters of oxygen desorption are the major factor in controlling the reaction, and one of the major parameters is the activation energy. In this section the effect of changing the value of activation energy for oxygen desorption process is analysed.

When the activation energy of oxygen desorption was changed, the reaction starting temperature also changed. If the activation energy is low, the reaction starts at a lower temperature, see Figure 7.35. Higher activation energy initiates the reaction at higher temperature and that results in negligible methane conversion with the chosen working temperature range (i.e. temperature less than 1000 K), see Figure 7.34.

Overall, the adsorption - desorption of oxygen on a Pd catalyst surface seems to control the reaction, as observed in Figure 7.30. The reaction starts only when the desorption of adsorbed oxygen starts and the complete extinction occurs when the surface is again full covered by adsorbed oxygen. This means that with lower activation energy of oxygen desorption, the oxygen adsorption - desorption process on the catalyst surface can occur at lower temperature as shown in Figure 7.35. In the same Figure 7.35, it can be observed that the hysteresis effects became more visible as the activation energy decreased.

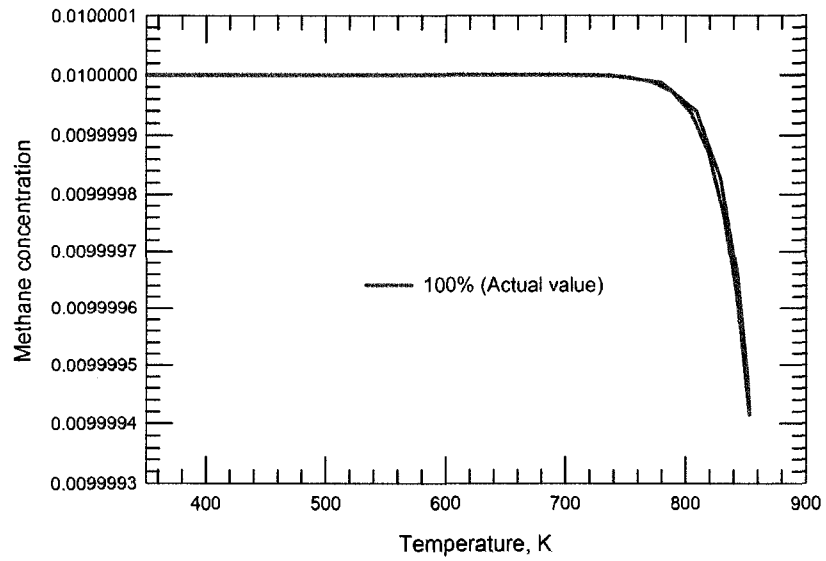


Figure 7.34: Oxygen desorption effect on methane conversion at actual value of activation energy.

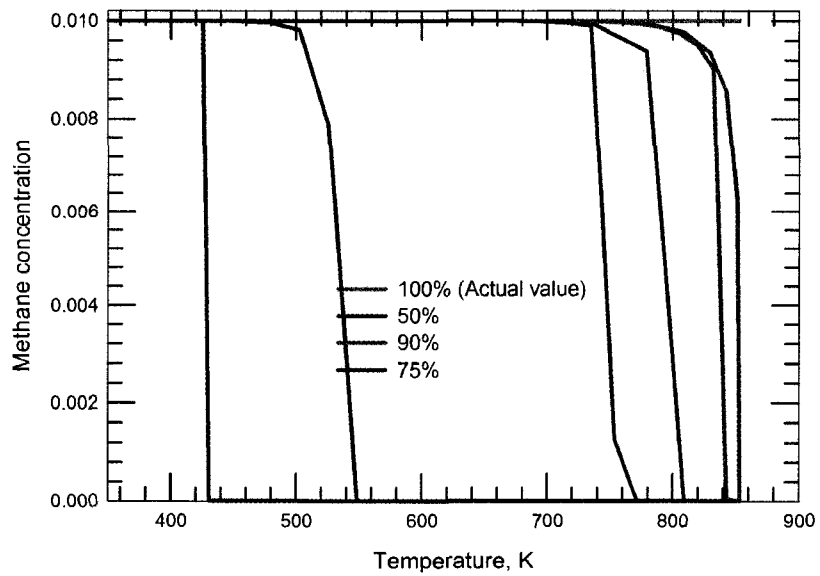


Figure 7.35: Effect of oxygen desorption by varying its activation energy.

7.2.4 Effect trends comparison

Based on the experimental results, it was concluded that methane, water and carbon dioxide inhibit the reaction. In this section the mechanistic model is used to examine the effect of methane, water and carbon dioxide on the ignition - extinction curves, the results were compared to the global model results. As observed earlier, the mechanistic model pretreated and unpretreated cases can not be differentiated, as the initial coverage showed no influence to reaction, thus the analysis was limited to unpretreated cases.

(i) Methane inlet concentration :

Figure 7.36 shows the ignition curves obtained from the mechanistic model for varying methane inlet concentration, while Figure 7.37 displays the extinction curves of the same study. From both ignition and extinction curves, it can be observed that the ignition points decrease with increasing methane inlet concentration, which is contrary to experimental observation. Figure 7.38 shows ignition - extinction curves for 500, 2000 and 9000 ppm methane inlet concentration to illustrate the same trend observed above.

Figure 7.39, 7.40 and 7.41 are temperature ignition - extinction and ignition-extinction curves respectively obtained from the mechanistic model, and show the same trend of increasing methane inlet concentration. The hysteresis behaviour is observed in this mechanistic model, but at low methane inlet concentration the hysteresis is almost negligible as show in Figure 7.42. Figure 7.43 shows that as methane inlet concentration increases the hysteresis effect is more visible. This can be explained as the effect of heat of reaction released once the mixture is ignited. The high concentration will release more thermal energy than low concentration mixture, and thus cause the difference in temperature rise.

Figures 7.41 to 7.43 show that as methane inlet concentration increases, the extinction curve needs much more cooler temperature to complete the process.

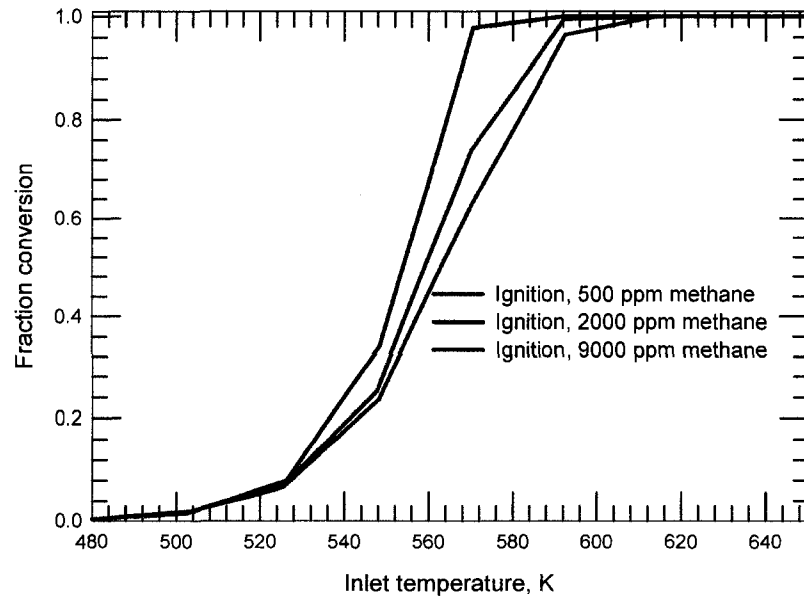


Figure 7.36: Ignition curves comparing the effect of methane initial concentration.

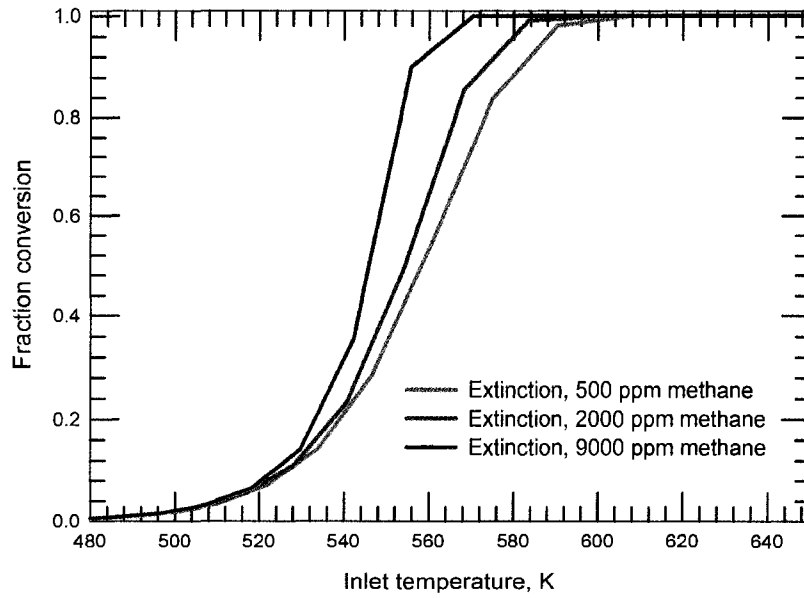


Figure 7.37: Extinction curves comparing the

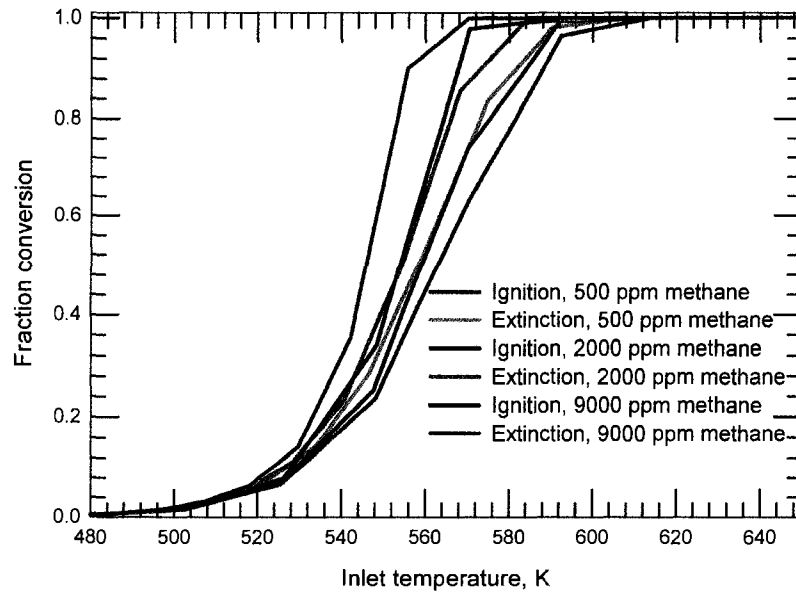


Figure 7.38: Ignition-extinction curves comparing the effect of methane initial concentration.

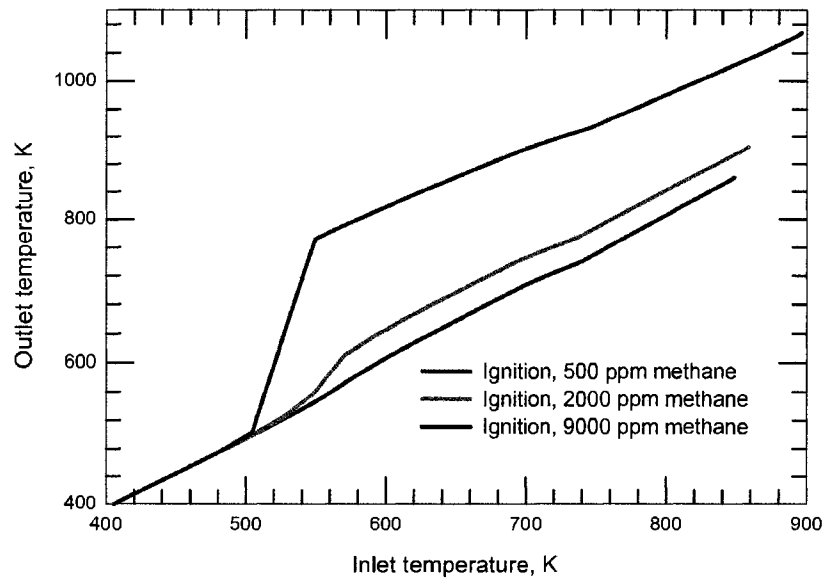


Figure 7.39: Temperature ignition curve comparing the effect of methane initial concentration.

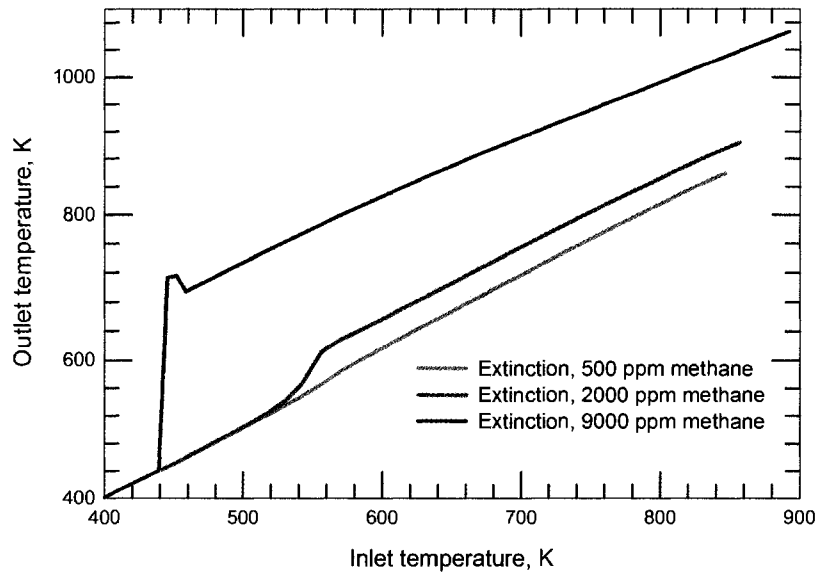


Figure 7.40: temperature extinction curves comparing the effect of methane initial concentration.

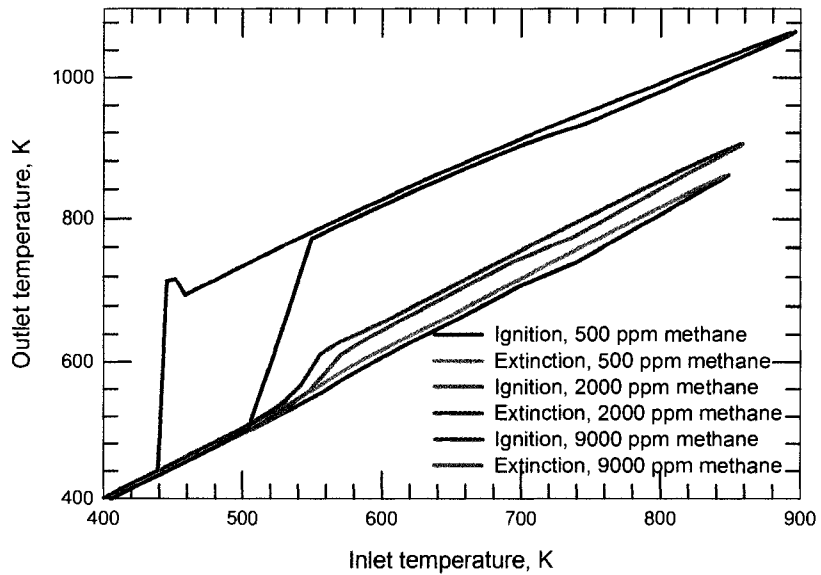


Figure 7.41: Temperature ignition-extinction curves comparing the effect of methane initial concentration.

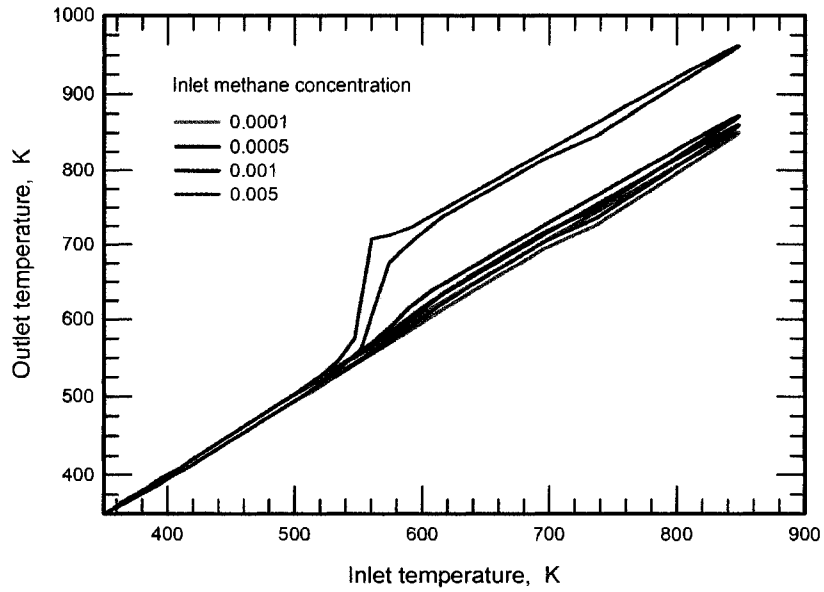


Figure 7.42: Ignition -extinction curves showing the effect of low methane initial concentration.

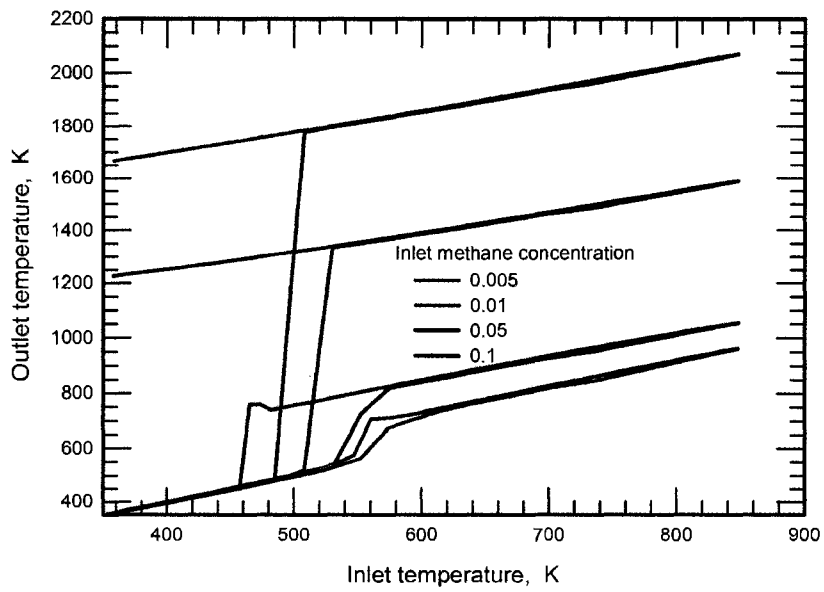


Figure 7.43: Ignition - extinction curves showing the effect of higher methane initial concentration.

(ii) Oxygen concentration :

In previous observation, using the mechanistic model, it was shown that oxygen desorption is important step for surface catalytic reaction to occur. Here, the effect of inlet oxygen concentration was examined and the results are shown in Figures 7.44 to 7.46. Figures 7.44 and 7.45 compare the ignition and extinction curves respectively for oxygen inlet concentration of 6% and 20%. From these figures, it can be observed that increasing oxygen concentration inhibits the reaction. The ignition - extinction curves in Figure 7.46 illustrate the same inhibition effect. This observation is contrary to experimental results where the main effect of oxygen concentration was to offset the influence of pretreatment.

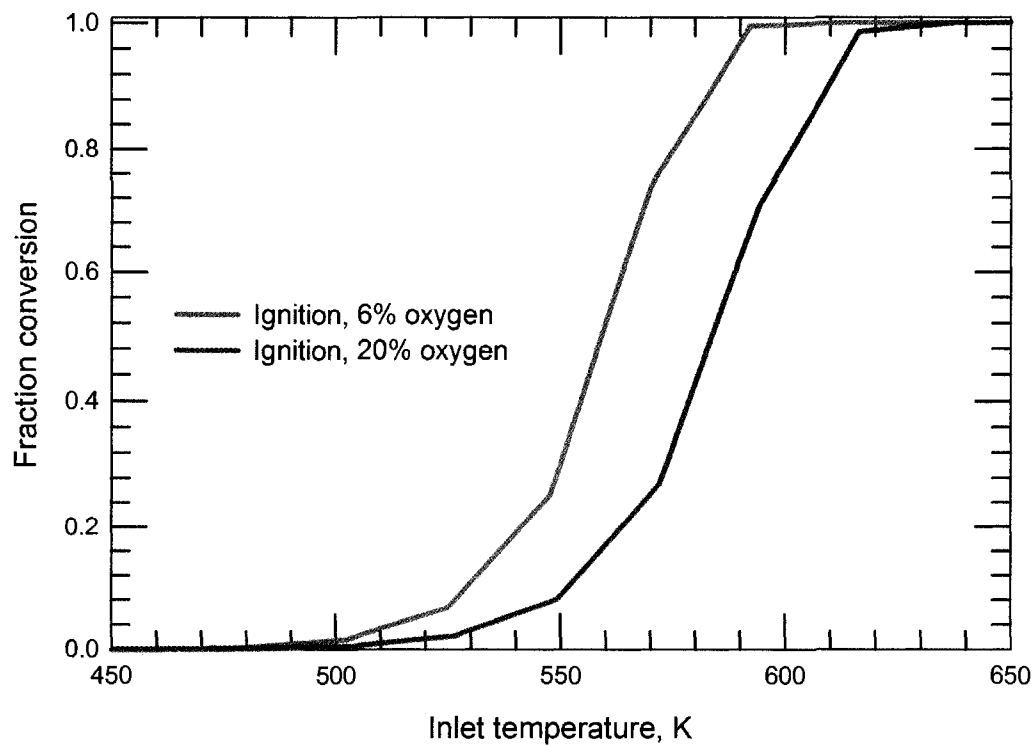


Figure 7.44: Ignition curves comparing the effect of oxygen concentration.

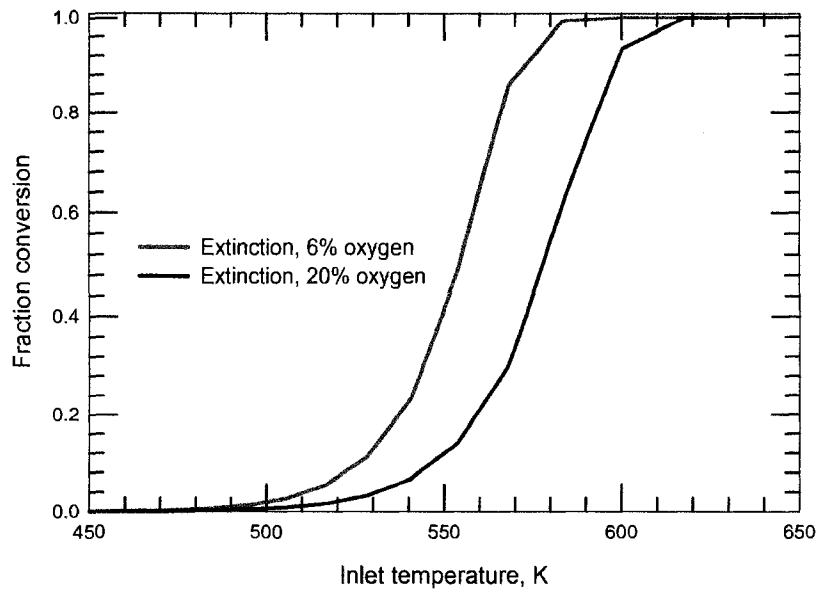


Figure 7.45: Extinction curves comparing the effect of oxygen concentration.

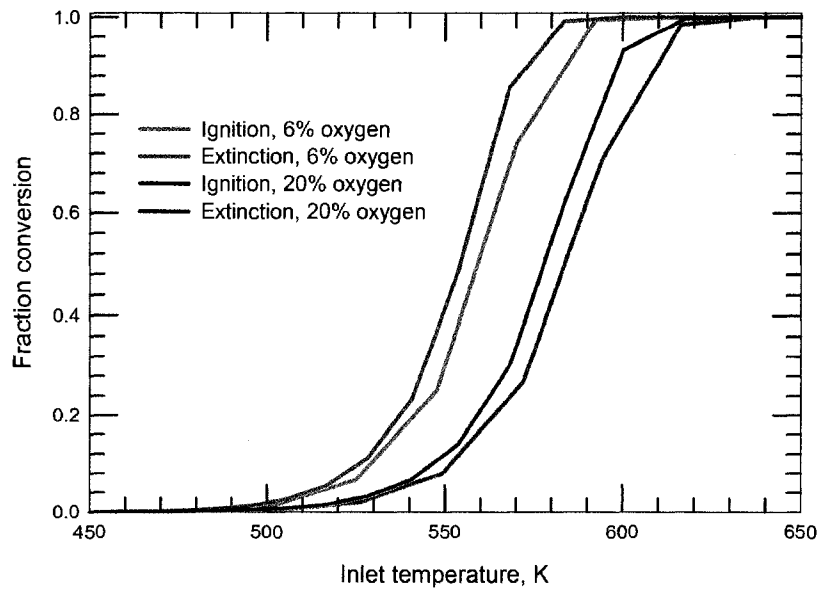


Figure 7.46: Ignition - extinction curves comparing the effect of oxygen concentration.

(iii) Water presence: Contrary to experimental observations, by using mechanistic model, the presence of water has no effect on the catalytic reaction for methane combustion as shown in Figure 7.47. Varying initial concentration of water in the feed stream has shown to exhibit the same activity in ignition and extinction periods.

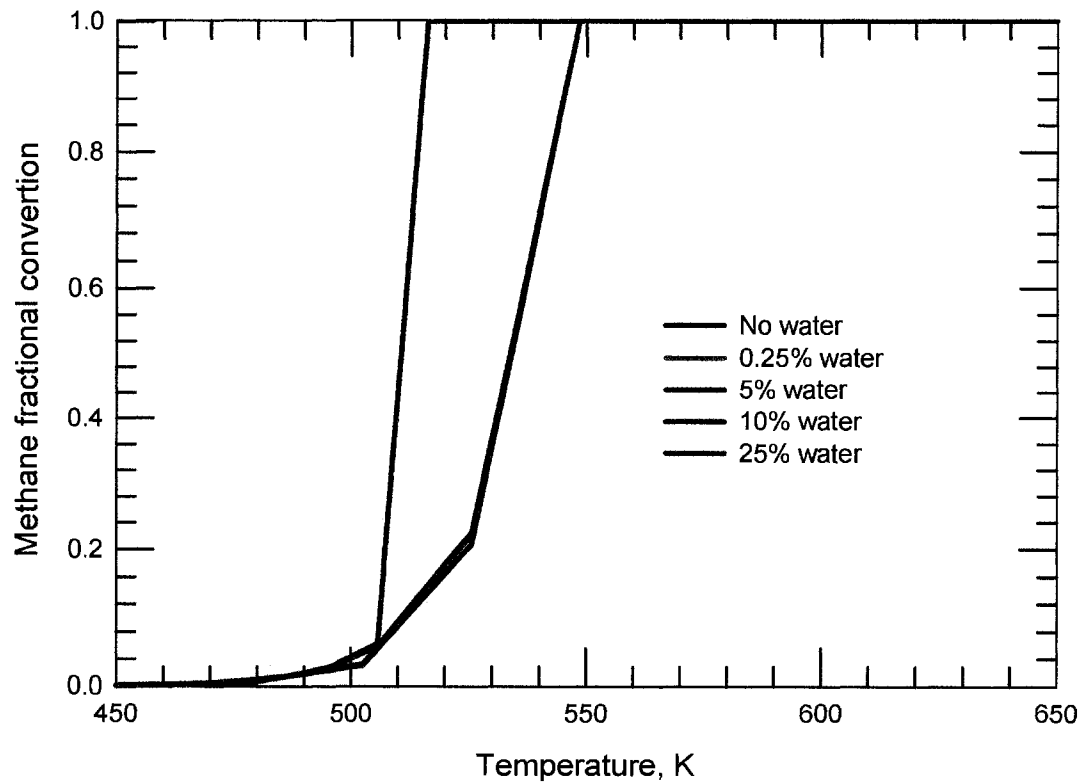


Figure 7.47: Ignition - extinction curves comparing the effect of water in the feed.

(iv) Carbon dioxide presence :

Figure 7.48 shows that by using the mechanistic model, the presence of carbon dioxide generally has no effect on the catalytic combustion of methane. Streams with varying concentration of carbon dioxide resulting essentially a similar performance particular during ignition period. During the extinction period, streams with more carbon dioxide observed to be slightly faster, see Figure 7.48.

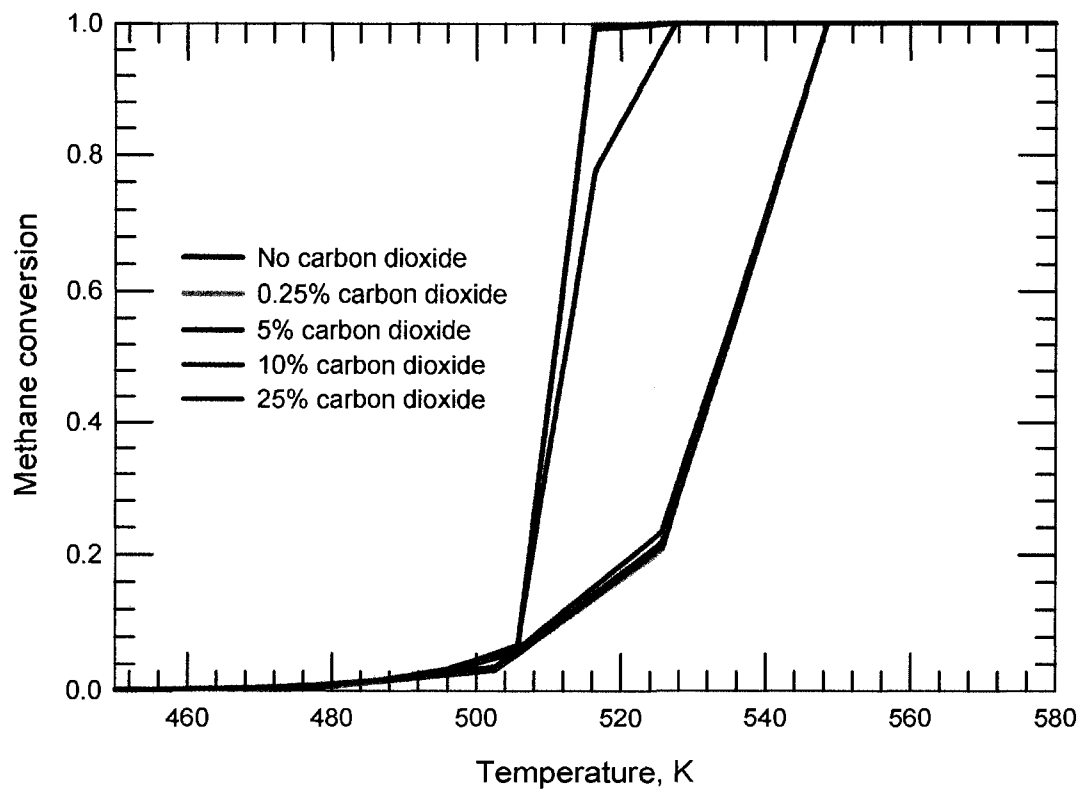


Figure 7.48: Ignition - extinction curves comparing the effect of carbon dioxide presence.

7.3 Concluding remarks

Current catalytic combustion research focuses on reactor design, to increase efficiency and productivity of the operation, for the given suitable catalyst in use. This notion stresses the need of better and clearer understanding of the physical and chemical processes occurring on the catalytic surface and their coupling to the flowing fluid.

For the data obtained on the experimental monolith, an empirical model based on the classical LHHW form was found to fit the data very well. It is felt that this model is sufficient for preliminary design purposes, and is used in Chapter 9 to explore the development of a new catalytic reverse flow reactor configuration.

Observations made experimentally, such as self inhibition by methane, and inhibition by carbon dioxide are at variance with many published models, however, this likely serves to emphasize the complexity of the palladium catalyzed combustion of methane.

The mechanistic model, based on the reduced Deutschmann scheme for platinum, is in general not able to capture the experimental observations. In particular, the ignition is enhanced by increasing methane concentration and inhibited by oxygen. These trends reflect the fact that the rate determining step in the Deutschmann mechanism is the desorption of oxygen from the surface. Furthermore, carbon dioxide and water do not show reaction inhibition effects. Although it might have been possible to develop a multi-step rate model, it was not felt that the data available justified the exercise. In conclusion, it seems what is happening on the Pd surface is more complex compared to what is happening on the Pt surface and thus the kinetics evaluated from Pt surfaces can not simply satisfy the mechanism on a Pd surface. There is clearly much work of fundamental interest that can be carried out in the palladium catalyzed methane combustion.

Catalytic flow reversal reactor: Background and model development

In Chapter 4 the capture of fugitive methane emissions from the natural gas compressor station was studied. It was demonstrated that based on typical emission levels, a stream containing about 0.2 to 1 % methane in air could be captured. In Chapters 5 to 7 the catalytic combustion of methane was discussed, and experimental and modelling results were presented. In this chapter the catalytic flow reversal reactor (CFRR) is presented, as a candidate for the combustion of the lean methane stream from the compressor building. This reactor has been shown to be effective for lean methane combustion in other situations, such as in coal mine vent gas.

8.1 Introduction

There are many reactor designs used in practice, including fixed and fluidized beds. Fixed bed reactors are the workhorse of the chemical process industries, especially for gas phase reactions, with the two most commonly used configurations being wall-cooled tubular fixed beds and adiabatic fixed beds. The former are used in many oxidation and hydrogenation reactions, and an example application of the latter is sulfuric acid production. They have also been used for the thermal com-

bustion of traces of VOC in tail gas. Traditionally, packed bed reactors operate at steady state and the key issues of interest, such as gas flow patterns, wall heat transfer coefficient, radial and axial effective bed conductivities, as well as inter-phase heat and mass transfer have been extensively studied. Steady-state operation offers simpler design and operation, including easier control. Such reactors typically operate over a narrow range of operating conditions. Over the last several years, there have been many papers published that discuss the advantages of operating in a forced unsteady manner, with benefits to conversion and selectivity being reported. There are different means by which unsteady operation can be forced, such as feed concentration cycling, or forced flowrate variations. One design, which is the focus of this investigation, is the catalytic flow reversal reactor (CFRR). In this mode of operation, the feed stream is periodically switched between the two ends of the reactor. A diagram of the reverse flow reactor is shown in Figure 8.1. In Figure 8.1 (a) the valves 1 and 4 are open and the feed flows to the reactor from left to right (forward flow). In Figure 8.1 (b) valves 2 and 3 are open and the feed flows to the reactor from right to left (reverse flow). The cycle time is the term given to the length of both the forward and reverse flow cycles. The partial cycle time or switch time (forward or reverse flow) may be the same (symmetric operation) or different (un-symmetric operation).

8.2 Heat trapping in a reverse flow reactor

The operating characteristic exhibited by a CFRR that can be successfully exploited for lean methane combustion is the so-called heat trap effect. This effect is observed in a CFRR for an exothermic reaction. Ideally, the operation of a fixed bed reactor for the destruction of methane should operate in the auto-thermal region. This region occurs when the thermal energy liberated in the reaction is sufficient to sustain the catalytic combustion at the given inlet reactor temperature. However, for low temperature feed (around room temperature) with a low concentration of methane, auto-thermal operation cannot be maintained for a standard uni-directional flow operation. Therefore, for this type of operation, the choice is either to pre-heat

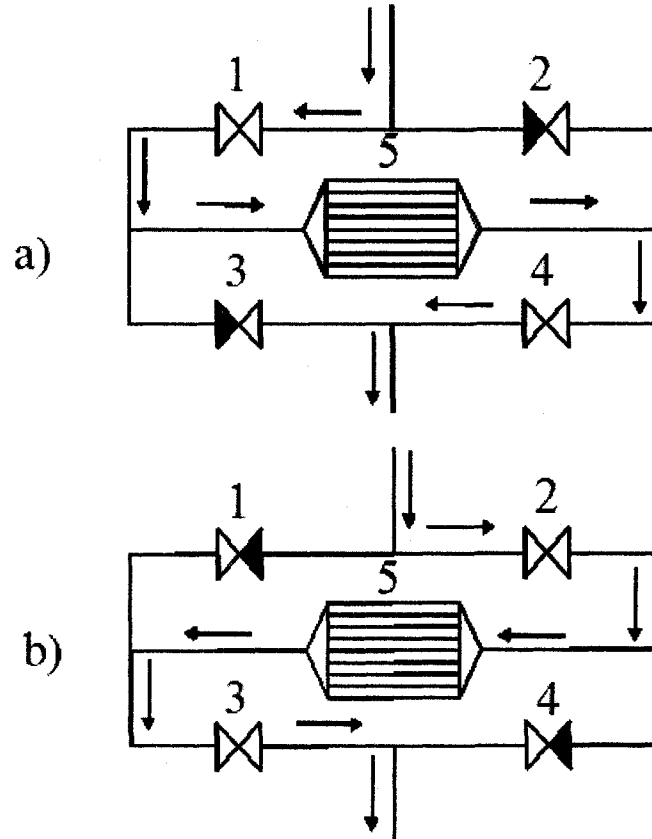


Figure 8.1: Typical arrangement for a CFRR in (a)forward flow and (b)reverse flow reactor mode(from Hayes(2004)).

the feed, add thermal energy to the bed or add additional fuel. However, with reverse flow operation, the heat trap effect can be used to maintain a high reactor temperature at low feed temperature and concentration. Figure 8.2 shows how the heat trap can develop in a reactor under reverse flow operation.

Figure 8.2 (a) illustrates a reactor temperature profile that might be observed with uni-directional flow operation for a combustion reaction under auto-thermal operation. This type of steady state could occur if, for example the feed was hot. Moving downstream in the reactor, it is seen that the temperature initially rises slowly as the reaction commences, and then more sharply as the heat liberated in the reaction accelerates the rate owing to the exponential temperature dependence

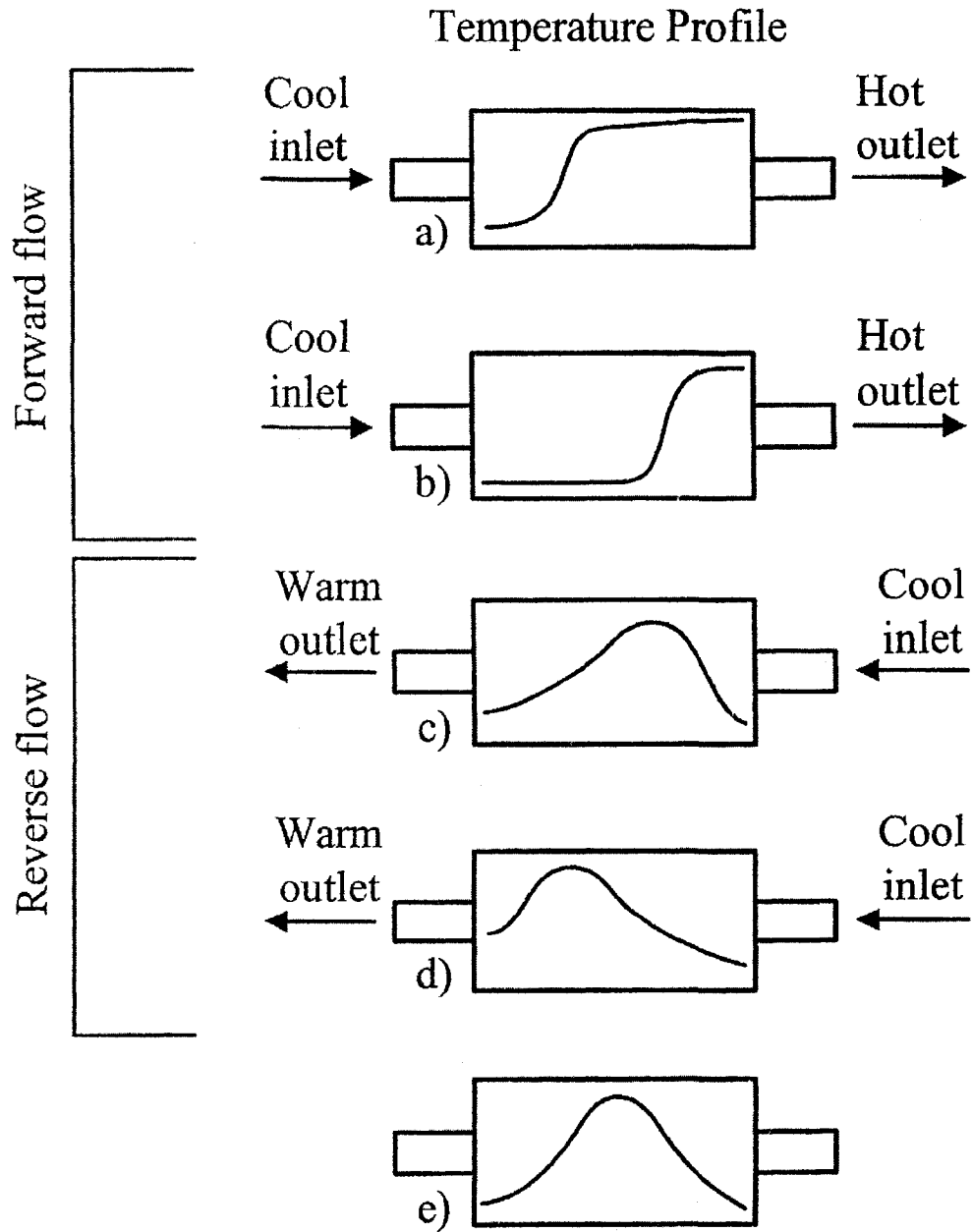


Figure 8.2: Illustration of heat trap effect in the reverse flow reactor (from Hayes(2004)).

of the rate constant. Downstream of this ignition front the temperature of the reactor will be essentially constant as the reactants are all depleted. If the reactor feed temperature were now lowered, then what would be observed is a reduction in reaction rate, and the reaction front would propagate downstream. If the feed temperature is sufficiently low, the reaction front will exit the reactor and the reaction will effectively be extinguished. However, consider the effect of switching the feed position to the other end of the reactor while the hot zone remains inside of the reactor. The incoming cold feed will be pre-heated by the energy stored in the catalyst bed, and the reaction can be maintained. The reaction profile will now move back towards the former entrance. Periodic switching will now trap the reaction zone within the reactor, and a stationary state will eventually develop, in which a hot zone oscillates back and forth between the two ends of the reactor. Because the stored energy is added to the feed stream, it is possible to achieve temperatures higher than the adiabatic temperature rise based on the fresh feed inlet temperature. Provided that the reactor is initially at a sufficiently high temperature (which may require some auxiliary heat source) and the cycle duration is carefully chosen, it is possible to achieve auto-thermal reactor operation at feed temperatures well below those required for auto-thermal operation with unidirectional flow. A reverse flow operation in which the solid phase temperature rise was as high as 13 times the adiabatic temperature rise has been reported (Hanamura et al., 1993).

8.3 Literature review of reverse flow reactors

The reverse flow reactor concept has been shown to be an effective technique for pollutant removal and has recently received attention in the literature (see for example, Hayes (2004)). It has been subjected to detailed numerical and experimental investigation. The first use of reverse flow was reported by Cottrell (1938), who observed that periodically switching the gas flow direction through a fixed bed traps heat in the centre of the bed. The extension to fixed bed reactors first appears in the literature in 1955 (Frank-Kamenetski, 1955). A detailed review of applications and studies of reverse flow reactor has been presented by Matros

and Bunimovich (1996).

Significant applications include the oxidation of SO_2 (Boreskov et al., 1982; Matros, 1989; Bunivovich et al., 1990; Boreskov and Matros, 1983; Boreskov and Matros, 1984), methanol synthesis (Vanden Bussche et al., 1993; Matros, 1989; Neophytides and Froment, 1992), NO_x reduction (Guit, 1993; Snyder and Subramaniam, 1998; Bobrova et al., 1988; Noskov et al., 1993), production of syngas (Blanks et al., 1990), ethylbenzene dehydration into styrene (Kolios and Eigenberger, 1999) and oxidation of carbon monoxide (Nieken et al., 1994; Purwono et al., 1994).

Many papers discuss the use of reverse flow in catalytic combustion, see, for example, Boreskov and Matros (1984), Eigenberger and Nieken, (1988), Matros et al. (1993), Sapundzhiev et al. (1993); van de Beld et al. (1994); Grozev and Sapundzhiev (1997) ; and Purwono et al. (1994), Salomons et al., (2003), and Kushwaha et al., (2004). The application to natural gas engine exhaust has also been reported by Strots et al. (1998); Matros et al. (1999); Liu et al. (2000; 2001b) , Liu et al. (2001c) and Liu et al. (2001a).

Recent investigations of reverse flow reactors focus more on the dynamics of the reaction, reactor stability, catalyst activity and catalyst selection as well as parametric studies. These studies have extended the usability of the reverse flow reactor in industrial applications and better understanding of the behavior of the reverse flow reactor, which may lead to new CFRR applications. Some of the significant studies are mentioned in the following Ferreira et al. (1996) and (1999) who used three different transient reactor models to study the effect of intra particle convection on the transient behavior of fixed bed reactors. The models which they used are the 1-D, heterogeneous, intra particle diffusion/convection model; the 1-D, heterogeneous, intra particle diffusion model; and the pseudo-homogeneous model. Their results show that the intra particle convective flow model allows higher reactant conversion with a higher hot spot temperature compared to the other two models. It is also interesting to note that the concentration waves that traverse through the reactor bed are delayed due to the additional reactant penetration that arises inside the solid catalyst by convection. Groote and Froment (1996) performed a number of simulations to investigate the feasibility of producing synthesis gas by partial

oxidation of natural gas on a Ni-catalyst in a fixed bed reactor with reversed flow, used the numerical model of one-dimensional unsteady state heterogeneous reactor with internal diffusional limitations. Based on their results, high selectivity and conversion can be obtained by using CFRR. These results imply that the production of synthesis gas by partial oxidation with air in a CFRR is feasible. The influence of several reactor operating conditions, such as interstitial velocity and reactor length, on the reactor performance was also studied. Their results showed that by decreasing the interstitial velocity, a lower maximum peak temperature in the catalyst bed can be observed, which is favorable from a controllability standpoint of view. The results also imply that longer half-cycle duration reduces the effect of the perturbations occurring upon the flow reversal. In addition, the influence of the reactor length mainly implies the influence of the duration of half-cycle. It is surprising to notice that the difference in reactor length only reflects in the reactants conversion, however, the selectivity of the products is practically unchanged.

Many studies of CFRR for complete lean methane combustion were carried out world wide. Eigenberger and Nieken (1988) discussed the influence of operating parameters on temperature profiles and stability of the CFRR operation. They demonstrated that an inert section determines the efficiency of hot gas withdraw from the system. Matros et al. (1999) showed that for treatment of exhaust from a natural gas fueled diesel engine using CFRR for oxidation of methane, the insufficient catalyst activity can be compensated by higher catalyst temperature and thus only thermal stability of the catalyst will determine the efficiency of methane oxidation in the system. Then, Aubé and Sapundjiev (2000) developed a transient two dimensional model for CFRR, which can be used for design of CFRR as well as in parametric studies. The model was validated by experimental data of lean methane mixture oxidation. Also, this model proved to be accurate in determining the dynamic behaviour of CFRR with small reactor diameter and low flow-rate with or without heat withdrawal. Salomons et al. (2003) through their experiments showed that CFRR is capable to destruct lean methane mixture in air of concentration as low as 0.19% by volume. Also, they showed that parameters (like space velocity, cycle time, feed concentration, inert section) govern the stability

of the reactor operation as well as determine the amount of energy to be trapped in the reactor. Kushwaha et al.(2004) carried out a parametric study on CFRR, using three different type of materials for inert sections. The results showed that the use of monolith inert sections reduces the pressure drops. Inert sections with lower thermal capacity gave a greater temperature front movement which will demand shorter cycles. Sheintuh (2005) showed that the main parameters that determines the maximum temperature in CFRR configuration are thermodynamic parameters, heat loss through reactor walls, conductivity and length of the inert sections. Later Marin et al. (2005) compared the performance of CFRR, when the catalyst section is either occupied by packed bed or monolith, in both cases the active catalyst was palladium supported on alumina. Using numerical analysis, they showed that for combustion of lean methane mixture in air, a packed bed gives stable operation at low velocity. As velocity increased the difference between packed bed and monolith become negligible, also packed bed always results in higher pressure drop compared to monolith catalyst. Hevia et al. (2007) concluded that noble metal catalysts are more suitable for leaner and stable mixture with constant concentration, while metal oxides catalyst should be used for richer mixture and can accommodate concentration variation to some extent. They also suggested that with enhancement of thermal stability, noble metal catalysts may increase the working window and thus further improve the CFRR performance.

8.4 Reverse flow reactor configurations

A number of catalytic reverse reactor configurations have been proposed. Figure 8.3 shows some of them. As discussed, CFRR are designed to trap the reaction thermal energy within the reactor. The temperature rise can be very dramatic, exceeding by far the adiabatic temperature rise. Although this is beneficial for achieving complete combustion, at the same time care must be taken to avoid excessive accumulation of heat energy, which can lead to excessively high temperatures that will damage the catalyst or the reactor walls. To avoid thermal runaway and to enhance the storage of energy in the reactor, inert sections are often included in

addition to the active catalyst. For example, in Figure 8.3 (a) the reactor is shown with a single catalyst bed, which will be responsible for all storage and reaction. Figure 8.3 (b) shows a three bed system where a bed without a catalyst is added on either side of the active catalyst. The two inert beds, in which no reaction occurs, are known as recuperators. The inert sections can have the same or different thermal properties as the catalytic beds. The inert sections also reduce thermal leakage from the system and may extend the catalyst life. Furthermore, inerts add thermal mass to the system and potentially reduce the need for expensive catalyst.

Because of the possibility of excessively high temperatures being achieved in the catalyst, it may be desired to remove excess thermal energy from the bed. Energy removal can be accomplished either by passing the hot effluent gases through external coolers (heat exchange) or withdrawing some mass of hot gases. Typically this heat exchange or mass removal would occur in the centre of the reactor, where the temperature will be high. For example, Figure 8.3 (c) shows a two bed system. For energy removal, typically a heat exchanger would be placed between the two beds, or hot gas extracted from this position. For energy extraction from a CFRR, Kushwaha et al. (2005) observed that the extraction of energy from the system by removal of hot gases from the centre is more efficient than using an heat exchanger, because it can maintain high conversion as well as avoid asymmetric temperature profiles as observed when the heat exchanger is used. Also, after studying the effect of the mode of heat withdrawal from CFRR, Gosiewski et al. (2007) agreed that heat withdrawal by withdrawing part of hot gases guarantees autothermal operation and stability in operations compared to the use of an external heat exchanger which may create an asymmetric temperature profile. Further, Gosiewski et al. (2007) suggested that although hot gases withdrawal is an efficient mode of energy extraction, care should be taken, because the conversion may be reduced.

8.5 Pilot reactor at CTEC Varennes

Studies by Salomons (2003), Kushwaha (2003) and Fuxman (2008) were all based on the pilot scale CFRR located at CANMET Energy Technology Centre Varennes. The

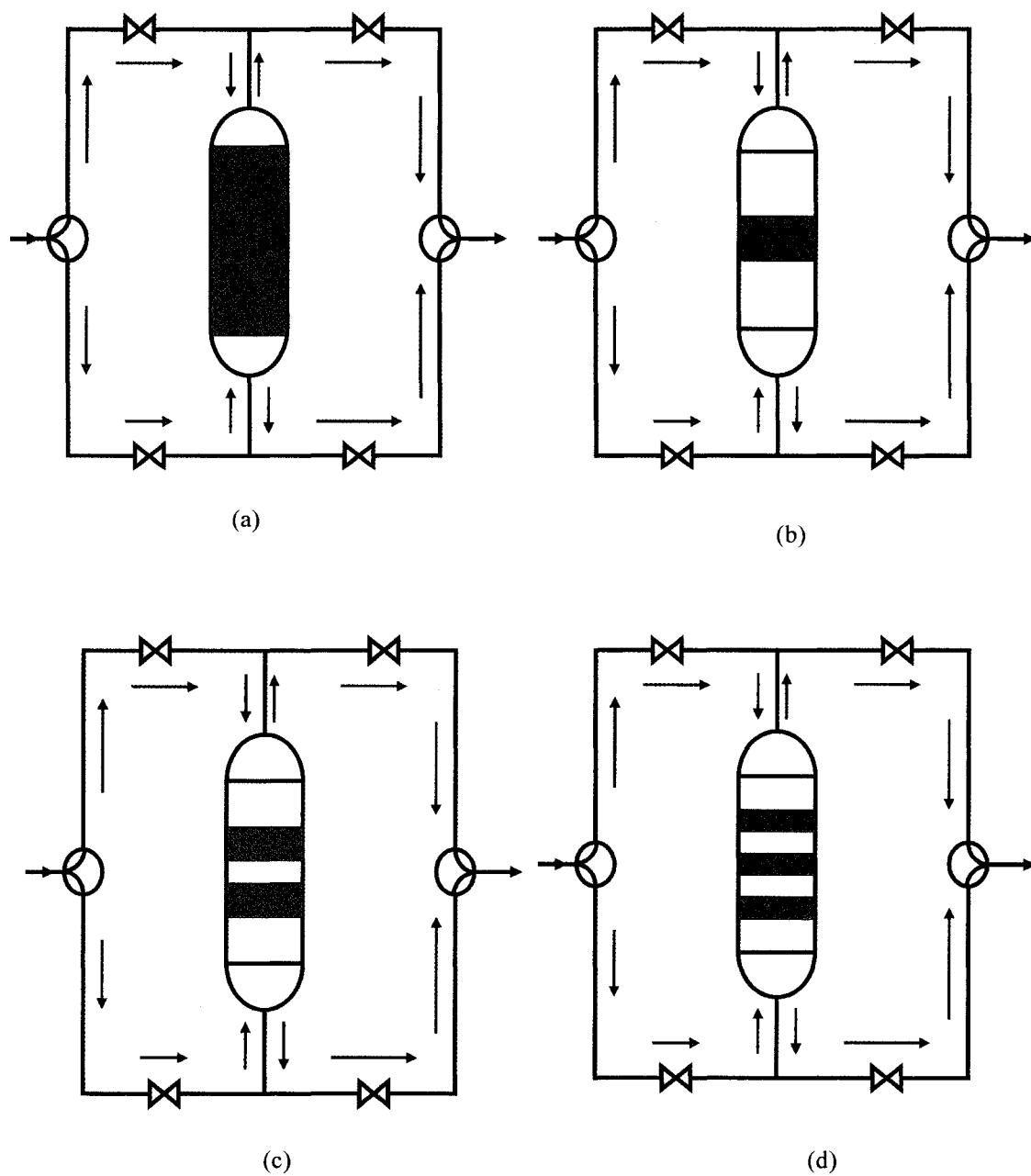


Figure 8.3: Common catalytic flow reverse reactor configuration, (a) single bed without inerts, (b) single bed with inerts and, (c) and (d) multiple beds.

same reactor forms the basis of the parametric studies presented shortly, and will be the test bed for the results presented here. Therefore a description of that reactor

is now given, based on the information provided in the three afore-mentioned references and by CTEC Varennes.

A diagram of the reactor is given in Figure 8.4 with the configuration used by Salomons (2003). In that study, the inert sections were ceramic monoliths. Kushwaha (2003) used the same system and varied the inert materials, using packed beds as well as monoliths (both metal and ceramic). As shown, the reactor was comprised of two cylindrical reaction sections in parallel joined by a U-bend at the bottom. Three-way valves are used to control the flow direction. The reactor system is made from Hastelloy to permit operation at temperatures up to 1300 K. The reactor walls were 3.2 mm thick with a density of 7800 kg/m^3 , a heat capacity of 460 J/(kgK) and a thermal conductivity of 14.3 W/(mK) . The reactor is insulated by a blanket 0.28 m thick with a density of 128 kg/m^3 , a heat capacity of 1340 J/(kgK) and a thermal conductivity of 0.144 W/(mK) .

The reactor internals consisted of a combination of open spaces, inert and catalyst sections. Salomons (2003) used three ceramic monolith sections in each side as inert material. Each monolith section was 0.2 m in height and had a 2.5 cm air gap between them, to give a total monolith height of 0.65 m. The monoliths were Celcor 9475 (EX-20) Cordierite with a density of 1683 kg/m^3 . The cell density was 100 cells per square inch (CPSI) with a fractional open frontal area (or porosity) of 0.75 to give a bulk density of 423 kg/m^3 . The hydraulic diameter of each cell was 2.16 mm. The heat capacity of the monolith was 1020 J/(kgK) . The thermal conductivity of the monolith substrate was 1.46 W/(m K) . Kushwaha (2003) used these ceramic monoliths in her study, but also examined the effect of other inert material. In one alternative, four metal monoliths was used in each reactor side. Each monolith section was 0.15 m long with a gap of 2.5 cm between them. The metal monoliths were supplied by Performance Industries Inc., and had a porosity of 93% and a bulk density of 532 kg/m^3 . The thermal conductivity of the metal substrate was 26 W/(m K) and the heat capacity was 461 J/(kgK) . The hydraulic diameter of each channel was 1.57 mm. Kushwaha (2003) also considered a packed bed of Denstone balls 0.7 m high in each reactor side. The ball diameter was 1 cm. The bulk density of the balls was 1440 kg/m^3 , the void fraction was 0.4 and the heat

capacity was 1040 J/(kgK).

The catalyst sections used in the cited investigations were packed beds of Raschig rings with a characteristic length of 7.5 mm and containing a non-noble metal catalyst. Properties of the catalyst packing were given by Aubé and Sapoundjiev, (2000). The solid density was 1240 kg/m³, the thermal conductivity was 0.5 W/(mK), the heat capacity was 1020 J/(kgK) and the bed porosity was 0.51. It is proposed to replace the catalyst sections with monoliths with Pd catalyst of loading of 15 g/ft³, that is, the same type of monolith as used in the kinetic studies reported in Chapter 6 but with a lower palladium loading. Investigations of the effect of changing the packed bed for Pd monoliths, and the effects of monolith length and position are reported later in the thesis.

Different methods have been used to pre-heat the catalyst bed. In Salomons (2003) an electric blanket was used on the right side reactor section. This catalyst section was heated from ambient temperature to about 830 K, measured at the electric blanket. Once the right reactor side was hot, the system was operated with inlet flow to the right side (forward flow mode), to push thermal energy to the left side. This method ensured that the reaction occurred in both sections, and that the left side made significant kinetic contributions to the system. In Kushwaha (2003) the apparatus was modified, and pre-heating was accomplished by adding hot air at the reactor mid-point (in the U-bend). Hot air was alternatively passed through both sides of the reactor, until a temperature in each catalyst bed of around 675 K was achieved. At this point, a stream with a relatively high methane stream was introduced, and the reactor operated in cyclical mode to achieve the desired starting temperature.

Kushwaha et al. (2004; 2005) discussed and compared the performance of the various types of inert. Also, they suggested that the rate of hot gas extraction at the centre of U - bend can be used as a means of controlling the reactor temperature. The latter point was used as a control strategy in the work of Fuxman (2008). In the current work, the effect of reaction parameters (inlet velocity, switch time, inlet methane concentration), thermal properties (thermal mass, thermal conductivity, insulator thickness), reactor geometry (radius, length of active catalyst, catalyst

activity), and the catalyst type (packed bed and Pd monolith catalyst) are further studied and investigated numerically.

8.6 Modelling the CFRR

8.6.1 Introduction to reactor modelling

Extensive investigation has been done to explore ways and means of maximizing the stored energy and its utilization externally. The stored energy depends much on reactor geometry, catalyst activity, thermal stability, thermal properties of internals and reaction parameters. Manipulation and clear understanding of these factors and their effects are beneficial in realizing maximum generation as well as utilization of energy released during the exothermic reaction (Litto et al., 2006).

Computer modelling is a valuable tool for understanding the processes and assisting with design. Modelling of catalytic monolith reactors was discussed in Chapter 7, with the focus there being on the single channel model. In the following paragraphs, a discussion of modelling of monoliths and packed beds will be presented, but the focus will be on the whole reactor.

As with any engineering process, a reactor model may vary from simple to complex, depending on the nature of design and the simplifying assumptions. Generally, it is advisable to use the simplest model possible, that is consistent with a useful solution, to minimize computer time. Generally speaking, heterogeneous reactors are usually modelled using a continuum approximation (e.g., (Zygourakis, 1989; Luoma and Smith, 1996)). In this method, the actual solid and fluid domains are not solved for at the pore level, but rather a volume averaging approach is used to approximate the domain, and account for the two phases. A continuum model can be either heterogeneous or pseudo-homogeneous. In the former case, the fluid and solid phases are both considered, and in general the temperature and concentration in the fluid and the solid are different, and are coupled by the appropriate mass and heat transfer mechanisms. In a pseudo-homogeneous model the fluid and solid temperatures and concentrations are assumed to be the same.

Another important criterion is the number of dimensions in the reactor model. Reactors are often tubular with a circular cross section, which leads naturally to the use of one and two dimensional (axi-symmetric) models. A one dimensional model assumes no radial gradients of temperature, concentration and velocity, which is not very realistic for a large diameter reactor. Two dimensional models are better, especially if there is axi-symmetry. Full three dimensional models are very expensive in terms of computer time. For the pilot plant reactor discussed earlier, a three dimensional model is really desired, but not possible to use in the time available.

The mathematical modelling of packed bed reactors is widely reported, see for example De Wash and Froment (1972), who gave a good summary and discuss the importance of the radial boundary conditions. Aubé and Sapoundjiev (2000) reported a two dimensional model for a packed bed flow reversal reactor. Monolith reactor models have also been widely presented in the literature. Models of a single channel of a monolith reactor as well as complete monolith reactors have been developed (see Chapter 7). A review of packed bed and monolith reactor models can also be found in Hayes and Kolaczkowski (1997).

Models specific to CFRR have been reported for a variety of applications, and used to investigate a variety of operating parameters, either from a theoretical point of view or coupled with experiments. Reported models include one dimensional, either pseudo-homogeneous or heterogeneous (Eigenberger and Nieken, 1988; Purwono et al., 1994; Bhatia, 1991; Gawdzik and Rakowski, 1988; Gawdzik and Rakowski, 1989; Gupta and Bhatia, 1991; Haynes et al., 1992; Liu et al., 2000; Liu et al., 2001b; Liu et al., 2001a), and two dimensional models (Aubé and Sapoundjiev, 2000; Salomons et al., 2004). Limited work on 3D has been reported (Liu et al., 2007).

The principle features of the CFRR and the phenomena occurring in it can be completely described by using transport phenomena, reaction kinetics, thermodynamics and the system properties. The resulting mathematical model is comprised of a system of partial differential and algebraic equations. The partial differential equations are obtained from the conservation equations, applied separately to the

gas and solid phases. Algebraic equations are used to estimate the physical and transport properties of the system. The following sections give a summary of the equations that were used to build the model for the system. The equations are essentially those used by Salomons (2003) and Kushwaha (2003), which are derived from many sources. The equations are also given in general form in Hayes and Kolaczowski (1997). Equations for reaction in monolith sections are also given, which are not used in the models of Salomons (2003) and Kushwaha (2003).

8.6.2 Basic transport equations

There are four basic conservation equations; the mole and energy balances for the fluid and solid phases. The form of these equations will vary depending on whether or not the solid is a packed bed or monolith, and whether or not there is a solid present. A fifth conservation equation, the momentum balance, may also be used. One of the numerical difficulties encountered when modelling transient systems containing a fluid and a solid is the different time scales involved. For example, for gas flow systems with a fairly short residence time, the response of the fluid phase occurs much more quickly than the solid. These different time scales can cause badly conditioned systems. If the solid response is relatively slow, therefore, it is usually sufficient to assume that the fluid temperatures and both concentrations are in a pseudo steady state with a slowly evolving temperature. This assumption is commonly used (Hayes et al., 1992; Lee and Aris, 1977).

Fluid phase mole balance:

The mole balance equation can be written to include convection and dispersion terms. In a packed bed and open section, mass transfer occurs by dispersion in both axial and radial directions, and by convection in the axial direction. In a monolith section, the structured packing effectively prevents radial dispersion. The mole balance for the packed bed reaction section is:

$$\frac{1}{r} \frac{\delta}{\delta r} \left(r D_{r,eff} C_f \frac{\delta Y_{CH_4,f}}{\delta r} \right) + \frac{\delta}{\delta z} \left(D_{a,eff} C_f \frac{\delta Y_{CH_4,f}}{\delta z} \right) - v_s C_f \frac{\delta Y_{CH_4,f}}{\delta z} \dots \quad (8.1)$$

$$- k_m a_v C_f (Y_{CH_4,f} - Y_{CH_4,s}) = 0$$

If there is no reaction, then the solid and fluid concentrations are the same, and the equation is:

$$\frac{1}{r} \frac{\delta}{\delta r} \left(r D_{r,eff} C_f \frac{\delta Y_{CH_4,f}}{\delta r} \right) + \frac{\delta}{\delta z} \left(D_{a,eff} C_f \frac{\delta Y_{CH_4,f}}{\delta z} \right) - v_s C_f \frac{\delta Y_{CH_4,f}}{\delta z} = 0 \quad (8.2)$$

This equation is also valid for the open sections. In a monolith with reaction, there is no radial dispersion in the fluid, and we have:

$$\epsilon \frac{\delta}{\delta z} \left(D_{a,eff} C_f \frac{\delta Y_{CH_4,f}}{\delta z} \right) - v_s C_f \frac{\delta Y_{CH_4,f}}{\delta z} - k_m a_v C_f (Y_{CH_4,f} - Y_{CH_4,s}) = 0 \quad (8.3)$$

The porosity appears in front of the dispersion term because of the way that the dispersion coefficient is defined. For the inert monolith sections the reaction is zero and the mole balance is:

$$\epsilon \frac{\delta}{\delta z} \left(D_{a,eff} C_f \frac{\delta Y_{CH_4,f}}{\delta z} \right) - v_s C_f \frac{\delta Y_{CH_4,f}}{\delta z} = 0 \quad (8.4)$$

Note also that the dispersion coefficients are defined differently for each medium, and will be described shortly.

Solid phase mole balance:

In the solid phase the rate of mass transfer to the solid surface equals the rate of reaction:

$$k_m a_v C_f (Y_{CH_4,f} - Y_{CH_4,s}) = (1 - \epsilon) \eta (-R_{CH_4}) \quad (8.5)$$

In the inert and open sections, the reaction rate is zero and the solid and fluid concentrations are equal.

Fluid phase energy balance:

The energy balance for the fluid also includes the effects of convection and conduction. As noted earlier, the fluid phase energy balance is written at steady state. The equation for a packed bed is:

$$\frac{1}{r} \frac{\delta}{\delta r} \left(r k_{r,eff} C_f \frac{\delta T_f}{\delta r} \right) + \frac{\delta}{\delta z} \left(k_{a,eff} C_f \frac{\delta T_f}{\delta z} \right) - v_s \rho_f C_p \frac{\delta T_f}{\delta z} + h a_v (T_f - T_s) = 0 \quad (8.6)$$

In a monolith there is no radial conduction in the fluid phase, and the radial term is dropped to give:

$$\epsilon \frac{\delta}{\delta z} \left(k_{a,eff} C_f \frac{\delta T_f}{\delta z} \right) - v_s \rho_f C_p \frac{\delta T_f}{\delta z} + h a_v (T_f - T_s) = 0 \quad (8.7)$$

For an open section the equation is:

$$\frac{1}{r} \frac{\delta}{\delta r} \left(r k_{r,eff} C_f \frac{\delta T_f}{\delta r} \right) + \frac{\delta}{\delta z} \left(k_{a,eff} C_f \frac{\delta T_f}{\delta z} \right) - v_s \rho_f C_p \frac{\delta T_f}{\delta z} = 0 \quad (8.8)$$

As with the mole balance, the effective thermal conductivities are defined differently for the different media.

Solid phase energy balance:

The energy balance in the solid phase includes the effects of accumulation, axial conduction, radial conduction, convection, and energy generation by the reaction, as necessary. The form of the equation is the same for both monoliths and packed bed reactors:

$$\begin{aligned} \frac{1}{r} \frac{\delta}{\delta r} \left(r k_{rs,eff} C_f \frac{\delta T_f}{\delta r} \right) + \frac{\delta}{\delta z} \left(k_{as,eff} C_f \frac{\delta T_f}{\delta z} \right) + h a_v (T_f - T_s) \dots \\ + (1 - \epsilon) \Delta H_R \eta (-R_{CH_4}) = (1 - \epsilon) \rho_s C_p \frac{\delta T_s}{\delta t} \end{aligned} \quad (8.9)$$

In the inert sections, the reaction rate term is dropped.

$$\frac{1}{r} \frac{\delta}{\delta r} \left(r k_{rs,eff} C_f \frac{\delta T_f}{\delta r} \right) + \frac{\delta}{\delta z} \left(k_{as,eff} C_f \frac{\delta T_f}{\delta z} \right) + h a_v (T_f - T_s) = (1 - \epsilon) \rho_s C_p \frac{\delta T_s}{\delta t} \quad (8.10)$$

For the solid reactor walls and insulation the conduction equation is applied:

$$\frac{1}{r} \frac{\delta}{\delta r} \left(r k_s \frac{\delta T_s}{\delta r} \right) + \frac{\delta}{\delta z} \left(k_s \frac{\delta T_s}{\delta z} \right) = \rho_s C p_s \frac{\delta T_s}{\delta t} \quad (8.11)$$

The solid thermal conductivity takes on the value for the wall or insulation.

Fluid phase momentum balance:

For essentially one dimensional flow, many investigators do not solve the momentum balance, but rather impose a velocity. If we make the ideal gas assumption, and ignore the pressure gradient, the velocity in the reactor can be simply described in terms of the inlet velocity and temperature, and the local temperature. The velocity of the fluid in the reactor is defined in terms of the superficial velocity, v_s , which is based on the empty cross sectional area, and the interstitial velocity, v , which is the actual fluid velocity in the void space. The relationship between the two is:

$$v_s = v \epsilon \quad (8.12)$$

The local velocity in terms of the inlet conditions is then defined as:

$$v_s = v_{s,\text{inlet}} \left(\frac{T_f}{T_{f,\text{inlet}}} \right) \quad (8.13)$$

For most of the simulations reported in this work, the above method was used to determine the velocity. Some work was also done using the momentum balance equation. For flow in porous media, the volume averaged Navier Stokes equation can be used to describe the flow. The equation is:

$$\frac{\delta}{\delta t} (\rho_f \bar{v}) + \Delta \cdot (\rho_f \bar{v} \bar{v}) = -\Delta p + \Delta \cdot (\bar{\tau}) + \rho_f \bar{g} + S_i \quad (8.14)$$

The source term, S_i , introduced for the porous medium can be generically defined in the form (Hayes et al., 1996; Hayes and Kolaczowski, 1997):

$$S_i = \left(\frac{\mu}{K} v_i + C_2 \frac{1}{2} \rho + f |v| v_i \right) \quad (8.15)$$

The first term on the right hand side accounts for the viscous loss and the second term the inertial loss. For laminar flow through porous media, the inertial loss is negligible and can be neglected. The viscous loss term is essentially a Darcy term, where K is the medium permeability. The permeability is a tensor. For a packed bed, the tensor nature of the permeability is retained, however, for a structured monolith the flow is permitted along the channel direction only. The permeability in the flow direction was determined from experimental pressure drop measurements. In the directions transverse to the flow, the permeability is set to an arbitrarily small value to ensure one dimensional flow.

8.6.3 Reaction kinetics

The reaction kinetics for the packed bed catalyst (Rashig rings) were reported by Aubé and Sapoundjiev (2000) to be first order with respect to methane, with the rate equation:

$$(-R_{CH_4}) = 1.35 \times 10^5 \exp\left(\frac{-6543}{T}\right) C_{CH_4} \quad (8.16)$$

For the palladium catalyst in the monolith support, the rate equation developed in Chapter 7 was used. The model parameters found were based on a catalyst loading of 80 g/ft^3 , and to simulate the reaction rate at different catalyst loading, the rate was multiplied by the ratio of Pd loading. For example, the rate at 15 g/ft^3 was found by multiplying by the ratio $15/80$. Further discussion is given in Chapter 9.

8.6.4 Diffusion in the catalyst

Both the packed bed catalyst and the Pd monolith catalyst will operate in the region of pore diffusion limitation. Interparticle diffusion resistance was expected to be significant owing to the large size of the catalyst pellets. The diffusion resistance was incorporated using an effectiveness factor based on the effective diffusivity in the catalyst, as described in Section 7.1.1.

The characteristic length of the particles, L_C , is defined as the volume divided by the surface area, which for the Rashigs rings used is equal to 1.25 mm. The generalized effectiveness factor for an isothermal first order reaction can be defined using either a flat plate, sphere or infinite cylinder geometry; all solutions give essentially the same answer (Froment and Bischoff, 1990). Here we used the flat plate equation:

$$\eta = \frac{\tanh(\phi)}{\phi} \quad (8.17)$$

For the palladium monolith, the rate equation was also derived using the first order flat plate assumption (see Chapter 7) and the same assumption was also used here.

8.6.5 Transport properties inside the reactor

There are many published works on the transport properties in packed beds and monoliths. In this work, those recommended by Hayes and Kolaczkowski (1997) and used by Salomons (2003) and Kushwaha (2003) were also used. They are summarized in the following. The packed bed radial and axial dispersion coefficients are calculated using a method cited by Carberry (1976). Define a hydraulic diameter for the particle:

$$D_H = \frac{D_R}{\frac{3D_R}{2D_C}(1 - \epsilon) + 1} \quad (8.18)$$

where D_R is the reactor diameter and D_C is the characteristic particle diameter, defined as:

$$D_C = 6\frac{V}{A} \quad (8.19)$$

The characteristic diameter of the Rashigs rings was 7.5 mm. The axial and radial Peclet numbers for mass transfer are defined as:

$$(Pe_r)_m = \frac{D_H v_s}{D_{r,eff}} \quad (Pe_a)_m = \frac{D_H v_s}{D_{a,eff}} \quad (8.20)$$

The Peclet numbers were calculated using the method of Dixon and Creswell (1979).

$$\frac{1}{(Pe_a)_m} = \frac{0.73\epsilon}{ReSc} + \frac{0.5}{(1 + \frac{9.7\epsilon}{ReSc})} \quad (8.21)$$

$$\frac{1}{(Pe_r)_m} = 0.1 + \frac{0.66\epsilon}{ReSc} \quad (8.22)$$

The Reynolds and Schmidt numbers are defined by:

$$Re = \frac{v_s D_C \rho_f}{\mu} \quad Sc = \frac{\mu}{\rho_f D_{AB}} \quad (8.23)$$

In the open sections, the axial and radial dispersion coefficients were calculated by multiplying the molecular diffusivity by 10 and 100 respectively. These terms were selected to approximate the degree of mixing in the open sections, as suggested by (Lee and Brodkey, 1964).

The dispersion coefficient for the monolith channels is calculated using Taylor-Aris dispersion (Taylor, 1953; Aris, 1956), as discussed in Chapter 7 for the single channel model.

The effective radial and axial thermal conductivity of the fluid $k_{rf,eff}$ and $k_{af,eff}$ in the packed bed were calculated from the Peclet number for heat transfer.

$$(Pe_a)_m = \frac{v_s D_C \rho_f C_p f}{k_{af,eff}} \quad (Pe_r)_m = \frac{v_s D_C \rho_f C_p f}{k_{rf,eff}} \quad (8.24)$$

The axial and radial fluid phase Peclet numbers were calculated using the method of Dixon and Creswell (1979), as given by Equations 8.21 and 8.22, with the Schmidt number replaced by the Prandtl number, where:

$$Pr = \frac{C_p \mu}{k_f} \quad (8.25)$$

The packed bed the model of Dixon and Creswell (1979) was used to calculate the effective thermal conductivity of the solid, which is the same in both axial and radial directions.

$$k_{as,eff} = k_{ar,eff} = \frac{2k_f \sqrt{1-\epsilon}}{1 - \frac{k_f}{k_s} B} \left(\frac{\left(1 - \frac{k_f}{k_s}\right) B}{\left(1 - B \frac{k_f}{k_s}\right)^2} \ln \left(\frac{k_s}{B k_f} \right) - \frac{B+1}{2} - \frac{B-1}{\left(1 - B \frac{k_f}{k_s}\right)} \right) \quad (8.26)$$

where:

$$B = 1.2 \left(\frac{1-\epsilon}{\epsilon} \right)^{\frac{1}{0.9}} = 1.15 \quad (8.27)$$

The effective thermal conductivity of the monolith solid is a function of the porosity in the axial direction and a function of the monolith structure in the radial direction, thus:

$$k_{as,eff} = k_s (1 - \epsilon) \quad \text{and} \quad k_{es,eff} = k_s G \quad (8.28)$$

The factor G accounts for the structure of the monolith in the radial direction. A value of 0.2 was used, based on the results of numerical simulations (unpublished work of Hayes, (2002)).

The effective axial thermal diffusivity of the fluid in the monolith was calculated by analogy to Taylor-Aris dispersion, again as discussed in Chapter 7.

Heat and mass transfer coefficients were required for both monolith and packed bed sections. The rate of heat and mass transfer depends on the fluid/solid interfacial area. The ratio of area to volume for a packed bed is given by Bird et al. (2001):

$$a_v = \frac{6(1-\epsilon)}{D_C} \quad (8.29)$$

The area to volume ratio for a monolith is calculated using the fractional open frontal area, or porosity, of the monolith structure and the hydraulic diameter of the channels.

$$a_v = \frac{4\epsilon}{D_H} \quad (8.30)$$

The mass transfer coefficient depends on the Reynolds and Schmidt numbers, and the heat transfer coefficient on the Reynolds and Prandtl numbers. For a packed bed, the Reynolds number and Prandtl numbers are given by Equation 8.23, and the Schmidt number is:

$$Sc = \frac{\mu}{\rho_f D_{AB}} \quad (8.31)$$

The Sherwood number was computed using the correlation of Wakao and Kagui (1982).

$$Sh = \frac{K_m D_C}{D_{AB}} = 2 + 1.1 Sc^{1/3} Re^{0.6} \quad (8.32)$$

The Nusselt number is:

$$Nu = \frac{h D_C}{k_f} = 2 + 1.1 Pr^{1/3} Re^{0.6} \quad (8.33)$$

The flow in the monolith channel was laminar and entrance effects are not significant because of the length of the monoliths used. For inert monoliths with square channels, the asymptotic value for the Nusselt number of 2.977 was used. For reactive monoliths, the value was calculated using the method described in Chapter 7.

8.6.6 Auxiliary equations

The fluid can be approximated as an ideal gas with mass and molar densities of:

$$\rho_f = \frac{\bar{M}P}{R_g T_f} \quad \text{and} \quad C = \frac{P}{R_g T_f} \quad (8.34)$$

The heat capacity of each gas species was described by a third-order polynomial function of temperature given by Hayes and Kolaczkowski (1997). The thermal

conductivity and viscosity of the fluid were functions of temperature. Functions were fit to the values for air using data from Incropera and DeWitt (1996). The thermal conductivity is:

$$k_f = 0.01679 + 5.073 \times 10^{-5}T_f \quad (8.35)$$

The viscosity is:

$$\mu = 7.701 \times 10^{-6} + 4.166 \times 10^{-8}T_f - 7.531 \times 10^{-12}T_f^2 \quad (8.36)$$

The enthalpy of the reaction in kJ/mol is (Hayes and Kolaczkowski, 1997):

$$(\Delta H_R)_{CH_4} = -806.9 + 1.586 \times 10^{-2}T - 8.485 \times 10^{-6}T^2 - 3.963 \times 10^{-9}T^3 + 2.16 \times 10^{-12}T^4 \quad (8.37)$$

8.6.7 Boundary and initial conditions

The radial boundary conditions were based on axial symmetry, and therefore all fluxes were zero at the centreline. The molar flux is zero at the impermeable walls. At the external surface of the reactor (outside of the insulation), heat transfer occurs by radiation and natural convection, although radiation was found to be negligible. The external heat transfer coefficient was assigned a value of 3 W/(m²K), and was estimated from a natural convection correlation (Incropera and Dewwit, 1996).

The axial boundary conditions were zero flux conditions for fluid phase mole and energy balances at the reactor outlet, and also for the inlet and outlet for the solid phase energy balance. For the inlet conditions, conditions of constant temperature and concentration were imposed for the fluid phase equations.

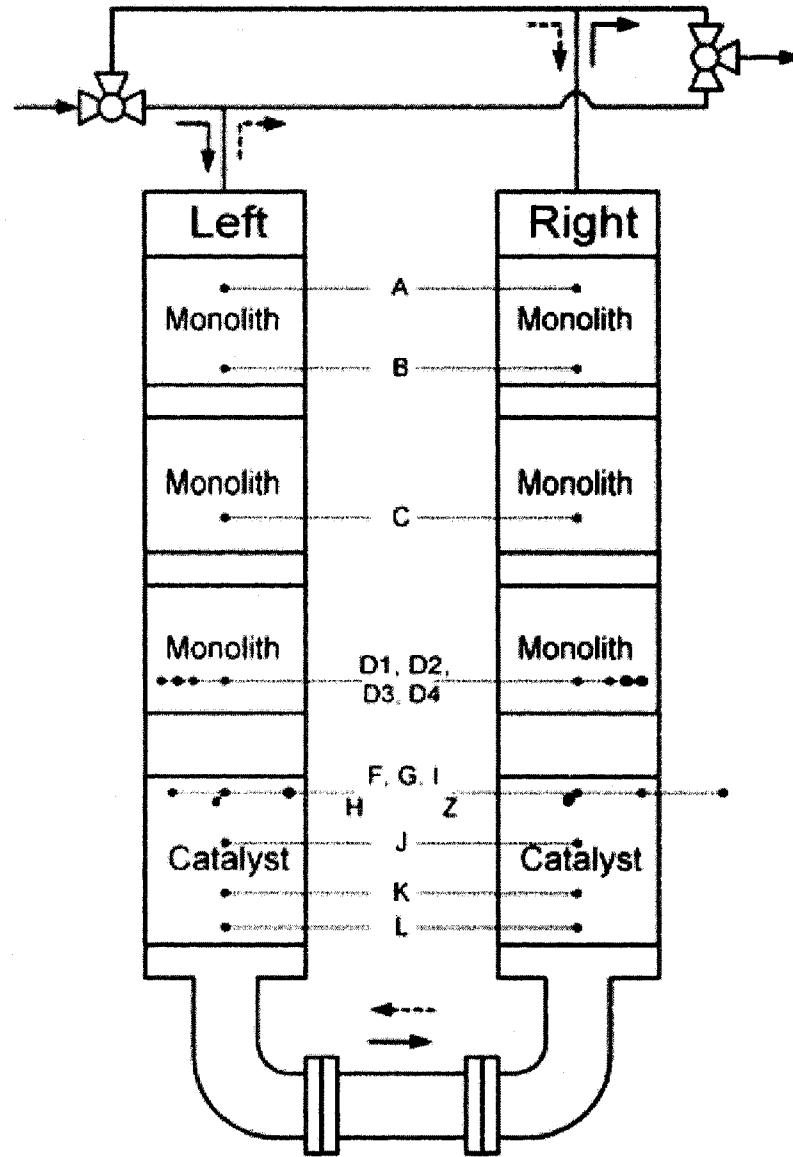


Figure 8.4: Diagram of the pilot scale CFRR at CTEC Varennes showing the configuration used by Salomons (2004). The catalyst was a packed bed and the inert sections were monoliths. The letters indicate thermocouple locations. Kushwaha (2003) used the same reactor and included different inert materials in her study. Diagram from Salomons (2003).

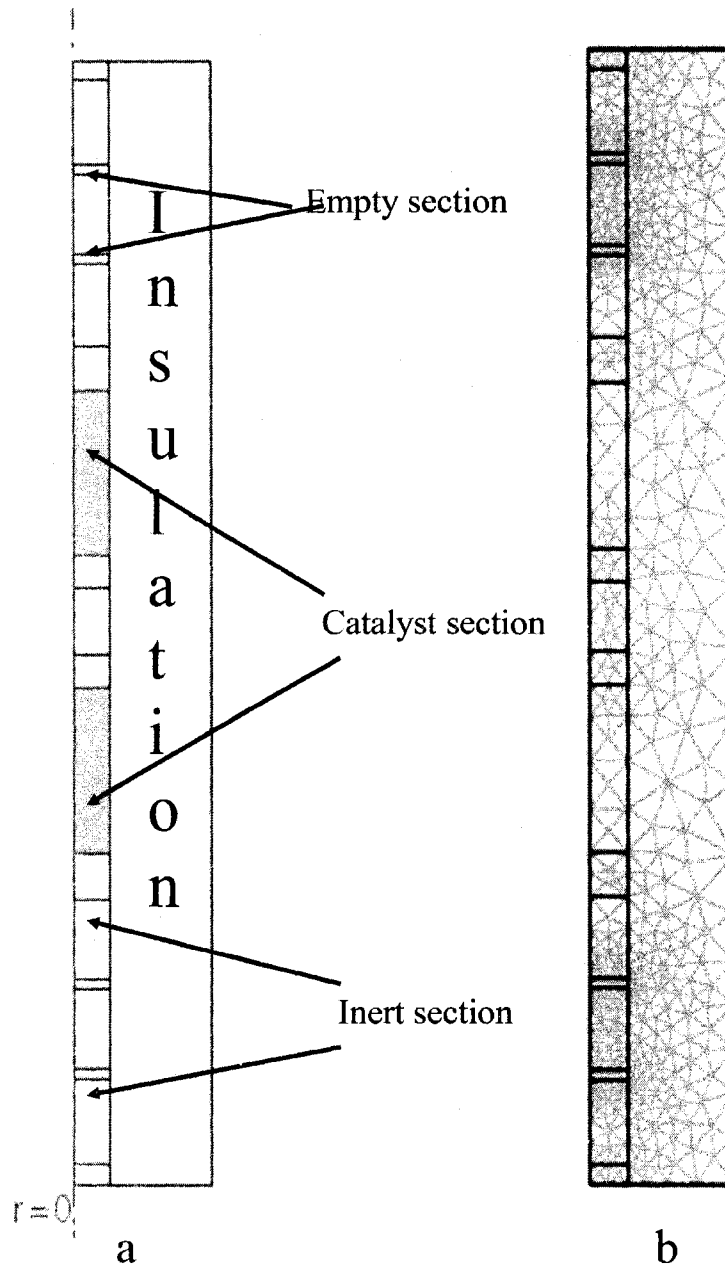


Figure 8.5: Two dimensional axi-symmetrical model for the CFRR used in the parameter study. (a) shows the sub-domains in the model and (b) shows a finite element mesh of the domains generated in COMSOL Multiphysics modelling package.

The initial conditions were imposed temperature profiles for the solid and fluid.

8.6.8 Solution methodology

The model described in Salomons (2003), was solved using the finite element method in a Fortran code which was based on software developed in the catalytic combustion group at the University of Alberta. Since that work was reported, the commercial software tool COMSOL Multiphysics has become available as a useful tool. COMSOL Multiphysics uses the finite element method to solve engineering problems. It facilitates all steps in the modelling process from defining the geometry, specifying physics, meshing, solving and then post-processing the results. It can be easily interfaced to Matlab, for a user friendly modelling environment. For this project, the model of Salomons (2003) , as summarized in the preceding sections, was implemented in a COMSOL environment. The model was developed in collaboration with Fuxman (2008), who used the model in the development and evaluation of control strategies for the CFRR. The COMSOL Multiphysics model was compared to the code of Salomons (2003) by Fuxman (2008) and found to give the same results.

In COMSOL Multiphysics it is easy to divide the overall domain into computational sub-domains, each of which can be assigned different properties. Further, the conservation equations to be solved in each sub-domain can be easily selected. The CFRR domain was sub-divided into different sub-domains depending on whether or not the sections contained a solid phase or not. Unstructured meshes were used in the solution, with a typical (coarse) mesh shown in Figure 8.5. In use, the mesh was refined until the solution obtained did not change.

8.7 Summary

This chapter has presented an overview of the catalytic flow reversal reactor and the development of a model for its study. In the next chapter, the model will be used to perform a parametric study of the reactor.

Parametric studies of the CFRR for lean methane combustion

9.1 Introduction

The catalytic flow reversal reactor (CFRR) was introduced in Chapter 8 as a potentially effective means for the destruction of lean methane. The CFRR has shown great promise for combustion of lean methane mixtures at ambient temperature. The technology has been successfully tested in underground coal mine applications, and has potential to be used in the oil and natural gas sector. However, outstanding issues to be resolved include optimisation of reactor design and development of robust control strategies. Control strategy was the subject of Fuxman (2008), and in this work a parametric study was performed to illustrate some of the critical operating parameters of the system. Numerical experiments were conducted to examine the effects of operating parameters, catalyst type, catalyst activity, reaction kinetics, equipment parameter and properties. The choice of catalyst was investigated, and the new palladium catalyst at different activity levels was compared to the existing non-noble metal catalyst. Higher catalyst activity affect the conversion and selectivity, and hence improve the reactor temperature in the positive way. However, excessive catalyst temperature can lead to deactivation and other harmful effects.

9.2 Energy extraction and reactor optimisation

CFRR operation is more complicated than standard chemical reactors, consequently, increasing conversion or selectivity can not be accomplished simply by increasing the reactor size or the amount of catalyst in the reactor. There are a number of concerns when developing CFRR units for practical use. A major concern is the scale-up or scale-down of these units. In particular, the performance change that can occur as the reactor diameter increases, leading to a diminution of the wall effect, has not been thoroughly explored. Many of the earlier modelling studies performed on CFRR used 1D models, which ignore the wall effects, including the effects of insulation. For large diameter reactors, such as those envisaged for coal mine vent gas operation, this may be a reasonable approximation. However, the current interest is the installation of smaller units in natural gas compressor stations, and it is expected that wall effects will be much more important in units of this size (diameter less than one meter). Hevia et al. (2006) showed that for bench to medium reactor sizes, the effect of the reactor wall in heat transfer phenomena is important. Therefore, the effects of various operating parameters on these relatively small reactors needs to be examined and analysed. The optimal operation of catalytic reactor needs a good compromise between pressure drop, flow uniformity, catalyst activity and stability. The monolith catalyst has shown the possibility of achieving this goal. Studies done by Salomons (2003) and Kushwaha (2003) used the CANMET CFRR, (see Chapter 8), with the packed bed catalyst. The detailed composition of the non-noble metal catalyst was not disclosed. To reduce pressure drop, increase catalyst activity and improve flow uniformity in this system, it is desirable to study the effect of using a monolith catalyst in comparison with a packed bed catalyst. The monolith catalyst is deposited in a thin washcoat film on the surface of a ceramic support, thence there is possibility of increasing the catalyst active area and hence improve catalyst activities as well as reactor performance. For methane combustion, Pd catalysts can have higher activity compared to non-noble metal catalyst, which makes it possible to work at lower temperature and leaner concentration (that may mean less energy requirement at start up). On the

other hand a Pd catalyst has inferior thermal stability and thus potentially limits the maximum temperature to be attained in the CFRR. A commercial Pd monolith catalyst developed by Umicore AG, Germany and discussed in Chapter 6 and 7 was used in this work.

As noted in the introduction, factors which cause stability problems to CFRR are directly related to changes of design parameters (bed length, cycle period, properties of reactor materials, fraction of inert materials, properties of inert materials), operating parameters (inlet concentration, flow rate, heat loss, heat extraction), catalyst activities and thermal stability. It is important to identify limits of their influence on CFRR performance and operational stability. In this chapter, the sensitivity of reactor performance due to varying the factors stated above will be analysed and studied numerically. Catalytic combustion of typical lean methane mixtures from fugitive emissions in the natural gas subsector, on non-noble metal catalyst in a packed bed and on a commercial Pd monolith catalyst will be considered.

Although catalytic combustion is carried out at lower temperature than homogeneous combustion, the reaction temperature is still high enough that it may be possible to extract energy from the system. As discussed in Chapter 8, the CFRR develops a stationary state in which the reactor temperature profile has a maximum value near the centre of the reactor, which slowly oscillates as the feed is switched between the two ends of the reactor. Because the temperature in the centre of the reactor can exceed by many times the adiabatic temperature rise, energy can be extracted from the centre both as a means of controlling the reactor operation and as a source of useful energy. Ideally, one would like to maximize the temperature in the reactor, both to maximize conversion with minimum catalyst requirement, as well as to maximize the extraction of useful energy. The stored energy and reactor temperature depend on reactor geometry, catalyst activity, thermal stability, thermal properties of internals and reaction parameters. Manipulation and clear understanding of these factors and their effects are beneficial in realizing maximum generation as well as utilization of energy released during the exothermic reaction (Litto et al., 2006).

The heat removed from the reactor may be used for tasks such as heating a building or driving a small turbine. Combating fugitive emissions in facilities usually means the addition of operating and capital cost, but with the possibility of heat removal from the reactor there is the chance of an economic payback.

9.3 Parametric study of CFRR

One of the key advantages of a computer model is that it may be used to explore the effects of changing parameters individually. Further, long time experiments can be performed which would be too expensive or time consuming to perform in the pilot or full scale experimental system.

In this work the computer model described in Chapter 8 was used to explore the influence of operating parameters, as a precursor step in the development of optimization and control strategies. From numerous previous experimental and modelling work, a number of variables are known to be important for proper operation. These include the thermal stability, design parameters, operating parameters and catalyst activities. Results showing trends due to variation of these parameters are presented and discussed.

9.3.1 Comparison of catalyst activity

As discussed earlier, the 200 mm ID pilot scale CFRR at CANMET Varennes has been extensively studied by Salomons (2003) and Kushwaha (2003). A significant amount of information was obtained in those studies, however, all of that work used the packed bed catalyst in the form of Rashigs rings. Their works demonstrated the advantages of using monolith inert materials in giving a lower pressure drop. A key purpose of the current work was to study the influence of replacing the packed bed catalyst with a commercial Pd monolith catalyst. The advantage of using monolith internals to give low pressure drop has been demonstrated, but the effects of changing the activity have not. For comparison purposes, a base case scenario was defined based on the current CFRR with non-noble metal catalyst in a packed

bed and the ceramic monolith in the inert sections, which is the configuration used by Salomons (2003).

The model studies for the packed bed catalyst used the rate expression given in Chapter 8, with the rate based on catalyst volume:

$$(-R_{CH_4}) = 1.35 \times 10^5 \exp\left(\frac{-6543}{T}\right) C_{CH_4} \quad \frac{\text{mol}}{\text{m}^3\text{s}} \quad (9.1)$$

For the palladium catalyst in the monolith support, the rate equation developed in Chapter 7 was used, where the rate is expressed in terms of washcoat volume.

$$(-R_{CH_4}) = \frac{k_v C_{CH_4}}{(1 + K_1 C_{CH_4} + K_2 C_{CO_2} + K_3 C_{H_2O})^2} \quad \frac{\text{mol}}{\text{m}^3\text{s}} \quad (9.2)$$

The parameters from Model B1 were used. These model parameters found were based on a catalyst loading of 80 g/ft³. There are five commercially available loadings for this catalyst, varying from 15 to 150 g/ft³, with 80 being the middle loading. To simulate the catalyst activity at different loadings of Pd, the rate was assumed to be linearly proportional to the Pd content. Thus, for example, to obtain the rate at 15 g/ft³, the rate at 80 was multiplied by the ratio 15/80. Liu et al. (2001a) showed that this approximation is reasonable. In this work, Pd loadings of 15, 80 and 150 g/ft³ were compared, which represent the lowest, middle and highest loadings.

A base case scenario was defined based on the CFRR configuration of Salomons (2003) with a non-noble metal catalyst in a packed bed and the ceramic monolith in the inert sections. The base case superficial velocity at STP was 0.21 m/s and the cycle time was 1000 s (switch time 500 s). The methane concentration was 0.5 % on volume basis. An arbitrary temperature profile was imposed as the initial condition.

The progression of the centreline axial temperature profile as a function of the number of cycles is shown in Figure 9.1.

The temperature profile observed in this simulation is typical of the operation of the CFRR. The initially imposed temperature is sufficient to initiate the reaction.

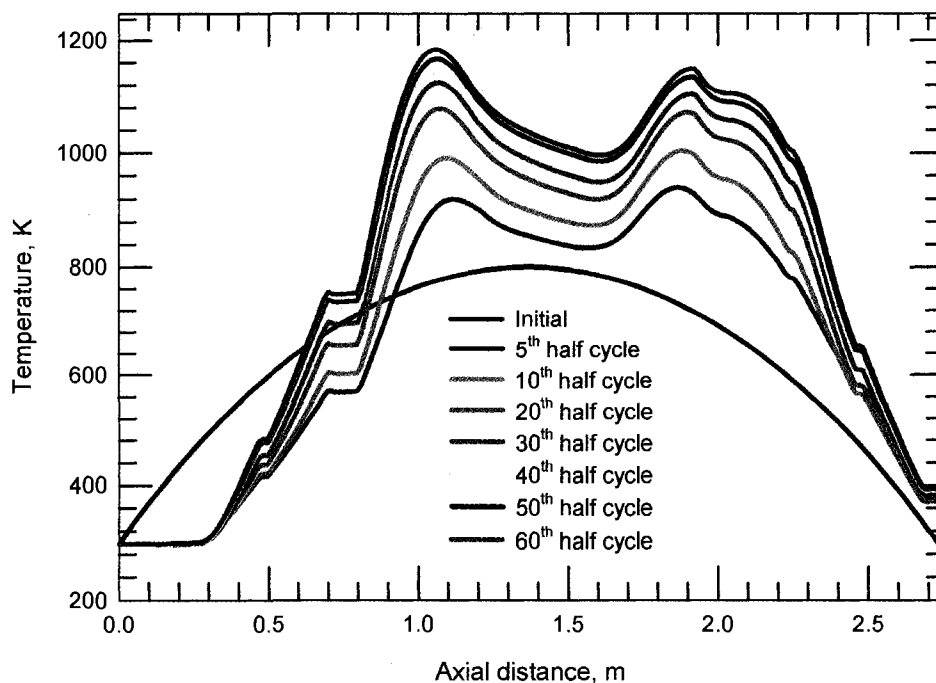


Figure 9.1: Centerline axial temperature profile for the base case with packed bed catalyst. The temperature continues to increase with each cycle, and a stationary state was approached.

The energy lost through the reactor walls and the exiting fluid is lower than the thermal energy generated by the combustion reaction, and the temperature in the reactor increases. After about sixty cycles it is seen that a stationary state is nearly reached, where the energy loss and generation are in balance.

The first test of the monolith reactor was made using a reaction section of the same length as the packed bed section. As noted above, three Pd loadings were tested. After having tested these three loadings, it was observed that the reactor response was essentially the same for all three catalyst activities. For example, Figure 9.2 shows the axial temperature profile achieved after 60 cycles for the three Pd loadings, with the packed bed result included for comparison purposes. It is seen that the profile for the three monolith catalysts are the same. Therefore, all further work was done using the lowest Pd loading, 15 g/ft³. Figure 9.3 shows the evolution of the axial temperature profile for this catalyst loading.

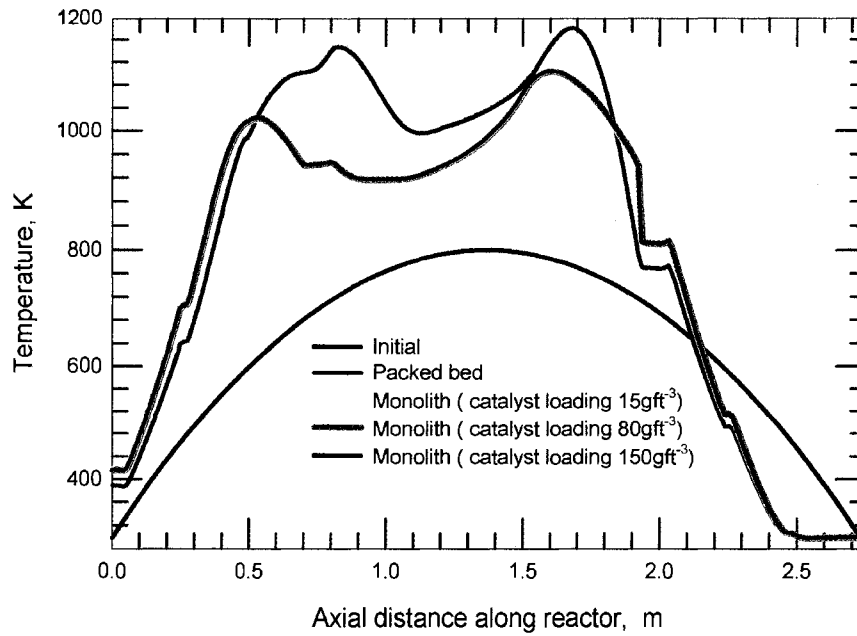


Figure 9.2: Centerline axial temperature profile at the end of 60th forward cycle, comparing packed bed and Pd monolith catalyst.

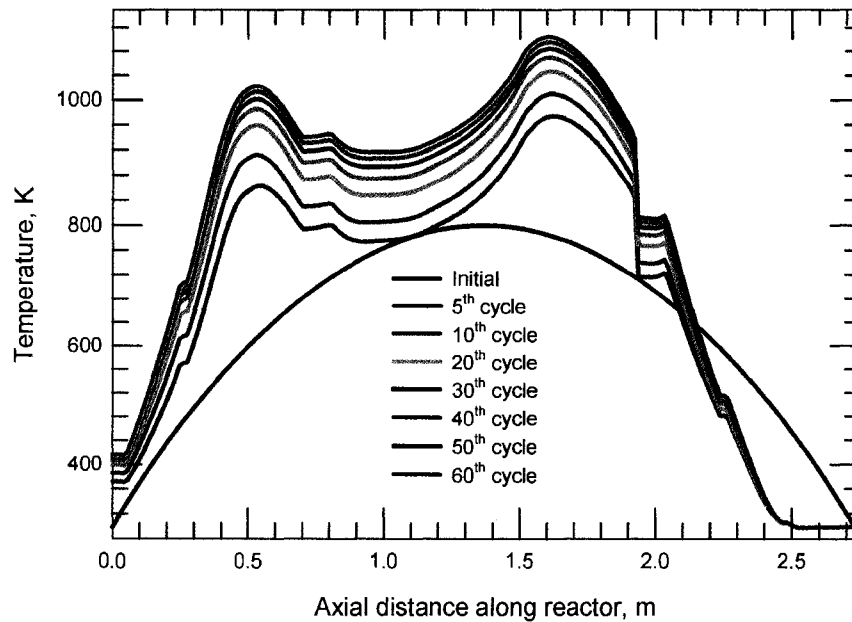


Figure 9.3: Centerline axial temperature profile progression for reactor with Pd monolith catalyst with loading at 15 g/ft³.

Figure 9.4 shows the evolution of the axial methane concentration profile with the cycle number. It is seen that at the initial conditions, most of the conversion in the packed bed occurs in the first encountered catalyst bed, with some additional conversion in the second bed. At the initial condition, there is some unreacted methane leaving the reactor, although as the temperature rises the conversion becomes complete. However, even at the stationary state value the second bed is required to obtain 100 % conversion. In contrast, the Pd catalyst shows a much higher activity, and even at the imposed initial condition 100 % conversion is achieved in the first monolith. Indeed, only a very short length of active reaction section is needed, and most of the catalyst is not utilized.

Both starting from the same arbitrary temperature profile, the packed bed catalyst had attained a higher fluid temperature in the central part of the reactor than

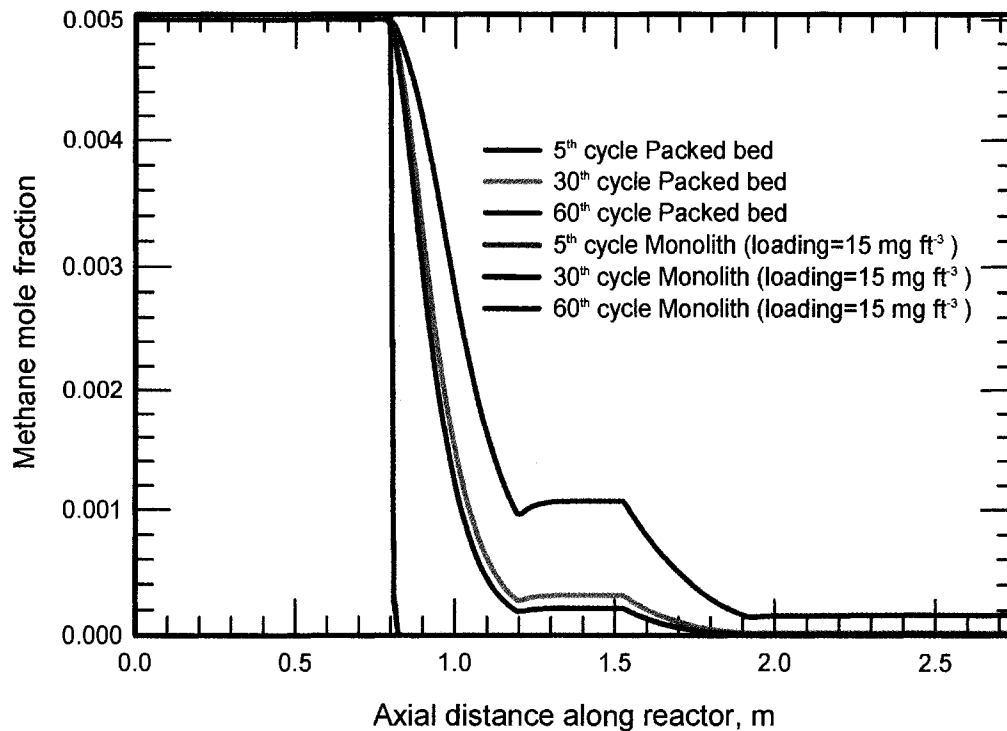


Figure 9.4: Methane concentration variation along length of reactor at centerline, comparing between the packed bed and Pd monolith catalyst activity.

Pd monolith reactor. At the same time, the Pd catalyst loses more energy in its effluent stream, as its fluid outlet temperature appears to be slightly higher, see Figure 9.2. Though complete combustion was achieved in the Pd monolith catalyst, more of the heat generated was lost by the outlet stream compared to the packed bed. Figures 9.5 and 9.6 show the radial temperature profile near the reaction zone during a forward and reverse operation respectively, for both packed bed and monolith reactors. For the Pd monolith, the radial temperature was taken at 1.05 m and 1.85 m positions, for forward and reverse flow respectively. In the packed bed the positions were 0.82 and 1.85 m for forward and reverse flow respectively. Radial temperature in the packed bed was raising fast compared to that in the monolith reactor and its walls appeared to be slightly hotter, while the monolith's radial temperature profile was almost flat.

Figure 9.4 shows that the Pd monolith catalyst is more active than the non-noble metal packed bed catalyst. Even with the lowest catalyst loading, the Pd monolith catalyst can achieve complete conversion of methane and only needs a small fraction of reactor length to accomplish the task. Thus, in further analysis only the minimum loading of 15 g ft^{-3} for Pd monolith catalyst was considered in the new CFRR setup. Because only a short length of active catalyst section was seen to be needed, further simulations were performed using a modified catalyst section of the reactor. The original catalyst section was 40 cm long on each side of U-bend. In the new setup, each catalyst section in the reactor was divided into two equal lengths of 20 cm to each section. One of the 20 cm sections was replaced with inert monolith. Tests were performed on two configurations. In the first configuration, called P1, the catalyst sections were far from U-bend, see Figure 9.7 a. In the other configuration, called P2, catalyst sections were close to U-bend, as shown in Figure 9.7 b.

With the new CFRR configurations P1 and P2, the performance of the reactor was evaluated and compared to the packed bed catalyst. Figures 9.8 to 9.10 compare the performance of the new setup of CFRR using the Pd monolith catalyst to the old CFRR setup with non-noble metal packed bed catalyst. The Pd monolith still shows higher activity and utilizes just a small fraction of reactor length at the entrance

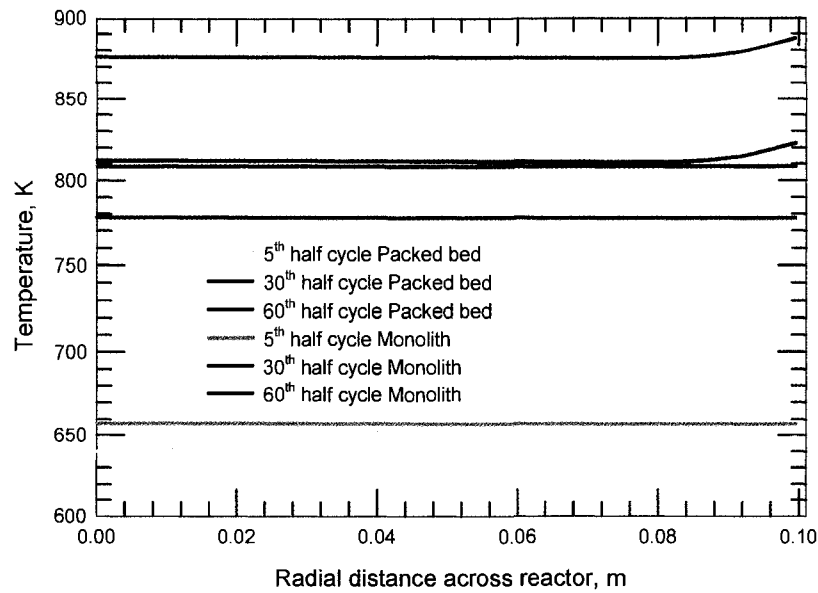


Figure 9.5: Radial temperature profile at the end of selected half - cycles forward flow, comparing packed bed and Pd monolith catalyst.

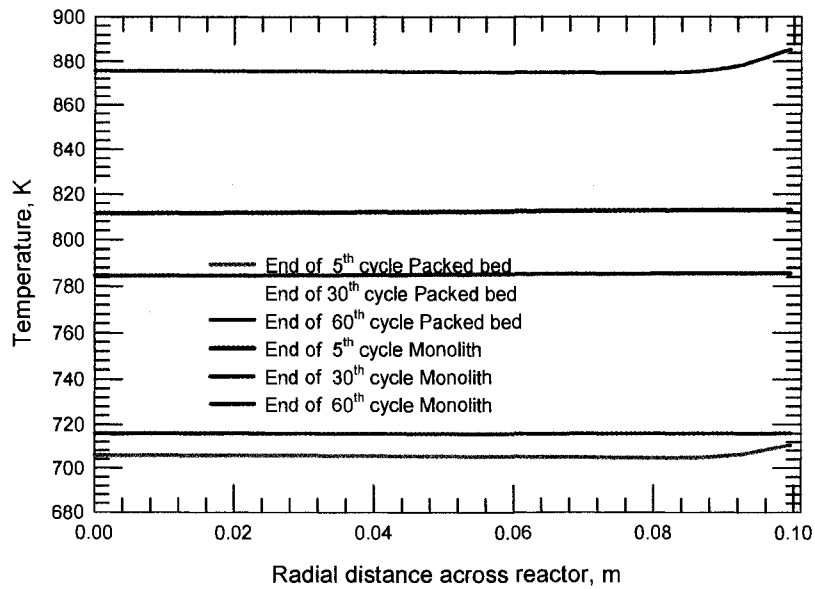


Figure 9.6: Radial temperature profile at the end of selected cycles reverse flow, comparing packed bed and Pd monolith catalyst.

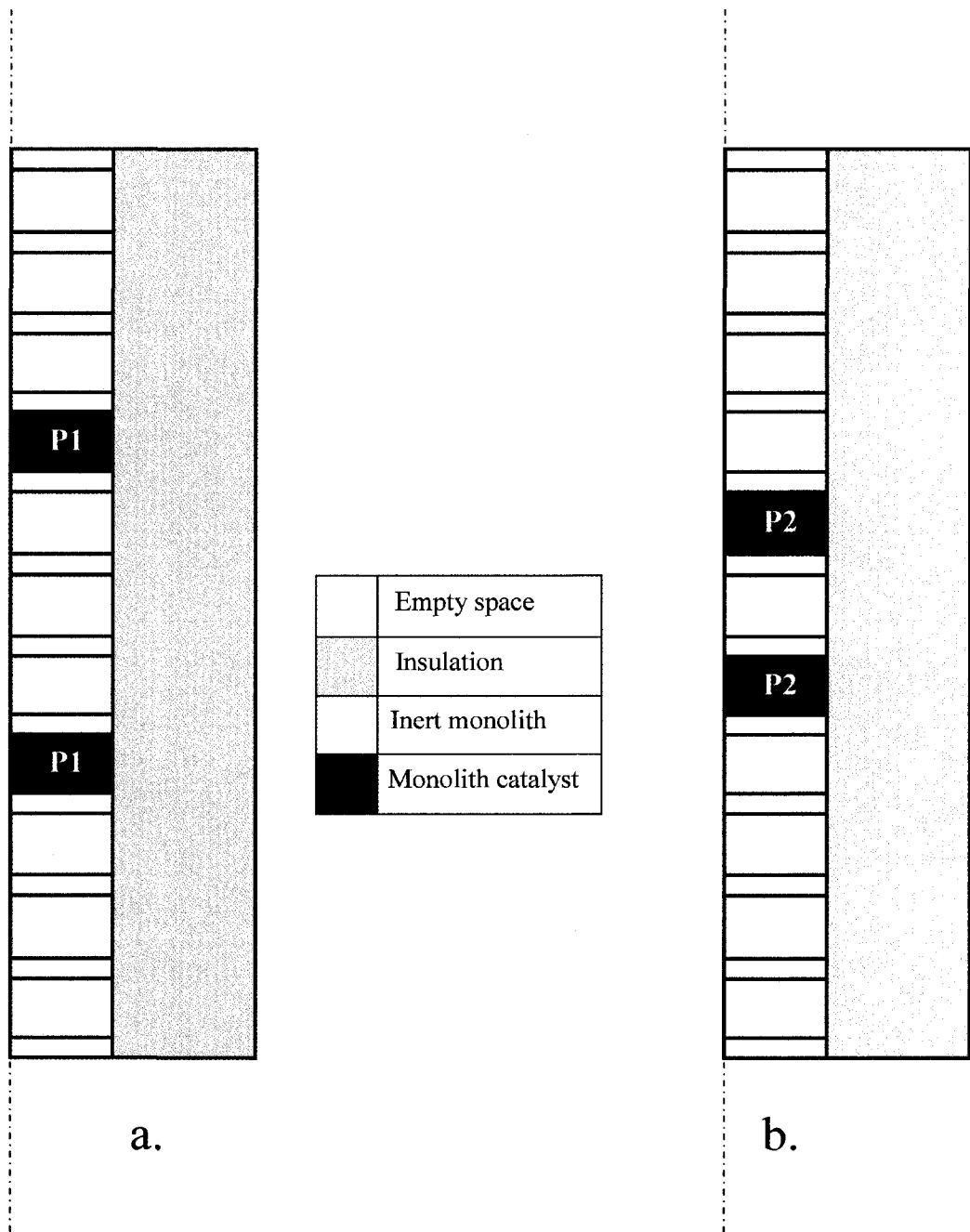


Figure 9.7: Symmetrical model of new proposed CFRR reactor to be used with Pd Monolith catalyst. Position P1 and P2 are possible position for catalyst.

point for complete reaction. Moreover, Figure 9.10 shows that the new CFRR setup has improved the temperature profile in the reactor, especially when the Pd monolith catalyst was inserted at position P2, near the U-bend. This configuration resulted in higher temperatures than those obtained from the packed bed catalyst, also the temperature profile became more narrow. When the Pd monolith catalyst was inserted into position P1, away from the U-bend, the temperature was lower than Pd monolith catalyst in position P2 and almost the same as the packed bed temperature profile in magnitude and shape except it became wider, see Figures 9.9 and 9.10. Figure 9.8 shows that almost complete conversion of methane can be realized independent of the catalyst location in the new CFRR setup and still only a small fraction of length of the active reactor section was used, as illustrated in Figure 9.11. In the Pd monolith, the reaction is localized at a point of active reactor zone entrance, while in the packed bed reactor the reaction is distributed along the whole length of the two catalyst section, when flow is in either direction, see Figure 9.11. For the new CFRR configuration, inserting the Pd monolith catalyst into position P2 is shown to result in higher temperature in the middle of the reactor and it is ideal for energy

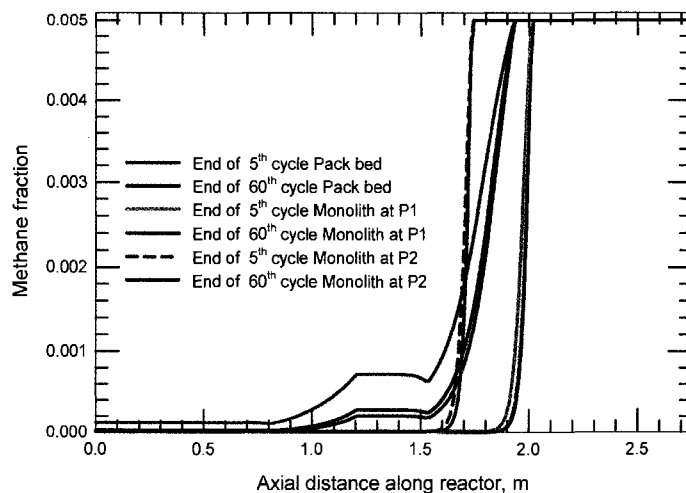


Figure 9.8: Methane concentration variation along centerline of reactor, comparing catalyst activity in the packed bed and new Pd monolith catalyst configuration.

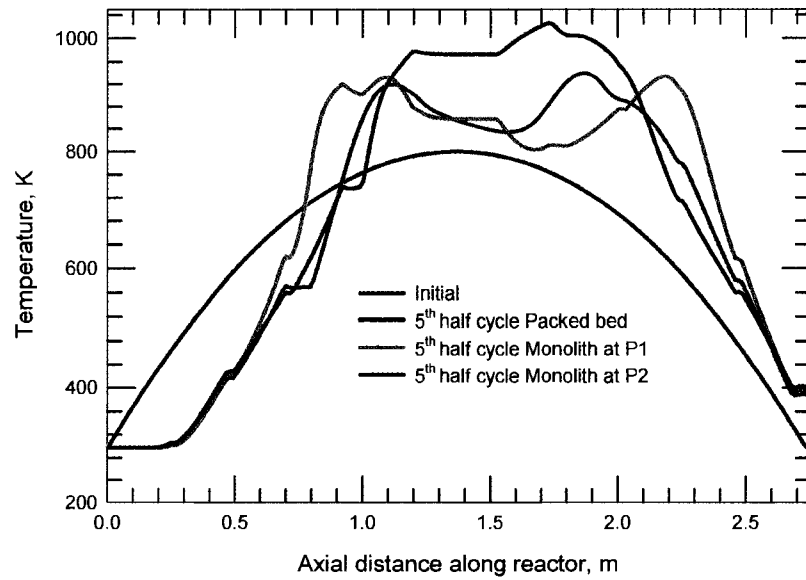


Figure 9.9: Temperature profile along centerline at end of 5th half cycle, comparing a packed bed and new Pd monolith configuration.

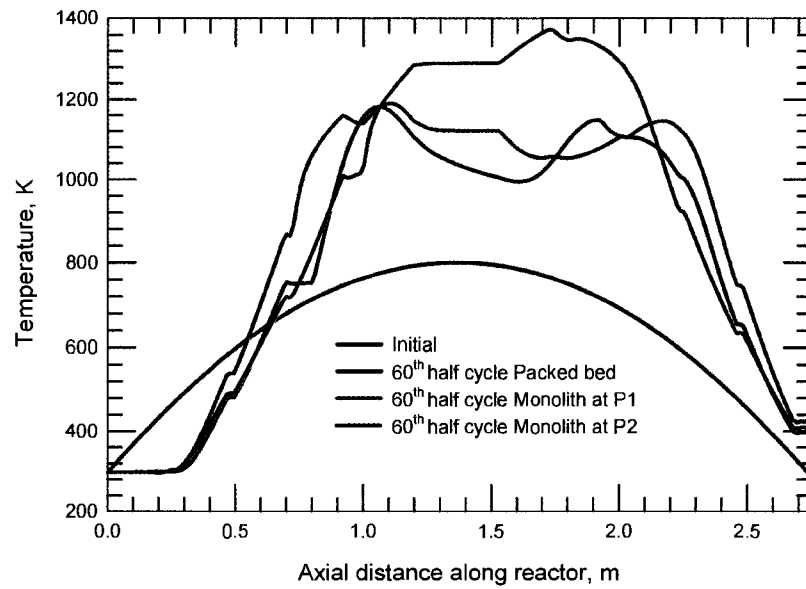


Figure 9.10: Temperature profile along centerline at end of 60th half cycle, comparing a packed bed and new Pd monolith configuration.

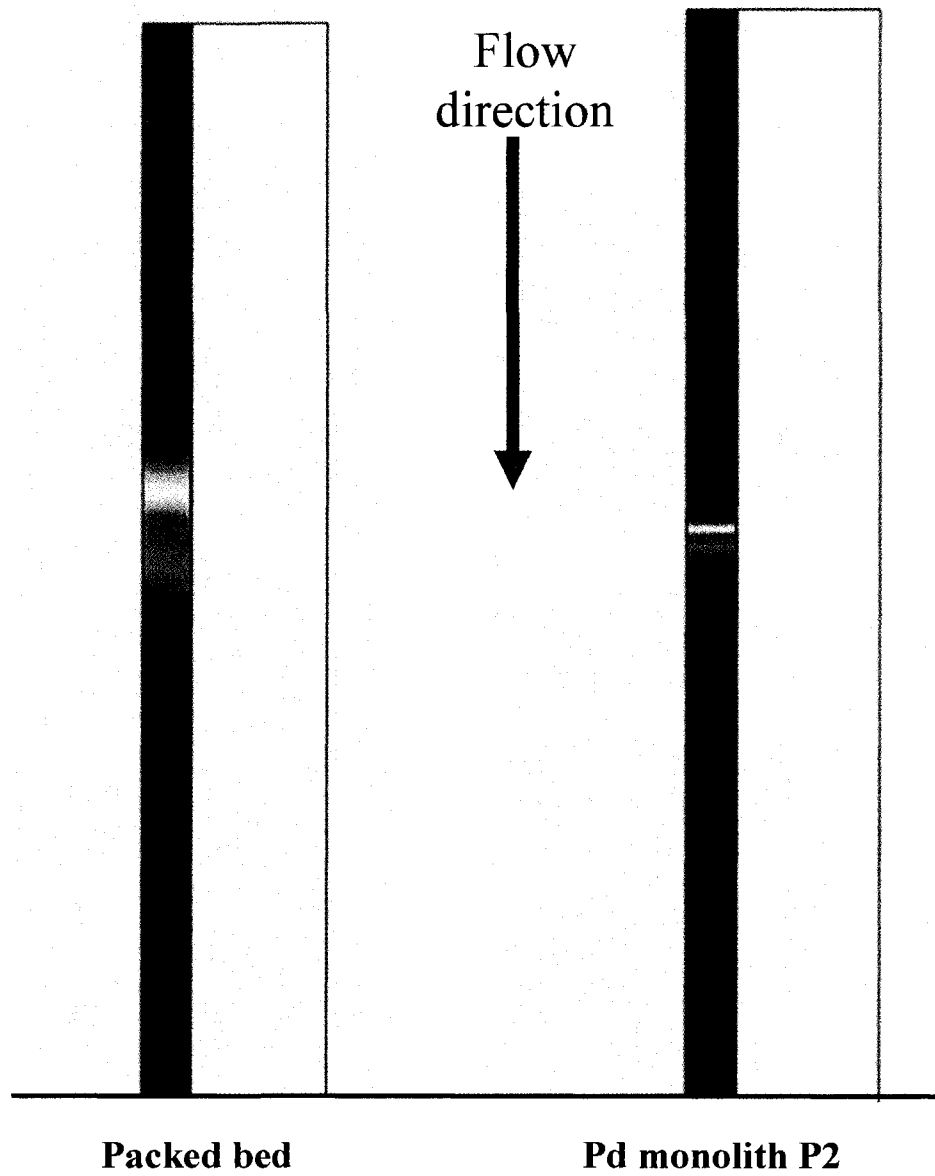


Figure 9.11: Surface plot of methane concentration showing the length of reactor zone used for reaction, left side is packed bed and right side is Pd monolith at P2. Red indicates high methane concentration and blue for zero concentration.

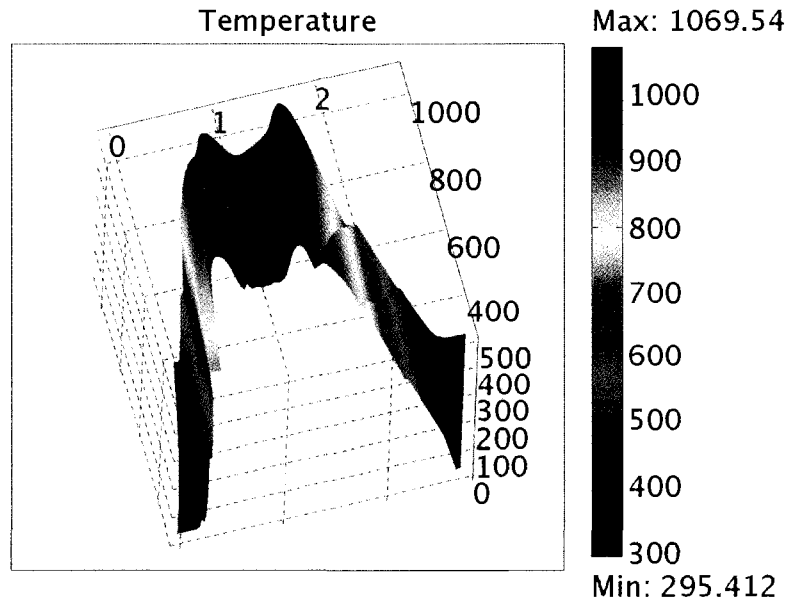


Figure 9.12: Centerline axial temperature profile in CFRR with packed bed catalyst.

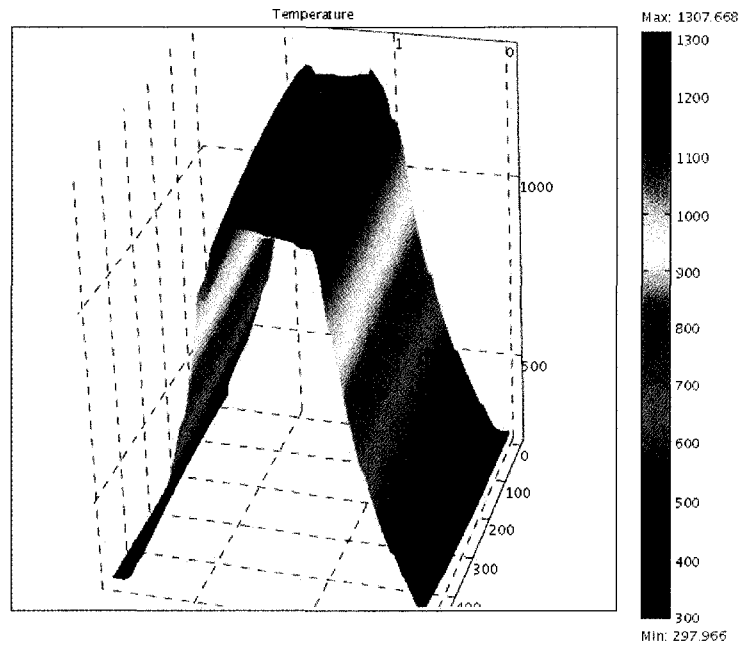


Figure 9.13: Centerline axial temperature profile in CFRR with Pd monolith at P2.

withdrawn, thus it has been recommended to have the Pd monolith at this position and all the following analysis is based on it. Figures 9.12 and 9.13 show surface plots of fluid temperatures for the packed bed and Pd monolith P2 respectively.

9.3.2 Velocity and switch time

The switch time is one of the key variables that can be used to control reactor operation. The best switch time will depend to an extent on the superficial gas velocity, which in turn may be related to the feed concentration. Velocity affects the residence time in the reactor, and hence affects the conversion. At low velocity there is decreased methane fed to reactor. The combination of velocity and switch time also determines the movement of the axial temperature profile. Increasing the velocity increases the flowrate and may diminish the contact time, which may lead to extinction of the reaction. A larger fluid residence time may lead to lower temperature and reaction extinction as well. The next set of results shows the effects of changing both the velocity and switch time such that the product of velocity and switch time is a constant. Figure 9.14 and 9.15 show the centreline axial temperature profiles after 60 cycles for a wide range of velocity and switch time combinations for the case of the Pd monolith and packed bed reactor respectively. When the superficial velocity is very low or very high, the reactor does not achieve the practical maximum temperature. Indeed, it was observed that for the lowest velocity of 0.1 m/s, the reactor reached a maximum temperature of about 800 K and 900 K in the packed bed and Pd monolith P2 respectively. Increasing the superficial velocity leads to a higher reactor temperature, provided that full conversion of the feed methane is obtained. It was observed that in the packed bed after 0.7 m/s, further superficial velocity increases resulted in incomplete conversion, and as a result the temperature begins to fall. Figure 9.17 illustrates that when the superficial velocity was increased to 2.0 m/s the methane conversion in the packed bed reactor was negligible. For the case of Pd monolith P2 catalyst, Figure 9.14 shows that it can sustain higher superficial velocity without any significant decrease in temperature, contrary to the packed bed behaviour, but above 1 m/s the temperature

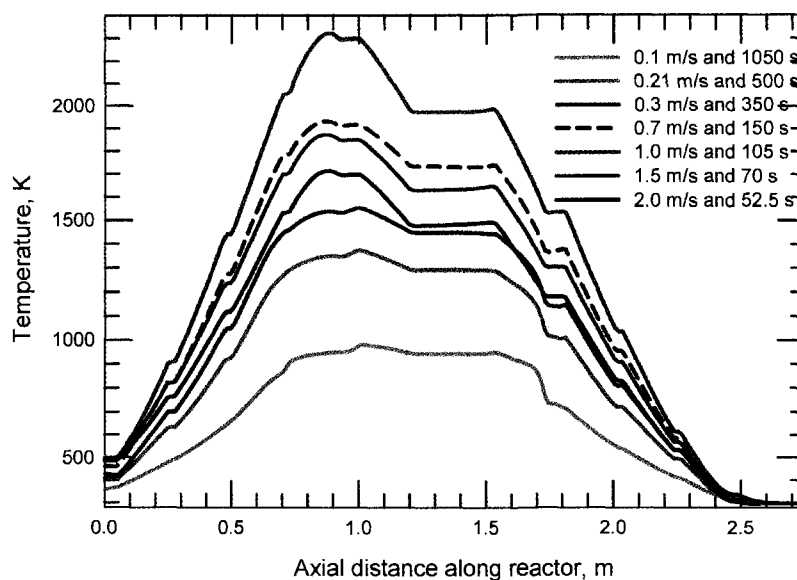


Figure 9.14: Centerline temperature profile after 60 cycles for different combinations of velocity and switch time on monolith reactor.

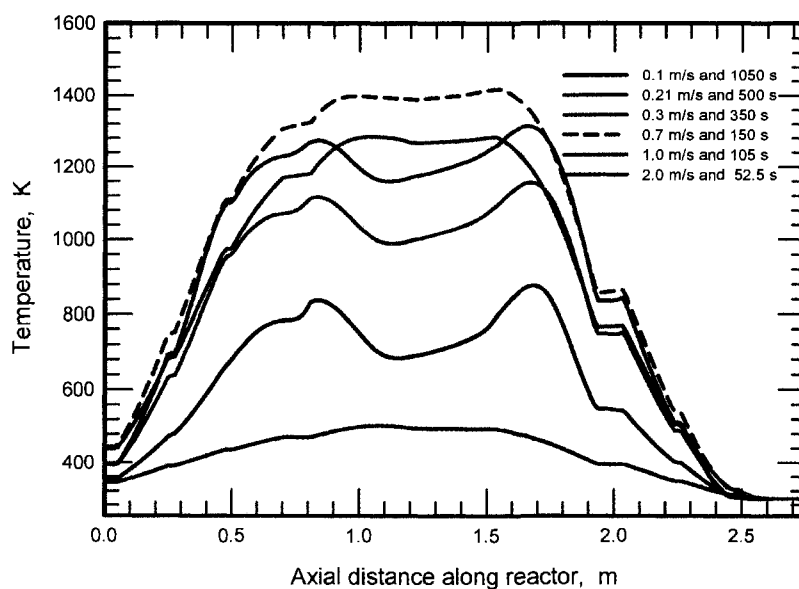


Figure 9.15: Centerline temperature profile after 60 cycles for different combinations of velocity and switch time on packed bed reactor.

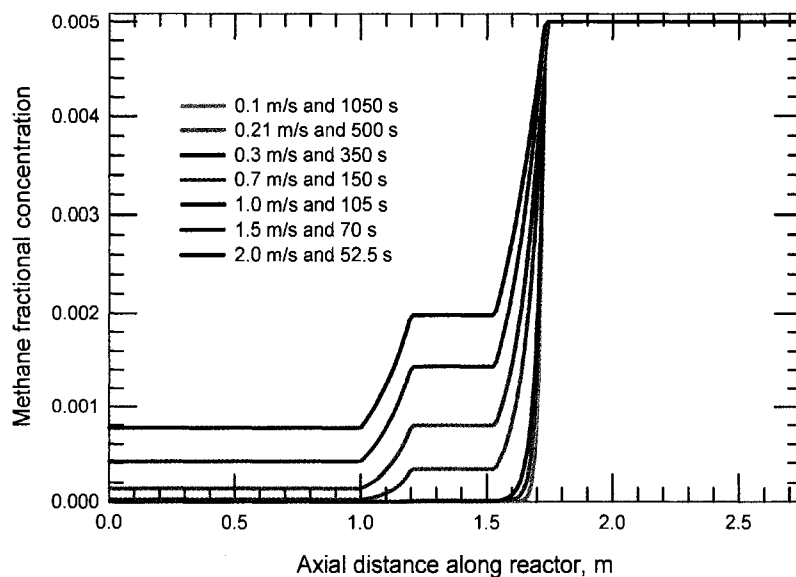


Figure 9.16: Centerline methane profile after 60 cycles for different combinations of velocity and switch time on monolith reactor.

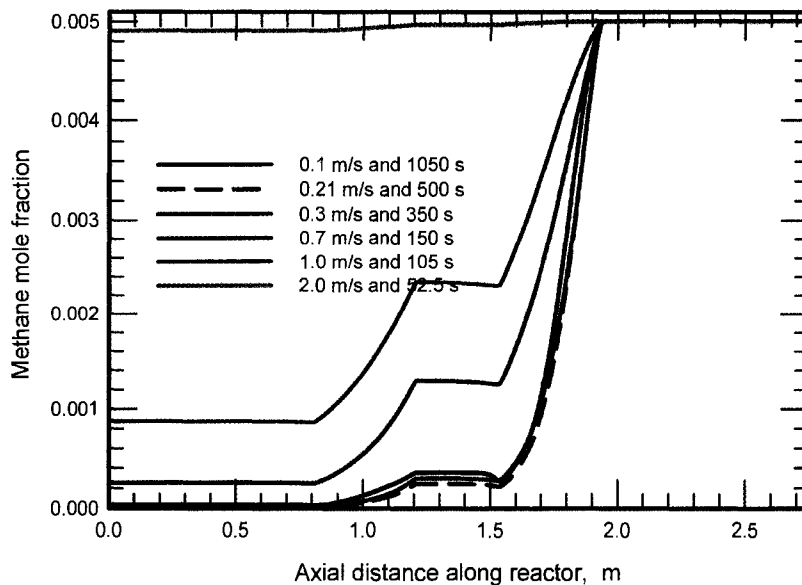


Figure 9.17: Centerline methane profile after 60 cycles for different combinations of velocity and switch time on packed bed reactor.

started to drop. Figure 9.16 show that still high conversion can be achieved in the Pd monolith catalyst with higher superficial velocity. Achieving complete conversion is the goal, but reactor temperature raising above 1000 K is against thermal stability of the catalyst, although heat extraction can be used to control the temperature, particularly for the palladium catalyst. Thus the CFRR with Pd catalyst can either operate at lower superficial velocity which also can achieve complete combustion, as shown in Figure 9.16 that when superficial velocity below 0.7 m/s is used the complete combustion is guaranteed, or at moderate superficial velocity with short switch time.

Changing the switch time alone at a constant velocity will result in more movement of the temperature front in the reactor. The effect is shown in Figure 9.18 for a range of cycle times, at a constant superficial velocity of 0.21 m/s. Longer cycle times lead to higher outlet temperatures, and thus energy loss from the system. Ultimately, longer switch times will lead to extinction of the reaction. With short switch time, the fluid stream was leaving the reactor at relatively lower temperature and most of the heat was retained in the reactor, as shown in Figure 9.18.

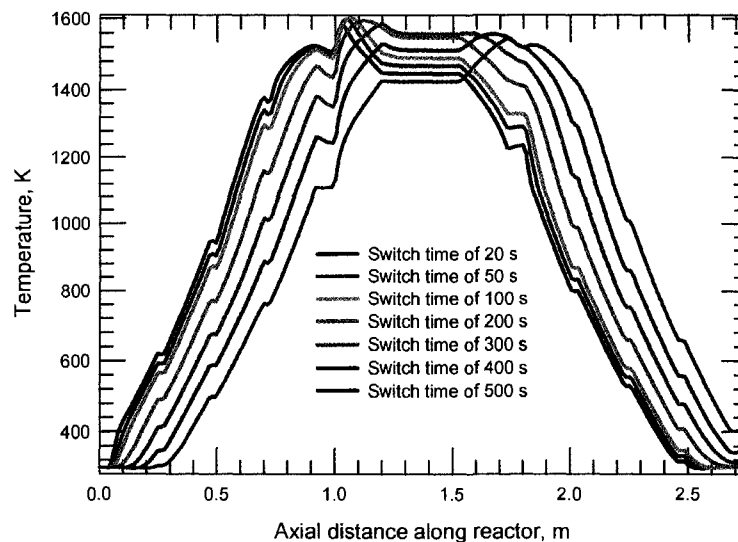


Figure 9.18: Centerline temperature profile at end of cycle 60 for different cycle time, in Pd monolith. The larger cycle time shows more motion of the profile.

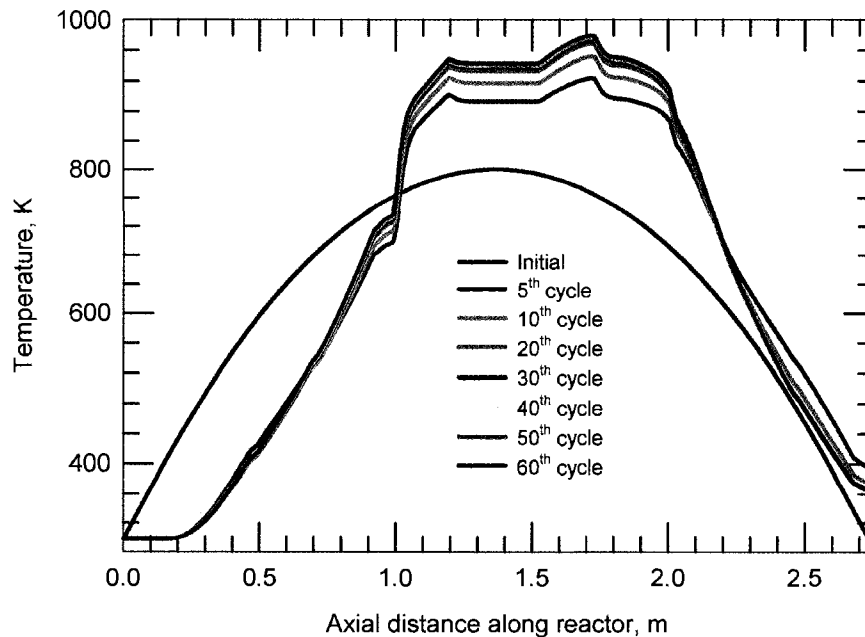


Figure 9.19: Centerline temperature profile at the mid-point for operation using superficial velocity of 0.1 m/s and switch time of 1050 s, in Pd monolith . Stationary state was attained after 12 cycles.

With lower superficial velocity, the stationary state can be attained in shorter time, and at low superficial velocity there is decreased amounts of methane fed to the reactor. For example, Figure 9.19 shows that with the lower superficial velocity of 0.1 m/s in the Pd monolith P2 the stationary state was reached after fewer than 15 cycles. Figure 9.20 shows that with higher superficial velocity, the stationary state is even not been approached after more than 59 cycles of operation. At the same time Figures 9.19 and 9.20 show that the higher superficial velocity case left the reactor at higher temperature, meaning a loss of useful energy. Though the higher temperature made it possible to attain the highest temperature compared to low superficial velocity case, in a practical point of view that may create another big problem on catalyst thermal stability. A heat extraction strategy can be used to control the higher reactor temperature to produce useful energy.

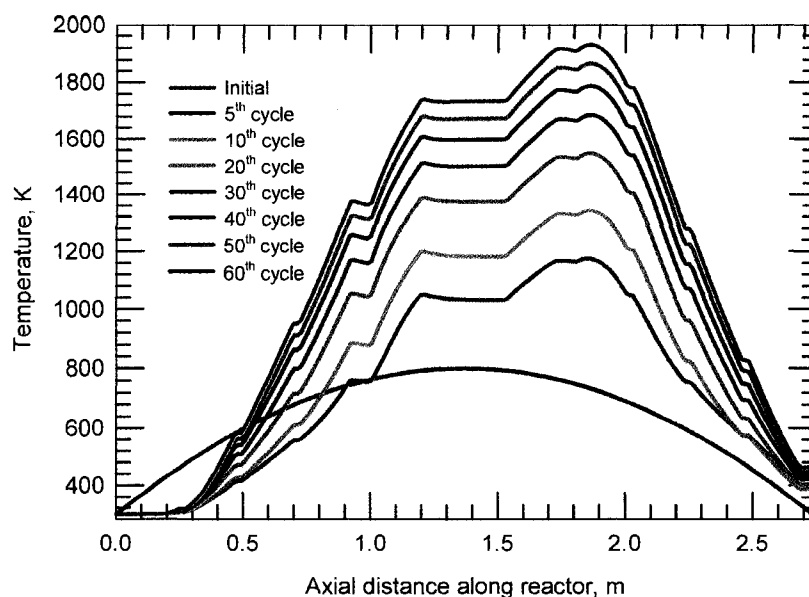


Figure 9.20: Centerline temperature profile at the mid-point of operation using superficial velocity of 0.7 m/s and switch time of 150 s, in Pd monolith. The stationary state was not attained even with 60 cycles.

9.3.3 Thermal properties

Heat transfer phenomena is an important factor influencing the stability of the CFRR operation. Therefore, material thermal properties of inert, reactor and catalyst are determining factors for operational stability and the amount of energy to be withdrawn from the system for external use. In this section the extent and limitation of material thermal properties was investigated as follows.

Catalyst thermal stability: The thermal stability of catalyst was discussed in Chapters 6 and 8. For this work the focus is a palladium catalyst and its operational limitation is around 1000 K. In that case the operation of CFRR should operate below this limiting temperature otherwise the catalyst will be damaged.

Thermal mass: In the earlier experimental investigations by Kushwaha et al. (2004; 2005), it was found that the higher thermal mass (product of density and

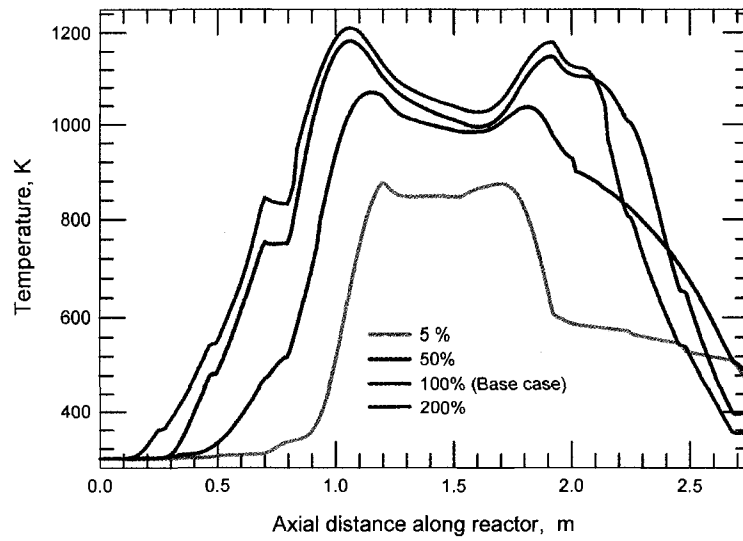


Figure 9.21: The centerline axial temperature profile at the end of cycle 60 (forward) for different thermal mass. For packed bed, the highest temperature and the least movement are seen with the highest thermal mass.

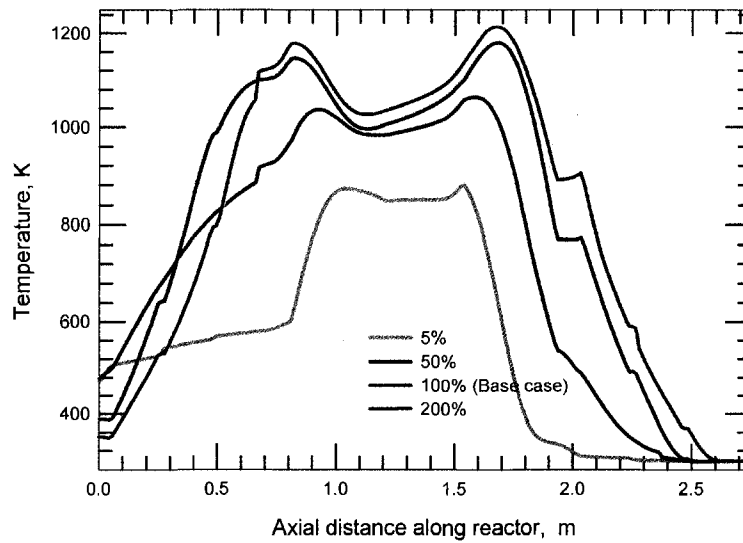


Figure 9.22: The centerline axial temperature profile at the end of cycle 60 (reverse) for different thermal mass. For packed bed, the highest temperature and the least movement are seen with the highest thermal mass.

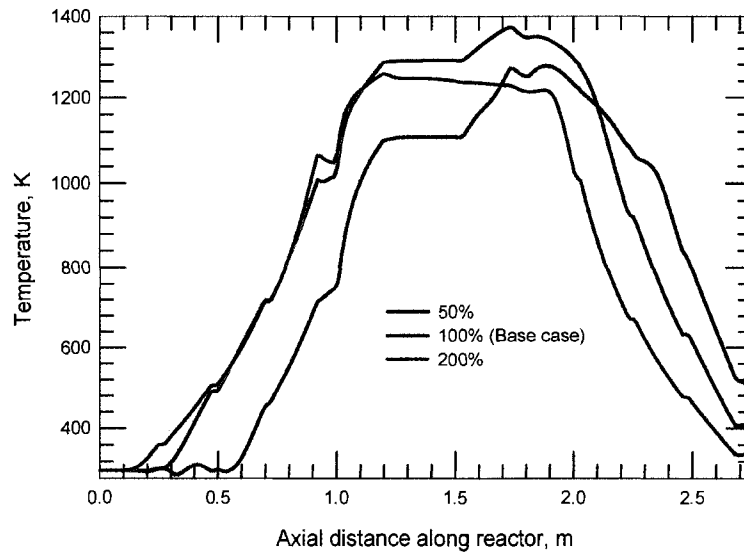


Figure 9.23: The centerline axial temperature profile at the end of cycle 60 (forward) for different thermal mass. For Pd monolith P2, the highest temperature and the least movement are seen with the highest thermal mass.

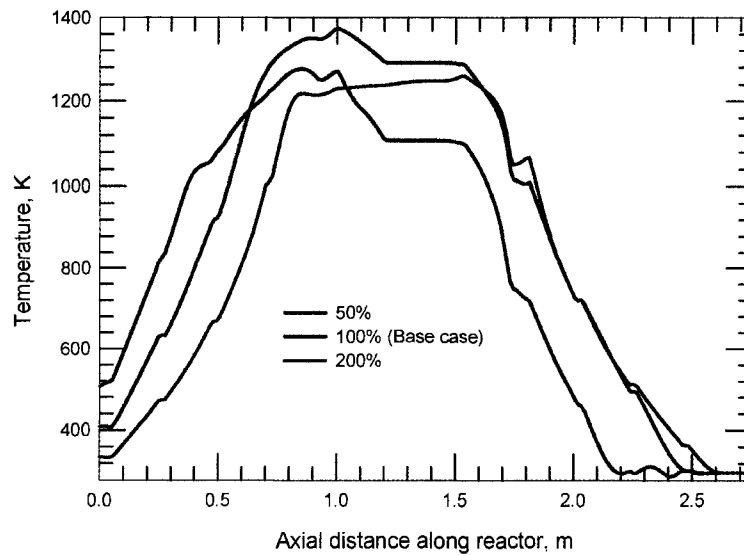


Figure 9.24: The centerline axial temperature profile at the end of cycle 60 (reverse) for different thermal mass. For Pd monolith P2, the stable temperature and the least movement are seen with the highest thermal mass.

heat capacity) inert sections gave less movement in the axial temperature profiles for a given cycle time. This observation is consistent with intuition; however, in the experimental runs it was not possible to change only a single variable. In this work thermal mass comparison for the axial temperature profiles obtained after 60 full cycles with different thermal mass only was done. It should be pointed out that a stationary state was not achieved at 60 cycles. Indeed, for these conditions, the stationary state occurs at a temperature higher than the safe operating region for the system. For a series of experiments, the thermal mass was set to a given percentage of the base case. Figure 9.21 shows the centerline axial temperature profiles obtained in the middle and at the end of cycle 60. It is clear that the highest temperatures are achieved with the highest thermal mass. This result is in line with expectations. It is evident that for low thermal mass, the outlet temperature of the gas increases, resulting in energy loss from the system, and hence a lower temperature. Further, the movement of the temperature wave during a cycle is the lowest with the highest thermal mass. It is clear that this variable is one of the most important, from a standpoint of reactor stability.

Thermal conductivity: The other principal thermal property is the thermal conductivity of the solid. The key effect of an increase in thermal conductivity is to increase the rate of heat transport through the solid phase. This effect could theoretically be beneficial in smoothing temperature gradients. It was noted by Kushwaha (2003) that metal monoliths gave quite different behaviour compared to ceramic ones, although as stated above, this difference could be caused by a number of property changes. It has been pointed out that in the flow direction in a monolith the solid thermal conductivity plays a minor role in axial transport. Figure 9.25 shows the result after 60 cycles of changing only the thermal conductivity over a wide range. It appears that the lower thermal conductivity gives a slightly higher centerline temperature, although overall the effect is not that large. The main effect is to promote increased radial conduction, which is the result of heat transfer into the insulation section. These results indicate that the role of the thermal conductivity, within physically attainable bounds, should not be that significant.

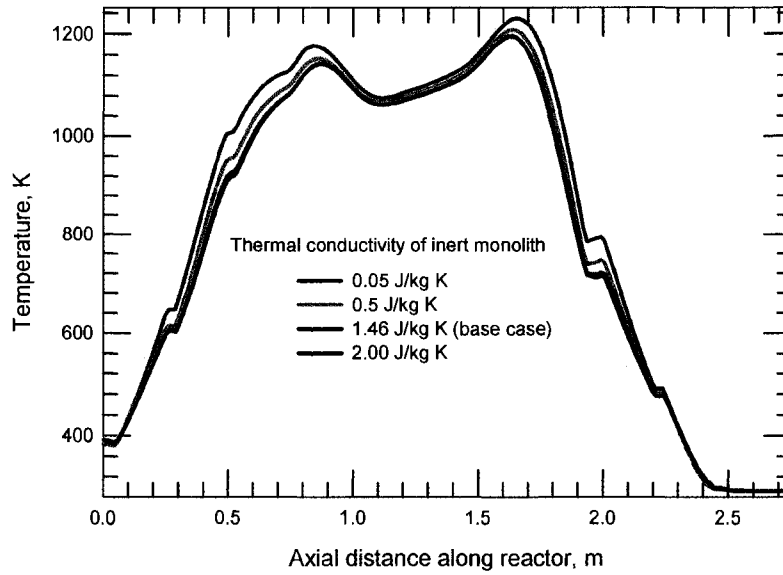


Figure 9.25: Centerline axial temperature profile for different thermal conductivities at the end of cycle 60. The effect is relatively minor in a packed bed.

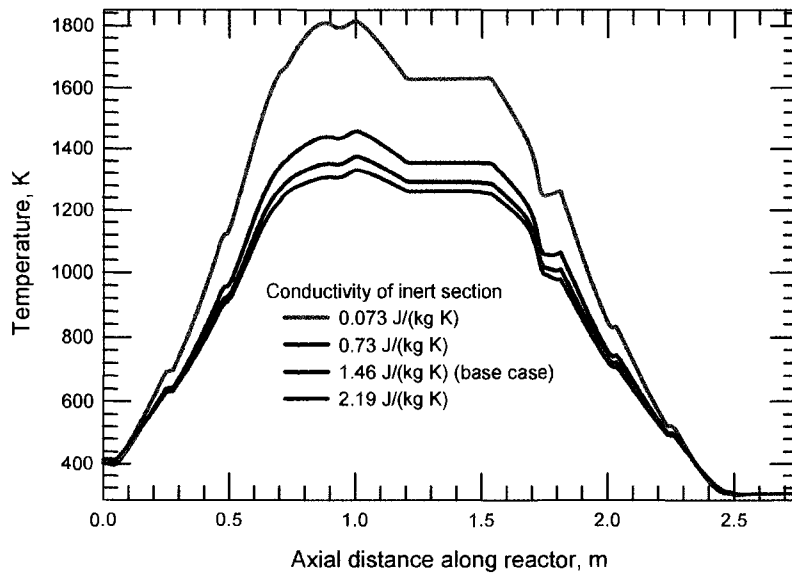


Figure 9.26: Centerline axial temperature profile for different thermal conductivities at the end of cycle 60. For reactor with Pd monolith P2, the effect is relatively minor.

This is especially important as a contribution to controlling heat transfer effects to and from the insulation.

Wall materials: Wall material, in particular its heat transfer phenomena, can not be neglected for smaller diameter reactors. This work analysed the effect of changing thermal capacities of reactor wall materials. Figure 9.27 shows that as thermal heat capacities of the wall decreases the fluid heat increases.

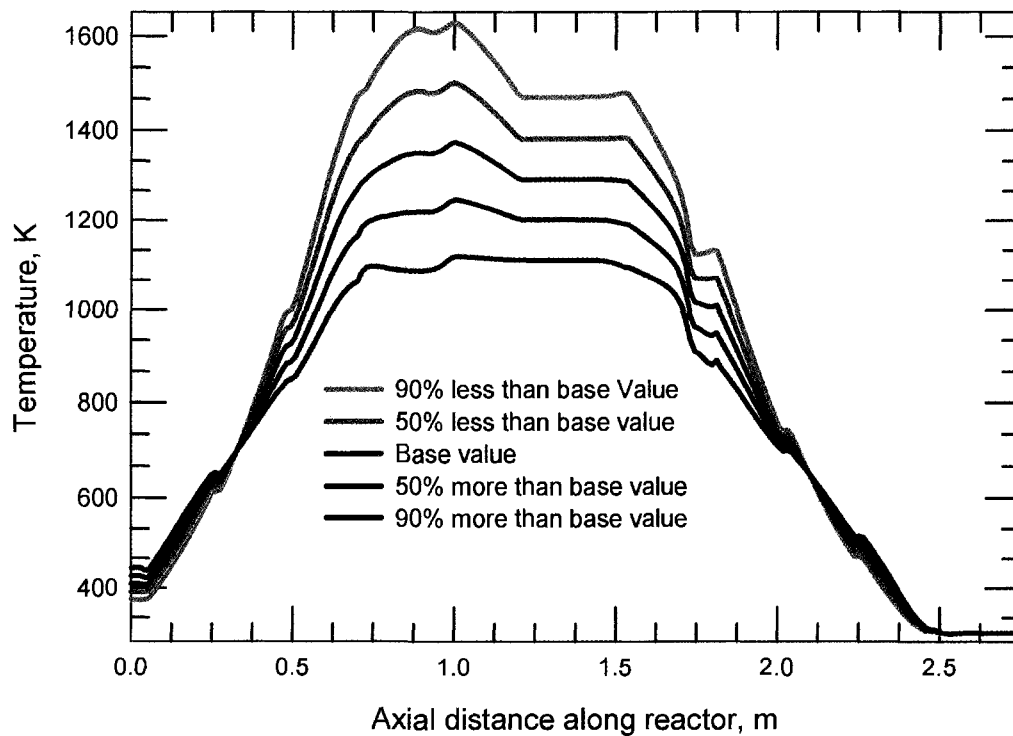


Figure 9.27: Axial temperature profiles after 60 cycles at varying values of wall thermal capacity, in reactor with Pd monolith P2.

9.3.4 Reactor geometry

Possibly the most important variable from a scale up standpoint is the effect of reactor geometry. Two important geometrical effects were considered; insulation thickness and reactor diameter.

Insulation thickness: It has previously been noted by Salomons et al. (2004; 2003) and Kushwaha et al. (2004; 2005), that the insulation plays a significant role in the reactor operation. The insulation adds thermal mass to the system, and during operation energy is transferred to and from the insulation. The effect of the insulation can be shown independently by adjusting the insulation thickness from 0.28 m insulation thickness as a base case. Figure 9.29 and 9.28 show the result of increasing the insulation thickness from 50 mm to 1000 mm in catalytic flow reversal reactor of reactor diameter of 200 mm, for packed bed and Pd monolith reactors respectively. For a thickness larger than 20 cm, no significant difference in the temperature profile was observed using the base case operating conditions. The thickness beyond which no change is observed is related ultimately to the heat transfer rate and the thermal properties of the insulation, which, in terms of a transient heat transfer analysis, are determined by the values of the Biot number and Fourier modulus.

Methane conversion in the Pd monolith was not affected by insulation thickness but with small thickness of insulation more heat energy will be lost to the surroundings thus causing the temperature in the reactor to drop even if complete combustion can be achieved. In the packed bed case, conversion and insulation thickness are closely related (see Figure 9.30), as mentioned earlier, reaction in the packed bed is distributed all over the bed, which is why the packed bed is victim to heat loss as heat is generated over the wide area.

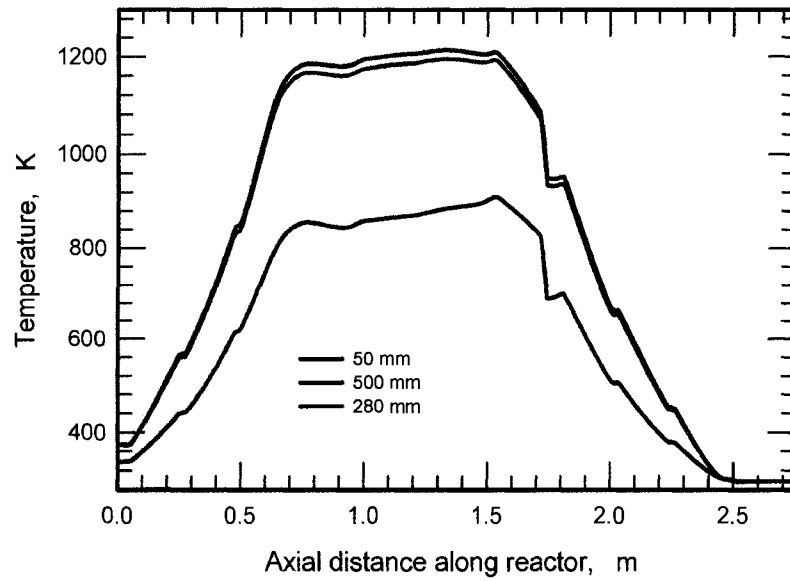


Figure 9.28: Axial temperature profiles after 60 cycles at various insulation thickness and constant reactor diameter. Above 200 mm thickness the effect is insignificant.

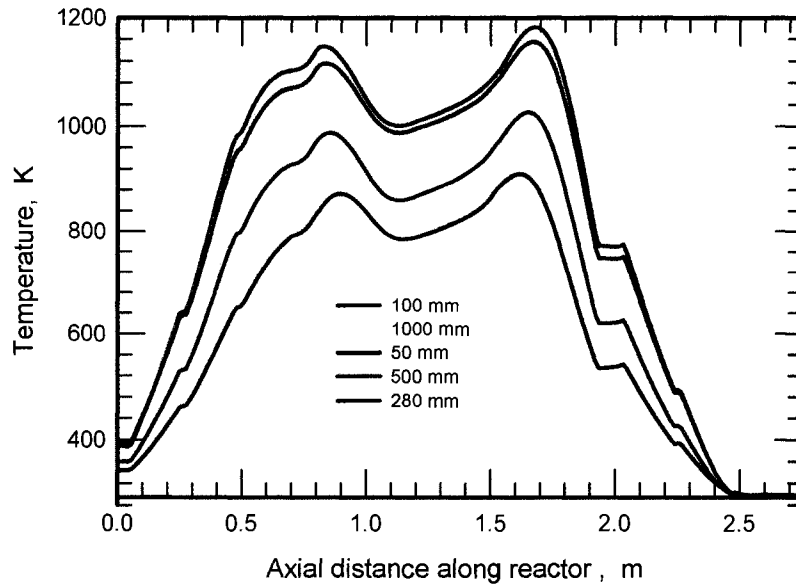


Figure 9.29: Axial temperature profiles after 60 cycles at various insulation thickness and constant reactor diameter. Above 200 mm thickness the effect is insignificant.

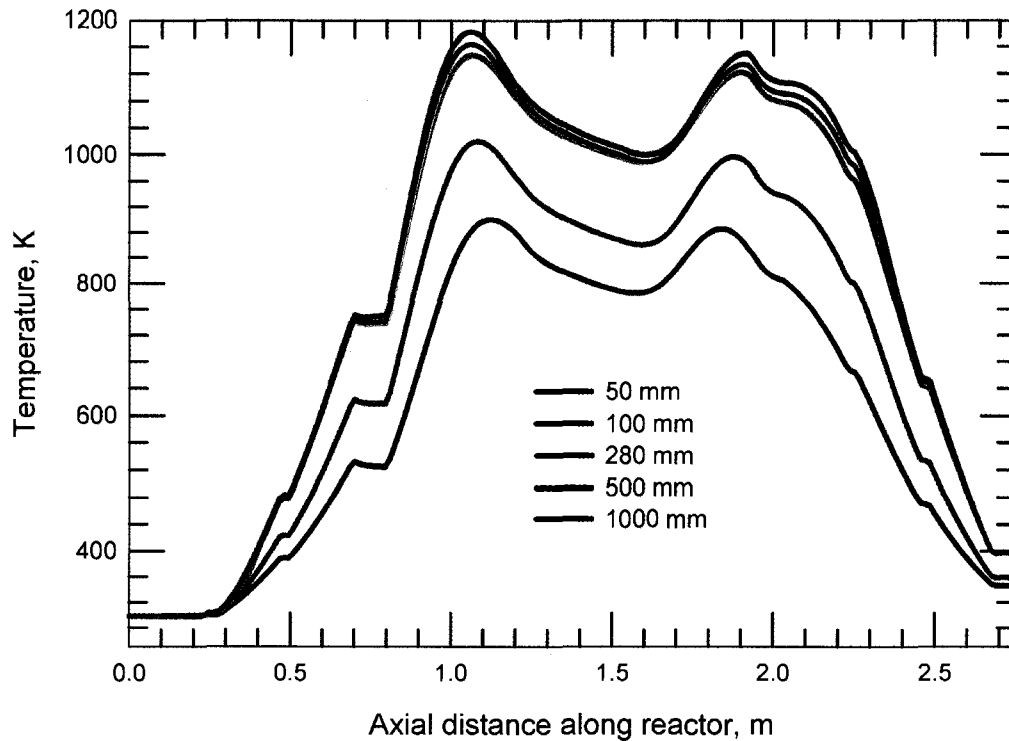


Figure 9.30: Axial methane profiles after 60 cycles at various insulation thickness and constant reactor diameter. Above 20 cm thickness the effect is insignificant.

Reactor diameter: Figure 9.31 shows the effect of changing reactor diameter using a constant insulation thickness. The axial centerline temperatures after 20 cycles are higher with larger reactor diameter by a significant amount. This result points to a significant wall effect, which is not surprising. As the reactor diameter increases, the radial temperature profiles become flatter, and the insulation effect diminishes. This in turn leads to higher centerline temperatures. These results must be included when scale-up is to be considered. Also it should be pointed out that based on estimates of gas flow rate from the applications in the oil and natural gas sector, reactor diameters less than one meter can be expected, hence careful attention must be paid to the insulation thermal properties and thickness.

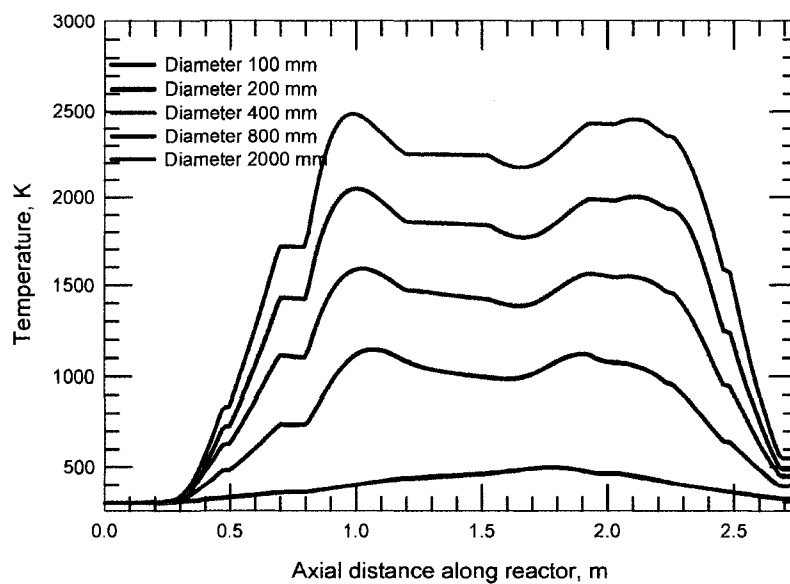


Figure 9.31: Axial temperature profiles after 60 cycles at various reactor diameter in packed bed.

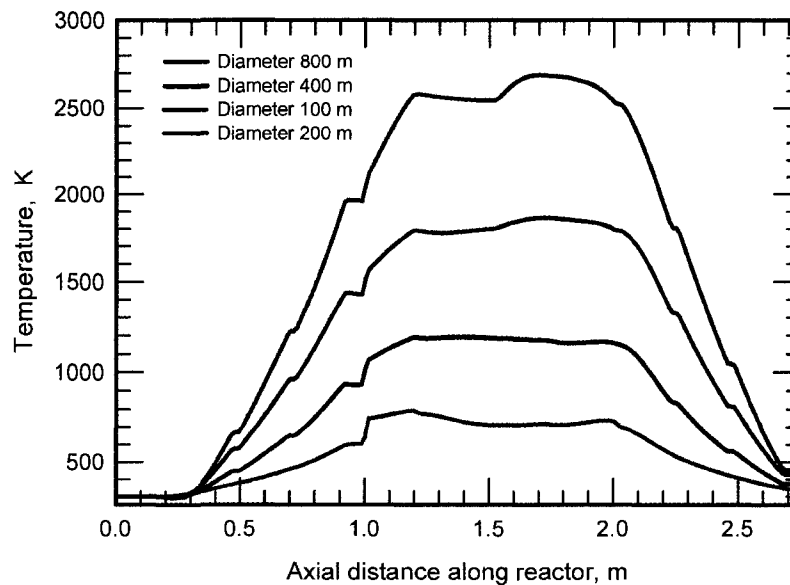


Figure 9.32: Axial temperature profiles after 60 cycles at various reactor diameter in reactor with Pd monolith P2.

9.3.5 Initial condition

The effect of initial condition on the operation of CFRR is investigated, in this work the investigation is limited to the initial temperature and methane concentration of the reactor. This investigation will help assess the influence of CFRR start-up on its operation. The results, see Figures 9.33 and 9.34, show that the initial temperature profile has little effect on the reactor operation. The trend of temperature progression in the reactor is independent of the initial temperature profile used, but the higher the initial temperature makes it quicker for the reactor temperature to attain the maximum temperature. Starting with any arbitrary profile, the final centreline profile looks the same. It is sufficient that the initial profile can start the ignition in the reactor. The results shown are for the Pd monolith P2, but also the packed bed showed the same general trend.

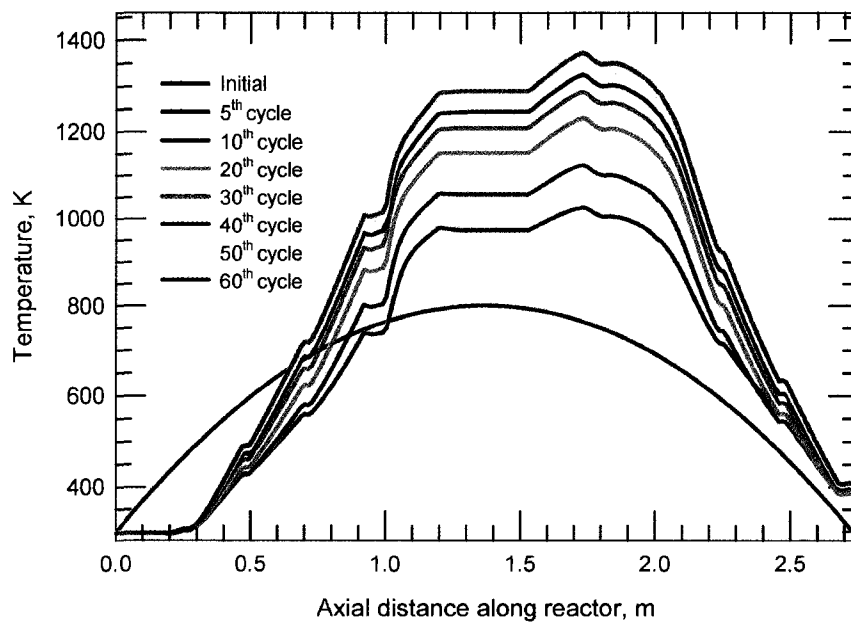


Figure 9.33: Axial temperature profiles progression starting from arbitrary initial temperature profile in reactor with Pd monolith P2..

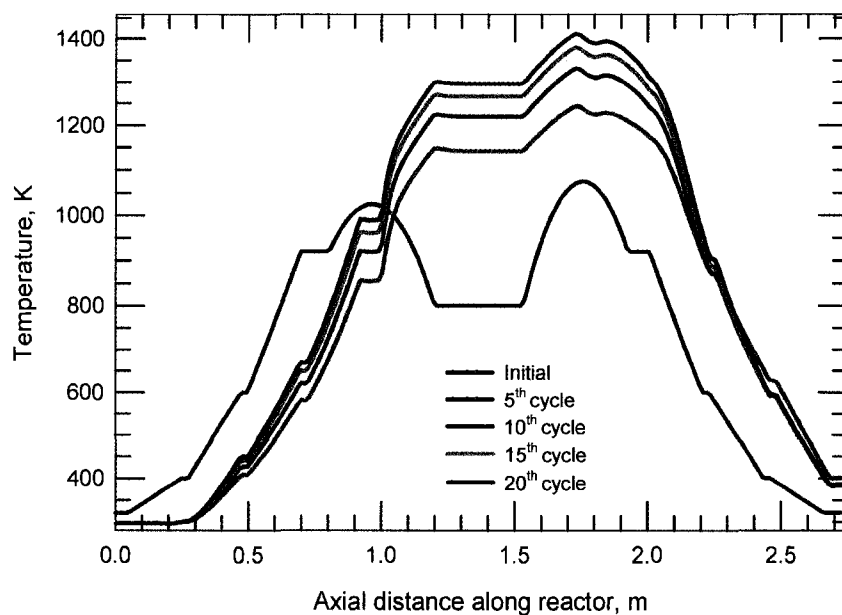


Figure 9.34: Axial temperature profiles progression starting from arbitrary initial temperature profile, in reactor with Pd monolith P2.

9.4 Discussion

It has been observed that systems such as the CFRR demonstrate intricate dynamic behaviour, with a complex inter-relationship among the operating and design variables. Development of optimization and control strategies must take such relationships into account, and a certain amount of customization towards a particular application is expected. The primary scaling parameter being the reactor diameter, special care must be paid to this variable. For large units, such as those used in coal mine applications, it is expected that the wall effects will be minimal; however, for smaller units in other applications, the two dimensional behaviour of the reactor cannot be ignored. Reactor wall and inert materials can influence reactor performance and thus determine the reactor stability in terms of general operation and scaling up of the reactor. Thermal properties of the reactor wall and inert materials have a particular major part to play. Velocity and switch time should be selected carefully, since their influence in reactor dynamics are very important.

Chapter 10

Conclusions and recommendations

Global warming is one of the most important environmental issues and poses exceptional challenges to the global environmental community. Scientists have suggested that global warming causes serious global climate changes and will have a great impact on human well being, and further suggested that human related activities are one of the main driving factors in global warming. It is a well known fact that atmospheric GHG have grown significantly since pre-industrial-times. These trends are largely attributed to human activities and mostly the usage of fossil fuel; the current, main challenge is to find and implement best available technologies and practices to minimize the GHG emission and possibly create an added value in the process.

The work presented focuses primarily on development of a suitable mitigation method for fugitive methane emissions occurring in the oil and natural gas sector. It was suggested that catalytic combustion is a suitable option to be used to combat this kind of emissions. CFRR technology was recommended to utilize the capability of this technology, in which a lean mixture of methane in atmospheric air (which is the main characteristic of fugitive methane emission) can be oxidized without need of an auxiliary fuel. There is also the possibility of tapping energy generated in the reactor which can offset energy demands required within the facility. To arrive to the solution this study was conducted in three major stages, which are: fugitive emissions capture, evaluation of catalyst activity and CFRR reactor analysis. The

main observation, results and conclusions of each stage are summarized in the following sections.

10.1 Conclusion

10.1.1 Fugitive emission capture

Fugitive methane emissions in the oil and natural gas sector are a major contributor to GHG emissions. At the same time, they are potentially much easier to reduce or eliminate than other GHG such as carbon dioxide, which is very expensive to capture and sequester using current technology. Fugitive emissions in natural gas compressor stations can potentially be collected using the building itself. Possibly the most important variable that affects the capture rate is the opening of the large doors. The large doors are often opened in the summer to keep the building cool. Using controlled extraction rates, typical emission rates can lead to an acceptable feed for a reverse flow catalytic reactor. This effluent can also be potentially combined with instrument vent streams, or the engine exhaust stream (which also contains significant methane and carbon monoxide), to increase the reduction of GHG emissions.

10.1.2 Catalytic activity

Important experimental observations from the catalytic combustion experiments using the commercial palladium based catalysts are: *Existence of hysteresis*: Hysteresis was observed across the range of methane concentration used, also with different levels of oxygen concentrations. Even with the presence of carbon monoxide, carbon dioxide and hydrogen the hysteresis behaviour persisted, but the presence of water seems to eliminate the occurrence of hysteresis behaviour as well as it inhibit the reaction rate.

Pretreatment: Pretreating the catalysts with reducing media (in this case 7% H₂ was used) promotes the reaction rate. The experimental results showed that pretreated cases were more active than non-pretreated cases. Another observation

on pretreatment is that the concentration of oxygen seems to influence the effect of pretreatment. As oxygen concentration increases, the difference in activity between pretreated and non-pretreated cases tends to disappear and this can be a sign of elimination of pretreatment effect at higher oxygen concentration. After some time of operation, the benefit of pretreatment disappears.

Reaction inhibition: Two types of inhibition were observed in the experiments; the first one is the self inhibition of methane itself. The experimental results showed that as methane concentration increases, the reaction rate decreases and requires a higher temperature to achieve complete combustion. The second type of inhibition is due to impurities in the feed or reaction products. Particularly, water showed a strong inhibition effect.

Surface Reaction Mechanism: Observations of hysteresis behaviour signify that the surface reaction mechanism is non-linear and complex. Using a detailed multi-step surface mechanism is the best way to capture the real chemistry and physics of surface reaction. Many have tried directly to translate the well developed multi-step mechanism of methane combustion on platinum based catalyst to palladium based catalyst. In this work, the platinum based mechanism was used to fit the experimental data and proved to be a failure and signifies that what is occurring on the palladium surface is quite different from the platinum surface. Thus, an independent detailed mechanism for palladium based catalysts is required. An empirical model of the LHHW form was able to fit the data successfully.

10.1.3 Performance of CFRR

Numerical modelling was used to evaluate the performance of the catalytic flow reversal reactor, and several important conclusions were made.

Catalyst activity: The Pd catalyst was seen to have a much higher activity than the non-noble metal catalyst. It was seen that with the Pd catalyst supported on a monolith, the position of the catalyst within the reactor had a strong influence on the axial temperature profiles. It is suggested that optimal performance is achieved when the catalyst is closest to the centre of the reactor. At typical reactor

temperatures achieved in the CFRR the reaction is strongly limited by the internal mass transfer.

Operating characteristics: The thickness of the insulation is an important parameter affecting the CFRR operation, especially at smaller reactor diameters. The insulation adds thermal mass to the system, which provides a heat sink and source during operation. The effect is diminished as the reactor diameter increases, and overall the wall effects are small at large reactor diameter.

The combination of velocity and switch time are important, and must be chosen with care to ensure complete conversion. the thermal mass of the reactor internals also plays an important role in the movement of the temperature profiles in the reactor.

10.2 Recommendation and future work

The current study has added some new information on the unusual behaviour of supported Pd in combustion of methane, fugitive emission capture and CFRR analysis. Overall the proposed approach for lean methane combustion looks viable, and testing should proceed at the pilot scale and field trial. Specifically, the monolith catalyst should be tested on the 200 mm diameter CFRR located in Vareennes. This validation is important to verify the results of the modelling studies. Once the pilot scale work has been completed, a trial project should be performed on a selected compressor station site.

There were also several interesting phenomena observed during the catalyst activity studies. In particular, the inhibition of the reaction by the methane, the catalyst activation by hydrogen and the behaviour with hydrogen present in the feed are all worthy of investigation. It is also clear that the development of a reaction mechanism for methane combustion on Pd needs to be investigated.

References

Aghalayam, P., Park, Y. K., Fernandes, N., Papavassiliou, V., Mhadeshwar, A. B., and Vlachos, D. G. (2003). A C1 mechanism for methane oxidation on platinum. *Journal of Catalysis*, 213(1):23–38.

Alberta Environment (2007). Alberta environment summary report on 2005 greenhouse gas emissions. Technical report, Alberta Environment.

Allocca, C., Chen, Q., and Glicksman, L. (2003). Design analysis of single-sided natural ventilation. *Energy and Building*, 35:785 – 795.

Anderson, D. (June,1996). Energy and the environment: Technical and economic possibilities. *Finance & Development World Bank*.

Araya, P., Guerrero, S., Robertson, J., and Gracia, F. (2005). Methane combustion over Pd/SiO₂ catalysts with different degrees of hydrophobicity. *Applied Catalysis A: General*, 283(1-2):225–233.

Aris, R. (1956). On the dispersion of a solute in a fluid flowing through a tube. In Aris, R., editor, *Proceedings of Royal Society I*, volume A235.

Au-Yeung, D., Bell, A., and Iglesia, E. (1999a). The dynamics of oxygen exchange with zirconia- supported PdO. *Catalysis*, 185:213–218.

Au-Yeung, D., Chen, K., Bell, A., and Iglesia, E. (1999b). Isotopic studies of methane oxidation pathways on PdO catalyst. *Catalysis*, 188:132–139.

- Aubé, F. and Sapoundjiev, H. (2000). Mathematical model and numerical simulations of catalytic flow reversal reactors for industrial applications. *Computers & Chemical Engineering*, 24(12):2623–2632.
- Audet, C. and Dennis, J. (2003). Analysis of generalized pattern searches. *SIAM Journal*, 13:889 – 903.
- Awbi, H. B. (1989). Application of computational fluid dynamics in room ventilation. *Building and Environment*, 24(1):73–84.
- Baldwin, T. R. and Burch, R. (1990). Catalytic combustion of methane over supported palladium catalysts : I. Alumina supported catalysts. *Applied Catalysis*, 66(1):337–358.
- Beguín, B., Garbowski, E., and Primet, M. (1991). Stabilization of alumina by addition of lanthanum. *Applied Catalysis*, 75(1):119 – 132.
- Behrendt, F., Deutschmann, O., and Warnatz, J. (1995). Simulation and sensitivity analysis of the heterogeneous oxidation of methane on platinum foil. *Journal of Vacuum Science and Technical Application*, 13(3):1373 – 1377.
- Belohlav, Z., Zamosny, P., Kluson, P., and Volf, J. (1997). Application of random-search algorithm for regression analysis of catalytic hydrogenations. *Canadian Journal of Chemical Engineering*, 75:735 – 742.
- Bhatia, S. (1991). Analysis of catalytic reactor operation with periodic flow reversal. *Chem. Eng. Sci.*, 46(1):361–367.
- Bird, R. B., Stewart, W. E., and Lightfoot, E. N. (2001). *Transport Phenomena*. New York: Wiley.
- Blanks, R. F., Wittrig, T. S., and Peterson, D. A. (1990). Bidirectional adiabatic synthesis gas generator. *Chemical Engineering Science*, 45(8):2407–2413.
- Bobrova, L. N., Slavinskaya, E. M., Noskov, A. S., , and Matros, Y. S. (1988). Unsteady-state performance of NO_x catalytic reduction by NH₃. *Reaction Kinetics and Catalysis Letters*, 37(2):267–272.

- Bond, T. C., Noguchi, R. A., Chou, C.-P., Mongia, R. K., Chen, J., and Dibble, R. W. (1996). Catalytic oxidation of natural gas over supported platinum: Flow reactor experiments and detailed numerical modeling. *Twenty-sixth Symposium (International) on Combustion/The Combustion Institute*, pages 1771–1778.
- Boreskov, G. and Matros, Y. (1984). Fixed catalyst bed reactors operated in steady and unsteady state conditions. *Recent Advances in the Engineering of Chemically Reacting Systems*, pages 142 – 155.
- Boreskov, G., Matros, Y., Bunimovich, G., and Ivanov, A. (1982). Catalytic processes under non-steady state conditions, II: Switching the direction for the feed of the reaction mixture to the catalyst bed. experimental results. *Kinetikai Kataliz*, 23:402–406.
- Boreskov, G. and Matros, Y. S. (1983). Unsteady state performance of heterogeneous catalytic reactions. *Catalysis Review Science Engineering*, 24(4):551 – 590.
- Bräuer, H. W. and Fetting, F. (1966). Stofftransport bei wandreaktion im einlaufgebiet eines strömungsrohres. *Chemie Ingenieur Technik - CIT*, 38(1):30 – 35.
- Briot, P. and Primet, M. (1991). Catalytic oxidation of methane over palladium supported on alumina : Effect of aging under reactants. *Applied Catalysis*, 68(1):301–314.
- Bui, P., Vlachos, D., and Westmoreland, P. (1997). Catalytic ignition of methane/oxygen mixtures over platinum surface: comparison of detailed simulation and experiments. *Surface Science*, 385:L1029–L1034.
- Bunivovich, G., Strots, V., and Goldman, O. (1990). Theory and industrial application of SO₂ oxidation reverse-process for sulfur acid production. *Unsteady State Processes in Catalysis, VPS BV, Utrecht*.
- Burch, R., Urbano, F. J., and Loader, P. K. (1995). Methane combustion over palladium catalysts: The effect of carbon dioxide and water on activity. *Applied Catalysis A: General*, 123(1):173–184.

- Burns, J. and Cliff, E., editors (1998). *Optimization using surrogate objectives on a helicopter test example, in Optimal Design*. SIAM, Philadelphia.
- Carberry, J. J. (1976). *Chemical and Catalytic reaction engineering*. McGraw Hill, Toronto.
- Cardoso, M. F., Salcedo, R. L., and Azevedo, S. F. (1996). The simplex simulated annealing approach to continuous non-linear optimization. *Computers and Chemical Engineering*, 20:1065 – 1080.
- Chen, K., Xie, S., Bell, A., and Iglesia, E. (2001). Structure and properties of oxidative dehydrogenation catalysts based on $\text{MoO}_3/\text{Al}_2\text{O}_3$. *Journal of Catalysis*, 198:232 – 243.
- Chen, M., Aleixo, J., Williams, S., Leprince, T., and Yong, Y. (2000). CFD Modelling of 3-way catalytic converter with detailed catalytic surface reaction mechanism. *SAE Sp*, pages 2271–2286.
- Chen, Q. (1996). Prediction of room air motion by reynolds-stress models. *Building and Environment*, 31:233 – 244.
- Chen, Q. and Xu, W. (1998). A zero-equation turbulence model for indoor airflow simulation. *Energy and Buildings*, 28(2):137–144.
- Chen, X., Li, C., and Silveston, P. (2003). Modeling of a reverse flow reactor for methanol synthesis. *Chinese Journal of Chemical Engineering*, 11(1):9–14.
- Chou, C.-P., Chen, J.-Y., Evans, G. H., and Winters, W. S. (2000). Numerical studies of methane catalytic combustion inside a monolith honeycomb reactor using multi-step surface reactions. *Combustion Science and Technology*, 150(1):27–57.
- Choudhary, T. V., Banerjee, S., and Choudhary, V. R. (2002). Catalysts for combustion of methane and lower alkanes. *Applied Catalysis A: General*, 234(1-2):1–23.

- Choudhary, V. and Rane, V. (1992). Pulse microreactor studies on conversion of methane, ethane, and ethylene over rare earth oxides in the absence and presence of free oxygen. *Journal of Catalysis*, 135(1):310–316.
- Church, J., Cant, N., and Trimm, D. (1993). Stabilisation of aluminas by rare and alkaline earth ions. *Applied Catalysis A: General*, 101(1):105–116.
- Ciuparu, D., Altman, E., and Pfefferle, L. (2001). Contribution of lattice oxygen in methane combustion over PdO-based catalysts. *Catalysis*, 234:64–74.
- Ciuparu, D., Lyubovsky, M., Altman, E., Pfefferle, L. D., and Datye, A. (2002). Catalytic combustion of methane over palladium based catalysts. *Catalysis Review*, 44(4):593–649.
- Ciuparu, D., Perkins, E., and Pfefferle, L. D. (2003). In situ DR-FTIR investigation of surface hydroxyls on γ -Al₂O₃ supported PdO catalysts during methane combustion. *Applied catalysis A: General*.
- Ciuparu, D. and Pfefferle, L. (2001). Support and water effects on palladium based methane combustion catalysts. *Applied Catalysis A: General*, 209(1-2):415–428.
- Cottrell, F. G. (1938). Purifying gases and apparatus therefore. *U.S. Patent 2*, 121:722.
- Crutzen, P. and Zimmermann, P. (1991). The changing photochemistry of the troposphere. *Tellus*, 43(A/B):136 – 151.
- Cullis, C. and Willatt, B. (1983). Oxidation of methane over supported precious metal catalysts. *Journal of Catalysis*, 83(2):267 – 285.
- Cullis, C. and Willatt, B. (1984). The inhibition of hydrocarbon oxidation over supported precious metal catalysts. *Journal of Catalysis*, 86(1):187–200.
- Datye, A. K., Bravo, J., Nelson, T. R., Atanasova, P., Lyubovsky, M., and Pfefferle, L. (2000). Catalyst microstructure and methane oxidation reactivity during

- Pd \rightleftharpoons PdO transformation on alumina supports. *Applied Catalysis A: General*, 198(1-2):179-196.
- De Wash, A. P. and Fromet, G. F. (1972). A two dimensional model for a fixed bed catalytic reactors. *Chem. Eng. Sci.*, 26:629 - 639.
- Deardorff, J. (1970). A numerical study of three-dimensional turbulent channel flow at large reynolds numbers. *Journal of Fluid Mechanics*, 41:453 - 480.
- Demoulin, O., Navez, M., Gracia, F., Wolf, E. E., and Ruiz, P. (2004). High throughput experimentation applied to the combustion of methane and a comparison with conventional micro-reactor measurements. *Catalysis Today*, 91-92:85-89.
- Demoulin, O., Navez, M., and Ruiz, P. (2005). Investigation of the behaviour of a Pd/ γ -Al₂O₃ catalyst during methane combustion reaction using in situ drift spectroscopy. *Applied Catalysis A: General*, 295(1):59-70.
- Deutschmann, O., Behrendt, F., and Warnatz, J. (1994). Modelling and simulation of heterogeneous oxidation of methane on a platinum foil. *Catalysis Today*, 21(2-3):461-470.
- Deutschmann, O., Behrendt, F., and Warnatz, J. (1998). Formal treatment of catalytic combustion and catalytic conversion of methane. *Catalysis Today*, 46(2-3):155-163.
- Deutschmann, O., Maier, L. I., Riedel, U., Stroemman, A. H., and Dibble, R. W. (2000). Hydrogen assisted catalytic combustion of methane on platinum. *Catalysis Today*, 59(1-2):141-150.
- Deutschmann, O., Schmidt, R., Behrent, F., and Warnatz, J. (1996). Numerical modelling of catalytic ignition. *The 26th symposium (international) on Combustion/Combustion Institute*, pages 747-1754.
- Dixon, A. G. and Creswell, D. L. (1979). Theoretical prediction of effective heat transfer parameters in packed beds. *AIChE Journal*, 25:663 - 676.

- Dlugokencky, E., Houweling, S., Bruhwiler, L., Masarie, K., Lang, P., Miller, J., and Tans, P. (2003). Atmospheric methane concentration: No longer rising. *Geophysical Research Letters*, 30(10).
- Dubien, C., Schweich, D., Mabilon, G., Martin, B., and Prigent, M. (1998). Three-way catalytic converter modelling: Fast- and slow-oxidizing hydrocarbons, inhibiting species, and steam reforming reaction. *Chemical Engineering Science*, 53:471 – 481.
- Dupont, V., Jones, J. M., Zhang, S.-H., Westwood, A., and Twigg, M. V. (2004). Kinetics of methane oxidation on Pt catalysts in the presence of H₂S and SO₂. *Chemical Engineering Science*, 59(1):17–29.
- Dupont, V., Zhang, S. H., and Williams, A. (2001). Experiments and simulations of methane oxidation on a platinum surface. *Chemical Engineering Science*, 56(8):2659–2670.
- Eftaxieas, A., Font, J., Fortuny, A., Fabregat, A., and Stuber, F. (2002). Nonlinear kinetic parameter estimation using simulated annealing. *Computers and Chemical Engineering*, 26:1725 – 1733.
- Eigenberger, G. and Nieken, U. (1988). Catalytic combustion with periodic flow reversal. *Chemical Engineering Science*, 43:2109 – 2115.
- Engel, T. and Ertl, G. (1978). A molecular beam investigation of the catalytic oxidation of CO on Pd(111). *Journal of Chemical Physics*, 69(3):1267–1281.
- Environment Canada (2007). Climate change overview. *web site*.
- EPA (1998). Inventory of U.S. Greenhouse Gas Emissions and Sinks: 1990-1995. Technical report, EPA.
- EPA (2006). Inventory of U.S. Greenhouse Gas Emissions and Sink: 1990 – 2005, epa-230-r-05-006. Technical report, U.S. Environmental Protection Agency.
- EPA (2007). Inventory of u.s. greenhouse gas emissions and sinks 1990-2005. Technical report, EPA.

- Escandon, L. S., Ordonez, S., Vega, A., and Di'ez, F. V. (2005). Oxidation of methane over palladium catalysts: Effect of the support. *Chemosphere*, 58(1):9–17.
- Esposito, W. and Floudas, C. (1998). Parameter estimation in nonlinear algebraic models via global optimization. *Computers and Chemical Engineering*, 22:S213 – S220.
- Euzen, P., Le Gal, J.-H., Rebours, B., and Martin, G. (1999). Deactivation of palladium catalyst in catalytic combustion of methane. *Catalysis Today*, 47(1-4):19–27.
- Farrauto, R., Lampert, J., Hobson, M., and Waterman, E. (1995). Thermal decomposition and reformation of PdO catalysts: Support effects. *Applied catalysis B: Environmental*, 6:263–270.
- Farrauto, R. J., Hobson, M. C., Kennelly, T., and Waterman, E. M. (1992). Catalytic chemistry of supported palladium for combustion of methane. *Applied Catalysis A: General*, 81(2):227–237.
- Fernandez, R. L., Mendis, M. S., and Schultz, H. L. (2003). Project finance opportunities for natural gas emission mitigation. *US EPA Natural Gas STAR Program*, page ng018.
- Ferreira, R. M. Q., Almeida-Costa, C. A., and Rodrigues, A. E. (1996). Effect of intraparticle convection on the transient behavior of fixed-bed reactors: Finite differences and collocation methods for solving unidimensional models. *Computers & Chemical Engineering*, 20(10):1201–1225.
- Ferreira, R. Q., Costa, C. A., and Masetti, S. (1999). Reverse-flow reactor for a selective oxidation process. *Chemical Engineering Science*, 54(20):4615–4627.
- Fluent Inc. (2002). *Airpak 2.1 User's Guide*. Fluent Inc.
- Fogler, H. S. (1992). *Elements of Chemical Reaction Engineering (2nd Edition)*. PRENTICE HALL INTERNATIONAL.

- Frank-Kamenetski, D. (1955). *Diffusion and heat exchanger in chemical kinetics*. Princeton University Press, Princeton, NJ, USA.
- Froment, G. and Bischoff, K. (1990). *Chemical reactor analysis and design (2nd ed.)*. Wiley, New York.
- Fujimoto, F., Ribiero, R., Avalos.borja, A., and Iglesia, E. (1998). Structure and reactivity of PdO_x/ZrO₂ catalysts for methane oxidation at low temperatures. *catalysis*, 179:431–442.
- Fuxman, A. (2008). *Automatic Control of CFRR*. PhD thesis, University of Alberta.
- Gan, G. (2000). Effective depth of fresh air distribution in rooms with single-sided natural ventilation. *Energy and Buildings*, 31:65 – 73.
- Garbowski, E., Feumi-Jantou, C., Mouaddib, N., and Primet, M. (1994). Catalytic combustion of methane over palladium supported on alumina catalysts: Evidence for reconstruction of particles. *Applied Catalysis A: General*, 109(2):277–292.
- Gawdzik, A. and Rakowski, L. (1988). Dynamic properties of the adiabatic tubular reactor with switch flow. *Chem. Eng. Sci.*, 43(11):3023–3030.
- Gawdzik, A. and Rakowski, L. (1989). Methods of analysis of the dynamic properties of the adiabatic tubular reactor with switch flow. *Computers and Chemical Engineering*, 13(10):1165–1173.
- Gelin, P. and Primet, M. (1999). Modeling heterogeneous and homogeneous reactions in the high-temperature catalytic combustion of methane. *Chemical engineering Science*, 54:5791–5807.
- Gelin, P. and Primet, M. (2002). Complete oxidation of methane at low temperature over noble metal based catalysts: A review. *Applied Catalysis B: Environmental*, 39(1):1–37.
- Gelin, P., Urfels, L., Primet, M., and Tena, E. (2003). Complete oxidation of methane at low temperature over Pt and Pd catalysts for the abatement of lean-

- burn natural gas fuelled vehicles emissions: Influence of water and sulphur containing compounds. *Catalysis Today*, 83(1-4):45–57.
- Golodets, G. I. (1983). Heterogeneous catalytic reactions involving molecular oxygen. *Studies in Surface Science and Catalysis*, 15:437 – 452.
- Gosiewski, K. and Warmuzinski, K. (2007). Effect of the mode of heat withdrawal on the asymmetry of temperature profiles in reverse-flow reactors. catalytic combustion of methane as a test case. *Chemical Engineering Science*, 62(10):2679–2689.
- Griffin, T. A., Calabrese, M., Pfefferle, L. D., Sappey, A., Copeland, R., and Crosley, D. R. (1992). The influence of catalytic activity on the ignition of boundary layer flows. Part III: hydroxyl radical measurements in low-pressure boundary layer flows. *Combustion and Flame*, 90(1):11–33.
- Groote, A. D., Froment, G., and Kobylinski, T. (1996). Synthesis gas production from natural gas in a fixed bed reactor with reversed flow. *Canadian Journal of Chemical Engineering*, 74:735 – 742.
- Groppi, G. (2003). Combustion of CH₄ over a PdO/ZrO₂ catalyst: an example of kinetic study under severe conditions. *Catalysis Today*, 77(4):335–346.
- Groppi, G., Cristiani, C., Lietti, L., Ramella, C., Valentini, M., and Forzatti, P. (1999). Effect of ceria on palladium supported catalysts for high temperature combustion of CH₄ under lean conditions. *Catalysis Today*, 50(2):399–412.
- Grozev, G. and Sapundzhiev, C. (1997). Modelling of the reversal flow fixed bed reactor for catalytic decontamination of waste gases. *Chemical Engineering and Technology*, 20:378 – 383.
- Guit, I. R. P. M. (1993). The selective catalytic reduction of NO in a reverse flow reactor: A quick design procedure. *Precision Process Technology*, pages 453–461.

- Gupta, V. and Bhatia, S. (1991). Solution of cyclic profiles in catalytic reactor operation with periodic flow reversal. *Computers and Chemical Engineering*, 15(4):229–237.
- Han, J., Zemlyanov, D. Y., and Ribeiro, F. H. (2006). Catalytic combustion of methane on palladium single crystals. *Catalysis Today*, 117(4):506–513.
- Hanamura, K., Echigo, R., and Zhdanok, S. (1993). Superadiabatic combustion in a porous medium. *International Journal of Heat Mass Transfer*, 36:3201 – 3209.
- Hayes, R. (2004). Catalytic solutions for fugitive methane emissions in the oil and gas sector. *Chemical Engineering Science*, 59(19):4073–4080.
- Hayes, R. and Checkel, M. (2001). Reversing flow catalytic converter for a natural gas/diesel dual fuel engine. *Chemical Engineering Science*, 56(8):2641–2658.
- Hayes, R. and Kolaczkowski, S. (1997). *Introduction to catalytic combustion*. Gordon and Breach Science Publishers.
- Hayes, R., Liu, B., and Votsmeier, M. (2005). Calculating effectiveness factors in non-uniform washcoat shapes. *Chemical Engineering Science*, 60(7):2037–2050.
- Hayes, R. E. (2002). Effective radial conductivity on monolith structure. Internal report.
- Hayes, R. E., Afcan, A., Boulanger, B., and Shenoy, A. V. (1996). Modelling the flow of power law fluids in a packed bed using a volume - averaged equation of motion. *Transport in Porous Media*, 23:175 – 196.
- Hayes, R. E., Bertrand, F. H., and Kolaczkowski, S. T. (2003). Catalytic combustion kinetics: Using a direct search algorithm to evaluate kinetic parameters from light - off curves. *Canadian Journal of Chemical Engineering*, 81:1192 – 1199.
- Hayes, R. E., Kolaczkowski, S. T., and Thomas, W. (1992). A finite element model for a catalytic monolith reactor. *Computer and Chemical Engineering*, 16(7):645 – 657.

- Hayes, R. E., Liu, B., Moxom, R., and Votsmeier, M. (2004). The effect of washcoat geometry on mass transfer in monolith reactors. *Chemical Engineering Science*, 59(15):3169–3181.
- Haynes, T., Georgakis, C., and Caram, H. (1992). Application of reverse flow reactors to endothermic reactions. *Chemical Engineering Science*, 47(9-11):2927–2932.
- Heck, R., Kelbert, G., Schmidt, K., and Zimmer, H. (1995). Hydrogen reduction following severe accidents using the dual recombiner-igniter concept. *Nuclear Engineering and Design*, 157:311–319.
- Henton, D. (2007). Let's make a carbon deal. Edmonton journal newspaper.
- Hevia, M. A., Ordonez, S., and Diez, F. V. (2007). Effect of the catalyst properties on the performance of a reverse flow reactor for methane combustion in lean mixtures. *Chemical Engineering Journal*, 129(1-3):1–10.
- Hevia, M. A. G., Ordonez, S., and Diez, F. V. (2006). Effect of wall properties on the behaviour of bench- scale reverse flow reactors. *Reactors, Kinetics and Catalysis*, 52(9):3203 – 3209.
- Hickman, D. A. and Schmidt, L. D. (1992). Synthesis gas formation by direct oxidation of methane over pt monoliths. *Journal of Catalysis*, 138(1):267–282.
- Hicks, R. F., Qi, H., Young, M. L., and Lee, R. G. (1990). Structure sensitivity of methane oxidation over platinum and palladium. *Journal of Catalysis*, 122(2):280–294.
- Houghton, J., Jenkins, G., and Ephraums, J. E. (1992). Climate change 1992: The supplement report to the ipcc scientific assessment. Technical Report 6, IPCC.
- Houghton, J., Y. Ding, D. J. G., Noguera, M., van der Linden, P., Dai, X., Maskell, K., and (Eds.), C. J. (2001). Contribution of working group I to the third assessment report of the intergovernmental panel on climate change. Technical report, IPCC.

- Ibashi, W., Groppi, G., and Forzatti, P. (2003). Kinetic measurement of CH₄ combustion over a 10% PdO/ZrO₂ catalyst using an annular flow microreactor. *Catalysis Today*, 83:115–129.
- Incropera, F. P. and Dewwit, D. P. (1996). *Introduction to heat transfer*. John Wiley & Sons, Toronto, 3rd edition.
- IPCC (2007). Climate change 2007: The physical science basis, summary for policy makers, contribution of working group I to the fourth assessment report of the IPCC. Technical Report 6, IPCC.
- Kenevey, K., Valdivieso, F., Soustelle, M., and Pijolat, M. (2001). Thermal stability of Pd or Pt loaded Ce_{0.68}Zr_{0.32}O₂ and Ce_{0.50}Zr_{0.50}O₂ catalyst materials under oxidising conditions. *Applied Catalysis B: Environmental*, 29(2):93–101.
- Kikuchi, E. and Matsuda, T. and Takahashi, N. (1997). Catalytic properties of Pd/Al₂O₃ calcined at high temperatures for methane combustion. *ACS Division of Petroleum Chemistry, Inc. Preprints*, 42(1):183–186.
- Kokkolaras, M., Audet, C., and Dennis, J. E. (2001). Mixed variable optimization of the number and composition of heat intercepts in a thermal insulation system. *Optimization and Engineering*, 2:5 – 29.
- Kolios, G. and Eigenberger, G. (1999). Styrene synthesis in a reverse-flow reactor. *Chemical Engineering Science*, 54(13-14):2637–2646.
- Kraikul, N., Jitkarnka, S., and Luengnaruemitchai, A. (2005). Catalytic methane combustion on Pd-Pt-La catalysts and their surface models. *Applied Catalysis B: Environmental*, 58(1-2):143–152.
- Kushwaha, A. (2003). Parametric studies of catalytic reverse flow reactor. Master's thesis, University of Alberta.
- Kushwaha, A., Poirier, M., Hayes, R., and Sapoundjiev, H. (2005). Heat extraction from a flow reversal reactor in lean methane combustion. *Chemical Engineering Research and Design*, 83(2 A):205–213.

- Kushwaha, A., Poirier, M., Sapoundjiev, H., and Hayes, R. (2004). Effect of reactor internal properties on the performance of a flow reversal catalytic reactor for methane combustion. *Chemical Engineering Science*, 59(19):4081–4093.
- Labalme, V., Bguin, B., Gaillard, F., and Primet, M. (2000). Characterisation and acid properties of some modified combustion catalysts: Pt/alumina with barium and Pt/zirconia with yttrium. *Applied Catalysis A: General*, 192(2):307–316.
- Lampert, J. K., Kazia, M. S., and Farrauto, R. J. (1997). Palladium catalyst performance for methane emissions abatement from lean burn natural gas vehicles . *Applied catalysis B: Environmental*, 14(3–4):211 – 223.
- Leclerc, J. and Schweich, D. (1993). Modeling catalytic monoliths for automobile emission control. In Lasa, H., editor, *Chemical Reactor Technology for Environmentally Safe Reactors and Products*, page 547576. Kluwer Academic Press, Dordrecht,.
- Lee, J. and Brodkey, R. S. (1964). Turbulent motion and mixing in a pipe. *AIChE Journal*, 10:187 – 193.
- Lee, J. H. and Trimm, D. L. (1995). Catalytic combustion of methane. *Fuel Processing Technology*, 42(2-3):339–359.
- Lee, S. and Aris, R. (1977). On the effects of radiative heat transfer in monoliths. *Chemical Engineering Science*, 32(8):827–837.
- Li, Z. and Flytzani-Stephanopoulos, M. (1999). On the promotion of AgZSM-5 by Cerium for the SCR of NO by Methane. *Catalysis*, 182(2):313–327.
- Li, Z., Xu, G., and Hoflund, G. B. (2003). In situ IR studies on the mechanism of methane oxidation over Pd/Al₂O₃ and Pd/Co₃O₄ catalysts. *Fuel Processing Technology*, 84(1-3):1–11.
- Libby, P. A. (1996). *Introduction to turbulence*. Taylor and Francis, Bristol PA.
- Litto, R., Hayes, R., and Liu, B. (2007). Capturing fugitive methane emissions from natural gas compressor buildings. *Journal of Environmental Management*, 84(3):347–361.

- Litto, R., Hayes, R., Sapoundjiev, H., Fuxman, A., Forbes, F., Liu, B., and Bertrand, F. (2006). Optimization of a flow reversal reactor for the catalytic combustion of lean methane mixtures. *Catalysis Today*, 117(4):536–542.
- Liu, B. (2000). *Experimental and modelling study of reverse flow catalytic converter for natural gas diesel dual engine pollution control*. PhD thesis, University of Alberta.
- Liu, B., Checkel, M., and Hayes, R. (2001a). Experimental study of a reverse flow catalytic converter for a dual fuel engine. *Canadian Journal of Chemical Engineering*, 79(4):491–506.
- Liu, B., Checkel, M., Hayes, R., Zheng, M., and Mirosh, E. (2000). Transient simulation of a catalytic converter for a dual fuel engine. *Canadian Journal of Chemical Engineering*, 78(3):557–568.
- Liu, B., Checkel, M. D., Hayes, R. E., Zheng, M., and Mirosh, E. A. (2001b). Experimental and modelling study of variable cycle time of a reverse flow catalytic converter for natural gas/diesel dual fuel engines. *SAE Trans, Journal of Fuels and Lubricants*, 109(4):15.
- Liu, B., Hayes, R., Yi, Y., Mmbaga, J., Checkel, M., and Zheng, M. (2007). Three dimensional modelling of methane ignition in a reverse flow catalytic converter. *Computers and Chemical Engineering*, 31(4):292–306.
- Liu, B., Hayes, R. E., Checkel, M. D., Zheng, M., and Mirosh, E. (2001c). Reversing flow catalytic converter for a natural gas/diesel dual fuel engine. *Chemical Engineering Science*, 56(8):2641–2658.
- Loong, C. K., Thiyagarajan, P., Richardson, J. W., Ozawa, M., and Suzuki, S. (1997). Microstructural evolution of zirconia nanoparticles caused by rare earth modification and heat treatment. *Journal of Catalysis*, 171(2):498–505.
- Luoma, M. and Smith, A. (1996). The use of PHOENICS in the design of catalytic converters. *PHOENICS Journal of CFD and its Applications*, 9:76 – 100.

- Lyubovsky, M., Karim, H., Menacherry, P., Boorse, S., LaPierre, R., Pfefferle, W. C., and Roychoudhury, S. (2003). Complete and partial catalytic oxidation of methane over substrates with enhanced transport properties. *Catalysis Today*, 83(1-4):183–197.
- Lyubovsky, M. and Pfefferle, L. (1998). Methane combustion over the [alpha]-alumina supported pd catalyst: Activity of the mixed pd/pdo state. *Applied Catalysis A: General*, 173(1):107–119.
- Lyubovsky, M. and Pfefferle, L. (1999). Complete methane oxidation over Pd catalyst supported on α -alumina. influence of temperature and oxygen pressure on the catalyst activity. *Catalysis Today*, 47(1-4):29–44.
- Marin, P., Hevia, M., Ordonez, S., and Diez, F. (2005). Combustion of methane lean mixtures in reverse flow reactors: Comparison between packed and structured catalyst beds. *Catalysis Today*, 105(3-4):701–708.
- Markatou, P., Pfefferle, L. D., and Smooke, M. D. (1993). A computational study of methane-air combustion over heated catalytic and non-catalytic surfaces. *Combustion and Flame*, 93(1-2):185–201.
- Matros, Y. (1989). *Catalytic Processes Under Unsteady-State Conditions*. Amsterdam, Elsevier.
- Matros, Y. and Bunimovich, G. (1996). Reverse flow operation in fixed bed catalytic reactors. *Catalytic Reviews: Science and Engineering*, 38:1 – 68.
- Matros, Y., Bunimovich, G., Strots, V., and Mirosh, E. (1999). Reversed flow converter for emission control after automotive engines. *Chemical Engineering Science*, 54(13-14):2889–2898.
- Matros, Y., Noskov, A., and Chumachenko, V. (1993). Progress in reverse process application to catalytic incineration problems. *Chemical Engineering and Processing*, 32(2):89–98.

- McCarty, J. G. (1995). Kinetics of PdO combustion catalysis. *Catalysis Today*, 26(3-4):283–293.
- McPhaden, M. (1999). Genesis and evolution of the 1997-98 el-nino. *Science*, 283.
- Methane to Market (2005). Oil and natural gas system methane recovery and use opportunities. <http://www.methanetomarkets.org/resources/oil-gas/docs/oil-gas.pdf>
Last viewed 2006.10.09.
- Mhadeshwar, M., Aghalayam, A., Papavassiliou, P., and Vlachos, V. (2002). Surface reaction mechanism development for platinum catalyzed oxidation of methane. *Proceedings of the combustion Institute*, 29:997–1004.
- Moallemi, M., Batley, B., Dupont, V., Foster, F., Pourkashanian, P., and Williams, W. (1999). Chemical modeling and measurements of the catalytic combustion of CH₄/air mixtures on platinum and palladium catalysts. *Catalysis Today*, 47:235–244.
- Monteiro, R. S., Zemlyanov, D., Storey, J. M., and Ribeiro, F. H. (2001). Turnover rate and reaction orders for the complete oxidation of methane on a palladium foil in excess dioxygen. *Journal of Catalysis*, 199(2):291–301.
- Montreuil, C. N., Williams, S. C., and Adamczyk, A. A. (1992). Modelling current generation catalytic converters: Laboratory experiments and kinetic parameter optimization – steady state kinetics. Technical report, SAE Paper 920096.
- Moore, S., Freund, P., Riemer, P., , and Smith, A., editors (1998). *Abatement of methane emissions, IEQ Greenhouse Gas R&D Programme Climate Change 1992: The Supplementary Report to the IPCC Scientific Assessment*. Cheltenham.
- More, H. (2007). Washcoat mass and heat transfer. Master's thesis, University of Alberta.

- Moros, R., Kalies, H., G., R. H., and Scaffarczyk, S. (1996). A genetic algorithm for generating initial parameter estimates for kinetic models of catalytic processes. *Computer and Chemical Engineering*, 20:1257 – 1270.
- Mukadi, L. S. and Hayes, R. (2002). Modelling the three-way catalytic converter with mechanistic kinetics using the Newton- Krylov method on parallel computer. *Computers and Chemicak Engineering*, 26:439 – 455.
- Mukadi, S. (2003). Summary of elementary mechanism. *Unpublished Document*.
- Müller, C. A., Koeppl, R. A., Maciejewski, M., Heveling, J., and Baiker, A. (1996). Methane combustion over catalysts prepared by oxidation of ternary Pd₁X₁₀Zr₇₅ (X = Co, Cr, Cu, Mn and Ni) amorphous alloys. *Applied Catalysis A: General*, 145(1-2):335–349.
- Müller, C. A., Maciejewski, M., Koeppl, R. A., and Baiker, A. (1997). Combustion of methane over Palladium/Zirconia derived from a glassy Pd-Zr alloy: Effect of Pd particle size on catalytic behavior. *Journal of Catalysis*, 166(1):36–43.
- Müller, C. A., Maciejewski, M., Koeppl, R. A., and Baiker, A. (1999). Combustion of methane over Palladium/Zirconia: effect of Pd-particle size and role of lattice oxygen. *Catalysis Today*, 47(1-4):245–252.
- Muto, K. I., Katada, N., and Niwa, M. (1996). Ccomplete oxidation of methane on supported palladium catalyst : Support effect. *Applied Catalysis A: General*, 134(2):203–215.
- Narui, K., Furuta, K., Yata, H., Nishida, A., Kohtoku, Y., and Matsuzaki, T. (1998). Catalytic activity of PdO/ZrO₂ catalyst for methane combustion. *Catalysis Today*, 45(1-4):173–178.
- Narui, K., Yata, H., Furuta, K., Nishida, A., Kohtoku, Y., and Matsuzaki, T. (1999). Effects of addition of Pt to PdO/Al₂O₃ catalyst on catalytic activity for methane combustion and TEM observation of supported poarticles. *Applied Catalysis A: General*, 179:165 – 173.

- NASA (2007). GISS surface temperature analysis. <http://data.giss.nasa.gov/gistemp/2007/> Last viewed 2008.01.15.
- Neophytides, S. and Froment, G. (1992). A bench scale study of reversed flow methanol synthesis. *Industrial & Engineering Chemistry Research*, 31(7):1583–1589.
- Nieken, U., Kolios, G., and Eigenberger, G. (1994). Control of the ignited steady state in autothermal fixed-bed reactors for catalytic combustion. *Chemical Engineering Science*, 49(24(2)):5507–5518.
- Noskov, A., Bobrova, L., and Matros, Y. (1993). Reverse-process for NO_x - off gases decontamination. *Catalysis Today*, 17(1-2):293–300.
- Oh, S. H., Mitchell, P. J., and Siewert, R. M. (1991). Methane oxidation over alumina-supported noble metal catalysts with and without cerium additives. *Journal of Catalysis*, 132(2):287–301.
- Okumura, K., Shinohara, E., and Niwa, M. (2006). Pd loaded on high silica beta support active for the total oxidation of diluted methane in the presence of water vapor. *Catalysis Today*, 117(4):577–583.
- Otto, K. (1989). Methane oxidation over Pt on α -alumina: Kinetics and structure sensitivity. *Langmuir*, 5:1364 – 1369.
- Pandya, A. (2006). Catalytic nox reduction from lean burn engine exhaust. Master's thesis, University of Alberta.
- Pecchi, G., Reyes, P., Concha, I., and Fierro, J. L. G. (1998). Methane Combustion on Pd/SiO₂ Sol Gel Catalysts. *Journal of Catalysis*, 179(1):309–314.
- Pfefferle, L. D., Griffin, T. A., Dyer, M. J., and Crosley, D. R. (1989). The influence of catalytic activity on the gas phase ignition of boundary layer flows Part II: Oxygen atom measurements. *Combustion and Flame*, 76(3-4):339–349.
- Prasad, R., Kennedy, L. A., and Ruckenstein, E. (1984). Catalytic combustion. *Catalysis Review: Science and Engineering*, 26(1):1–58.

- Purwono, S., Budman, H., Hudgins, R. R., Silveston, P. L., and Matros, Y. S. (1994). Runaway in packed bed reactors operating with periodic flow reversal. *Chemical Engineering Science*, 49:5473–5487.
- Reinke, M., Mantzaras, J., Bombach, R., Schenker, S., and Inauen, A. (2005). Gas phase chemistry in catalytic combustion of methane/air mixtures over platinum at pressures of 1 to 16 bar. *Combustion and Flame*, 141(4):448–468.
- Reinke, M., Mantzaras, J., Schaeren, R., Bombach, R., Inauen, A., and Schenker, S. (2004). High-pressure catalytic combustion of methane over platinum: In situ experiments and detailed numerical predictions. *Combustion and Flame*, 136(1-2):217–240.
- Revkin, A. C. (2004). Climate debate gets its icon: Mt. kilimanjaro. *The New York Times*.
- Ribeiro, F. H., Chow, M., and Dallabetta, R. A. (1994a). Kinetics of the complete oxidation of methane over supported palladium catalysts. *Journal of Catalysis*, 146(2):537–544.
- Ribeiro, F. H., Chow, M., and Dallabetta, R. A. (1994b). Kinetics of the complete oxidation of methane over supported palladium catalysts. *Journal of Catalysis*, 146(2):537–544.
- Rodi, W. and Fueyo, N., editors (1993). *Engineering Turbulence Modelling and Experiments 5*, volume 5. International symposium on Engineering Turbulence Modelling and Measurement.
- Roth, D., Gelin, P., Primet, M., and Tena, E. (2000). Catalytic behaviour of Cl-free and Cl-containing Pd/Al₂O₃ catalysts in the total oxidation of methane at low temperature. *Applied Catalysis A: General*, 203(1):37–45.
- Salomons, S. (2003). Modelling the behaviour of a reverse flow reactor for the combustion of lean methane. Master's thesis, University of Alberta.

- Salomons, S. (2008). *Kinetic Models for a diesel oxidation catalyst*. PhD thesis, University of Alberta.
- Salomons, S., Hayes, R. E., Poirier, M., and Sapoundjiev, H. (2003). Flow reversal reactor for the catalytic combustion of lean methane mixtures. *Catalysis Today*, 83(1-4):59–69.
- Salomons, S., Hayes, R. E., Poirier, M., and Sapoundjiev, H. (2004). Modelling a reverse flow reactor for the catalytic combustion of fugitive methane emissions. *Computers & Chemical Engineering*, 28(9):1599–1610.
- Sapundzhiev, C., Chaouki, J., Guy, C., and Klvana, D. (1993). Catalytic combustion of natural gas in a fixed bed reactor with flow reversal. *Chemical Engineering Communications*, 125:171–186.
- Satterfield, C. (1970). *Mass Transfer in Heterogeneous Catalysis*. Cambridge, MA: MIT Press.
- Schnepper, C. A. and Stadtherr, M. A. (1996). Robust process simulation using interval methods. *Computer and Chemical Engineering*, 20:187 – 199.
- Seimanides, S. and Stoukides, M. (1986). Catalytic oxidation of methane on polycrystalline palladium supported on stabilized zirconia. *Journal of Catalysis*, 98(2):540–549.
- Seinfeld, J. H. and Pandis, S. N. (2006). *Atmospheric chemistry and physics: From Air pollution to climate change*. John Wiley & Sons, Inc., Hoboken, New Jersey, second edition.
- Sheintuh, M. (2005). Analysis of design sensitivity of flow reversal reactor: Simulation, approximation and oxidation experiments. *Chemical Engineering Science*, 60(11):2991 – 2998.
- Sidwell, R. W., Zhu, H., Kee, D. T., Wickham, C. S., and Jackson, G. S. (2002). Catalytic combustion of premixed methane/air on palladium-substituted hexaluminate stagnation syrface. *Proceedings of the Combustion Institute*, 29:1013–1020.

- Simone, O. D., Kennelly, T., L. Brungard, N., and J. Farrauto, R. (1991). Reversible poisoning of palladium catalysts for methane oxidation. *Applied Catalysis*, 70(1):87–100.
- Snyder, J. D. and Subramaniam, B. (1998). Numerical simulation of a reverse-flow NO_x - SCR reactor with side-stream ammonia addition. *Chemical Engineering Science*, 53(4):727–734.
- Song, X., William, W., Schmidt, L., and Aris, R. (1991). Bifurcation behavior in homogeneous-heterogeneous combustion: II. computations for stagnation-point flow. *Combustion and Flame*, 84:292–311.
- Srebric, J., Chen, Q., , and Glicksman, L. (1999). Validation of a zero-equation turbulence model for complex indoor airflows. *ASHRAE Transactions*, 105 (2):414 – 427.
- Stathopoulos, T. and Zhou, Y. (1995). Numerical evaluation of wind pressures on flat roofs with the $k - \epsilon$ model. *Building and Environment*, 30:267 – 276.
- Steele, L., Dlugokencky, E., Lang, P., Tans, P., Martin, R., and Masarie, K. (1992). Slowing down of the global accumulation of atmospheric methane during the 1980s. *Nature*, 358(6384):313–316.
- Steele, L., Fraser, P., Rasmussen, R. A., Khalil, M. A. K., Conway, T., Crawford, A., Gammon, R., Masarie, K., and Thoning, K. W. (1987). The global distribution of methane in the troposphere. *Atmos. Chem.*, 5:125 – 171.
- Strots, V., Bunimovich, G., Matros, Y., Zheng, M., and Mirosh, E. (1998). Advanced catalytic converter system for natural gas powered diesel engines. *Studies in Surface Science and Catalysis*, 119:907–912.
- Taylor, G. I., editor (1953). *Dispersion of soluble matter in solvent flowing slowly through a tube*, volume A219, 186 – 203. Royal Society.
- Thomas, J. M. and Thomas, W. J. (1967). *Principles and practice of heterogeneous catalysis*. Academic Press, Inc., Ltd, London.

- Tronconi, E. and Forzatti, P. (1992). Adequacy of lumped parameter models for scr reactors with monolith structure. *AIChE Journal*, 38:201 – 210.
- Uchida, H., Takashima, F., and Imaseki, Y. (1994). *Science Technology in Catalysis*, pages 383 – 386.
- Van De Beld, B., Borman, R., Derkx, O., Van Woezik, B., and Westerterp, K. (1994). Removal of volatile organic compounds from polluted air in a reverse flow reactor: An experimental study. *Industrial and Engineering Chemistry Research*, 33(12):2946–2956.
- Van de Beld, L. (1996). A kinetic study of the complete oxidation of ethene, propane and their mixtures on a Pd/Al₂O₃ catalyst. *Fuel and Energy Abstracts*, 37(3):176–292.
- Van Giezen, J., van den Berg, F., Kleinen, J., van Dillen, A., and Geus, J. (1999). The effect of water on the activity of supported palladium catalysts in the catalytic combustion of methane. *catalysis today*, 47:287–293.
- Vanden Bussche, K. M., Neophytides, S. N., Zolotarskii, I., and Froment, G. (1993). Modelling and simulation of a reversed flow operation of a fixed-bed reactor for methanol synthesis. *Chemical Engineering Science*, 48(19):3335 – 3345.
- Versteeg, H., , and Malalasekera, W. (1995). *An introduction to computational fluid dynamics- The finite volume method*. Pearson Education Limited.
- Veser, G. and Frauhammer, J. (2000). Modelling steady state and ignition during catalytic methane oxidation in a monolith reactor. *Chemical Engineering Science*, 55(12):2271–2286.
- Wakao, N. and Kaguei, S. (1982). *Heat and mass transfer in packed beds*. Gordon and Breach, London.
- Wang, L., Xu, Y., Wong, S.-T., Cui, W., and Guo, X. (1997). Activity and stability enhancement of Mo/HZSM-5-based catalysts for methane non-oxidative

- transformation to aromatics and C₂ hydrocarbons: Effect of additives and pre-treatment conditions. *Applied Catalysis A: General*, 152(2):173–182.
- Wang, X. and Chang Xie, Y. (2001). Low-temperature CH₄ total oxidation on catalysts based on high surface area SnO₂. *Reaction Kinetics and Catalysis Letters*, 72(1):115–123.
- Watson, R., Zinyowera, M., Moss, R., and Dokken, D. E. (1995). Climate change 1995: Scientific technical analysis, contribution of working Group II to the second assessment report of the IPCC. *IPCC Publications*, 41(6):362–5967.
- Watson, R., Zinyowera, M., Moss, R., and Dokken, D. E. (1996). Climate change 1995: Scientific technical analysis, contribution of working Group II to the second assessment report of the IPCC. *IPCC Publications*, pages 362–5967.
- Williams, W. R., Stenzel, M. T., Song, X., and Schmidt, L. D. (1991). Bifurcation behavior in homogeneous-heterogeneous combustion: I. experimental results over platinum. *Combustion and Flame*, 84(3-4):277–291.
- Wolf, D. and Moros, R. (1997). Estimating rate constants of heterogeneous catalytic reactions without supposition of rate determining step - an application of a genetic algorithm. *Chemical Engineering Science*, 52:1189 – 1199.
- Zhang, H., Gromek, J., Fernando, G., and Marcus, H. L. (2004). Novel nanostructured Pd-Zr oxides. *Materials Science and Engineering A*, 366(2):248–253.
- Zheng, G. and Altman, E. (2000). The oxidation of Pd(111). *Surface Science*, 1 - 3:151 – 168.
- Zhu, H. (2001). *Numerical modeling of methane combustion on palladium catalyst for gas turbine applications*. PhD thesis, University of Maryland.
- Zwinkels, M., Jaras, S., Menon, P., and Griffin, T. (1993). Catalytic materials for high-temperature combustion. *Catalysis Review-Science and Engineering*, 35(3):319–358.

Zygourakis, K. (1989). Transient operation of monolith catalytic converter: A two-dimensional reactor model and the effect of radially non-uniform flow distribution. *Chemical Engineering Science*, 44:2075–2086.

Single channel model derivation

This appendix shows the derivation of a one dimensional single channel model for a monolith reactor. The single monolith channel is represented as a right circular cylinder with a uniform washcoat and substrate thickness. Consider a short section of monolith channel, as shown in Figure A.1

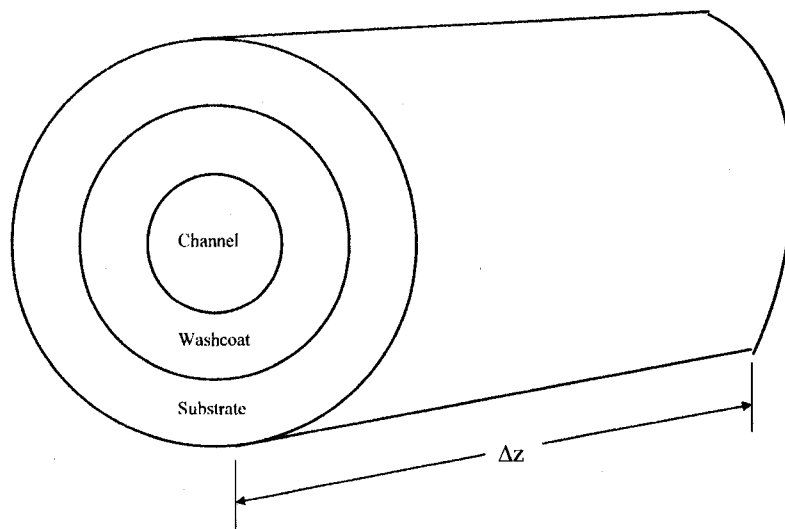


Figure A.1: Section of monolith channel

Let

- D_H = inside diameter of channel
- D_{WC} = diameter to outside surface of washcoat
(Washcoat/substrate interface)
- D_S = diameter to outside of substrate

The cross sectional area of channel, washcoat and substrate are set equal to those of the real channel. Consider a small length of channel, Δz . The reaction occurs in the washcoat volume. The changes in temperature and concentration are considered in the axial direction only. Perform a steady state shell balance for specie A over the increment ΔZ :

$$\left(-D_l A_c C_f \frac{\delta Y_{Af}}{\delta z}\right)_z - \left(-D_l A_c C_f \frac{\delta Y_{Af}}{\delta z}\right)_{z+\Delta z} + (A_c U_m C_f Y_{Af})_z \dots - (A_c U_m C_f Y_{Af})_{z+\Delta z} - k_m a_m C_f (Y_{Af} - Y_{As}) = 0 \quad (A.1)$$

The symbols represent:

- D_l = the dispersion coefficient, which includes the molecular diffusion and the effect of laminar flow.
- A_c = cross sectional are of the channel
- C_f = total molar density of the fluid
- U_m = mean velocity of the fluid
- k_m = mass transfer coefficient
- a_m = area for mass transfer
- Y_{Af} = mole fraction of A in the fluid, which is the mixing cup value
- Y_{As} = mole fraction of A at the surface

Take the limit as $\Delta z \rightarrow dz$ and substitute for the two areas:

$$\frac{\delta}{\delta z} \left(-D_l C_f \frac{\delta Y_{Af}}{\delta z}\right) - U_m C_f \frac{\delta Y_{Af}}{\delta z} - \frac{4}{D_H} k_m C_f (Y_{Af} - Y_{As}) = 0 \quad (A.2)$$

The above Equation represent the fluid phase mole balance for species A. The equation can be written for each species in the mixture.

The reaction rate for the washcoat is sometimes written in terms of the washcoat/channel interface area, with units of mol/(m²s). With this convention the solid phase mole balance for species A is:

$$k_m a_m C_f (Y_{Af} - Y_{As}) = \eta (-R_A)_s \quad (\text{A.3})$$

The factor η is the effectiveness factor that accounts for diffusion resistance in the washcoat.

In this thesis, the reaction rate is written in terms of the washcoat volume. the rate of mass transfer balances the rate of reaction, or:

$$k_m a_m C_f (Y_{Af} - Y_{As}) = \eta (-R_A)_v \Delta V_w \quad (\text{A.4})$$

Here ΔV_w represents the washcoat volume contained in length increment Δz , which is the volume of the annular washcoat segment

$$\Delta V_w = \frac{\pi}{4} (D_{wc}^2 - D_H^2) \Delta z \quad (\text{A.5})$$

Recall that

$$a_m = \pi D_H \Delta z \quad (\text{A.6})$$

The solid phase mole balance is therefore:

$$\eta (-R_A)_v = \frac{4D_H}{(D_{wc}^2 - D_H^2)} k_m C_f (Y_{Af} - Y_{As}) \quad (\text{A.7})$$

The volumetric reaction rate is evaluated at the surface concentration, Y_{As} .

The steady state fluid phase energy balance can also be written as a shell balance:

$$\begin{aligned} \left(-k_l A_c \frac{\delta T_f}{\delta z} \right)_z - \left(-k_l A_c \frac{\delta T_f}{\delta z} \right)_{z+\Delta z} + \left[(\rho C_p)_f U_m T_f \right]_z A_c \dots \\ - \left[(\rho C_p)_f U_m T_f \right]_{z+\Delta z} A_c - h a_m (T_f - T_s) = 0 \end{aligned} \quad (\text{A.8})$$

Substitute for a_m and take the limit:

$$\frac{\delta}{\delta z} \left(k_l \frac{\delta T_f}{\delta z} \right) - (\rho C p)_f U_m \frac{\delta T_f}{\delta z} - \frac{4h}{D_H} (T_f - T_s) = 0 \quad (\text{A.9})$$

Note that k_l is an effective thermal conductivity that incorporates the fluid conductivity.

The solid phase energy balance equation retains the transient term, because the solid temperature changes slowly with respect to the gas temperature. The shell balance for single reaction is :

$$\begin{aligned} \left(-k_s A_{cs} \frac{\delta T_s}{\delta z} \right)_z - \left(-k_s A_{cs} \frac{\delta T_s}{\delta z} \right)_{z+\Delta z} - h a_m (T_s - T_f) \dots \\ + \Delta V_w \eta (-R_A)_v \Delta H_R = A_{cs} \Delta z (\rho C p)_s \frac{\delta T_s}{\delta t} \end{aligned} \quad (\text{A.10})$$

The symbols are:

- k_s = thermal conductivity of the solid, which is a combination of washcoat and substrate.
- A_{cs} = cross sectional area of the solid, both catalyst and washcoat
- ΔV_w = Volume of washcoat, as before

Note that the solid cross sectional area is given as:

$$A_{cs} = (D_s^2 - D_H^2) \frac{\pi}{4} \quad (\text{A.11})$$

Take the limit, perform substitution and simplifications:

$$\frac{\delta}{\delta z} \left(k_s \frac{\delta T_s}{\delta z} \right) - \frac{4D_H h}{(D_s^2 - D_H^2)} (T_s - T_f) + \left(\frac{D_{WC}^2 - D_H^2}{D_s^2 - D_H^2} \right) \eta (-R_A)_v \Delta H_R = (\rho C p)_s \frac{\delta T_s}{\delta t} \quad (\text{A.12})$$